CHARACTERISATION OF A CONTINUOUS OSCILLATORY BAFFLED TUBULAR REACTOR

NITIN EMELYAN PEREIRA

Thesis submitted for the degree of
Doctor of Philosophy
to Heriot-Watt University, Edinburgh,U.K.
on completion of research in the
Centre for Oscillatory Baffled Reactor Application (COBRA)
Department of Mechanical and Chemical Engineering

March 2002

DECLARATION

This is to declare that the thesis is an account of the author's work carried out at Heriot-Watt University, Edinburgh, except where acknowledgement is made, and has not been submitted for any other degrees.

NITIN EMELYAN PEREIRA (Candidate)

PROF. XIONGWEI NI (Supervisor)

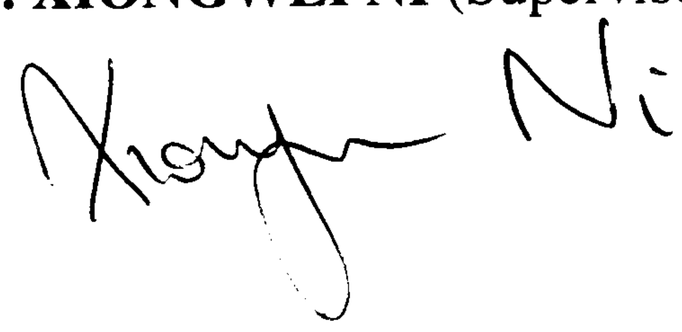

To my parents, Ruby and Emelyan for all their love, warmth, support and understanding

ABSTRACT

The oscillatory baffled tubular reactor (OBTR) is a relatively recent development in mixing and reactor technology and has shown a number of advantageous properties in uniform mixing, plug flow, particle suspension and reaction both at laboratory and pilot scales. Recent studies have shown that the OBTR can successfully be employed to control drop/particle size distribution. The objective of the present study is to characterise a continuous OBTR for a pioneering application in continuous suspension polymerisation of methyl methacrylate.

The characterisation was performed by studying both single and two phase flow behaviours over a range of oscillation amplitudes, frequencies and net flow rates. The single phase flow study was carried out in terms of axial dispersion by examining residence time distribution characteristics. The plug flow with axial dispersion model was employed to evaluate the axial dispersion coefficient. Over the operating conditions investigated, very close to plug flow behaviour was observed in the OBTR. The two phase flow behaviours were studied in terms of droplet size distribution (DSD) and mean drop size. A silicone oil (Dow corning 200) of a similar density and viscosity to the monomer used in the suspension polymerisation was utilised as the dispersed phase and water as the continuous phase. Samples containing droplets were measured by direct photography and DSD and the Sauter mean drop size were obtained. The DSD and the mean drop size were strongly influenced by the oscillation amplitude or frequency but were found to be not sensitive to the changes in the net flow rates over the operating conditions examined in this study. Drop hold-up was also measured as a means to understand droplet behaviour in the vertical OBTR. A numerical model based on population balance method was also developed in order to understand drop breakage and coalescence.

ABSTRACT

CONTENTS I

PUBLICATIONS BY AUTHOR VI

LIST OF FIGURES VII

LIST OF TABLES XXIX

ACKNOWLEDGEMENTS XXX

NOMENCLATURE XXXII

1 INTRODUCTION 1

1.1 MOTIVATION FOR THIS STUDY 1

1.2 OSCILLATORY BAFFLED TUBULAR REACTOR (OBTR)-
MECHANISM AND PRINCIPLE 2

1.3 THESIS LAYOUT 7

2 LITERATURE REVIEW 8

2.1 BACKGROUND TO OBTR 8

2.1.1 A GENERAL DESCRIPTION OF OBTR 8

2.1.2 OSCILLATORY BAFFLED TUBULAR REACTOR –
POWER CONSUMPTION 9

2.1.3 EFFECT OF BAFFLE GEOMETRY 11

2.1.4 AN OVERVIEW OF RESEARCH INTO OBTR 13

2.2 BACKGROUND OF SYSTEMS ANALOGOUS TO OBTR 15

2.2.1 RECIPROCATING PLATE COLUMN (RPC) 16

2.2.2 PULSED SIEVE – PLATE COLUMN (PSPC) 20

2.2.3 MULTI-STAGE VIBRATIONAL DISK COLUMN (MVDC) 23

3 CHARACTERISATION OF THE VERTICAL OBTR 25

3.1 SINGLE PHASE FLOW STUDY 25

3.1.1 INTRODUCTION 25

3.1.1.1 EXPERIMENTAL STUDIES OF AXIAL DISPERSION IN OBTR SYSTEMS 26

3.1.1.2 IN SYSTEMS ANALOGOUS TO OBTR 30

3.1.2 EXPERIMENTAL SET UP 32

3.1.2.1 THE OSCILLATORY BAFFLED TUBE REACTOR 32

3.1.2.2 BAFFLES 35

3.1.2.3 THE OSCILLATION UNIT 36

3.1.3 EXPERIMENTAL PROCEDURE 37

3.1.3.1 OPERATING VARIABLES 37

3.1.3.2 PROBE CALIBRATION 38

3.1.4 RESULTS AND DISCUSSIONS 38

3.1.4.1 EFFECT OF OPERATING PARAMETERS ON RESIDENCE TIME DISTRIBUTION 38

3.1.4.2 AXIAL DISPERSION COEFFICIENT 44

3.1.4.2.1 THE DIFFUSIONAL MODEL 44

3.1.4.2.2 TANKS –IN- SERIES MODEL 48

3.1.4.2.3 EFFECT OF OSCILLATION PARAMETERS 52

3.1.5 SUMMARY OF RESULTS 58

3.2 TWO PHASE FLOW STUDY 59

3.2.1 INTRODUCTION 59

3.2.2 DROPLET MEASUREMENT 60

3.2.2.1 DIRECT PHOTOGRAPHIC 60

3.2.2.2 CAPILLARY SAMPLING PROBE 60

3.2.2.3 DROP STABILISATION 61

3.2.2.4 LIGHT TRANSMISSION 62

3.2.2.5 CHEMICAL METHOD 62

3.2.3 EXPERIMENTAL PROCEDURE AND IMAGE ACQUISITION SET UP 63

3.2.3.1 ANALYSIS ROUTINE 66

3.2.3.2 NUMBER OF DROPS 67

3.2.3.3 REPEATABILITY 69

3.2.4 RESULTS AND DISCUSSIONS 70

3.2.4.1 DROP STABILITY 71

3.2.4.2 EFFECT OF OSCILLATION PARAMETERS 79

3.2.4.2.1 EFFECT OF OSCILLATION AMPLITUDE 79

3.2.4.2.2 EFFECT OF OSCILLATION FREQUENCY 82

3.2.4.2.3 EFFECT OF OSCILLATION VELOCITY 84

3.2.4.2.4 EFFECT OF NET FLOW RATE 87

3.2.4.2.5 EFFECT OF OSCILALTION VELOCITY ON d_{32} 88

3.2.5 SUMMARY OF RESULTS 92

3.3 WHAT HAVE WE LEARNT 93

4 CHARACTERISATION OF THE HORIZONTAL OBTR 94

4.1 SINGLE PHASE FLOW STUDY 94

4.1.1 EXPERIMENTAL SET-UP AND PROCEDURE 94

4.1.2 EXPERIMENTAL PROCEDURES 97

4.1.3 RESULTS AND DISCUSSIONS 98

4.1.3.1 EFFECT OF OPERATING PARAMETERS ON

RESIDENCE TIME DISTRIBUTION 98

4.1.4 AXIAL DISPERSION COEFFICIENT 104

4.1.4.1 EFFECT OF OSCILLATION PARAMETERS 104

4.1.5 SUMMARY OF RESULTS 107

4.2 TWO PHASE FLOW STUDY 113

4.2.1 DROPLET ANALYSIS 113

4.2.1.1 NUMBER OF DROPS 113

4.2.1.2 REPEATABILITY 116

4.2.2 RESULTS AND DISCUSSIONS 117

4.2.2.1 DROP STABILITY 118

4.2.2.2 EFFECT OF OSCILLATION PARAMETERS 125

4.2.2.2.1 EFFECT OF OSCILLATION AMPLITUDE 125

4.2.2.2.2 EFFECT OF OSCILLATION FREQUENCY 127

4.2.2.2.3 EFFECT OF OSCILLATION VELOCITY 128

4.2.2.2.4 EFFECT OF NET FLOW RATE 132

4.2.3 SUMMARY OF RESULTS 133

4.3 WHAT HAVE WE LEARNT 134

5 MODELLING OF DROPLET BREAKAGE AND COALESCENCE 135

5.1 INTRODUCTION 135

5.2 POPULATION BALNCE APPROACH 135

5.2.1 OVERVIEW 135

5.2.2 DISCRETISATION 136

5.3 THE MODEL 138

5.3.1 GENERAL ASSUMPTIONS 138

5.3.2 DROP CLASSES 139

5.3.3 VOLUME FRACTION CONTINUITY EQUATION 140

5.4 POPULATION BALANCE MODEL 141

5.4.1 BREAKAGE MODEL 141

5.4.2 COALESCENCE MODEL 143

5.4.3 COMBINED MODEL 149

5.5 RESULTS 150

5.6 OPTIMISATION ISSUES 156

5.7 SUMMARY OF RESULTS 159

6 CONCLUSIONS AND FUTURE WORK 160

6.1 CONCLUSIONS 160

6.1.1 SINGLE PHASE STUDY 160

6.1.2 TWO PHASE STUDY 161

6.2 FUTURE WORK 162

APPENDIX 1 CHARACTERISATION OF THE VERTICAL OBTR 163

APPENDIX 2 CHARACTERISATION OF THE HORIZONTAL OBTR 183

APPENDIX 3 MODELLING OF DROPLET BREAKAGE AND COALESCENCE 212

REFERENCES 216

PUBLICATIONS BY THE AUTHOR

JOURNAL PAPERS

1. X.Ni and Nitin E.Pereira, "On the parameters that affect axial mixing in a continuous oscillatory baffled reactor" *AIChE Journal*, Vol. 46, pp. 37-45, 2000.

2. Nitin E.Pereira and Ni, X., "Droplet size distribution in a continuous oscillatory baffled reactor", *Chemical Engineering Science*, Vol. 56, No. 3, pp.735-739, 2001.

CONFERENCE PRESENTATIONS

1. Nitin E.Pereira and X.Ni, "On the parameters that affect axial mixing in a continuous oscillatory baffled tube ", Oscillatory Flow Mixing (OFM) conference, Manchester, December 1998.

2. Nitin E.Pereira, X.Ni and Julie C.Johnstone, "Droplet size distribution in a continuous oscillatory baffled tube", International Symposium of Chemical Reaction Engineering (ISCRE),Poland, Sep.2000.

3. Nitin E.Pereira and X.Ni, "Droplet size distribution and dispersed phase hold-up in a continuous oscillatory baffled tube", Oscillatory Flow Mixing (OFM) conference, Cambridge, December 2001

LIST OF FIGURES

Figure 1.1. Mixing mechanism in an OBTR

Figure 1.2. Representation of oscillator response (x_o = 1 mm, f =1 Hz, period of oscillation, T = 1 s)

Figure 2.1. Reciprocating Plate Column

Figure 2.2. Types of RPC plates

Figure 2.3. Schematic diagram of a pulsed sieve – plate column

Figure 2.4. Multistage vibrating disk contactor (MVDC)

Figure 3.1. Schematic diagram of the vertical OBTR system for single phase investigation

Figure 3.2. Orifice baffles

Figure 3.3. Calibration graph for piston

Figure 3.4. Concentration measurements, Re_o = 9036 (12 mm, 3 Hz), Re_n = 469

Figure 3.5. Concentration measurements, Re_o = 6024 (10 mm, 3 Hz), Re_n = 452

Figure 3.6. Concentration measurements, Re_o = 7531 (8 mm, 3 Hz), Re_n = 490

Figure 3.7. Concentration measurements, Re_o = 4518 (6 mm, 3 Hz), Re_n = 452

Figure 3.8. Concentration measurements, Re_o = 6024 (12 mm, 2 Hz), Re_n = 452

Figure 3.9. Concentration measurements, Re_o = 9036 (12 mm, 1 Hz), Re_n = 490

Figure 3.10. Concentration measurements, Re_o = 9036 (12 mm, 3 Hz); Re_n = 268

Figure 3.11. Concentration measurements, Re_o = 9036 (12 mm, 3 Hz); Re_n = 912

Figure 3.12. Imperfect pulse technique

Figure 3.13. The "Tanks – in – Series'' Model

Figure 3.14. The "Tanks – in – Series with Back mixing" Model

Figure 3.15. Effect of oscillation amplitude on axial dispersion coefficient, f = 3 Hz

Figure 3.16. Effect of oscillation frequency on axial dispersion coefficient, x_o = 12 mm

Figure 3.17. Effect of oscillatory Reynolds number on axial dispersion coefficient

Figure 3.18. Effect of velocity ratio on Peclet number

Figure 3.19. Schematic diagram of the vertical OBTR system for two phase investigation

Figure 3.20. Schematic diagram of Image Acquisition System

Figure 3.21. Typical droplet image

Figure 3.22. The effect of droplet number on droplet size distribution, Re_o = 5020 (x_o = 10 mm, f = 2.0 Hz), Re_n = 541, Riser

Figure 3.23. The effect of droplet number on droplet size distribution, Re_o = 5020 (x_o = 10 mm, f = 2.0 Hz), Re_n = 541, Downcomer

Figure 3.24. Repeatability of droplet size distribution, Re_o = 5020 (x_o = 10 mm, f = 2.0 Hz), Re_n = 554, Downcomer

Figure 3.25. Drop size distribution as a function of flow length, Re_o = 7530 (x_o = 15 mm, f = 2 Hz), Re_n = 554

Figure 3.26. Drop size distribution as a function of flow length, Re_o = 5020 (x_o = 10 mm, f = 2 Hz), Re_n = 544

Figure 3.27. Drop size distribution as a function of flow length, Re_o = 9036 (x_o = 18 mm, f = 2 Hz), Re_n = 554

Figure 3.28. Drop size distribution as a function of flow length, Re_o = 11295 (x_o = 15 mm, f = 3 Hz), Re_n = 551

Figure 3.29. Drop size distribution as a function of flow length, Re_o = 13554 (x_o = 18 mm, f = 3 Hz), Re_n = 564

Figure 3.30. Drop size distribution as a function of flow length, Re_o = 10040 (x_o = 10 mm, f = 4 Hz), Re_n = 554

Figure 3.31. Drop size distribution as a function of flow length, Re_o = 15060 (x_o = 15 mm, f = 4 Hz), Re_n = 550

Figure 3.32. Drop size distribution as a function of flow length, Re_o = 18072 (x_o = 18 mm, f = 4 Hz), Re_n = 550

Figure 3.33. Drop size distribution at N = 222, Re_n = 554

Figure 3.34. Axial Variation of hold–up

Figure 3.35. Axial variation of Sauter mean drop diameter, Re_n = 554

Figure 3.36. Effect of oscillation amplitude on droplet size distribution (f = 2.0 Hz, Re_n = 554), Riser

Figure 3.37. Effect of oscillation amplitude on droplet size distribution (f = 2.0 Hz, Re_n = 554), Downcomer

Figure 3.38. Effect of oscillation amplitude on Sauter mean drop diameter (f = 2 Hz, Re_n = 554)

Figure 3.39. Effect of oscillation frequency on droplet size distribution (x_o = 15 mm, Re_n = 554), Riser

Figure 3.40. Effect of oscillation frequency on droplet size distribution (x_o = 15 mm, Re_n = 554), Downcomer

Figure 3.41. Effect of oscillation frequency on Sauter mean drop diameter (x_o = 2 Hz, Re_n = 554)

Figure 3.42. Effect of oscillation velocity on drop size distribution, Re_n = 554, Riser

Figure 3.43. Effect of oscillation velocity on drop size distribution, Re_n = 554, Downcomer

Figure 3.44. Drop size distribution at riser and downcomer for $x_o f$ = 60 mm/s, Re_n = 554

Figure 3.45. Effect of net flow rate on drop size distribution, Re_o = 7530 (x_o = 15 mm, f = 2 Hz), Riser

Figure 3.46. Effect of net flow rate on drop size distribution, Re_o = 7530 (x_o = 15 mm, f = 2 Hz), Downcomer

Figure 3.47. Effect of oscillation Reynolds number on dimensionless mean drop diameter (Riser)

Figure 3.48. Effect of oscillation Reynolds number on dimensionless mean drop diameter (Downcomer)

Figure 3.49. Effect of energy dissipation on mean drop diameter (Riser)

Figure 3.50. Effect of energy dissipation on mean drop diameter (Downcomer)

Figure 4.1. Schematic diagram of the horizontal OBTR system for single phase investigation

Figure 4.2. Concentration measurements, Re_o = 3012 (4 mm, 3 Hz), Re_n = 488

Figure 4.3. Concentration measurements, Re_o = 4518 (6 mm, 3 Hz), Re_n = 504

Figure 4.4. Concentration measurements, Re_o = 9036 (12 mm, 3 Hz), Re_n = 498

Figure 4.5. Concentration measurements, Re_o = 6024 (12 mm, 2 Hz), Re_n = 525

Figure 4.6. Concentration measurements, Re_o = 3012 (12 mm, 1 Hz), Re_n = 525

Figure 4.7. Concentration measurements, Re_o = 9036 (12 mm, 3 Hz) Re_n = 268

Figure 4.8. Concentration measurements, Re_o = 9036 (12 mm, 3 Hz), Re_n = 944

Figure 4.9. Effect of oscillation amplitude on axial dispersion coefficient, f = 3 Hz

Figure 4.10. Effect of oscillation frequency on axial dispersion coefficient, x_o = 12 mm

Figure 4.11. Effect of oscillation Reynolds number on axial dispersion coefficient

Figure 4.12. Effect of velocity ratio on Peclet number

Figure 4.13. Schematic diagram of the horizontal OBTR system for two phase investigation

Figure 4.14. The effect of droplet number on droplet size distribution, Re_o = 5020 (x_o = 10 mm, f = 2.0 Hz), Re_n = 541, Port 1

Figure 4.15. The effect of droplet number on droplet size distribution, Re_o = 5020 (x_o = 10 mm, f = 2.0 Hz), Re_n = 541, Port 4

Figure 4.16. Repeatability of droplet size distribution, Re_o = 5020, (x_o = 10 mm, f = 2.0 Hz), Re_n = 541) Port 1

Figure 4.17. Repeatability of droplet size distribution, Re_o = 5020 (x_o = 10 mm, f = 2.0 Hz), Re_n = 541, Port 4

Figure 4.18. Drop size distribution as a function of flow length, Re_o = 2510 (x_o = 10 mm, f = 1 Hz), Re_n = 538

Figure 4.19. Drop size distribution as a function of flow length, Re_o = 3012 (x_o = 12mm, f = 1 Hz), Re_n = 528

Figure 4.20. Drop size distribution as a function of flow length, Re_o = 3765 (x_o = 15 mm, f = 1 Hz), Re_n = 544

Figure 4.21. Drop size distribution as a function of flow length, Re_o = 4016 (x_o = 8 mm, f = 2 Hz), Re_n = 535

Figure 4.22. Drop size distribution as a function of flow length, Re_o = 5020 (x_o = 10 mm, f = 2 Hz), Re_n = 541

Figure 4.23. Drop size distribution as a function of flow length, Re_o = 6024 (x_o = 12 mm, f = 2 Hz), Re_n = 541

Figure 4.24. Drop size distribution as a function of flow length, Re_o = 7530 (x_o = 15 mm, f = 2 Hz), Re_n = 541

Figure 4.25. Drop size distribution as a function of flow length, Re_o = 9036 (x_o = 12 mm, f = 23 Hz), Re_n = 541

Figure 4.26. Drop size distribution as a function of flow length, Re_o = 11295 (x_o = 15 mm, f = 3 Hz), Re_n = 541

Figure 4.27. Axial variation of Sauter mean drop diameter

Figure 4.28. Axial variation of hold- up, Re_n = 541

Figure 4.29. The effect oscillation amplitude on droplet size distribution (f = 2.0 Hz, Re_n = 541)

Figure 4.30. Effect of oscillation amplitude on Sauter mean drop diameter, f = 2 Hz

Figure 4.31. The effect oscillation frequency on droplet size distribution, (x_o = 15 mm, Re_n = 541)

Figure 4.32. Effect of oscillation frequency on Sauter mean drop diameter, (x_o = 15 mm, Re_n = 541)

Figure 4.33. Effect of oscillation velocity on drop size distribution, Re_n = 541

Figure 4.34. Effect of oscillation Reynolds number on dimensionless mean drop diameter

Figure 4.35. Effect of energy dissipation on mean drop diameter

Figure 4.36. Effect of net flow rate on Sauter mean drop diameter, Re_o = 7530 (x_o = 15 mm, f = 2 Hz)

Figure 5.1. The discretised volume bins of droplets used in the model

Figure 5.2. Experimental data and reconstructed distributions, Re_o = 6024 (x_o = 12 mm, f = 2 Hz), Re_n = 541, χ^2 = 0.004123

Figure 5.3. Experimental data and reconstructed distributions, Re_o = 6024 (x_o = 12 mm, f = 2 Hz), Re_n = 541, χ^2 = 0.002989

Figure 5.4. Variation of breakage rate constants with drop size, Re_o = 6024 (x_o = 12 mm, f = 2 Hz), Re_n = 541, χ^2 = 0.004123

Figure 5.5. Variation of coalescence rate constants with drop size, Re_o = 6024 (x_o = 12 mm, f = 2 Hz), Re_n = 541, χ^2 = 0.004123

Figure 5.6. Variation of breakage rate constants with drop size, Re_o = 6024 (x_o = 12 mm, f = 2 Hz), Re_n = 541, χ^2 = 0.002989

Figure 5.7. Variation of coalescence rate constants with drop size, Re_o = 6024 (x_o = 12 mm, f = 2 Hz), Re_n = 541, χ^2 = 0.002989

Figure 5.8. Breakage and total coalescence rates as functions of drop size, Re_o = 6024 (x_o = 12 mm, f = 2Hz), Re_n = 541, χ^2 = 0.002989

Figure 5.9. Breakage and total coalescence rates as functions of drop size, Re_o = 6024 (x_o = 12 mm, f = 2Hz), Re_n = 541, χ^2 = 0.002989

Figure 5.10. Optimisation of breakage rate constants, Re_o = 6024 (x_o = 12 mm, f = 2 Hz), Re_n = 541, χ^2 = 0.002989

Figure 5.11. Optimisation of breakage rate constants, Re_o = 6024 (x_o = 12 mm, f = 2 Hz), Re_n = 541, χ^2 = 0.002989

Figure 5.12. Optimisation of coalescence rate constants, Re_o = 6024 (x_o = 12 mm, f = 2 Hz), Re_n = 541, χ^2 = 0.002989

Figure 5.13. Optimisation of coalescence rate constants, Re_o = 6024 (x_o = 12 mm, f = 2 Hz), Re_n = 541, χ^2 = 0.002989

APPENDIX 1 CHARACTERISATION OF THE VERTICAL OBTR

Figure A1.1. Concentration measurement, $Re_o = 4518$ ($x_o = 6$ mm, $f = 3$ Hz), $Re_n = 256$

Figure A1.2. Concentration measurement, $Re_o = 4518$ ($x_o = 6$ mm, $f = 3$ Hz), $Re_n = 964$

Figure A1.3. Concentration measurement, $Re_o = 7530$ ($x_o = 10$ mm, $f = 3$ Hz), $Re_n = 256$

Figure A1.4. Concentration measurement, $Re_o = 7530$ ($x_o = 10$ mm, $f = 3$ Hz), $Re_n = 920$

Figure A1.5. Concentration measurement, $Re_o = 0$, $Re_n = 260$

Figure A1.6. Concentration measurement, $Re_o = 0$, $Re_n = 464$

Figure A1.7. Concentration measurement, $Re_o = 0$, $Re_n = 1024$

Figure A1.8. Prediction of concentration profile 3 from profile 1 using axial dispersion model, $Re_o = 9036$ ($x_o = 8$ mm, $f = 3$ Hz), $Re_n = 490$

Figure A1.9. Prediction of concentration profile 3 from profile 1 using axial dispersion model, $Re_o = 9036$ ($x_o = 10$ mm, $f = 3$ Hz), $Re_n = 452$

Figure A1.10. Prediction of concentration profile 3 from profile 1 using axial dispersion model, $Re_o = 9036$ ($x_o = 12$ mm, $f = 3$ Hz), $Re_n = 469$

Figure A1.11. Prediction of concentration profile 3 from profile 1 using axial dispersion model, Re_o = 9036 (x_o = 12 mm, f = 1 Hz), Re_n = 490

Figure A1.12. Prediction of concentration profile 3 from profile 1 using axial dispersion model, Re_o = 9036 (x_o = 12 mm, f = 2 Hz), Re_n = 452

Figure A1.13. Prediction of concentration profile 3 from profile 1 using axial dispersion model, Re_o = 9036 (x_o = 12 mm, f = 3 Hz), Re_n = 268

Figure A1.14. Prediction of concentration profile 3 from profile 1 using axial dispersion model, Re_o = 9036 (x_o = 12 mm, f = 3 Hz), Re_n = 912

Figure A1.15. Drop size distribution as a function of flow length, Re_o = 7530 (x_o = 15 mm, f = 2 Hz), Re_n = 285

Figure A1.16. Drop size distribution as a function of flow length, Re_o = 9036 (x_o = 18 mm, f = 2 Hz), Re_n = 299

Figure A1.17. Drop size distribution as a function of flow length, Re_o = 13554 (x_o = 18 mm, f = 3 Hz), Re_n = 299

Figure A1.18. Drop size distribution as a function of flow length, Re_o = 7530 (x_o = 15 mm, f = 2 Hz), Re_n = 974

Figure A1.19. Drop size distribution as a function of flow length, Re_o = 9036 (x_o = 18 mm, f = 2 Hz), Re_n = 989

Figure A1.20. Drop size distribution as a function of flow length, Re_o = 11295 (x_o = 15 mm, f = 3 Hz), Re_n = 975

Figure A1.21. Drop size distribution as a function of flow length, Re_o = 13554 (x_o = 18 mm, f = 3 Hz), Re_n = 1006

Figure A1.22. Drop size distribution as a function of flow length, Re_o = 15060 (x_o = 15 mm, f = 4 Hz) Re_n = 975

Figure A1.23. Effect oscillation amplitude on droplet size distribution (f = 2.0 Hz, Re_n = 554), Riser 1

Figure A1.24. The effect oscillation amplitude on droplet size distribution (f = 2.0 Hz, Re_n= 554), Downcomer 2

Figure A1.25. The effect oscillation frequency on droplet size distribution (x_o = 15 mm, Re_n = 554), Riser 1

Figure A1.26. The effect oscillation frequency on droplet size distribution (x_o = 15 mm, Re_n = 554), Downcomer 2

Figure A1.27. Effect of oscillation velocity on drop size distribution (DSD) (Re_n =289), Riser 1

Figure A1.28. Effect of oscillation velocity on drop size distribution (DSD) (Re_n =289), Riser 2

Figure A1.29. Effect of oscillation velocity on drop size distribution (DSD) (Re_n = 289), Downcomer 1

Figure A1.30. Effect of oscillation velocity on drop size distribution (DSD) (Re_n = 554), Riser 1

Figure A1.31. Effect of oscillation velocity on drop size distribution (DSD) (Re_n = 554), Downcomer 2

Figure A1.32. Effect of oscillation velocity on drop size distribution (DSD) (Re_n = 982), Riser 1

Figure A1.33. Effect of oscillation velocity on drop size distribution (DSD) (Re_n = 982), Riser 2

Figure A1.34. Effect of oscillation velocity on drop size distribution (DSD) (Re_n = 982), Downcomer 1

Figure A1.35. Effect of oscillation velocity on drop size distribution (DSD) (Re_n = 982), Downcomer 2

Figure A1.36. Effect of net flow rate on drop size distribution (x_o = 15 mm, f = 2 Hz), Riser 1

Figure A1.37. Effect of net flow rate on drop size distribution (x_o = 15 mm, f = 2 Hz), Downcomer 2

APPENDIX 2 CHARACTERISATION OF THE HORIZONTAL OBTR

Figure A2.1. Concentration measurement, Re_o = 3012 (x_o = 4 mm, f = 3 Hz), Re_n = 266

Figure A2.2. Concentration measurement, Re_o = 3012 (x_o = 4 mm, f = 3 Hz), Re_n = 955

Figure A2.3. Concentration measurement, Re_o = 7530 (x_o = 10 mm, f = 3 Hz), Re_n = 256

Figure A2.4. Concentration measurement, Re_o = 7530 (x_o = 10 mm, f = 3 Hz), Re_n = 987

Figure A2.5. Concentration measurement, Re_o = 0, Re_n = 272

Figure A2.6. Concentration measurement, Re_o = 0, Re_n = 504

Figure A2.7. Concentration measurement, Re_o = 0, Re_n = 955

Figure A2.8. Prediction of concentration profile 3 from profile 1 using axial dispersion model, Re_o = 9036 (4 mm, 3 Hz), Re_n = 488

Figure A2.9. Prediction of concentration profile 3 from profile 1 using axial dispersion model, Re_o = 9036 (6 mm, 3 Hz), Re_n = 504

Figure A2.10. Prediction of concentration profile 3 from profile 1 using axial dispersion model, Re_o = 9036 (12 mm, 3 Hz), Re_n = 525

Figure A2.11. Prediction of concentration profile 3 from profile 1 using axial dispersion model, Re_o = 9036 (12 mm, 1 Hz), Re_n = 525

Figure A2.12. Prediction of concentration profile 3 from profile 1 using axial dispersion model, Re_o = 9036 (12 mm, 2 Hz), Re_n = 498

Figure A2.13. Prediction of concentration profile 3 from profile 1 using axial dispersion model, Re_o = 9036 (12 mm, 3 Hz), Re_n = 244

Figure A2.14. Prediction of concentration profile 3 from profile 1 using axial dispersion model, Re_o = 9036 (12 mm, 3 Hz), Re_n = 945

Figure A2.15. Drop size distribution as a function of flow length, Re_o = 3012 (x_o = 12 mm, f = 1 Hz), Re_n = 234

Figure A2.16. Drop size distribution as a function of flow length, Re_o = 3012 (x_o = 12 mm, f = 1 Hz), Re_n = 997

Figure A2.17. Drop size distribution as a function of flow length, Re_o = 3765 (x_o = 15 mm, f = 1 Hz), Re_n = 235

Figure A2.18. Drop size distribution as a function of flow length, Re_o = 3765 (x_o = 15 mm, f = 1 Hz), Re_n = 997

Figure A2.19. Drop size distribution as a function of flow length, Re_o = 4016 (x_o = 8 mm, f = 2 Hz), Re_n = 1004

Figure A2.20. Drop size distribution as a function of flow length, Re_o = 5020 (x_o = 10 mm, f = 2 Hz), Re_n = 1010

Figure A2.21. Drop size distribution as a function of flow length, Re_o = 6024 (x_o = 12 mm, f = 2 Hz), Re_n = 239

Figure A2.22. Drop size distribution as a function of flow length, Re_o = 6024 (x_o = 12 mm, f = 2 Hz), Re_n = 998

Figure A2.23. Drop size distribution as a function of flow length, Re_o = 7530 (x_o = 15 mm, f = 2 Hz), Re_n = 252

Figure A2.24. Drop size distribution as a function of flow length, Re_o = 7530 (x_o = 15 mm, f = 2 Hz), Re_n = 1016

Figure A2.25. Drop size distribution as a function of flow length, Re_o = 9036 (x_o = 12 mm, f = 3 Hz), Re_n = 264

Figure A2.26. Drop size distribution as a function of flow length, Re_o = 9036 (x_o = 12 mm, f = 3 Hz), Re_n = 1016

Figure A2.27. Drop size distribution as a function of flow length, Re_o = 11295 (x_o = 15 mm, f = 3 Hz), Re_n = 264

Figure A2.28. The effect oscillation amplitude on droplet size distribution (f = 2.0 Hz, Re_n=541), Port 1

Figure A2.29. The effect oscillation amplitude on droplet size distribution (f = 2.0 Hz, Re_n = 554), Port 2

Figure A2.30. The effect oscillation amplitude on droplet size distribution (f = 2.0 Hz, Re_n = 541), Port 4

Figure A2.31. The effect oscillation frequency on droplet size distribution (x_o = 15 mm, Re_n = 541), Port 1

Figure A2.32. The effect oscillation frequency on droplet size distribution (x_o = 15 mm, Re_n = 541), Port 2

Figure A2.33. The effect oscillation frequency on droplet size distribution (x_o = 15 mm, Re_n =541), Port 4

Figure A2.34. Effect of oscillation velocity on drop size distribution (DSD) (Re_n = 541), Port 1

Figure A2.35. Effect of oscillation velocity on drop size distribution (DSD) (Re_n = 541), Port 2

Figure A2.36. Effect of oscillation velocity on drop size distribution (DSD) (Re_n = 541), Port 4

Figure A2.37. Effect of oscillation velocity on drop size distribution (DSD) (Re_n = 248), Port 1

Figure A2.38. Effect of oscillation velocity on drop size distribution (DSD) (Re_n = 248), Port 2

Figure A2.39. Effect of oscillation velocity on drop size distribution (DSD) (Re_n = 248), Port 3

Figure A2.40. Effect of oscillation velocity on drop size distribution (DSD) (Re_n = 248), Port 4

Figure A2.41. Effect of oscillation velocity on drop size distribution (DSD) (Re_n = 1002), Port 1

Figure A2.42. Effect of oscillation velocity on drop size distribution (DSD) (Re_n = 1002), Port 2

Figure A2.43. Effect of oscillation velocity on drop size distribution (DSD) (Re_n = 1002), Port 3

Figure A2.44. Effect of oscillation velocity on drop size distribution (DSD) (Re_n = 1002), Port 4

Figure A2.45. Effect of net flow rate on Sauter mean drop diameter, (x_o = 15 mm, f = 2 Hz), Port 1

Figure A2.46. Effect of net flow rate on Sauter mean drop diameter, (x_o = 15 mm, f = 2 Hz), Port 2

Figure A2.47. Effect of net flow rate on Sauter mean drop diameter, (x_o = 15 mm, f = 2 Hz), Port 4

Figure A2.48. Effect of oscillatory Reynolds number on dimensionless mean drop diameter, Re_n = 249

Figure A2.49. Effect of oscillation velocity on Sauter mean drop diameter, Re_n = 541

Figure A2.50. Effect of oscillation velocity on Sauter mean drop diameter, Re_n = 1004

APPENDIX 3 MODELLING OF DROPLET BREAKAGE AND COALESCENCE

Figure A3.1. Experimental data and reconstructed distributions, Re_o = 5020 (x_o = 10 mm, f = 2 Hz), Re_n = 541, χ^2 = 0.004487

Figure A3.2. Breakage and total coalescence rates as functions of drop size, Re_o = 5020 (x_o = 10 mm, f = 2Hz), Re_n = 541, χ^2 = 0.004487

Figure A3.3. Variation of breakage rate constants with drop size, Re_o = 5020 (x_o = 10 mm, f = 2 Hz), Re_n = 541, χ^2 = 0.004487

Figure A3.4. Variation of coalescence rate constants with drop size, Re_o = 5020 (x_o = 10 mm, f = 2 Hz), Re_n = 541, χ^2 = 0.004487

Figure A3.5. Experimental data and reconstructed distributions, Re_o = 7530 (x_o = 15 mm, f = 2 Hz), Re_n = 541, χ^2 = 0.00110575

Figure A3.6. Breakage and total coalescence rates as functions of drop size, Re_o = 7530 (x_o = 15 mm, f = 2Hz), Re_n = 541, χ^2 = 0.00110575

Figure A3.7. Variation of breakage rate constants with drop size, Re_o = 7530 (x_o = 15 mm, f = 2 Hz), Re_n = 541, χ^2 = 0.00110575

Figure A3.8. Variation of coalescence rate constants with drop size, Re_o = 7530 (x_o = 15 mm, f = 2 Hz), Re_n = 541, χ^2 = 0.0133909

LIST OF TABLES

Table 3.1. Calculated *E* and *Pe*

Table 3.2. Velocity ratio

Table 4.1. Calculated *E* and *Pe* for different probe locations

Table 4.2. Velocity ratio

Table 4.3 Comparison of *E* for different OBTRs

Table 4.4 Comparison of drop stability between horizontal and vertical OBTR

Table 4.5 Comparison of horizontal and vertical OBTR

ACKNOWLEDGEMENTS

I would like to give special thanks to my supervisor, *Prof. Xiongwei Ni* for providing inestimable help and motivation throughout this project without which this project would not have been completed. Fellow COBRA colleagues, *Andy, Bruce, Benoit, Dmitiri, Greig, Hongbing, Hemraj, Julie, Lekraj*, *Monica* and *Yan* are thanked for their encouragement and help. Also special thanks to Heriot-Watt University for providing Postgraduate Research scholarship that helped me to live comfortably and enjoy my time in beautiful Scotland.

I would also like to extend thanks to staff of the Department of Mechanical and Chemical Engineering for their sincere co-operation. I am highly indebted and would like to give very special thanks to technical service manager, *Mr. Malcolm McWilliams*, and technicians, *Mr. John "Big" Thomson* and *Mr. Richard Kinsella* for helping build the experimental rigs used in this project. Also thanks to technicians *Mr. Mark McCaskey, Mr. Ian Galloway, Mr. Ronnie Millar* and *Mr. Craig Bell*. Special thanks to *Mr. Aftab Aziz* and *Mr. John Prichard* for computing assistance and *Mr. Alf Buchan* and *Mr. Les Morris* for processing order forms.

Special "cheers" to office mates *Charlotte, Elaine*, *Myrna, Rose, Vanna, Greig* and *Mikey* for providing a nice, fun loving atmosphere and encouragement during the course of this project. Also thanks to two other good friends, *Steven* and *Jaime* providing valuable advice and support during the course of this project. Special thanks to special friends *Al, Antonio, Andreas, Collin, Daniel, Juanita, Meera, Nuno, Rosa* and *Zul*.

XXX

Finally, I would like to thank my parents, *Ruby* and *Emelyan*, sister, *D'laila* and grandparents for their unwavering support and above all almighty "God" who has always been a guardian angel, especially during thesis writing.

NOMENCLATURE

a_o	Oscillation acceleration	$m.s^{-2}$
A	Cross-sectional area of the tube	m^2
$B_i^+(t)$	Birth rate of drops in bin i due to breakage	s^{-1}
$B_i^-(t)$	Death rate of drops in bin i due to breakage	s^{-1}
C	Concentration of the tracer	$mg.l^{-1}$
$C^{'}$	Normalised concentration of the tracer	
$C_i^+(t)$	Birth rate of drops in bin i due to coalescence	s^{-1}
$C_i^-(t)$	Death rate of drops in bin i due to coalescence	s^{-1}
C_o	Orifice discharge coefficient (= 0.6)	
D	Internal tube / column diameter	m
D_d	Disk diameter	m
d_i	Average droplet diameter of bin class, i	m
d_{32}	Sauter mean drop diameter	m
D_o, D_h	Orifice or hole diameter	m
E	Axial dispersion coefficient	$m^2.s^{-1}$
$\frac{E}{uL}$	Dimensionless axial dispersion coefficient	
f	Oscillation frequency	Hz
f_b	Backmixing coefficient ($=\frac{F_b}{F}$)	
f_i	Volume fraction of drops in class i	
F	Net forward flow rate	$m^3.s^{-1}$
F_b	Net backmixing flow rate	$m^3.s^{-1}$
$\boldsymbol{g}$	Vector of breakage rates	
g_i	Breakage rate of droplets in bin (i)	s^{-1}

H	Inter-baffle / plate spacing	m
$k_{b,1}$	Fraction of drops allocated to bin (j+1) from type (b) coalescence (= $1-\frac{1}{2\sqrt{2}}$)	
$k_{b,2}$	Fraction of drops allocated to bin (j+1) from type (b) coalescence (= $\frac{1}{2\sqrt{2}}$)	
$k_{c,1}$	Fraction of drops allocated to bin (j+1) from type (b) coalescence (= $\frac{3}{2}-\sqrt{2}$)	
$k_{c,2}$	Fraction of drops allocated to bin (j+1) from type (b) coalescence (= $\sqrt{2}-\frac{1}{2}$)	
$K_l a$	Mass transfer coefficient	s^{-1}
L	Length of the OBTR	m
L	Distance between probes	m
n	Mass of tracer injected	mg
n_i	Number of droplets with diameter i	
n_d	Number of drops	
N	Number of inter-baffle cells/cavities	
$\boldsymbol{P}$	Vector consisting of all coalescence and breakage rate constants	
$\frac{P}{V}$	Power density	$W.m^{-3}$
ΔP	Frictional pressure drop across orifice plate/baffle	$N.m^{-2}$
Pe	Peclet number (=$\frac{uL}{E}$)	

Re_o	Oscillatory Reynolds number $(=\frac{D\omega x_o}{\nu})$	
Re_n	Net flow Reynolds number $(=\frac{Du}{\nu})$	
St	Strouhal number $(=\frac{D}{4\pi x_o})$	
t	Time variable	s
Δt	Time interval	s
T	Period of oscillation $(=1/f)$	s
$T(t)$	Transfer function	s^{-1}
u	Net steady flow velocity	$m\ s^{-1}$
V	Volume	m^3
V_{cell}	Volume of an inter-baffle cell	m^3
V_d	Dispersed phase Volume	m^3
x	Oscillation amplitude	m
x_o	Centre to peak oscillation amplitude	m
$x_o f$	Oscillation velocity	$m.s^{-1}$

Greek letters

α	Ratio of the effective baffle orifice area to the tube area $(=\frac{D_o^2}{D^2})$	
β	Vector of coalescence rates	
$\beta_{i,j}$	Rate of coalescence between drops in bin (i) and drops in bin (j)	s^{-1}
ε	Energy dissipation rate	$W.kg^{-1}$
ψ	Velocity ratio $(=\frac{Re_o}{Re_n})$	
ϕ	Dispersed phase hold-up	

γ	Interfacial tension	$N.m^{-1}$
$\delta(x)$	Dirac delta function	m^{-1}
μ	Dynamic viscosity	$(kgm^{-1}s^{-1})$
π	3.1416	
υ	inematic viscosity $(=\mu/\rho)$,	$m^2.s^{-1}$
ρ	Fluid density,	$kg.m^{-3}$
$\Delta\rho$	Density difference between phases	$kg.m^{-3}$
σ	Surface tension	$N\ m^{-1}$
	Standard deviation	
σ^2	Variance	
ω	Angular oscillation frequency $(=2\pi f)$	$rad.s^{-1}$

Subscripts

c	Continuous phase
d	Dispersed phase
n	Net flow
o	Oscillatory

CHAPTER 1

INTRODUCTION

1.1 MOTIVATION FOR THIS STUDY

It has often been the goal of chemical engineers to construct a reactor design which would give perfect plug flow, even under variable throughput conditions. Tubular reactors are a close approximation, yet in general are reliant on turbulent flow, are susceptible to variations in throughput and can for long residence times require very long tubes with resulting high pressure differences along the length of the reactor.

The oscillatory baffled tubular reactor (OBTR) is a relatively recent development in mixing and reactor technology which has been researched over the past decade. It has a number of similarities to other tubular mixing technologies, particularly pulsed and reciprocating columns, but at the laboratory and pilot scales has demonstrated a number of advantageous properties (Mackley, 1987). Most notably control of the oscillatory conditions when operating as a continuous process allows axial dispersion to be minimised (Dickens *et al.* 1989), permittting the control of residence time distributions independently of the throughput rate (Mackley and Ni, 1991, 1993). In this way the technology can be operated as a near perfect plug flow device, unaffected by changes in throughput. In a batch mode, control of the oscillatory conditions in oscillatory baffled columns allow Guassian drop/particle size distributions to be obtained in suspension polymerisation (Ni *et al.* 1998, 1999, 2001) leading to significant waste reductions, *i.e.* under sized as well as over sized particles.

The OBTR is generally considered to consist of periodically spaced annular baffles inside a long tube in which either a liquid or a multiphase mixture is oscillated axially. This flow past the baffles induces vortices which provide both axial and radial mixing in the tube. The intensity of mixing can be varied by tuning the oscillatory conditions (amplitude and frequency of oscillation) and several different mixing regimes have been identified ranging from creeping laminar to fully turbulent flow (Howes 1988).

The ability to generate radial mixing gives a unique form of control in respect of intensity of mixing, axial dispersion, drop/particle suspension and other transfer processes, this presents a unique opportunity to characterise an OBTR for a pioneering application in continuous suspension polymerisation. Although some of the mentioned properties of OBTR have been studied on a number of occasions by previous researchers, such studies have in general been limited to single phase applications. There is therefore a clear need to understand the behaviour of an OBTR in the context of continuous suspension polymerisation by characterising such a reactor in terms of axial dispersion in single phase, furthermore droplet size distribution and the mean drop size in a two phase system.

1.2 OSCILLATORY BAFFLED TUBULAR REACTOR (OBTR) - MECHANISM AND PRINCIPLE

It should be mentioned that the term of OBTR has been used throughout the thesis, yet no reaction was performed. As the objective of this work is to characterise OBTR in application of continuous suspension polymerisation, the retention of the

word "reactor" allows continuity of the work as well as a reduction in using too many acronyms.

The mechanism of fluid mixing in an OBTR can be understood with the help of Figure 1.1. On the upward stroke of the oscillation eddies are formed downstream of the baffle. On flow reversal these eddies are pushed into the centre of the tube while new eddies are formed at the same time and the cycle is repeated. In this way intense mixing can be achieved in the inter-baffle region where the events are similar both at the wall and centre of the tube. Hence each inter-baffle cell can be assumed to behave as a unit perfectly mixed stirred tank, so mixing over the length of the tube is a cumulative effect of all discrete mixing units leading to a plug flow behaviour.

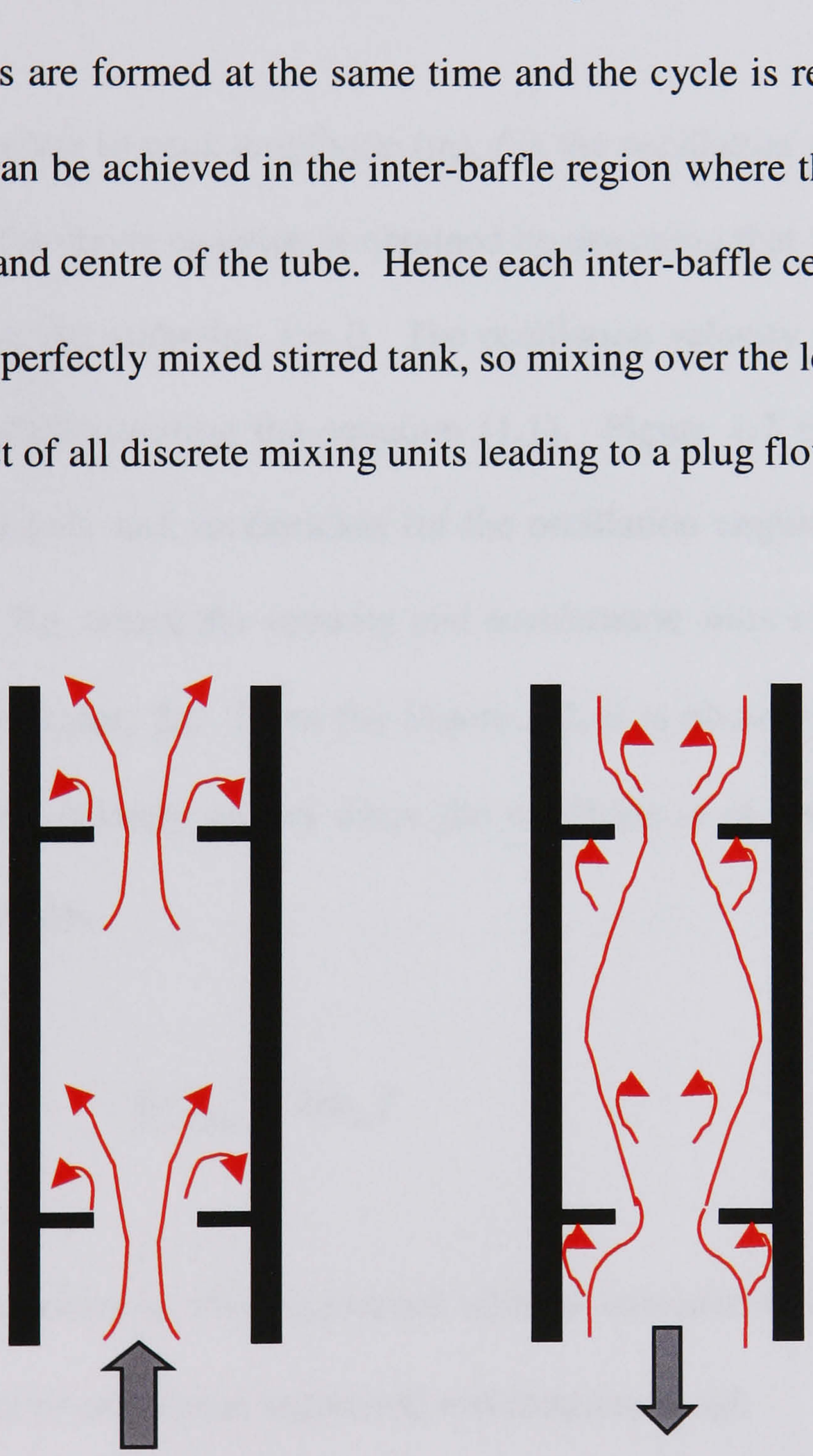

Figure 1.1. Mixing mechanism in an OBTR

An oscillator like a piston or bellows driven by an electric geared motor usually provides the oscillations. The displacement of the oscillator, x, is usually sinusoidal and is described by the equation,

$$x = x_o \sin(2\pi ft) \tag{1.1}$$

where x_o is the centre to peak amplitude (m), f is the oscillation frequency (Hz) and t is the time (s). The above equation is obtained by assuming that the initial position of the oscillator is at the midpoint, $x = 0$. The oscillation velocity and acceleration can be obtained by differentiating the equation (1.1). Figure 1.2 shows the oscillation displacement, velocity and acceleration for the oscillation amplitude, x_o = 1 mm and frequency, f = 1 Hz, where the velocity and acceleration were evaluated by dividing by the waveform factor, 2π. From the Figure 1.2, it is observed that the maximum angular oscillation velocity occurs when the oscillator is at the mid-position of its travel and is given by,

$$(v_o)_{\max} = 2\pi x_o f \tag{1.2}$$

The oscillatory velocity is often expressed without considering the waveform factor, 2π, as the product of oscillation amplitude and frequency, $x_o f$.

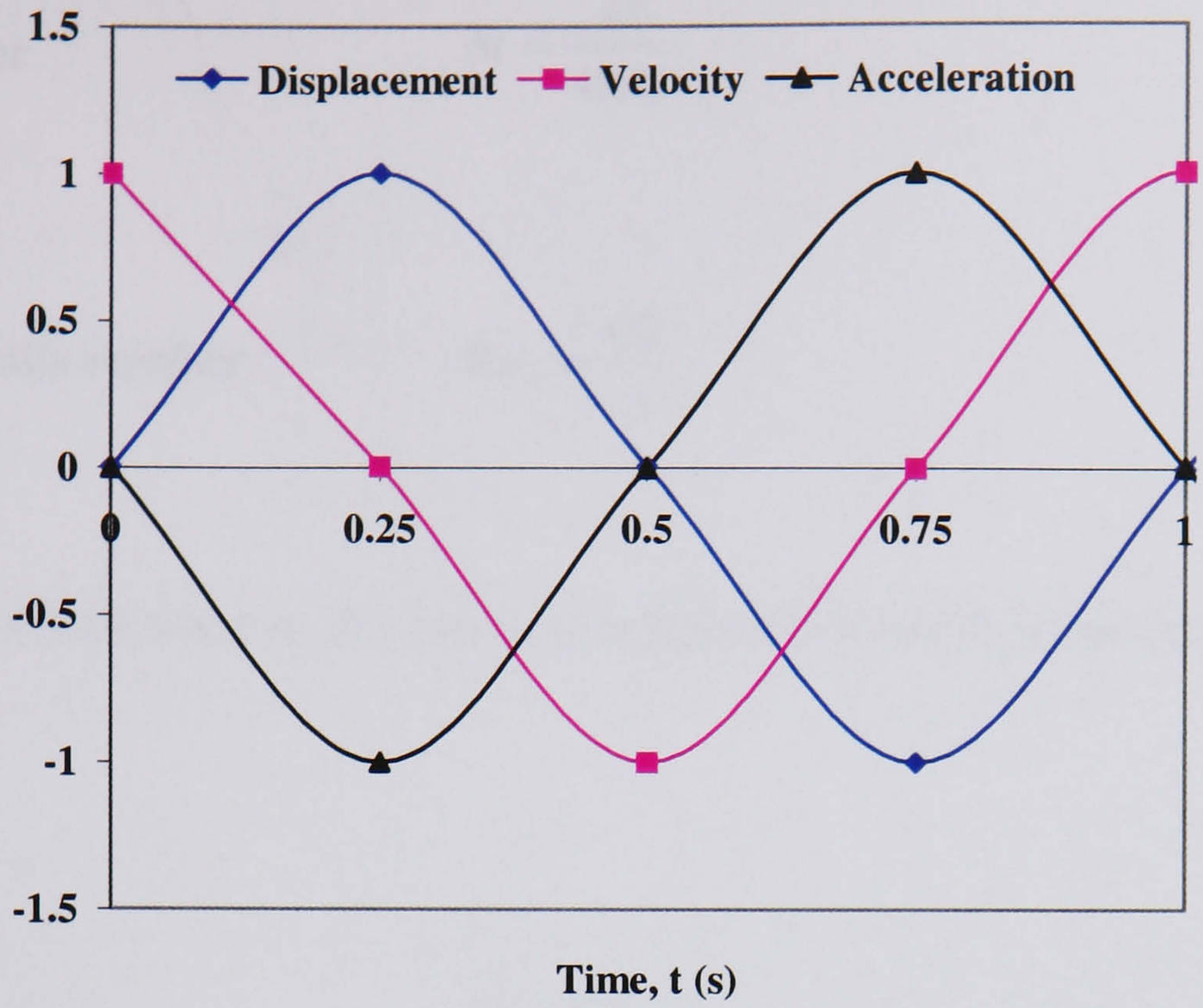

Figure 1.2. Representation of oscillator response (x_o = 1 mm, f =1 Hz, period of oscillation, T = 1 s)

The dynamic nature of the oscillatory flow in an OBTR can be characterised by two dimensionless groups, the oscillatory Reynolds number and the Strouhal number. The oscillatory Reynolds number, Re_o, defined in equation (1.3) describes the intensity of oscillation applied to the system.

Oscillatory Reynolds number $$\mathrm{Re}_o = \frac{x_o \omega D}{\nu} \qquad (1.3)$$

The Strouhal number, St, defined in equation (1.4), represents effectively the ratio of tube diameter to oscillation amplitude. In a continuous OBTR system, the net flow Reynolds number, Re_n is also relevant and defined as:

Strouhal number $$St = \frac{D}{4\pi x_o} \quad (1.4)$$

Net flow Reynolds number $$\mathrm{Re}_n = \frac{uD}{\nu} \quad (1.5)$$

In addition, the Peclet number, *Pe*, has been adopted to quantify axial dispersion and is defined as:

Peclet number $$Pe = \frac{uL}{E} \quad (1.6)$$

where D is the internal tube diameter (m), E is the axial dispersion coefficient ($m^2.s^{-1}$), L is the distance between two measuring points (m), u the characteristic mean net flow velocity ($m.s^{-1}$), x_o the centre –to – peak oscillation amplitude (m), ν the fluid kinematic viscosity (Pa.s), ρ the fluid density ($kg.m^{-3}$) and ω the angular oscillation frequency ($rad.s^{-1}$).

The thesis characterises the behaviour of an OBTR operating continuously. Axial dispersion has been chosen as the principal parameter in the single phase investigation. Knowledge of axial dispersion allows for the prediction of residence time distributions. In two phase studies, a Silicone oil of density 920 kg/m^3 and viscosity 4.6 cP is used as the dispersed phase and water as the continuous phase. Drop size distribution and mean drop size have been studied under various operating conditions. A model based on population balance approach is also developed to predict DSD in the present system.

1.3 THESIS LAYOUT

Following this introduction, the thesis commences in Chapter 2 with a survey of background literature relevant to the characteristics of OBTR. The background to analogous systems such as pulsed plate columns and reciprocating plate columns is also discussed in so far as it is relevant to this work. Chapter 3 describes the experimental set-up used in the characterisation of a vertical OBTR, followed by characterisation of a horizontal OBTR in Chapter 4. The droplet behaviour was modelled by using the population balance approach and is presented in Chapter 5. The main part of the thesis is concluded in Chapter 6 along with the recommendations for future work put forward by the author. A list of references and appendices are given at the end.

CHAPTER 2

LITERATURE REVIEW

This chapter surveys the background literature which is relevant to the characterisation of an oscillatory baffled tube reactor (OBTR) and is divided into two sections: 2.1 presents a basic description of OBTR and a summary of the range of direct research into the various properties of OBTR from which industrial interest in the technology has arisen. Then follows a chronology and description of the results and conclusions drawn from the various published OBTR experimental and modelling studies most relevant to this thesis. In 2.2, the background to analogous systems such as reciprocating and pulsed plate columns are discussed so far as it is relevant to OBTR, particularly in respect of continuous single and two phase operations.

2.1 BACKGROUND TO OBTR

2.1.1 A GENERAL DESCRIPTION OF OBTR

An oscillatory baffled tube reactor (OBTR) is generally understood to be a cylindrical tube of typically from 12 mm up to 800 mm diameter containing periodically spaced baffles and in which a liquid or multiphase fluid is oscillated axially by means of diaphragms, bellows or piston at one or both ends of the tube. The resulting flow of fluid past the baffles induces vortex formation and hence radial mixing from which the various useful properties of OBTR stem. For batch operations, the OBTR is usually operated vertically. Fluid oscillation can be achieved either by pulsing the fluid using bellows or piston at the base of the reactor or by oscillating a set of baffles at the top of the reactor. In a continuous mode, the OBTR is usually a long tube, of typically

between 5 and 50 m depending on residence time of any particular reaction. It can be operated either vertically or horizontally with a net flow of fluid along the tube. The work reported in this thesis concerns the continuous operation.

2.1.2 OSCILLATORY BAFFLED TUBULAR REACTOR – POWER CONSUMPTION

Power dissipation is an important parameter in assessing the efficiency of any given reactor. Jealous and Johnson (1955) first evaluated power dissipation in pulsed columns using a quasi-steady state model. The model assumed that the flow at any moment in the fluid oscillation cycle is fully developed. They related the instantaneous power consumption to the static pressure, the inertia force to accelerate the liquid, and the hydrodynamic frictional force imposed by the baffles and other fittings. During the oscillating cycle the inertial effects due to the accelerating and decelerating motion of the liquid cancelled each other out, but the frictional power dissipation is irreversible due to baffle restrictions and is derived as

$$\frac{\Delta P}{L} = \left(\frac{1-\alpha^2}{\alpha^2} \right) \frac{\rho N}{2C_d^2} (\omega x_o)^2 \qquad (\mathrm{N.m^{-3}}) \qquad (2.1)$$

where N is the number of baffled cells per unit length ($\mathrm{m^{-1}}$), ρ the density of the system ($\mathrm{kg.m^{-3}}$), α the fractional free area and is defined as $\left(\frac{D_o}{D} \right)^2$, where D_o and D are the orifice and tube diameters (m) respectively and C_d is the orifice coefficient for the flow

through the baffle hole and is assumed to be 0.6 for fully developed conditions. Hence the time-averaged power consumption in a pulsed column is a function of the frictional pressure drop of the liquid as it is displaced through the plate hole according to the quasi-steady state model. Integrating equation (2.1) over an oscillation cycle, the energy dissipation per unit volume (power density) is expressed as:

$$\frac{P}{V} = \frac{2\rho N}{3\pi C_d^2}\frac{\left(1-\alpha^2\right)}{\alpha^2}\left(\omega x_o\right)^3 \qquad (\mathrm{W.m^{-3}}) \qquad (2.2)$$

The power dissipation rate, ε, is evaluated as,

$$\varepsilon = \frac{P}{\rho V} = \frac{16\pi^2 N}{3C_d^2}\frac{\left(1-\alpha^2\right)}{\alpha^2}\left(x_o f\right)^3 \qquad (\mathrm{W.kg^{-1}}) \qquad (2.3)$$

Baird and Stonestreet (1995) observed that the pressure drop and power dissipation measured agreed with the well-known quasi-steady state model at large amplitudes and low frequencies, but at lower amplitudes and higher frequencies the predictions using the quasi steady theory were exceeded by a significant degree. To account for this deviation, a new flow model based on acoustic principles and eddy viscosity was proposed and is defined by the equation (2.4),

$$\varepsilon = 1.5\frac{\omega^3 x_o^2 l}{H\alpha} \qquad (\mathrm{W.kg^{-1}}) \qquad (2.4)$$

where l is the mixing length (m), which is an adjustable parameter of the same order as that of the tube diameter. This new eddy acoustic model gave good agreement with the data on pressure fluctuations, power density and phase shift angle for conditions of high frequency and low amplitude, e.g.(3 to 14 Hz; 1 to 5 mm), where the quasi-steady state model appears to fail. This model appears to be promising, however more work on the estimation of the mixing length needs to be done in order to generalise the equation (2.4). In this study, the range of oscillation amplitudes and frequencies is from 0 to 18 mm and 0 to 4 Hz, respectively and fall into the former model. Hence in this study, the quasi-steady state model was used throughout.

2.1.3 EFFECT OF BAFFLE GEOMETRY

In an OBTR the baffle geometry such as baffle type, baffle spacing and baffle free area influences the size of the eddy generation and therefore the onset of the fluid mechanical conditions. A number of different configurations for baffles have been tested including central, helical and orifice geometries (Hewgill *et al.* (1993), but the most commonly adopted is the single orifice (or annular) baffle. The baffle spacing is a key design parameter since it affects the shape / length of the eddies within each baffle cavity while the baffle free area controls the width of vortices within each baffled cell. Much research has been carried out in order to optimise those baffle properties.

Brunold *et al.* (1989) were among the first to study the effect of baffle spacing. They carried out flow visualisation studies on flow patterns for a single phase oscillatory flow in a baffled U-tube. Baffle spacings of 1, 1.5 and 2 times the tube diameter were investigated. It was observed that the baffle spacing of 1.5 tube diameter

gave the most effective mixing over the range of operating conditions used. They also reported that the baffle free area ratio, α, being 34 % was the optimal value for effective mixing. This optimum inter – baffle spacing (1.5 tube diameter) and baffle free area ratio (α = 34 %) have since been used as a standard by many investigators, see for example, Dickens *et al.* (1989), Howes *et al.* (1990,1991), Mackay *et al.* (1991) and Mackley and Ni (1991, 1993).

Ni and Gao (1996) studied the effect of baffle spacing on mass transfer characteristics and scale-up parameters involved in the batch oscillatory baffled reactors. The baffle spacing to tube diameter ratio was varied between 1 and 2. They observed that the baffle spacing of 1.8 times the tube diameter gave the highest mass transfer. Similar observation was made by Gough *et al.* (1997) in their flow visualisation studies for the optimum of the flow patterns.

Ni et al. (1998a) carried out a symmetrical experimental investigation on the effect of baffle free area, baffle spacing and baffle thickness on mixing time in various batch oscillatory baffled columns. The free baffle area ratio was varied between 11 % to 51 %, and an optimum ratio of 20 to 22 % was recommended, which is smaller than 34 % that has been used in the past. A baffle spacing of 2 times tube diameter was found to be the optimum one for oscillating baffle configuration at the top of the column while 1.8 times tube diameter was identified as the optimum spacing for OBC with pulsing fluid mechanism at the base. Also thinner baffles favoured the generation of vortices, an optimum baffle thickness of 2 –3 mm was reported.

From the above discussion, a baffle spacing of 1.8 times tube diameter (72 mm), a free baffle area (α) of 21 % and baffle thickness of 3 mm was used throughout the work reported in this thesis.

2.1.4 AN OVERVIEW OF RESEARCH INTO OBTR

Over the last decade the OBTR has been applied to different process engineering applications. Heat transfer enhancement was reported by Mackley *et al.* (1990), who observed a sevenfold increase in the tube-side Nusselt number (relative to steady, unbaffled flow) in a tube subjected to low Reynolds numbers. Mackley and Stonestreet (1995) observed a 30-fold increase in the heat transfer when oscillation and baffles were combined together as compared to a steady flow unbaffled tube.

Hewgill *et al.*(1993) investigated mass transfer of oxygen into water in an oscillatory baffled column and observed a six fold increase in the mass transfer rate in comparison to a bubble column. Ni *et al.* (1995a) observed an 11% increase in oxygen mass transfer coefficient relative to a stirred tank. Ni et al. (1995b) extended the mass transfer study using yeast re-suspension and yeast culture in an OBTR bioreactor and a commercially available ST fermenter. The mean transfer coefficient, $K_l a$, in the former were on average 75% higher than those in the latter.

Finnigan and Howell (1989) improved filtration performance by a factor of around 3 when they incorporated baffles and pulsatile flow in a tubular ultrafiltration membrane unit. The improved filtration performance in yeast cell harvesting was also

reported by Howell *et al.* (1993). A 100% increase in the flux was obtained relative to the conventional technique with a reduction in fouling across the membrane surface. Ni and Mackley (1993) observed that the OBTR was much more energy efficient than the stirred tank reactor in a study of the reaction between sodium hydroxide and ethyl acetate in terms of conversion vs. power dissipation.

Mackley *et al.* (1993) successfully applied OBTR to keep sedimenting particles in suspension. This offers considerable potential benefit for liquid solid separation both in batch and continuous mode of operation. In a two phase system of oil and water, Zhang *et al.* (1996) showed that it is possible to control the mean droplet size and size distribution by varying the oscillatory conditions (amplitude and frequency). The continuation of Zhang's work was the application of a batch OBTR to suspension polymerisation of methylmethacrylate and greater controllability and repeatability on particle size were obtained (Ni *et al.* 1998, 1999, Zhang 1998). Inverse phase polymerisation of acrylamide was also carried out in a batch OBTR, Gaussian particle size distributions were obtained (Ni *et al.* 2001). The significance of those studies is that the Gaussian particle size distribution can be maintained over a wide range of mean particle size from 200 mm to 800 mm by varying oscillation conditions. This is an effective way to provide process intensification.

Suspension polymerisation processes have predominantly been operated batchwise in polymer industry. The ability of generating radial mixing in OBTR gives a unique form of control in respect of intensity of mixing, axial dispersion, drop size control and other transfer processes. This is ideal for suspension polymerisation application. The advantages for such operations are the reduction of waste, downtimes

and more consistent product quality. Until now there has been not much research in continuous suspension polymerisation, and this work is the prelude of the big picture at the Heriot-Watt University COBRA group and it evaluates, for the first time, OBTR operating continuously in terms of axial dispersion in a single phase and drop size distribution in a two phase system. The work provides the scientific knowledge and technical know-how to the mission of continuous suspension polymerisation in OBTR.

2.2 BACKGROUND OF SYSTEMS ANALOGOUS TO OBTR

This section is not intended as a comprehensive review of pulsed packed beds and reciprocating plate columns, but aims to highlight similarities with OBTR in respect of operations. It is divided into two sections, dealing respectively with the relevant literature on reciprocating plate column (2.2.1) and pulsed plate column (2.2.2)

Oscillatory flow has been around for a long time, Van Dyke (1935) was the first who applied pulsation to improve liquid-liquid efficiency. Generally there are two types of columns, the reciprocating plate column (RPC) which moves a set of perforated plates up and down the column and the pulsed sieve plate column (PPC) which pulses the liquid phase hydraulically by external means. There are a number of similarities between the behaviour of these and OBTR and some of the observations from those columns can probably be applied to the latter.

2.2.1 RECIPROCATING PLATE COLUMN (RPC)

RPCs are the most often used device for contacting immiscible liquids for separation processes and as such are well described by Long (1967). Karr (1959) developed a laboratory column. Since then several types of Karr RPC (KRPC) have been used world wide. Common features of RPCs are illustrated in Figure 2.1. The column shell is usually made from stainless steel or titanium on industrial scale while glass or plastic is used on laboratory scale. The plate stack is usually supported on a vertical shaft via a reciprocating scotch yoke driven by a geared – down electric motor. Typically the frequency can be in the range 0.5 to 5 Hz and the stroke is in the range 5 to 40 mm. The plates are usually made from metal or Teflon. Usually a gap of about 1–2 mm is provided between the outer edge of the plate and the column wall. Sometimes Teflon borders are provided on metal plates to reduce wall friction. The plates are usually placed at a distance of about 25 to 150 mm.

In the Karr column, the plate featured large diameter perforations, D_o between 10-16 mm and an open area fraction, α of about 0.6, as shown Figure 2.2. No downcomers were provided on the plate, since the open structure of the plate is sufficient for countercurrent flow. This type of RPC is operated only in the emulsion regime (high agitation rates). Simple but reliable procedures for design and scale-up from pilot plants have been established (Karr, 1971, 1976 and 1987). General applications of KRPC have been in copper extraction (Sharma and Baird, 1978), Penicillin extraction (Reschke and Schugerl, 1985) and extraction of products from fermentation broth (Karr *et al.* 1980). This type of column has been very popular in the U.S.A. and Europe. In the last few decades, much research has been carried

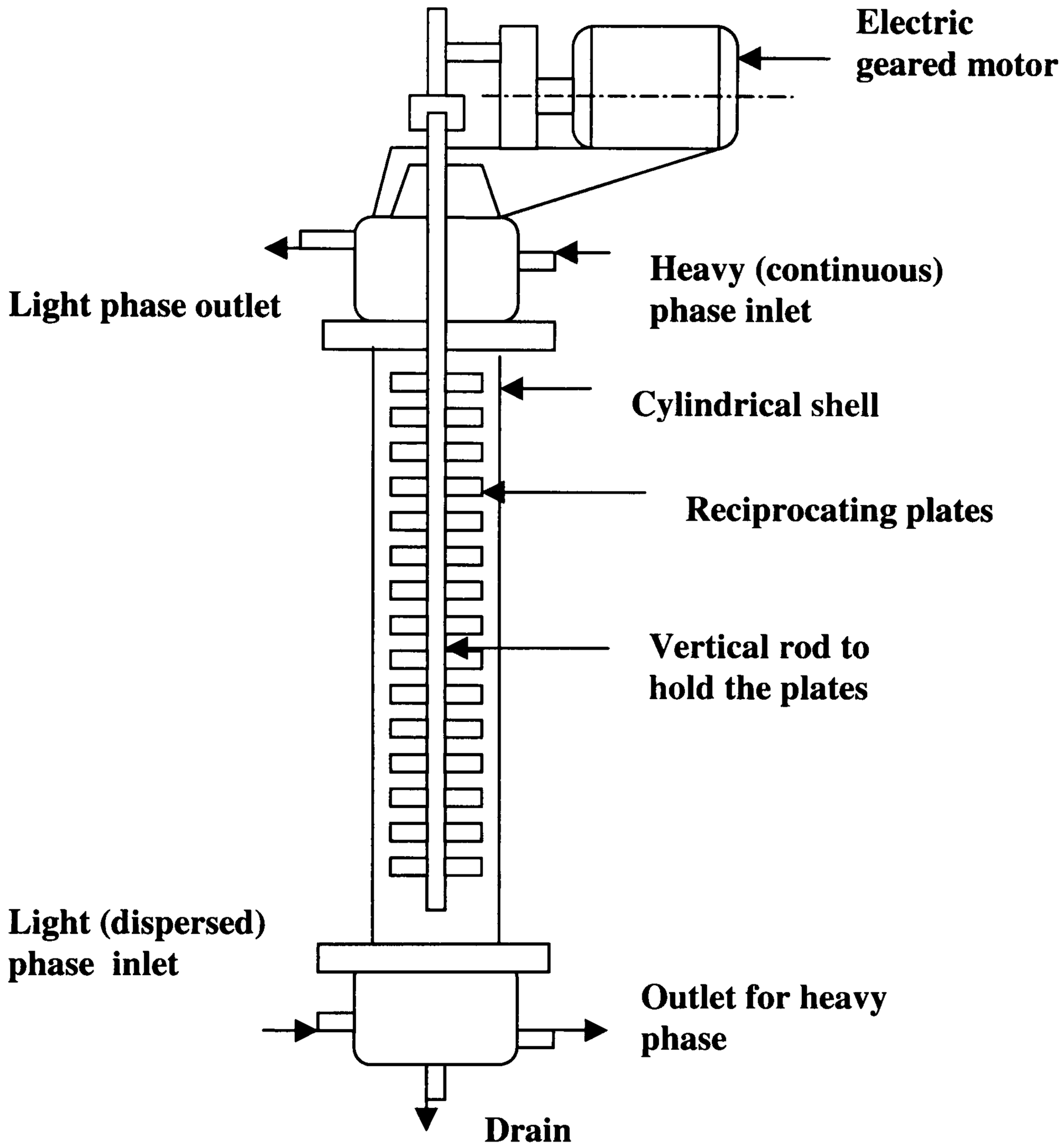

Figure 2.1. Reciprocating Plate Column

out on hydrodynamic characteristics of the KRPC in terms of axial mixing, drop hold-up, mean drop diameter and mass transfer, see for example, Baird and Lane (1973), Baird (1974), Hafez *et al.* (1979), Kim and Baird (1976a,b), Boyadzhiev and Spassov (1982), Rama Rao *et al.* (1983), Baird and Shen (1984), Resche and Schugerl (1985), Yang *et al.* (1986b), Karr *et al.* (1987), Baird and Rama Rao (1988), Vejkovic and Skala (1988) and Stevens and Baird (1990). Most of the research has been carried out in

diameters up to 150 mm. On industrial scale, columns up to 1.7 m in diameter have been used (Lo *et al.* 1991). In such large scale operations, doughnut-shaped baffles were inserted at intervals of the plate stack to reduce radial non-uniformities in the flow.

Prochazka and co-workers in the 1960s developed an RPC characterised by a perforated plate having less free area (Figure 2.2). The plate also has a downcomer to allow the continuous phase to flow through. The diameter of perforations ranged from 2 to 5 mm and occupied a fractional free area between 4 to 20 %. The fractional free area of downcomers was between 10 and 25 %. Depending on the application and requirement, the Prochazka RPC can be operated at different agitation speeds. The plates usually move in a uniform motion or with a 180^0 phase difference especially in large diameter columns. A plate spacing between 60 – 150 mm was usually employed. Several studies on axial mixing, drop size and hold-up have been reported (Nemecek and Prochazka, 1974, Jares and Prochazka, 1987 and Vohradsky and Sovava, 1990).

Two more plate configurations, shown in Figure 2.2, were also introduced, namely KRIMZ RPC and GIAP RPC. These RPC plates were characterised by rectangular punched perforations with the displaced metal strips remaining attached as inclined vanes (Godfrey and Slater, 1994, Lo *et al.* 1991). The purpose of the vanes is to enhance the radial motion as liquid passes through the perforations so as to reduce the axial mixing in larger diameter columns. The dimensions of the rectangular openings varied between 200 to 9800 mm^2 and the open area was about 45 %. Both the KRIMZ and GIAP plates had similar geometries, except for the segmental downcomers on the GIAP plates with open free area of 5 to 15 %. The plate spacing varied from 50 to 150 mm. These RPCs were operated at up to 3 Hz in frequency and 10 mm in amplitude,

and have been used in the USSR since the early 60s, most widely used in caprolactam production, mainly for the extraction of caprolactam. Industrial applications up to 1.6 m diameter have been documented. Extensive work on drop hold up and size, axial mixing and mass transfer has also been reported in the former Soviet Union (Godfrey and Slater, 1994).

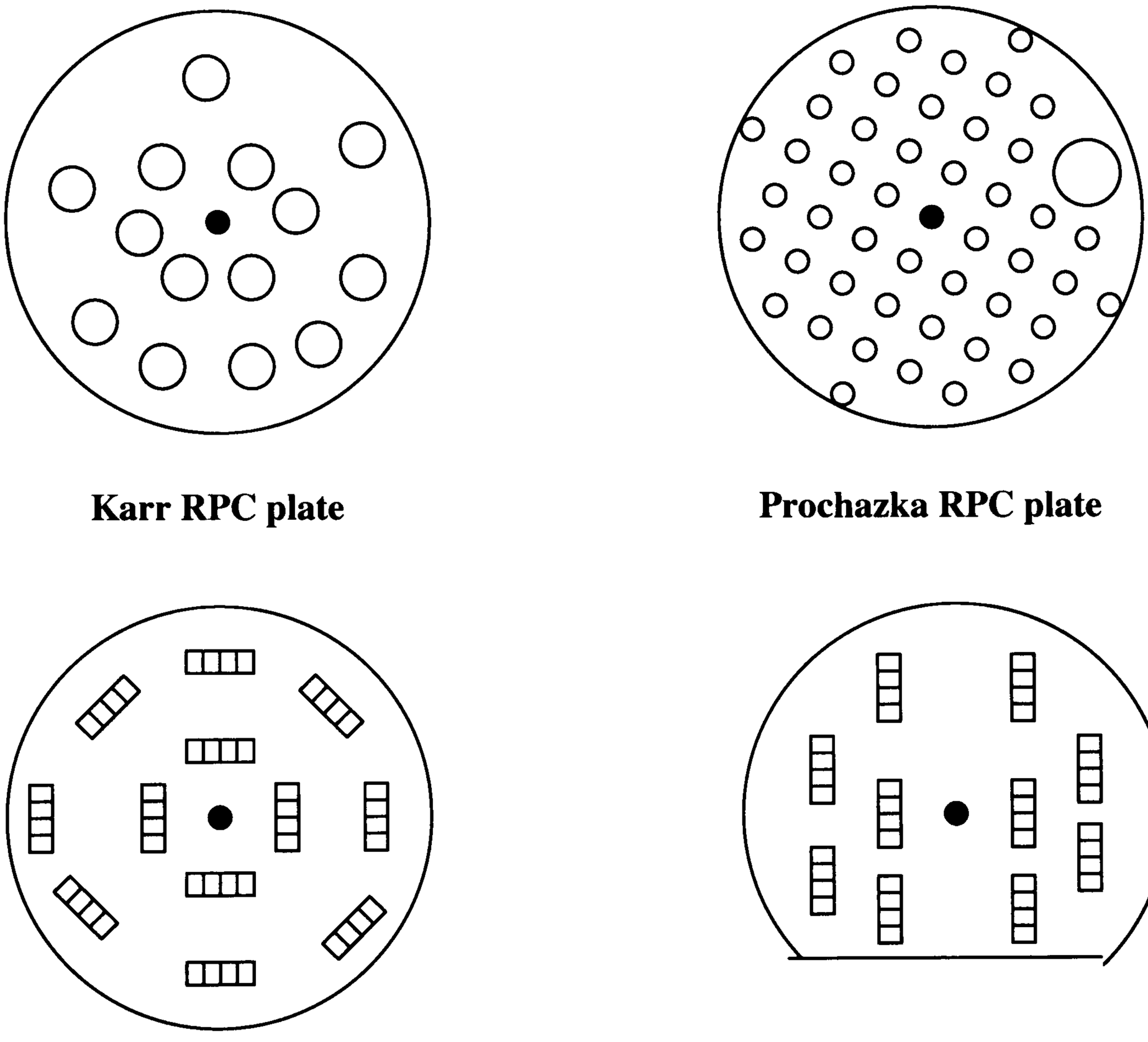

Figure 2.2. Types of RPC plates

2.2.2 PULSED SIEVE – PLATE COLUMN (PSPC)

The pulsed sieve – plate column consists of a cylindrical column, shown in Figure 2.3, equipped with horizontally installed sieve – plates without downcomers. Generally the sieve plates have cylindrical holes and a triangular pitch. For maximum performance, the plate geometry can be tailored for a particular process. Usually plates with hole diameters from 2 to 4 mm with free areas of 23 – 40 % were used, with 23 % used for high and 40 % for low interfacial tension systems. The plate material is usually stainless steel or plastic. When the plates are installed in the column, special attention has to be given to the clearance between the plate and the column wall. If this gap is very large, then it can lead to a significant increase in the back mixing of the liquid and hence lower the column efficiency. Optimum plate spacings, between 50 and 100 mm, are used, because larger plate spacings favour backmixing and reduce the column efficiency.

The pulses are introduced in the column by means of a pulsator (piston, bellows, air pump) located at the bottom of the column. The pulsing motion is usually sinusoidal but can also be triangular. The operating behaviour of a pulsed sieve – plate column can be controlled by changing the pulsation intensity, the product of pulsation amplitude and frequency, as this determines the energy input in the system. When the pulsing action is applied at the base of the column, the dispersed phase is forced through the plate perforations and the continuous phase flows downward on the downstroke. Thus the pulsing action disperses the dispersed phase into drops as it is forced through the plate perforations without the need of internal moving parts, which is an advantage over the reciprocating plate column (RPC).

The liquids are fed continuously to the column counter currently. The column also has settling zones both at the top and bottom, the dispersed phase rises through the column, coalesces in the upper settling zone and leaves the extractor at the top of the column, while the continuous phase leaves from the bottom. The dispersed phase is fed into the column through a distributor. The mean drop diameter of the drops entering the column should be larger than the mean drop size in the column, otherwise the column hydrodynamics would be influenced by the distributor and not the plates or the pulsation intensity.

Numerous investigators have carried out extensive research to study fluid dynamic characteristics of pulsed sieve-plate columns, for example, Sege and Woodfield (1954), Miyauchi and Oya (1965), Prabhakar *et al.* (1988), Sreenivasulu *et al.* (1997), Pietzsch and Blass (1987) and Kumar and Hartland (1986). Depending on the pulsation intensity, a pulsed sieve-plate column can operate in 3 different regimes: mixer-settler, dispersion or transition and emulsion regime. The mixer-settler regime occurs at low pulsation intensity, $x_o f < 15$ mm/s and is characterised by heavy (continuous) and light (discrete) phases forming discrete clear layers in each compartment (Prabhakar *et al.* 1988, Godfrey and Slater, 1994 and Sreenivasulu *et al.* 1997) and has rather large mean drop diameter, d_{32} . With further increase in the agitation rate, the energy input into the column increases, which in turn, increases the drop break-up thus reducing the mean drop diameter. The dispersed phase is uniformly distributed throughout the column and hence this regime is called the dispersion regime. With further increase in the agitation intensity, very small drops are produced which results in very narrow size distribution. Since small drops have low terminal velocity, the drop hold-up increases in the emulsion regime. If the pulsation intensity is increased beyond the emulsion regime, the column becomes unstable and results in

flooding. These regimes are also observed in reciprocating plate columns, Rama Rao *et al.* (1983).

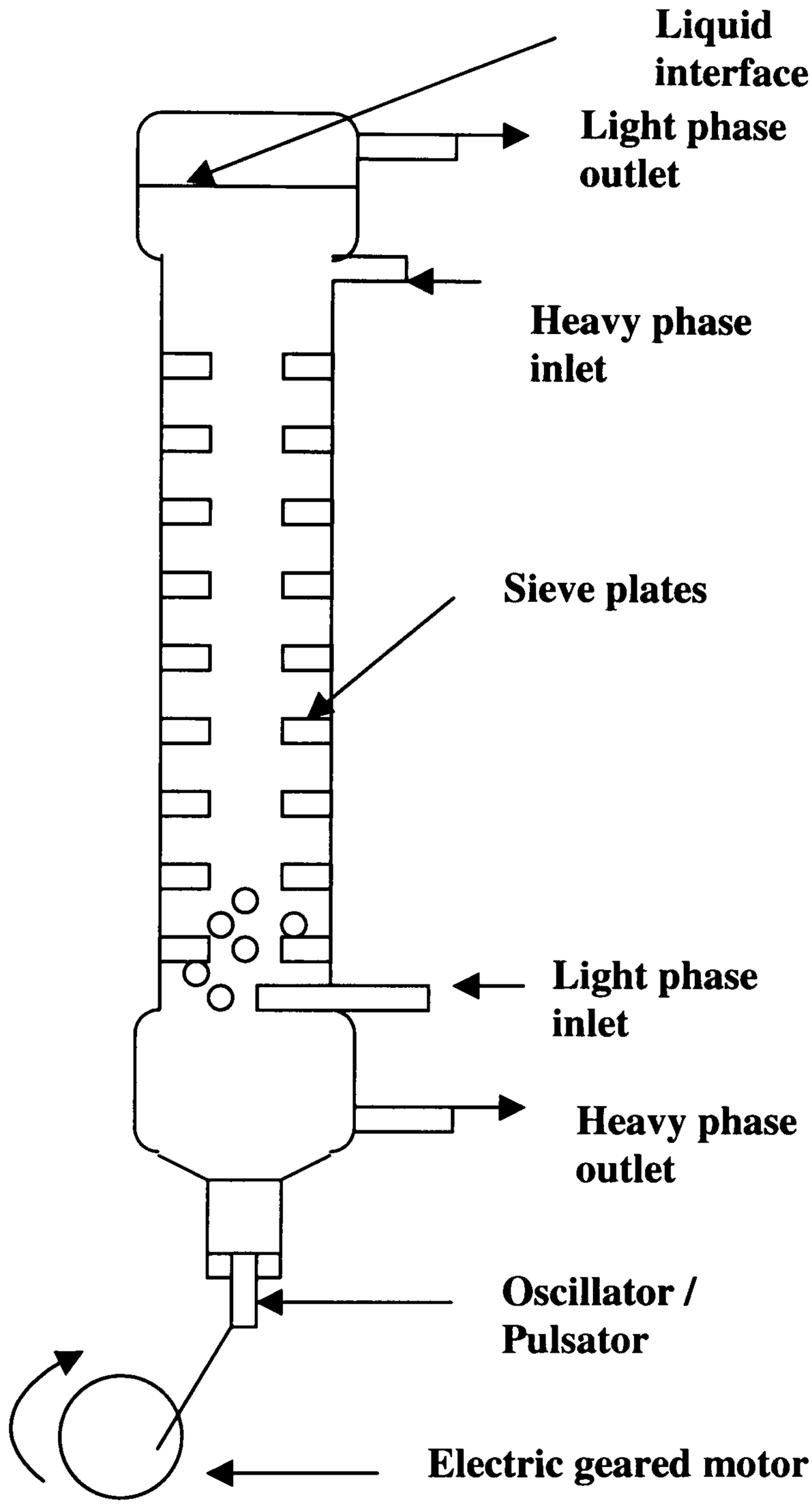

Figure 2.3. Schematic diagram of a pulsed sieve – plate column

2.2.3 MULTI-STAGE VIBRATIONAL DISK COLUMN (MVDC)

Multistage vibrating disk column (MVDC), as shown in Figure 2.4, can be considered as a modification of the reciprocating plate column. There is a characteristic difference between the MVDC and RPC; the RPC vibrates the perforated plates whose diameter nearly equals the internal column diameter, while the MVDC vibrates the disks placed at the centre of each stage in which the contents are vigorously mixed, thus promoting mass transfer between the phases. The disks can be vibrated by different mechanisms, e.g. crank mechanism, cam or electromagnet, resulting in different waveform. Tojo *et al.* (1975b) investigated different oscillation waveforms (trapezoidal, triangular and square) and observed that the trapezoidal vibration produced the greatest effect on the mass transfer rate. The open area for flow depends on the ratio of disk to column diameter, $\frac{D_d}{D}$; an optimum value of 0.75 – 0.8 for disk diameter and $\frac{D_o}{D}$=0.5 – 0.7 for hole diameter of the partition plate and $\frac{H}{D} \approx 1$ for stage height has been recommended by Tojo *et al.* (1975a). This type of column has primarily been used as a gas-liquid contactor (Miyanami *et al.* 1973, 1978 and Tojo *et al.* 1979). Liquid-liquid dispersion characteristics have also been investigated by studying axial mixing (Miyanami *et al.* 1973), drop size distribution and hold-up (Miyanami *et al.* 1975).

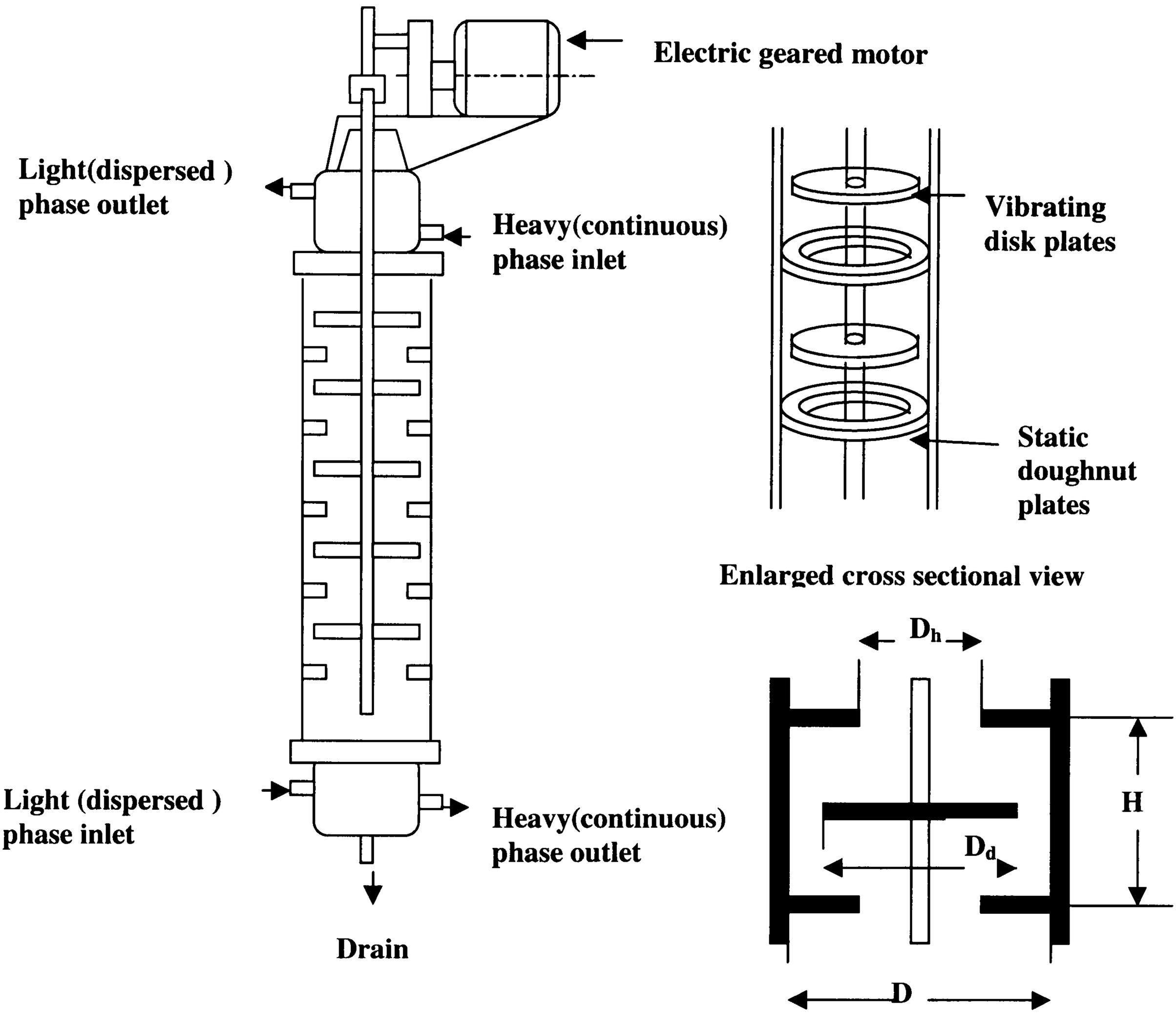

Figure 2.4. Multistage vibrating disk contactor (MVDC), Tojo *et al*. (1980)

Although a number of similarities exist between various RPCs, PSPCs and OBTR, the major difference lies in the plate design, and the consequence of this leads to significant different flow characteristics, and behaviour of reactors. It is therefore essential to characterise an OBTR in context of continuous operation with a direct application to continuous suspension polymerisation.

CHAPTER 3

CHARACTERISATION OF THE VERTICAL OBTR

This chapter describes the characterisation of a vertical OBTR in terms of a single phase flow study and a two flow case.

3.1 SINGLE PHASE FLOW STUDY

3.1.1 INTRODUCTION

Axial dispersion is a measure of the rate at which an inert tracer spreads axially along a tube such as in an OBTR. It can be a measure of macro-mixing (e.g. mechanical mixing of the bulk fluid) or of micro-mixing (e.g. molecular diffusion) or most commonly a combination of both types of mixing. Quantification of axial dispersion is of particular interest for OBTR since the results can tell us the extent of non-ideality of the reactor deviated from plug flow, and the results can also be used to predict residence time distribution for both large and small reactors. The single phase flow study is the stage one characterisation of the vertical OBTR, and this Chapter deals in more detail with the experimental facilities, measurement and modelling of axial dispersion and is divided into three parts. The first presents the literature available on experimental techniques of axial dispersion measurement and on the models that have been used to quantify axial dispersion. Emphasis is placed upon the diffusion model, or the plug flow with axial dispersion model (model adopted in this thesis). The second part describes the set-up of the experimental measurement and treatment of the experimental raw data acquired for axial dispersion measurements. In part three, the

experimental results and evaluation of axial dispersion coefficient are presented and discussed.

3.1.1.1 EXPERIMENTAL STUDIES OF AXIAL DISPERSION

The earliest observation of oscillatory flow in a baffled tube took place in the early 1980s in the University of Cambridge as part of a 4th year research project, which was later published as Brunold *et al.* (1989). Using a manometer-style 46 mm diameter tube containing annular baffles they observed the flow over a large range of amplitudes created by unforced simple harmonic oscillation of the fluid following an initial height displacement on one side of the U-shape tube. They estimated viscous and eddy dissipation energy losses in the flow by measuring damping. They also demonstrated that 1.5 tube diameter was a good compromise between excessive channelling of the flow (1 tube diameter) and insufficient vortex interaction (2 tube diameter spacing).

In a subsequent 4th year research project in 1984 Dickens and Williams measured residence time distributions (RTDs) in a 23 mm diameter baffled tube with an oscillatory flow superimposed upon a net flow. They injected a potassium chloride (KCl) solute tracer into the baffled tube inflow and placed a conductivity cell at the outflow and measured RTDs for a range of oscillatory amplitudes. Their findings were subsequently published as Dickens *et al* (1989). They quantified dispersion using a diffusion model and assumed a perfect pulse of tracer: the variance of the resulting conductivity tracer for each experiment was used to calculate an inverse Peclet number ($Pe = \frac{uL}{E}$) using the result derived by Levenspiel and Smith (1957),

$$\sigma^2 = 2\left(\frac{E}{uL}\right) + 8\left(\frac{E}{uL}\right)^2 = 2\left(\frac{1}{Pe}\right) + 8\left(\frac{1}{Pe}\right)^2 \qquad (3.1)$$

where σ^2 is the calculated variance of the exit concentration profile, E is the axial dispersion coefficient ($m^2.s^{-1}$), u is the mean net flow velocity ($m.s^1$) and L is the distance between two measuring points (m). They discovered a minimum value of the inverse Peclet number of about 0.025 which compared closely with the value that would be obtained using a simple tanks-in-series model (Levenspiel, 1999), where N is the number of perfectly-stirred tank if it was assumed that each inter-baffle cavity represented a perfectly-stirred tank,

$$\sigma^2 = \frac{1}{N} \qquad (3.2)$$

and since the value of $\frac{E}{uL}$ was much less than one,

$$\frac{E}{uL} = \frac{1}{2N} \qquad (3.3)$$

This important result established that OBTR could be used as a method for producing tightly controlled RTDs in a tubular reactor with only weak dependence on

the net flow rate through the tube and apparently mimicking the effect of having many continuous stirred tank reactors in series.

Following on from this discovery, a detailed study of axial dispersion was made by Howes (1988) in his Ph.D. thesis, which included both experimental results and theoretical modelling. Howes also used KCl solution as the tracer and used conductivity cell probes to measure tracer concentration. The assumption was made that the measured conductivity was the average value of the concentration in the inter-baffle cell containing the conductivity cell probe, but the author noted that this gave poor results when there were large concentration differences within the cell and that the range of experiments were limited by the shortness of the tube. Howes (1988) analysed the concentration data with a tanks-in-series with back-mixing model; the model assumed that each inter-baffle cavity was a perfectly mixed tank with flow to both the upstream and downstream neighbouring tanks. He presented an algorithm for calculating a backmixing coefficient and the model could be fitted to give a reasonable agreement with his experimental dispersion data. Howes varied Re_o, St and Re_n, similarly to Dickens *et al.* (1989) and found that imposing the oscillatory flow upon the steady net flow could substantially reduce the axial dispersion, which could be minimised for a given net flow rate by adjusting the oscillation conditions.

Mackley and Ni (1991) injected NaCl solution as a tracer in a 25 mm diameter baffled tube and measured the changing concentration using point conductivity probes which drew off a small volume of fluid and had a reported resolution of about 1 mm^3. The spatial resolution of the probes allowed Mackley and Ni to determine differences in the dispersion as a function of radial position and they concluded that OBTR greatly

enhanced the radial distribution of the tracer. The oscillation used by Mackley and Ni (1991) was driven by a pneumatic cylinder at each end of the closed tube, giving a square displaced wave form. This unfortunately leaves uncertainity as to the peak velocity (which in theory must have been infinite !).

A similar experiment was performed by Mackley and Ni (1993) on a much longer tube of about 6.3 m containing approximately 160 baffles including U-bends. This extra length allowed measurement of the dispersion in the baffled tube as a function of net flow Reynolds number without oscillation; a minimum value in the diffusion coefficient was observed for a net flow Reynolds number of about 400. They also reported an experiment using a bundle of five parallel 25 mm diameter tubes to demonstrate a potential method for scale-up.

Smith (2000) investigated the scale-up in OBTR by considering the effect of column diameter on axial dispersion and observed a linear dependence, $E \alpha d$. Ni *et al.* (2001a,b) introduced the concept of a hydraulic diameter that allowed the axial dispersion coefficients for various plate geometry and scales to be related in this way, so that the mixing characterisation in oscillatory baffled tubes and other pulsed flow devices can be correlated on a single linear basis. They also reported the influence of tracer density on axial dispersion in a 50 mm diameter batch oscillatory baffled column and observed that for density of the tracer solution from 1.0 to 1.5, the axial dispersion showed an increase between 2 and 269 %.

3.1.1.2 IN SYSTEMS ANALOGOUS TO OBTR

Considerable amount of information is available in the literature on single phase axial dispersion in the reciprocating plate column (RPC) and the pulsed plate column (PPC) over a range of operating parameters and a brief summary of the work carried out by different investigators is presented in a concise form as far as it is relevant to this investigation.

Axial dispersion has been found to increase with the oscillation velocity expressed as $x_o f$. Several researchers, such as, Kim and Baird (1976a,b), RamaRao *et al.* (1983) and Stevens and Baird (1990), have observed that the amplitude, x_o has stronger effect than f, while Lounes and Thibault (1996) observed the opposite effect in a 101 mm RPC, i.e. $E \propto x_o^{0.756} f^{1.066}$. Kim and Baird (1976a) found that for single phase operation, the dispersion varied linearly with the frequency and approximately as the 1.74 power of the amplitude, i.e. $E \propto x_o^{1.74} f$. The higher power effect of x_o was similar to that reported by Baird (1974) where $E \propto x_o^2 f$ for perforated plates in a 5 cm RPC and was similar to that by Godfrey *et al.* (1988) in a pulsed sieve plate column. However, Hafez *et al.* (1979) studied axial mixing in a 150 mm Karr type column for different plate types and arrangements and found axial dispersion coefficient to increase linearly with respect to the product, $x_o f$, in the well–agitated regime. Baird and Rama Rao (1988, 1998) reported a similar linear dependence in a 5 and 15 cm reciprocating plate bubble columns respectively. Nabli *et al.* (1997) from their numerical studies on a 288 mm diameter pulsed extraction column reported that for small values of x_o/H, e.g. 0.5, axial dispersion coefficient varied linearly with the oscillation velocity, however for higher values of x_o/H, a complex relationship was obtained between E and x_o.

Dispersion studies were carried out by Miyauchi and Oya (1965) in 32 and 54 mm diameter pulsed perforated – plate columns. They reported a linear variation of the continuous axial phase dispersion E with x_o and f. Similar correlation was proposed by Miyauchi and Vermeulen (1963) at higher agitation rates. A linear dependence on amplitude and frequency was also reported by Kagan *et al.* (1973) in 56 mm and 300 diameter pulsed plate columns. A varying dependence of axial dispersion coefficient E on $x_o f$ to $x_o^{1.5} f$ was observed by Ingham *et al.* (1995) in their single phase axial mixing studies in pulsed sieve plate liquid - liquid extraction columns for column diameters over the range 40 to 152 mm.

On the effect of continuous phase velocity, Kim and Baird (1976a) reported no significant effect of the liquid flow rate on E, and was in agreement with the observations of Godfrey *et al.* (1988), Ingham *et al.* (1995) Baird (1974), Hafez *et al.* (1979), Baird and RamaRao (1988, 1998), RamaRao and Baird (2000). This is because usually in a pulsed application the net flow velocity is an order of magnitude less than the velocity due to pulsation.

In conclusion, the axial dispersion coefficient is strongly influenced by the oscillation condition in both RPC and PPC.

3.1.2 EXPERIMENTAL SET UP

3.1.2.1 THE OSCILLATORY BAFFLED TUBE REACTOR

The OBTR was designed and fabricated in-house, operated vertically as shown schematically in Figure 3.1. It consisted of 14 QVF glass tubes, each of 40 mm in diameter. The first tube was 1 meter in length while the remaining tubes were each 1.5 m long. These tubes were connected by U-bends, each about 0.35 m in curvature length, as shown in Figure 3.1. The straight sections and bends formed a single flow path of about 25 m. A non-return valve, NRV1, was used in the flow inlets in order to reduce any propagation of oscillation upstream. A self-priming SP series LOWARA centrifugal pump was used for pumping water continuously through the system. It was a close coupled pump with a liquid side channel and a star impeller, which is designed to remain primed even when the suction line is not filled with water. It had a nickel plated brass impeller housed between two brass wear plates in the pump body to prevent jamming due to oxidation. The flow rate was controlled by means of rotameters, R1 and R2, (KDG Mobrey 2000) and was varied between 0.45 – 1.8 l/min., which gives a residence time from 30 to 60 minutes. A Cole Palmer variable-flow drive gear pump (Model no. P-75225-05, CP Instruments Co Ltd.) was used to pump the dispersed phase (silicone oil) into the system. It had a single turn potentiometer for speed control, which produces a flow rate in the range of 2.5 to 85 ml/min. In this study the flow rate of oil was fixed at 45 ml/min. There are three measuring ports downstream of the injection port along the length of the tube, as marked in red in Figure 3.1.

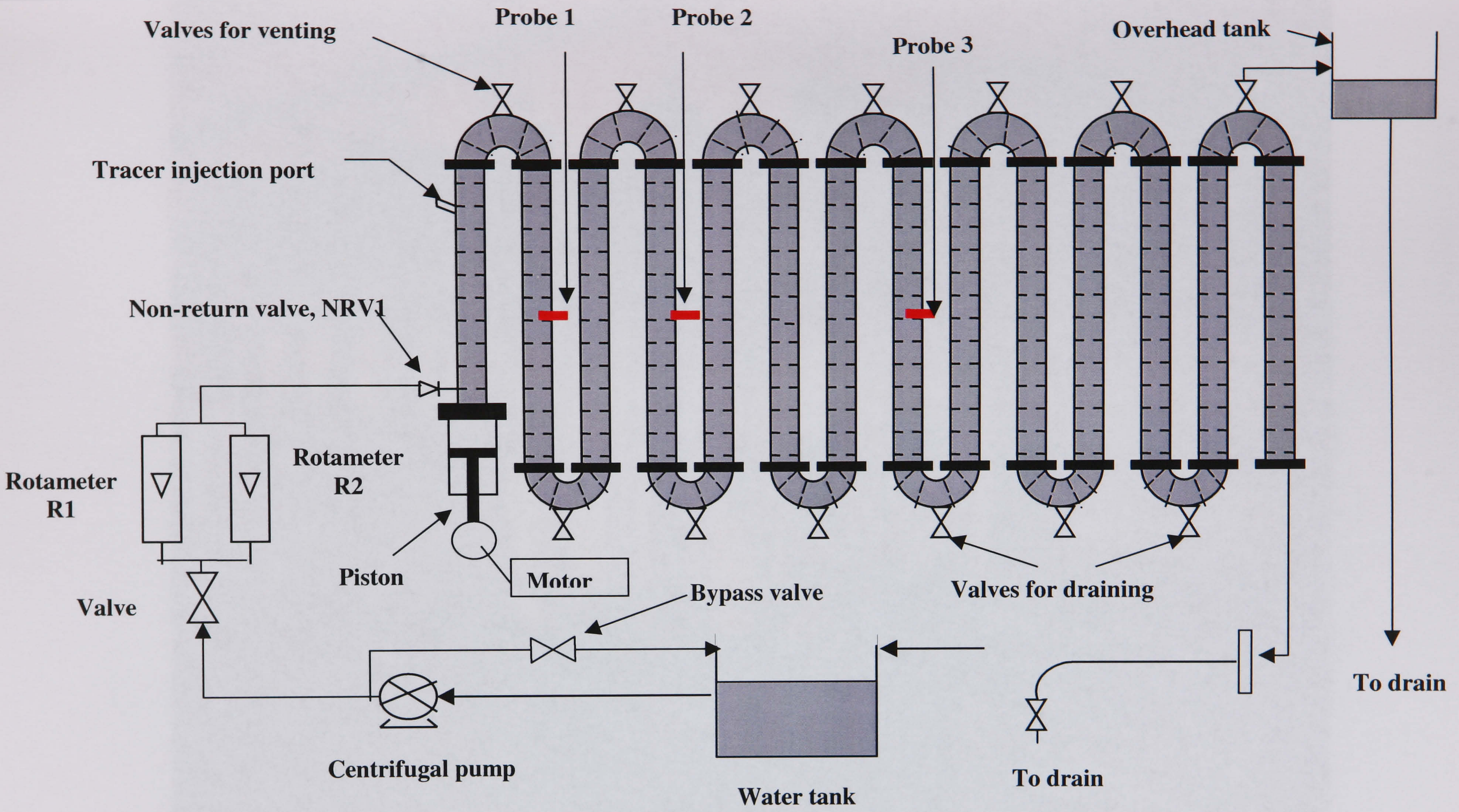

Figure 3.1. Schematic diagram of the vertical OBTR system for single phase investigation

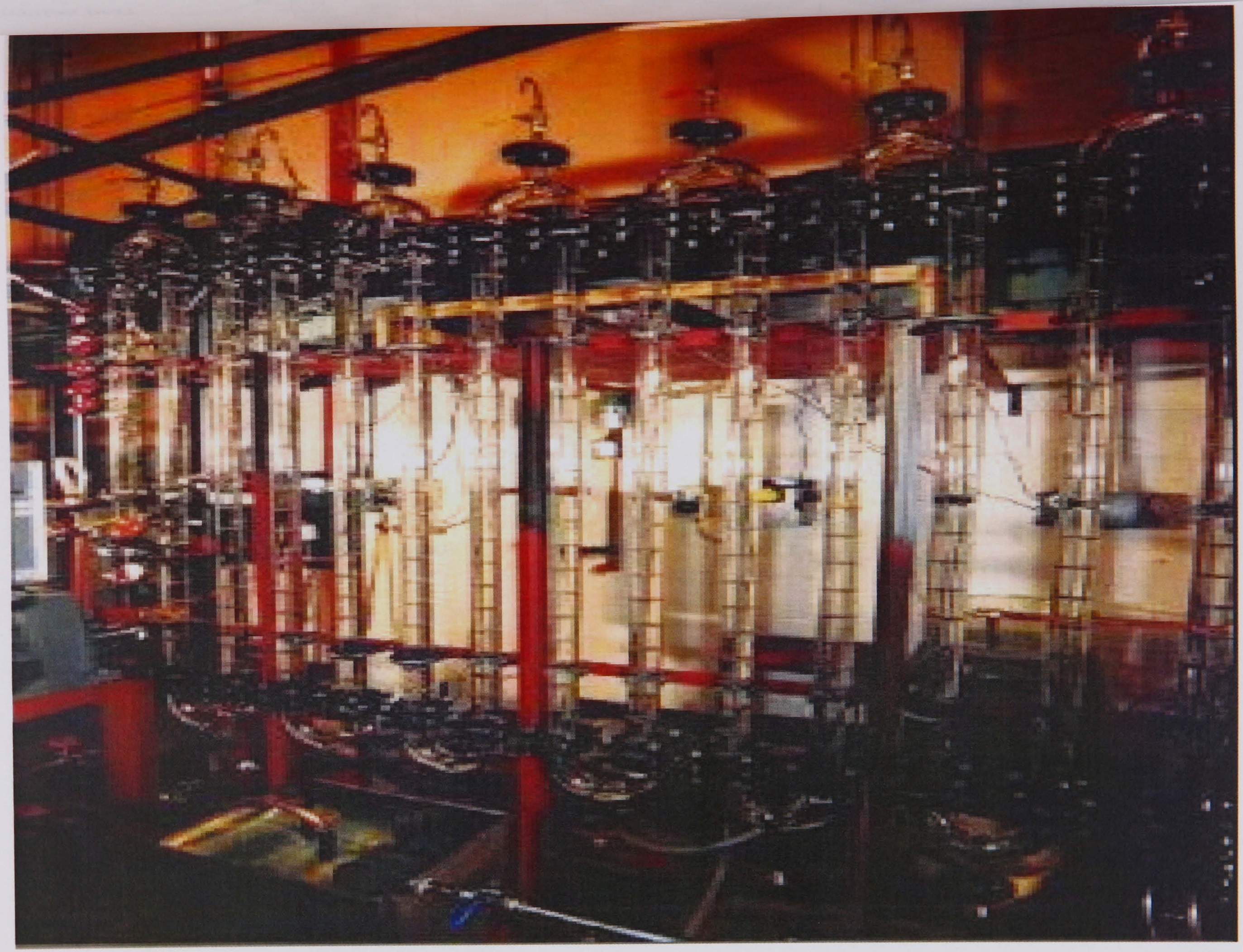

PLATE 1. VERTICAL OSCILLATORY BAFFLED TUBULAR REACTOR

3.1.2.2 BAFFLES

Orifice baffles as in Figure 3.2 were used. The baffles were made of stainless steel 316 and were 38 mm in diameter and 3 mm in thickness. The orifice diameter is of 18 mm, giving a free area ratio, α, of 21%. They were designed to give a 'push fit' seal when placed inside the tube. The baffles were supported by two 3 mm diameter longitudinal rods. The baffle spacing, *H*, used was 1.8 times the tube diameter, *D*. Baffles are periodically placed along the length of the system including bends. There were total of 346 baffles.

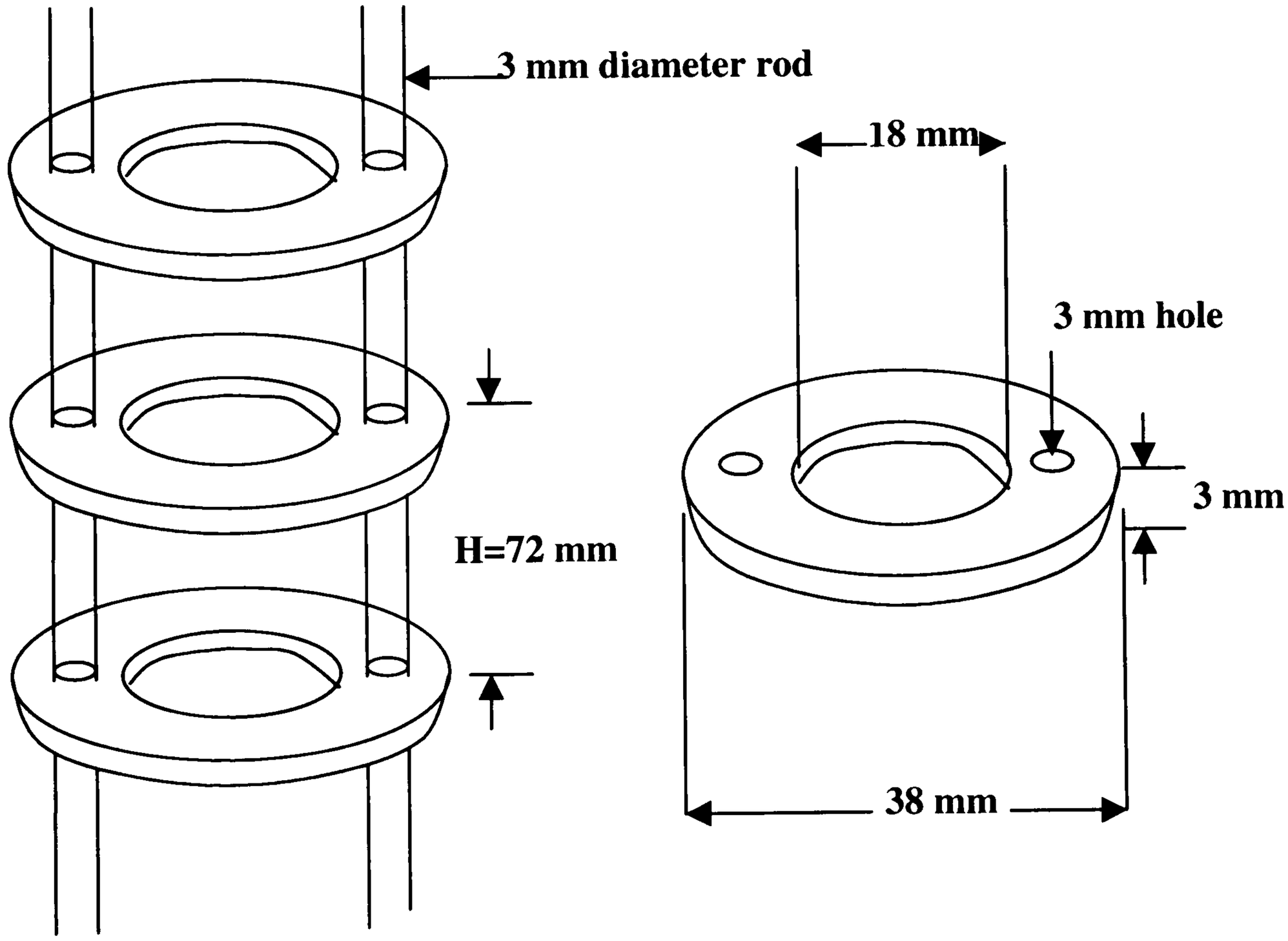

Figure 3.2. Orifice baffles

3.1.2.3 THE OSCILLATION UNIT

The oscillation unit consisted of a stainless steel piston, a NORD helical geared motor linked with a NORDAC vector AC frequency inverter. Prior to the experiments calibration was done to correlate the amplitude of the piston displacement with that of the fluid and is given in Figure 3.3. In later data analysis, the fluid oscillation amplitudes were used. A frequency range of 0-4 Hz can be achieved along with oscillation amplitude of 0 to 20 mm (centre to peak). The frequency was achieved by changing the inverter frequency and the amplitude by adjusting the off-centre positions of the rod linking the piston and the drive unit.

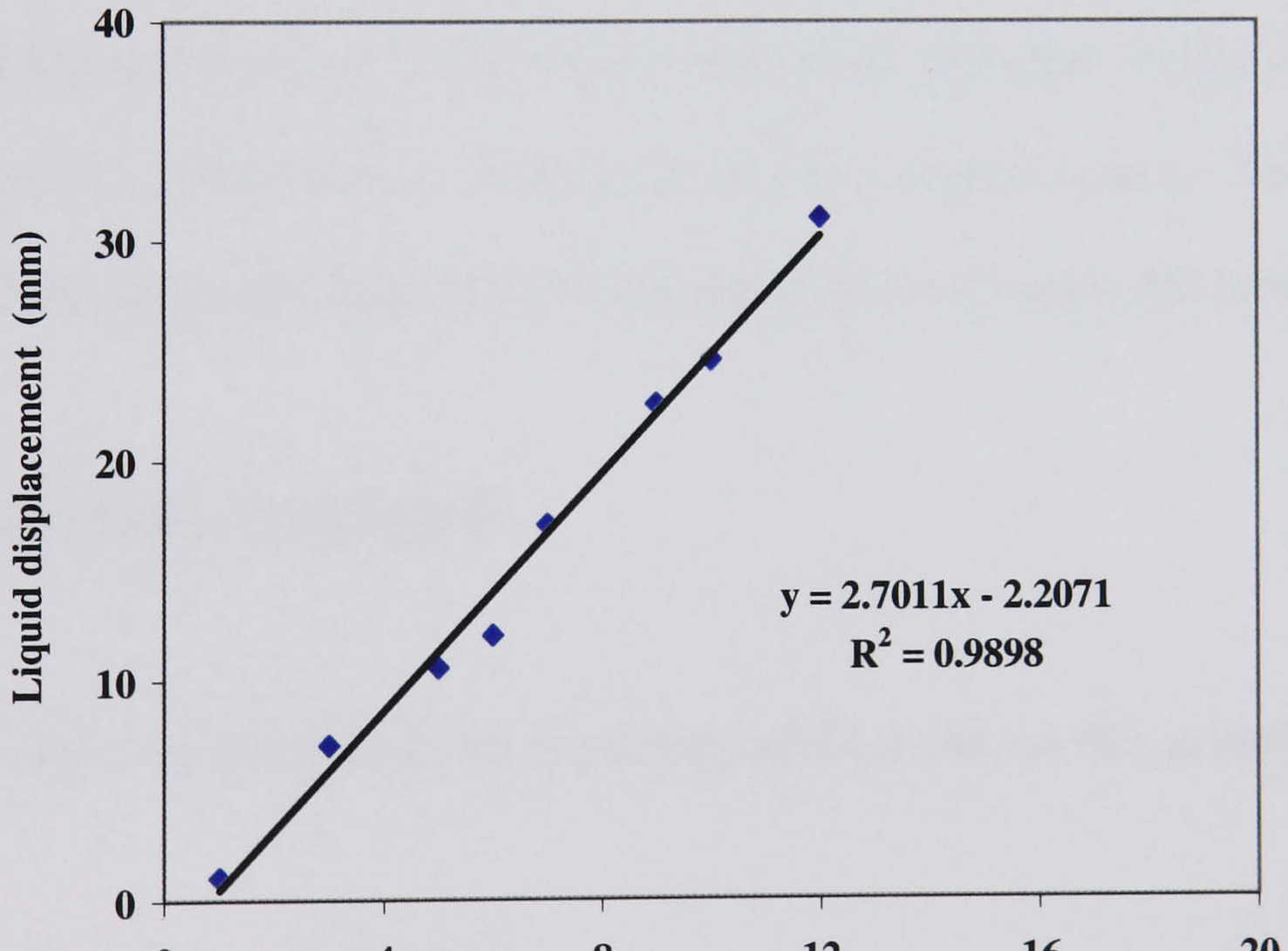

Figure 3.3. Calibration graph for piston

3.1.3 EXPERIMENTAL PROCEDURE

The tracer method was employed to measure the residence time distribution (RTD) of the tracer concentration. Potassium nitrite (KNO_2) was used as the tracer, 20 ml of 40 g/l. of potassium nitrite tracer solution was rapidly injected into the continuous phase through the injection port as shown in Figure 3.1 and its concentration was monitored at three locations downstream. The data from the conductivity probes was continuously logged on to a PC and the variation of the tracer concentration displayed on the screen with help of a "Logger Pro" software. The probes were connected to the PC through an universal lab interface (ULI) with 9V power supply and a serial interface cable. This interface is controlled by the software and converts the signals from the probes to a form that a computer can read. The data were collected in a real time mode and the sampling speed can be varied with the help of the software. In this investigation data were typically sampled at a fixed speed of 120 samples/minute. The plug flow with axial dispersion model was applied to calculate the axial dispersion coefficient.

3.1.3.1 OPERATING VARIABLES

The following summarises the operating variables used in this investigation:

Oscillation amplitude, x_o = (0-12) mm

Oscillation frequency, f = (0-3) Hz

Oscillation velocity, $x_o f$ = (0-36) mm/s

Oscillatory Reynolds number, Re_o – (0-9036)

Continuous phase flow rate, u_c = (0.5–1.9) l./min

Net flow Reynolds number, Re_n = 260-1024

3.1.3.2 PROBE CALIBRATION

The Vernier Conductivity Probes (VCP) were used to measure concentration of tracer in the system. Before calibrating the probe, it was made sure that the probe surface was free of residue by dipping it in distilled water for about 5 minutes and then dried. The conductivity probe was then connected to one of the ports of the Vernier interface box and was calibrated by using the standard two–point method, where distilled water corresponds to a zero calibration point and a solution of 1g/l of KNO_2 refers to the maximum point.

3.1.4 RESULTS AND DISCUSSIONS

3.1.4.1 EFFECT OF OPERATING PARAMETERS ON RESIDENCE TIME DISTRIBUTION

Figure 3.4 shows one of the typical concentration profiles obtained at a net Reynolds number of 469 superimposed with an oscillation amplitude of 12 mm and an oscillation frequency of 3 Hz. It can be seen that the concentration curve of the probe 1 responded first as it was located nearest to the injection. This was then followed by probes 2 and 3 at about 5 and 13 minutes later post to the tracer injection. From Figure 3.4, it is observed that the RTD curves were well-defined, narrow and essentially of a Gaussian form. The profiles of the RTD curves show that a near to plug flow characteristic has been achieved in the vertical OBTR system. The RTD responses illustrated here are well in line with the previous studies as mentioned earlier.

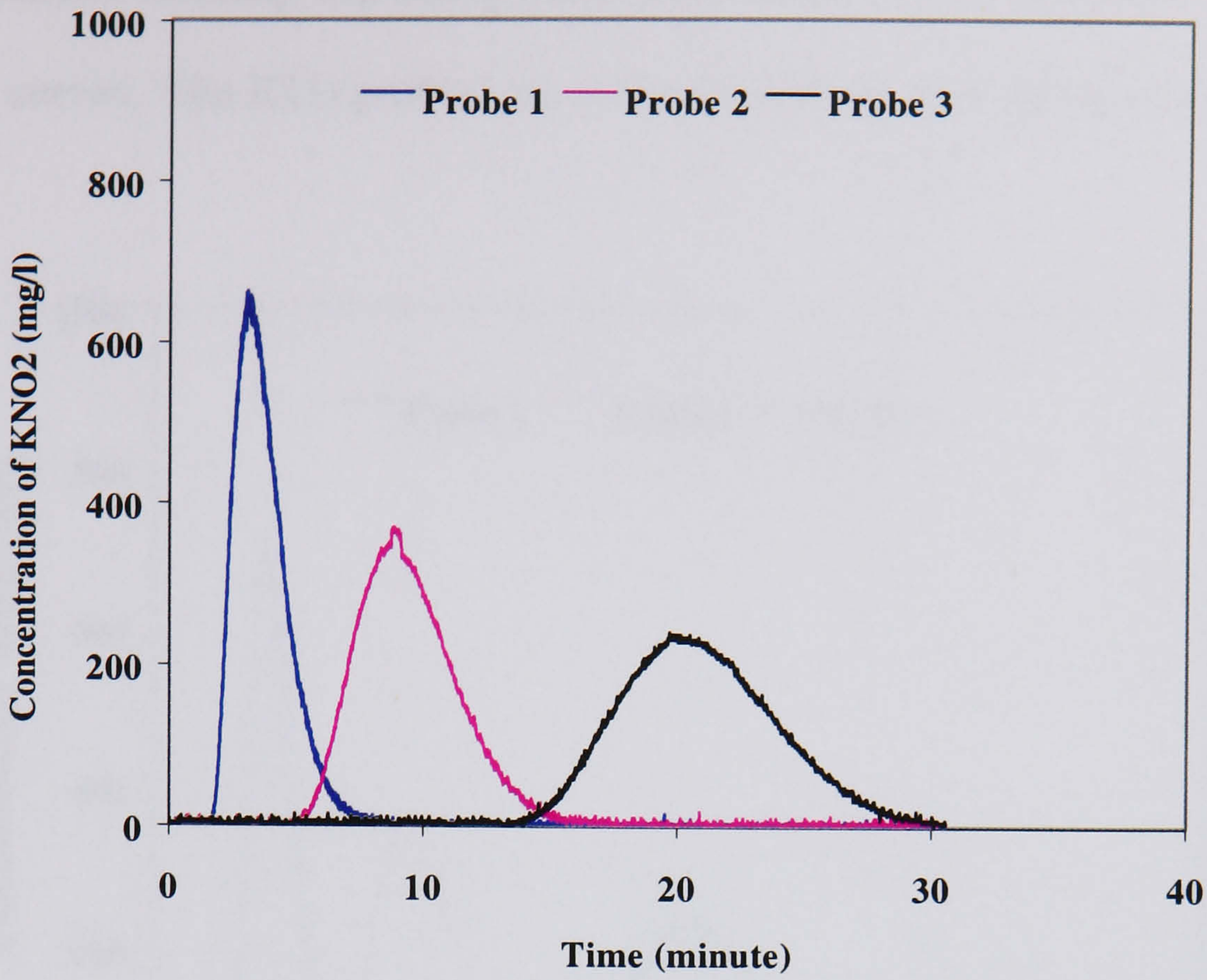

Figure 3.4. Concentration measurements, Re_o = 9036 (12 mm, 3 Hz), Re_n = 469

The effect of oscillation conditions on the RTD characteristics was examined by varying either the oscillation amplitude or frequency while keeping the other operating conditions constant, Figures 3.5-3.9 show the RTD profiles. The effect of oscillation amplitudes on RTD was studied at a fixed oscillation frequency of 3 Hz and at a fixed net flow Reynolds number of around about 500, while varying the amplitude from 12 mm (Figure 3.4), 10 mm (Figure 3.5) to 8 mm (Figure 3.6) to 6 mm (Figure 3.7). Practically it was difficult to keep the net flow rate absolutely constant due to the presence of fluid oscillation, as a direct result, there is a 10 % discrepancy in the flow rate settlement. It can clearly be seen from these Figures that the symmetrical and well defined RTD curves are identical to that shown in Figure 3.4, and the increase in the oscillation amplitude seems to slightly broaden the RTD profile. Similarly the effect of oscillation frequency on RTD is shown in Figures 3.9, 3.8 and 3.4 for 1, 2 and 3 Hz, respectively at a fixed oscillation amplitude of 12 mm. It can be noted that the RTD curves become broader with the increase of the oscillation frequency. This is expected,

as the oscillation intensity increases, more axial dispersion is expected, hence more broad RTD curves. The RTD profiles are still well-defined, symmetrical and narrow.

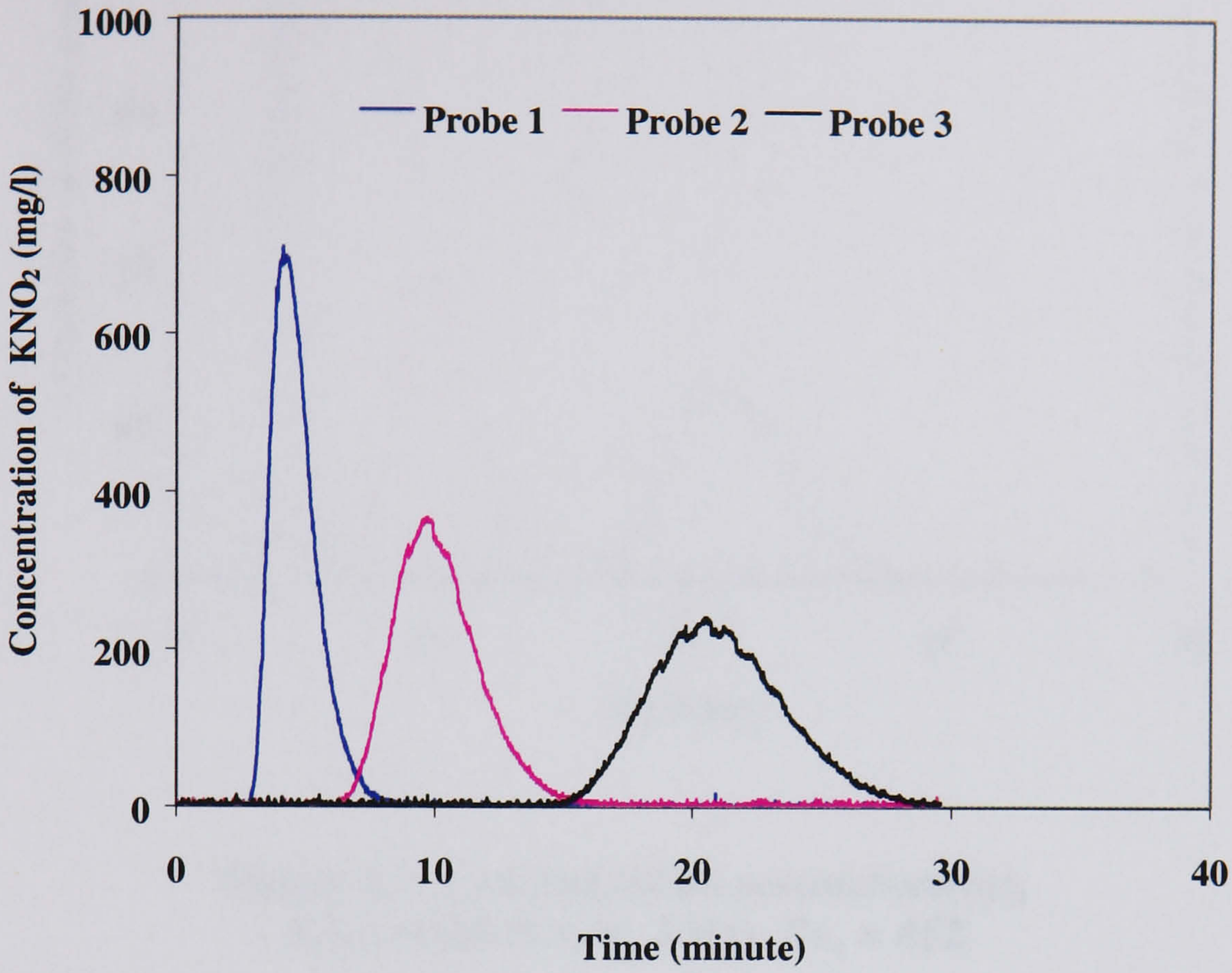

Figure 3.5. Concentration measurements, Re_o = 7531 (10 mm, 3 Hz), Re_n = 452

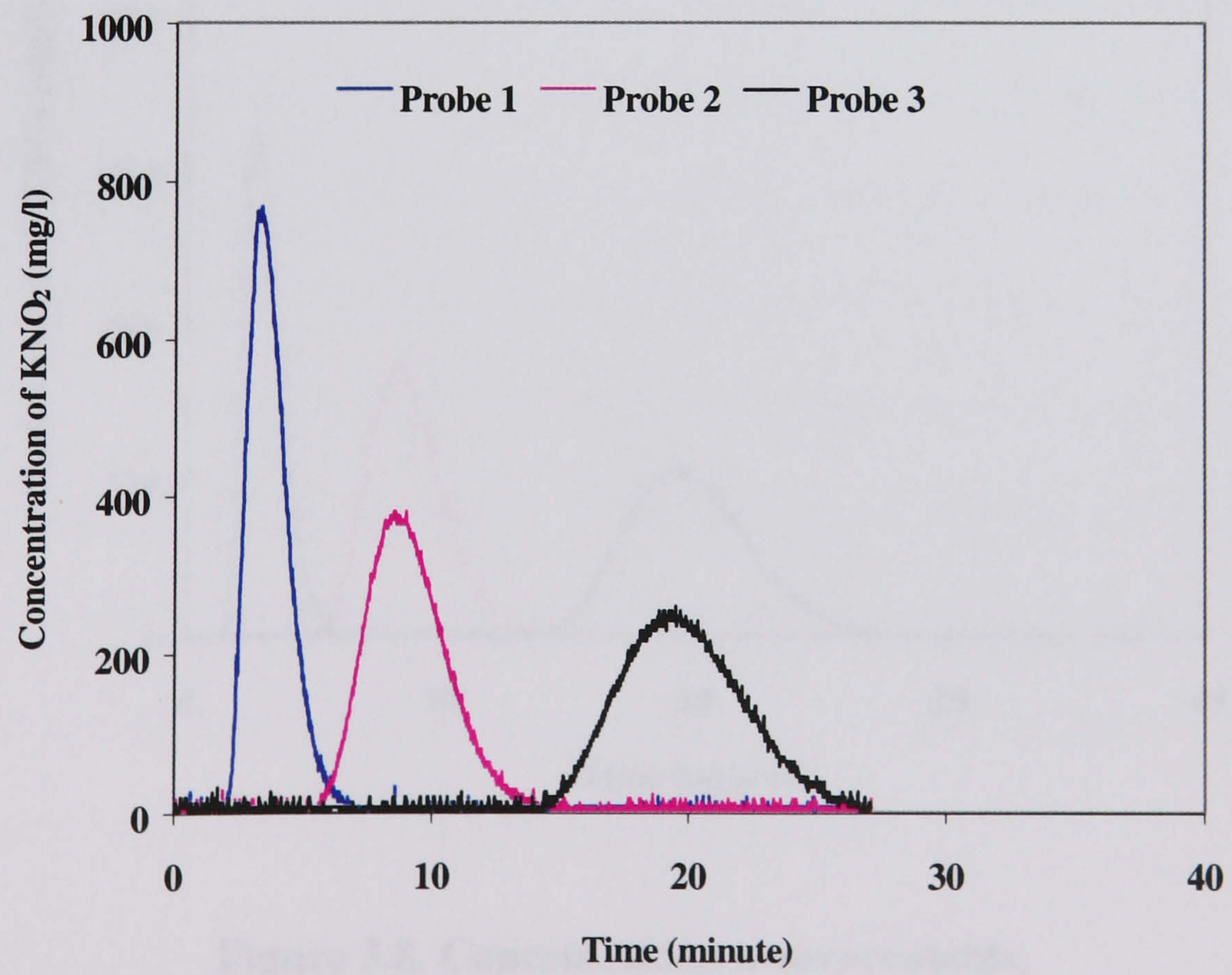

Figure 3.6. Concentration measurements, Re_o = 6024 (8 mm, 3 Hz), Re_n = 490

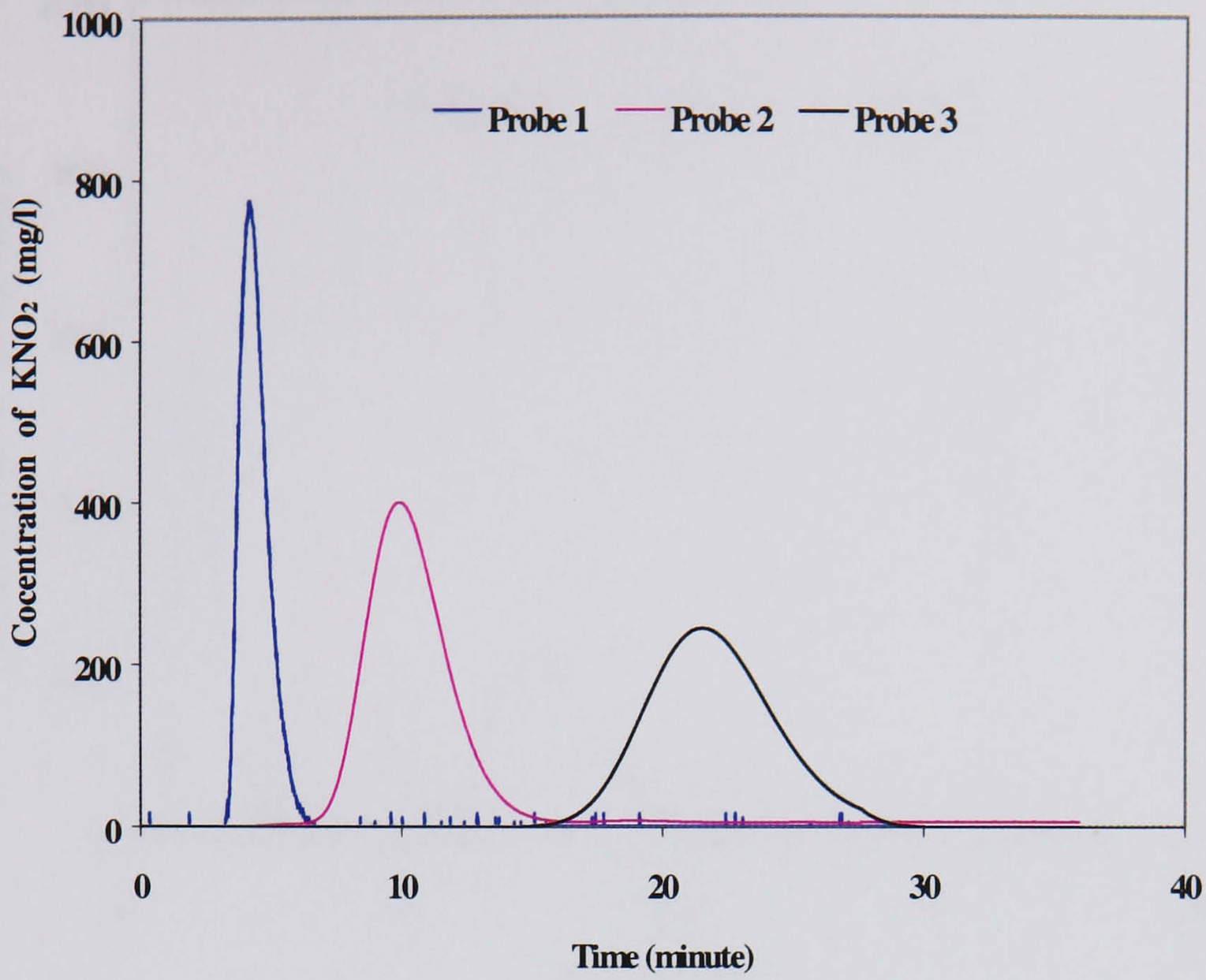

Figure 3.7. Concentration measurements, Re_o = 4518 (6 mm, 3 Hz), Re_n = 452

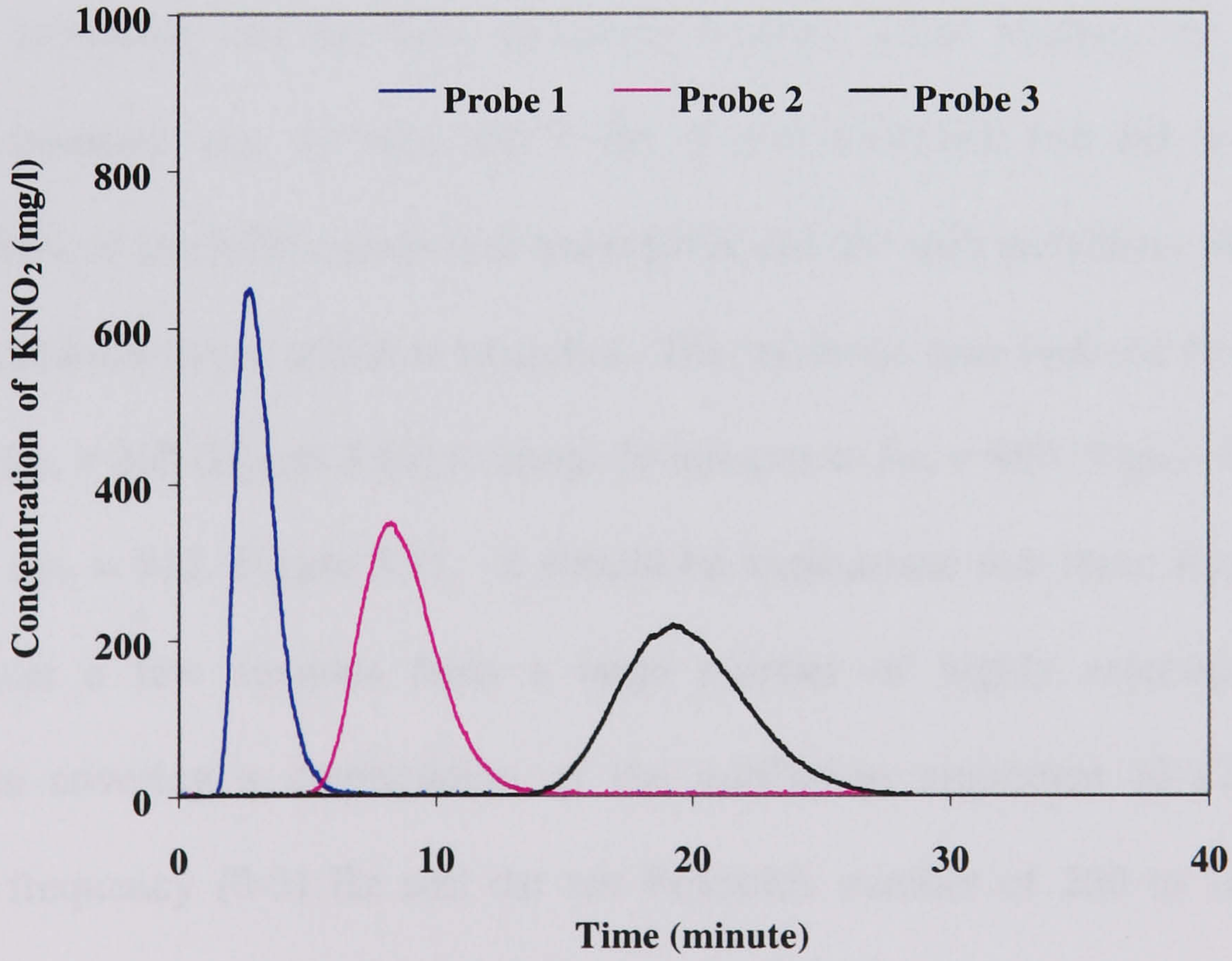

Figure 3.8. Concentration measurements, Re_o = 6024 (12 mm, 2 Hz), Re_n = 452

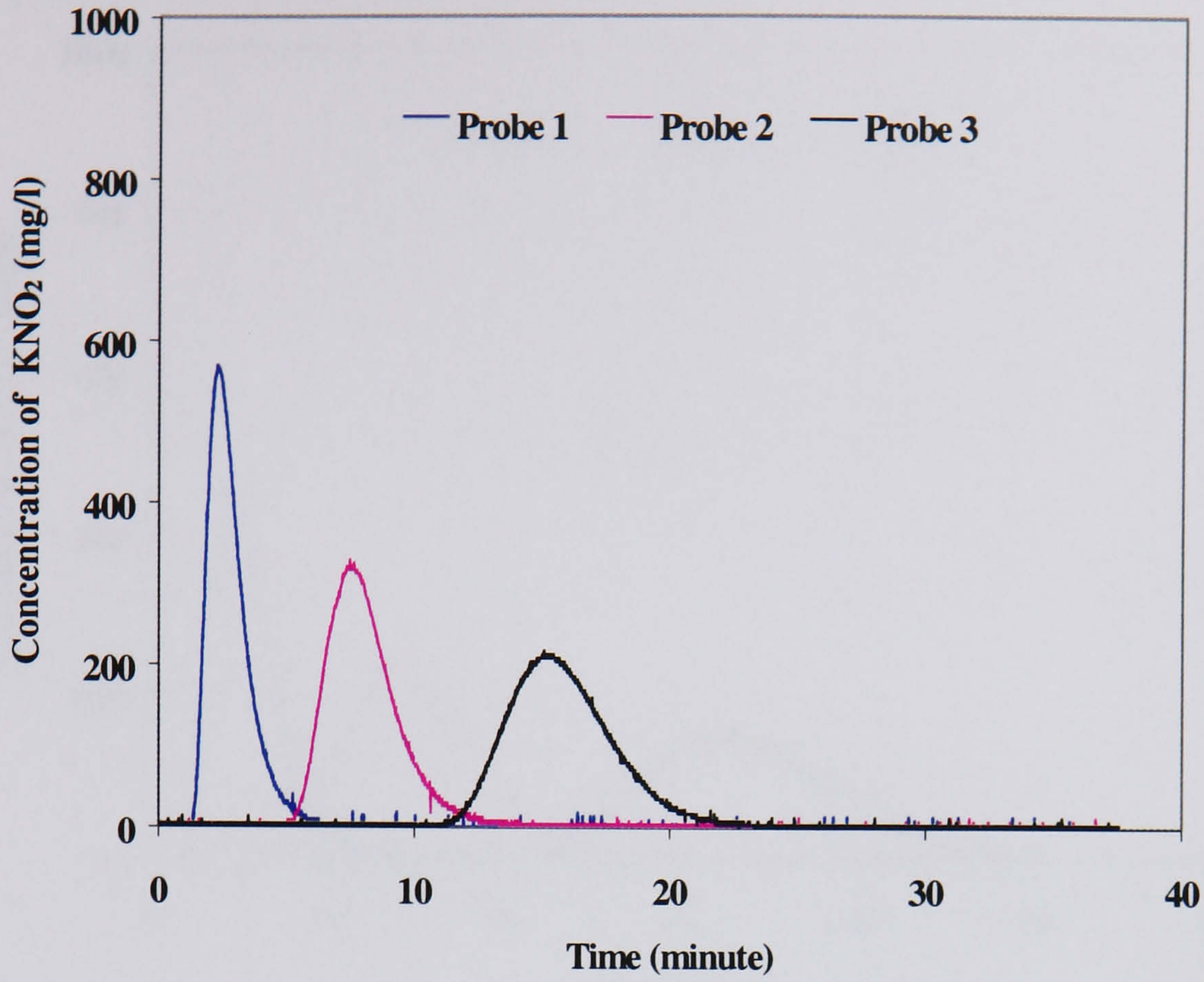

Figure 3.9. Concentration measurements, Re_o = 9036 (12 mm, 1 Hz), Re_n = 490

On increasing the net flow Reynolds number, while keeping the oscillatory conditions constant, e.g. 12 mm and 3 Hz, it was observed that the well defined Gaussian form of the RTD curves was maintained and the only parameter changed was the mean residence times, which is expected. The residence time reduced from about 49 minutes at Re_n = 268 (Figure 3.10) to about 29 minutes at Re_n = 469 (Figure 3.4), and 14 minutes at Re_n = 912, Figure 3.11. It should be emphasised that these figures shown here are just a few samples from a large number of highly reproducible RTD experiments covering a combination of the oscillation amplitude (0-12) mm and oscillation frequency (0-3) Hz and the net Reynolds number of 260 to 1024, which corresponds to a flow rate of 0.5 to 1.92 l/min respectively.

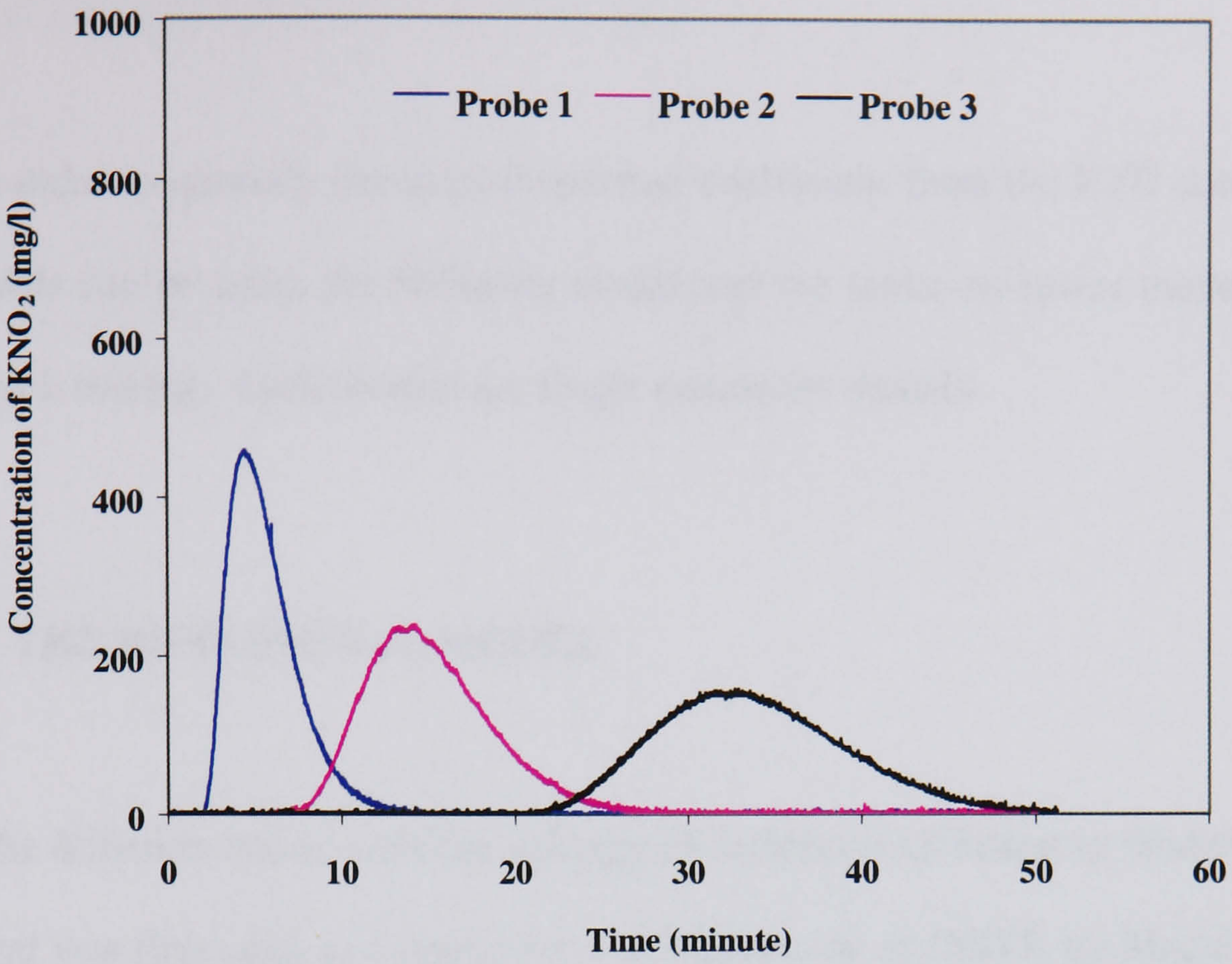

Figure 3.10. Concentration measurements, Re_o = 9036 (12 mm, 3 Hz); Re_n = 268

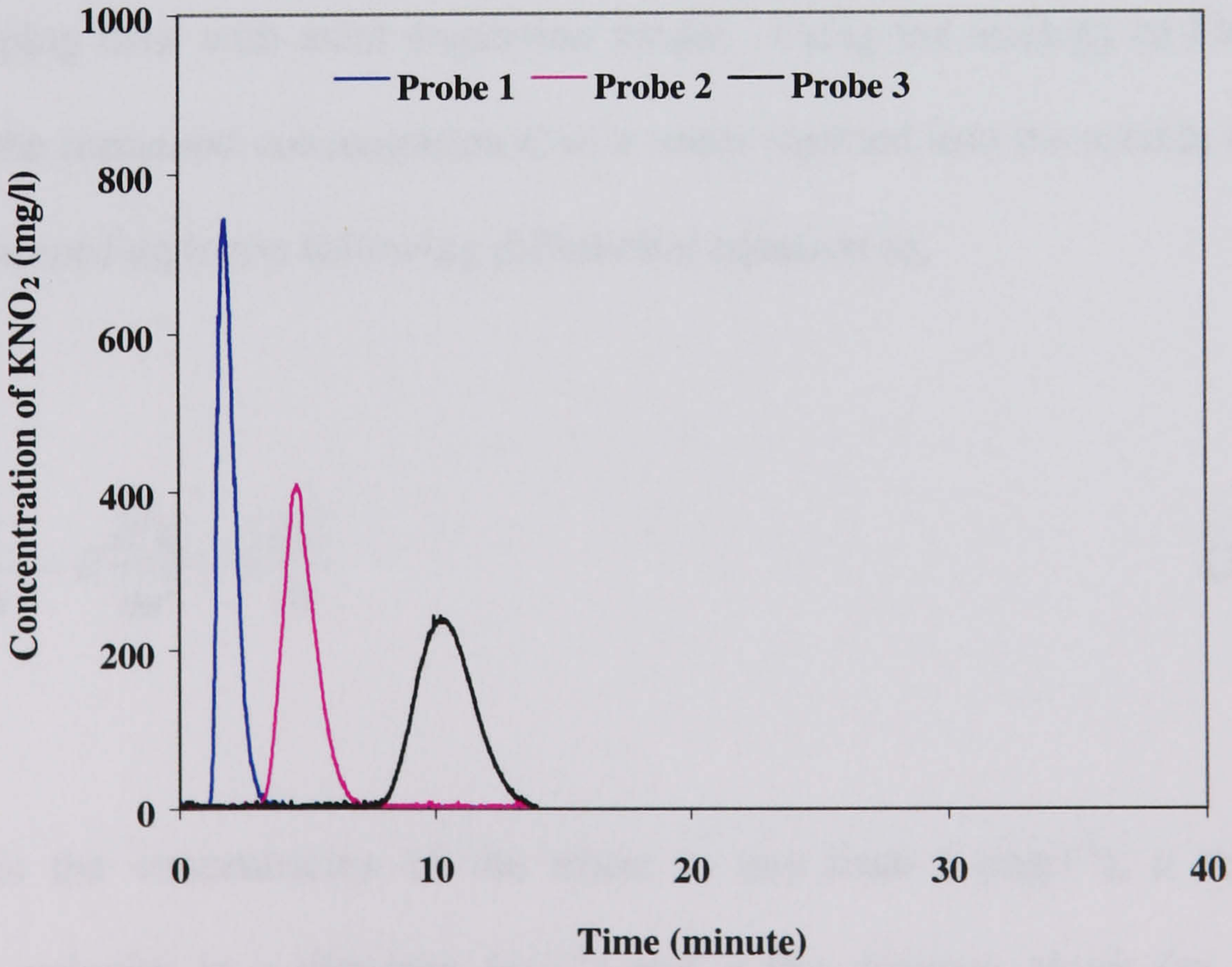

Figure 3.11. Concentration measurements, Re_o = 9036 (12 mm, 3 Hz); Re_n = 912

3.1.4.2 AXIAL DISPERSION COEFFICIENT

In order to quantify the axial dispersion coefficient from the RTD data, the two main models can be used, the diffusion model and the tanks–in–series model, with or without back mixing. Both models are single parameter models.

3.1.4.2.1 THE DIFFUSIONAL MODEL

The diffusion model uses the analogy of molecular diffusion to describe macro-mixing and was first used as a model for axial dispersion in OBTR by Mackley and Ni (1991). This model essentially assumes near to plug flow conditions in the systems. The non-ideality is considered as a deviation from plug flow caused by stochastic fluctuations of local flow velocities which are superimposed on the average flow velocity and is represented by the axial dispersion coefficient, E. This model is also called the plug flow with axial dispersion model. Using the analogy of Fick's law of diffusion, the measured concentration C of a tracer injected into the system is predicted to change according to the following differential equation as,

$$\frac{\partial C}{\partial t} = E\frac{\partial^2 C}{\partial x^2} - u\frac{\partial C}{\partial x} \tag{3.4}$$

where C is the concentration of the tracer at any time t ($mg.l^{-1}$), u the net flow superficial velocity in x-direction ($m.s^{-1}$) and x the distance along the tube. The diffusion model is inherently appropriate for describing a physical situation where homogenous mixing exists (Levenspiel, 1999). It may therefore be supported that it is a

good model for OBTR when substantial mixing occurs (i.e. under chaotic mixing conditions), but that it may fail if there are large segregated volumes of fluid in the flow (e.g. at low Reynolds number flows). A potential disadvantage of the diffusion model with respect to OBTR is that it takes no account of the geometry of OBTR, i.e. the presence of periodically spaced orifice baffles which compartmentalise the flow.

BOUNDARY PROBLEM

A number of research workers have discussed analytical solution with respect to equation (3.4), for example, Dankwerts (1953), Aris (1959), Levenspiel and Smith (1957) and Bischoff (1964). The boundary conditions for equation (3.4) are dependent on the physical structure of the system and its boundaries, as well as on the method of injection. If a perfect input pulse of tracer is injected into an infinitely long tube, the typical boundary conditions are:

$$C(x,0) = \frac{n}{A}\delta(x) \tag{3.5}$$

$$\lim_{x \to \pm\infty} C(x,t) = 0 \tag{3.6}$$

where n is the mass of tracer injected (mg), A the cross-sectional area of the tube (m^2) and $\delta(x)$ is a Dirac delta function (m^{-1}). Solving equation (3.4) with the above boundary conditions yields an analytical solution as a function of time and distance (Goebel *et al.* 1986),

$$C(x,t)=\frac{n}{A}\left[\frac{1}{\sqrt{4\pi Et}}\right]\exp\left\{-\frac{(x-ut)^2}{4Et}\right\} \tag{3.7}$$

The above solution assumes a perfect input pulse of tracer injected at t = 0, which is very difficult to achieve in reality and can not be measured experimentally. This problem can be avoided by the use of the imperfect pulse technique (Aris, 1959) where the form of the input tracer does not matter so long as the tracer concentration can be measured at two or more points in the tube both downstream of the injection point and separated by a certain distance L, see Figure 3.12. The method of analysis of the results is typically to use the upstream data to predict the downstream response with the help of the diffusion model and by trial and error to obtain a best fit value for E, such that the experimental and predicted downstream profiles are as similar as possible. This approach was adopted for OBTR by Mackley and Ni (1991) who used a solution taken from Goebel *et al.* (1986). They argued that the normalised concentration $c_1'(t)$ of tracer measured at the upstream point over a short time interval Δt could be thought of as being equivalent to injecting a perfect pulse of tracer with volume $c'(t')\Delta t$ at time t = t'. Taking the limit as Δt tends to zero and integration over all possible injection times t' would enable one to predict the concentration at the downstream measuring point, which is a convolution integral and must be integrated numerically.

$$c'_{con.}(t)=c'(L,t)=\int_0^t c_1'(t')\frac{u}{\sqrt{4\pi E(t-t')}}\exp\left[-\frac{x-u(t-t')^2}{4E(t-t')}\right]dt' \tag{3.8}$$

The value of the dispersion coefficient, E was adjusted iteratively to give the best fit between c'_{con} and the measured concentration c_2' using either a least squares algorithm or by visual inspection.

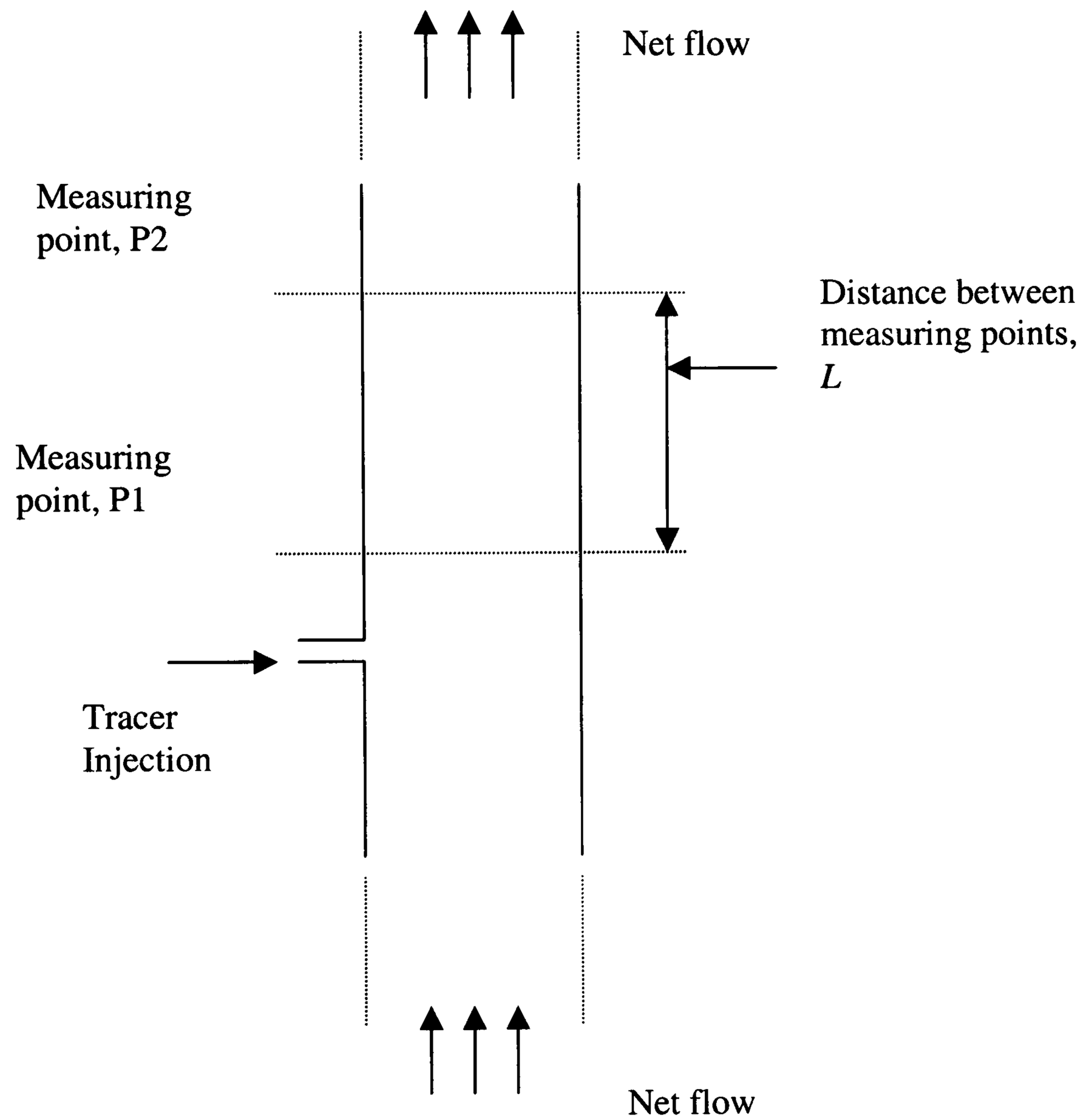

Figure 3.12. Imperfect pulse technique

From equation (3.8), the appropriate transfer function between the measuring points one and two can be extracted as (Smith, 2000),

$$T(t)=\frac{1}{\sqrt{4\pi E\frac{t^3}{x^2}}}\exp\left[\frac{-(x-ut)^2}{4Et}\right] \tag{3.9}$$

This is however different from $\frac{u}{\sqrt{4\pi Et}}\exp\left[\frac{-(x-ut)^2}{4Et}\right]$, as appeared in equation (3.7) and (3.8). This subtle difference in the pre-exponential terms accounts for the errors in best fit programme (Smith, 2000). In fact, the transfer function of equation (3.9) provided the smallest error (Smith, 2000) and is adopted in this work.

3.1.4.2.2 TANKS-IN-SERIES MODEL

The concept of representing OBTR as a series of stirred tanks dates back to Dickens *et al.* (1989). This model gives a good physical representation of OBTR and is appealing to most chemical engineers because of its simplicity. In this model, N equal size completely mixed compartments arranged in series are considered. An advantage of this model is that it can easily be applied for complex reactions by simple calculations from mixer to mixer.

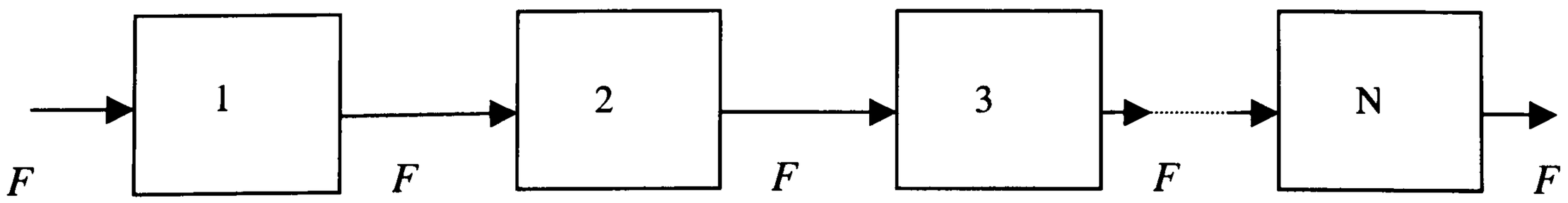

Figure 3.13. The ''Tanks – in – Series'' Model

The advantages of this model were outlined by Wen and Fan (1975):

- The transient mixing behaviour of such a model can be represented by a set of linear first - order ordinary differential equations instead of a partial differential equation. Therefore, the model is amenable to well – established and generalised mathematics of the linear ordinary differential equations and linear algebra.

- If a chemical reaction is taking place in a system, the above model can be represented by a set of finite difference equations rather than differential equations. The solution of the algebraic equations is generally easier than that of the differential equations.

The ability to specify the sizes of compartments and the mode of interconnection among them makes the compartments model one of the most flexible, but this model has limitations when it is applied to oscillatory flow systems, as it does not take into account the possibility of upstream mixing of the fluid due to oscillations, in particular, it can not model the situation of oscillation only with no net flow. Hence modified forms in terms of either, "tanks-in–series with back mixing" or "stagewise backmixing model" (Levenspiel, 1999; Mecklenborough and Hartland, 1975) were derived.

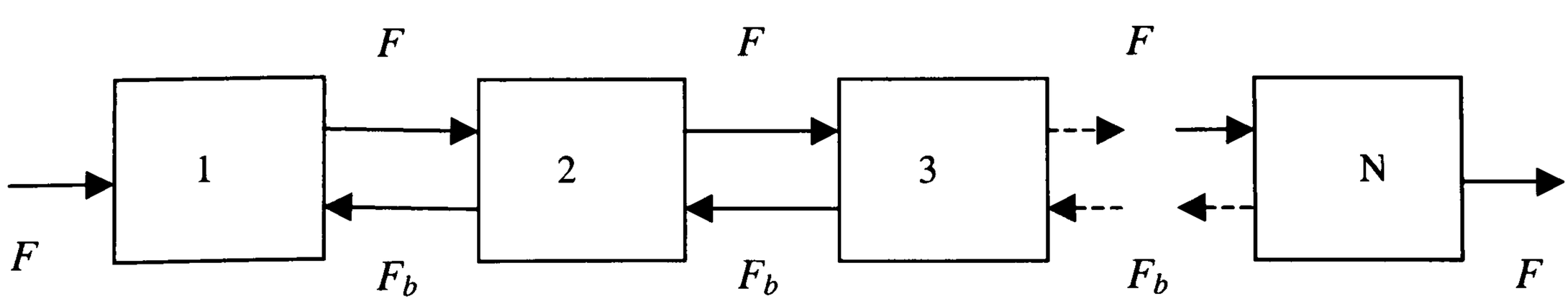

Figure 3.14. The "Tanks – in – Series with Back mixing " Model

The "Tanks–in–Series with Back mixing" model is schematically represented in Figure 3.14. According to this model, the system is assumed to consist of N perfectly mixed cells of equal volume, V_c, with flow to both the upstream and downstream neighbouring tanks. The parameter characterising this model is the equivalent backmixing coefficient f_b and is defined as the ratio of backmixing to the net forward flow rate, $\frac{F_b}{F}$. The model can be solved by applying the mass balance across each cell. A disadvantage of the model is that the equivalent backmixing coefficient, f_b is not a true measure of the actual physical backmixing since a degree of short-circuiting also occurs and contributes to the value of f_b.

Only a small difference exists between the axial dispersion and the tanks-in-series models (Mecklenburg and Hartland, 1975) and the backmixing coefficient can be related to the axial dispersion coefficient through the following equation:

$$\frac{E}{uL} = \frac{f_b + 0.5}{N} \tag{3.10}$$

For not too large a deviation from plug flow both models are equivalent, it is perhaps largely a matter of taste as to which model is preferred. From the RTD curves presented earlier, near to plug flow characteristics have been displayed in all the RTD profiles. In this thesis, the plug flow with axial dispersion model was used to evaluate the axial dispersion coefficient, E.

As mentioned in the experimental procedure, the tracer was recorded at three different locations, *i.e.* probe 1, probe 2 and probe 3 respectively, along the axial length of the OBTRs. The distances between probes 1 and 2, probes 2 and 3 and probes 1 and 3 were 3.7 m, 7.4 m and 11.1 m, respectively. The corresponding axial dispersion

coefficients are denoted as E_{12}, E_{23} and E_{13}, respectively and are given in Table 3.1 over different operating parameters. It can be observed that all the three axial dispersion coefficients are almost identical for all the conditions tested and anyone of the three coefficients can be used as the representative of the system. In the following presentation, E_{13} has been used and the Peclet number, Pe $(=\frac{uL}{E})$ was based on E_{13}. Some of the comparison between the measured concentration profiles and the modelled one while evaluating the axial dispersion coefficient are shown in Appendix 1.

Table 3.1. Calculated *E* and *Pe*

x_o	f	Re_o	Re_n	E_{12}	E_{23}	E_{13}	Pe_{13}
0	0	0	260	0.0006	0.0005	0.0006	120.3
6	0.5	753	260	0.0005	0.0006	0.0005	150.9
6	1	1506	272	0.0005	0.0006	0.0005	150.9
8	1	2008	272	0.0009	0.0009	0.0009	80.2
12	1	3012	260	0.001	0.0011	0.001	73.3
8	2	4016	264	0.0011	0.0012	0.0011	65.6
12	2	6024	260	0.0013	0.0014	0.0013	54.6
10	3	7530	256	0.0011	0.0014	0.0013	57.2
12	3	9036	268	0.0014	0.0015	0.0014	53.1
0	0	0	464	0.0006	0.0007	0.0006	259.0
6	0.5	753	560	0.0005	0.0005	0.0005	248.6
6	1	1506	448	0.0005	0.0006	0.0005	230.9
8	1	2008	416	0.0008	0.0009	0.0008	169.9
12	1	3012	490	0.0009	0.0008	0.0009	138.1
8	2	4016	448	0.001	0.0011	0.001	125.4
12	2	6024	452	0.0012	0.0013	0.0012	104.5
10	3	7530	452	0.0013	0.0014	0.0013	100.1
12	3	9036	469	0.0014	0.0013	0.00014	92.9
0	0	0	1024	0.0008	0.0008	0.0008	330.2
6	0.5	753	952	0.0006	0.0006	0.0006	440.3
6	1	1506	952	0.0006	0.0005	0.0005	519.5
8	1	2008	936	0.0008	0.0006	0.0007	380.6
12	1	3012	960	0.0009	0.001	0.0009	297.2
8	2	4016	964	0.0011	0.0009	0.001	277.5
12	2	6024	1000	0.0013	0.0012	0.0012	201.7
10	3	7530	920	0.0012	0.0014	0.0013	194.7
12	3	9036	912	0.0013	0.0011	0.0013	194.7

3.1.4.2.3 EFFECT OF OSCILLATION PARAMETERS

The effects of oscillation amplitude and frequency on axial dispersion coefficient are presented in Figures 3.15 - 3.16, respectively. It was observed that the axial dispersion coefficient increased with the increase in both the oscillation amplitude and frequency. With increase in the oscillations, the RTD curves generally become broader, resulting in higher axial dispersion within the system. The absolute increase in the axial dispersion coefficient is rather small. The significance of the axial dispersion coefficient plots is that the value of the coefficient is very low indeed, confirming that near to plug flow characteristics have been achieved in the OBTR under the conditions investigated.

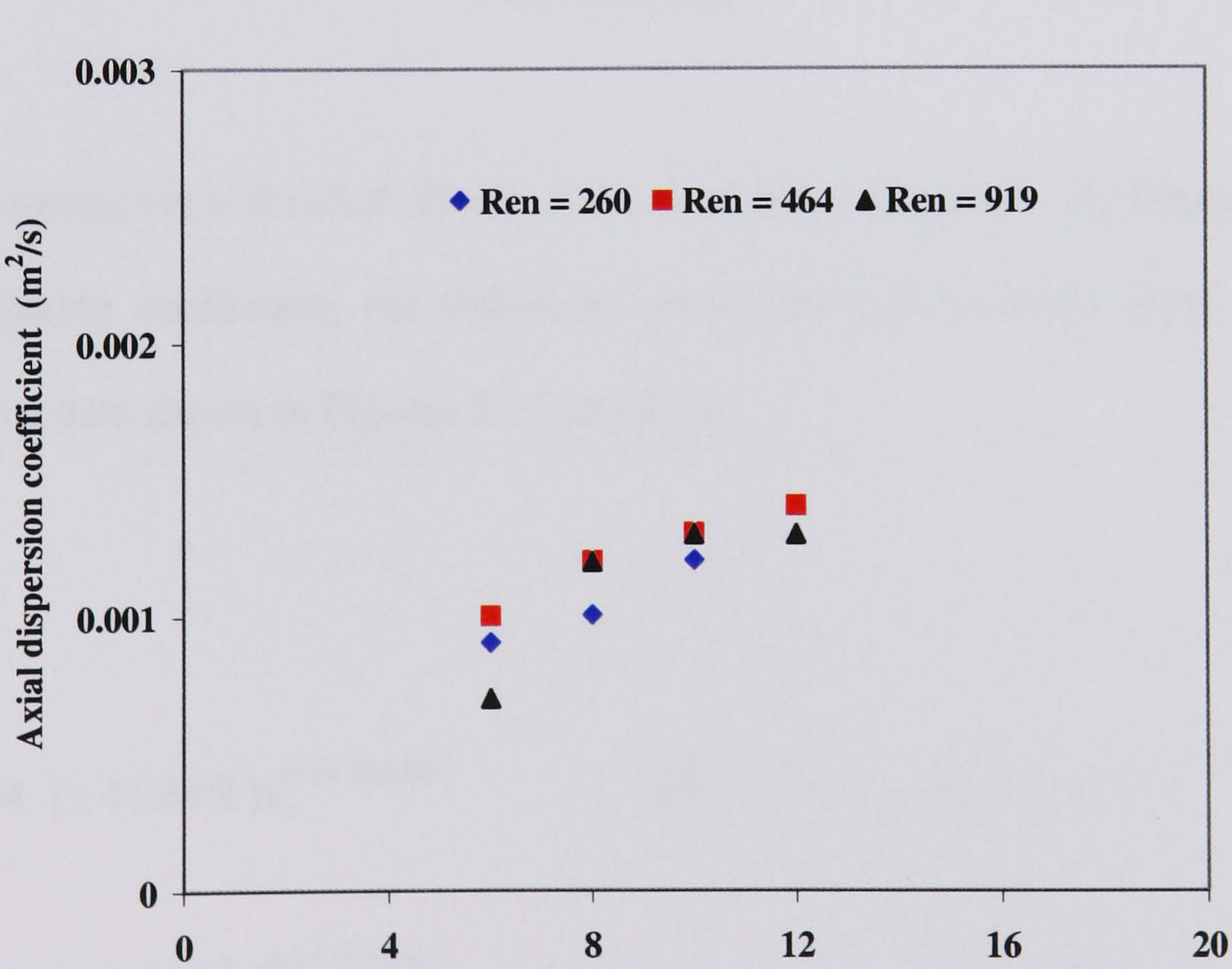

Figure 3.15. Effect of oscillation amplitude on axial dispersion coefficient, f = 3 Hz

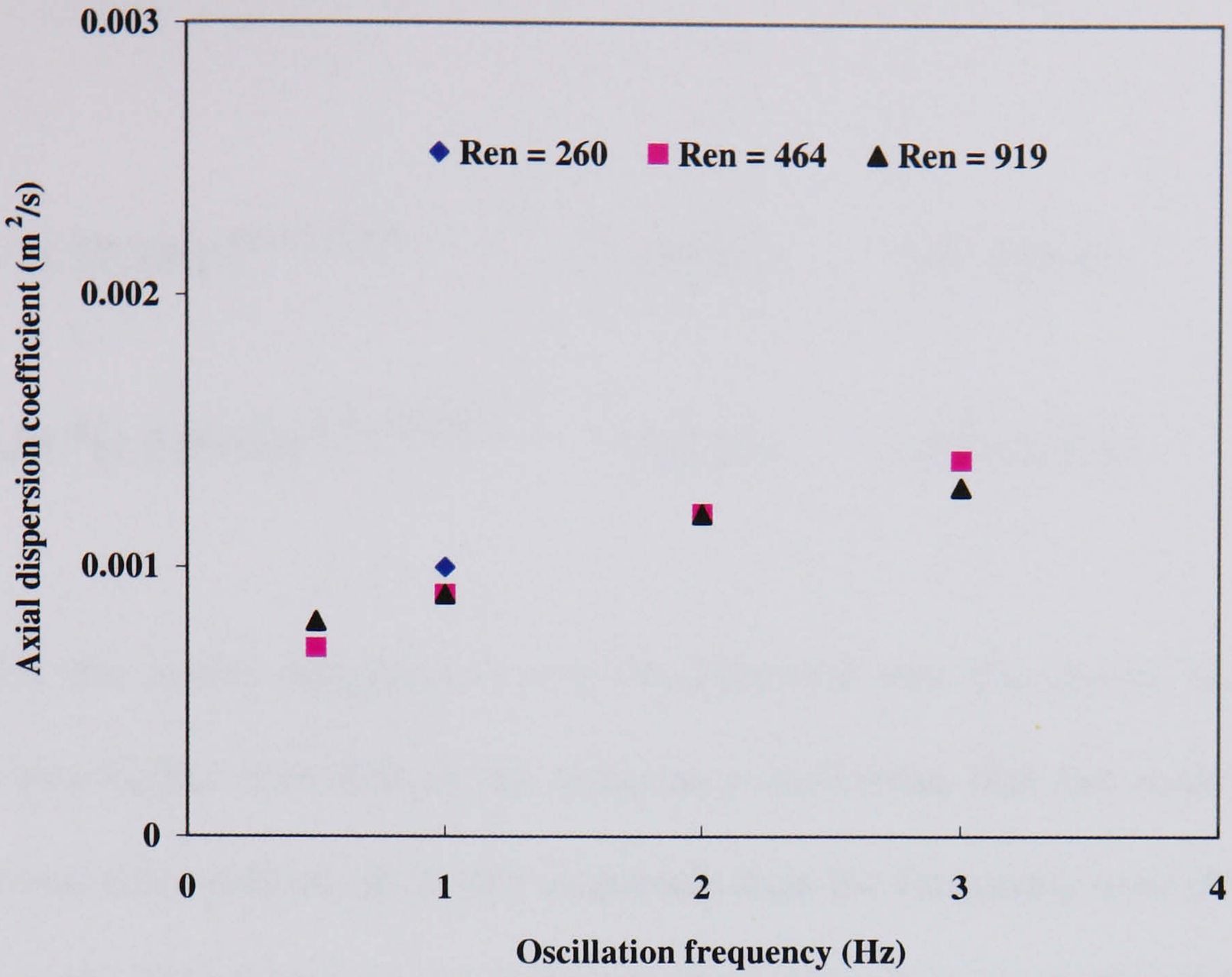

Figure 3.16. Effect of oscillation frequency on axial dispersion coefficient, x_o = 12 mm

To assess the individual effects of the oscillation amplitude and frequency on the axial dispersion coefficient, the following power law relationships were established based on the data shown in Figures 3.15 and 3.16.

$Re_n = 260$

$$E = 0.0234\ (\pm 41.84\%) x_o^{0.64\ (\pm 8.8\%)} \qquad (\mathrm{m^2.s^{-1}}) \qquad (R^2 = 0.964); \qquad (3.11)$$

$$E = 0.0009\ (\pm 3.25\%) f^{0.37\ (\pm 3.8\%)} \qquad (\mathrm{m^2.s^{-1}}) \qquad (R^2 = 0.975); \qquad (3.12)$$

$Re_n = 464$

$$E = 0.0118\ (\pm 22.5\%) x_o^{0.47\ (\pm 4.74\%)} \qquad (\mathrm{m^2.s^{-1}}) \qquad (R^2 = 0.98) \qquad (3.13)$$

$$E = 9.11\times10^{-4}\ (\pm 0.57\%) f^{0.38\ (\pm 0.77\%)} \qquad (\mathrm{m^2.s^{-1}}) \qquad (R^2 = 0.951) \qquad (3.14)$$

$Re_n = 919$

$$E = 0.066\ (\pm 77.2\%) x_o^{0.53\ (\pm 21.8\%)} \qquad (\mathrm{m^2.s^{-1}}) \qquad (R^2 = 0.845) \qquad (3.15)$$

$$E = 9.51\times10^{-4} (\pm 2.65\%) f^{0.29\ (\pm 3.6\%)} \qquad (\mathrm{m^2.s^{-1}}) \qquad (R^2 = 0.924) \qquad (3.16)$$

From the above equations, it can be observed that the power index of the amplitude was higher than that of the frequency, indicating that the axial dispersion coefficient was more influenced by the amplitude than the frequency over the operating conditions used. This finding is in good agreement with previous studies (Mackley and Ni, 1991, 1993).

The effect of the net flow rates on the axial dispersion coefficients is plotted in Figure 3.17, where the oscillatory Reynolds number is used in the horizontal axis. Note that the axial dispersion coefficients showed a non-zero value at $Re_o = 0$ and then generally decreased to a minimum before increasing. This observation is similar to that by Smith (2000) in oscillatory baffled tube systems and Hafez *et al.* (1979), Karr *et al.* (1987) and Baird and Rama Rao (1988,1998) in their studies in RPC. At zero oscillatory Reynolds number, the radial mixing in the system is due to the steady continuous net flow alone. The superimposition of oscillations enhances the radial mixing in the inter-baffle cells and hence the axial dispersion coefficient shows a decrease. At certain conditions both the radial and axial mixing components are balanced and this corresponds to the minimum value of the axial dispersion coefficient, which corresponds to the closest condition to the true plug flow. With further increase

in the oscillatory Reynolds number, axial mixing component dominates and results in an increase in the axial dispersion coefficient.

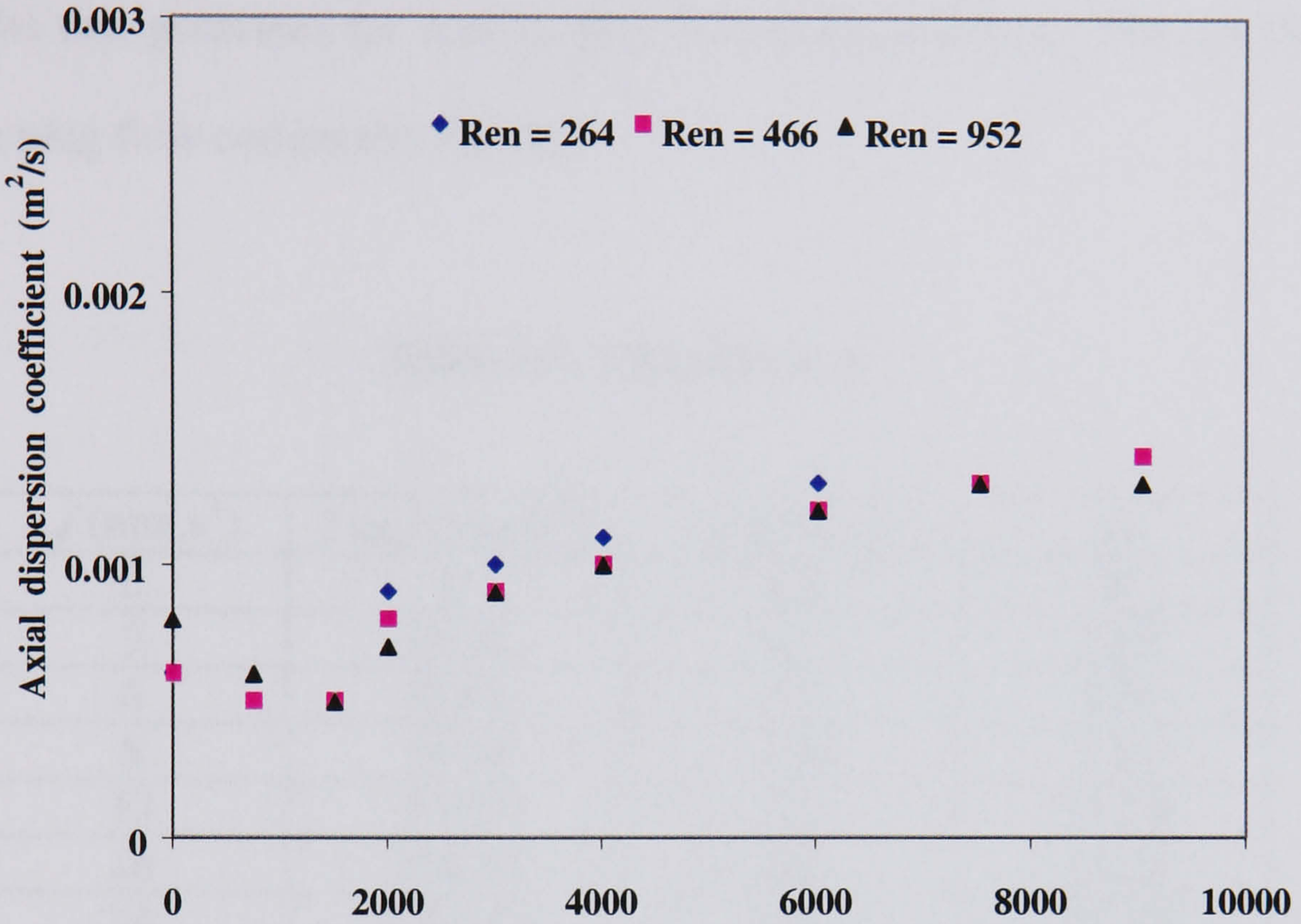

Figure 3.17. Effect of oscillatory Reynolds number on axial dispersion coefficient

As far as the effect of the net flow rate on the axial dispersion coefficient, the influence is not significant at any given oscillatory Reynolds number. In order to understand the combined effect of oscillatory and net flows on the axial dispersion coefficient, a velocity ratio, ψ was introduced and defined as,

$$\psi = \frac{\mathrm{Re}_o}{\mathrm{Re}_n} = \frac{\omega x_o}{u_c} = \frac{2\pi x_o f}{u_c} \tag{3.17}$$

The velocity ratio gives a measure of the dominance of the oscillatory motion over the net flow component. Table 3.2 shows the ratios examined in this work over all

the operating conditions. It is easily seen that the velocity ratios are greater than one when $x_o f > 3$ mm/s, and increase with an increase in the oscillatory Reynolds number. This indicates that the effect of oscillatory motion dominates over that of the net flow over a significant range of the operational conditions. It is the oscillatory motion in the baffled tube that generates the near to plug flow characteristics. The net flow merely carries the plug flow component forward.

Table 3.2. Velocity ratio

$x_o f$ (mm.s^{-1})	$2\pi x_o f$ (mm.s^{-1})	u_c (mm.s^{-1})	ψ
0	0	6.5	0
3	18.84	6.5	2.89
6	37.68	6.8	5.54
8	50.24	6.8	7.39
12	75.36	6.5	11.59
16	100.48	6.6	15.22
24	150.72	6.5	23.18
30	188.4	6.4	29.43
36	226.08	6.7	34.78
0	0	11.6	0
3	18.84	14	1.34
6	37.68	11.2	3.36
8	50.24	10.4	4.83
12	75.36	12.2	6.12
16	100.48	11.2	8.97
24	150.72	11.6	12.99
30	188.4	10.8	17.44
36	226.08	12	18.84
0	0	25.6	0
3	18.84	23.8	0.79
6	37.68	23.8	1.58
8	50.24	23.4	2.14
12	75.36	24	3.14
16	100.48	24.1	4.16
24	150.72	25	6.02
30	188.4	23.0	8.19
36	226.08	22.8	8.69

By plotting the dimensionless Peclet number, Pe $(=\frac{u_c L}{E})$ against the velocity ratio in Figure 3.18, a correlation relating Pe with ψ can be established as,

$$Pe = \frac{uL}{E} = 462 \left(\pm\ 13.67\%\right) \psi^{-0.60\ (\pm\ 6.44\%)} \quad (R^2 = 0.798) \qquad (3.18)$$

The correlation plotted in Figure 3.18 gave a reasonable good fit with the coefficient of variance, $R^2 = 0.8$. The above equation was inverted and modified to account for the axial dispersion coefficient as a function of oscillation and net flow components by the following equation:

$$E = 0.072 \left(x_o f\right)^{0.6} u^{0.4} \qquad (\mathrm{m^2.s^{-1}}) \qquad (3.19)$$

The axial dispersion coefficient is more influenced by the oscillatory flow component and is less sensitive to the net flow component. This is in agreement with the results reported in Figure 3.17. From Figure 3.18, the Peclet number, Pe varied from 54–519 over the operating conditions used. A Peclet number, Pe, greater than 20 indicates a relatively small effect of axial mixing and above 50 indicates a negligible effect (Godfrey *et al.* 1988). Since in this investigation most of the Peclet numbers, Pe, were well above 50, this means that the vertical OBTR has been operating very close to plug flow behaviour over the experimental operating conditions used.

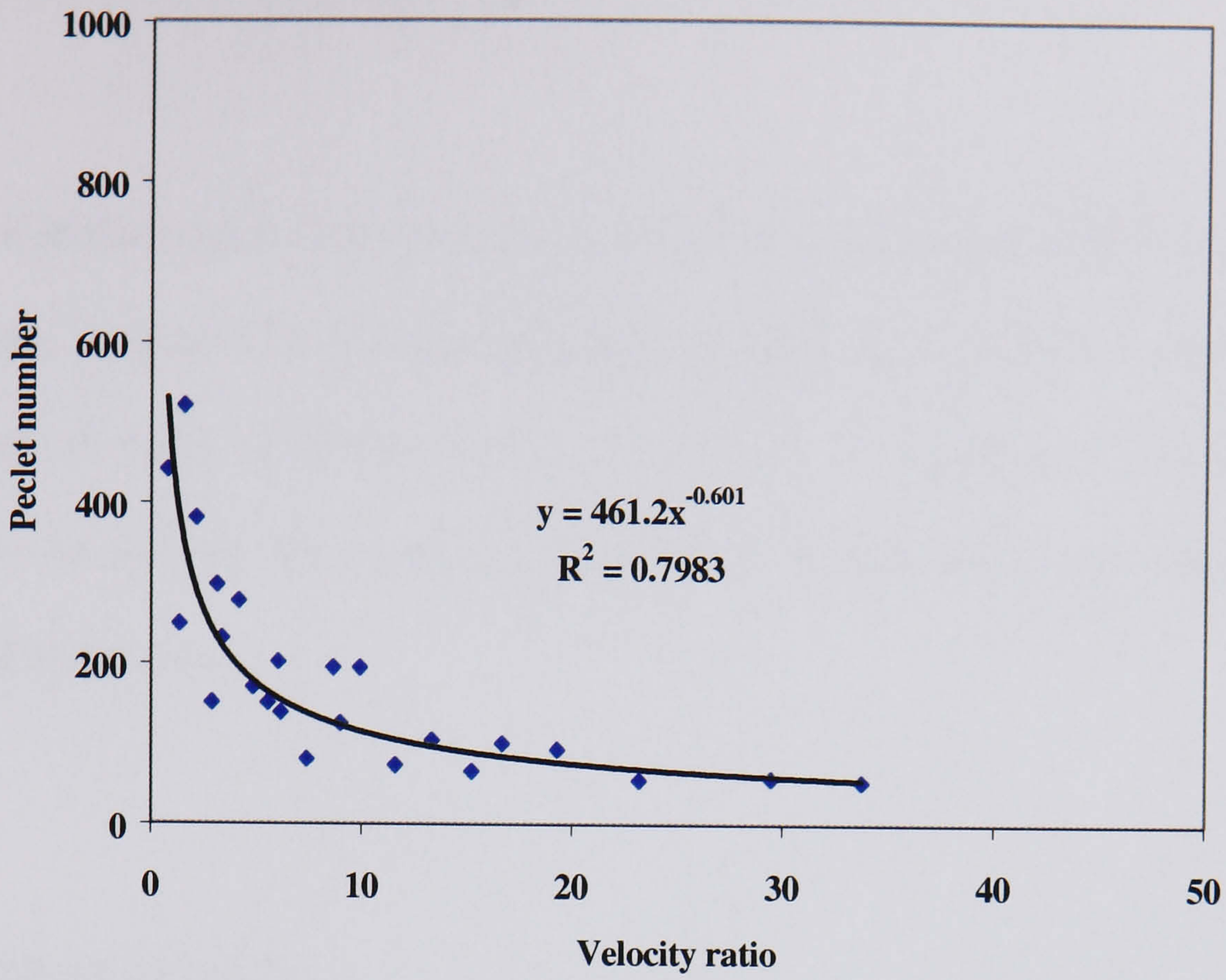

Figure 3.18. Effect of velocity ratio on Peclet number

3.1.5 SUMMARY OF RESULTS

Highly reproducible and controlled RTDs with near to plug flow behaviour were obtained. The axial dispersion coefficient was evaluated over a range of oscillation amplitudes, frequencies and net flow rates and was found to be sensitive to both the oscillation amplitude and frequency, but less to changes in the net flow rates. A correlation was established relating the axial dispersion coefficient with both the oscillatory and net flow Reynolds number. The correlation also confirms the experimental finding. In summary from the single phase flow experimental results, the vertical OBTR was observed to behave very close to a plug flow tubular reactor.

3.2 TWO PHASE FLOW STUDY

This section deals with the studies of droplet size and size distributions in a two phase system. It starts with the experimental method of acquiring drops, the procedures and the data analysis techniques and is followed by experimental results along with discussions. As each subject appears, a short review of relevant literature is given as the background information.

3.2.1 INTRODUCTION

When two immiscible liquids are agitated in a vessel, a dispersion of one phase into another is expected, and the former refers to the dispersed phase, and the latter the continuous phase. In most applications, the densities and viscosities of the two liquids are different, resulting in dispersed droplets in the continuous phase. Suspension polymerisation process is one of the typical examples of this type of dispersion. Droplets are usually suspended in a mixing vessel and subjected to continuous break-up and coalescence. Due to imperfect mixing in reactors, a droplet size distribution (DSD) is often encountered. Clearly the mean droplet size and DSD depend on many factors from chemistry and chemical engineering. The chemistry factors include the make-up of the dispersed / continuous phases, the catalysts, the initiators, etc. and governs the final properties of droplets/particles, such as surface tension, density, phase fraction and molecular weights. The chemical engineering factors are associated with the fluid mechanics conditions in a given reactor, e.g. mixing intensity, operating temperature/pressure and control the size distribution of these droplets and particles. On characterising the OBTR for the purpose of continuous suspension polymerisation,

it is desirable to understand how the chemical engineering factors affect such a distribution in the OBTR while keeping the chemistry factors the same. The starting point of this is to establish a reliable dynamic technique for acquiring droplet samples and measuring droplet sizes. There has been a number of research studies carried out in this field in stirred tanks, Bae and Tavlarides (1989) and Allen, T. (1997) have provided a good review on different techniques, such as direct photographic method, capillary sampling probe, drop stabilisation method, light transmission and chemical reaction method. The following is a short introduction on each technique.

3.2.2 DROPLET MEASUREMENT

3.2.2.1 DIRECT PHOTOGRAPHY

The most common method is the direct photography and has been used by many investigators in the past, for example, Brown and Pitt(1972), Van Heuven (1971), Coulaloglou and Tavlarides (1976), Calabrese *et al.* (1986), Wang and Calabrese (1986), Miyauchi and Oya (1965), Baird and Lane (1973), Miyanami et al. (1975), Boyadzhiev and Spassov (1982), Prabhakar *et al.* (1988), and Sreenivasulu *et al.* (1997). It involves illuminating a plane through a vessel and taking photographs of interest perpendicular to the plane.

3.2.2.2 CAPILLARY SAMPLING PROBE

The capillary method employs a fine bore capillary of the order of the drop size for sampling from a liquid dispersion. As drops pass through the capillary they are transformed into cylindrical slugs of an equivalent volume. A laser beam is split into

two rays using a beam splitter and a plane mirror and the rays pass directly through the capillary 0.1 mm apart. The emergent beam is collected by a × 10 microscope objective lens and focused on to a photodiode. From the measurement of the passage time of a slug at one detector and its travel time between two detectors the velocity and diameter of the drop can be calculated. The method can be used to obtain broad drop size distribution in the range above 50 μm in real time and automatically.

Verhoff *et al.* (1977) developed a special technique to measure bivariate drop size, where they used a photometer assembly to measure both the drop size and concentration. A similar method, Laser Capillary Spectrophotometry, was developed by Bae and Tavlarides (1989) for rapid and accurate determination of bivariate drop size concentration distribution for reactive liquid-liquid dispersions. Goldmann and Blass (1984) employed three different sizes (0.7, 1.12 and 1.7 mm) of capillaries for measurement of mono-dispersed drops of butyl-acetate in water in the range of 2 to 5 mm in diameter. Pietzsch and Blas (1987) adapted this capillary sampling method to measure drop sizes for toluene – water and tri-butyl phosphate – n-alkane / water systems in a pulsed sieve-tray extraction column.

3.2.2.3 DROP STABILISATION

Drop stabilisation involves trapping of a small dispersion solution into a specially designed cylinder and encapsulating it by a thin polymer film. The thin polymer film prevents any coalescence and stabilises the drops. A small portion is then transferred to a flat glass dish and photographed. This method is simple, easy and accurate, but it requires many images and lengthy analysis times and can be used for low volume fraction measurements. McCoy and Madden (1969), Shinnar (1961), Van

Heuven (1971), Mlynek and Resnick (1972), Tanaka (1985), Wright and Ramakrishna (1994), Zerfa and Brooks (1996), Tobin *et al.* (1990) and Ni *et al.* (1998) are those who utilised this technique.

3.2.2.4 LIGHT TRANSMISSION

The light transmission technique has widely been used in determining the interfacial area in dispersion studies, from which the average drop size, not size distribution, is calculated. The method involves inserting optical probes in a two phase mixture and detecting light signals. It is simple and gives the advantage of quick measurement and on-line operation, Calderbank (1958), Weinstein and Treybal (1973) and Brown and Pitt (1970, 1972). But this technique is best suited for systems with low hold up because at higher hold up values, a correction factor has to be used for multiple reflections of light as it traverses a dense swarm of drops, Caldrebank (1958) and Giles *et al.* (1971). Optical probes can also cause hydrodynamic disturbance at the point of measurement.

3.2.2.5 CHEMICAL METHOD

Interfacial area and hence average drop size can be determined by using a chemical reaction. This involves a reaction of a relatively unchanging dispersed – phase concentration diffusing to the continuous phase. The effective interfacial area can be obtained from the extraction rate and physiochemical properties of the system, Nanda and Sharma (1966). This technique has extensively been used for gas – liquid

dispersion. The disadvantage of this method is the effect of mass transfer on the dispersion physiochemical properties, e.g. the interfacial tension, which can affect the interfacial area and thus the average drop size.

In conclusion, it is the direct photographic method that has been employed throughout this work.

3.2.3 EXPERIMENTAL PROCEDURE AND IMAGE ACQUISITION SET UP

The experimental set-up to study the two phase characteristics is presented in Figure 3.19. Before each experiment the OBTR system was rinsed with water and then completely filled with water, which constitutes the continuous phase. Any trapped air was bled off at this stage. The system was oscillated for about five minutes at a desired oscillation amplitude and frequency before the dispersed phase was injected into the system at a constant rate of 45 ml/min. The dispersed phase was Silicone oil (920 kg/m^3, 4.6 mPa.s). All the experiments were carried out at a room temperature and in absence of surfactants and colloids. The dispersed phase was allowed to disperse uniformly through the entire system prior to capturing droplet images using a CV-M1 CCD camera. The photographs were taken at four different positions along the path of the vertical OBTR system as shown in Figure 3.19. The four locations are in the middle of the straight sections. The arrangement for acquiring droplet images is shown in Figure 3.20. The position of the tube, where the camera was focussed, was surrounded by a rectangular box made of perspex and filled with water in order to eliminate distortions due to curvature effect. Most of the photographs were taken with a focal length between 0.3 and 0.4 and an aperture of 2.8. A short exposure time of 1/3000 sec was employed. The illumination was provided by a 650 W floodlight. A diffusing

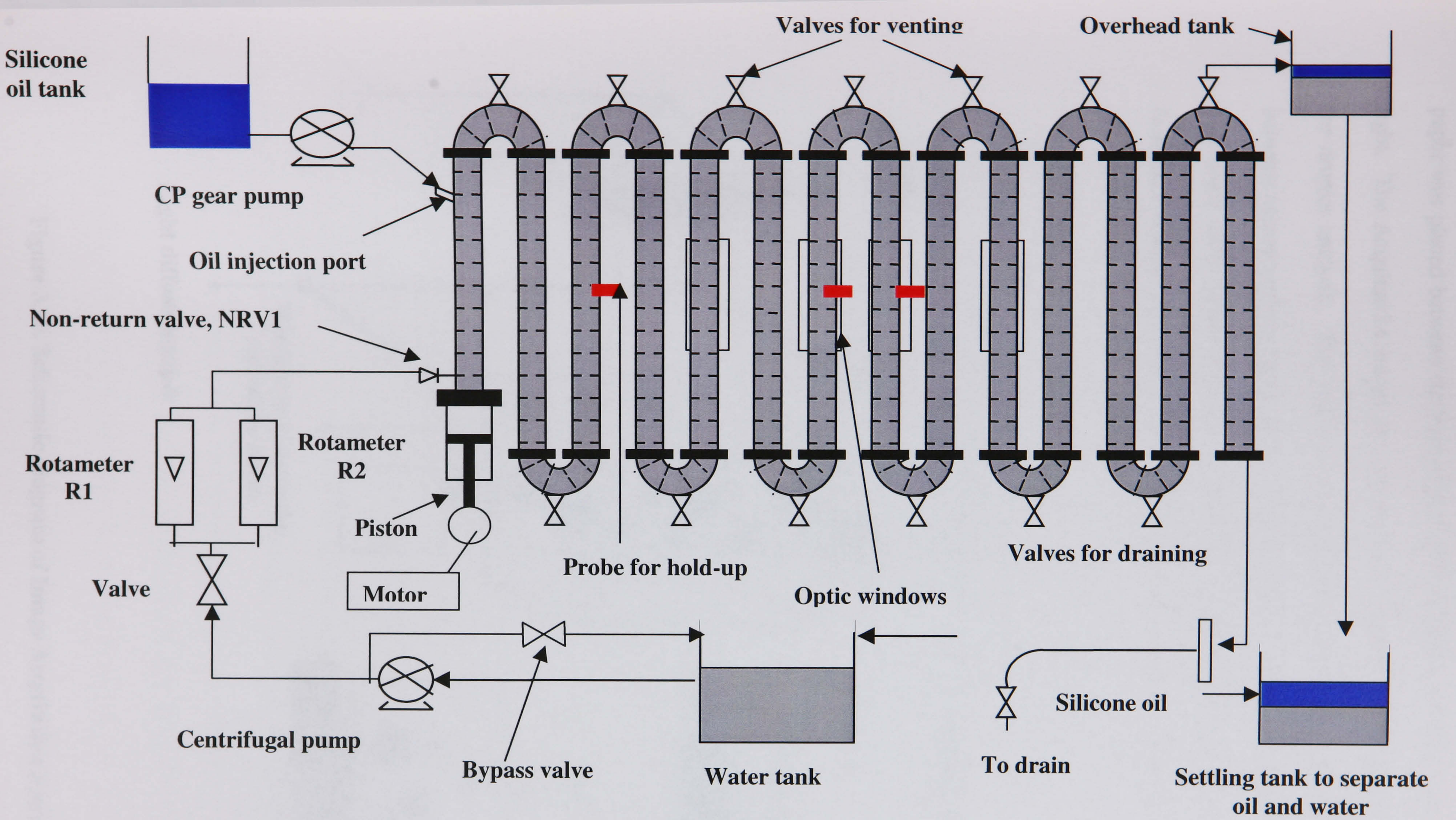

Figure 3.19. Schematic diagram of the vertical OBTR system for two phase investigation

paper was placed between the light source and rectangular perspex box to disperse the light. The Aequitas IA image analysis software (Dynamic Data Links Ltd.) was used for droplet analysis. The software uses difference in colour intensity to distinguish between objects and the background. To improve the contrast, the silicone oil was dyed blue using BDH waxoline blue dye. The Sauter mean diameter (d_{32}) was calculated from the corresponding DSD, which was obtained at an interval of about 50 μm.

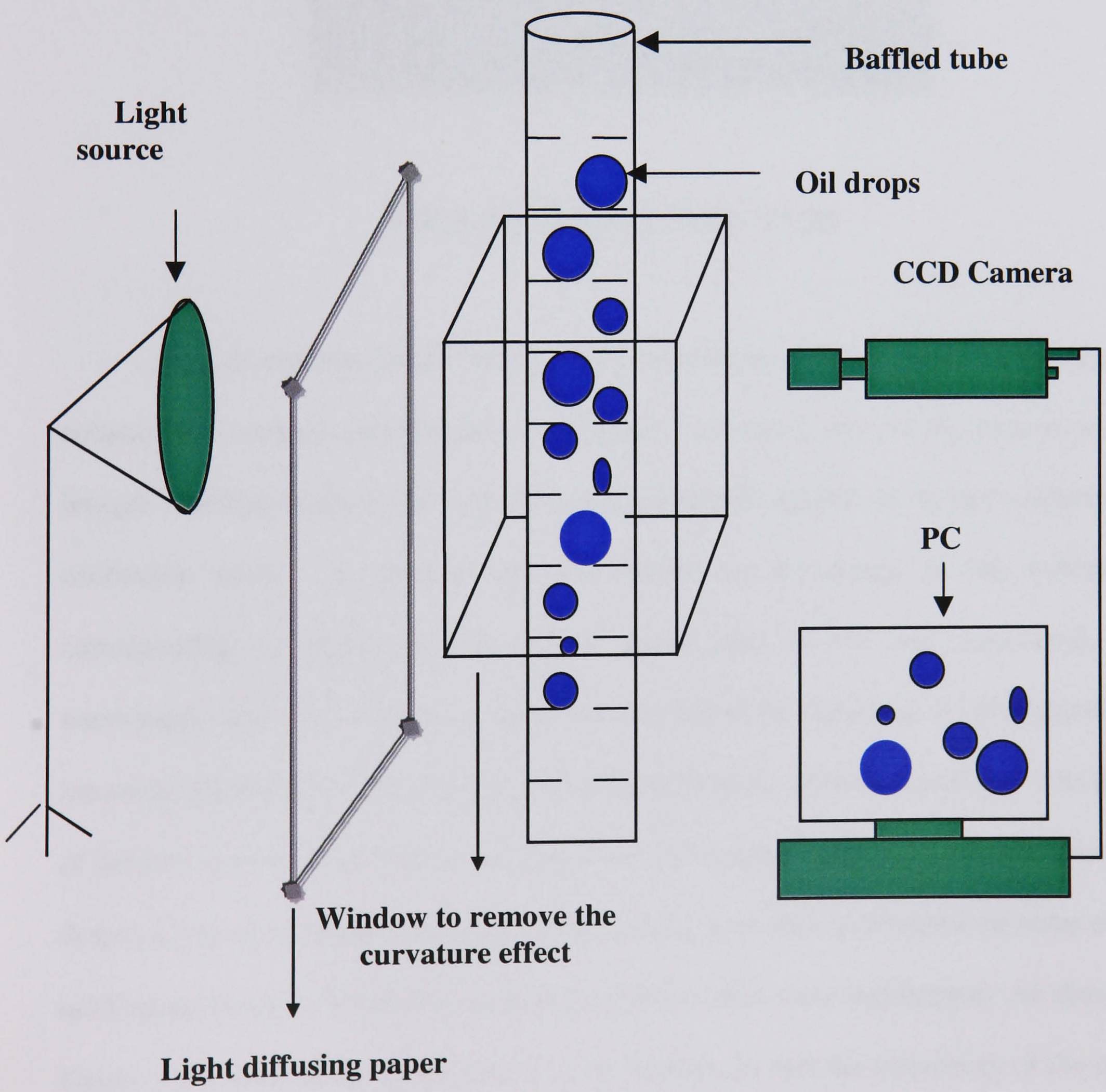

Figure 3.20. Schematic diagram of Image Acquisition System

3.2.3.1 ANALYSIS ROUTINE

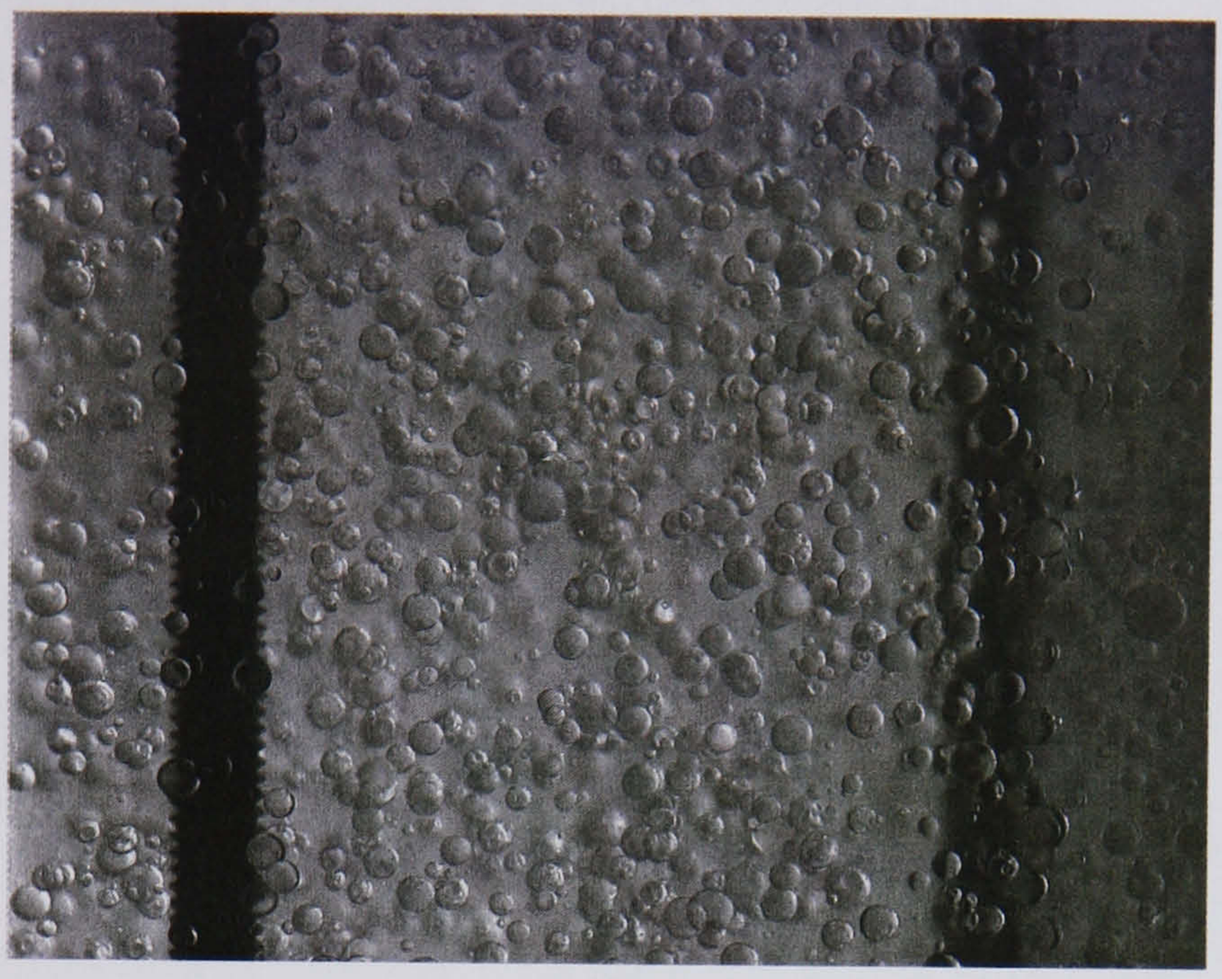

Figure 3.21. Typical droplet image

Prior to analysis, droplet images were treated using the Microsoft Photo editor to enhance the contrast and brightness. Figure 3.21 shows one of the typical treated images. Before analysis, the software was calibrated against an image containing a calibration scale. A straight line was drawn on the image in the x-direction corresponding to 10000 microns and an aspect ratio of 1.0 was maintained. As mentioned above this software relies on the threshold function to distinguish the measured objects from the redundant ones based on their colour or intensity. The depth of field for a given focus lens means that there are focussed drops as well as unfocussed drops shown up in images. Manual binary editing was often performed on some of the unfocussed images. Drops that were only clearly visible were highlighted. As shown in Figure 3.21, most of the drops appear to be circular, in fact the circularity of the drops varied between 85 and 95 %. By manually moving the cursor on each drop, the co-ordinates of two diametrically opposite points were selected and a straight line was

drawn connecting the two points to give the drop diameter. This procedure was repeated for all drops within each photographic image. As a consequence of this, one would appreciate the effort and time spent on the data analysis.

The measured drop diameters were then grouped at a class interval of 50 μm and to each interval a number frequency, n, was assigned, generating a discretised frequency histogram or drop size distribution. From the drop size distribution, the Sauter mean drop size was obtained by using the equation,

$$d_{32}=\frac{\sum n_i d_i^3}{\sum n_i d_i^2} \tag{3.20}$$

where n_i represents the number of drops (frequency) in an interval i and d_i is the corresponding mean drop diameter of that class i. d_{32} represents that a drop that has the same volume-to-surface area ratio as the entire population of drops and is the most important one of all the mean diameters, since it is directly related to the interfacial area per unit volume, which determines energy, mass and/or chemical reaction rates in dispersions. The Sauter mean drop diameter has been used in this thesis.

3.2.3.2 NUMBER OF DROPS

Since the droplet analysis is time consuming, it is important to find out a minimum number of drops that is required to provide a representative and reliable size distribution for a given operation. In this work, droplet numbers from 200 to 1000 were examined and their effects on drop size distribution are shown in Figures 3.22-3.23. The term of "riser" and "downcomer" in Figures 3.22 and 3.23 refers to a tube in which

the continuous phase flows up and down, respectively. Generally, the DSDs are much broader and less well defined in the risers than those in the downcomers. The stability of DSD will be discussed latter. Now back to the drop number, it is clear that the distributions remained more or less constant for droplets above 250. This is the guide used in this thesis on determination of the minimum droplet number. On balance of accuracy and time consumption, 600-800 drops were used throughout the work. In fact the error due to the selection of the drop numbers, n_d can be estimated using an empirical equation proposed by Hayslett (1972) as

$$e = \frac{1.96}{\sqrt{n_d}} \tag{3.21}$$

On this account, the error was about 8%.

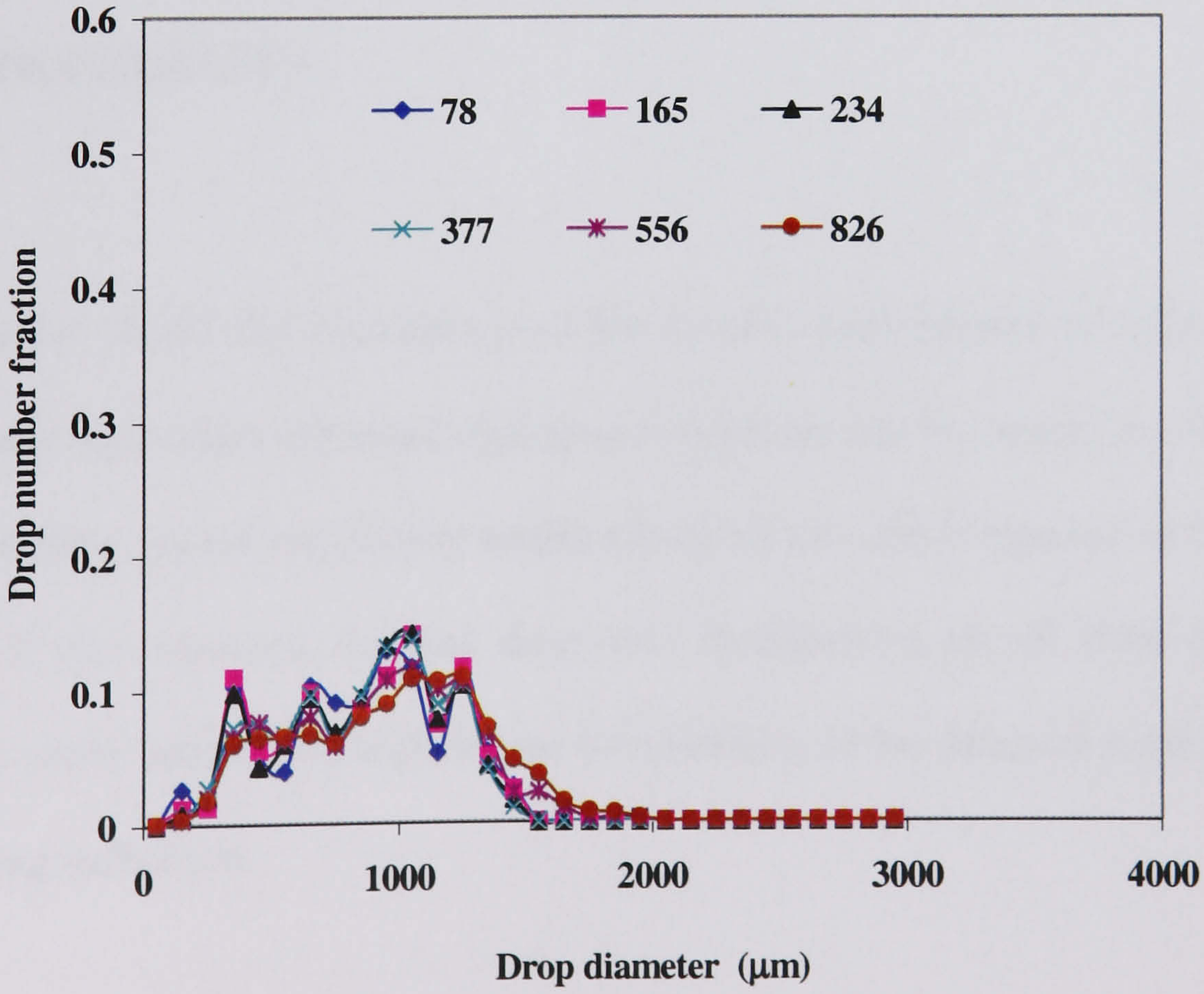

Figure 3.22. The effect of droplet number on droplet size distribution, Re_o = 5020 (x_o = 10 mm, f = 2.0 Hz), Re_n = 544, Riser

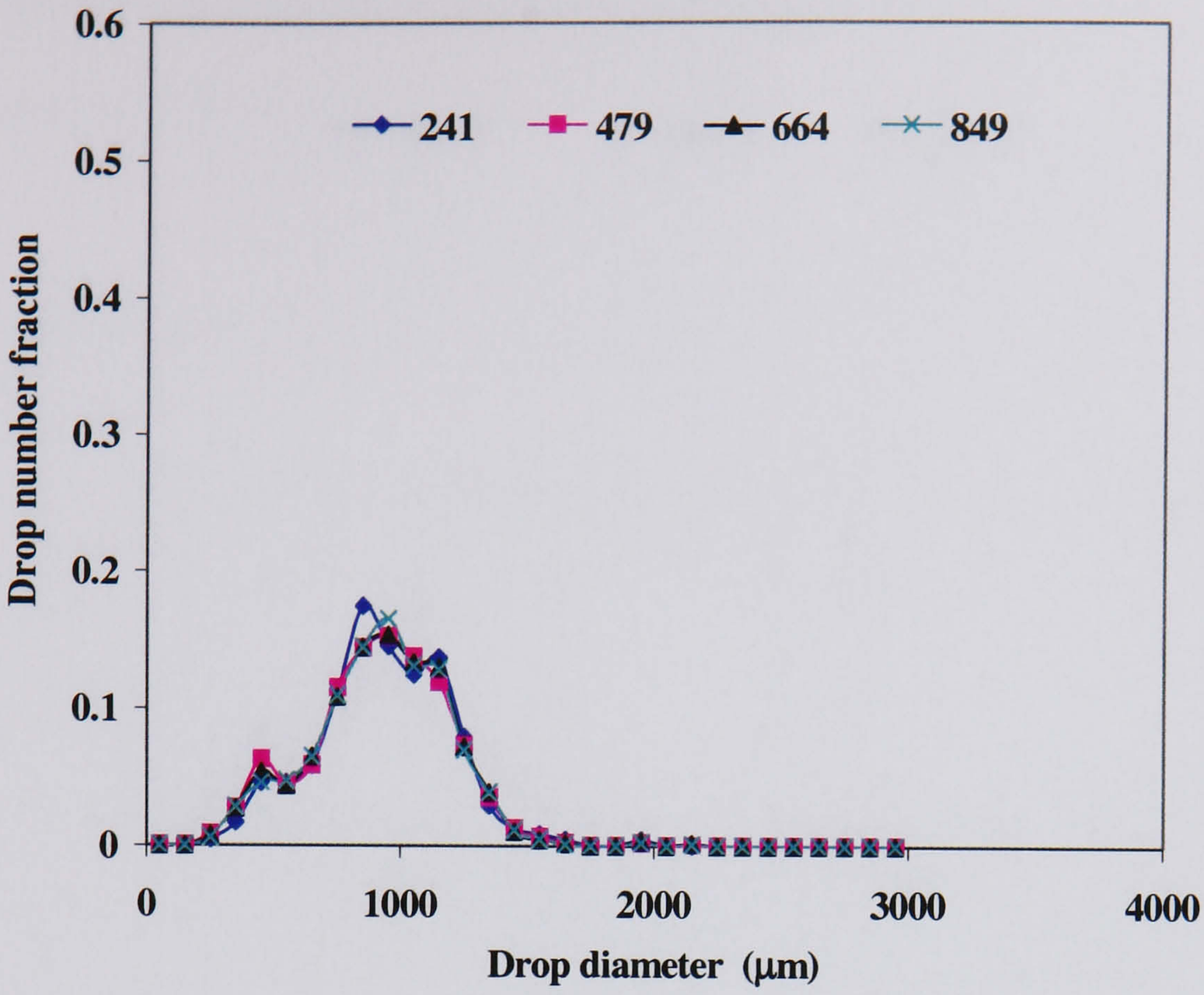

Figure 3.23. The effect of droplet number on droplet size distribution, Re_o = 5020 (x_o = 10 mm, f = 2.0 Hz), Re_n = 544, Downcomer

3.2.3.3 REPEATABILITY

In order to test the consistency of the results, experiments were performed on three different days under the same operating conditions and the results are illustrated in Figures 3.24 for a typical oscillatory amplitude of 10 mm and frequency of 2 Hz. From the Figure it was observed that the drop size distributions on all three days almost overlapped, which indicates a high degree of reliability of the data and good accuracy of the measuring technique.

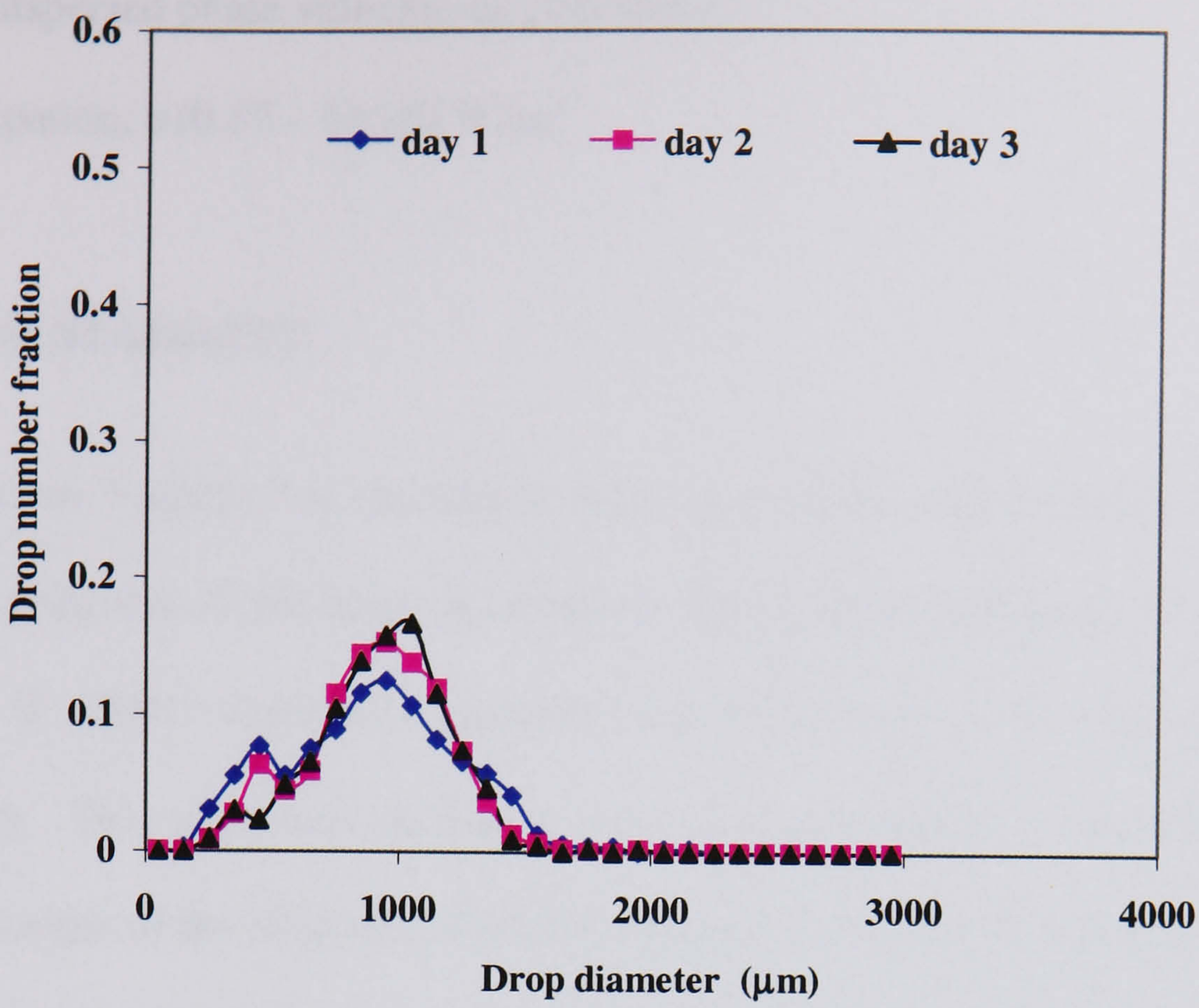

Figure 3.24. Repeatability of droplet size distribution, Re_o = 5020 (x_o = 10 mm, f = 2.0 Hz), Re_n = 544, Downcomer

3.2.4 RESULTS AND DISCUSSION

The main parameters that govern droplet interactions in the OBTR are the oscillation amplitude, frequency and the net flow rate. Investigations were carried out to study the effect of these operational parameters on drop size distribution and mean droplet size by varying one parameter at a time. Experiments were performed over a range of operating conditions, which are listed below:

Oscillation amplitude, x_o : (10-18) mm

Oscillation frequency, f : (2-4) Hz

Oscillation velocity, $x_o f$: (20 – 72) mm.s^{-1}

Oscillation Reynolds number, Re_o : (5020 - 18072)

Net flow velocity, u_c :(5.8 – 25) mm.s^{-1}

Net flow Reynolds number, Re_n : (234 -1004)

Superficial dispersed phase velocity, u_d : 0.6 mm.s^{-1}

Energy dissipation, ε (0.37 – 17.28) W.kg^{-1}

3.2.4.1 DROP STABILITY

The term "stability" in this thesis refers to a steady state at which well defined symmetrical drop size distribution are obtained. Previous investigators, Ni *et al.* (1998) and Nelson, G. (2001) observed a minimum oscillation time of 30 minutes to achieve drop stability. This minimum oscillation time is termed as the "transition" period in which the changes of the drop size distributions and drop size with time become steady. In this investigation, the dispersed phase is introduced continuously and hence in order to examine the drop stability, the drop size measurements were carried out at different positions along the length of the flow.

The variation of drop size distribution along the tube length is shown in Figure 3.25 for a typical oscillation Reynolds number, $Re_o = 7530$ ($x_o = 15$ mm, $f = 2$ Hz) and a net flow Reynolds number, $Re_n = 554$. Note that the symbol N in the Figure 3.25 refers to the number of baffles, in turn the length of the tube. It was observed that initially the DSDs were generally bi-modal and not well defined at locations closer to the oil input, but became progressively unimodal further away downstream of the oil input. In the process, the DSD profiles get sharper and narrower, e.g. at $N = 326$ corresponding to a flow length of 23.4 m, the DSD is well defined. However, the time taken for such well defined DSD to establish is about 28 minutes at $Re_n = 554$. The time is too long. The reason for this is the combination of risers and downcomers presented in the system, where the difference in density between oil and water plays a significant role in droplet movement. Since the drops are lighter than the continuous medium (water) they have a natural tendency to rise, hence in the riser the residence time of the drops is less than

that in the downcomer. In other words, the drops travel faster in the riser. This in fact presented complication to the process of drop stability. Visually it can clearly be observed that drops are accumulating at the top of risers, just before the bends. The accumulation causes coalescence and the presence of large drops become apparent. Due to the buoyancy, these large drops are further stretched in the bends and their shapes are elongated and irregular. After the bends, the drops in the downcomer are then subjected to a sort of compression due to the combination of the net flow and fluid oscillation. The action of such compression reverses the elongation of drops and causes drop to break.

Further along the downcomers, drops tend to "float" under oscillation and travel increasingly slower towards the bottom bends before flowing upwards in the risers. The combination of the risers and downcomers has disrupted and therefore prolonged the drop stabilisation process, and in turn affected the DSD profiles. There is no definite trend on the variation of DSDs along the tube length, Figures 3.26 – 3.32 supports this observation. Here one can see that DSDs behave differently as compared to those shown in Figure 3.25. As a matter of fact, the stability of DSDs along the tube length has not been observed for all the experimental conditions. Figures 3.33 compiles DSDs at one location, say, N = 222, a downcomer under different operating conditions, the degree of the overlapping is clearly poor.

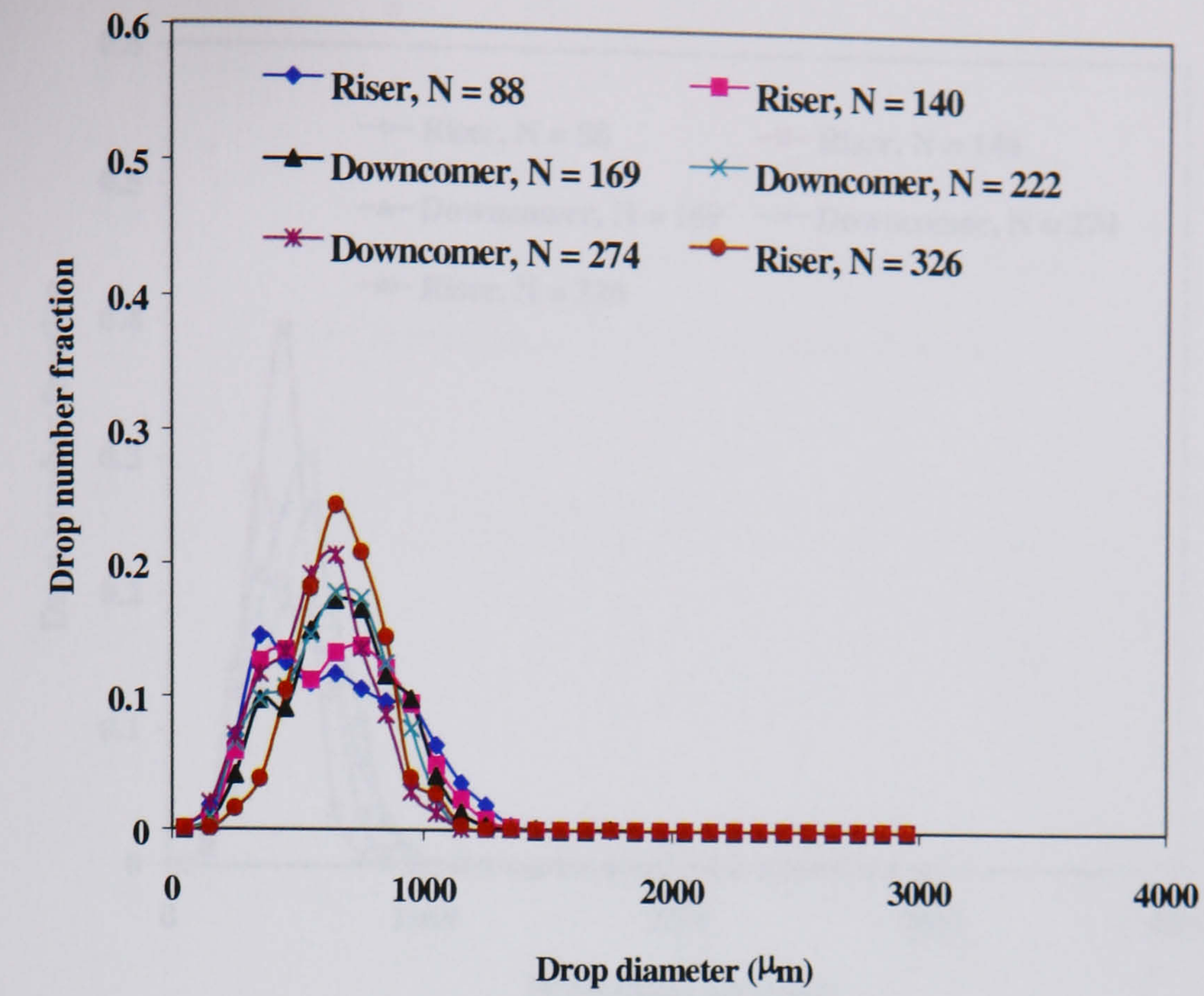

Figure 3.25. Drop size distribution as a function of flow length, Re_o = 7530 (x_o = 15 mm, f = 2 Hz); Re_n = 554

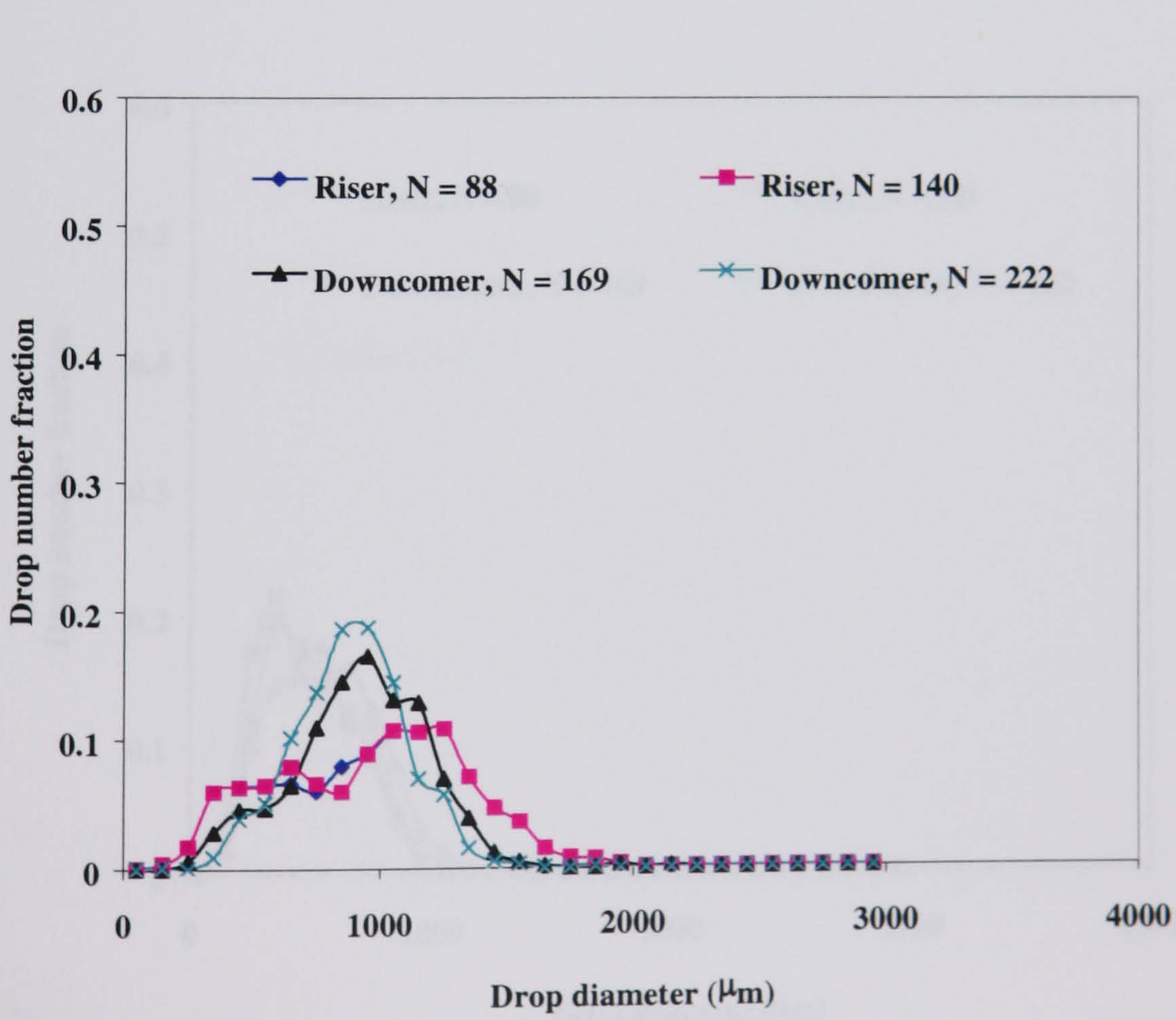

Figure 3.26. Drop size distribution as a function of flow length, Re_o = 5020 (x_o = 10 mm, f = 2 Hz); Re_n = 544

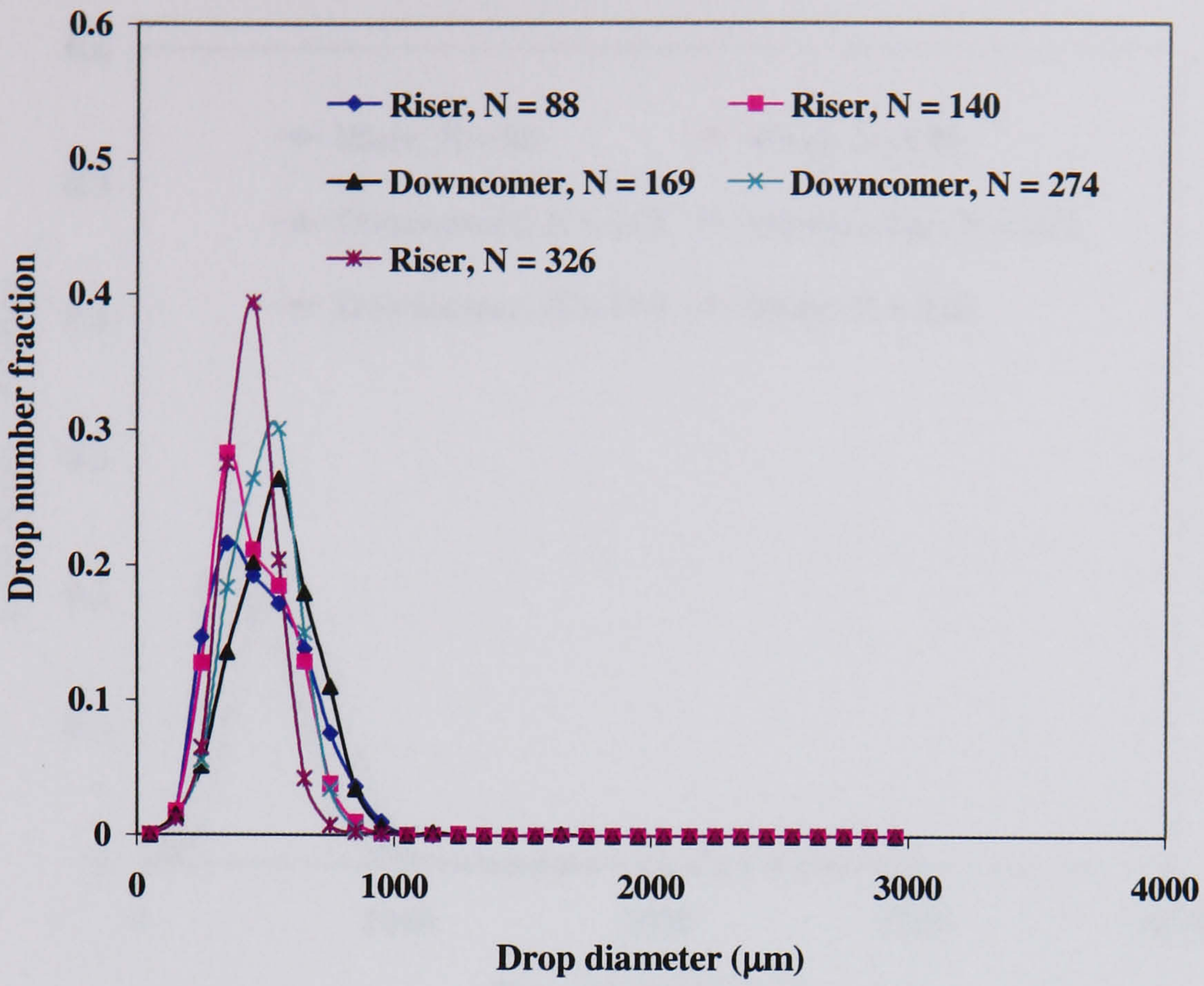

Figure 3.27. Drop size distribution as a function of flow length, Re_o = 9036 (x_o = 18 mm, f = 2 Hz); Re_n = 554

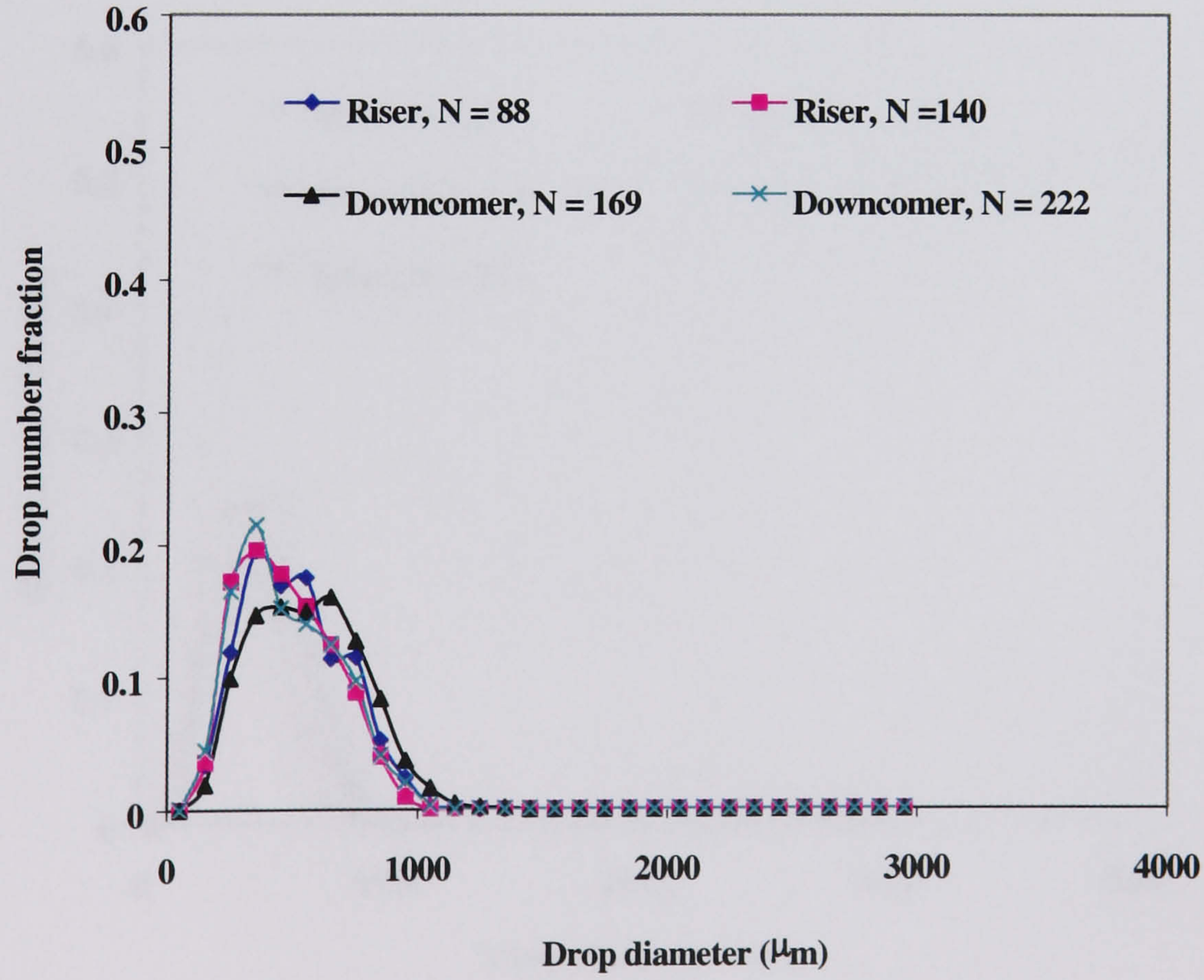

Figure 3.28. Drop size distribution as a function of flow length, Re_o = 11295 (x_o = 15 mm, f = 3 Hz); Re_n = 551

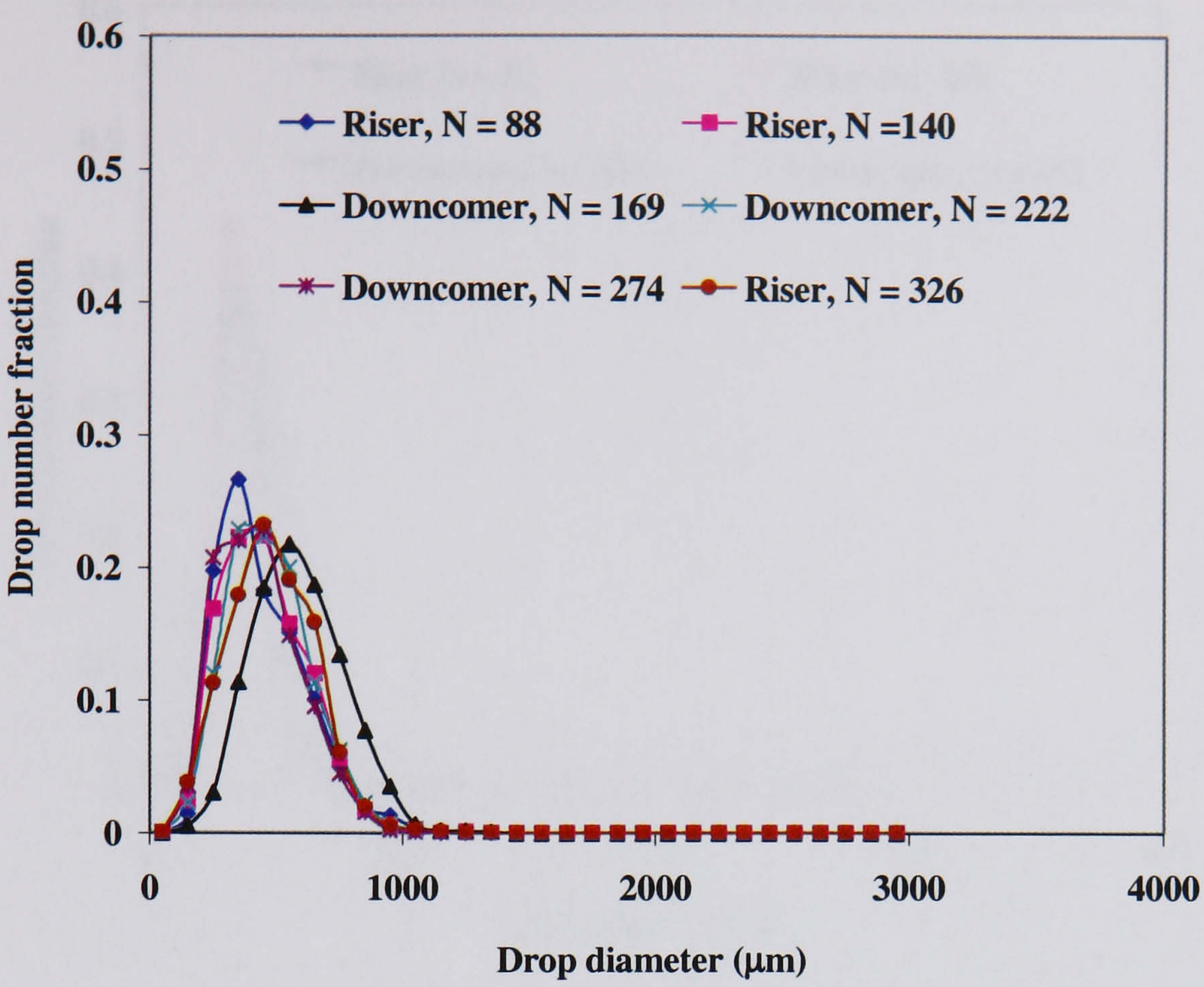

Figure 3.29. Drop size distribution as a function of flow length, Re_o = 13554 (x_o = 18 mm, f = 3 Hz); Re_n = 564

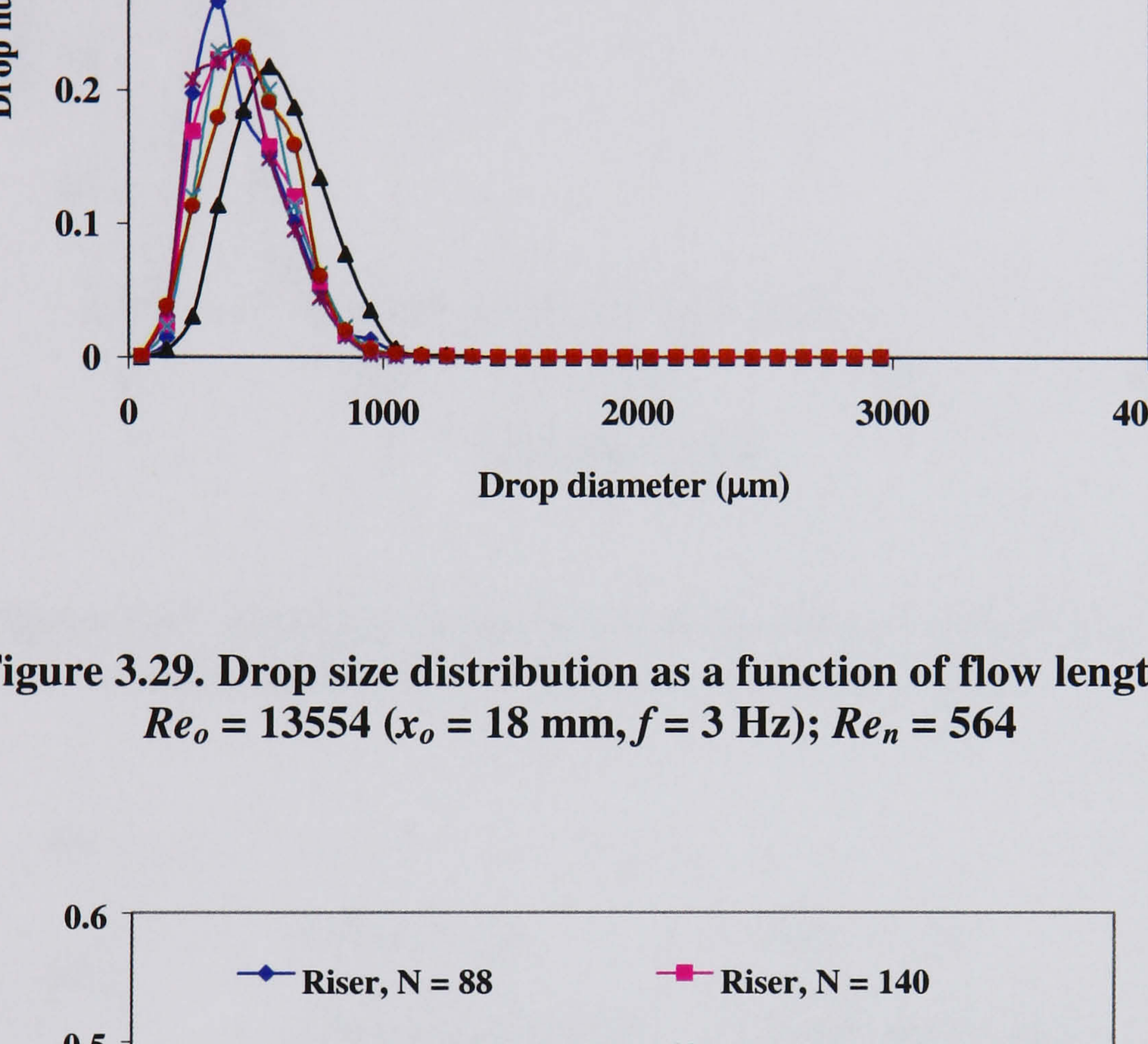

Figure 3.30. Drop size distribution as a function of flow length, Re_o = 10040 (x_o = 10 mm, f = 4 Hz); Re_n = 552

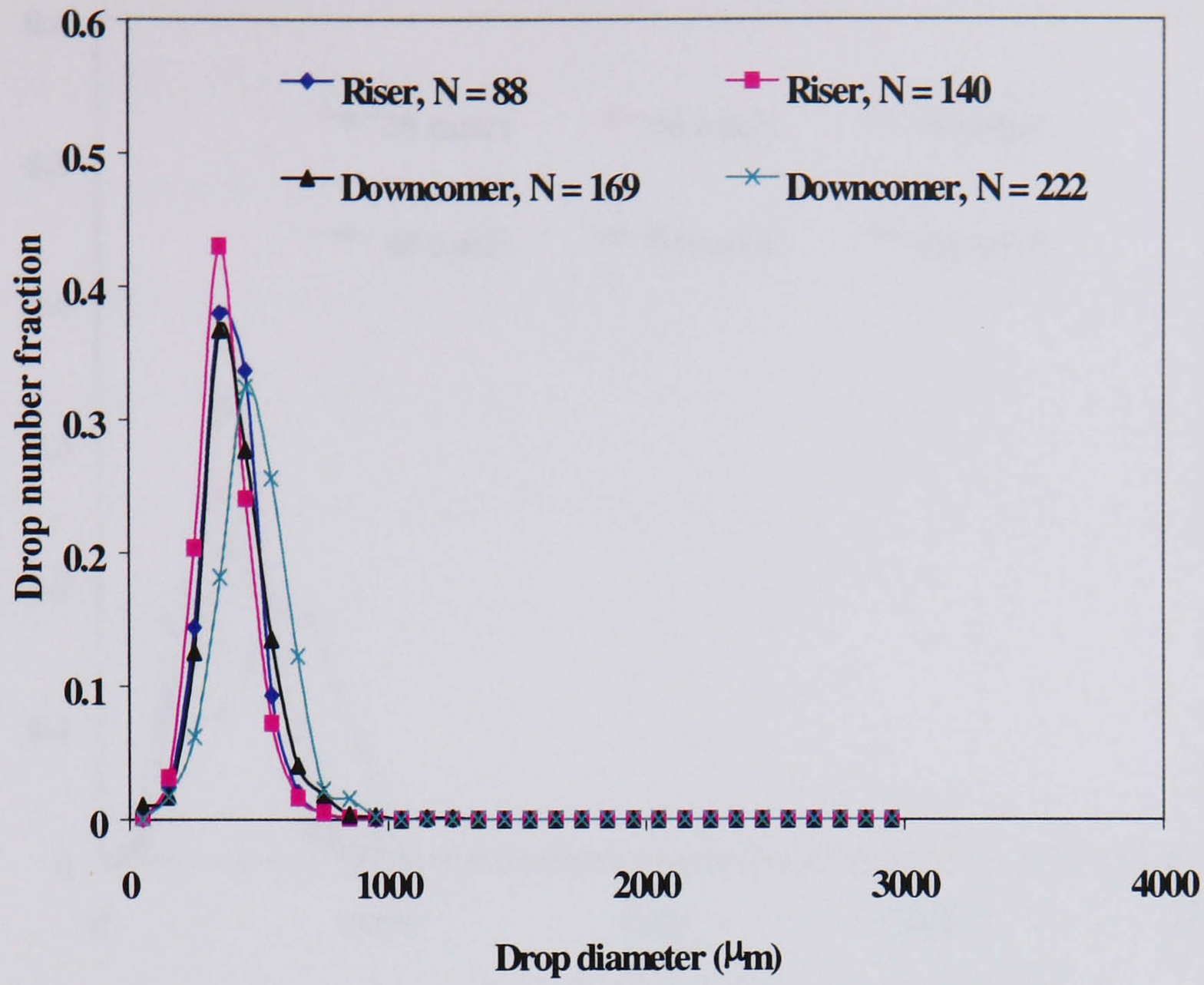

Figure 3.31. Drop size distribution as a function of flow length, Re_o = 15060 (x_o = 15 mm, f = 4 Hz); Re_n = 550

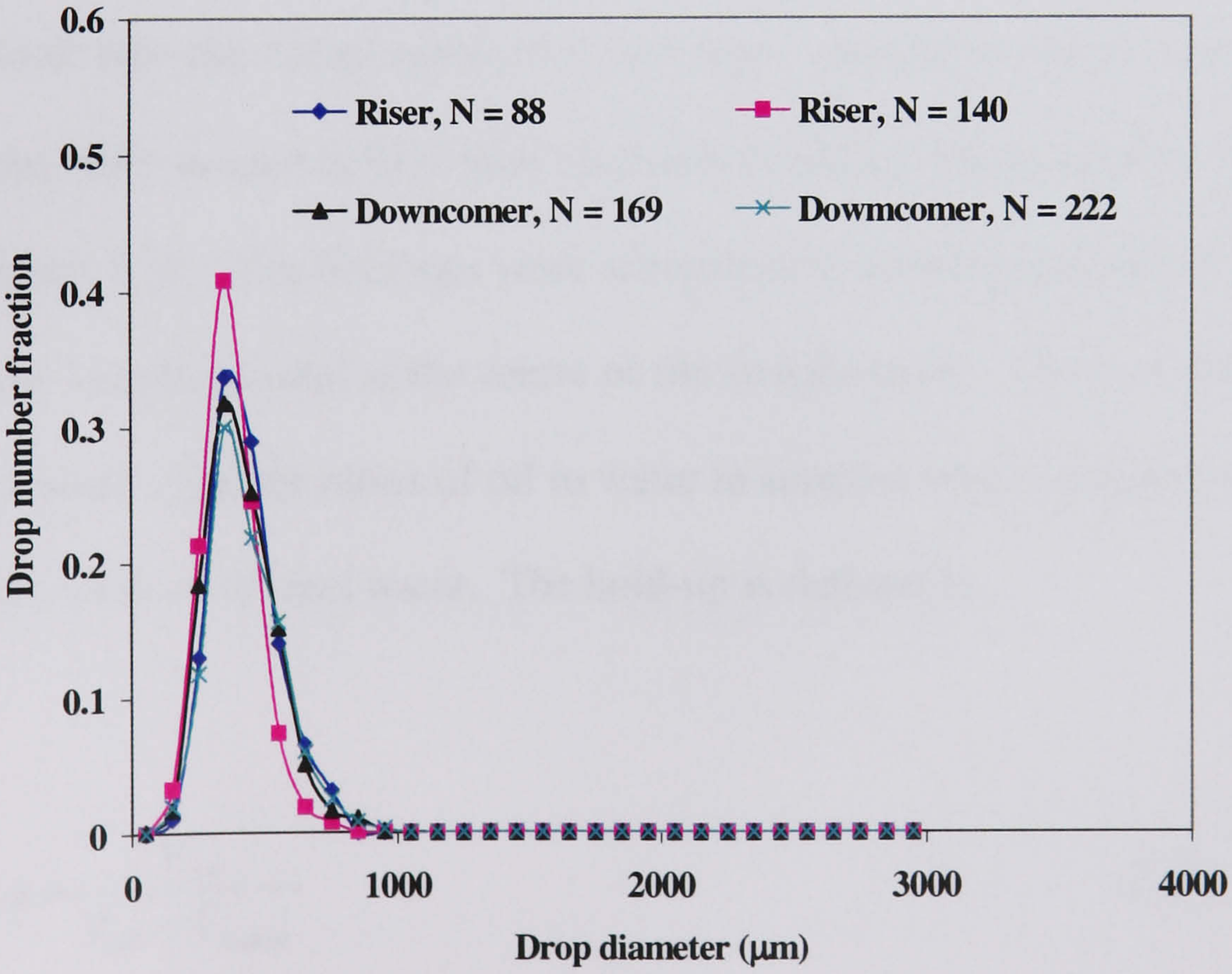

Figure 3.32. Drop size distribution as a function of flow length, Re_o = 18072 (x_o = 18 mm, f = 4 Hz); Re_n = 550

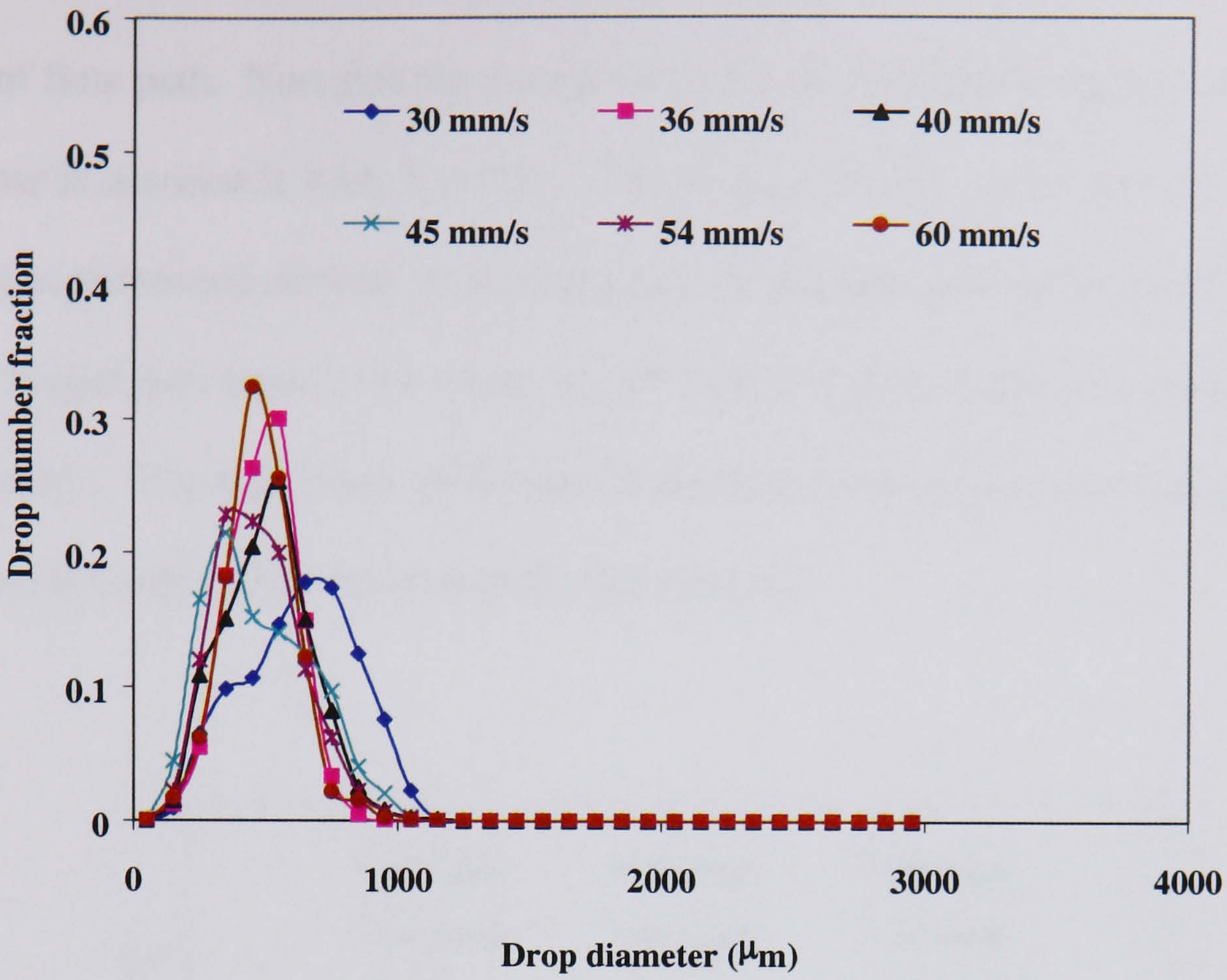

Figure 3.33. Drop size distribution at N = 222, Re_n = 554

To look into the complication that the risers and downcomers caused further, drop hold-ups were measured in a riser and a downcomer, the locations of which are shown in Figure 3.19. The hold-ups were measured by drawing samples at three ports along the tube length, situated at the centre of the straight tubes. The samples were then allowed to separate, and the ratios of oil to water in samples were compared with that of the initial flow rates of oil and water. The hold-up is defined as,

$$\phi = \frac{V_{oil}}{V_{oil} + V_{water}} \tag{3.22}$$

where V_{oil} and V_{water} are volumes of oil and water in sample, respectively. In order to increase the accuracy of hold-up data, three samples were taken at each port and an

average of the three was used in the analysis. Figure 3.34 shows the hold-ups as a function of flow path. Note that the riser refer to N = 43 and 140 in Figure 3.34 and the downcomer is associated with N = 169. The drop hold-ups in the risers are similar, validating experimental method. It is clear however that the hold-ups in the downcomer are much higher than those in the risers, in particular, at lower oscillation velocities, e.g. $x_o f$ < 20 mm/s. The significant difference in the drop hold-ups between the risers and the downcomer support the experimental DSD profiles.

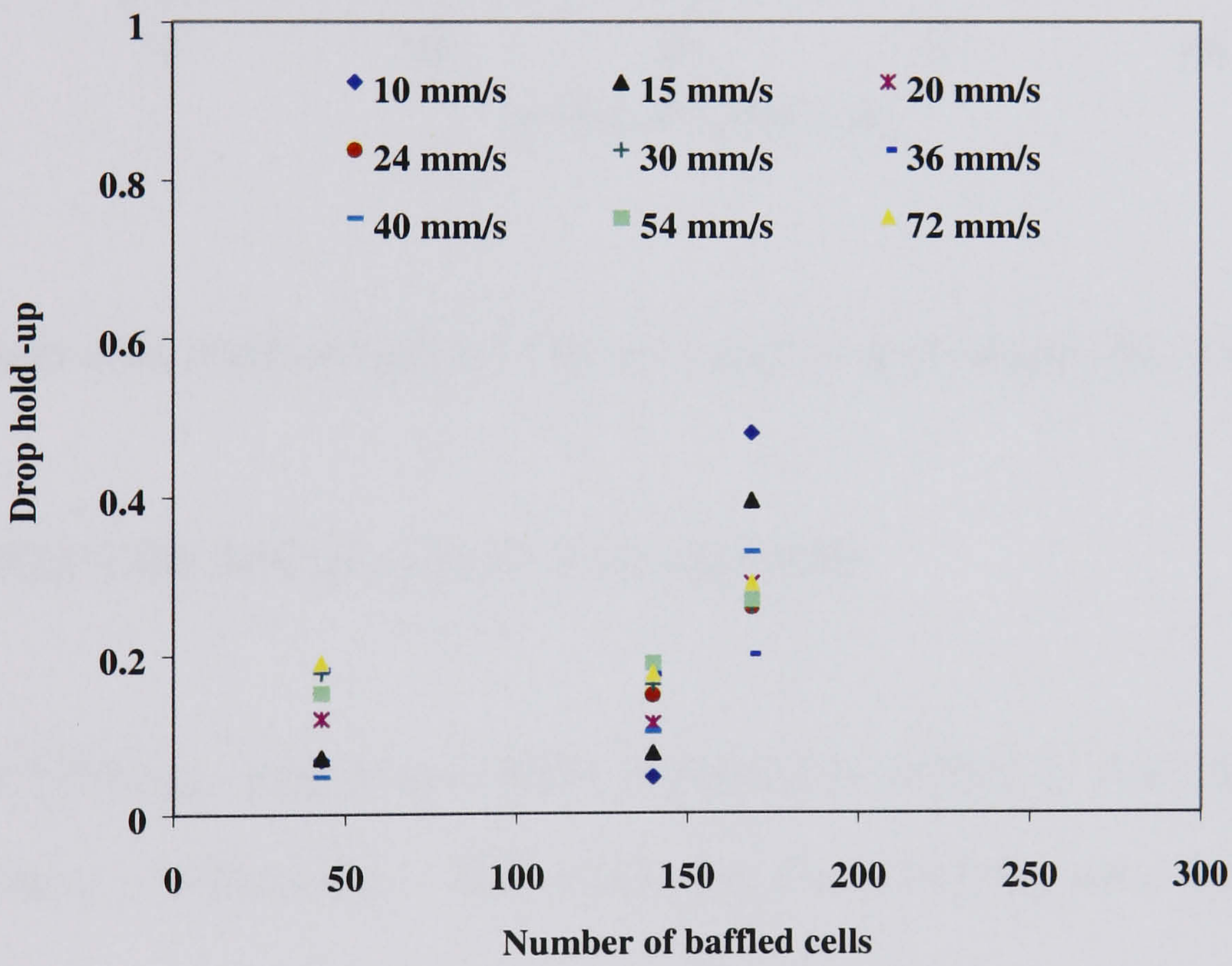

Figure 3.34. Axial Variation of hold–up

The pattern of the Sauter mean drop diameter along the reactor length shows, however, little change, see Figure 3.35 for different oscillation conditions. This is not surprising, as one can deduce from the DSDs in Figures 3.25 - 3.32 that there is little change in the ranges of drop sizes, although the changes in DSD profiles are substantial. As a result, The overall absolute change in d_{32} along the length was found to be about 16 %.

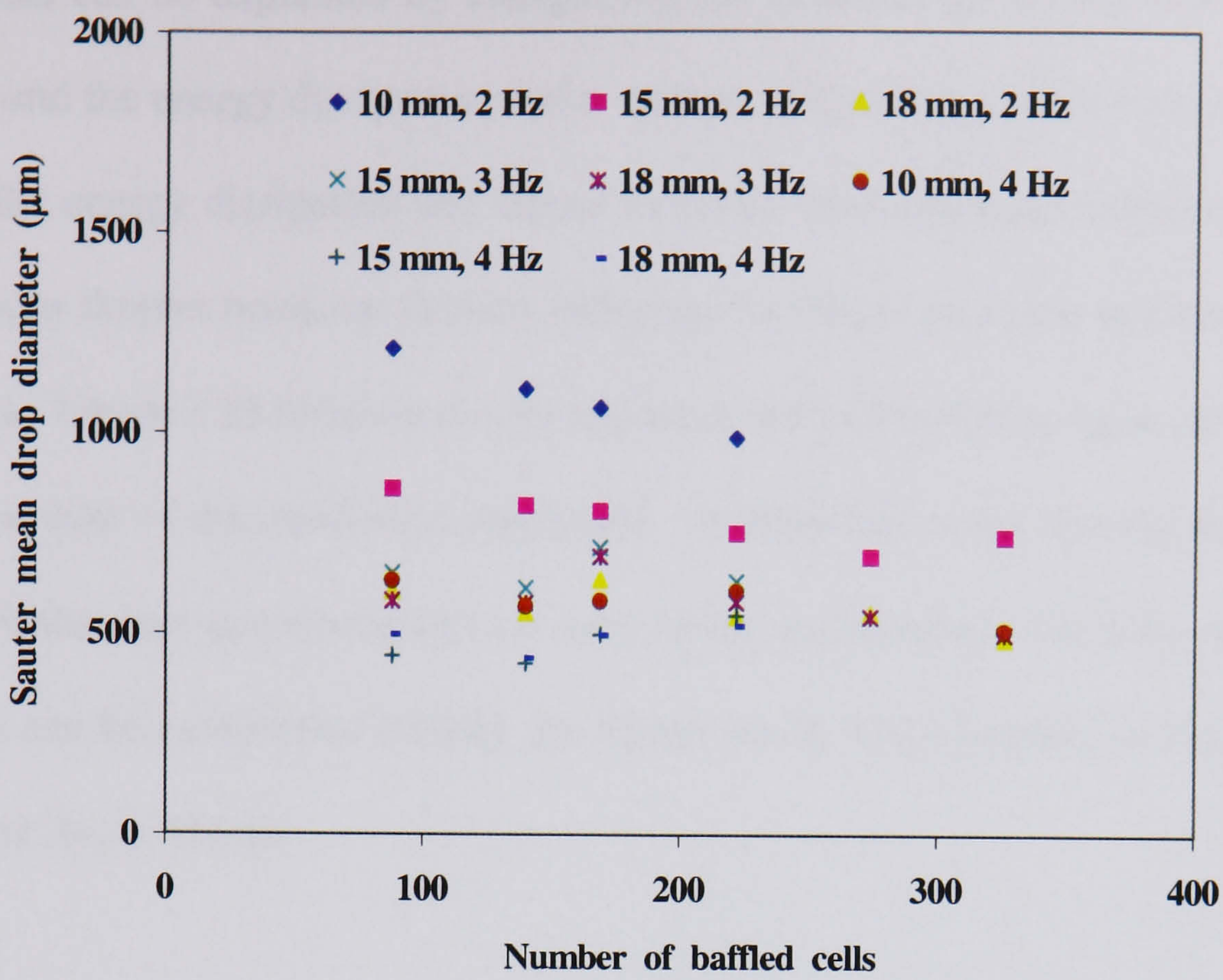

Figure 3.35. Axial variation of Sauter mean drop diameter, Re_n = 552

3.2.4.2 EFFECT OF OSCILLATION PARAMETERS

The following results to be reported correspond to the port 2, "riser" and the port 3, "downcomer", respectively. The results for the remaining ports are given in Appendix 1.

3.2.4.2.1 EFFECT OF OSCILLATION AMPLITUDE

Figures 3.36-3.37 show the effect of oscillation amplitude on drop size distribution (DSD) for a typical net flow Reynolds number of 551. From the Figures 3.36-3.37, one can see that with the increase in the oscillation amplitude the drop size distribution narrowed with the mean diameter shifting towards the lower end of the size scale, and the drop number fraction corresponding to smaller sizes also increased.

These results can be explained by considering the relationship between the oscillation amplitude and the energy dissipation in the system. Increasing the oscillation amplitude increases the energy dissipation and hence increases the turbulence intensity, which in turn enhances droplet break-up thereby reducing the mean drop size and narrowing the distribution. Figure 3.38 displays the decreasing trend of the Sauter mean drop diameter with the increase of the oscillation amplitude. It should be noted that the difference in d_{32} for both the riser and downcomer is very small, as expected. On this note, a single correlation can be established linking the Sauter mean drop diameter at the oscillation amplitude at $Re_n = 551$ as,

$$d_{32} = 1.75\times10^{-5}(\pm 70.9\%)\ x_o^{-0.89\ (\pm 16.5\%)} \quad \text{(m)}, \quad (R^2 = 0.878) \qquad (3.23)$$

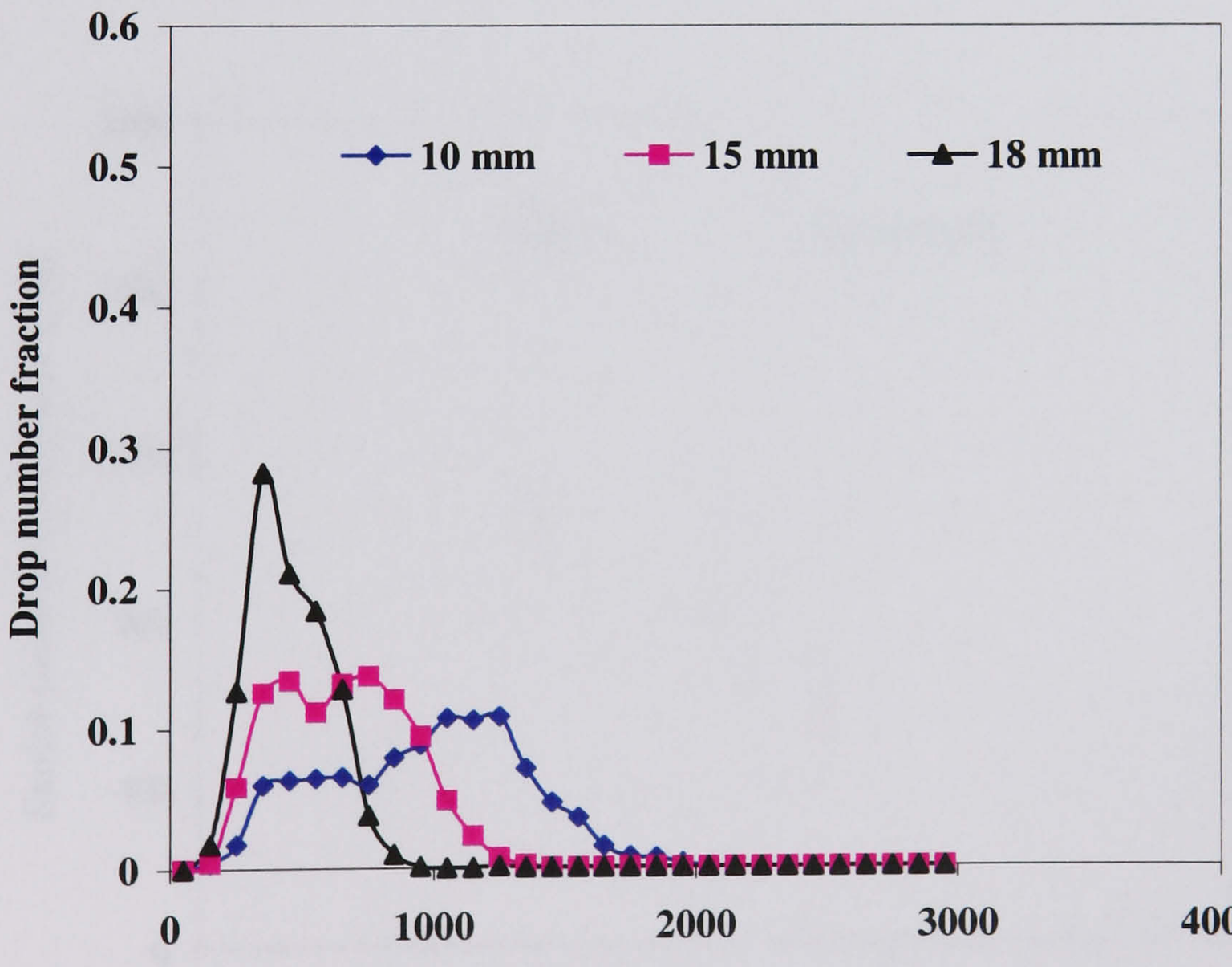

Figure 3.36. Effect of oscillation amplitude on droplet size distribution (f = 2.0 Hz, Re_n = 551), Riser

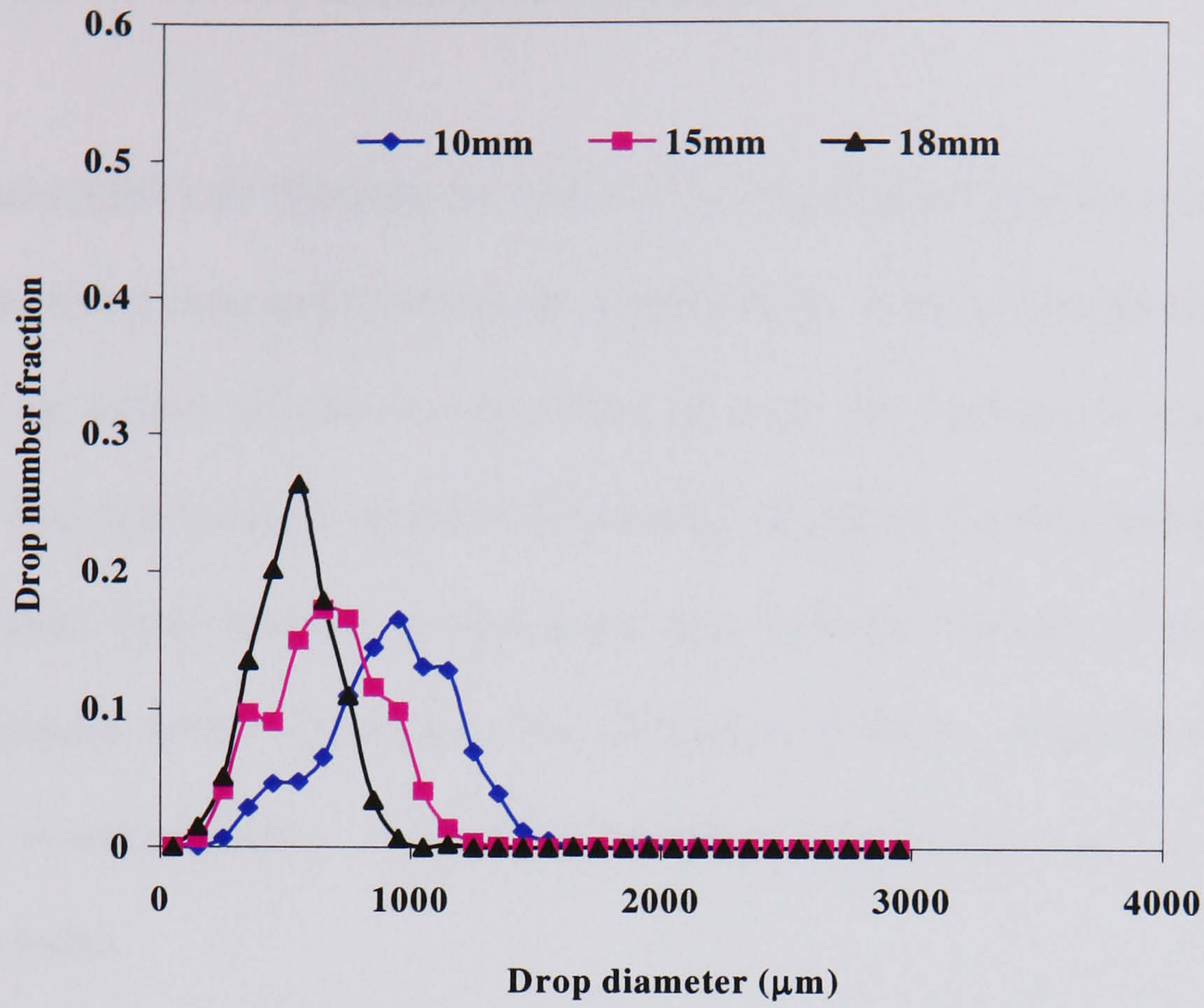

Figure 3.37. Effect of oscillation amplitude on droplet size distribution (f = 2.0 Hz, Re_n = 551), Downcomer

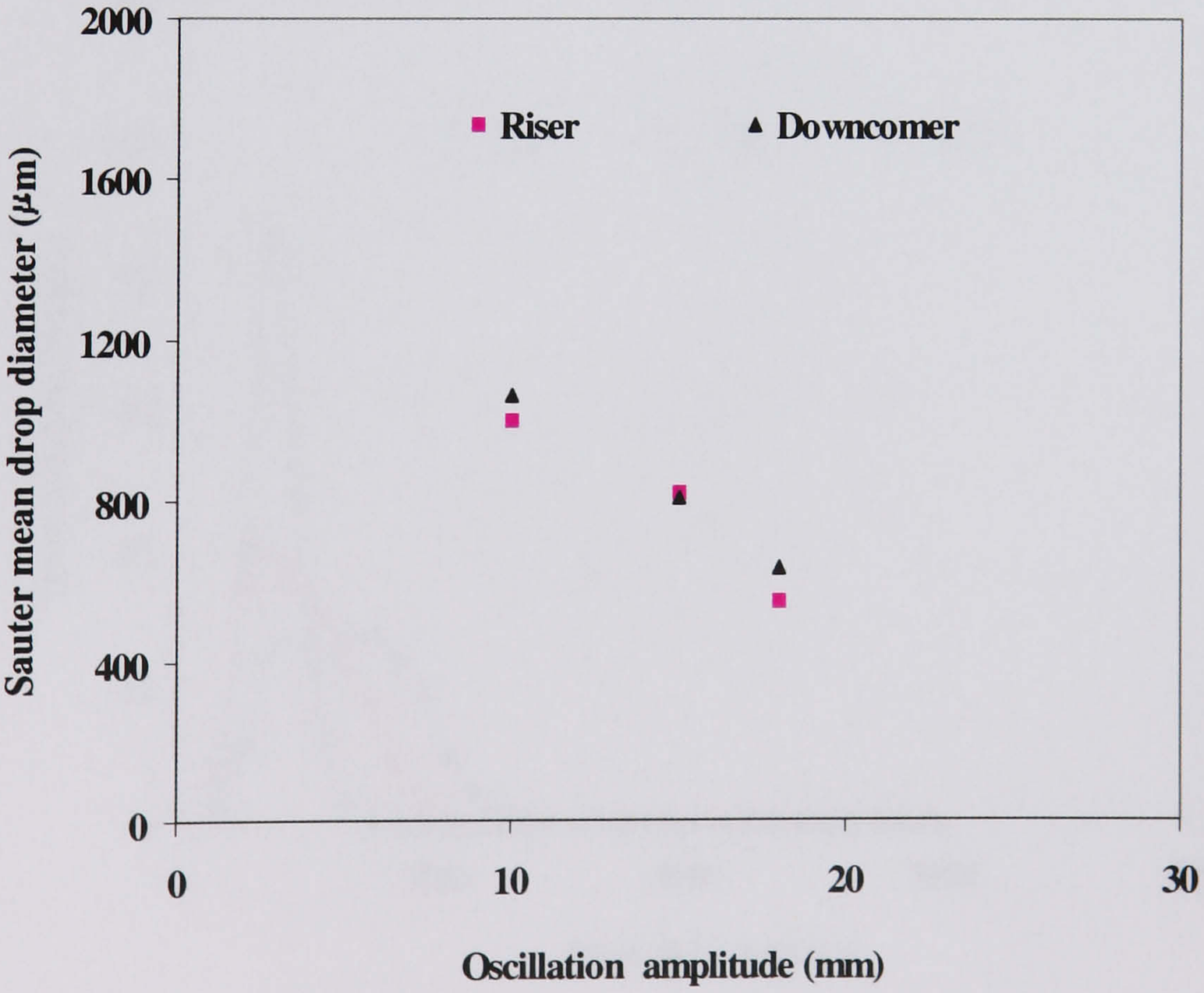

Figure 3.38. Effect of oscillation amplitude on Sauter mean drop diameter, (f = 2.0 Hz, Re_n = 551)

3.2.4.2.2 EFFECT OF OSCILLATION FREQUENCY

Figures 3.39-3.40 illustrate the effect of the oscillation frequency on the Sauter mean drop size in a riser and downcomer, respectively. A similar trend in DSDs as to that of the oscillation amplitude was observed with the increase in the oscillation frequency. This again can be related to the energy dissipation in the system. Likewise, the Sauter mean drop diameter is also decreasing with the increase of the oscillation frequency (Figure 3.41). Once again the difference in the d_{32} between the riser and downcomer is insignificant. A single correlation between d_{32} and f is justified to describe the trend,

$$d_{32} = 1.178\times10^{-3}(\pm 8.69\%)\ f^{-0.53\ (\pm 7.92\%)} \quad \text{(m)}, \quad (R^2 = 0.918) \tag{3.24}$$

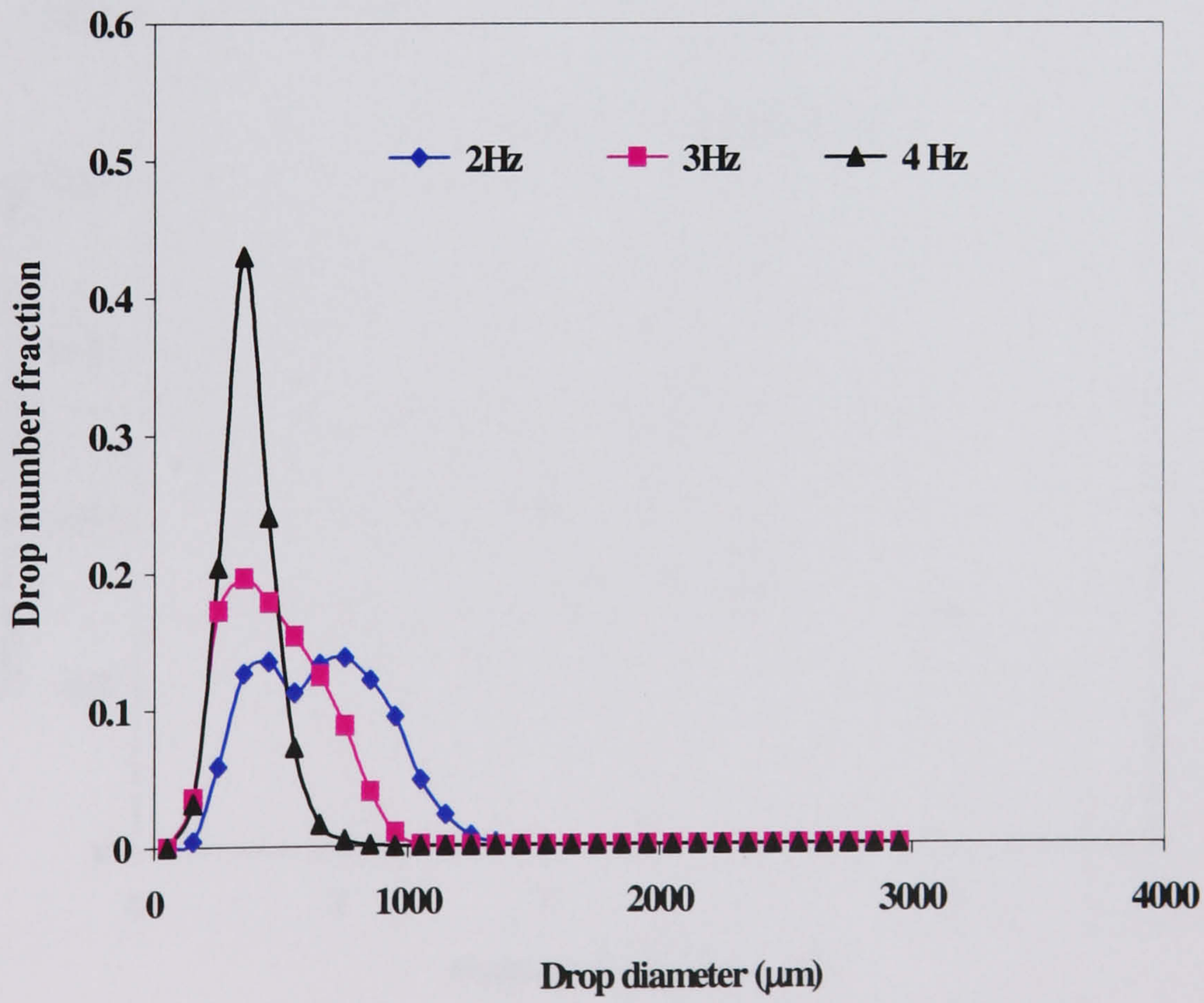

Figure 3.39. Effect of oscillation frequency on droplet size distribution (x_o = 15 mm, Re_n = 551), Riser

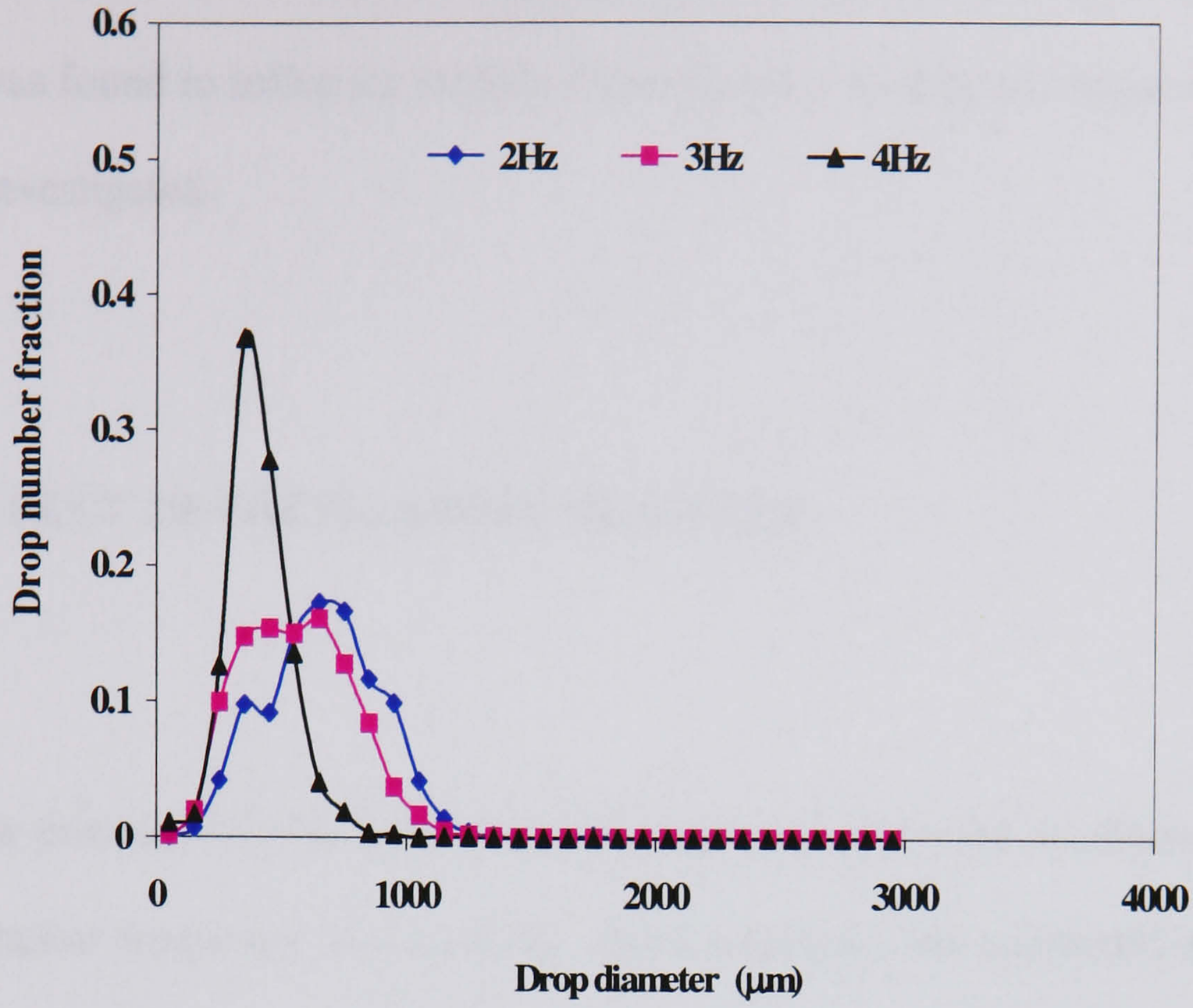

Figure 3.40. Effect of oscillation frequency on droplet size distribution (x_o = 15 mm, Re_n = 551), Downcomer

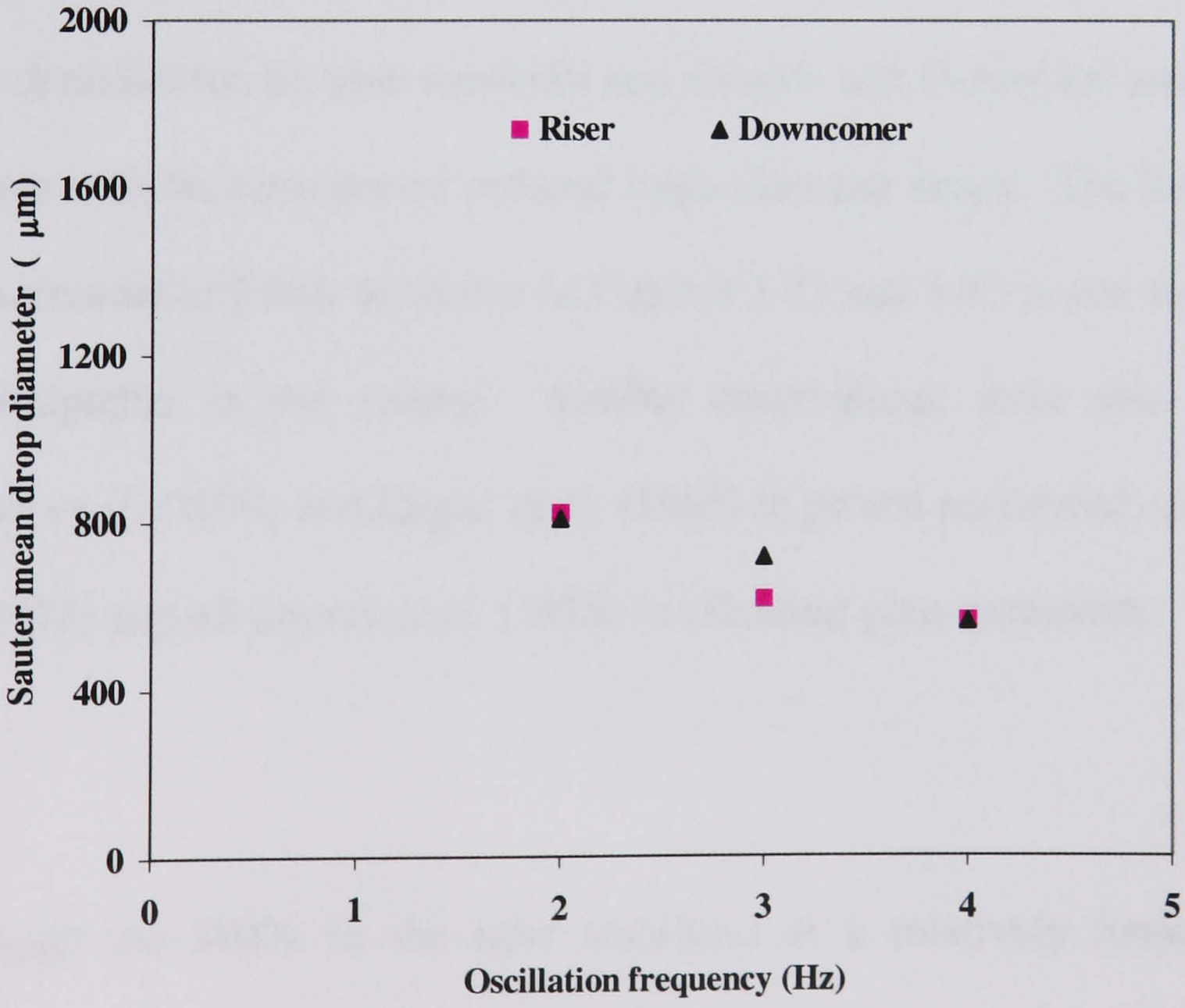

Figure 3.41. Effect of oscillation frequency on Sauter mean drop diameter, (x_o = 15 mm, Re_n = 551)

On comparison of the two correlations, one can deduce that the oscillation amplitude was found to influence slightly more than the oscillation frequency under the conditions investigated.

3.2.4.2.3 EFFECT OF OSCILLATION VELOCITY

In the previous sections, the individual effect of either the oscillation amplitude or the oscillation frequency was studied. In this section, the combined effect of the oscillation velocity, $x_o f$ on the drop size distribution (DSD) is reported. Figures 3.42 – 3.43 show the experimental DSD profiles for both the riser and the downcomer, respectively. At lower oscillations, e.g., $x_o f$ = 20 mm/s, the drop size distribution was very broad and displayed bimodal characteristics. With the increase in the oscillation velocity, the distributions became unimodal and sharper and shifted towards the smaller drop diameters with the presence of reduced large diameter drops. The transition from bimodal to unimodal in DSDs as shown in Figures 3.42 and 3.43 is due to the increase in power dissipation in the system. Similar observations were also reported by Khemangkorn *et al.* (1977) and Kagan *et al.* (1965) in pulsed perforated –plate column; Tojo *et al.* (1975) and Miyanami *et al.* (1975) in vibrating plate extractors.

Although the DSDs in the riser stabilised at a relatively lower oscillation velocity than those in the downcomer, the DSDs were essentially identical at high oscillation velocities, e.g. 60 mm/s. This in fact provides the vehicle in the vertical OBTR to achieve drop stability. A further graph in Figure 3.44 confirms this claim. In

fact the DSDs virtually overlap at all the risers and downcomers starting from 10.5 m away from the oil injection, which is about 42 % of the total length. This finding presents potential problems in applying the vertical OBTR to the continuous suspension polymerisation process, as it is desirable that the initiator is added after the stabilisation of drop has been reached, the later the stability, the longer the tubes that are required. A further drawback is that such a stability of drops is achieved at the expense of very high oscillatory velocities, hence high power input.

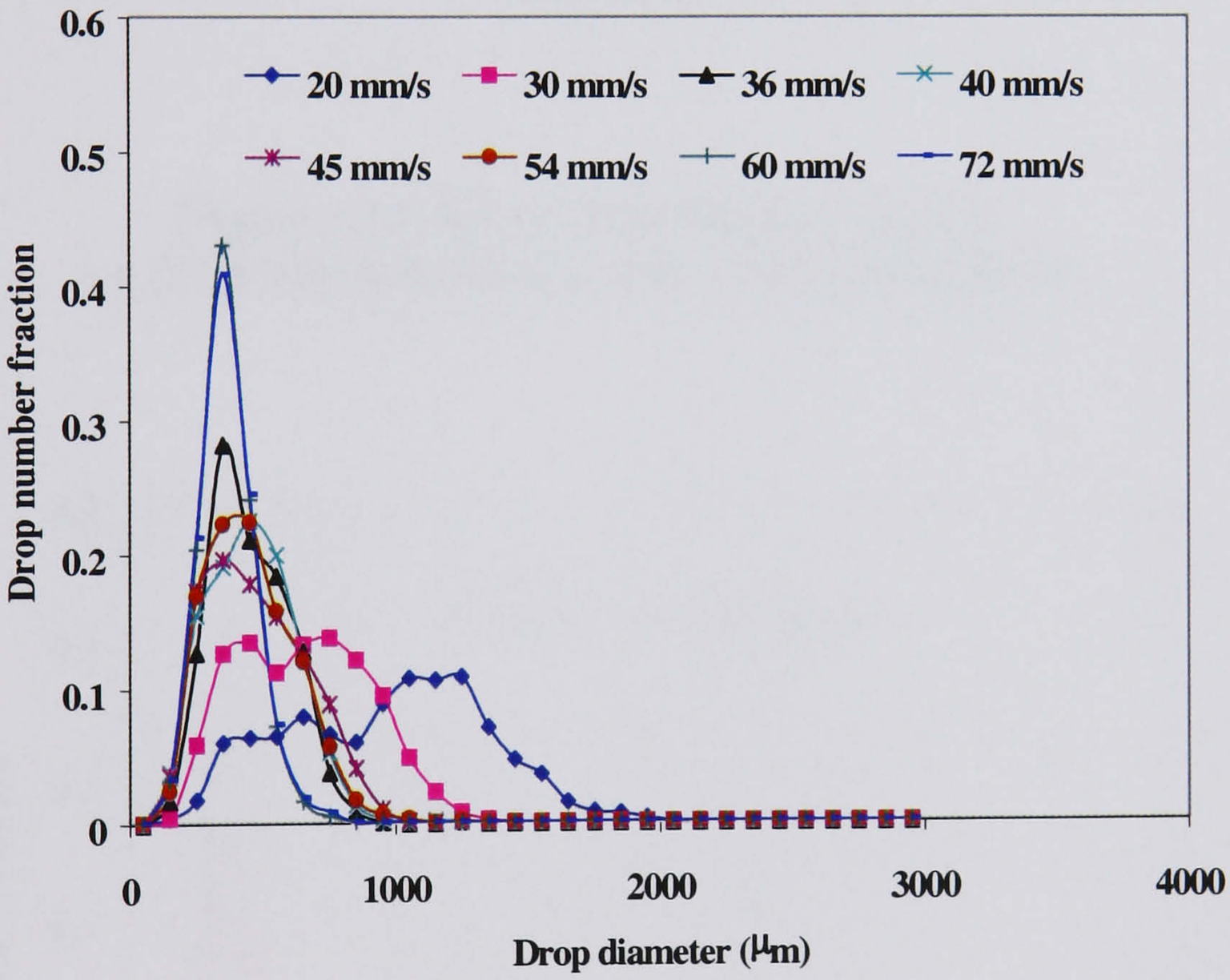

Figure 3.42. Effect of oscillation velocity on drop size distribution, Re_n = 554, Riser

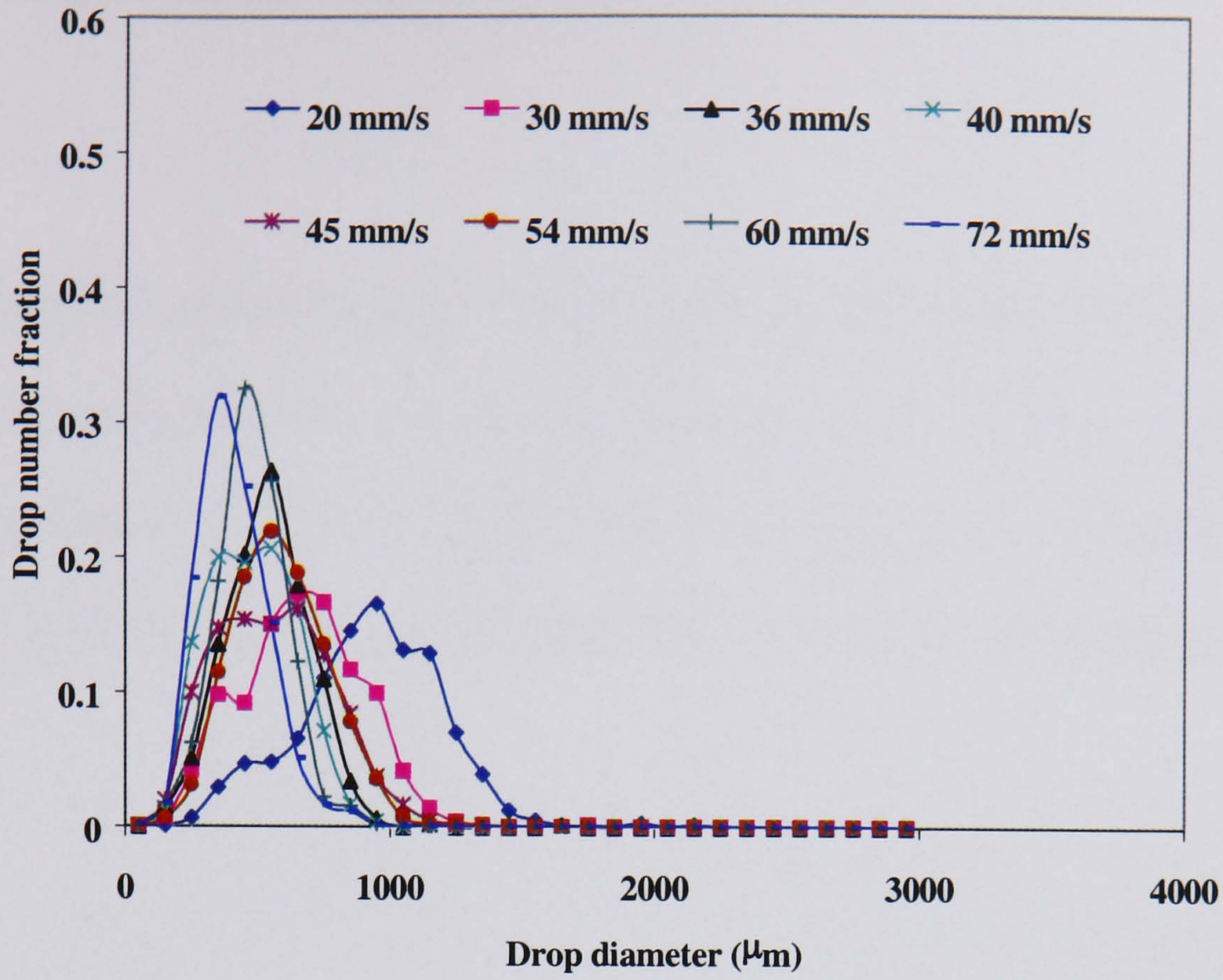

Figure 3.43. Effect of oscillation velocity on drop size distribution, Re_n = 554, Downcomer

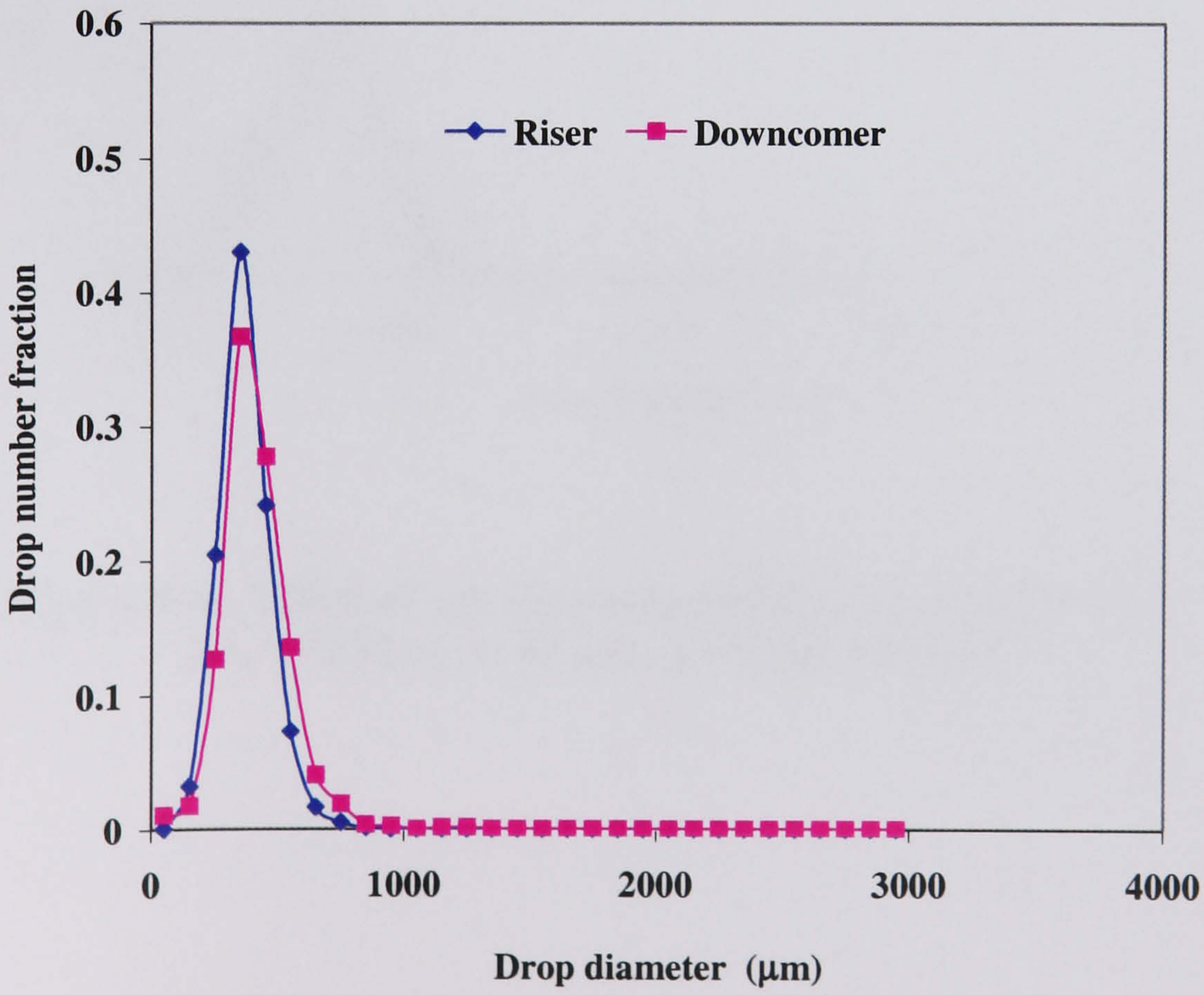

Figure 3.44. Drop size distribution at riser and downcomer for $x_o f$ = 60 mm/s, Re_n = 550, N = 140 & 169

3.2.4.2.4 EFFECT OF NET FLOW RATE

The effect of the net flow rate on DSD in the riser is shown in Figure 3.45, at a fixed oscillation amplitude of 15 mm and frequency of 2 Hz (Re_o = 7530). The corresponding Figure for the downcomer is given in Figure 3.46. Generally speaking, the behaviour of DSDs is somewhat similar in both type of flow arrangements.

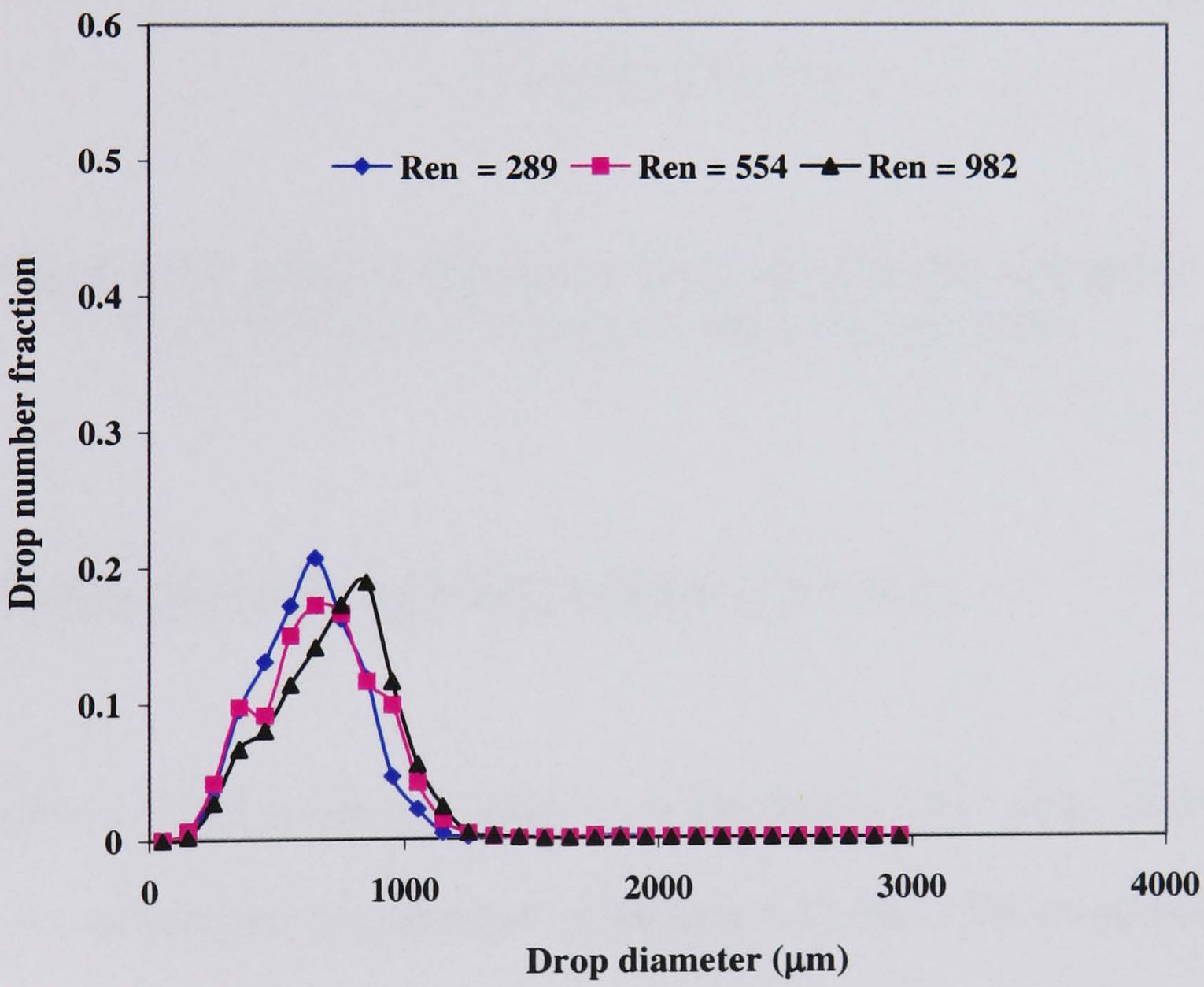

Figure 3.45. Effect of net flow rate on drop size distribution, Re_o = 7530 (x_o = 15 mm, f = 2 Hz), (Riser)

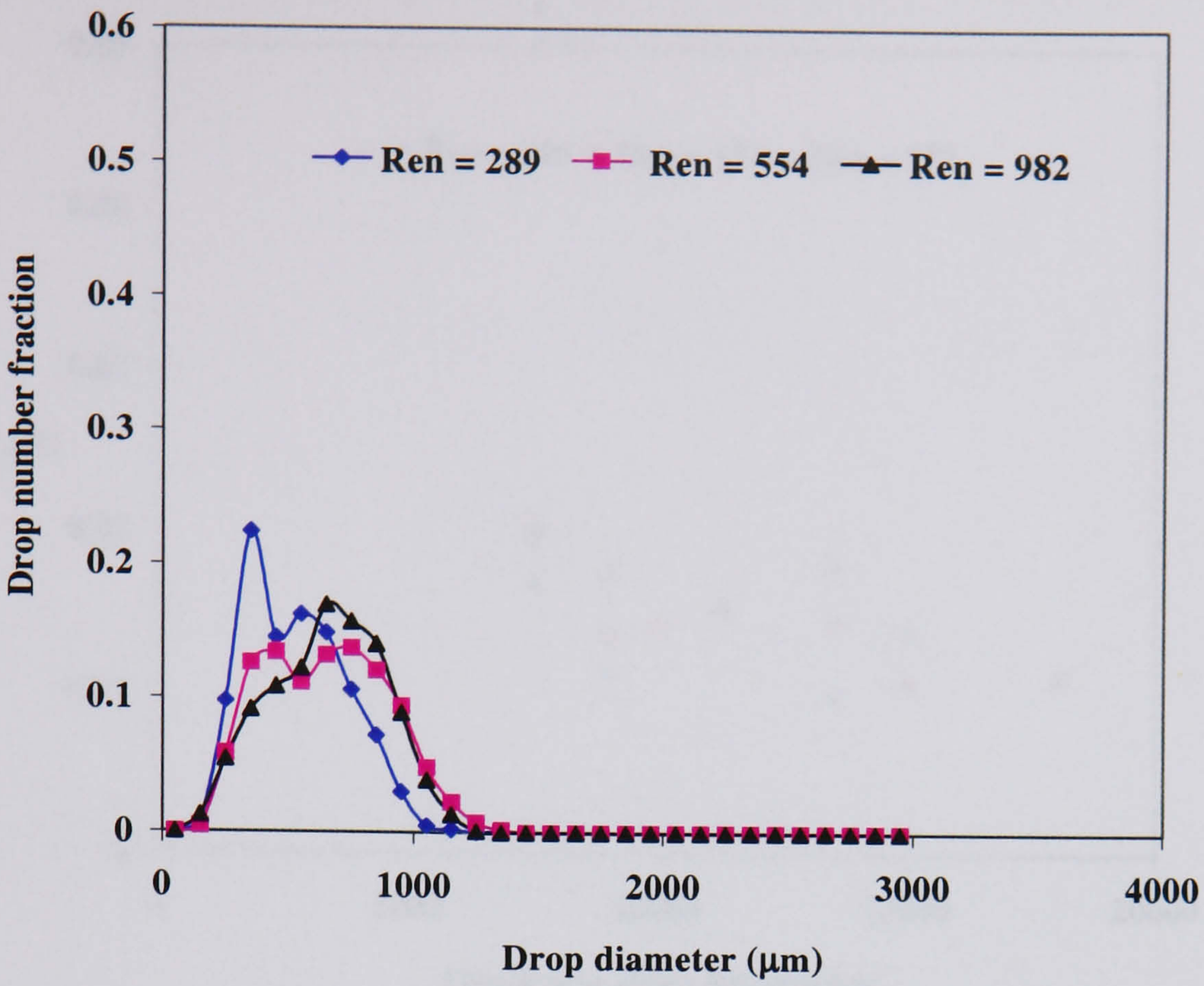

Figure 3.46. Effect of net flow rate on drop size distribution, Re_o = 7530 (x_o = 15 mm, f = 2 Hz), (Downcomer)

3.2.4.2.5 EFFECT OF OSCILLATION VELOCITY ON d_{32}

The effect of the oscillation velocity on the Sauter mean drop diameter in both the riser and the downcomer is presented in Figures 3.47 and 3.48, respectively over the entire operating conditions used. In these Figures, $\frac{d_{32}}{D}$ is plotted against the oscillation Reynolds number. In both the riser and the downcomer, the mean drop diameter showed an overall decrease with the increase in the oscillatory Reynolds number, *i.e.* the oscillation velocity, and more so in the downcomer. From the previous discussion, this is expected.

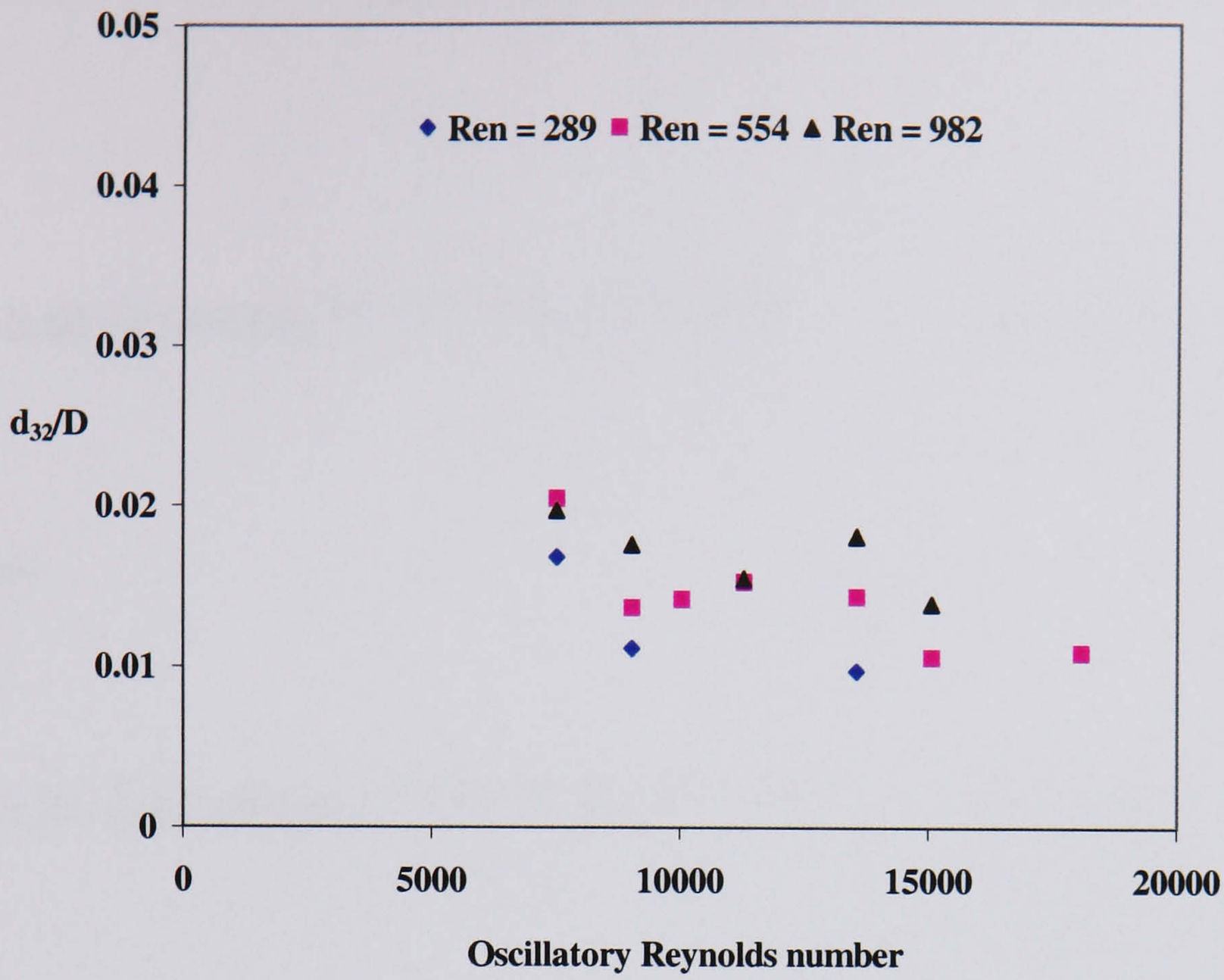

Figure 3.47. Effect of oscillatory Reynolds number on dimensionless mean drop diameter (Riser)

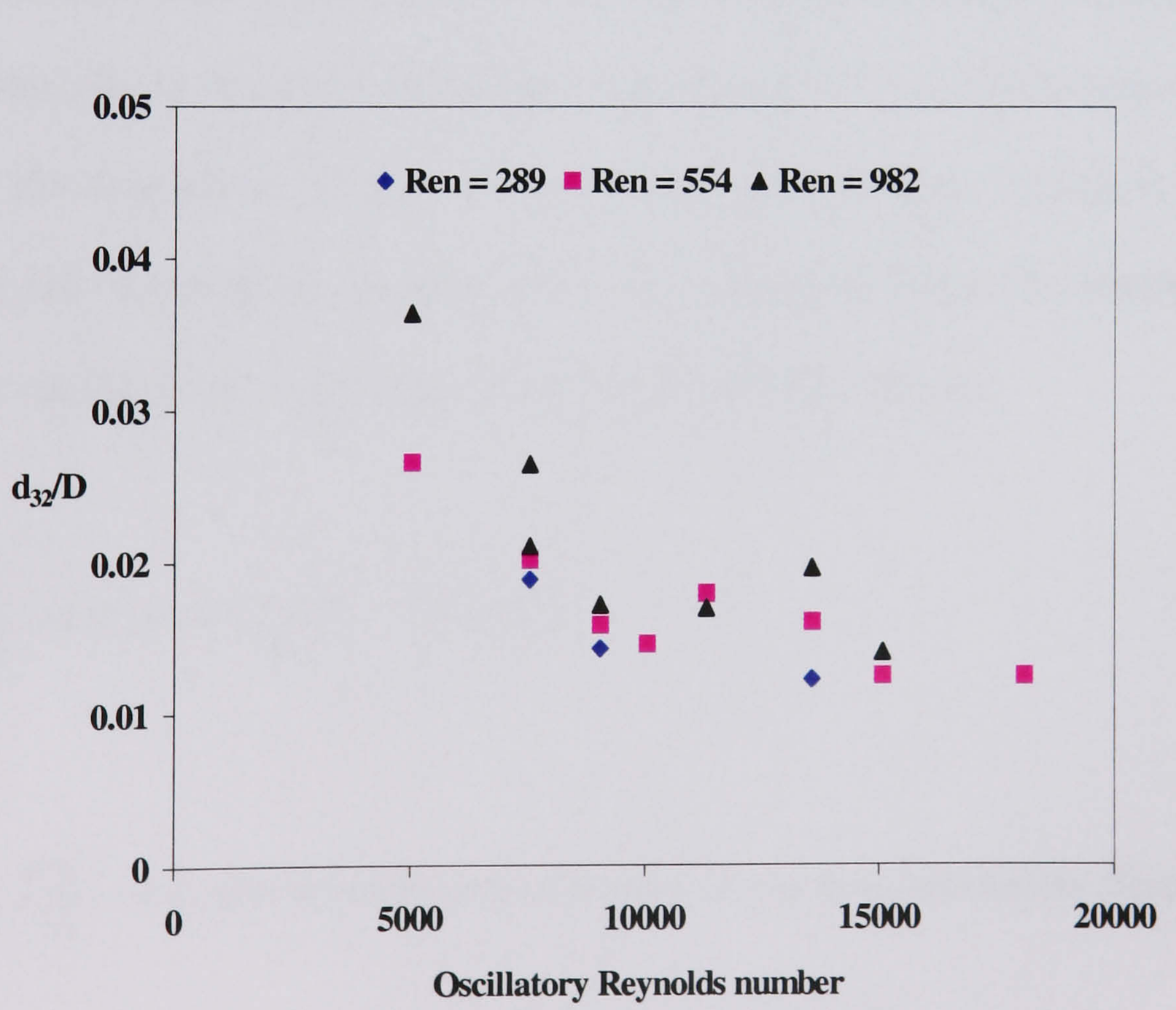

Figure 3.48. Effect of oscillatory Reynolds number on dimensionless mean drop diameter (Downcomer)

The data shown in the above Figures were fitted with a power law relationship as:

Riser

$$\frac{d_{32}}{D} = 0.40\ (\pm 54\%)\mathrm{Re}_o^{-0.57\ (\pm 17.72\%)}\mathrm{Re}_n^{0.31\ (\pm 12.25\%)} \qquad (R^2 = 0.744) \quad (3.25)$$

Downcomer

$$\frac{d_{32}}{D} = 1.24\ (\pm 41.88\%)\mathrm{Re}_o^{-0.66\ (\pm 10.9\%)}\mathrm{Re}_n^{0.29\ (\pm 15.65\%)} \qquad (R^2 = 0.867) \quad (3.26)$$

It can be seen that the net flow has a similar effect on d_{32} in both the riser and the downcomer, and the outcome is in line with the experimental DSDs shown in Figures 3.45 and 3.46. The oscillation, however, affected d_{32} more in the downcomer than the riser, due to the prolonged droplet residence time in the downcomer. In order to expand the correlation in both the riser and the downcomer linking to the power dissipation rate as given in equation (2.3), the oscillatory Reynolds number, *i.e.* the oscillation velocity, was converted to the power dissipation rate as,

$$\varepsilon = \frac{P}{V\rho} = 4.63\times 10^4 \left(x_o f\right)^3 \qquad (\mathrm{W.kg^{-1}}) \qquad (3.27)$$

Replotting $\frac{d_{32}}{D}$ vs ε provides the graphs needed for such a correlation. Figures 3.49 is the one for the riser and Figures 3.50 for the downcomer. $\frac{d_{32}}{D}$ again decreases with the increase in the power dissipation, with more for the downcomer, the trend matches well with the expectation. From the trends the following correlations are obtained:

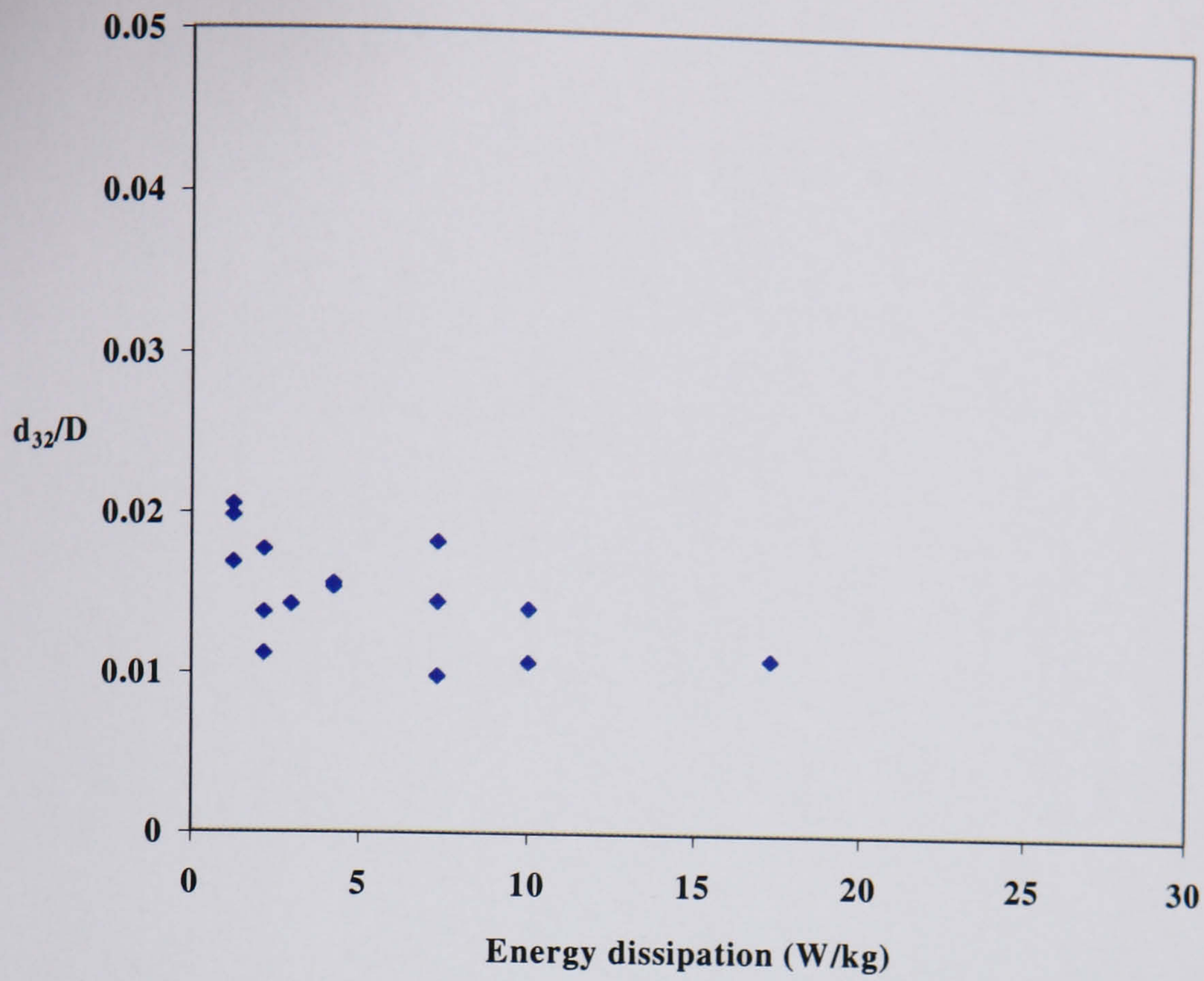

Figure 3.49. Effect of energy dissipation on mean drop diameter (Riser)

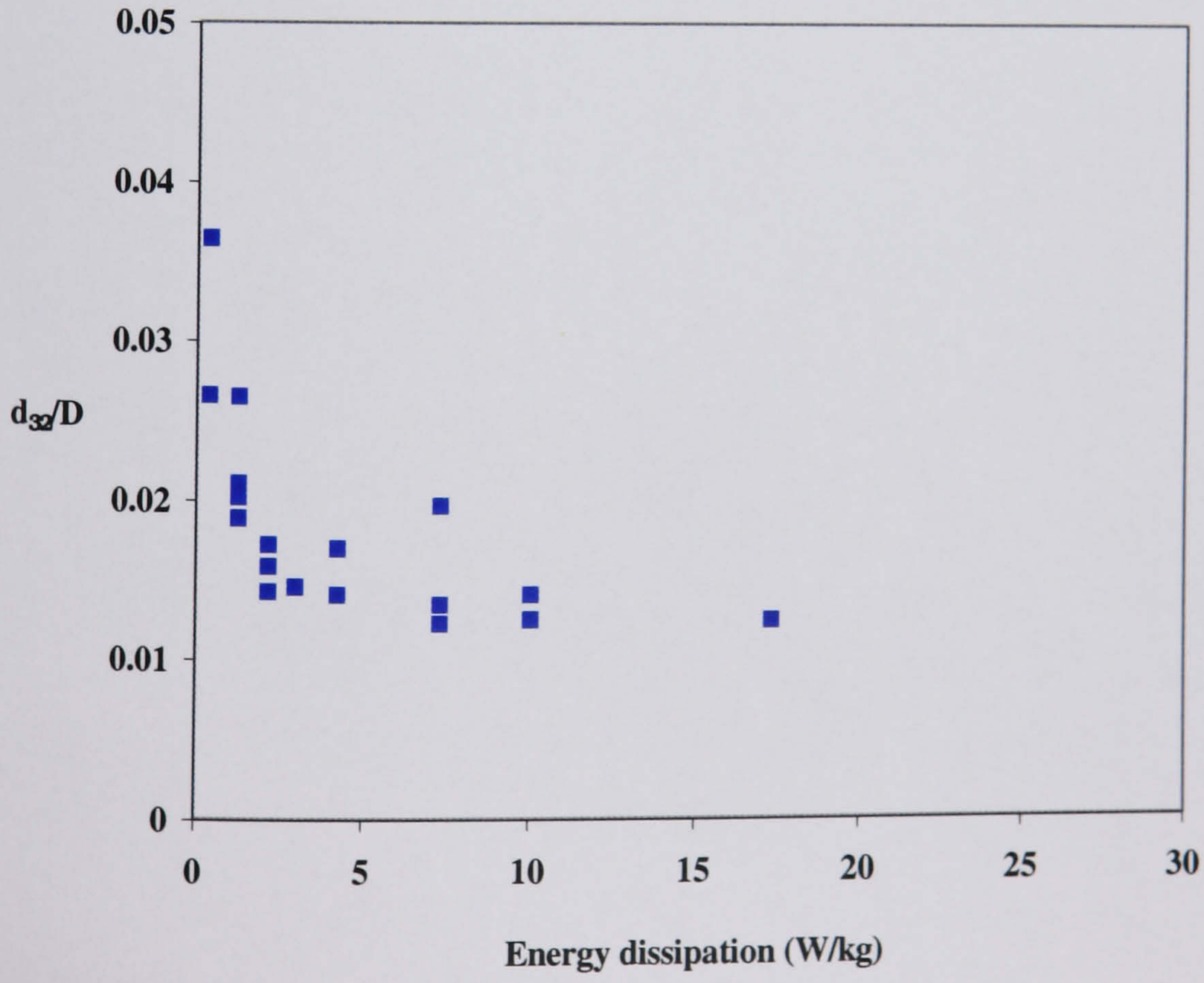

Figure 3.50. Effect of energy dissipation on mean drop diameter (Downcomer)

Riser

$$\frac{d_{32}}{D} = 0.018\ (\pm 9.38\%)\varepsilon^{-0.16\ (\pm 5.9\%)} \qquad (R^2 = 0.37) \qquad (3.28)$$

Downcomer

$$\frac{d_{32}}{D} = 0.022\ (\pm 5.4\%)\varepsilon^{-0.23\ (\pm 3.63\%)} \qquad (R^2 = 0.72) \qquad (3.29)$$

From the correlations, it was observed that the value of power index is slightly higher in the downcomer indicating more large drops appearing per unit power input, due to high drop hold-up in the downcomer.

3.2.5 SUMMARY OF RESULTS

From the experimental two phase flow results, it was observed the drop size distributions and the Sauter mean drop diameter were strongly influenced by the oscillation amplitude, frequency and the combination of the two in both the risers and the downcomers. However, the effect of the net flow rate on DSD and mean drop size was much smaller compared to the oscillation velocity conditions.

The drop stability was examined by measuring the DSD and d_{32} along the length of the tube, as well as by examining the oscillation conditions. In the presence of risers and downcomers in the vertical OBTR, the degree of DSDs overlapping at a given

operational condition is low along the length of the tube, indicating poor stability. The shape of the DSDs is generally not well defined.

The drop stability along the flow path was achieved at high oscillation velocities, e.g. ≥ 60 mm/s. At such oscillation velocities, the Sauter mean drop size was between 498 to 550 μm, which is effectively the maximum drop size achievable in the vertical OBTR system. Further increase in the oscillation velocity will allow smaller Sauter mean drop size. In terms of controllability, however, it is rather limited.

3.3 WHAT HAVE WE LEARNT?

On characterising the vertical OBTR, there are two major conclusions to be drawn from this work:

- The vertical OBTR is well suited for single phase applications as near to plug flow characteristics have been achieved over all the experimental conditions explored.

- The vertical OBTR is however not well suited for two phase flow applications, in particular, suspension polymerisation processes. The presence of risers and downcomers has led to poor drop stability and excessive oscillation in order to achieve such a drop stability.

CHAPTER 4

CHARACTERISATION OF THE HORIZONTAL OBTR

The employment of a horizontal OBTR was the direct result of the progress and development in our understanding of characterisation of a continuous OBTR with a special reference to continuous suspension polymerisation reaction. Following the investigation in the vertical OBTR, the single and two phase flow studies have been carried out in a horizontal OBTR. The results are presented in a similar style as those in the previous chapter.

4.1 THE SINGLE PHASE FLOW STUDY

4.1.1 EXPERIMENTAL SET UP AND PROCEDURE

The experimental horizontal OBTR used in the present investigation is shown in Figure 4.1. It consisted of seven QVF glass tubes, each of 40 mm in diameter. The first tube was 1 meter in length while the remaining tubes were 1.5 m each in length. These tubes were connected by U-bends, each about 0.35 m in curvature length, as shown in Figure 4.1. The straight sections and bends formed a single-flow path of about 12.5 m. A non-return valve, NRV2, was used in the flow inlet in order to reduce any propagation of oscillation upstream. A LOWARA centrifugal pump was used to pump the continuous phase (water) through the system. The flow rate was controlled by means of a rotameter, R3. The flow rate was varied between 0.45 – 1.8 l/min. in the system, which gives a residence time from 15 to 30 minutes. A NORD helical geared motor was used to control the oscillations in the system by changing the amplitude and

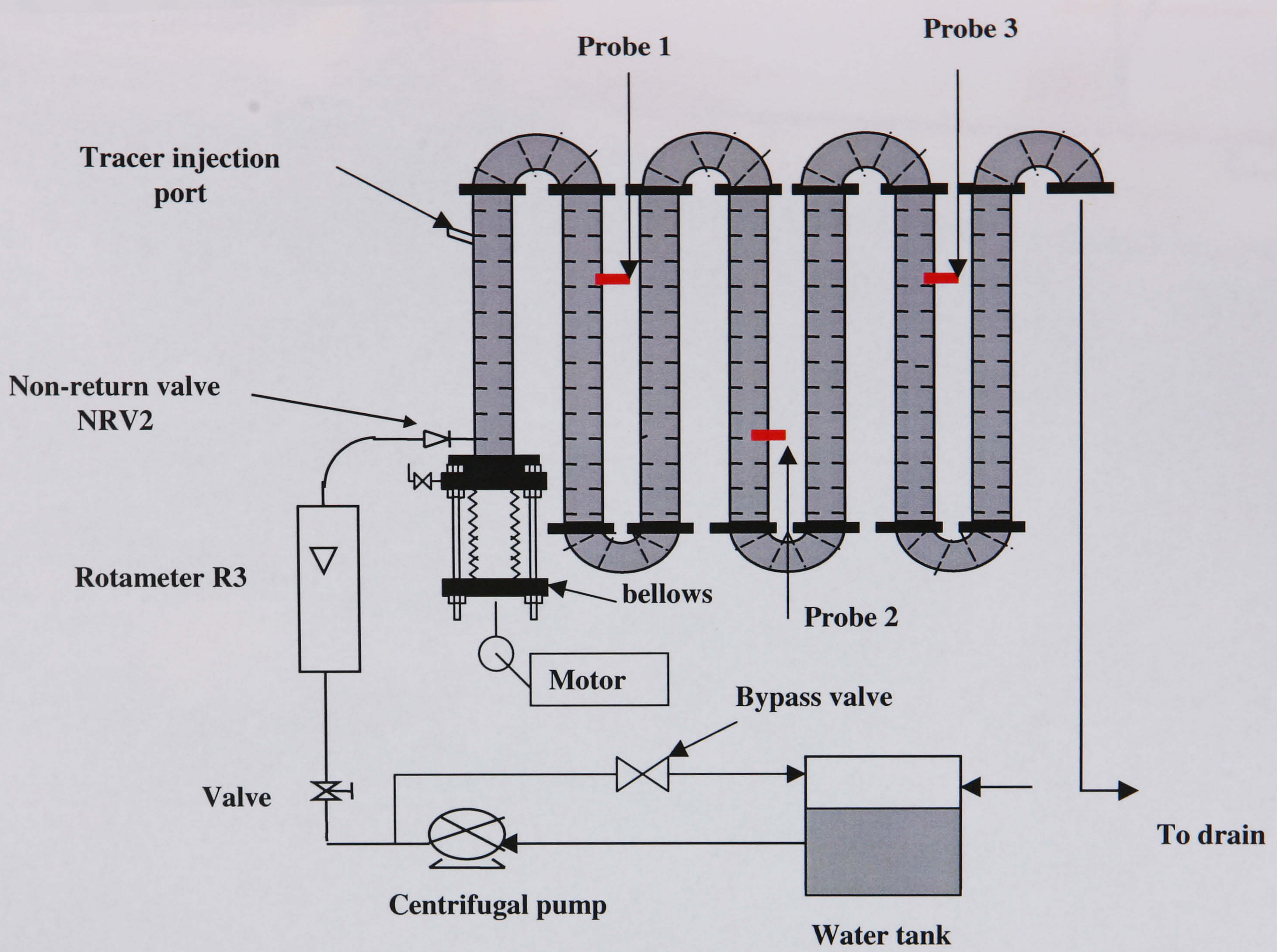

Figure 4.1. Schematic diagram of the Horizontal OBTR for single phase investigation

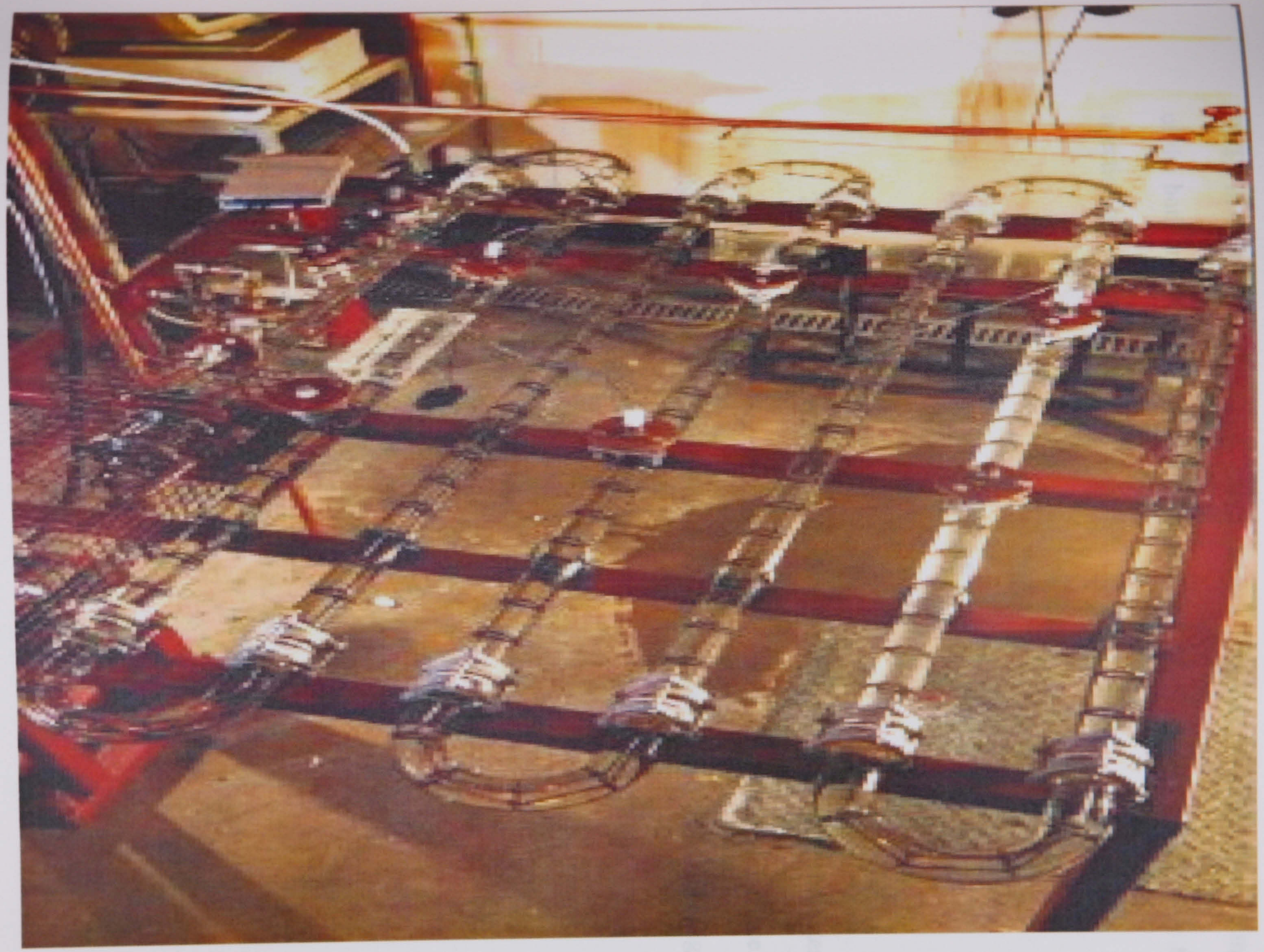

PLATE 2. HORIZONTAL OSCILLATORY BAFFLED TUBULAR REACTOR

frequency. The dispersed phase was introduced by means of a CP gear pump. The baffles and other auxillary equipments were the same as that were used in the vertical OBTR in Chapter 3. Three conductivity probes were used, Figure 4.1, along the length of the horizontal OBTR, which are located at 1 m, 5.2 m and 8.4 m away from the injection tracer, respectively.

4.1.2 EXPERIMENTAL PROCEDURES

The same procedures used to study the single and two phase characteristics in the vertical OBTR were adopted here in the horizontal OBTR and hence are not described in this Chapter. The operating conditions used in the present investigation are given below:

Oscillation amplitude, x_o = (0-12) mm

Oscillation frequency, f = (0-3) Hz

Oscillation velocity, $x_o f$ = (0-36) mm/s

Oscillatory Reynolds number, Re_o – (0-9036)

Continuous phase flow rate, u_c = (0.5–1.9) lt./min

Net flow Reynolds number, Re_n = 260-1037

4.1.3 RESULTS AND DISCUSSIONS

4.1.3.1 EFFECT OF OPERATING PARAMETERS ON RESIDENCE TIME DISTRIBUTION

Figure 4.2 shows one of the typical concentration profiles obtained at a net Reynolds number of 488 superimposed with an oscillation amplitude of 4 mm and an oscillation frequency of 3 Hz. Once again it can be seen that the concentration curve of the probe 1 responded first as it was located the nearest to the injection. This was then followed by the probes 2 and 3 at about 6 and 9 minutes post to the tracer injection. From Figure 4.2, the RTD curves were well-defined, narrow and essentially of a Gaussian form. The profiles of the RTD curves show that a near to plug flow characteristic has been achieved in the horizontal OBTR system. The RTD responses illustrated here are again well in line with the previous studies as mentioned in Chapter 2.

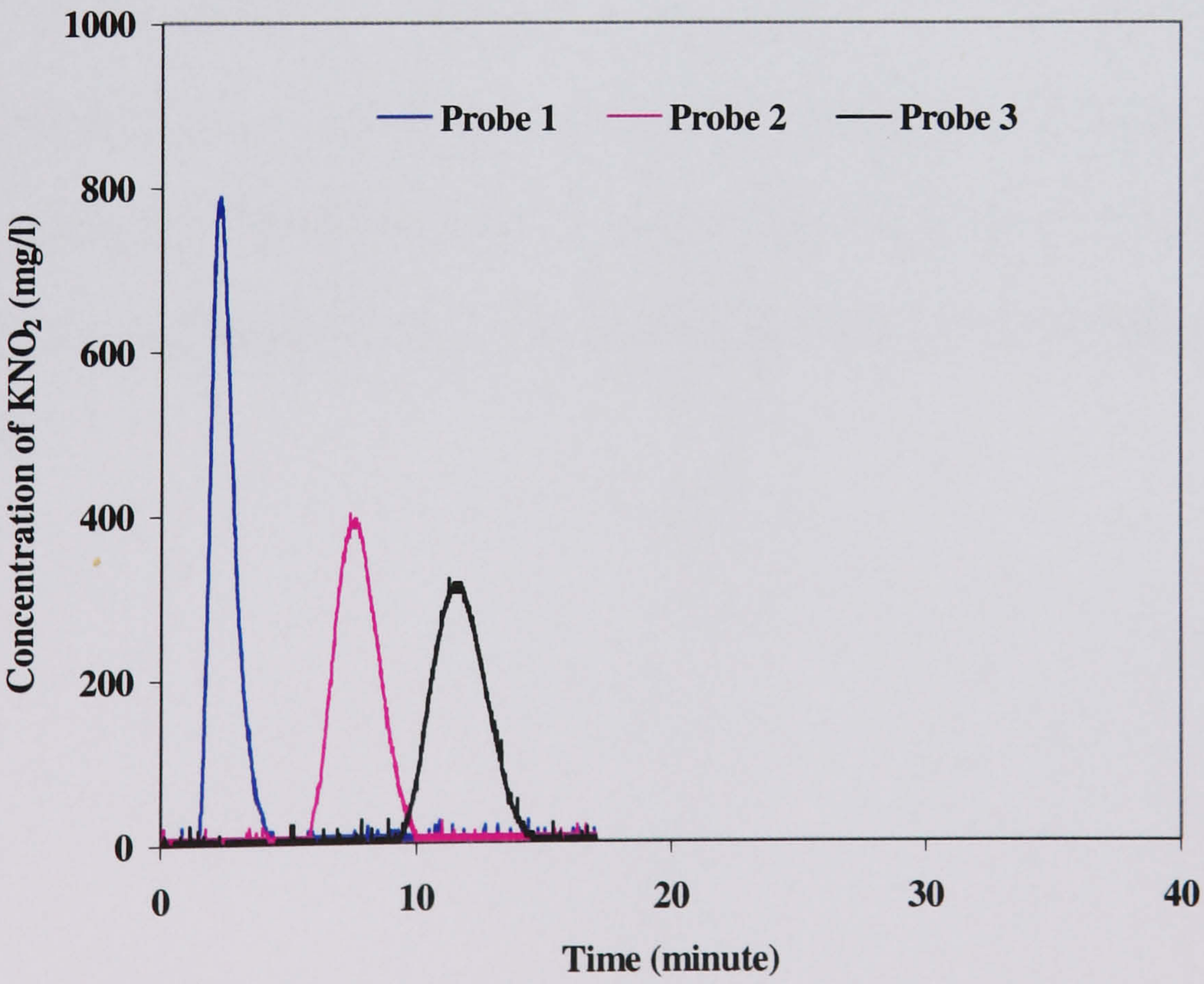

Figure 4.2. Concentration measurements, Re_o = 3012 (4 mm, 3 Hz), Re_n = 488

The effect of oscillation conditions on the RTD characteristics was examined by varying either the oscillation amplitude or frequency while keeping the other operating conditions constant, Figures 4.3-4.6 show the RTD profiles. The effect of oscillation amplitudes on RTD was studied at a fixed oscillation frequency of 3 Hz and at a fixed net flow Reynolds number of around about 504, while varying the amplitude from 4 mm (Figure 4.2), 6 mm (Figure 4.3) to 12 mm (Figure 4.4). There is again about 6.8 % discrepancy in the flow rate settlement due to the same reason as described in Chapter 3. It can clearly be seen from these Figures that the symmetrical and well defined RTD curves are identical to that shown in Figure 4.2, and the increase in the oscillation amplitude seems to make the RTD curves broader due to the increase in the axial dispersion. Similarly the effect of oscillation frequency on RTD is shown in Figures 4.4, 4.5 and 4.6 for 3, 2 and 1 Hz, respectively at a fixed oscillation amplitude of 12 mm. Visually it seems that there are little variations in the RTD curves for the increase of the oscillation frequency. However, the RTD curves do become slightly broader with the increase of the oscillation frequency, when Figure 4.4 is overlapped with either Figure 4.5 or 4.6. This is expected, as the oscillation intensity increases, more axial dispersion is expected, hence broader RTD curves. Importantly, the RTD profiles were still well-defined, symmetrical and narrow with the increase in the oscillation amplitude or frequency.

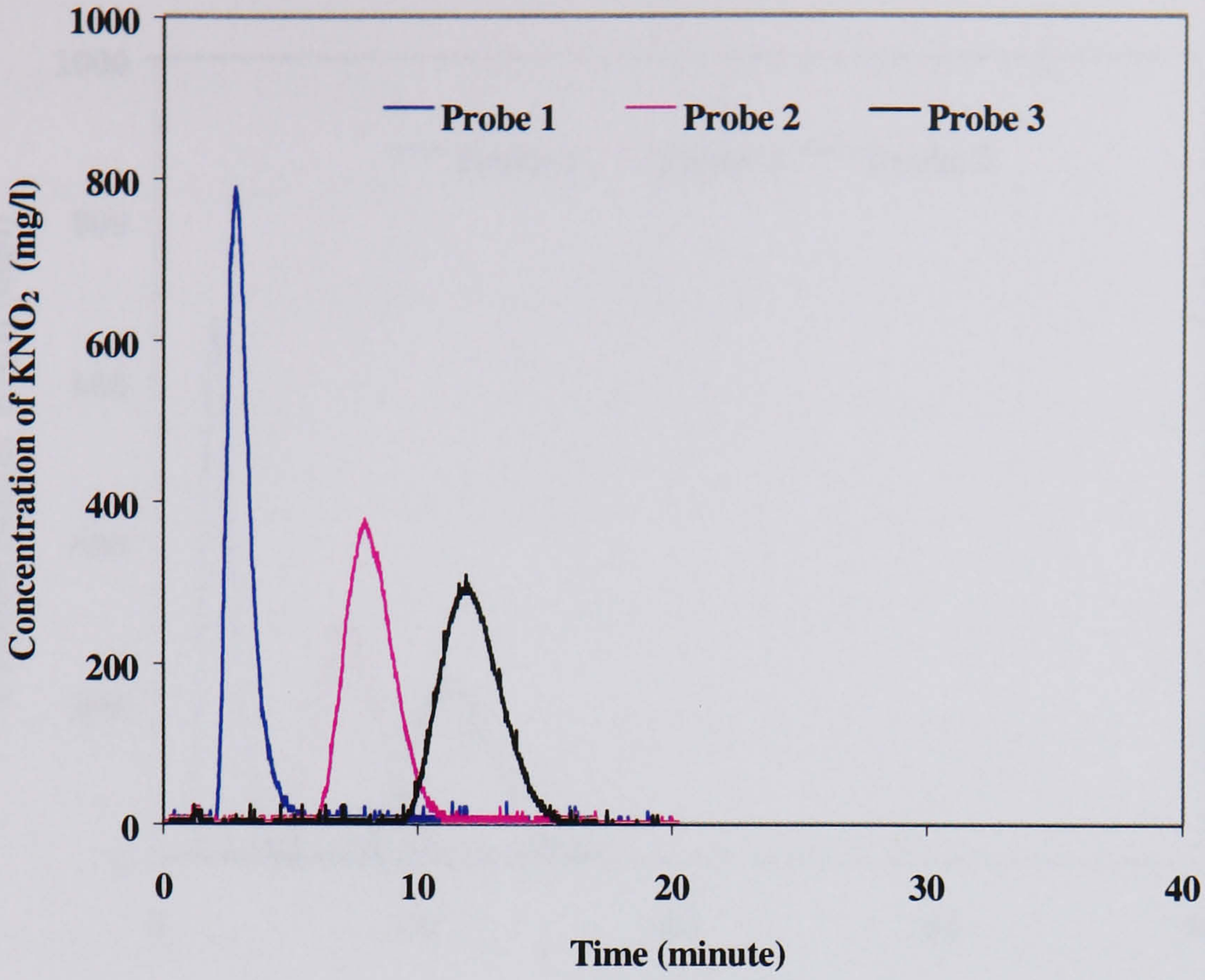

Figure 4.3. Concentration measurements, Re_o = 4518 (6 mm, 3 Hz), Re_n = 504

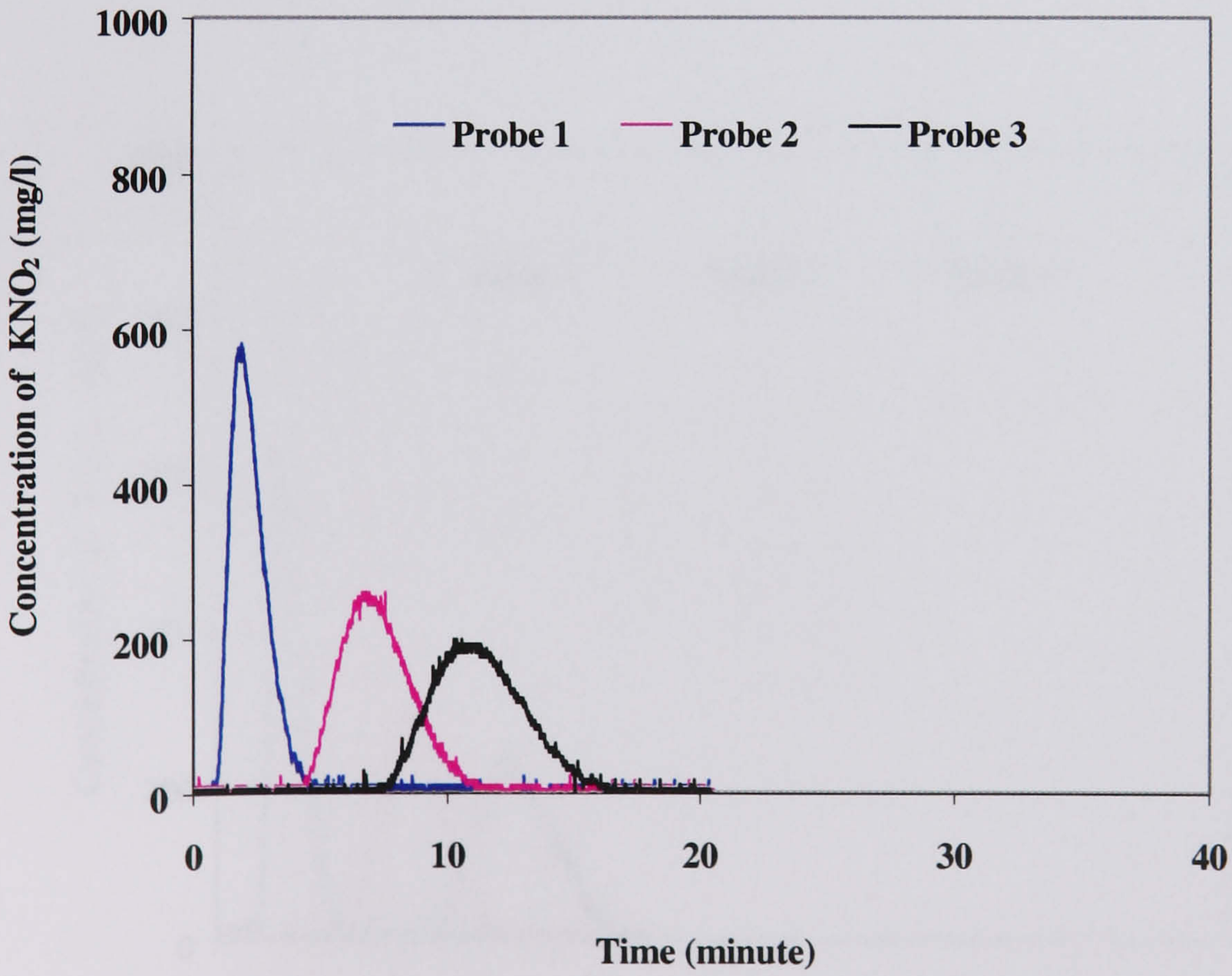

Figure 4.4. Concentration measurements, Re_o = 9036 (12 mm, 3 Hz), Re_n = 498

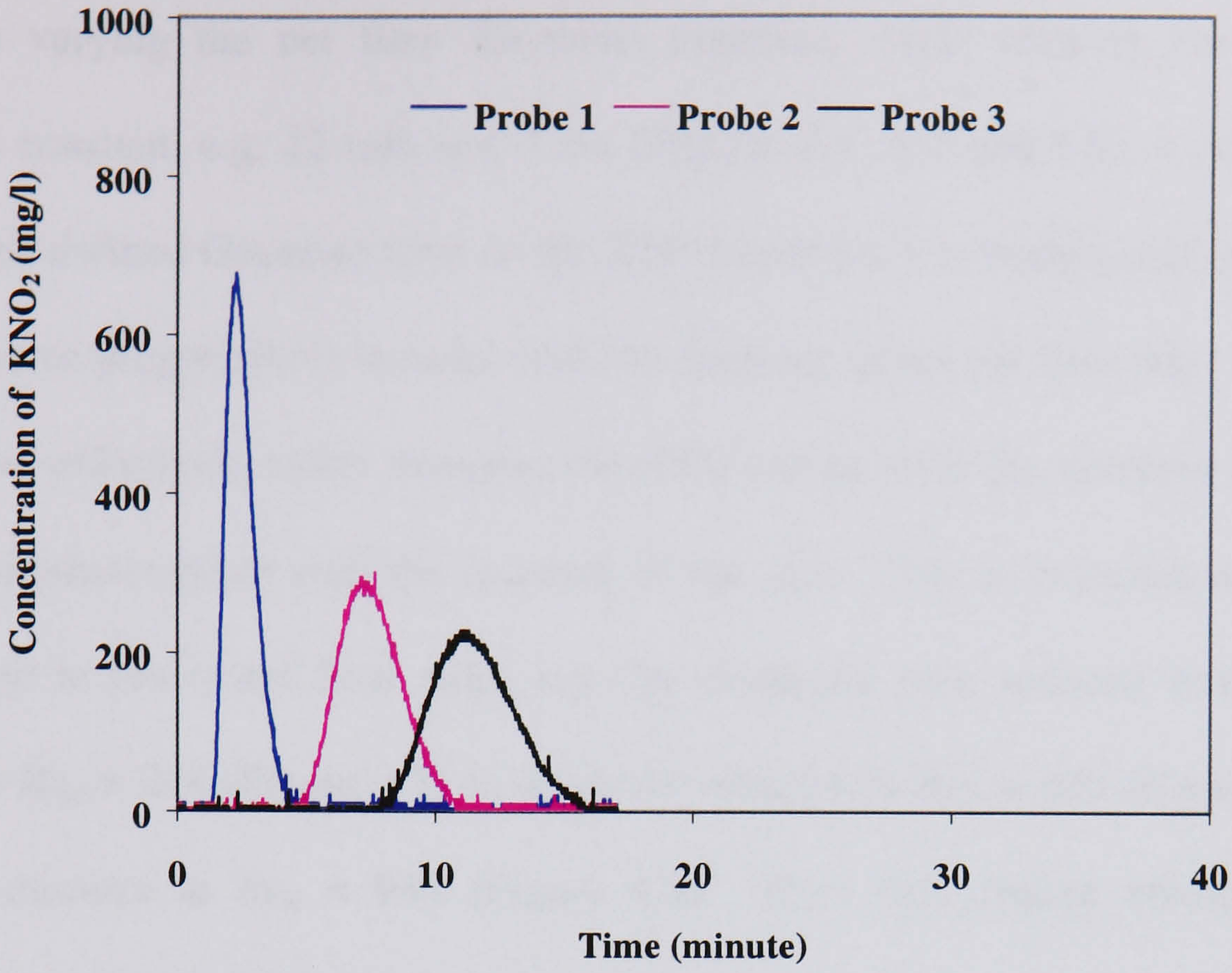

Figure 4.5. Concentration measurements, Re_o = 6024 (12 mm, 2 Hz), Re_n = 525

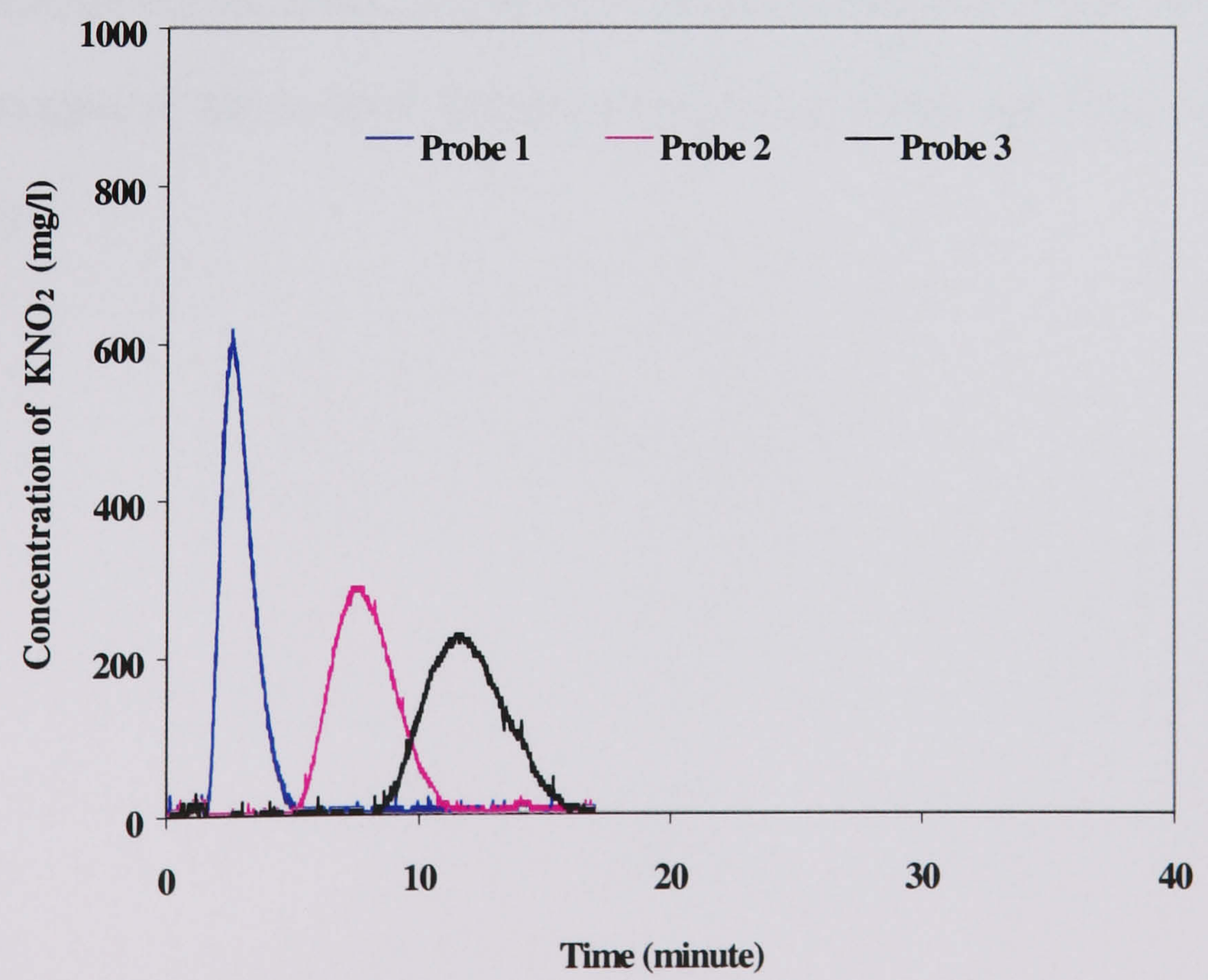

Figure 4.6. Concentration measurements, Re_o = 3012 (12 mm, 1 Hz), Re_n = 525

On varying the net flow Reynolds numbers, while keeping the oscillatory conditions constant, e.g. 12 mm and 3 Hz (Figures 4.4, 4.7 and 4.8), it was observed that the well defined Gaussian form of the RTD responses was maintained, but the RTD curves become progressively broader with the decrease in the net flow rate. The role of the net flow effectively either stretches the RTD curves with the decrease of the flow rate or compresses them with the increase of the rate. This is expected as the tracer stays longer at lower net flow rates, e.g. the residence time reduced from about 35 minutes at Re_n = 268 (Figure 4.7) to about 18 minutes at Re_n = 525 (Figure 4.4), and under 10 minutes at Re_n = 944 (Figure 4.8). How this change affects the axial dispersion coefficient will be looked at later.

It should be emphasised that these figures shown here are just a few samples from a large number of highly reproducible RTD experiments covering a combination of the oscillation amplitude (0-12) mm and oscillation frequency (0-3) Hz and the net Reynolds number of 256 to 1037, which corresponds to a flow rate of 0.5 to 1.89 l/min respectively.

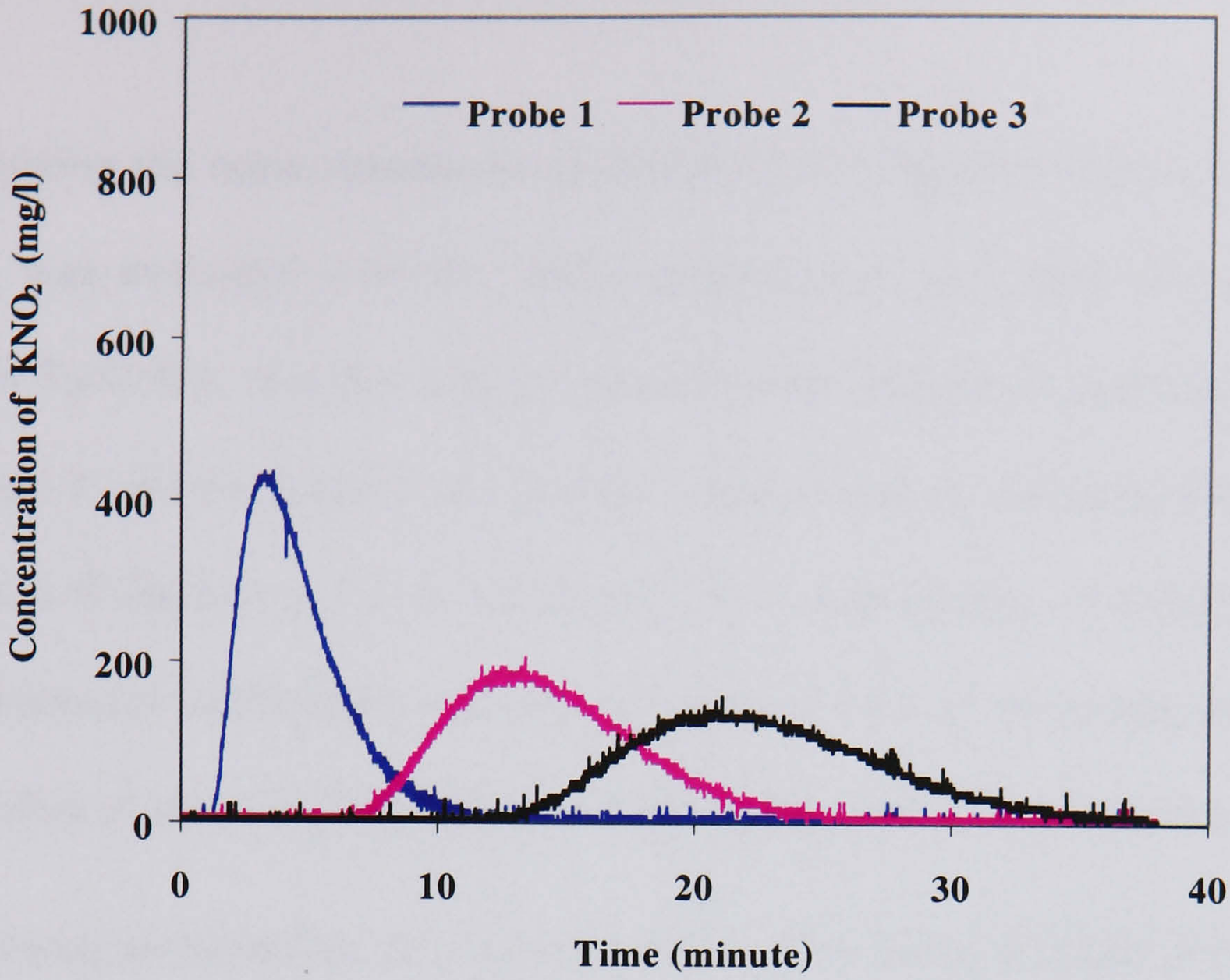

Figure 4.7. Concentration measurements, Re_o = 9036 (12 mm, 3 Hz) Re_n = 268

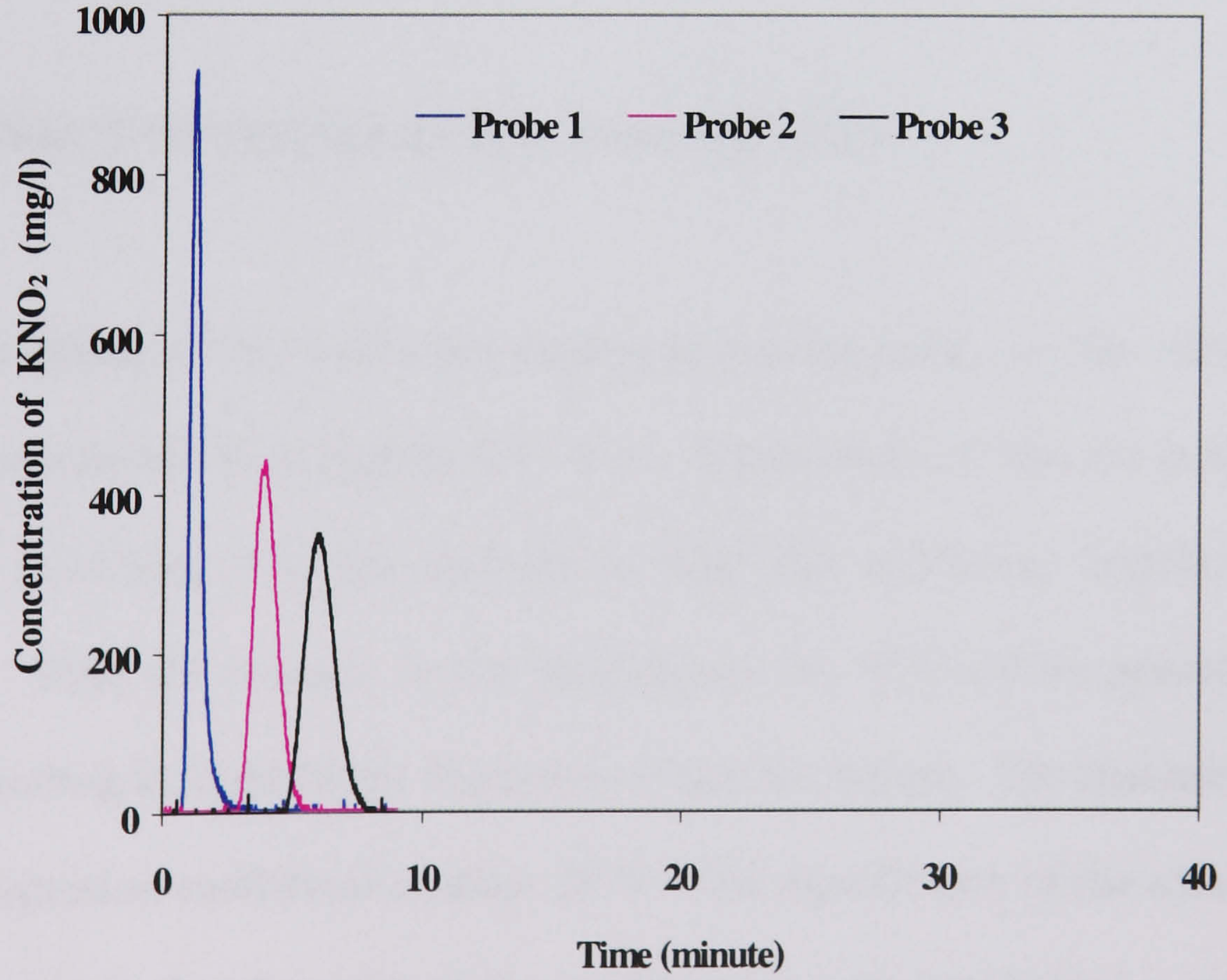

Figure 4.8. Concentration measurements, Re_o = 9036 (12 mm, 3 Hz), Re_n = 944

4.1.4 AXIAL DISPERSION COEFFICIENT

Applying the same procedures as described in Chapter 3, the axial dispersion coefficient was evaluated over the entire experimental conditions investigated and tabulated in Table 4.1. E_{12}, E_{23} and E_{13} represent axial dispersion coefficients between probes 1 and 2, probes 2 and 3 and probes 1 and 3 and the corresponding distances between each of them were 4.2 m, 3.2 m and 7.4 m, respectively. It was observed that the axial dispersion coefficients were almost identical over all the conditions tested. It is thus justified to select anyone from the three coefficients to represent the system and in the following presentation, E_{13} has been used. The Peclet number, Pe ($=\frac{uL}{E}$) was also based on E_{13}. Some of the comparison between the measured concentration profiles and the modelled ones while evaluating the axial dispersion coefficients are shown in Appendix 2.

4.1.4.1 EFFECT OF OSCILLATION PARAMETERS

The effects of the oscillation amplitude and frequency on the axial dispersion coefficient are presented in Figures 4.9 - 4.10. It was observed that the axial dispersion coefficient increased with the increase in both the oscillation amplitude and the frequency. With the increase in the oscillations, the RTD curves generally became broader, resulting in higher axial dispersion within the system. The absolute increase in the axial dispersion coefficient is about 24 %. The significance of the axial dispersion coefficient plots is that the value of the coefficient is very low indeed, confirming that near to plug flow characteristics have been achieved in the OBTR under the conditions investigated.

Table 4.1. Calculated *E* and *Pe*

x_0f	Re_o	Re_n	E_{12}	E_{23}	E_{13}	Pe_{13}
0	0	272	0.0004	0.0004	0.0004	125.8
3	753	264	0.0003	0.0003	0.0003	162.8
6	1506	266	0.0007	0.0006	0.0007	70.3
12	3012	266	0.0006	0.0006	0.0006	70.3
18	4518	260	0.0009	0.0008	0.0009	50.2
24	6024	276	0.0018	0.0015	0.0018	28.4
30	7530	256	0.0016	0.0012	0.0015	31.6
36	9036	268	0.0018	0.0021	0.0018	27.5
0	0	504	0.0005	0.0006	0.0005	186.5
3	753	552	0.0005	0.0005	0.0005	204.2
6	1506	437	0.0007	0.0006	0.0008	134.7
12	3012	437	0.0005	0.0005	0.0005	161.7
18	4518	504	0.0007	0.0006	0.0007	133.2
24	6024	525	0.0016	0.0017	0.0016	60.7
30	7530	488	0.0014	0.0014	0.0013	69.4
36	9036	525	0.002	0.0019	0.0018	54.0
0	0	955	0.0011	0.0014	0.0011	160.0
3	753	934	0.0006	0.0006	0.0006	288.0
6	1506	1037	0.0008	0.0008	0.0007	274.1
12	3012	902	0.0006	0.0008	0.0009	278.1
18	4518	997	0.0007	0.0006	0.0007	263.5
24	6024	955	0.0011	0.0011	0.001	176.7
30	7530	987	0.0012	0.0013	0.0012	152.2
36	9036	944	0.0014	0.0018	0.0014	124.7

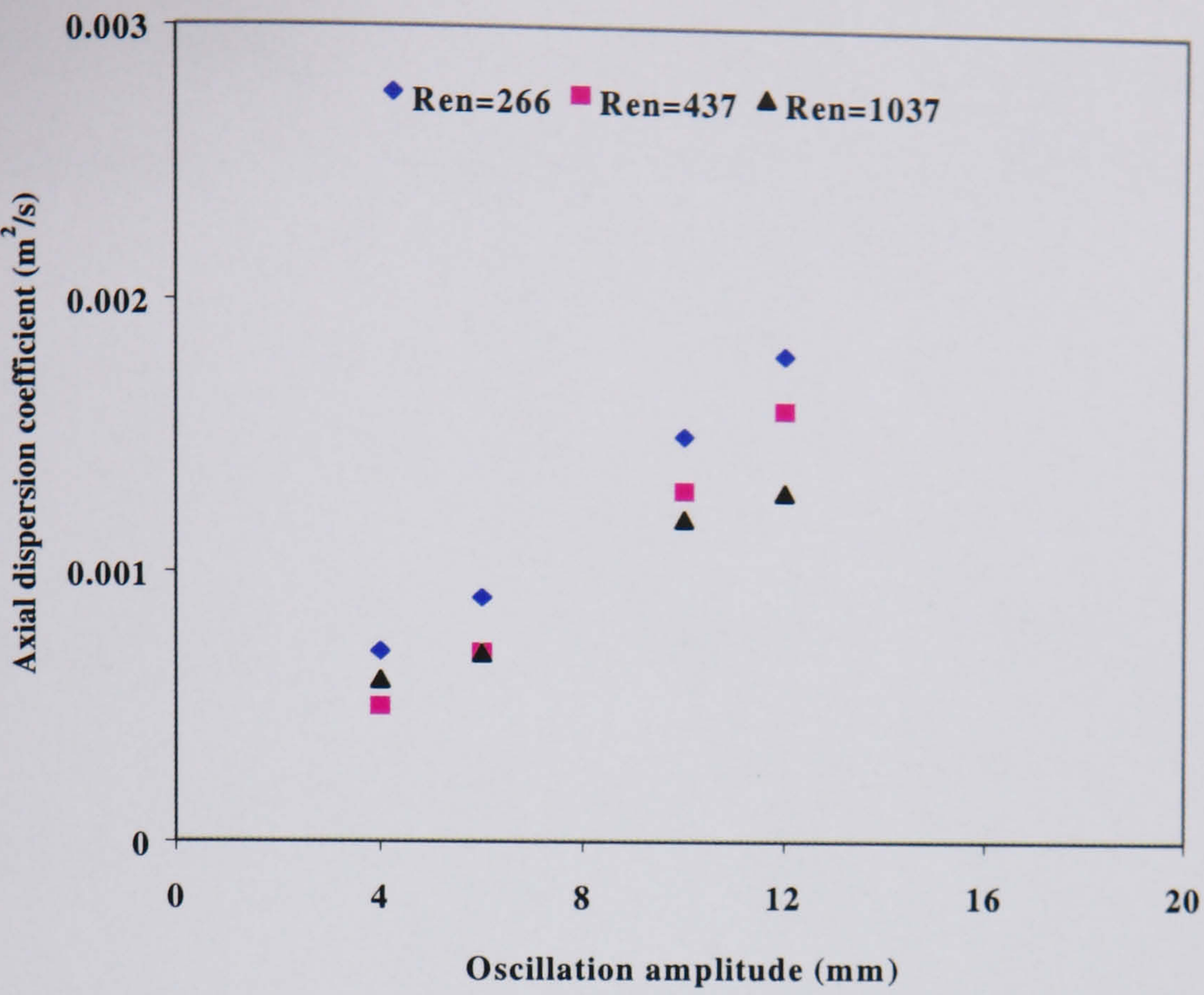

Figure 4.9. Effect of oscillation amplitude on axial dispersion coefficient, f = 3 Hz

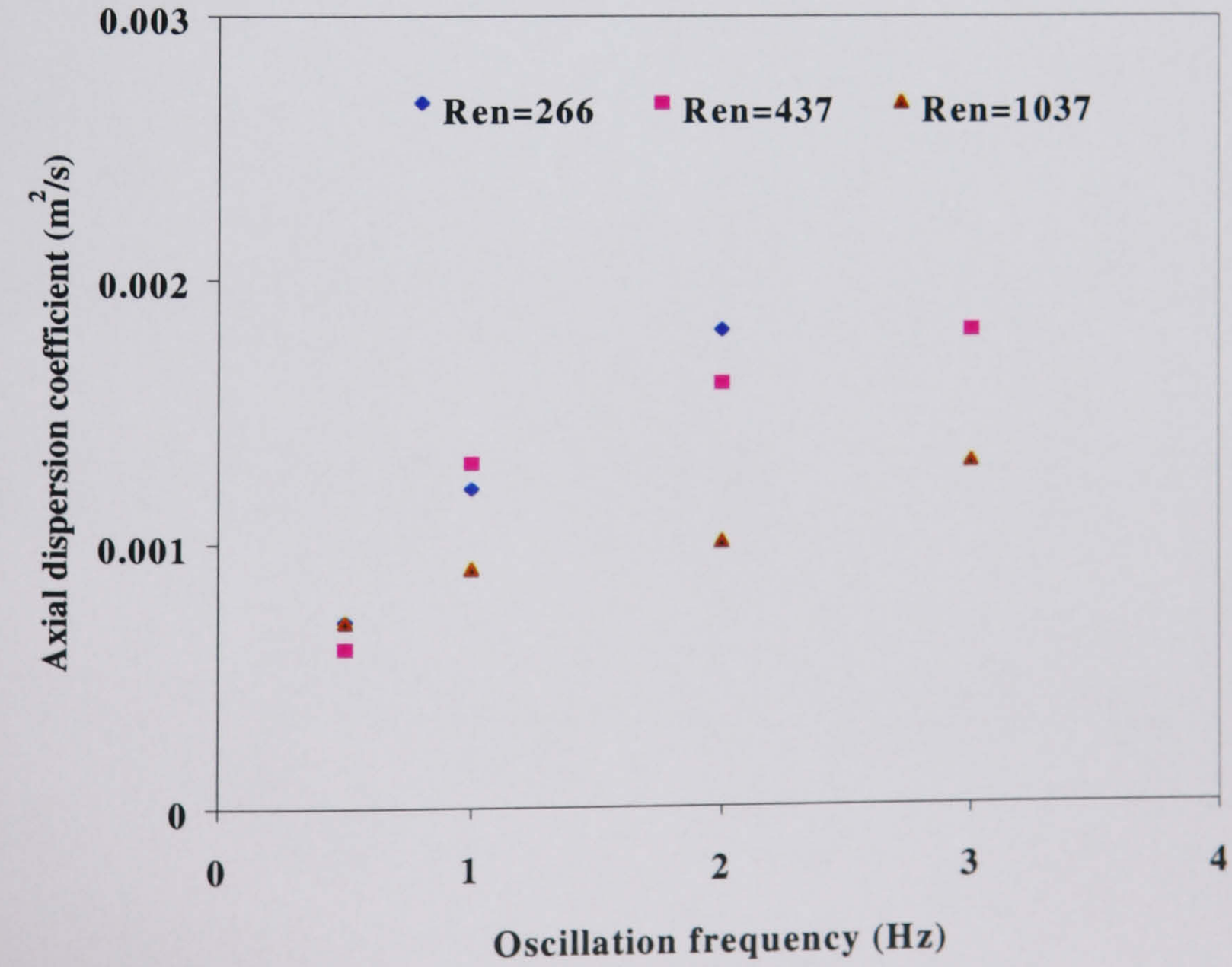

Figure 4.10. Effect of oscillation frequency on axial dispersion, x_o = 12 mm

To assess the individual effects of the oscillation amplitude and frequency on the axial dispersion coefficient, the following power law relationships together with the estimation of errors are established based on the data shown in Figures 4.9-4.10:

$Re_n = 266$

$$E = 0.0843\ (\pm 31.71\%)\ x_o^{0.88\ (\pm\ 6.4\%)} \qquad (\mathrm{m^2.s^{-1}}) \qquad (R^2 = 0.989) \qquad (4.1)$$

$$E = 0.0011\ (\pm\ 7.36\%)\ f^{0.55\ (\pm\ 10\%)} \qquad (\mathrm{m^2.s^{-1}}) \qquad (R^2 = 0.94) \qquad (4.2)$$

$Re_n = 460$

$$E = 0.1845\ (\pm 30.44\%) x_o^{1.07\ (\pm 6.16\%)} \qquad (\mathrm{m^2.s^{-1}}) \qquad (R^2 = 0.99) \qquad (4.3)$$

$$E = 0.001\ (\pm 10.78\%) f^{0.59\ (\pm 14.15\%)} \qquad (\mathrm{m^2.s^{-1}}) \qquad (R^2 = 0.89) \qquad (4.4)$$

$Re_n = 1037$

$$E = 0.0585\ (\pm 50.37\%) x_o^{0.84\ (\pm 12.62\%)} \qquad (\mathrm{m^2.s^{-1}}) \qquad (R^2 = 0.96) \qquad (4.5)$$

$$E = 0.00088\ (\pm 5.4\%) f^{0.35\ (\pm 7.36\%)} \qquad (\mathrm{m^2.s^{-1}}) \qquad (R^2 = 0.92) \qquad (4.6)$$

The errors were generated by using the "Regression" function in Microsoft excel. From the above equations, it can be observed that the power index of the amplitude was generally higher than that of the frequency, indicating that the axial dispersion coefficient was more influenced by the amplitude than the frequency over the operating conditions used. This finding is in good agreement with the vertical OBTR results.

The effect of the net flow rates on the axial dispersion coefficients is plotted in Figure 4.11, where the oscillatory Reynolds number is used in the horizontal axis. Note that the axial dispersion coefficients showed a non-zero value at $Re_o = 0$ and then an increasing trend with the increase in the oscillation Reynolds number. As far as the effect of the net flow rate was concerned, the variations of the axial dispersion coefficients were generally very small at a given oscillation condition.

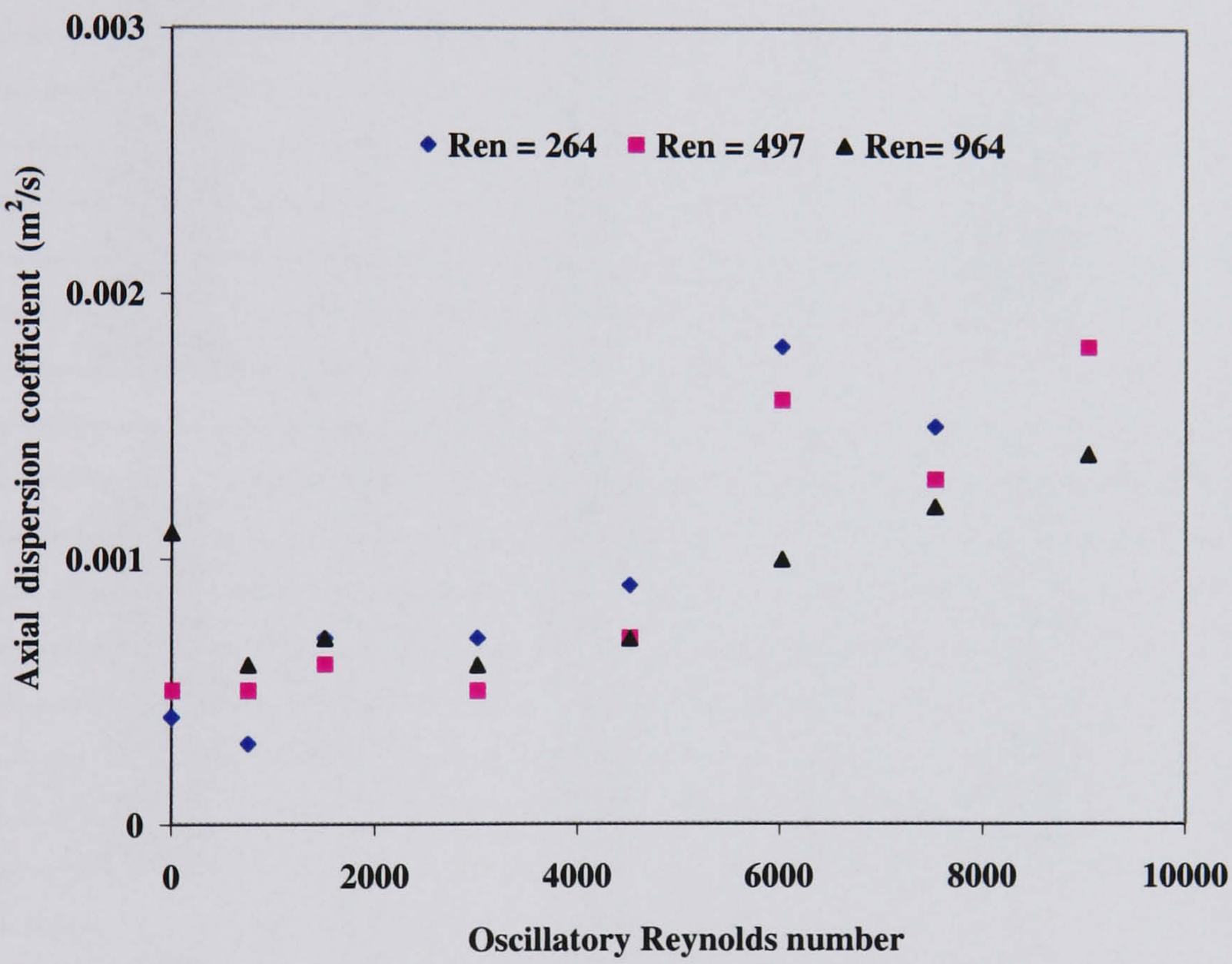

Figure 4.11. Effect of oscillatory Reynolds number on axial dispersion coefficient

In order to understand the combined effect of the oscillatory and net flows on the axial dispersion coefficient, the velocity ratio, ψ defined in equation (3.17) in Chapter 3 is again used here. Table 4.2 shows the ratios examined in this work over all the operating conditions. It is easily seen that the velocity ratios are greater than one when $x_o f > 3$ mm/s, and increase with an increase in the oscillatory Reynolds number. This indicates that the effect of oscillatory motion dominates over that of the net flow

over a significant range of the operational conditions. It is the oscillatory motion in the baffled tube that generates the near to plug flow characteristics, while the net flow only aids the plug flow component to move forward.

Table 4.2. Velocity ratio

$2\pi x_o f$ (mm.s^{-1})	u_c (mm.s^{-1})	ψ
0	6.8	0
18.84	6.6	2.85
37.68	6.6	5.67
75.36	6.6	11.33
113.04	6.5	18.53
150.72	6.9	21.84
188.4	6.4	29.44
226.08	6.7	33.74
0	12.6	0
18.84	10.9	1.36
37.68	10.9	3.45
75.36	10.9	6.89
113.04	12.6	8.97
150.72	13.1	11.48
188.4	12.2	15.44
226.08	13.1	17.22
0	23.8	0
18.84	25.9	0.81
37.68	25.9	1.45
75.36	22.5	3.34
113.04	24.9	4.53
150.72	23.8	6.31
188.4	24.6	7.63
226.08	23.6	9.58

By plotting the dimensionless Peclet number, Pe $(=\frac{u_c L}{E})$ against the velocity ratio in Figure 4.12, a correlation relating Pe with ψ can be established as,

$$Pe = \frac{uL}{E} = 378\ (\pm\ 18.29\%)\psi^{-0.66\ (\pm\ 8.37\%)} \qquad (R^2 = 0.766) \qquad (4.7)$$

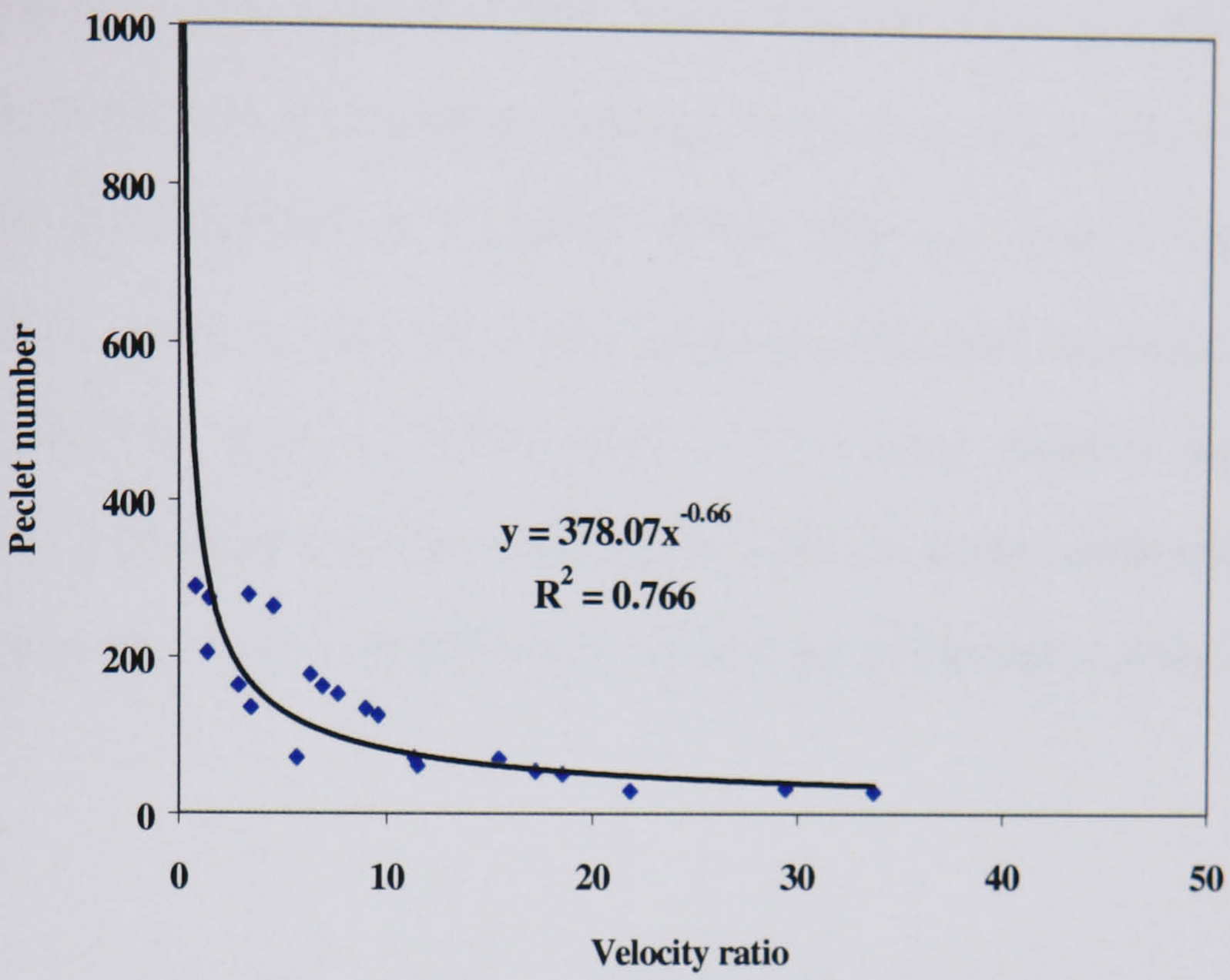

Figure 4.12. Effect of velocity ratio on Peclet number

The above correlation and the errors were established by using the "Regression" function in Microsoft excel. From Figure 4.12, the Peclet number, Pe $(=\frac{u_c L}{E})$ varied from 28 to 287. As mentioned in Chapter 3, a Peclet number, Pe, above 50 indicates a negligible effect of axial mixing and since most of the Peclet numbers, Pe, were well above 50 (Table 4.1), this means that the horizontal OBTR approached very close to plug flow behaviour over the operating conditions used. The equation (4.7) can be modified as,

$$E = 0.0658(x_o f)^{0.66} u^{0.34} \qquad (\mathrm{m^2.s^{-1}}) \qquad (4.8)$$

From the above equation, it is again confirmed that the axial dispersion coefficient is more influenced by the oscillation velocity than that of the net flow velocity. This agrees well with the observation reported in Figure 4.11. On comparing the equation (4.8) with equation (3.19), it was observed that the axial dispersion coefficients obtained were of the same magnitude. Hence over the operating conditions used, both the horizontal and vertical OBTR displayed similar single phase characteristics. Table 4.3 lists the axial dispersion coefficients obtained in both the horizontal and the vertical OBTRs together with those reported by previous investigators. One can see that the values of the axial dispersion coefficients obtained in this thesis were on a par with the others, assuring the performance of the OBTR set-up.

Table 4.3 Comparison of *E* for different OBTRs

Investigator	**Diameter/Length (mm)/ (m)**	Re_o	Re_n	E ($m^2.s^{-1}$)
Present Investigation	40 / 12.5, 25	0-9036	244-1037	$(3 - 18) \times 10^{-4}$
Dickens et al. (1989)	23 / 0.67	100-3300	110	$(0.64 - 49) \times 10^{-4}$
Howes (1988)	51 / 2.5	160-2500	40,106	$(0.5 - 7) \times 10^{-4}$
Mackley and Ni (1991)	26 / 1.08	40-3600	128	$(0.2 - 2) \times 10^{-4}$
Mackley and Ni (1993)	25 / 6.3	0-750	106-3400	$(2 - 45) \times 10^{-4}$
Smith, K. (2000)	24, 54, 150 / 1, 2, 4.5	0 – 25000	107 – 3100	$(1 - 90) \times 10^{-4}$

4.1.5 SUMMARY OF RESULTS

Highly reproducible and controlled RTDs with near to plug flow behaviour have been obtained in the horizontal OBTR. The axial dispersion coefficient was evaluated over a range of operating conditions and was found to be more sensitive to both the oscillation amplitude and frequency than the net flow rate. This experimental observation was confirmed by a correlation established relating the axial dispersion coefficient with both the oscillatory and the net flow components. On comparing the results with that from the vertical OBTR, it was observed that both the OBTRs had similar single phase characteristics and produced very close to plug flow behaviour.

4.2 TWO PHASE FLOW STUDY

The objective of this part of the work is to investigate the effect of operating conditions on the characteristics of the DSD and mean drop diameter in the horizontal OBTR. The experimental method and procedures of acquiring drops, and the data analysis techniques are same as that in the vertical OBTR in Chapter 3, as a result, they are not mentioned here. The only differences are the locations of the optical windows along the length of the system. Four optical windows are used (see Figure 4.13), and the distances from the oil input are 1.42 m, 3.45 m, 7.5 m and 11.4 m from left to right in the direction of flow respectively. The location on the far left is named as port 1 and that on the furthest right is termed as port 4. In the presentation of the results, a similar style together with similar subtitles to that in Chapter 3 is employed here.

4.2.1 DROPLET ANALYSIS

4.2.1.1 NUMBER OF DROPS

Droplet numbers from 200 to 1000 were examined and their effects on drop size distribution are given in Figures 4.14 and 4.15. It is clear that the distributions remained more or less constant for droplets above 250. On balance of accuracy and time consumption, 600-800 drops were used in the horizontal OBTR.

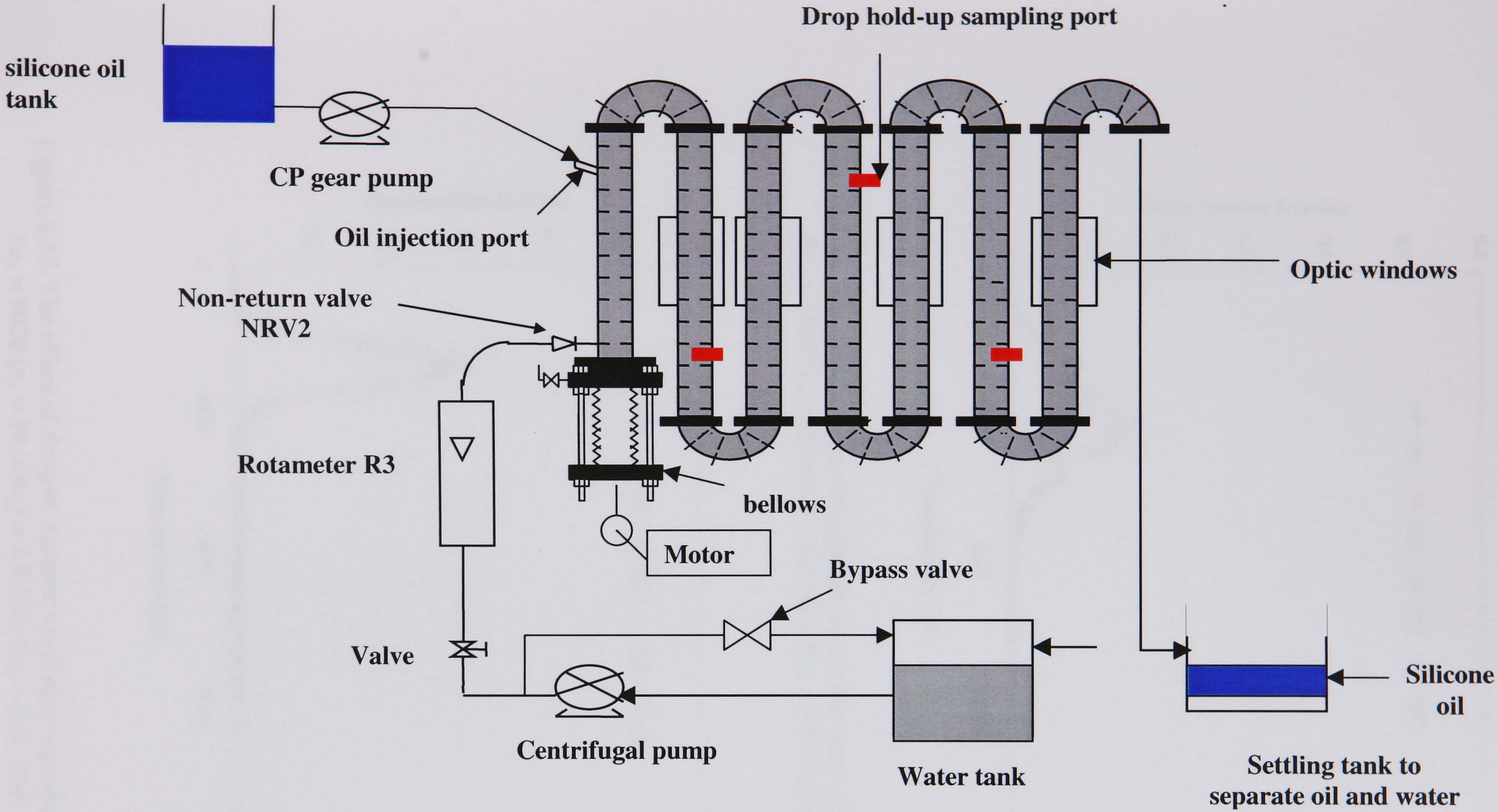

Figure 4.13. Schematic diagram of the Horizontal OBTR for two phase investigation

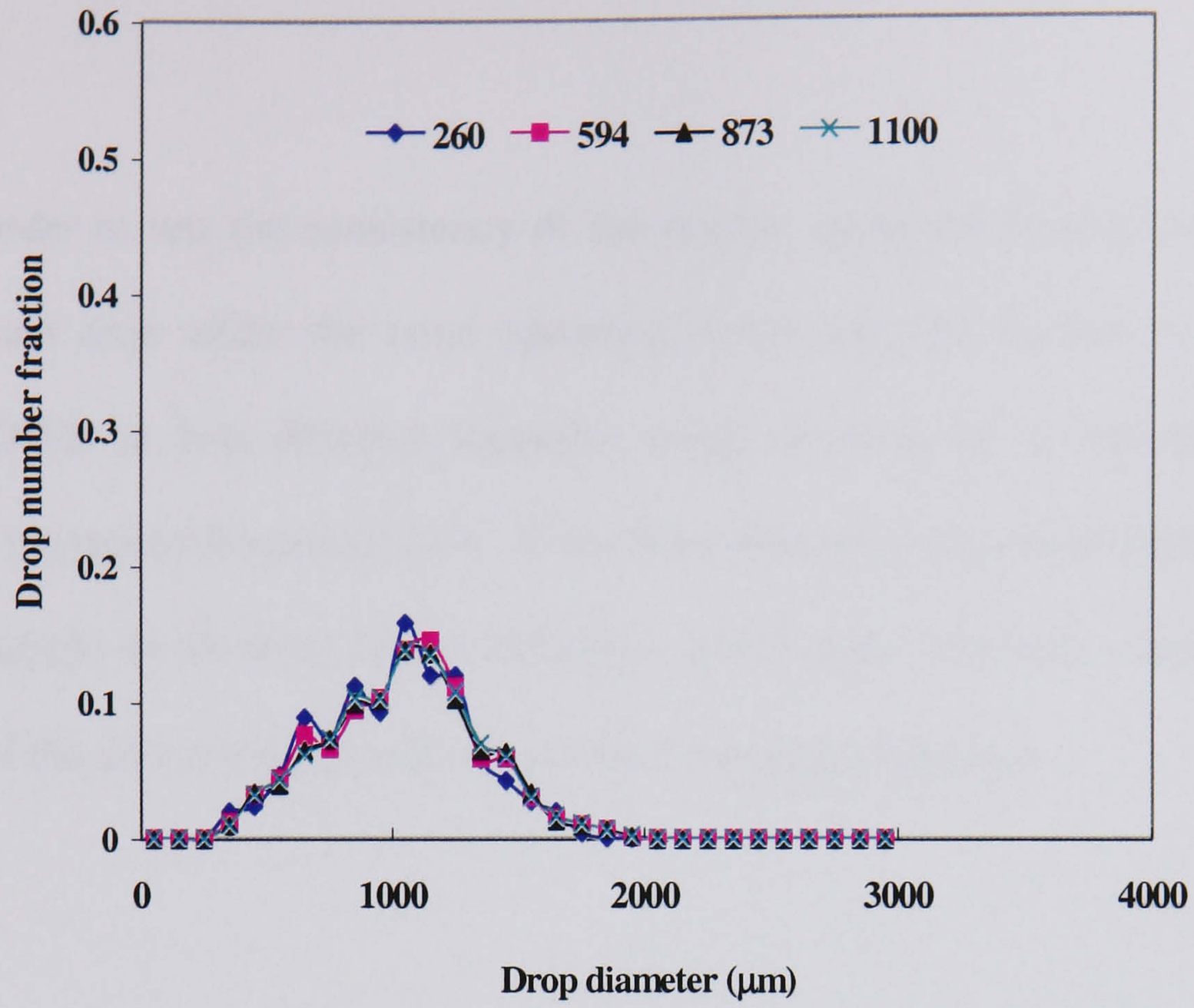

Figure 4.14. The effect of droplet number on droplet size distribution, Re_o = 5020 (x_o = 10 mm, f = 2.0 Hz), Re_n = 541, Port 1

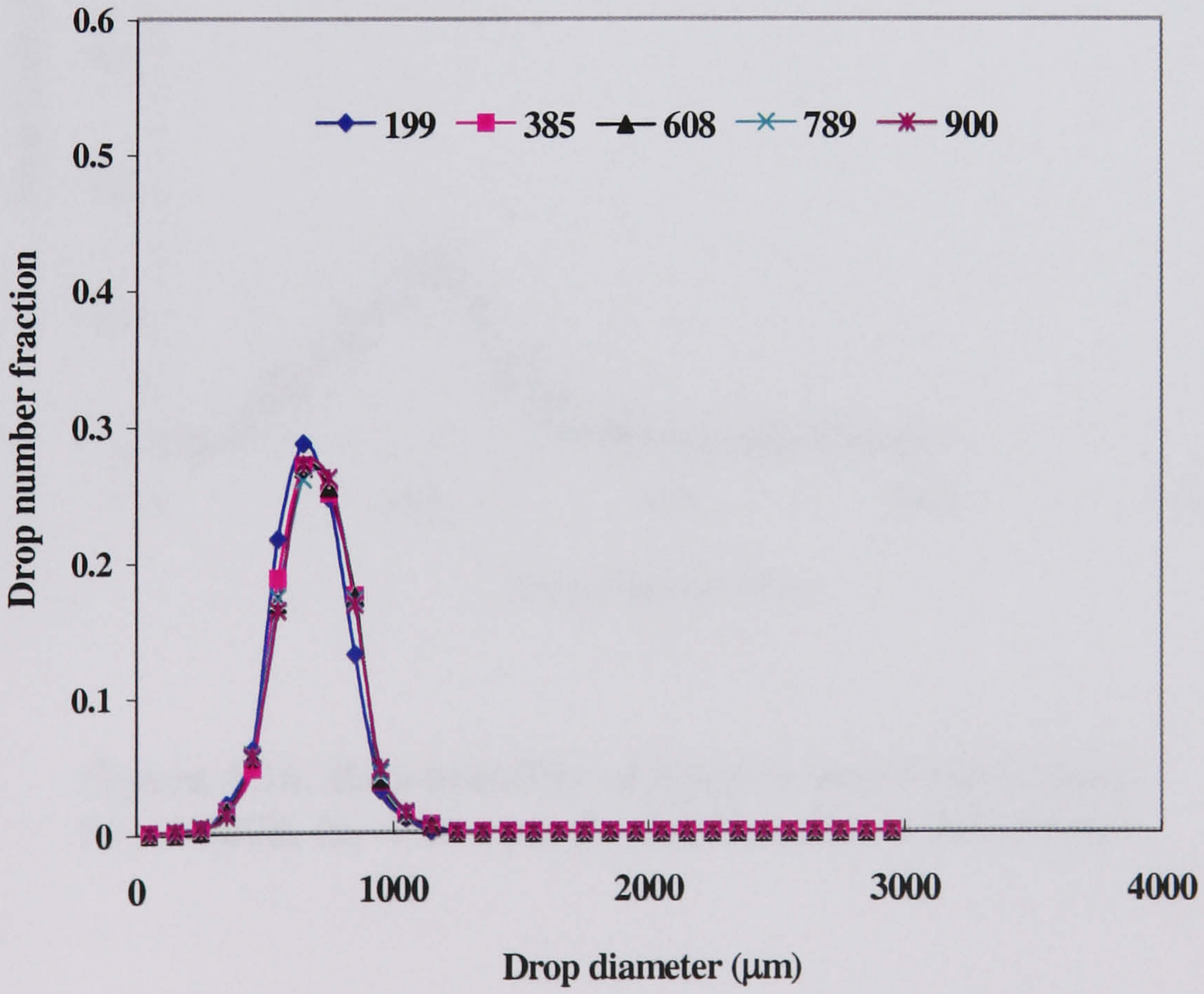

Figure 4.15. The effect of droplet number on droplet size distribution Re_o = 5020 (x_o = 10 mm, f = 2.0 Hz), Re_n = 541, Port 4

4.2.1.2 REPEATABILITY

In order to test the consistency of the results, experiments were performed on three different days under the same operating conditions and Figures 4.16 and 4.17 show the DSDs at two different locations along the tube for a typical oscillatory amplitude 10 mm and frequency 2 Hz. From these Figures it was observed that the drop size distributions on all three days overlapped, which again indicates a high degree of reliability of the data and good accuracy of the measuring technique.

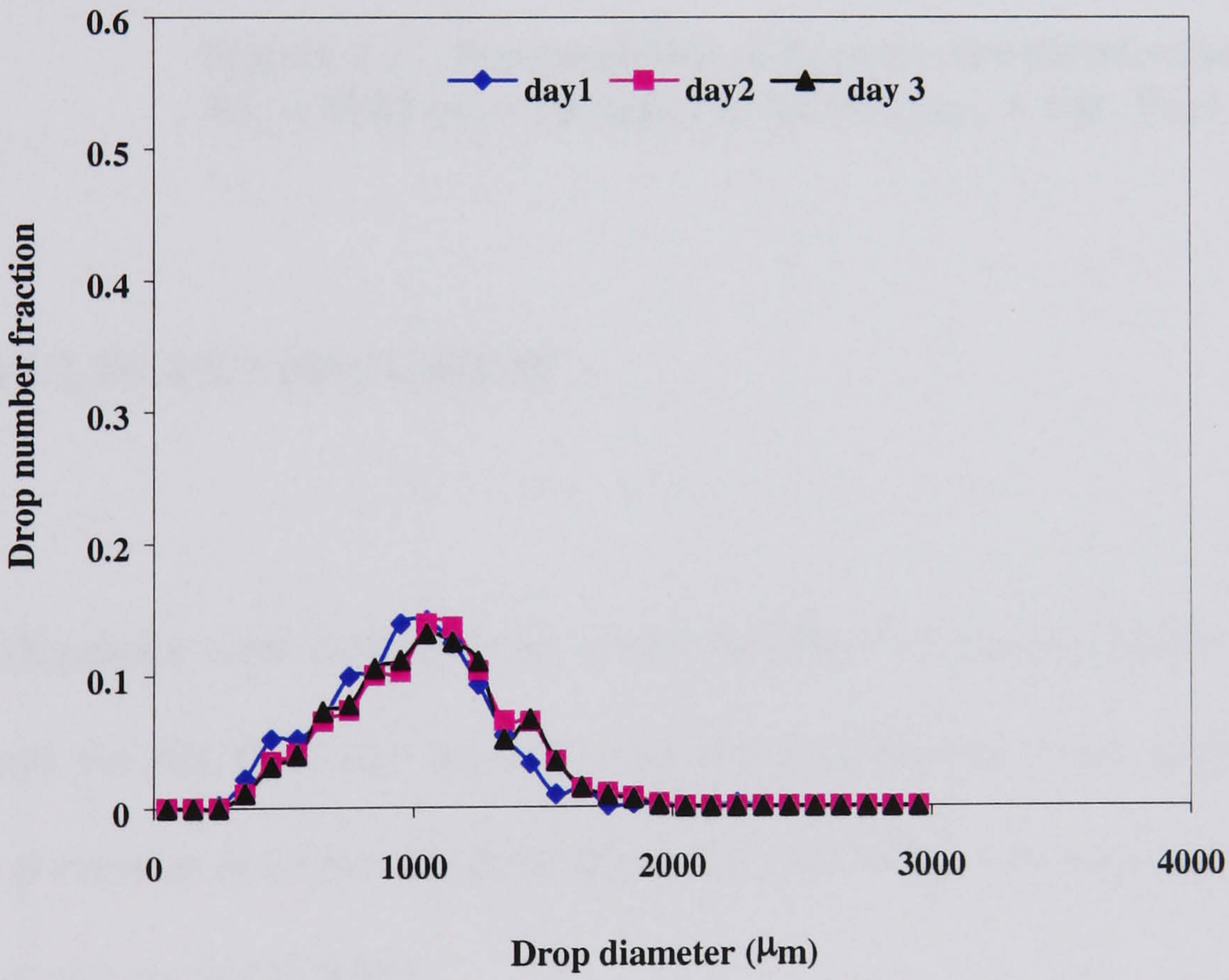

Figure 4.16. Repeatability of droplet size distribution, Re_o = 5020, (x_o = 10 mm, f = 2.0 Hz), Re_n = 541, Port 1

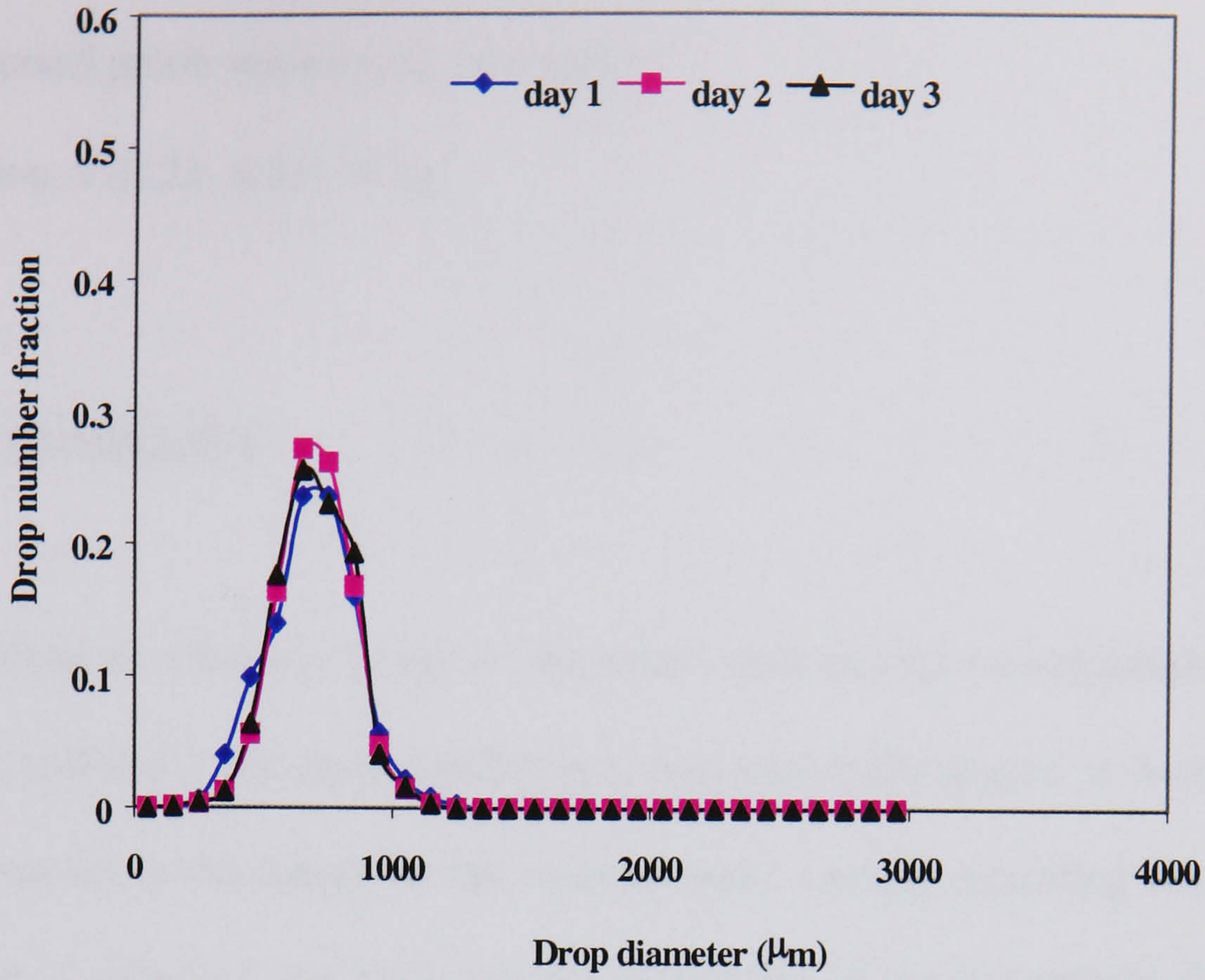

Figure 4.17. Repeatability of droplet size distribution, Re_o = 5020 (x_o = 10 mm, f = 2.0 Hz), Re_n = 541, Port 4

4.2.2 RESULTS AND DISCUSSION

Investigations were carried out to study the effect of the oscillation amplitude, frequency and the net flow rate on drop size distribution and mean droplet size by varying one parameter at a time. Experiments were performed over a range of operating conditions, which are listed below:

Oscillation amplitude, x_o : (8-15) mm

Oscillation frequency, f : (1-3) Hz

Oscillation velocity, $x_o f$: (8 – 45) mm.s^{-1}

Oscillation Reynolds number, Re_o (2008 - 11295)

Flow velocity, u :(5.8 – 25) mm.s^{-1}

Net flow Reynolds number, Re_n : (234 -1004)

Superficial dispersed phase velocity, u_d : 0.6 mm.s^{-1}

Energy dissipation, ε (0.23- 4.21) W.kg^{-1}

4.2.2.1 DROP STABILITY

As explained in Chapter 3, one of the main aims of this investigation was to examine droplet stability. The drop stability is a measure of the degree of overlapping of DSDs with respect to the length of the system under various operating conditions. To achieve such a stability, the DSD curves should be of an essentially Gaussian function with a high degree of overlapping. Figures 4.18-4.26 show the development of the stability for different operating conditions. One can see that the DSDs in Figure 4.18 overlap fairly well, but the shape was too broad, while the DSDs in Figure 4.19 were broad in profile and poor in overlapping. On increasing the oscillation amplitude and frequency, the DSDs started to become sharper and sharper and the overlapping got better. In Figure 4.24, the stability of DSDs has clearly been established from the port 2 onwards. Importantly such stability can be reproduced accurately at the given condition. When the stability is achieved, the Sauter mean drop size remained more or less constant as shown in Figure 4.27. Table 4.4 compares the stability with that in the vertical OBTR.

One can draw the conclusion that the stability is achieved earlier in the horizontal OBTR than that in the vertical OBTR and at considerably less power input. The significant difference in the stability of DSDs in the horizontal OBTR lies in the set-up of the systems. As in horizontal operation, there are no risers and downcomers present in the system leading to marked different characteristics in the dispersed phase

hold-up, as illustrated in Figure 4.28. Here the hold-ups are much more uniform than those in the vertical OBTR, hence more constant mean drop size and earlier stability of DSDs.

4.4. Comparison of Drop stability between horizontal and vertical OBTR

	Horizontal OBTR	**Vertical OBTR**
Drop stability achieved at	7.49 m from injection port	10.49 m from injection port
x_o (mm)	15	15
f (Hz)	2	4
ε (W.kg^{-1})	1.25	10.08

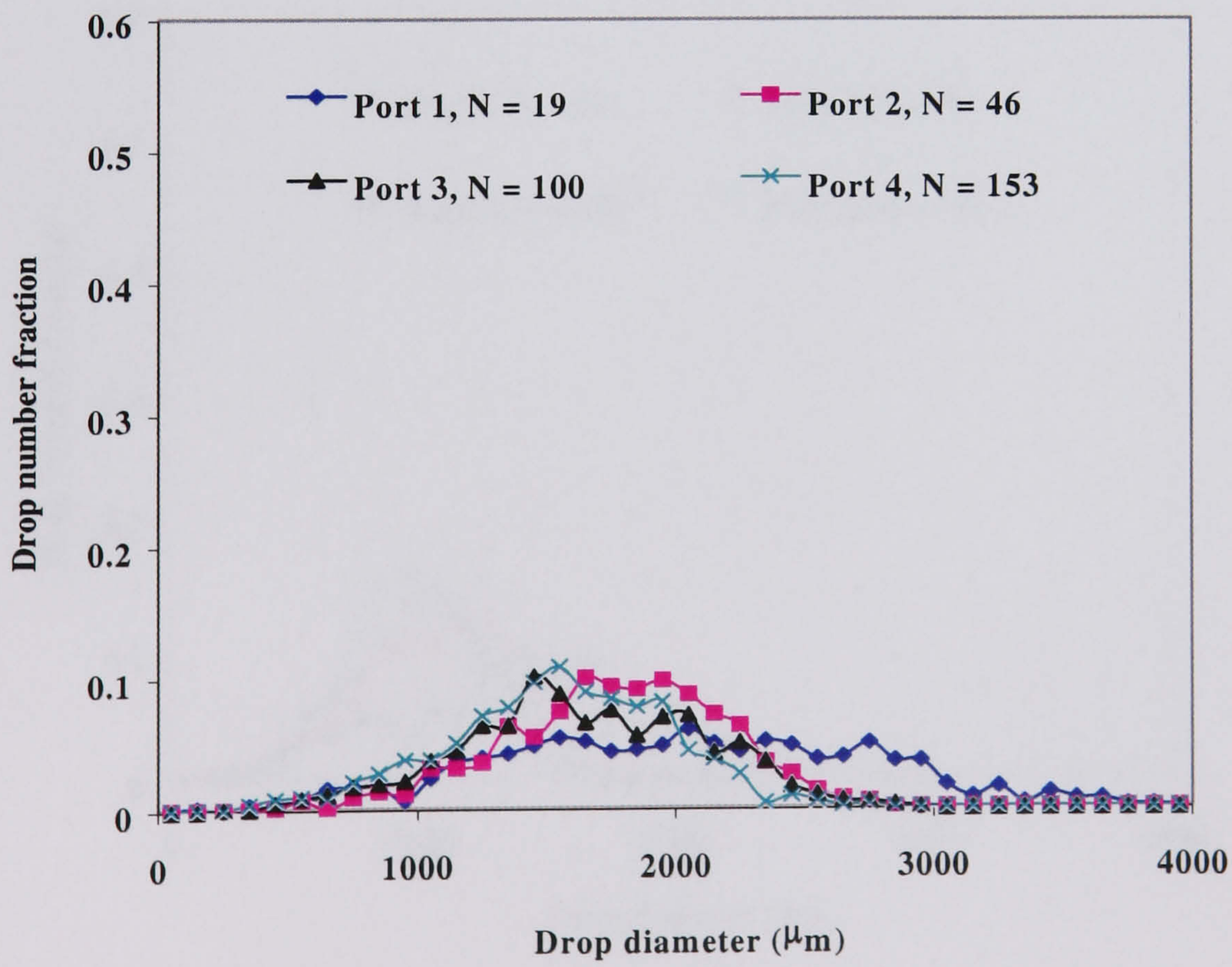

Figure 4.18. Drop size distribution as a function of flow length, Re_o = 2510 (x_o = 10 mm, f = 1 Hz); Re_n = 538

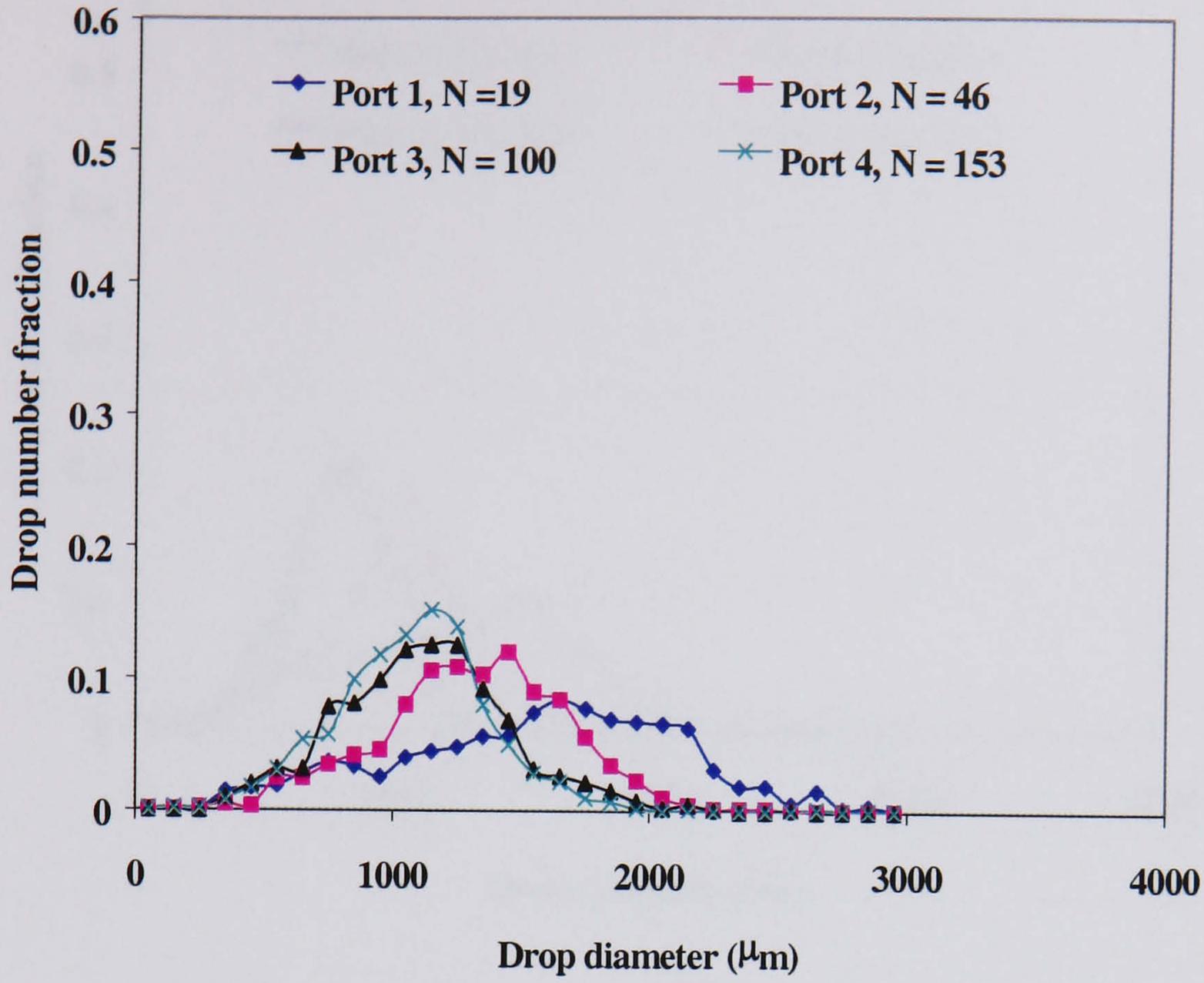

Figure 4.19. Drop size distribution as a function of flow length, Re_o = 3012 (x_o = 12 mm, f = 1 Hz); Re_n = 528

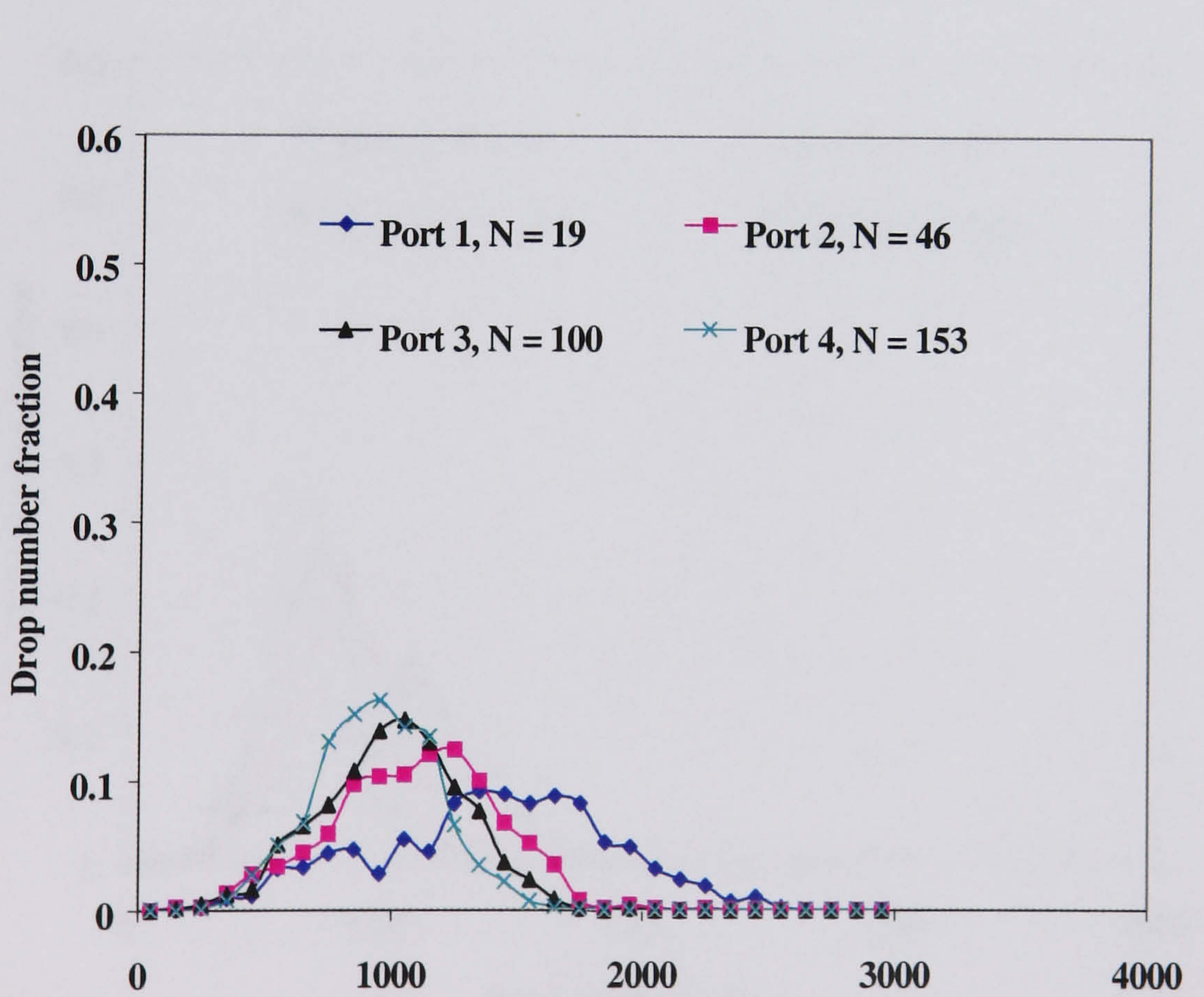

Figure 4.20. Drop size distribution as a function of flow length, Re_o = 3765 (x_o = 15 mm, f = 1 Hz); Re_n = 544

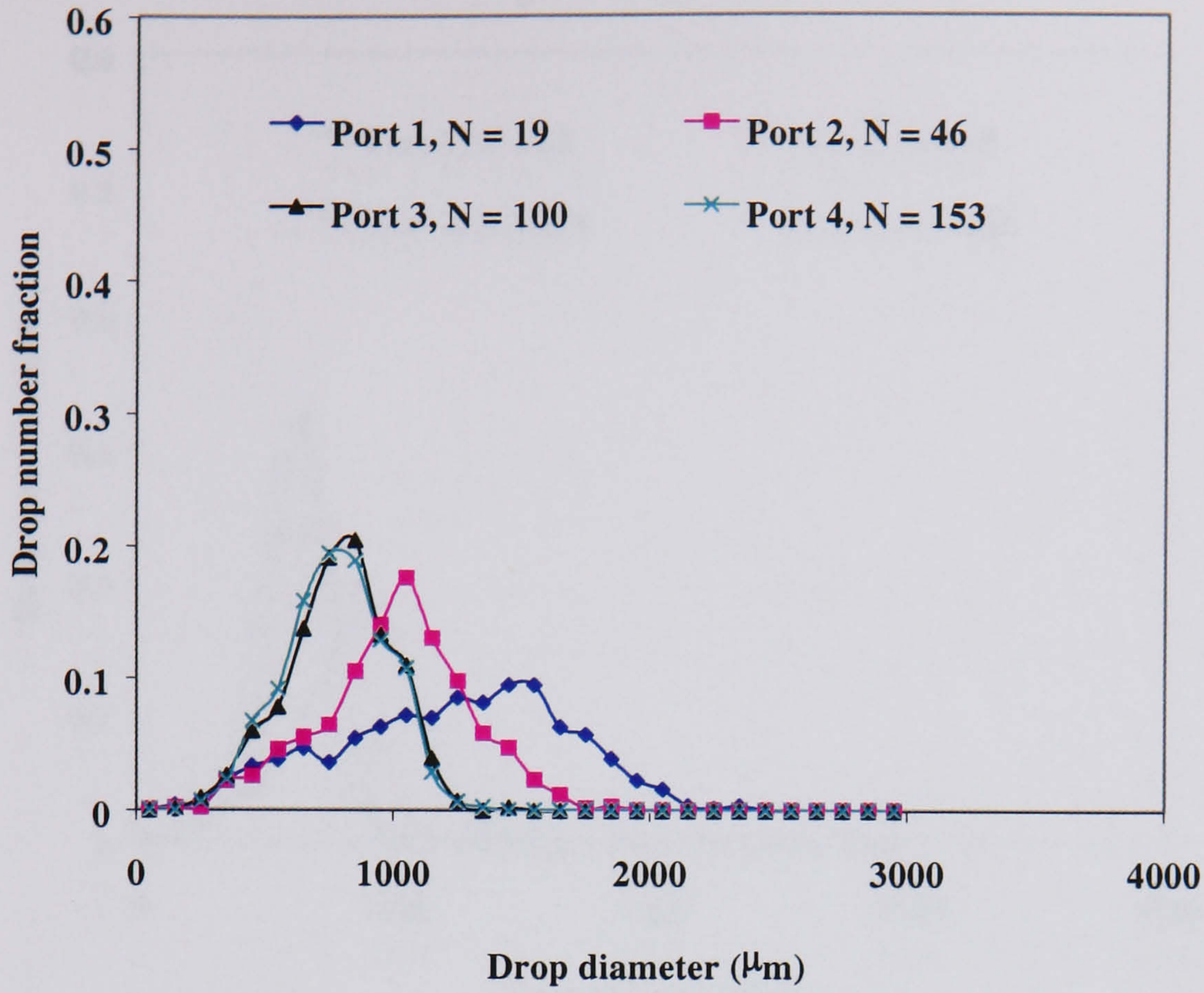

Figure 4.21. Drop size distribution as a function of flow length, Re_o = 4016 (x_o = 8 mm, f = 2 Hz); Re_n = 535

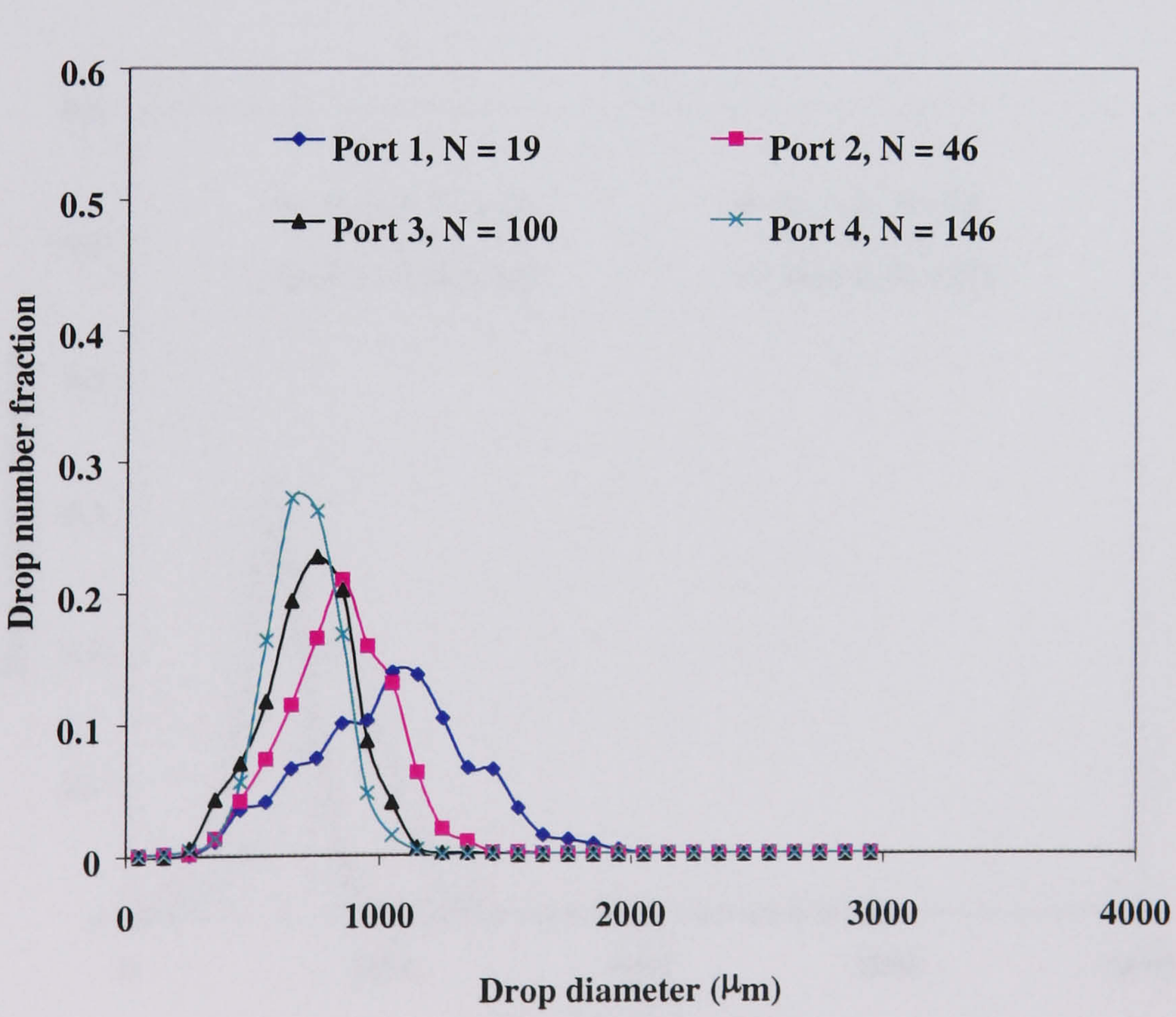

Figure 4.22. Drop size distribution as a function of flow length, Re_o = 5020 (x_o = 10 mm, f = 2 Hz); Re_n = 541

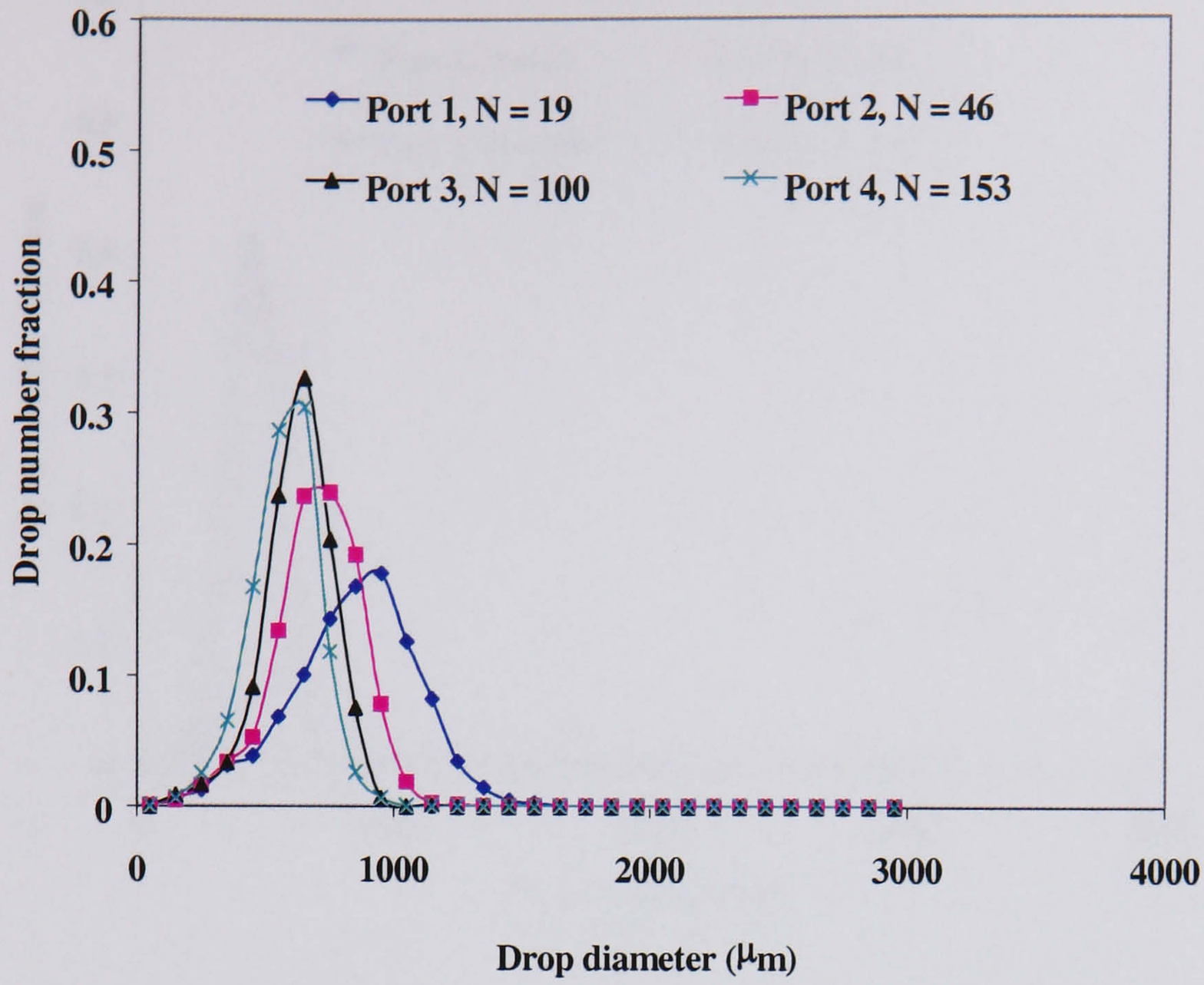

Figure 4.23. Drop size distribution as a function of flow length, Re_o = 6024 (x_o = 12 mm, f = 2 Hz); Re_n = 541

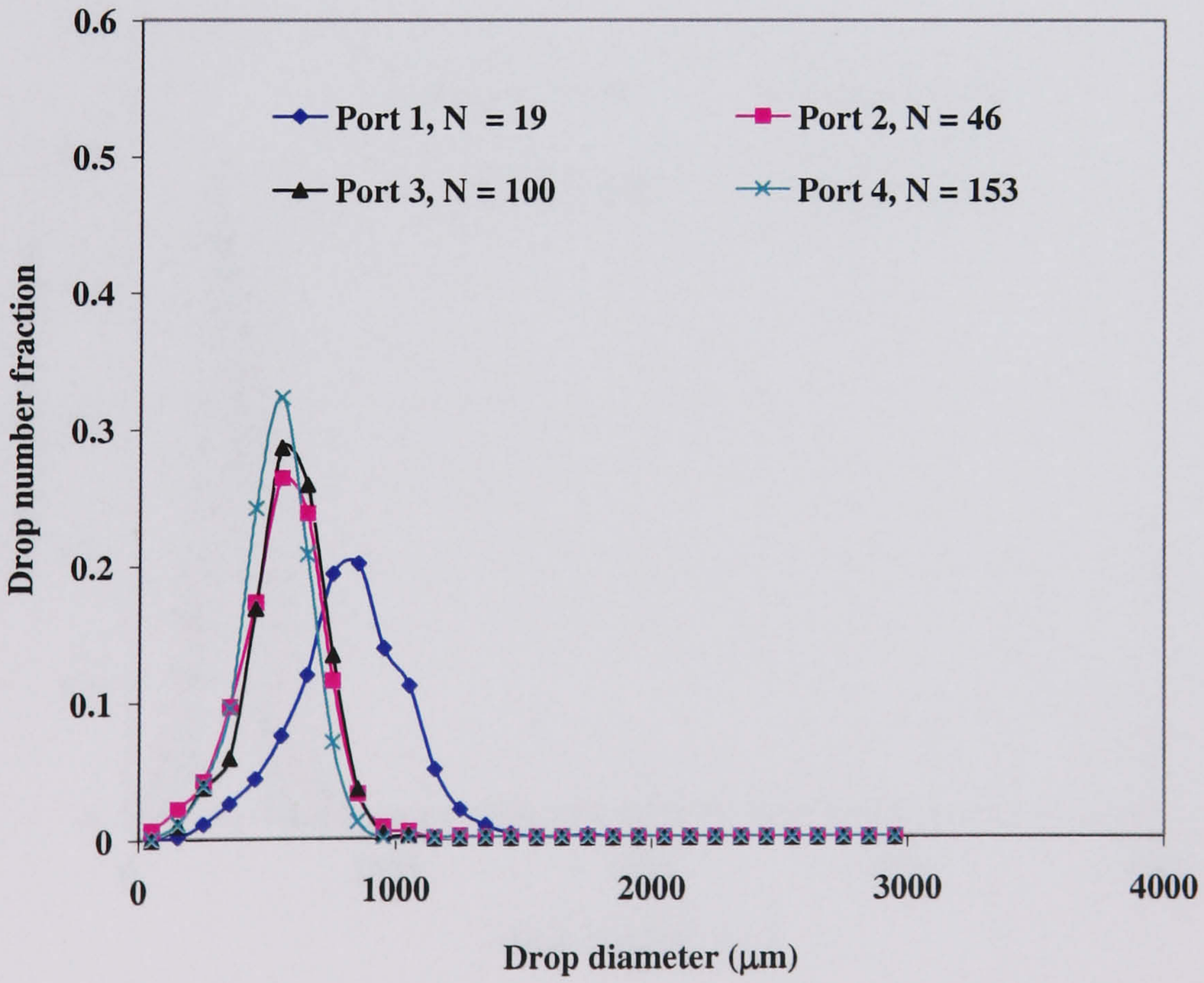

Figure 4.24. Drop size distribution as a function of flow length, Re_o = 7530 (x_o = 15 mm, f = 2 Hz); Re_n = 541

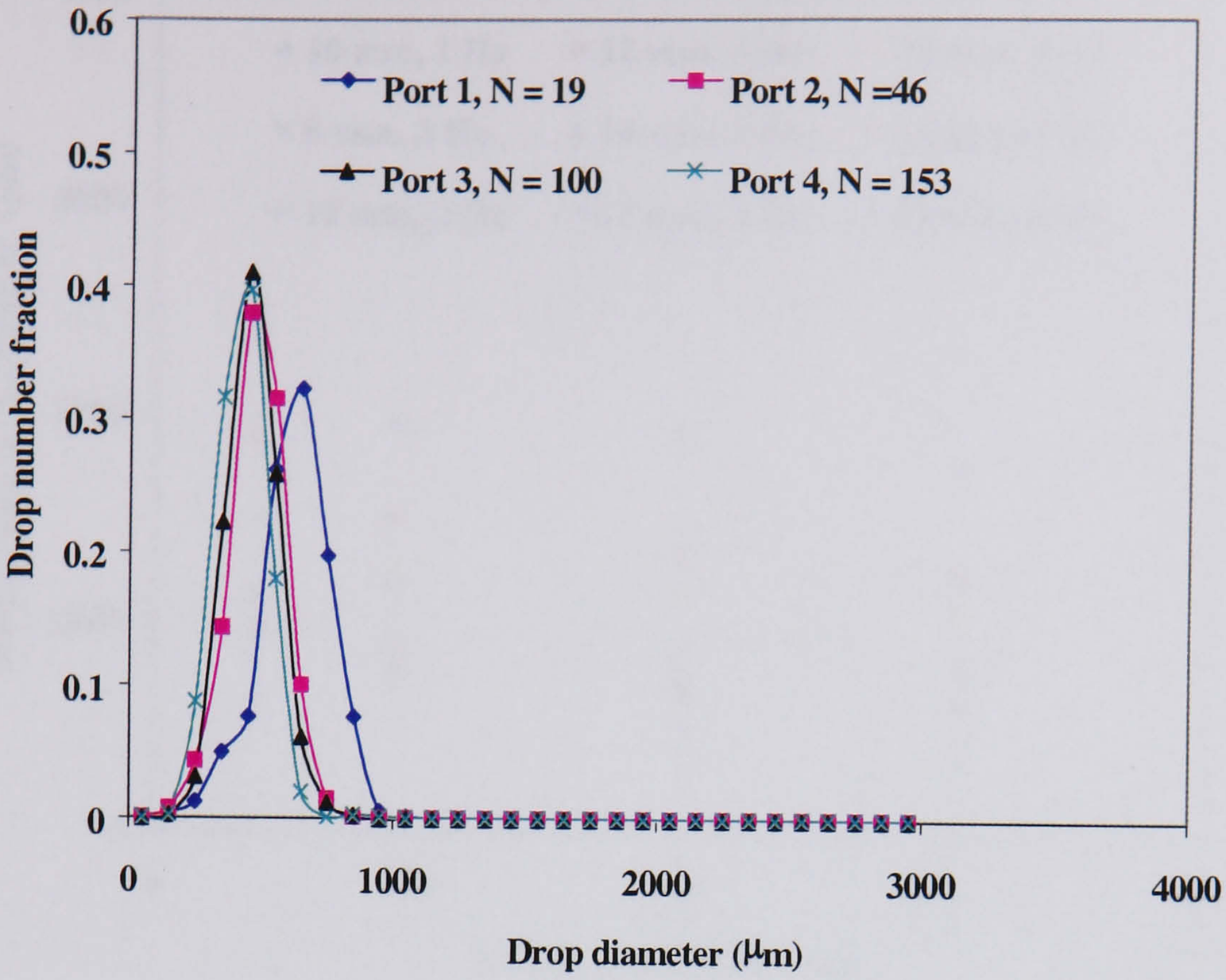

Figure 4.25. Drop size distribution as a function of flow length, Re_o = 9036 (x_o = 12 mm, f = 3 Hz); Re_n = 541

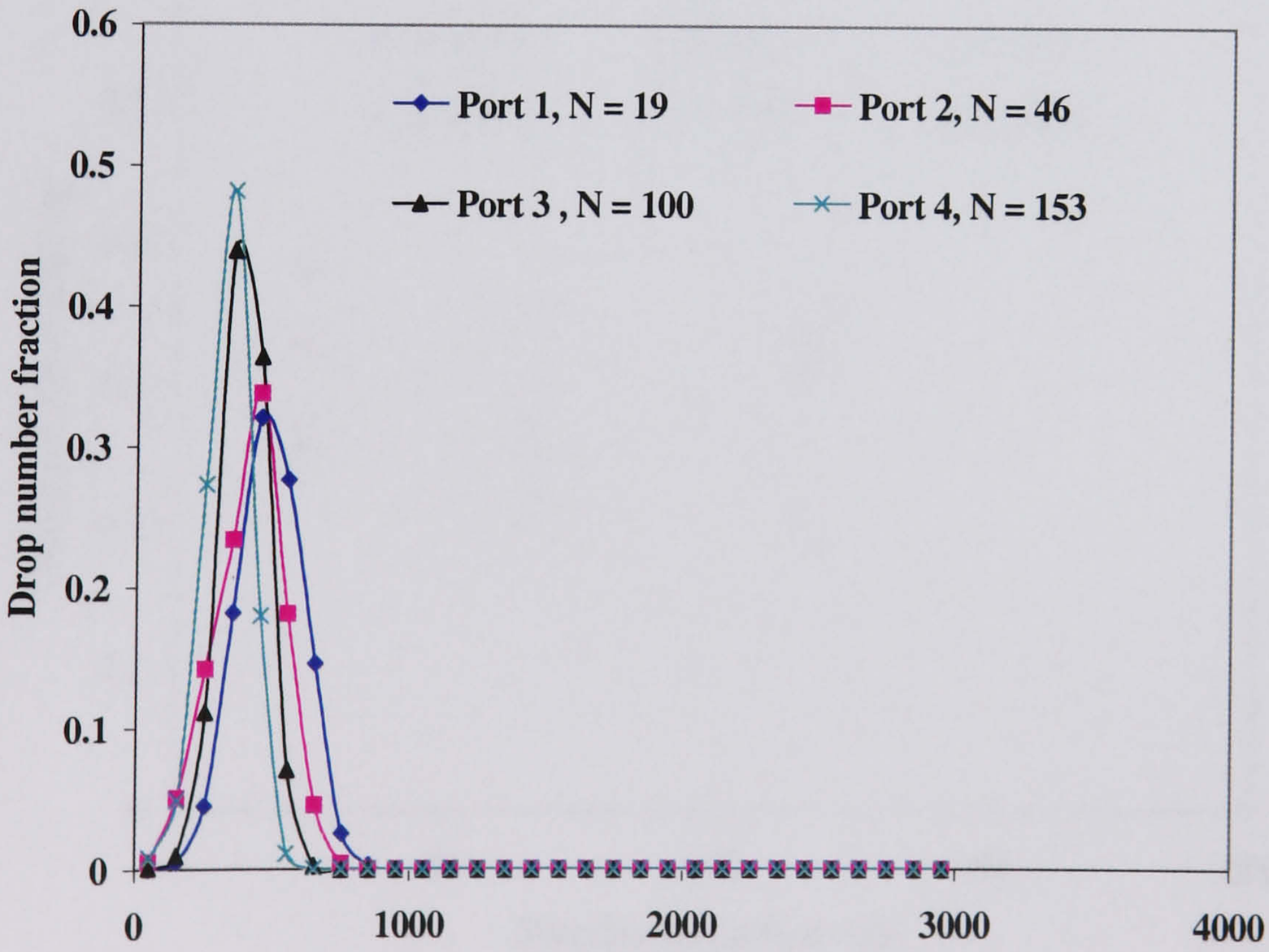

Figure 4.26. Drop size distribution as a function of flow length, Re_o = 11295 (x_o = 15 mm, f = 3 Hz); Re_n = 541

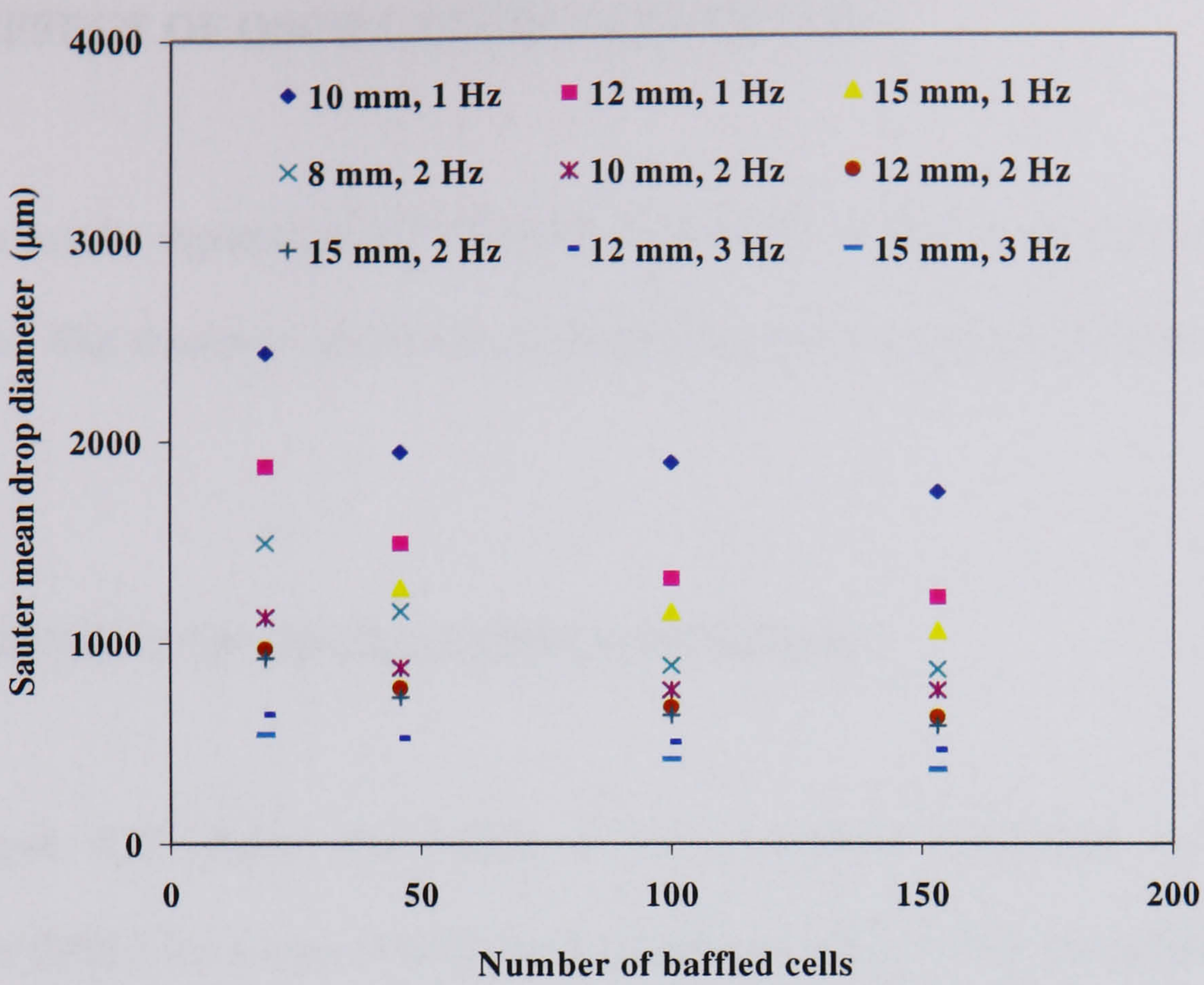

Figure 4.27. Axial variation of Sauter mean drop diameter

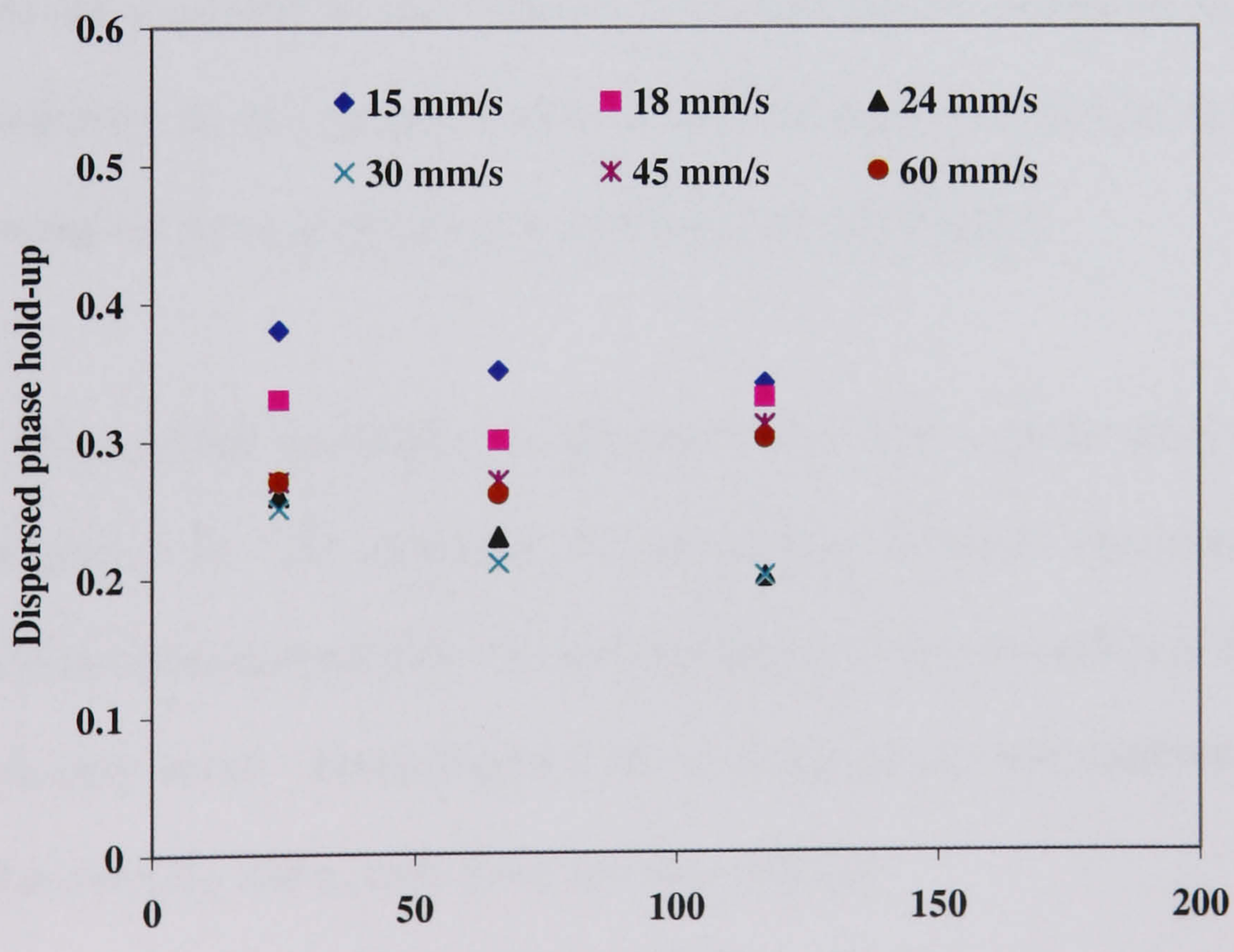

Figure 4.28. Axial variation of hold- up, Re_n = 541

4.2.2.2 EFFECT OF OSCILLATION PARAMETERS

The results reported in this Chapter correspond to Port 3, as it is closest to the steady state. The results corresponding to remaining ports are given in Appendix 2.

4.2.2.2.1 EFFECT OF OSCILLATION AMPLITUDE

Figure 4.29 shows the effect of the oscillation amplitude on drop size distribution (DSD) for a typical net flow Reynolds number of 541. It was observed that with the increase in the oscillation amplitude the drop size distribution narrowed with the mean shifting towards the lower end of the size scale. The drop number fraction corresponding to smaller drops also showed a general increase with the amplitude. Those results are expected as the increase in the oscillation amplitude increases the turbulence intensity in the system, which in turn increases the droplet breakage rate thereby reducing the mean drop size and narrowing the distribution.

The effect of the oscillation amplitude on the Sauter mean drop diameter is plotted in Figure 4.30. As expected, the mean drop diameter decreased with the increase in the oscillation amplitude. It was also observed that the effect of the net flow rate on d_{32} is very small. From Figure 4.30, a single power law relationship can be established between d_{32} and x_o over three net flow rates as:

$$d_{32} = 2.2\times10^{-5}(\pm\ 24.93\%)x_o^{-0.76\ (\pm5.5\%)}\ \text{(m)},\ (R^2 = 0.95) \qquad (4.9)$$

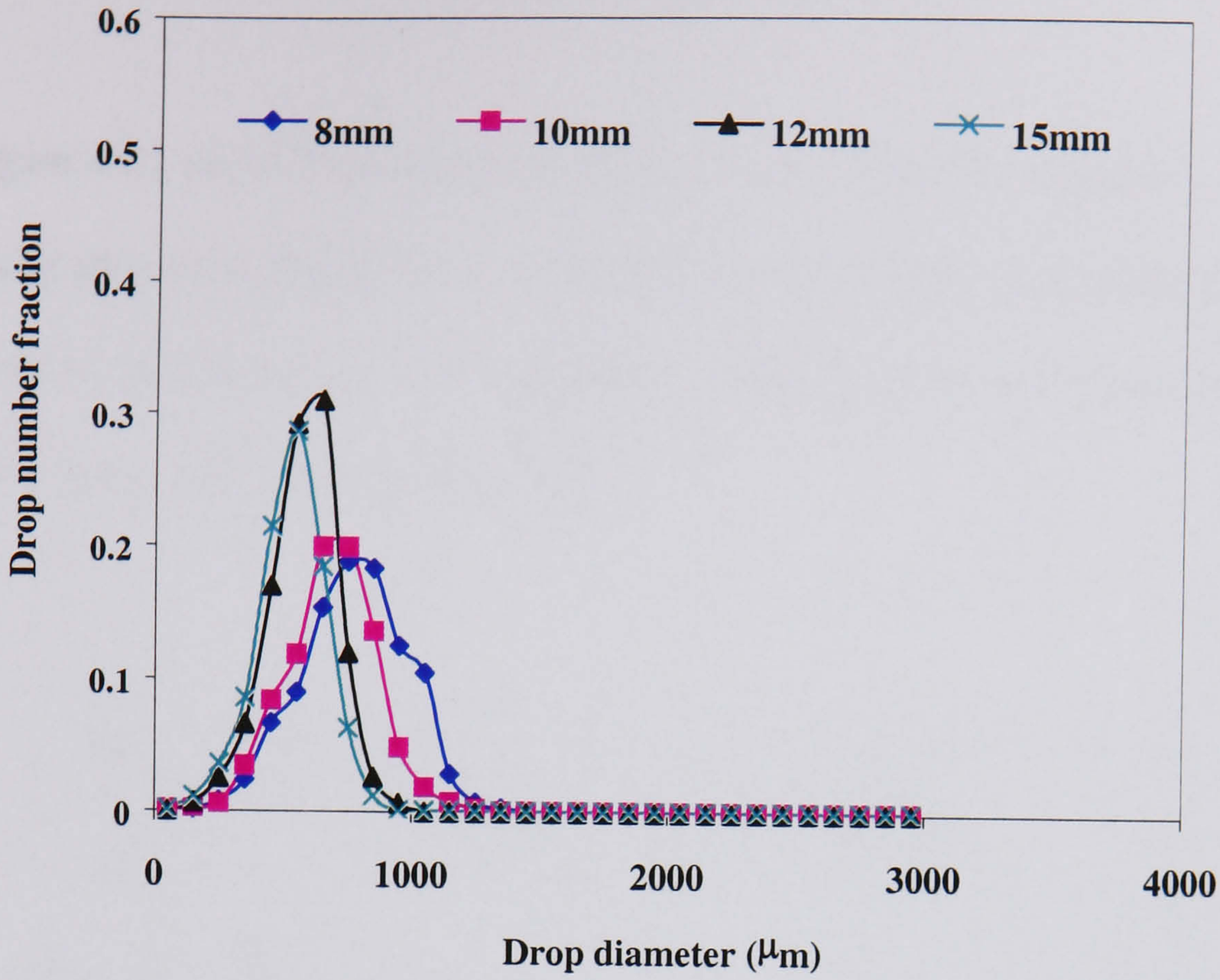

Figure 4.29. The effect oscillation amplitude on droplet size distribution (f = 2.0 Hz, Re_n = 541)

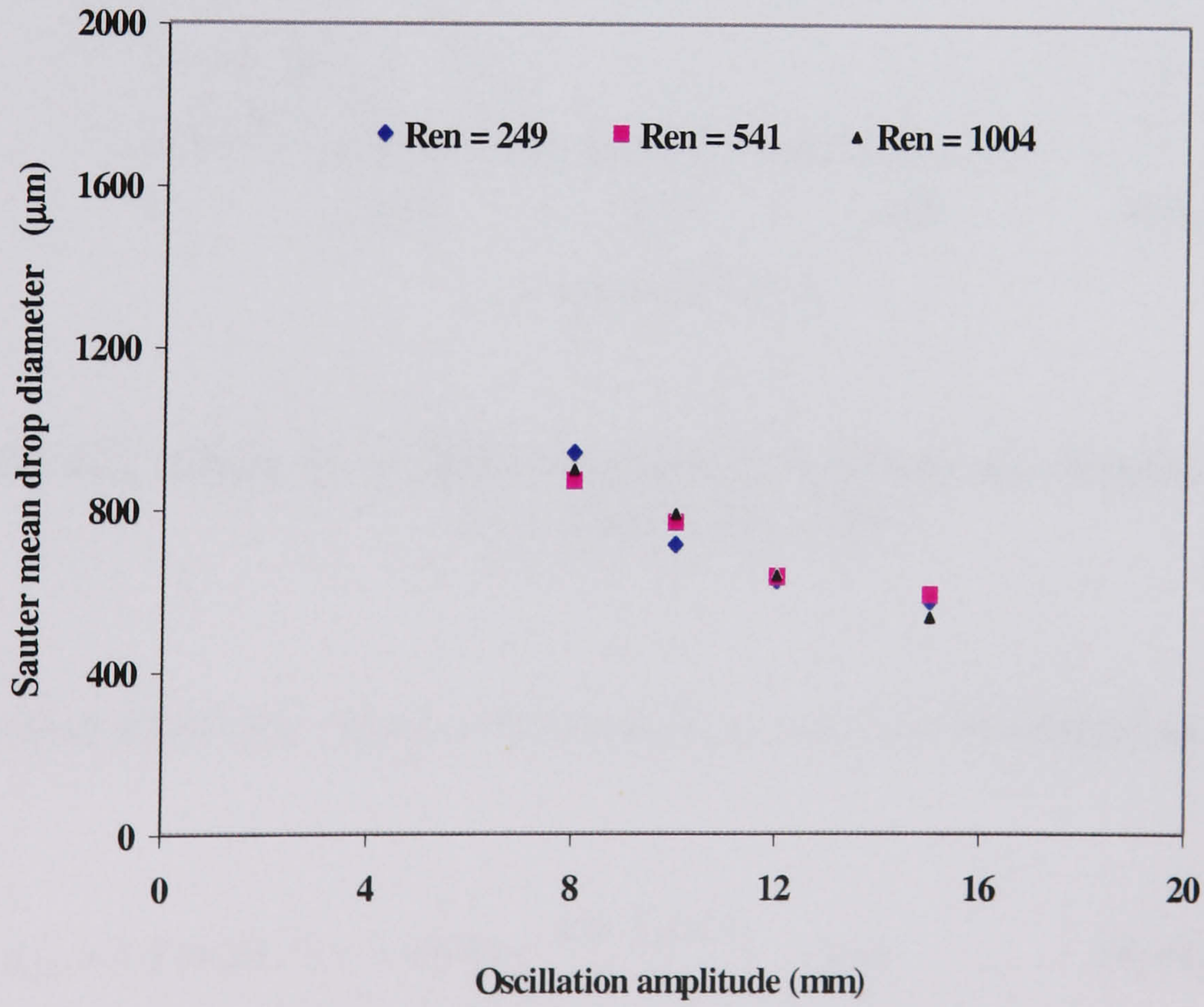

Figure 4.30. Effect of oscillation amplitude on Sauter mean drop diameter, f = 2 Hz

4.2.2.2.2 EFFECT OF OSCILLATION FREQUENCY

Figure 4.31 and 4.32 display the effect of the oscillation frequency on the DSD and the mean drop size, respectively. The DSDs and the mean drop diameter showed a similar trend as that observed in the amplitude. This again can be related to the energy dissipation in the system (see equation 2.3).

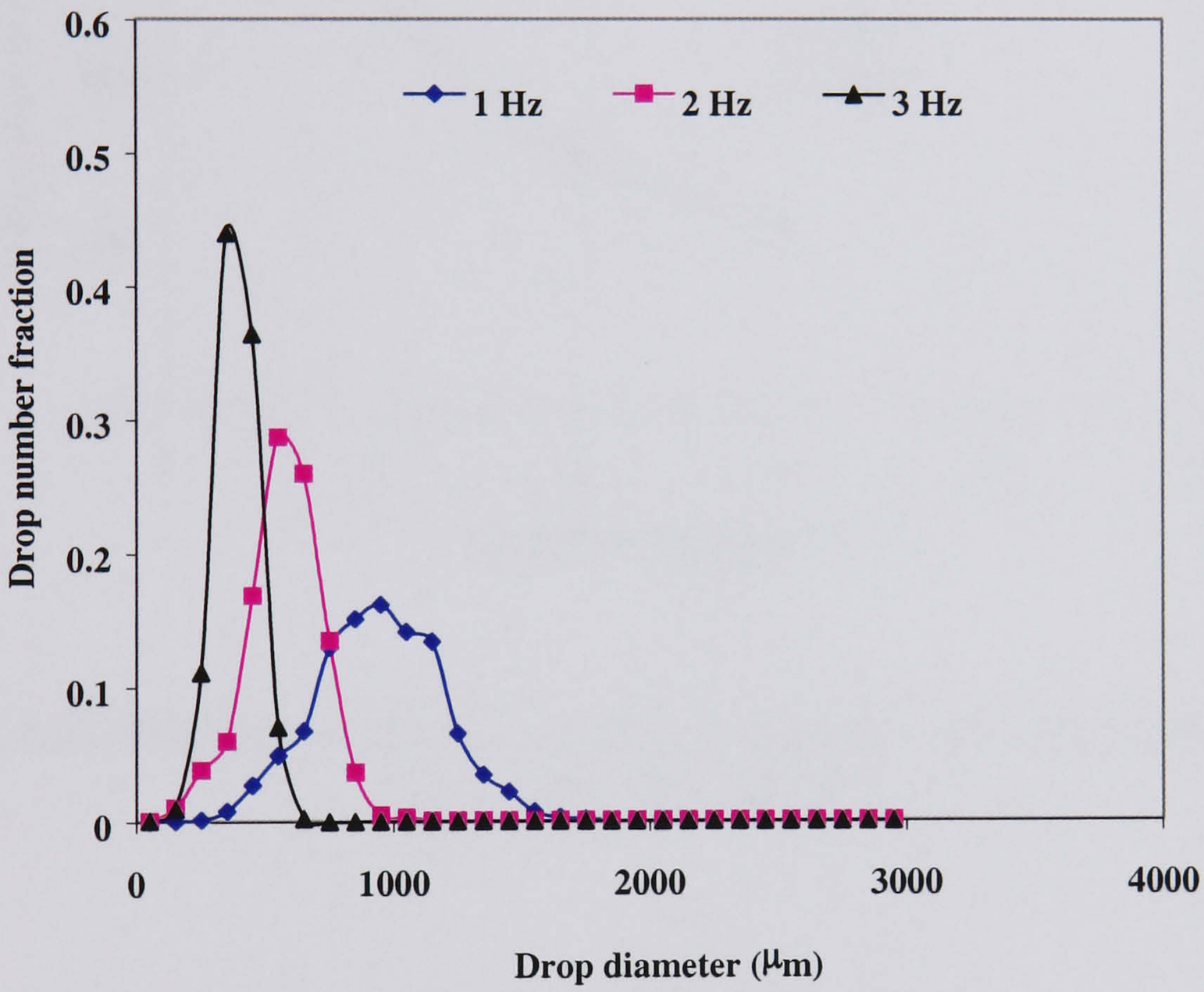

Figure 4.31. Effect of oscillation frequency on droplet size distribution (x_o = 15 mm, Re_n =541)

A similar power law relationship between d_{32} and f was developed as,

$$d_{32} = 1.11\times10^{-3}(\pm\ 1.93\%)\, f^{-0.85\ (\pm\ 2.56\%)} \quad \text{(m)} \qquad (4.10)$$

On comparing the power indices of equations 4.9 - 4.10, it was observed that the oscillation frequency has slightly larger effect on d_{32} than the oscillation amplitude.

This is different from that observed in the vertical OBTR, but the difference is very small.

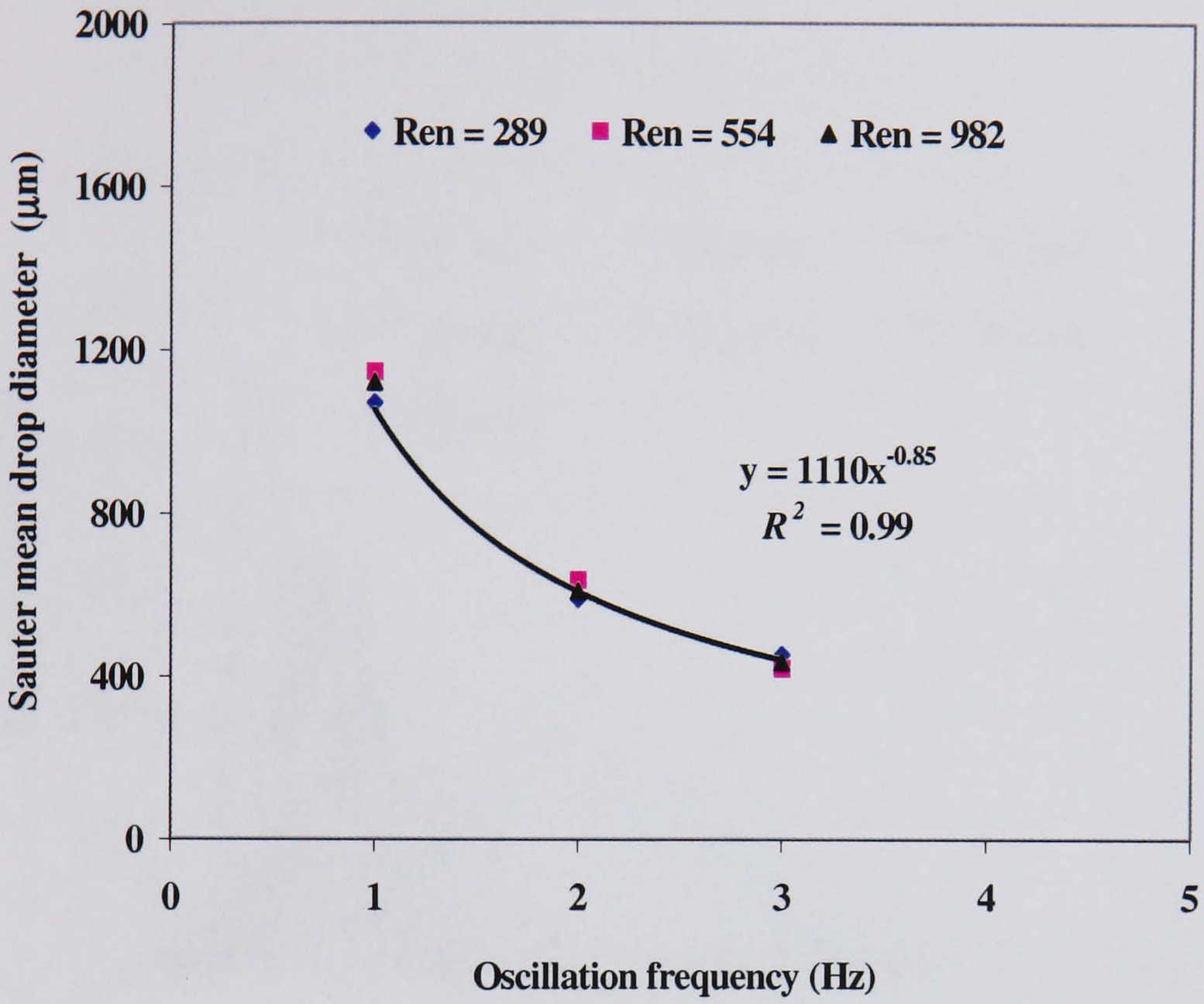

Figure 4.32. Effect of oscillation frequency on Sauter mean drop diameter, (x_o = 15 mm, Re_n = 541)

4.2.2.2.3 EFFECT OF OSCILLATION VELOCITY

In the previous sections, the individual effect of either the oscillation amplitude or the oscillation frequency was studied. In this section, the combined effect of the oscillation velocity, $x_o f$ on the drop size distribution (DSD) are examined in Figure 4.33. At lower oscillations, e.g., $x_o f$ = 10 mm/s, the drop size distribution was very broad and not unimodal. With the further increase in the oscillation velocity, the distributions became unimodal and narrower in width, and shifted towards the smaller drop diameters with the presence of reduced large diameter drops. This is because with an increase in

the oscillation velocity, $x_o f$, the drop breakage increases, thus decreasing the number of large drops and increasing the density of smaller drops, which results in narrow drop size distributions.

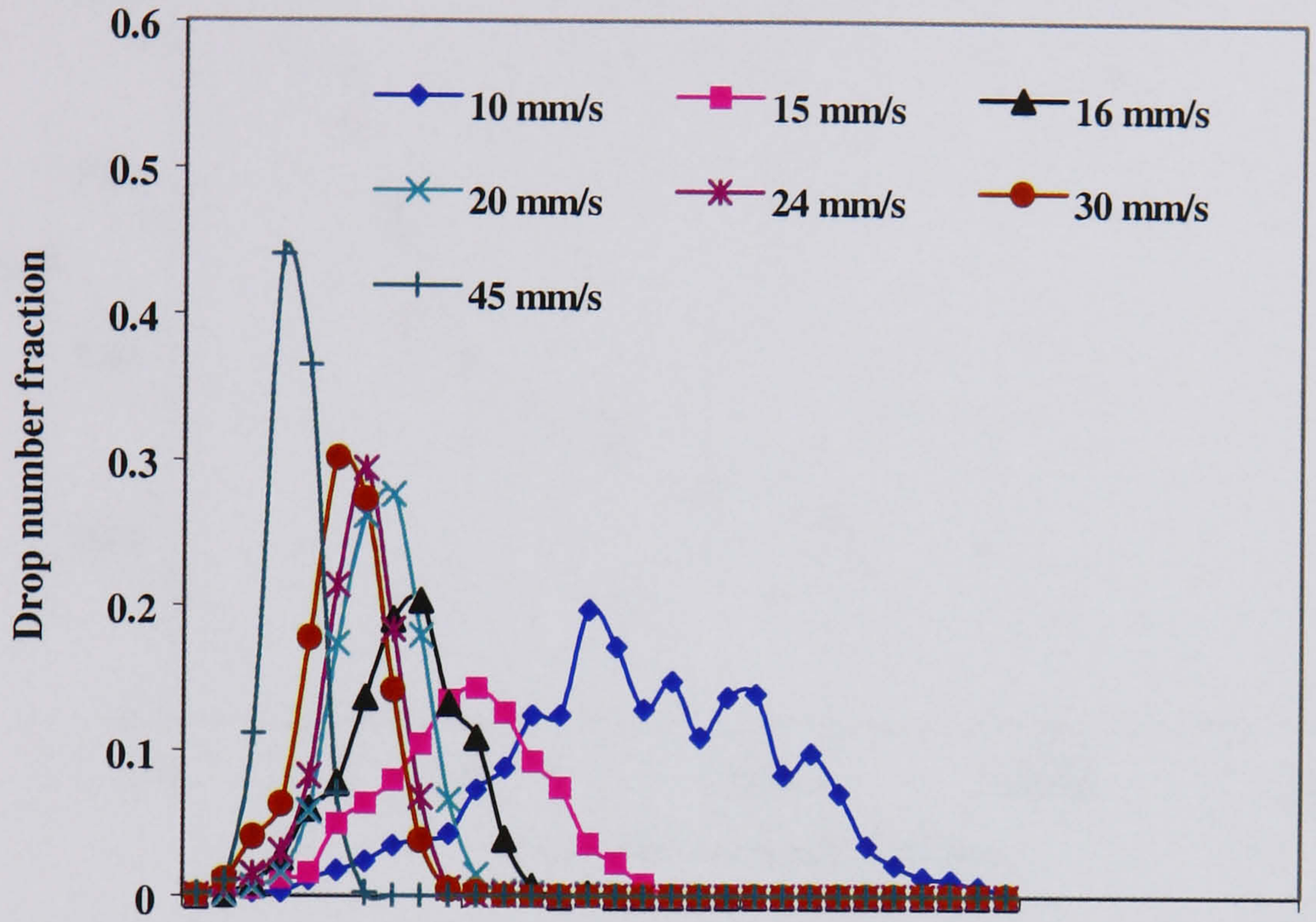

Figure 4.33. Effect of oscillation velocity on drop size distribution, Re_n = 541

The effect of the oscillation velocity on the Sauter mean drop diameter is presented in Figure 4.34 over the entire operating conditions used, where $\frac{d_{32}}{D}$ is plotted against the oscillation Reynolds number. From Figure 4.34, one can see that over the operating conditions, the mean drop diameter decreased with the increase in the oscillation velocity. Visually the decrease in $\frac{d_{32}}{D}$ is steeper here than that in the vertical OBTR (Figure 3.43 and 3.44). The data from Figure 4.34 was fitted with a power law relationship as:

$$\frac{d_{32}}{D} = 107\ (\pm 45.30\ \%)\,\mathrm{Re}_o^{\,-0.90\ (\pm 3.33\ \%)}\,\mathrm{Re}_n^{\,0.13\ (\pm 15.95\ \%)} \qquad (R^2 = 0.942) \qquad (4.11)$$

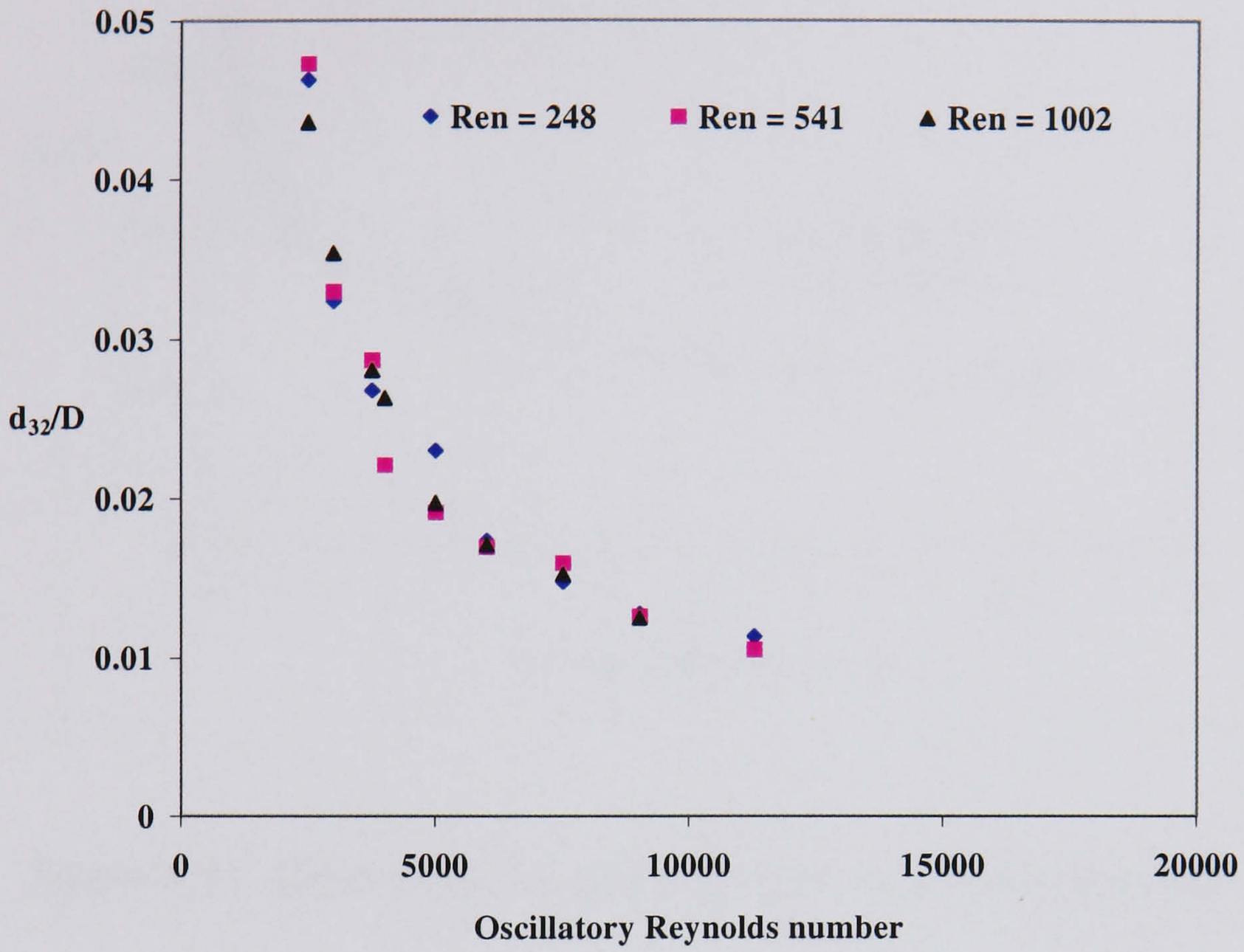

Figure 4.34. Effect of oscillation Reynolds number on dimensionless mean drop diameter

Similarly, the $\frac{d_{32}}{D}$ can also be plotted against the power dissipation rate, ε of the OBTR as in Figure 4.35, resulting

$$\frac{d_{32}}{D} = 0.0159\ (\pm\ 1.80\%)\varepsilon^{\,-0.30\ (\pm\,1.11\%)} \qquad (R^2 = 0.957) \qquad (4.12)$$

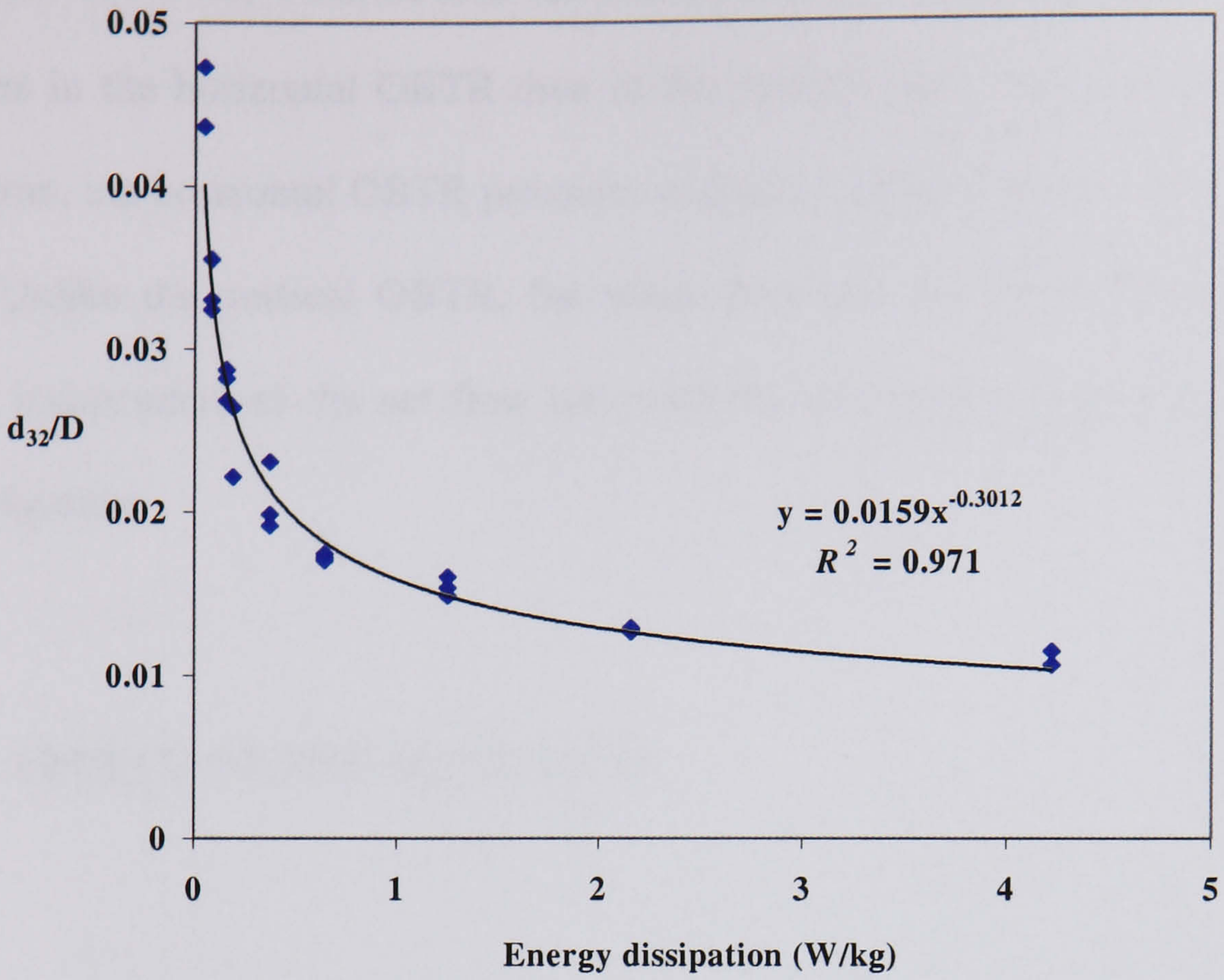

Figure 4.35. Effect of energy dissipation on mean drop diameter

In order to make a comparison with those in the vertical OBTR, Table 4.5 tabulates the correlation for both cases.

Table 4.5. Comparison of Horizontal and Vertical OBTR

Horizontal OBTR	Vertical OBTR
$\frac{d_{32}}{D} = 107\,\mathrm{Re}_o^{-0.90}\,\mathrm{Re}_n^{0.13}$	$\frac{d_{32}}{D} = 0.40\,\mathrm{Re}_o^{-0.57}\,\mathrm{Re}_n^{0.31}$ (Riser) $\frac{d_{32}}{D} = 1.24\,\mathrm{Re}_o^{-0.66}\,\mathrm{Re}_n^{0.29}$ (Downcomer)
$\frac{d_{32}}{D} = 0.0159\varepsilon^{-0.30}$	$\frac{d_{32}}{D} = 0.018\varepsilon^{-0.16}$ (Riser) $\frac{d_{32}}{D} = 0.022\varepsilon^{-0.23}$ (Downcomer)

From Table 4.5, it can be seen that the mean drop size is more influenced by the oscillations in the horizontal OBTR than in the vertical one. Also for an unit power consumption, the horizontal OBTR produces a smaller stable drop size than the vertical OBTR. Unlike the vertical OBTR, the mean drop size in the horizontal OBTR is relatively independent of the net flow rate over the operating conditions employed in this investigation.

4.2.2.2.4 EFFECT OF NET FLOW RATE

Figure 4.36 shows the variation of DSDs for different net flow rates at a fixed oscillation condition. The DSDs well overlapped each other, indicating the effect of the net flow rate on DSD is negligible. This is in line with the observation in Figure 4.30 and 4.32, as well as the investigation in the vertical OBTR. The results are again significant as it indicates that the DSD and the mean drop diameter can be controlled just by changing the oscillation conditions, independent of the net flow rates. This is the ideal situation for continuous suspension polymerisation processes.

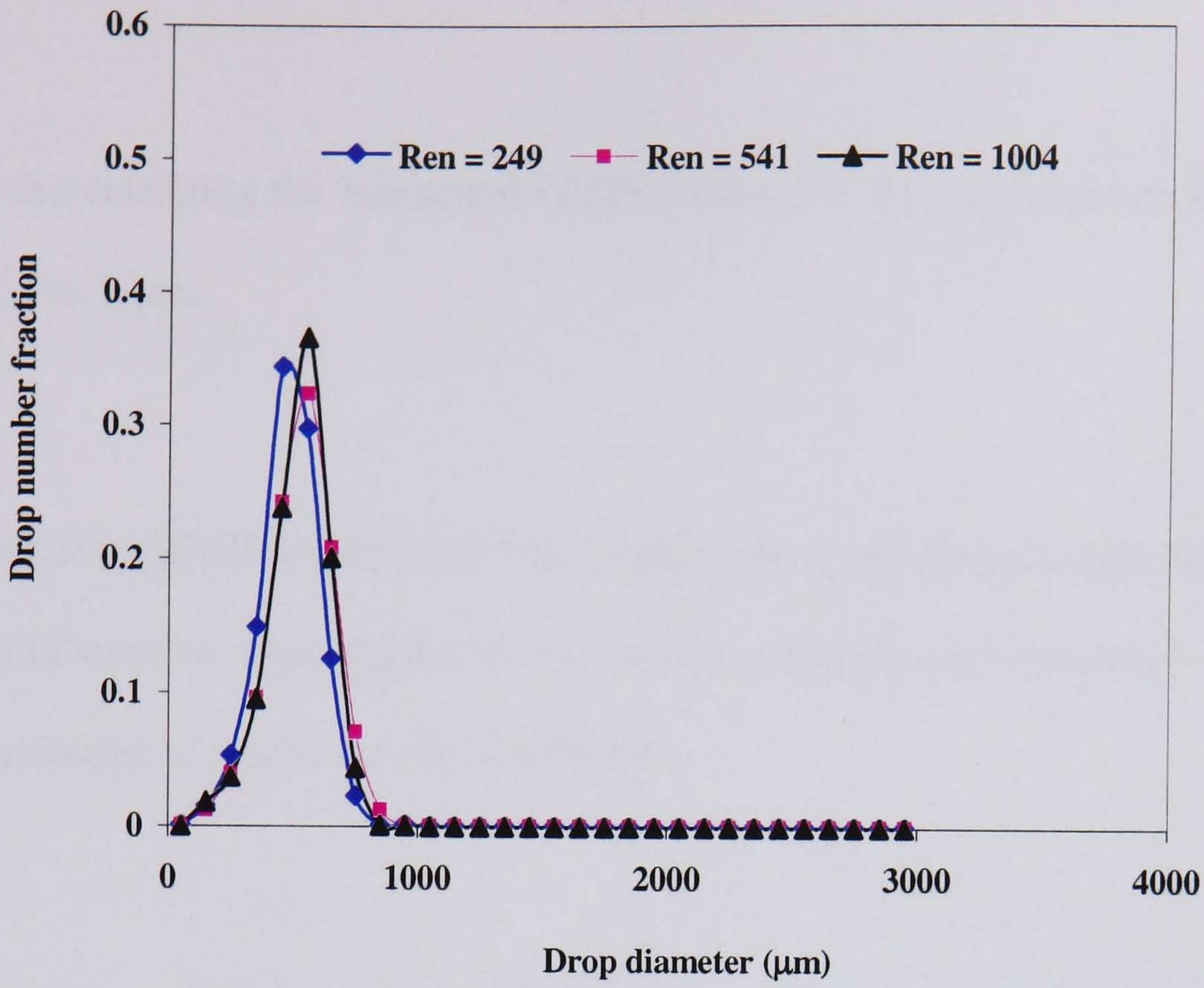

Figure 4.36. Effect of net flow rate on Sauter mean drop diameter, Re_o = 7530 (x_o = 15 mm, f = 2 Hz)

4.2.3 SUMMARY OF RESULTS

From the experimental two phase flow results, it was observed that the drop size distributions and the Sauter mean drop diameter were strongly influenced by the oscillation amplitude, frequency, but independent of the net flow rate conditions.

The drop stability was examined by measuring the DSD and d_{32} along the length of the tube, as well as by examining the oscillation conditions. It was observed that drop size distribution stability was achieved at Port 2 onwards at a relatively low oscillation velocity, i.e. 30 mm/s as compared to 60 mm/s in the vertical OBTR.

4.3 WHAT HAVE WE LEARNT?

On characterising the horizontal OBTR, there are two major conclusions to be drawn from this work:

- The horizontal OBTR is well suited for single phase application as near to plug flow characteristics have been achieved over all the experimental conditions explored, which is similar to that of the vertical OBTR.

- The horizontal OBTR is also well suited for two phase flow applications, in particular, suspension polymerisation processes, as observed from the DSD stability study.

As a result, the horizontal OBTR offers better control over the drop size distribution and the mean drop diameter compared to the vertical OBTR.

CHAPTER 5

MODELLING OF DROPLET BREAKAGE AND COALESCENCE

5.1 INTRODUCTION

The evolution of the dispersed phase droplet size distribution in a liquid-liquid dispersion is governed by both the droplet breakage and coalescence. The nature of these interactions is dependent on a number of parameters, such as mixing intensity, geometry of vessel and agitator, phase fraction, fluid physical properties, temperature, initial state of the system, presence of stabilisers, ionic species and so on. This makes the prediction of breakage and coalescence rates difficult. This chapter describes the development, evaluation and validation of a model for evaluating droplet breakage and coalescence rates based on the population balance equation. The population balance approach leads to a single integro-differential equation that can be solved only numerically, which requires long running time, without the assurance that computations actually converge (Bajpai *et al.*, 1976, Narsimhan *et al.*, 1984). To simplify the problem, the population balance equation can be applied in a discretised form. In this work a discretised population balance approach has been applied.

5.2 POPULATION BALANCE APPROACH

5.2.1 OVERVIEW

Population balance equation modelling is not a recent concept and has been applied to various fields of science and engineering. Among them, modelling

particulate processes have made intensive use of the population balance technique to model the behavior of particle size distributions (Ramkrishna, 1985). The first attempt to apply the population balance model to liquid-liquid systems was made by Valentas and Amundson (1966) by using empirical breakage and coalescence rate functions. Coulaloglou and Tavlarides (1977) reused the population balance equation and derived phenomenological functions to predict the rates from Kolmogoroff's theory of isotropic turbulence. Ever since, a number of expressions for breakage and coalescence rates have been proposed for application in the same equation. The population balance approach can thus be regarded as a frame that can be applied to various systems provided suitable rates are used given the assumptions of the system. Another important feature of the population balance approach is that it can be applied to droplets, bubbles or solid particles.

5.2.2 DISCRETISATION

Discretising the population balance model is a convenient way of solving the problem. By discretisation the entire drop volume range [v_{min} , v_{max}] is divided into a number of intervals of the type [v_i , v_{i+1}] by using a standard finite-element technique. The intervals of volume in turn define the classes of drops with volumes falling in the corresponding intervals. The intervals can be defined either linearly or geometrically.

The linear discretisation is carried out such that,

$$v_i = v_{i-1} + \Delta v \tag{5.1}$$

In this case all intervals are of the same width, Δv. The geometric discretisation is defined as,

$$v_i = \mathrm{R} v_{i-1}, \mathrm{R}>1, \tag{5.2}$$

where R is a geometric constant, Equation (5.2) can be rewritten as,

$$\ln(v_i) = \ln(v_{i-1}) + \ln(\mathrm{R}) \tag{5.3}$$

As a result, this type of discretisation is also called logarithmic discretisation. It can be noticed that the interval width increases with volume v_i, assuring that the model has a very good resolution in the region of small drops (Laso *et al.*, 1987; Hounslow, 1988).

Hounslow *et al.* (1988) applied the population balance approach to crystal size distributions. Although dealing with particles of very different type than liquid drops, their modeling work provides valuable insight to discretising the population balance equation. The model accounted for nucleation, growth and aggregation of crystals. The population balance equation was discretised using a geometric discretisation of the size domain, with ratio $\mathrm{R} = \sqrt{2}$. In a later publication (Litster *et al.*, 1995), the discretisation was made adjustable, using a ratio $\mathrm{R} = 2^{1/q}$ where q is an integer with a value greater than 1. Their work emphasized that higher-order moments of the distribution can be accurately predicted, provided that q is high enough. Laso *et al.* (1987) proposed another model of particular interest for this present work. The simplified model by Laso

et al. (1987) used a six-class approximation to solve the population balance equation. The range of drop volume was discretised logarithmically, using a ratio $R = 2$, meaning that in each class the volume of drops is twice the volume of drops in the previous class.

5.3 The Model

The model used in this work was initially written by Saye (2001) within the C.O.B.R.A. group for the evaluation of droplet breakage and coalescence rates from experimental drop size distributions. The model utilises an approach that is similar to that of the discretised population balance method by Laso *et al.* (1987), but in absence of any *a priori* assumption of functional form for breakage and coalescence rates. This itself is in contrast to the traditional approach. In the model, the conservation of volume is satisfied, and both breakage and coalescence rates are the unknowns, and have to be evaluated from the experimental data.

5.3.1 GENERAL ASSUMPTIONS

The following assumptions were made to develop the model used in this investigation:

1. It is assumed that the law of conservation of volume holds true. The effect of pressure variation on drop volume in the OBTR is neglected. Therefore, no growth term needs to be accounted for, and coalescence of two drops of sizes v_1 and v_2 will

result in a droplet with volume v_1+v_2. Similarly, the volumes of drops formed by breakage have sum equal to the volume of the initial mother drop.

2. Mixing is assumed to be efficient enough for droplets to be uniformly distributed. This is a relevant assumption given that the enhanced mixing capabilities are offered by OBRs. The size distributions are modelled only as a function of time and not space.

3. It is also assumed that the variation of the DSD with time depends only on breakage and coalescence and hence the model does not account for effect of droplet transport or any effect of gravity.

5.3.2 DROP CLASSES

The drop classes were discretised by using a geometric ratio of $\sqrt{2}$ such that the characteristic volume of drops in any given class is $\sqrt{2}$ times the characteristic volume of the previous class, corresponding to a diameter ratio of $2^{1/6}$ between each adjacent drop class. A similar approach was used by Hounslow *et al.* (1988). Because the ratio is $\sqrt{2}$, the characteristic volume of the classes doubles every other class. It should be noted that any other value could have been used for this ratio. Figure 5.1 is the schematic diagram showing the discretisation of drop classes. The $\sqrt{2}$ ratio was found to be fine enough without generating too many classes from the experimental measurements and not requiring excessive CPU times.

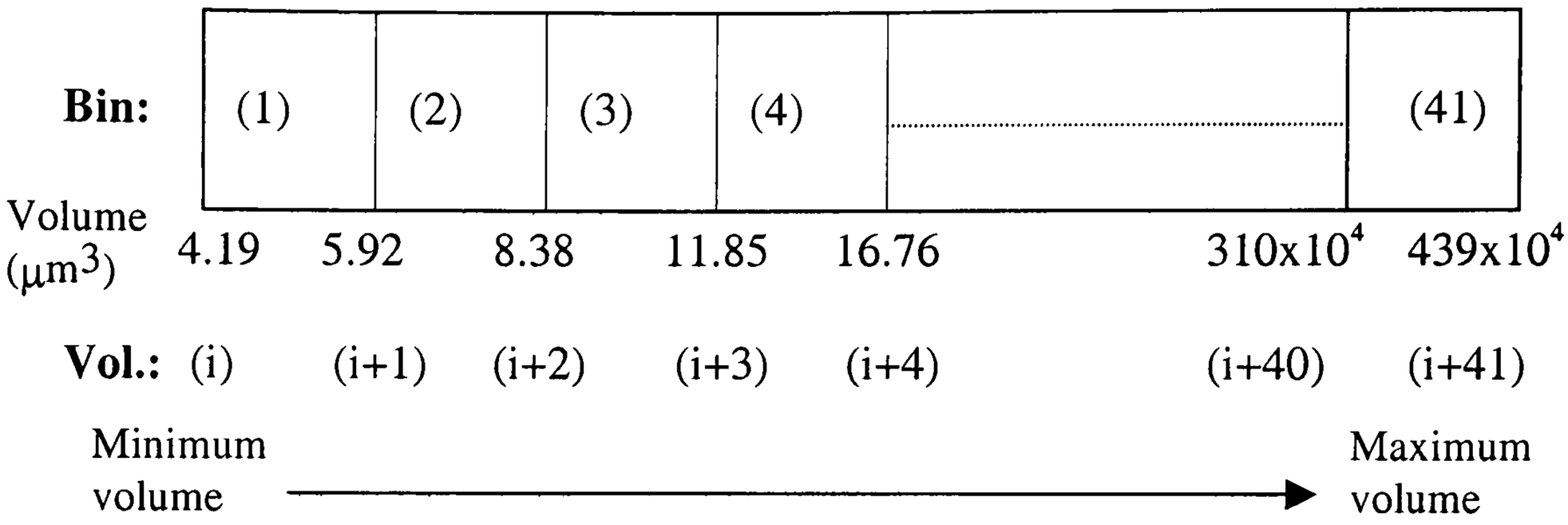

Figure 5.1. The discretised volume bins of droplets used in the model

5.3.3 VOLUME FRACTION CONTINUITY EQUATION

On applying the assumptions and the discretisation, the drop distribution continuity equation can be simplified to the following expression:

$$\frac{\partial}{\partial t} f_i(t) = B_i^+(t) + B_i^-(t) + C_i^+(t) + C_i^-(t) \tag{5.4}$$

where $B_i^+(t)$ and $B_i^-(t)$ stand for the birth and death rates of drops occurring in class i because of breakage, $C_i^+(t)$ and $C_i^-(t)$ are the birth and death rates in class i due to coalescence and $f_i(t)$ is the volume fraction of drops in class i of a distribution defined as:

$$f_i = \frac{\sum_k v_k n_{k,i}}{\sum_j \left(\sum_k v_k n_{k,j} \right)} \tag{5.5}$$

where $n_{k,j}$ is the number of drops with volume v_k in any class j of the distribution. Hence

$$\sum_i f_i = 1 \tag{5.6}$$

5.4 POPULATION BALANCE MODEL

5.4.1 BREAKAGE MODEL

In the breakage model, it was assumed that the "mother" drop breaks up into two equally sized "daughter" droplets, thus making the daughter droplet distribution rather simple. According to this assumption a drop of volume v will break up into two equally sized drops of volume $v/2$, which in our distribution according to the discretisation used is two classes down from the mother drop class. The conservation of volume implies that breakage of drops from a class i will result in a fraction of volume available in class i travelling two classes down to class (i-2). This is a rather simple assumption, however when other matters related to the computational complexity of the model are solved, it will be possible to extend the model to more elaborate daughter distributions.

Let g_i be the fraction of volume leaving class i per unit of time. Then class i undergoes a loss of volume $g_i f_i V_d$ per unit of time, which in terms of volume fraction is expressed as:

$$\frac{\partial f_i}{\partial t} = -g_i f_i \tag{5.7}$$

Applying the conservation of volume, the same amount of volume is allocated to class (i-2), according to:

$$\frac{\partial f_{i-2}}{\partial t} = g_i f_i \tag{5.8}$$

From equations, (5.7) and (5.8), one identifies

$$B_i^-(t) = -g_i f_i(t) \tag{5.9}$$

$$B_i^+(t) = g_{i+2} f_{i+2}(t) \tag{5.10}$$

In a more concise manner, $\mathbf{g}$ is defined as the vector formed by the breakage rate constants over all classes (or frequencies) of the distribution. Breakage rate constants are assumed to be independent of time and their dimension is the reciprocal of time (s^{-1}). To keep the breakage model consistent with the drop classes, no droplets

with volume less than the minimum volume in the distribution should be formed by breakage. To prevent the formation of such droplets, breakage is not allowed in the first two classes. This is enforced by setting the first two breakage rates to zero, as expressed by

$$g_1 = g_2 = 0. \tag{5.11}$$

5.4.2 COALESCENCE MODEL

Coalescence is a more complex phenomenon than breakage as it involves drops from various classes of the distributions. The general scheme would be a drop from a class i interacting with a drop from a class j, and the resulting coalesced drop falling into a suitably identified class k. Because the distributions incorporate many classes, the total number of possible interactions is high, and hence only three types of interactions are considered in developing the coalescence model:

- Type (a): coalescence of drops from the same class ($j=i$),
- Type (b): coalescence of drops from two adjacent classes ($j=i\pm1$),
- Type (c): coalescence of drops from classes one class apart ($j=i\pm2$).

In other words, a drop from any given class can interact with drops from five other classes. It is assumed that coalescence always involves the same number of coalescing drops. This is necessary in order to identify the class into which the resulting coalesced drop falls. In the model, coalescence is a binary process, meaning

that one given drop will coalesce with one single other drop. This is in line with the assumptions reported in the literature (Coulaloglou and Tavlarides, 1976 and Tsoursis and Tavlarides, 1994). To completely model the effect of drop coalescence, one needs to determine to which class k this total volume corresponds. This operation is made difficult by the choice of a geometric discretization of the volume range.

For the three interactions described above, one can identify class k as described below. For example, for Type (a), $k = i+2$. For Types (b) and (c), the coalesced droplets do not fall into one single class, but two adjacent classes, $(j+1)$ and $(j+2)$, with $j>i$. In those cases, ratios are used to properly describe how the total volume is split between the two classes $(j+1)$ and $(j+2)$ after coalescence. For Type (b), a fraction $k_{b,1}$ will be allocated to class (j+1), and a fraction $k_{b,2}$ to class (j+2). For Type (c), a fraction $k_{c,1}$ will be allocated to class (j+1), and a fraction $k_{c,2}$ to class (j+2). The values of $k_{b,1}$, $k_{b,2}$, $k_{c,1}$ and $k_{c,2}$ presented in equations (5.12) to (5.15) were computed based on the assumption that drop volumes are uniformly distributed in each class as:

$$k_{b,2} = \frac{1}{2\sqrt{2}} \tag{5.12}$$

$$k_{b,1} = 1 - \frac{1}{2\sqrt{2}} \tag{5.13}$$

$$k_{c,1} = \frac{3}{2} - \sqrt{2} \tag{5.14}$$

$$k_{c,2} = \sqrt{2} - \frac{1}{2} \tag{5.15}$$

The coalescence rate constant, $\beta_{i,j}$, is defined as the fraction of volume in class i interacting with class j per unit of time. The rate of coalescence describing a loss of volume fraction in class i that is due to coalescence with class j, is given by,

$$\left.\frac{\partial f_i}{\partial t}\right)_{i+j} = -\beta_{i,j} f_i f_j \tag{5.16}$$

in which $\beta_{i,j}$ is the coalescence rate constant for this interaction (i+j). In a similar manner, class j undergoes a loss of volume fraction,

$$\left.\frac{\partial f_j}{\partial t}\right)_{j+i} = -\beta_{j,i} f_j f_i \tag{5.17}$$

By equality of coalescence, $\left.\frac{1}{v_i}\frac{\partial f_i}{\partial t}\right|_{i+j} = \left.\frac{1}{v_j}\frac{\partial f_j}{\partial t}\right|_{j+i}$

$$\text{hence, } \beta_{j,i} = \frac{v_j}{v_i}\beta_{ij} \tag{5.18}$$

This will result in gains in both classes (j+1) and (j+2) respectively

$$\frac{\partial f_{j+1}}{\partial t} = k_{x,1}(\beta_{i,j} f_i f_j + \beta_{j,i} f_j f_i) = k_{x,1}(1 + \frac{\nu_j}{\nu_i})\beta_{i,j} f_i f \tag{5.19}$$

$$\frac{\partial f_{j+2}}{\partial t} = k_{x,2}(\beta_{i,j} f_i f_j + \beta_{j,i} f_j f_i) = k_{x,2}(1 + \frac{\nu_j}{\nu_i})\beta_{i,j} f_i f_j \tag{5.20}$$

where x stands for the type of interactions involved (x = 'b' or 'c'). In the particular case of type (a), this results in a loss in class i as:

$$\frac{\partial f_i}{\partial t}\Big)_i = -\beta_{i,i} f_i^2 \tag{5.21}$$

and a gain in class (i+2) being:

$$\frac{\partial f_{i+2}}{\partial t}\Big)_i = \beta_{i,i} f_i^2 \tag{5.22}$$

To summarise, we present here the losses and gains that coalescence incur to class i. Type (a) will cause a loss:

$$C^-_{i,(a)} = \frac{\partial f_i}{\partial t}\Big)_{loss(a)} = -\beta_{i,i} f_i^2 \tag{5.23}$$

as well as a gain:

$$C^{+}_{i,(a)} = \frac{\partial f_i}{\partial t}\Big)_{gain(a)} = \beta_{i-2,i-2} f^{2}_{i-2} \tag{5.24}$$

In class i, type (b) will induce the loss:

$$C^{-}_{i,(b)} = \frac{\partial f_i}{\partial t}\Big)_{loss(b)} = -\beta_{i,i-1} f_i f_{i-1} - \beta_{i,i+1} f_i f_{i+1} = -\frac{v_i}{v_{i-1}} \beta_{i-1,i} f_i f_{i-1} - \beta_{i,i+1} f_i f_{i+1} \tag{5.25}$$

as well as the gain:

$$C^{+}_{i,(b)} = \frac{\partial f_i}{\partial t}\Big)_{gain(b)} = k_{b,1} \beta_{i-2,i-1} f_{i-2} f_{i-1} (1 + \frac{v_{i-1}}{v_{i-2}}) + k_{b,2} \beta_{i-3,i-2} f_{i-3} f_{i-2} (1 + \frac{v_{i-2}}{v_{i-3}}) \tag{5.26}$$

In class i, type (c) will cause a loss:

$$C^{-}_{i,(c)} = \frac{\partial f_i}{\partial t}\Big)_{loss(c)} = -\beta_{i,i-2} f_i f_{i-2} - \beta_{i,i+2} f_i f_{i+2} = -\frac{v_i}{v_{i-2}} \beta_{i-2,i} f_i f_{i-2} - \beta_{i,i+2} f_i f_{i+2} \tag{5.27}$$

and a gain:

$$C^{+}_{i,(b)} = \frac{\partial f_i}{\partial t}\Big)_{gain(c)} = k_{c,1} \beta_{i-3,i-1} f_{i-3} f_{i-1} (1 + \frac{v_{i-1}}{v_{i-3}}) + k_{c,2} \beta_{i-4,i-2} f_{i-4} f_{i-2} (1 + \frac{v_{i-2}}{v_{i-4}}) \tag{5.28}$$

The coalescence rate constants $\beta_{i,j}$ can be gathered into a non-symmetrical matrix. However, the simple relationship between $\beta_{i,j}$ and $\beta_{j,i}$ means that knowledge of $\beta_{i,j}$ for $i \le j$ is sufficient. The total coalescence rate C_i^- describing loss undergone by class i, is derived as the sum of the losses in equations (5.23), (5.25) and (5.27), thus:

$$\begin{aligned} C_i^- &= -\left(\beta_{i,i} f_i + \beta_{i,i-1} f_{i-1} + \beta_{i,i+1} f_{i+1} + \beta_{i,i-2} f_{i-2} + \beta_{i,i+2} f_{i+2}\right) f_i \\ &= -\left(\beta_{i,i} f_i + \frac{v_i}{v_{i-1}} \beta_{i-1,i} f_{i-1} + \beta_{i,i+1} f_{i+1} + \frac{v_i}{v_{i-2}} \beta_{i-2,i} f_{i-2} + \beta_{i,i+2} f_{i+2} \right) f_i \end{aligned} \tag{5.29}$$

It can be seen from that equation that at most five coefficients $\beta_{i,j}$ are needed to completely describe the effects of coalescence on class i. This is the consequence of only three coalescence interactions being accounted for in the model.

All coalescence rate constants are considered to be independent of time and their dimension is the reciprocal of time (s^{-1}). Not all interactions are always possible or fully permissible, as coalescence in some of the classes would result in drops with size larger than the maximum size in the distribution. These coalescence interactions include the last four classes. In these classes, only the interaction of drops that result in drop volumes being less than or equal to the maximum volume are considered.

5.4.3 COMBINED MODEL

The breakage and coalescence equations (5.4, 5.10, 5.10) and (5.25-5.28) can be put together to give a combined model describing breakage and coalescence altogether and is presented by equation (5.30),

$$\frac{d}{dt} f = A(f).P \tag{5.30}$$

In this equation, $\boldsymbol{f}$ stands for the vector consisting of the volume fractions f_i and is a function of time, $\boldsymbol{P}$ stands for a vector consisting of all coalescence and breakage rate constants. Equation (5.30) represents a system of linear differential equations. Assuming N size classes, we get $4N$-9 parameters, and

$$\boldsymbol{P} = (\beta_{1,1}, \beta_{1,2}, \beta_{1,3}, \beta_{2,2}, \beta_{2,3}.....\beta_{N-2,N-2}, \beta_{N-2,N-1}, g_{3,}.....g_N)$$

Finally, **A** is a matrix of N lines and $4N$-9 columns, representing a quadratic function of f coordinates (the coefficients are linear functions of $f_i f_j$ or f_i). For a given $\boldsymbol{P}$, the numerical solution to the system is the volume fraction in all the classes as a function of time. To solve the system, an initial condition is required, which is a drop size distribution at any given time in the experiment. Alternatively, for a given $f(t)$, the solution is $\boldsymbol{P}$.

By varying the vector $\boldsymbol{P}$, i.e. g and β, the solution f can be modified to fit the experimental distributions f_{exp}. An objective function can be built that uses g and β as variables to compute the norm of the error vector $(f-f_{exp})$. The error returned by the objective function is minimised by varying vector g and matrix β. When the global minimum of the objective function is reached, then g and β are the breakage and coalescence rates that govern the evolution of the volume fractions f_{exp} with time. The model equations are solved using a C-programme written by D.Mignard within COBRA. Initially, the Fletcher's version of Marquardt's algorithm was used. However, the scaling of the method for so many different parameters (typically about a hundred) proved extremely difficult, and the method would look for parameters far beyond the domain boundaries. Generally, a recursive, one parameter-at-a time method was adopted. The integration is carried out using the Michelsen method, which is called the Caillaud-Padmanabhan's method with a variable integration step. It can be seen that the advantage of not assuming any functional form for breakage and coalscence rates in the model is achieved at the expense of minimizing a large number of parameters.

5.5 RESULTS

Note that the model is at an early stage of development, and hence only one set of results corresponding to the oscillation amplitude of 12 mm and 2 Hz is shown here to illustrate the implementation of the model and the scope of future work. The others are shown in the APPENDIX 3.

The DSDs predicted by the model were obtained for two different values of χ^2, where χ^2 is the error between the experimental and model data and is defined by the equation,

$$\chi^2 = \sum_{i,t} \left(f_i - f_{\exp} \right)^2 \qquad (5.31)$$

Where t represents the sampling times for the recorded DSDs. From Figures 5.2 and 5.3, it was observed that a relatively good fit in DSDs was achieved between the experimental and the model prediction. Notice that only three DSDs corresponding to port 2, port 3 and port 4 are shown in Figures 5.2 and 5.3, this is because the DSD corresponding to port 1 was used as an initial condition to solve the differential equations in the model. There appeared to be little or no difference in the DSDs below a certain value of χ^2, as can be seen when comparing Figures 5.2 and 5.3.

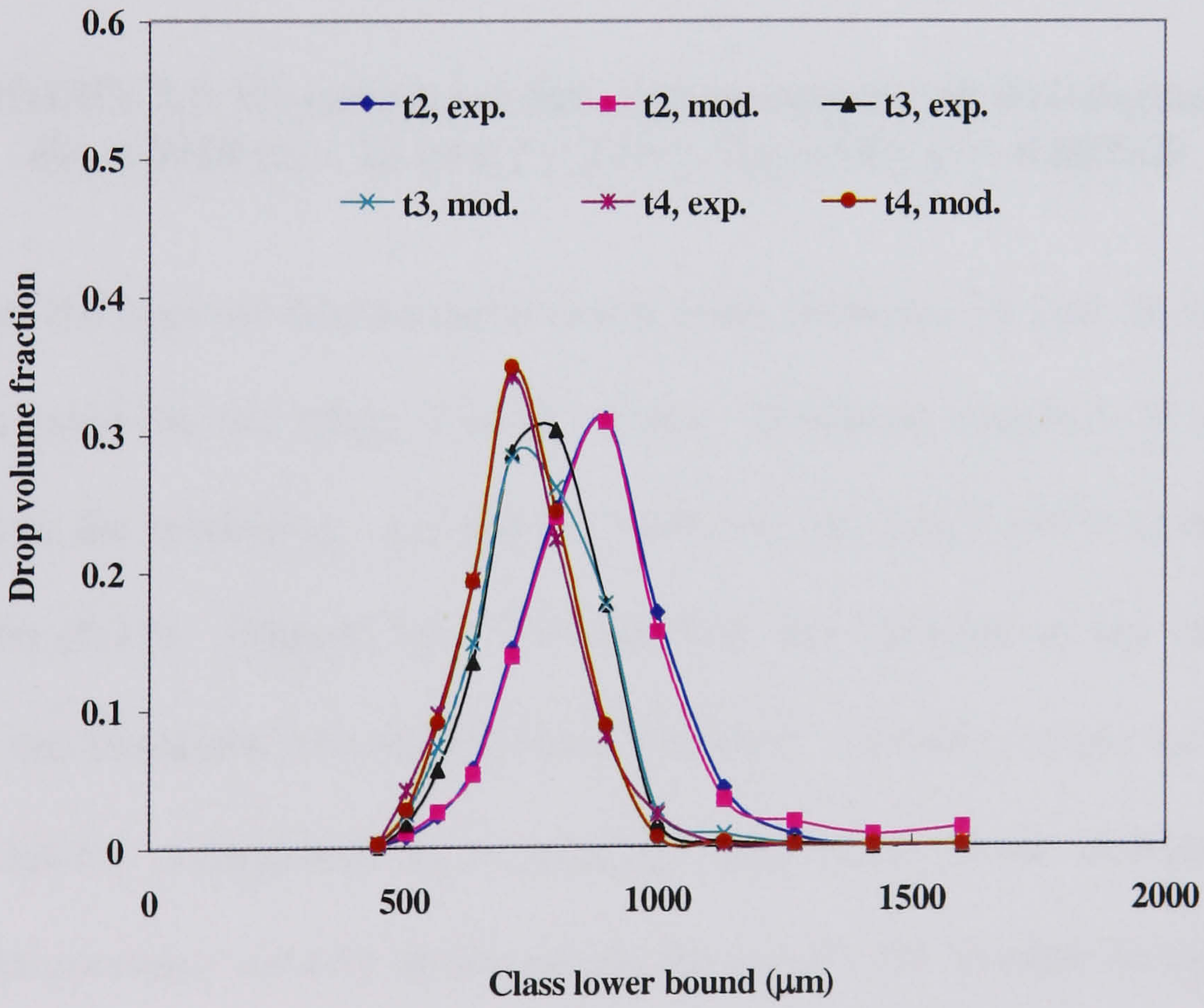

FIGURE 5.2. Experimental data and reconstructed distributions Re_o = 6024 (x_o = 12 mm, f = 2 Hz), Re_n = 541, χ^2 = 0.004123

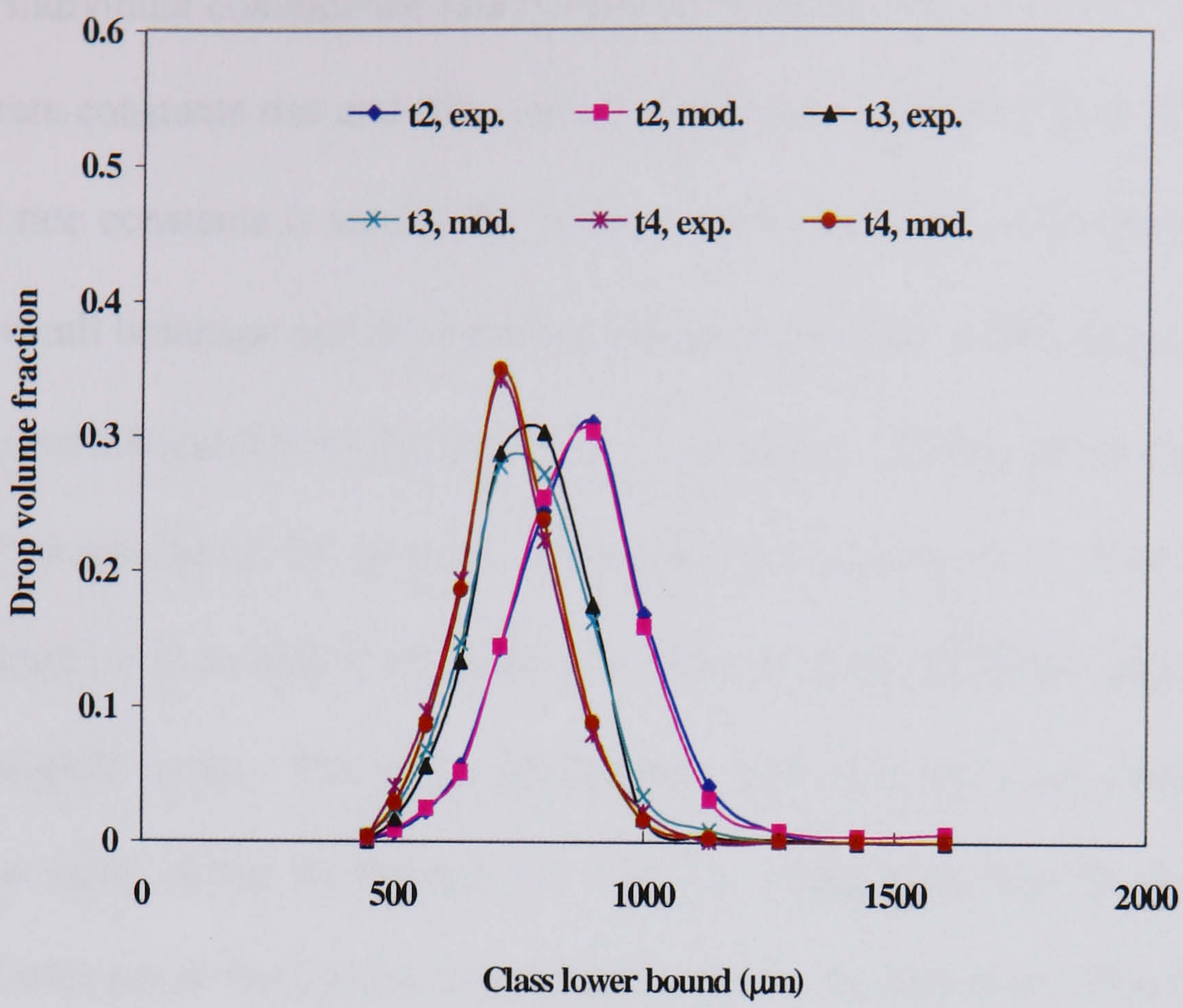

FIGURE 5.3. Experimental data and reconstructed distributions
Re_o = 6024 (x_o = 12 mm, f = 2 Hz), Re_n = 541, χ^2 = 0.002989

Given the type of discretisation being used, between 24 and 26 classes were necessary to cover the full range of drop volume. However, classes 1-13 were empty, and ignored in the modelling. g_{14} and g_{15} were set very small (10^{-6}) to be consistent with equation (5.11). Figures 5.4 – 5.9 illustrate the variation of the breakage and coalescence rate constants with the drop size for two χ^2 numbers, where each data point in Figures 5.4-5.9 corresponds to a particular drop class in the distribution. The breakage rate constants showed an increasing trend with the increase in the drop class size, but followed by sudden decrease for the last or the last two drop classes (Figure 5.4 and 5.6). It should be noted that the two values of the breakage rate constants are different in Figures 5.4 and 5.6, even though the same DSDs were used in the evaluation. This is because of the use of too many variables in the model, one parameter can easily offset the error produced by other variables, thus producing the same DSDs. This issue will be addressed later in this Chapter.

The individual coalescence rate constants, however, did not exhibit any specific trend. The rate constants rise and fall over the drop class sizes, but the magnitude of the coalescence rate constants is similar for the two different values of χ^2 (Figures 5.5 and 5.7). The overall breakage and coalescence rates as a function of the drop class size are given in Figures 5.8 and 5.9 for the same two χ^2 numbers. The negative value indicates the losses of drops during the process of breakage and coalescence. One can see that both rates exhibit a sharp fall at the drop class sizes of about 1200 μm and then a steep rise to the original value. The value corresponds well with the mean drop size in the DSDs of the same colour in Figures 5.2 and 5.3, suggesting that the breakage and coalescence rates are at the highest when close to the mean drop size. This is intuitively true, as at an equilibrium state, the breakage and coalescence rates reach the maximum and close to be equal, as illustrated by Figures 5.8 and 5.9. The rate constants at other oscillation conditions show similar trends and are given in APPENDIX 3.

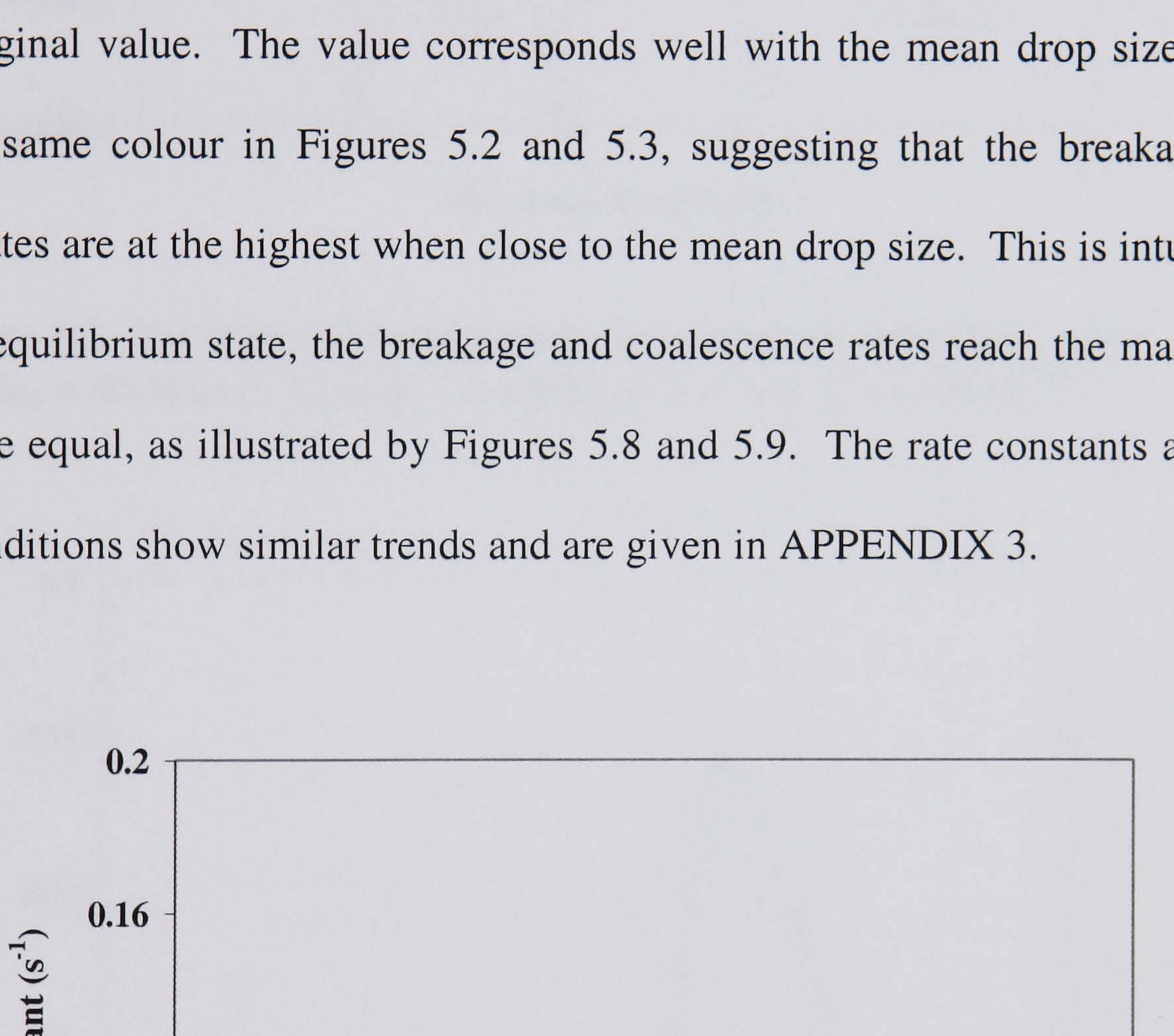

Figure 5.4. Variation of breakage rate constants with drop size, Re_o = 6024 (x_o = 12 mm, f = 2 Hz), Re_n = 541, χ^2 = 0.004123

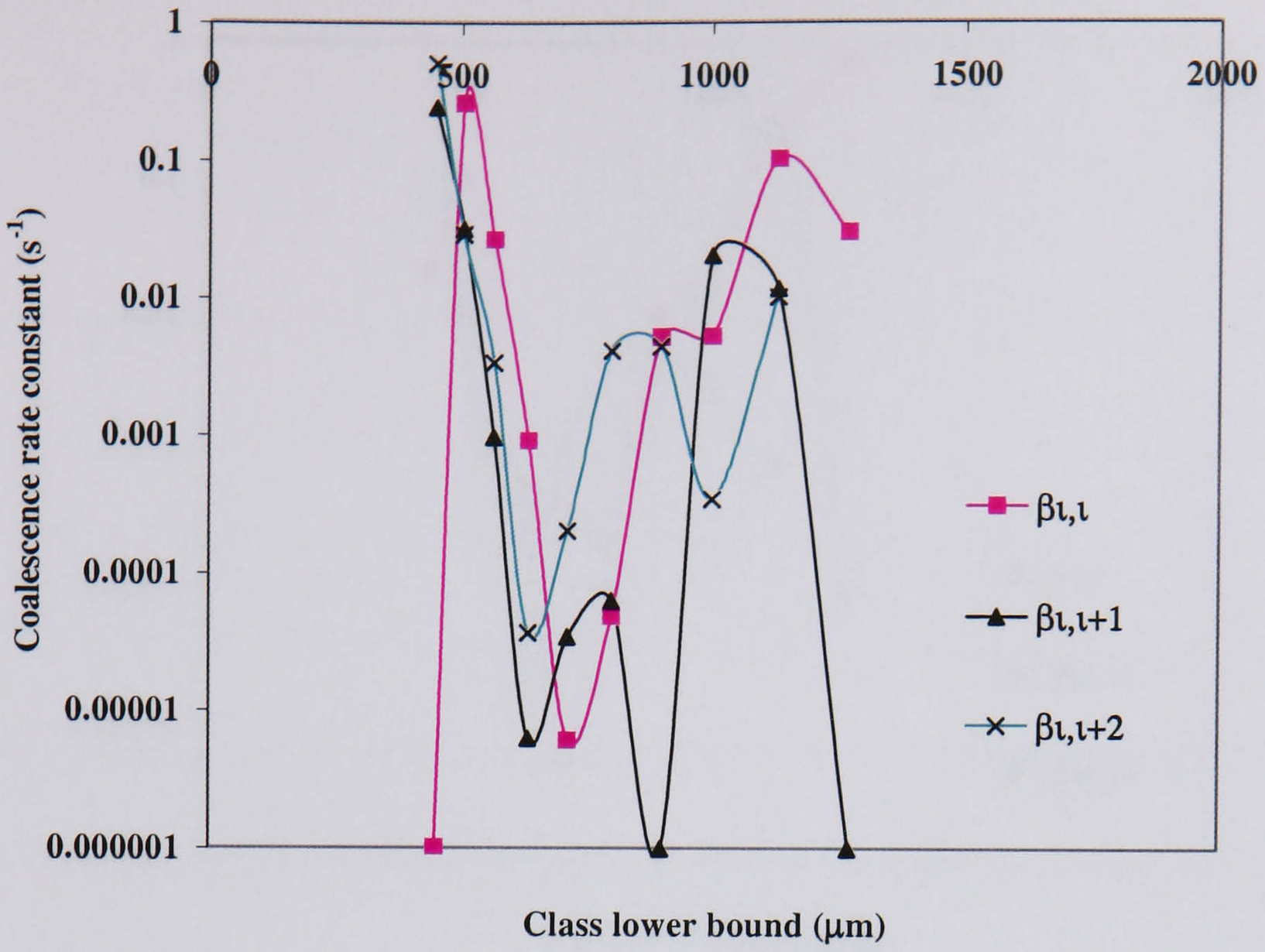

Figure 5.5. Variation of coalescence rate constants with drop size, Re_o = 6024 (x_o = 12 mm, f = 2 Hz), Re_n = 541, χ^2 = 0.004123

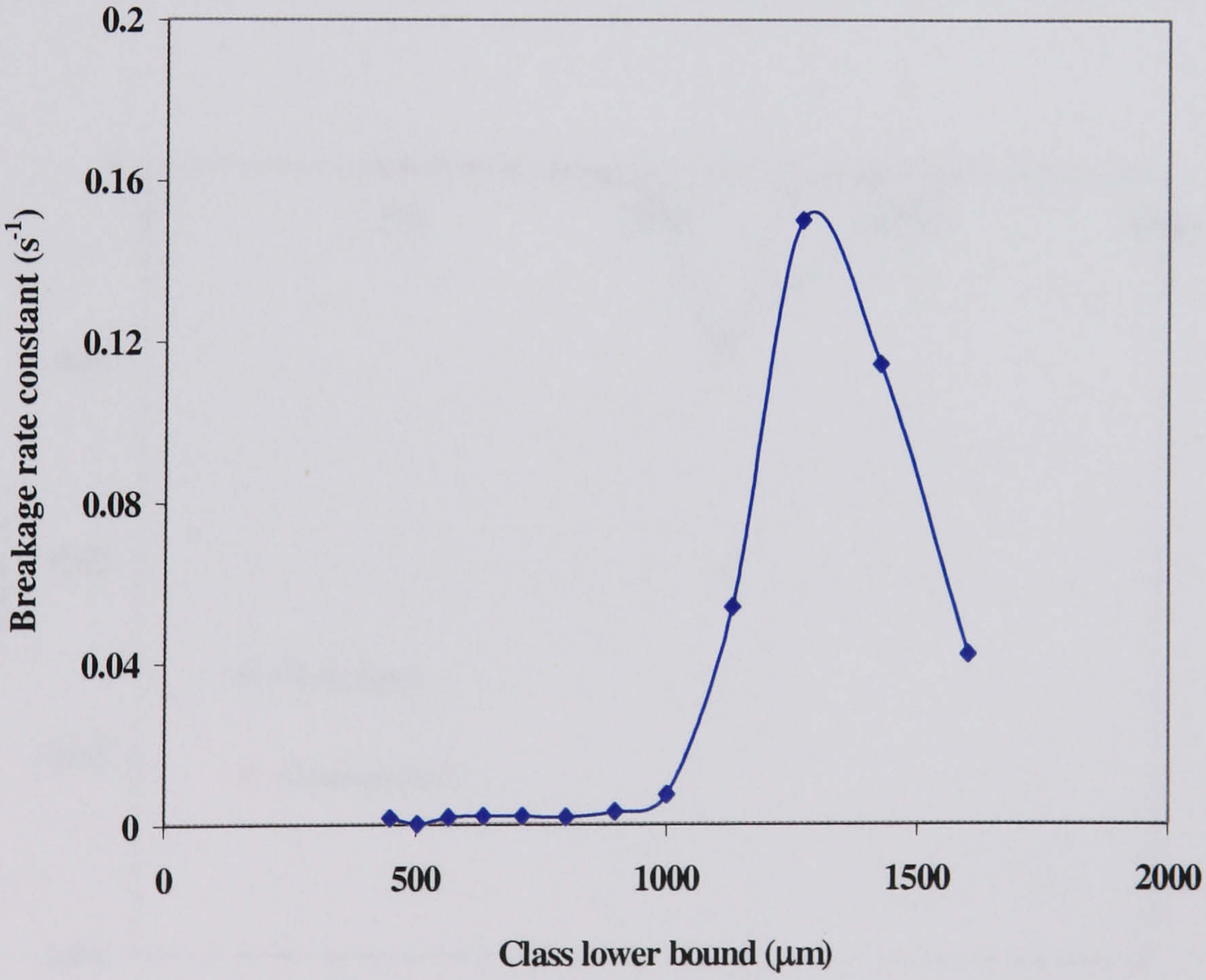

Figure 5.6. Variation of breakage rate constants with drop size, Re_o = 6024 (x_o = 12 mm, f = 2 Hz), Re_n = 541, χ^2 = 0.002989

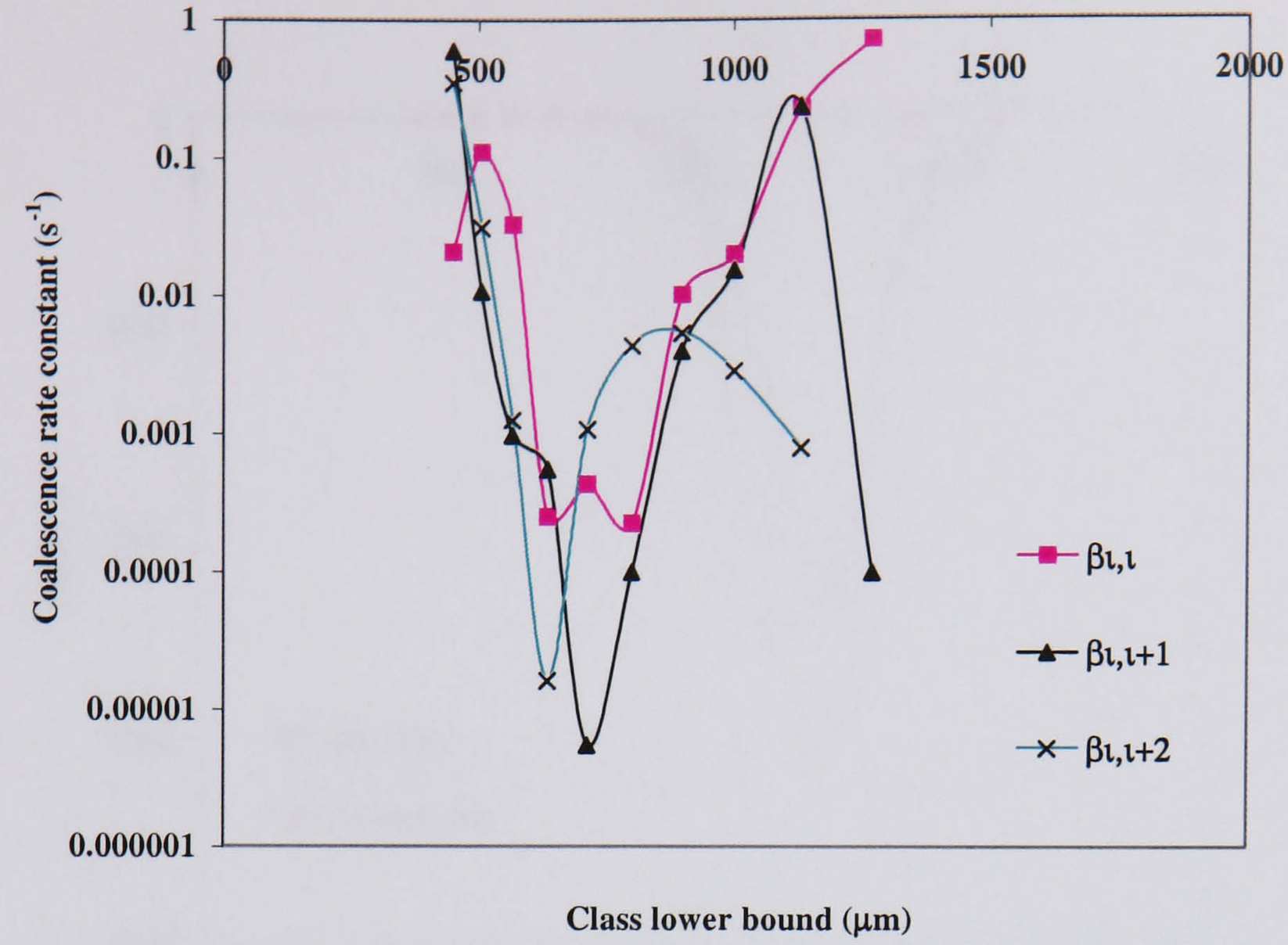

Figure 5.7. Variation of individual coalescence rate constants with drop size, Re_o = 6024 (x_o = 12 mm, f = 2 Hz), Re_n = 541, χ^2 = 0.002989

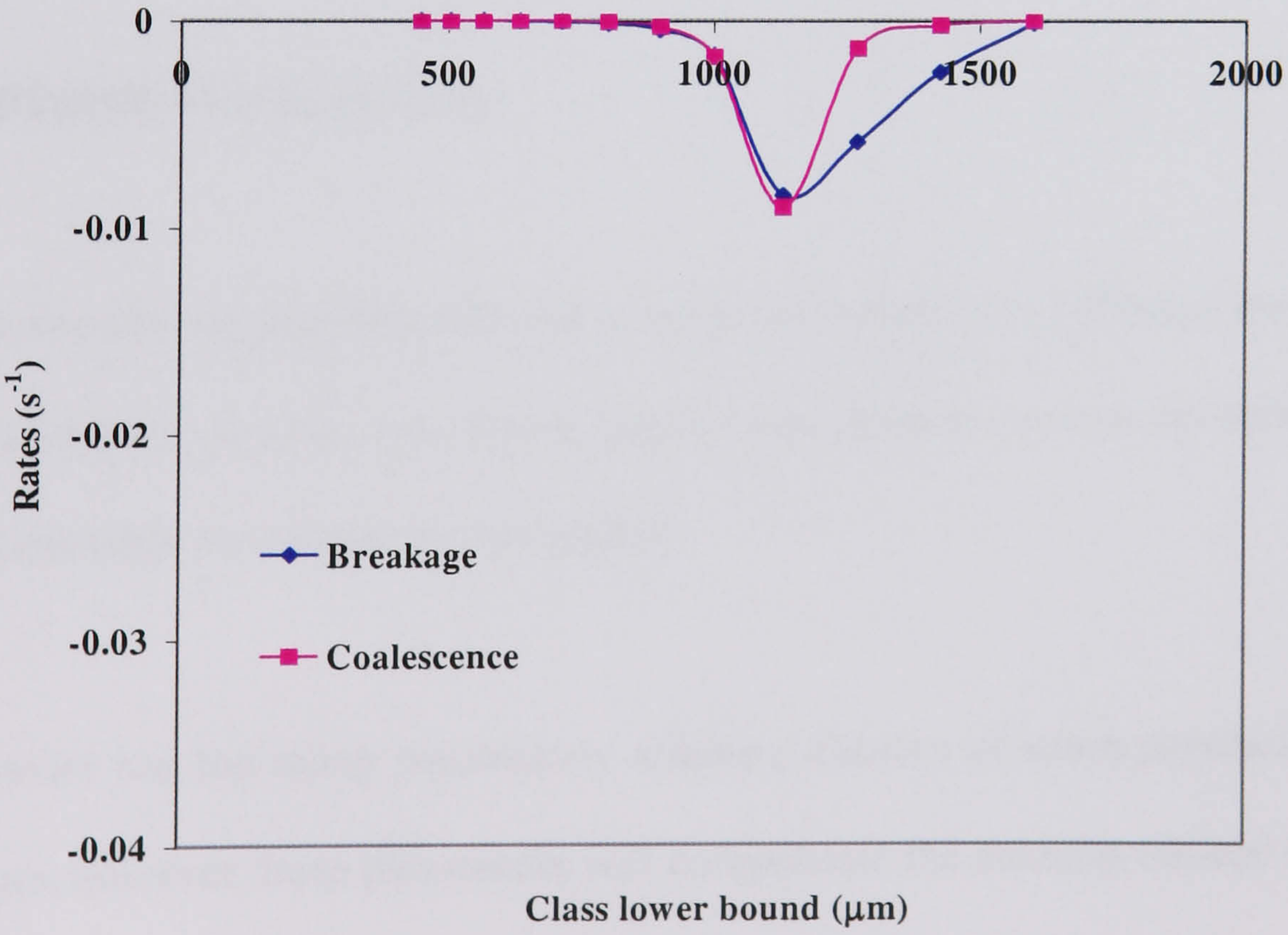

FIGURE 5.8. Breakage and total coalescence rates as functions of drop size, Re_o = 6024 (x_o = 12 mm, f = 2Hz), Re_n = 541, χ^2 = 0.004123

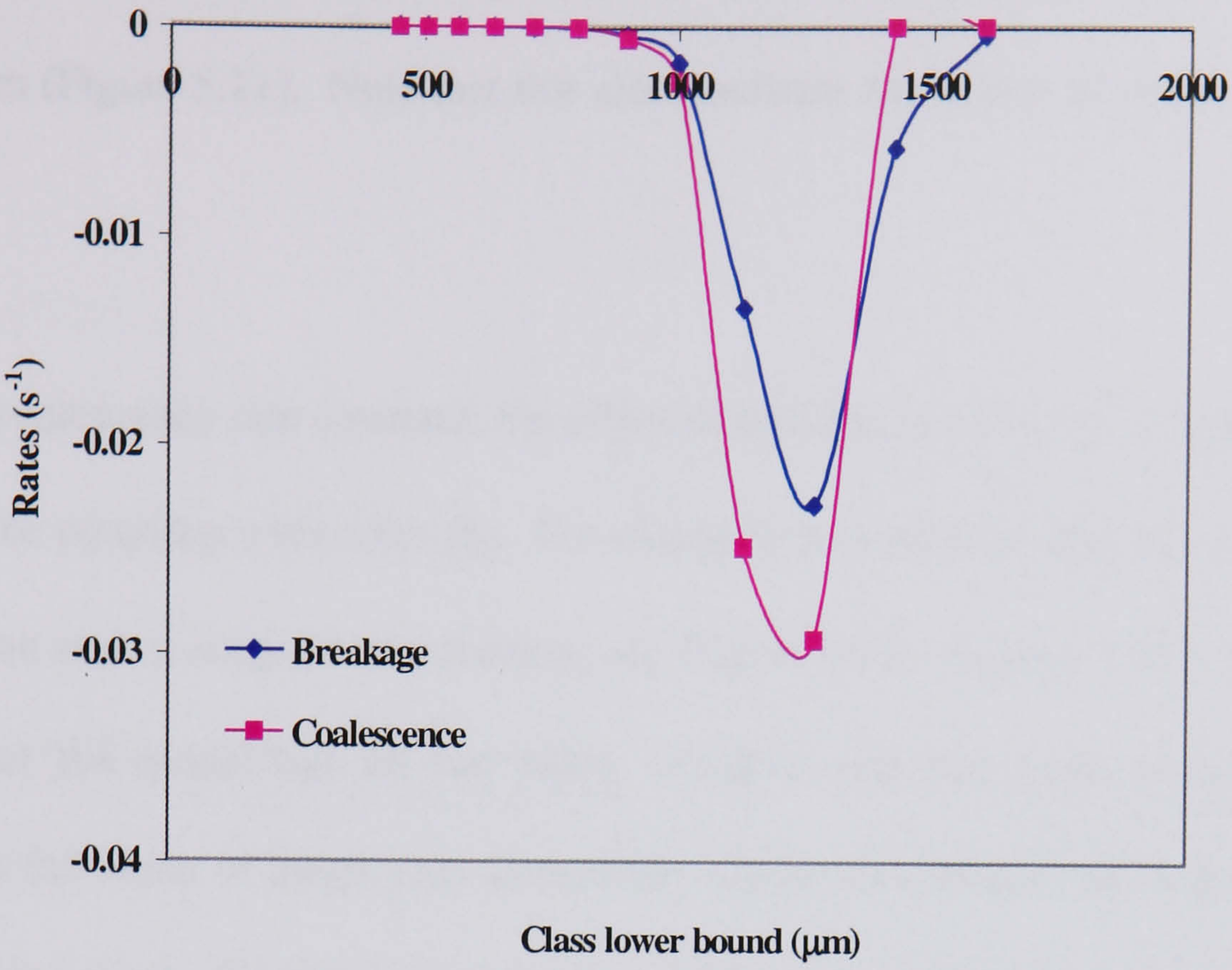

FIGURE 5.9. Breakage and total coalescence rates as functions of drop size, Re_o = 6024 (x_o = 12 mm, f = 2Hz), Re_n = 541, χ^2 = 0.002989

5.6 OPTIMISATION ISSUES

As one can see that different rate constants resulted from different levels of error in the minimisation process, this clearly raises some concerns on the optimisation. The following are some comments on this aspect:

- The model has too many parameters, arbitrary choices of some parameters may be possible, however those parameters will compensate the errors produced by others.

- There are different degrees of flat valleys approaching the minimum, as shown in Figures 5.10-5.13. For the breakage rate constants, some rate constants showed clear minima on optimisation (Figure 5.10), e.g. g_i for i = 16-21, associating the

most populated classes. Under those conditions, the rate errors should have a stronger effect on χ^2. Other rate constants did not display any characteristics of minimum (Figure 5.11). Note that this also confirms the action of setting g_{13} and g_{14} to zero.

- For the coalescence rate constant, the effect of the rate errors on χ^2 is more subtle as $\beta_{i,i}$ may be coupling with other $\beta_{i,j}$. For example, it is unclear why $\beta_{17,17}$, $\beta_{18,18}$ and $\beta_{19.19}$ have such a range of uncertainity, see Figure 5.13. Figures 5.10 – 5.13 are the proof that the model has far too many variables and that some parameters may change a full order of magnitude around the minimum without inducing any change in the value of χ^2. Further improvement of the model should consider reducing the number of variables by establishing experimental relationship between certain drop classes.

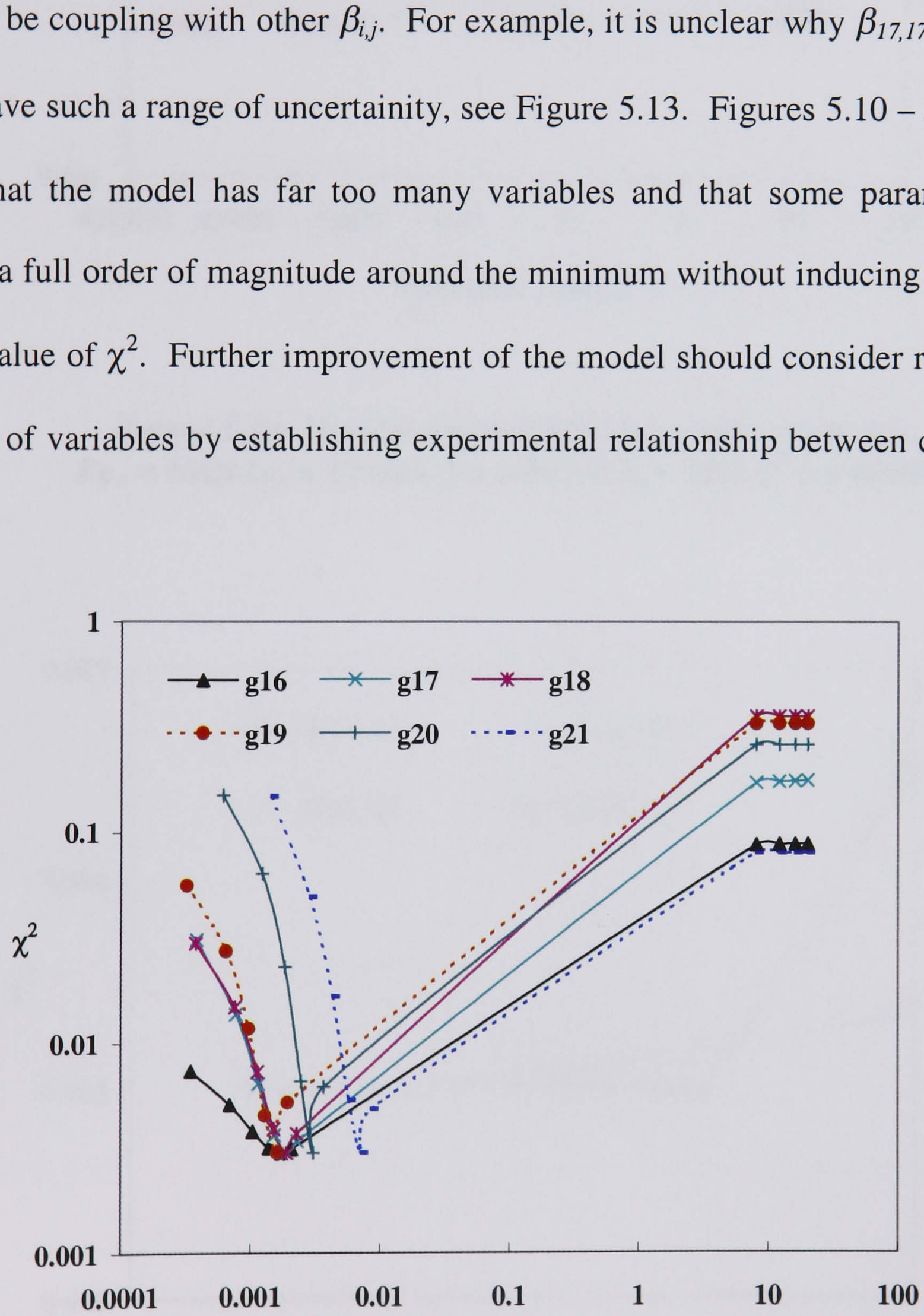

Figure 5.10. Optimisation of breakage rate constants, Re_o = 6024 (x_o = 12 mm, f = 2 Hz), Re_n = 541, χ^2 = 0.002989

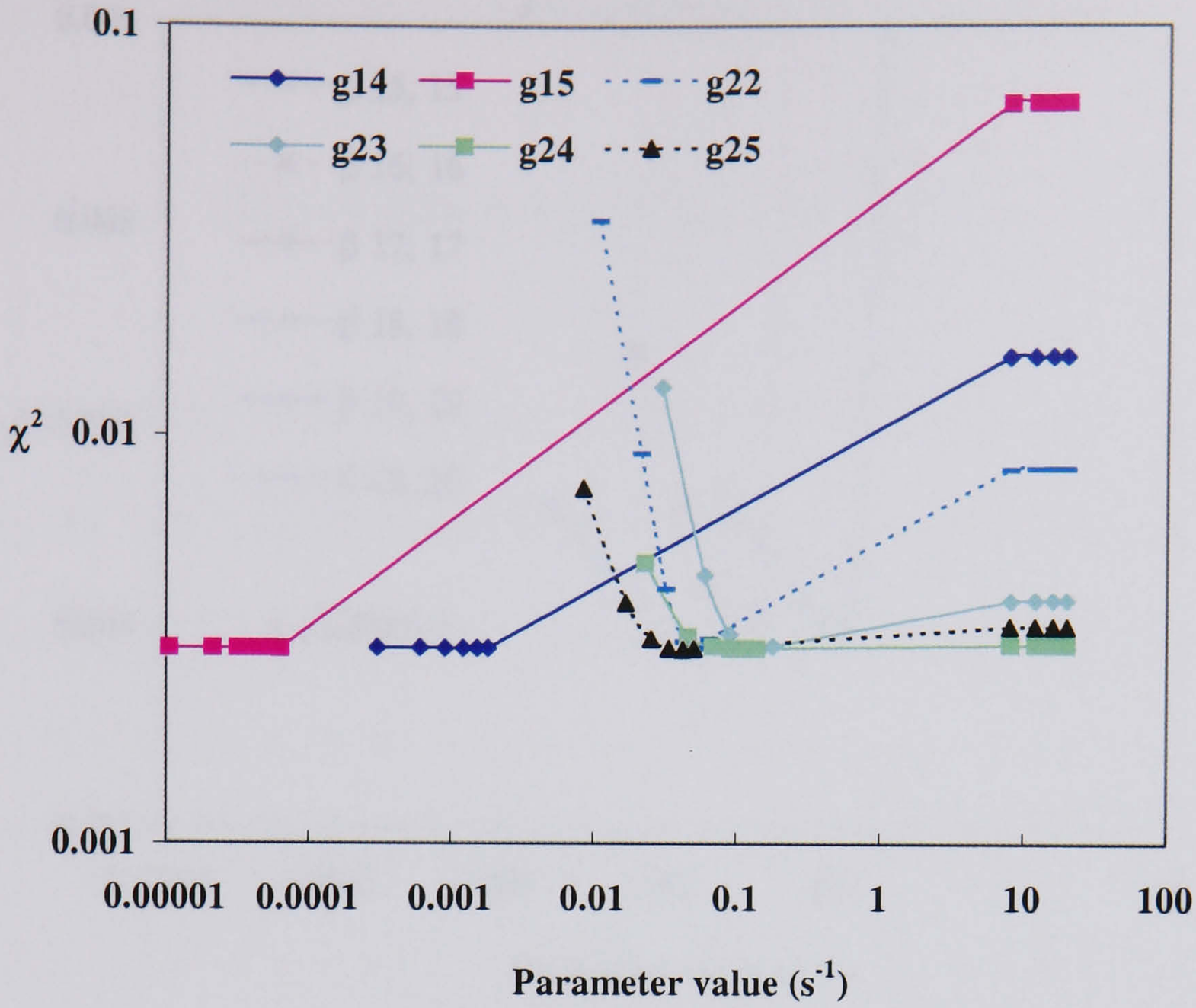

Figure 5.11. Optimisation of breakage rate constants, Re_o = 6024 (x_o = 12 mm, f = 2 Hz), Re_n = 541, χ^2 = 0.002989

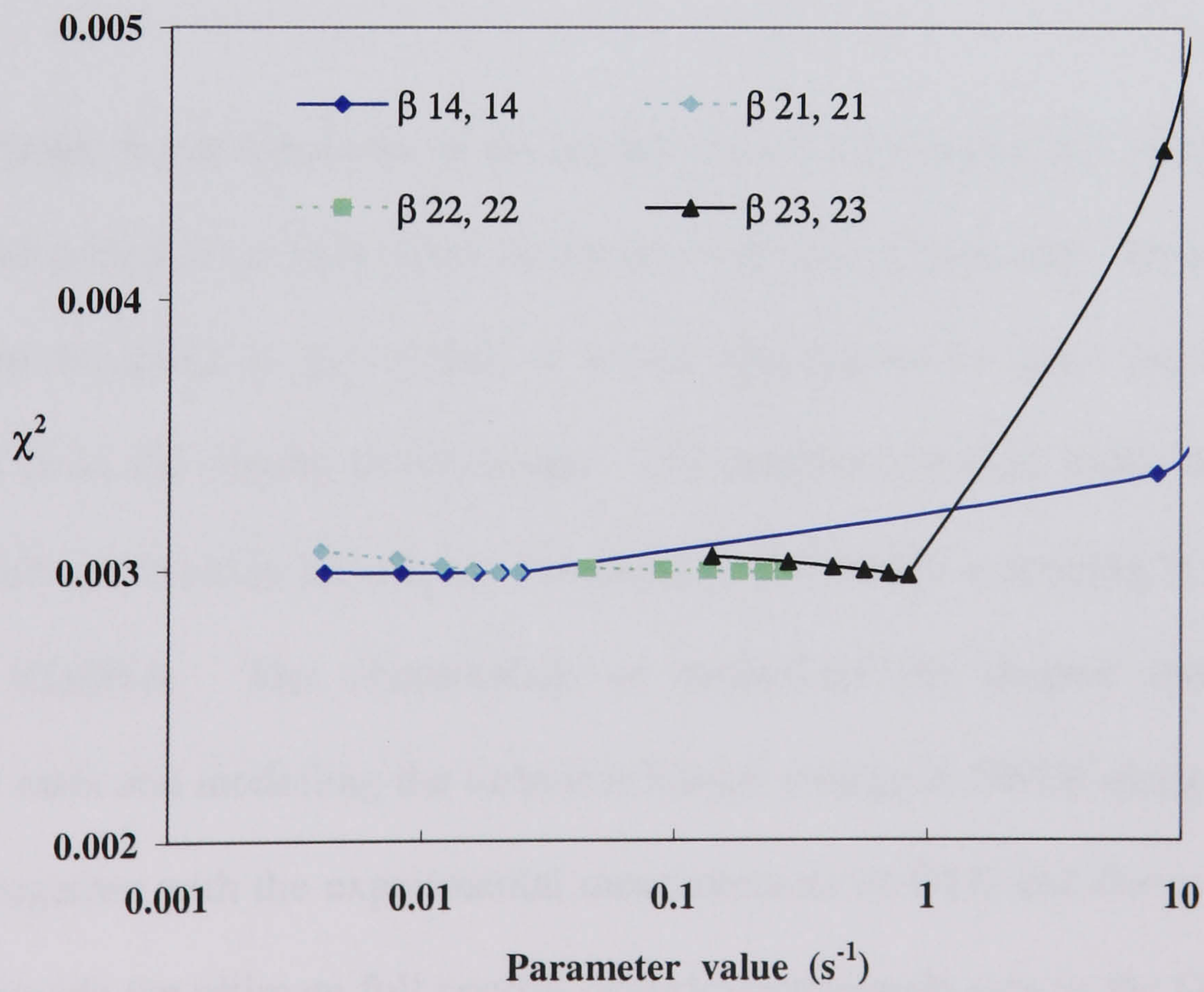

Figure 5.12. Optimisation of coalescence rate constants, Re_o = 6024 (x_o = 12 mm, f = 2 Hz), Re_n = 541, χ^2 = 0.002989

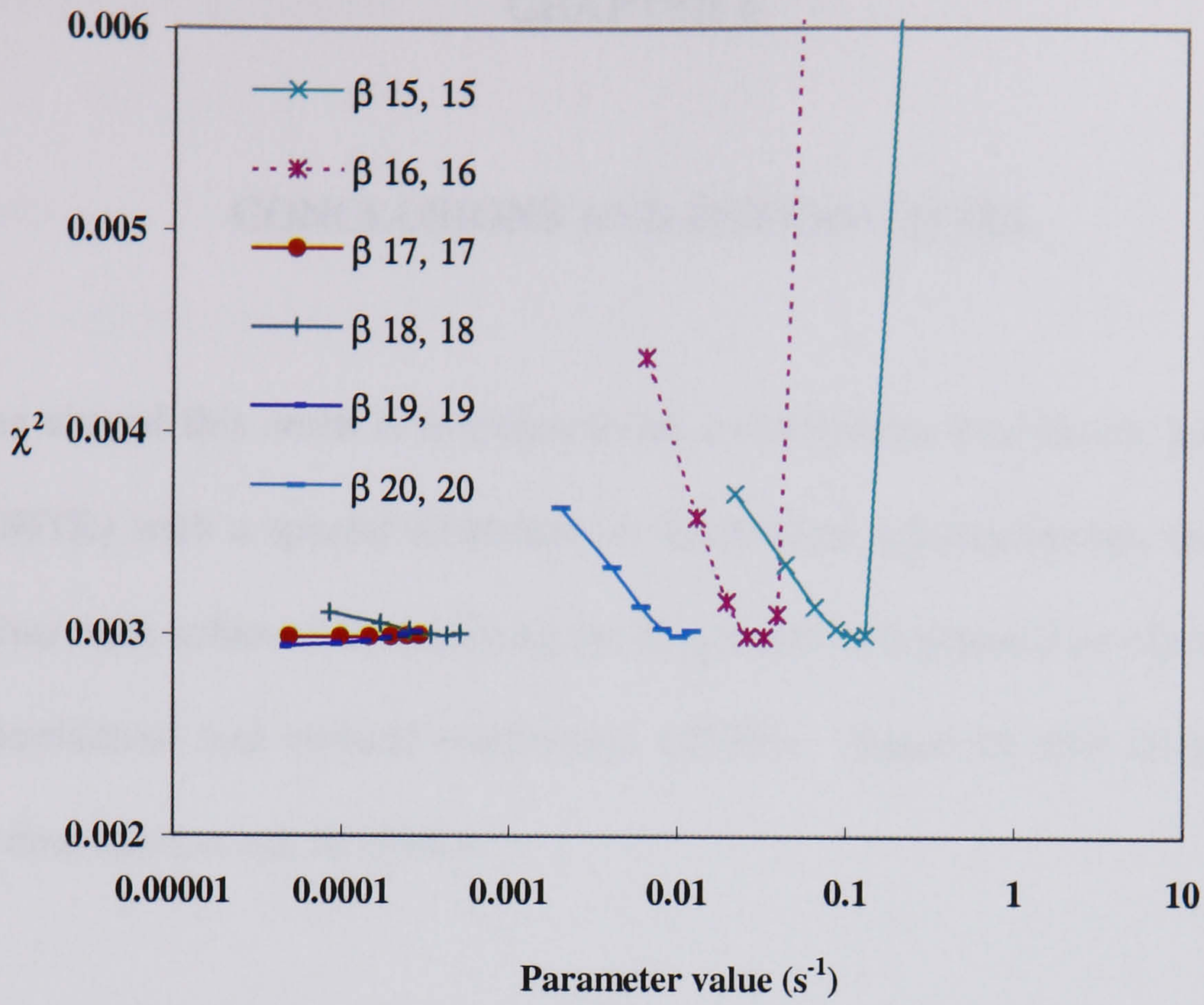

Figure 5.13. Optimisation of coalescence rate constants, Re_o = 6024 (x_o = 12 mm, f = 2 Hz), Re_n = 541, χ^2 = 0.002989

5.7 SUMMARY OF RESULTS

Although the development of the model is at its early stage, the initial modelled breakage and coalescence rates agree intuitively with our expectation. Since too many variables are involved in the model, it is not appropriate to draw any significant conclusions from the results at this stage. The emphasis should rather be spent on improving the optimisation technique. Fortunately, the droplet modelling is an ongoing project in COBRA. The combination of modelling the droplet breakage and coalescence rates and modelling the turbulent kinetic energy in OBTR using large eddy simulation together with the experimental measurements of DSD and the mean droplet sizes will provide the ultimate full control over droplet/particle size in the OBTR, from science to engineering and from empirical to theoretical. The work described in this thesis partially contributes toward this core theme of COBRA.

CHAPTER 6

CONCLUSIONS AND FUTURE WORK

The aim of this work is to characterise a continuous oscillatory baffled tubular reactor (OBTR) with a special emphasis on suspension polymerisation reaction. This objective has been achieved by studying the single and two phase flow characteristics of both the horizontal and vertical continuous OBTRs. Based on this investigation the following conclusions can be drawn:

6.1 CONCLUSIONS

6.1.1 SINGLE PHASE STUDY

The single phase flow study showed that very close to plug flow behaviour was obtained in both horizontal and vertical OBTR over all the operating conditions. The axial dispersion coefficient, E used to quantify deviation from true plug flow, was found to be more influenced by both the oscillation amplitude and frequency than the net flow component. Over the operating conditions investigated, the values of E are very small indeed for both the horizontal and vertical OBTRs, indicating that the deviation from the true plug flow is very small. On comparison of the performance of the horizontal and vertical OBTRs, there are little differences in RTDs and E.

6.1.2 TWO PHASE STUDY

Drop size distribution (DSD) and the Sauter mean drop diameter, d_{32} were measured at different axial positions in both the horizontal and vertical OBTRs over a range of oscillation amplitudes, frequencies and net flow rates. In the vertical OBTR, the stability of DSDs was found difficult to attain due to the presence of risers and downcomers in the system. As a direct result, there was significant difference in the drop hold-up between the risers and downcomers, resulting in no definite trend in DSDs along the flow path. The DSDs are generally broad and poorly defined, which is far from a Guassian function. However, the drop stability can be achieved in the vertical OBTR, but at much higher power input and longer flow path. In the horizontal OBTR, on the other hand the drawbacks of the vertical OBTR are overcome. The stability of DSDs is achieved earlier due to little difference in the drop hold-ups along the flow path and is achieved at much less power input.

In spite of the shapes of the DSDs in both the horizontal and vertical OBTRs, the common features are that the DSDs become narrower and d_{32} smaller as the oscillation intensity increases. The response of the changes in DSDs and d_{32} are found more with the oscillation condition than the net flow component. Overall, the horizontal OBTR produced more uniform mixing, attained stability earlier and smaller drops for unit power input than the vertical one. As a consequence of this, for continuous suspension polymerisation process the horizontal OBTR should be preferred over the vertical one.

The droplet interactions were modelled using a population balance approach to evaluate droplet breakage and coalescence rates. The early results are promising, though further development of the model is required.

6.2 FUTURE WORK

The author recommends that the following investigation should be of particular interest:

- To investigate the effect of viscosity and density difference on the drop size distribution and mean drop size.

- To evaluate the mean drop size, d_{32} at high phase hold-up, ϕ.

- To further develop the model in order to improve the accuracy.

APPENDIX 1-CHARACTERISATION OF THE VERTICAL OBTR

TYPICAL RESIDENCE TIME DISTRIBUTION

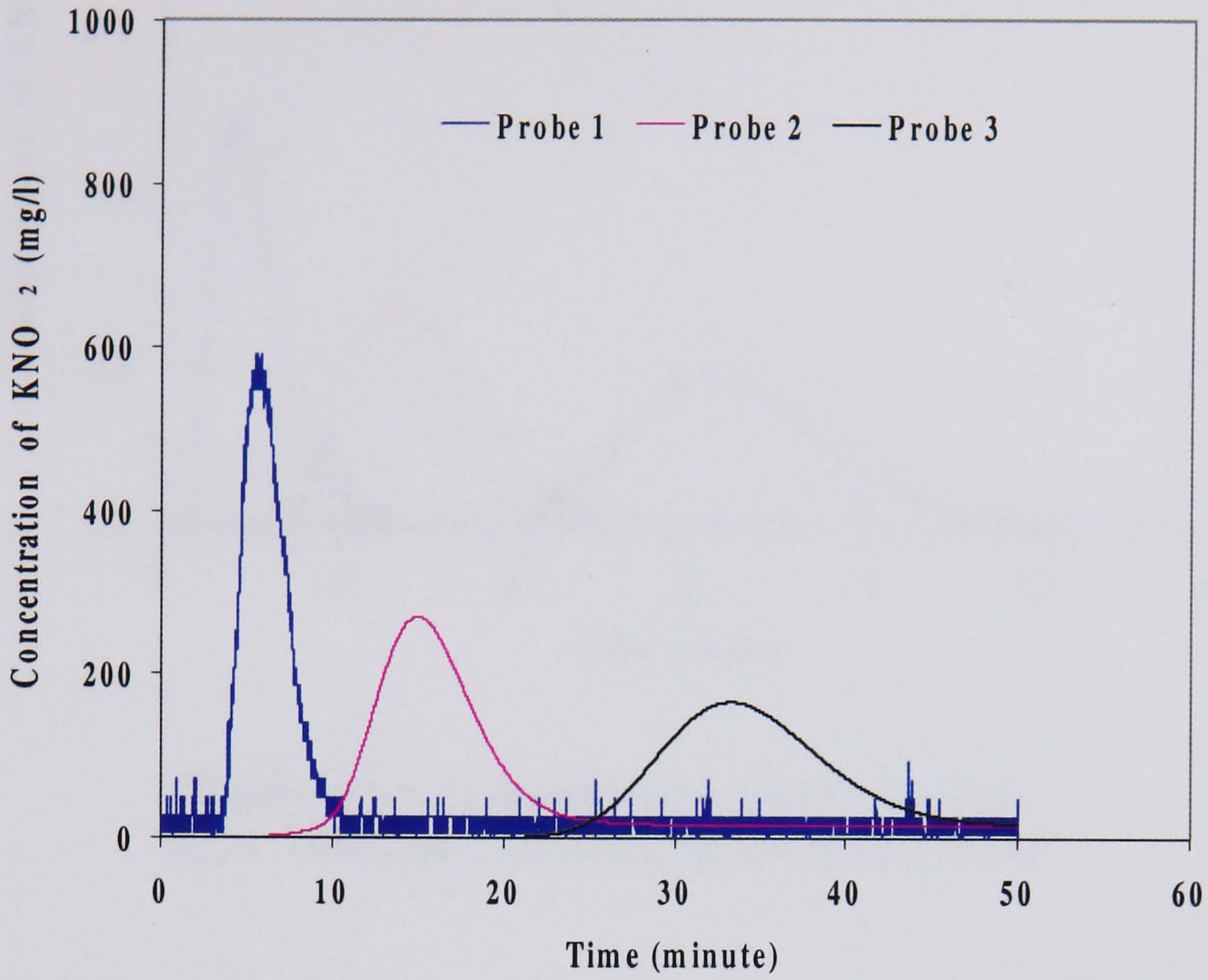

Figure A1.1. Concentration measurement,
Re_o = 4518 (x_o = 6 mm, f = 3 Hz), Re_n = 256

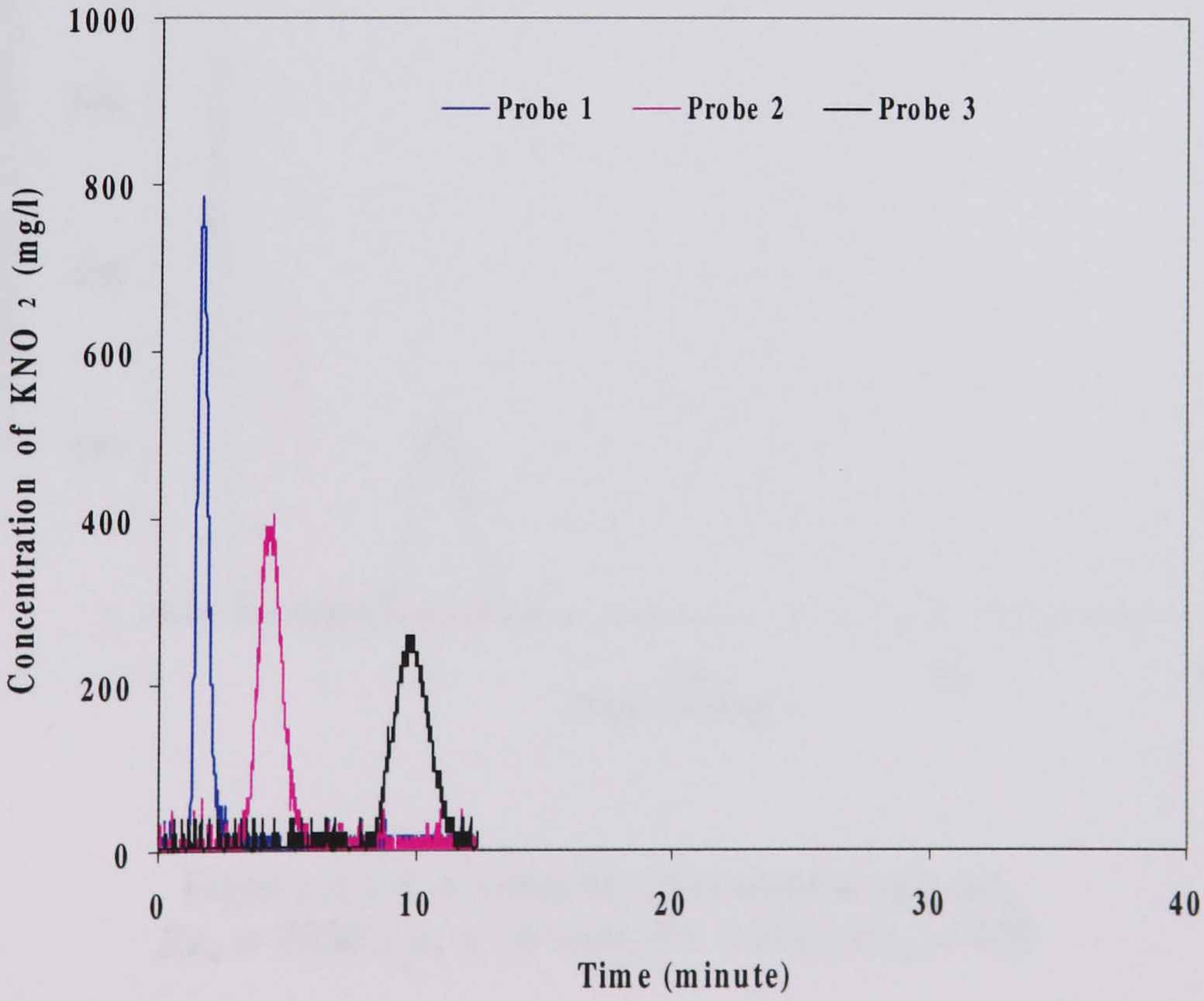

Figure A1.2. Concentration measurement,
Re_o = 4518 (x_o = 6 mm, f = 3 Hz), Re_n = 964

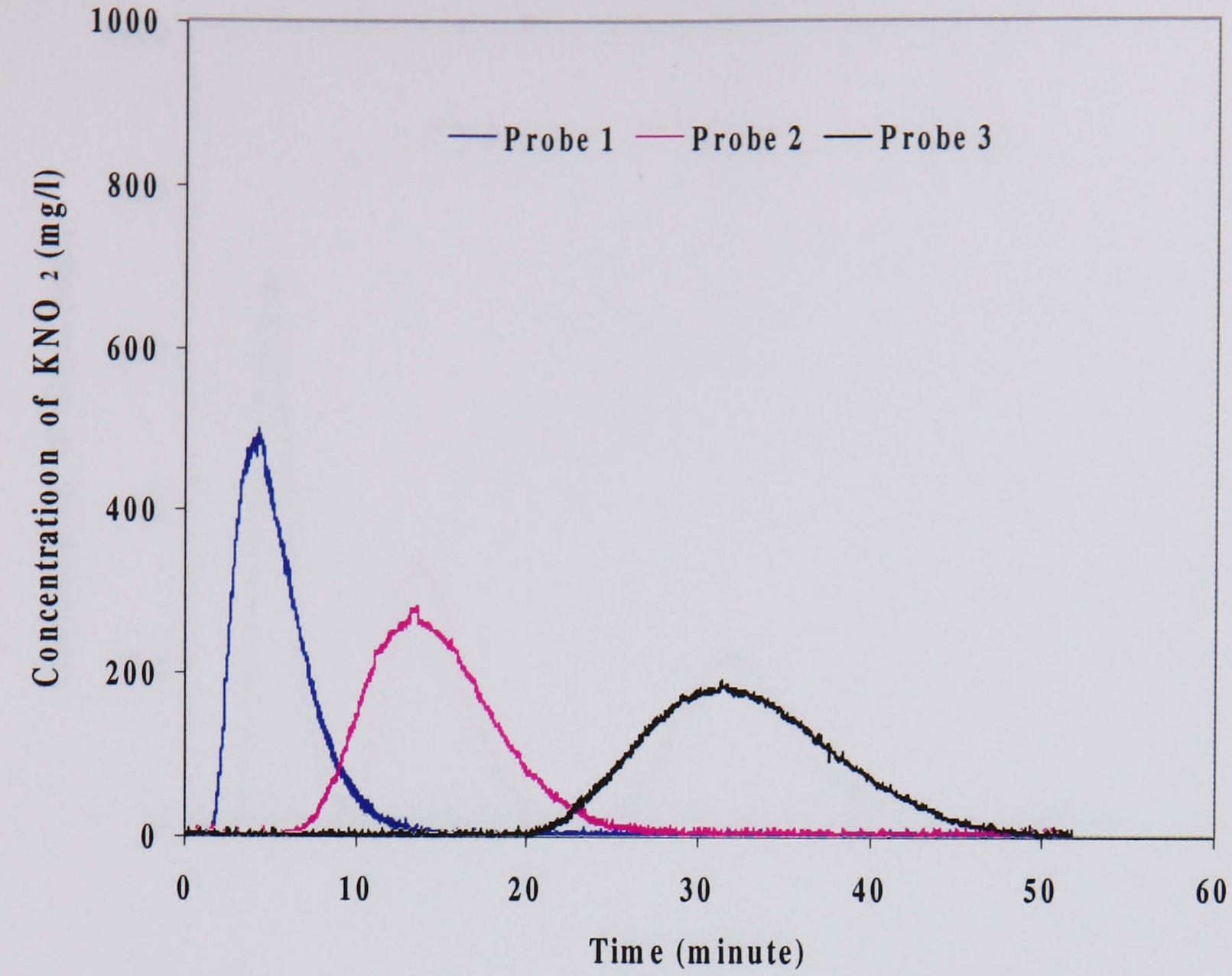

Figure A1.3. Concentration measurement,
Re_o = 7530 (x_o = 10 mm, f = 3 Hz), Re_n = 256

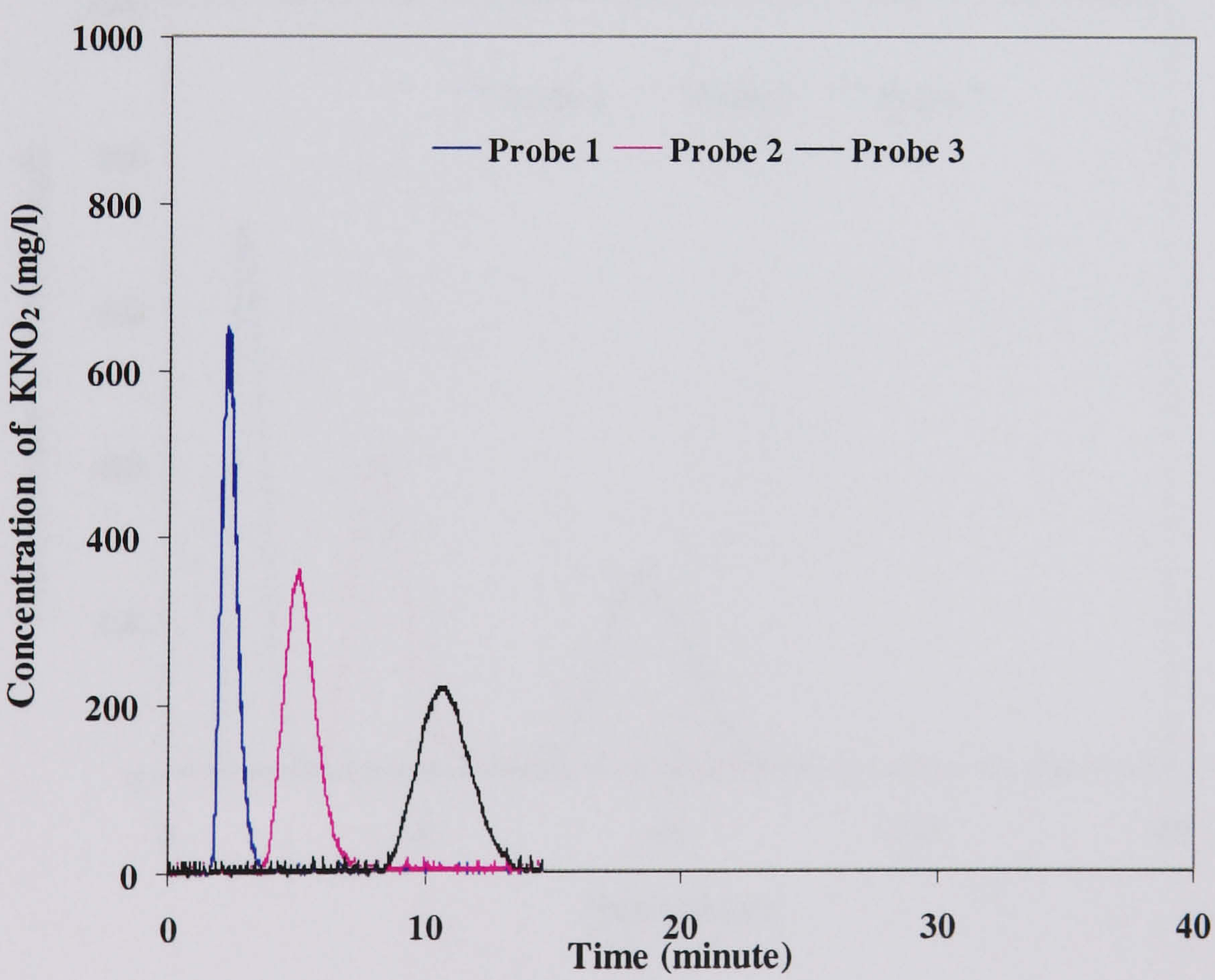

Figure A1.4. Concentration measurement,
Re_o = 7530 (x_o = 10 mm, f = 3 Hz), Re_n = 920

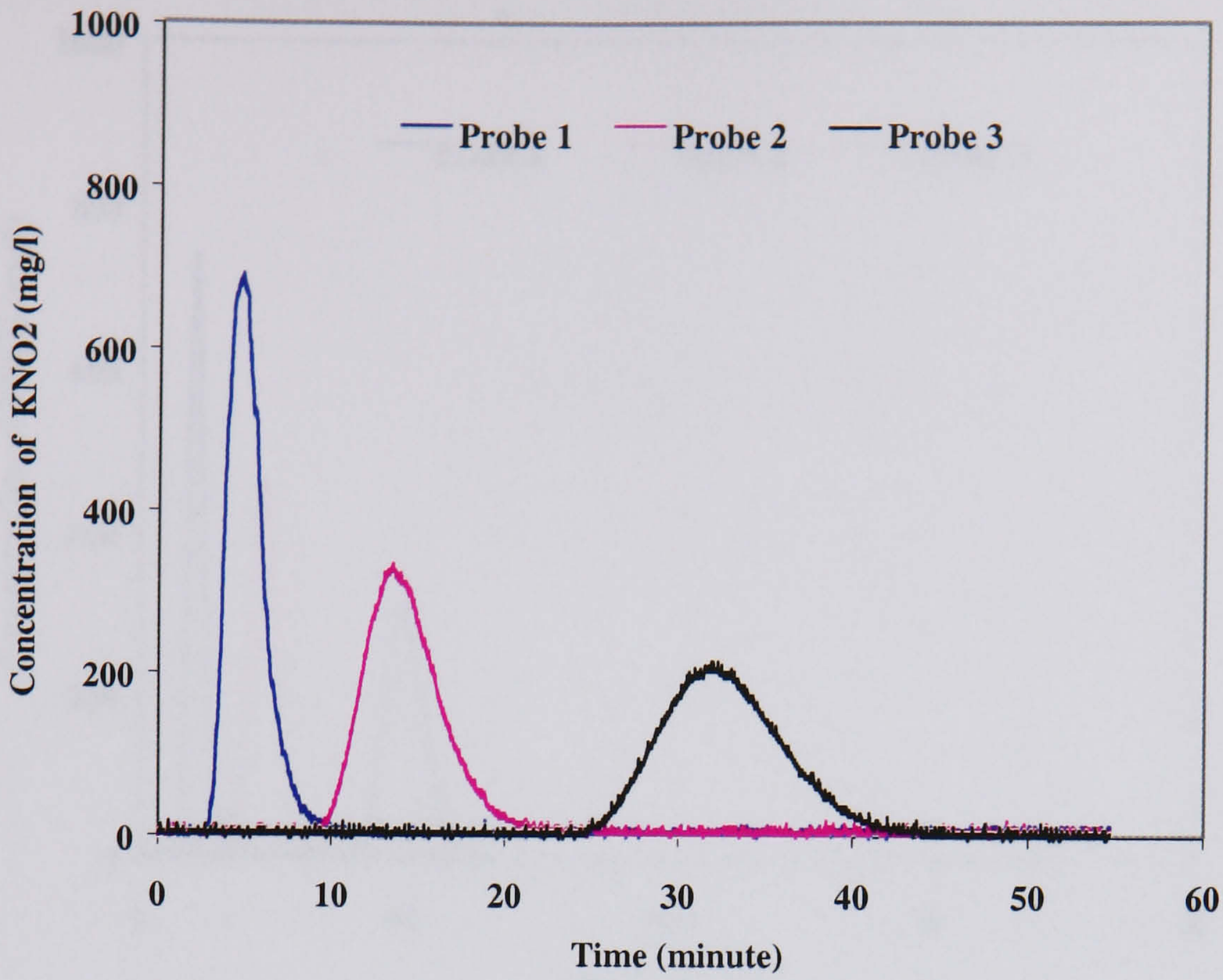

Figure A1.5. Concentration measurement,
$Re_o = 0$, $Re_n = 260$

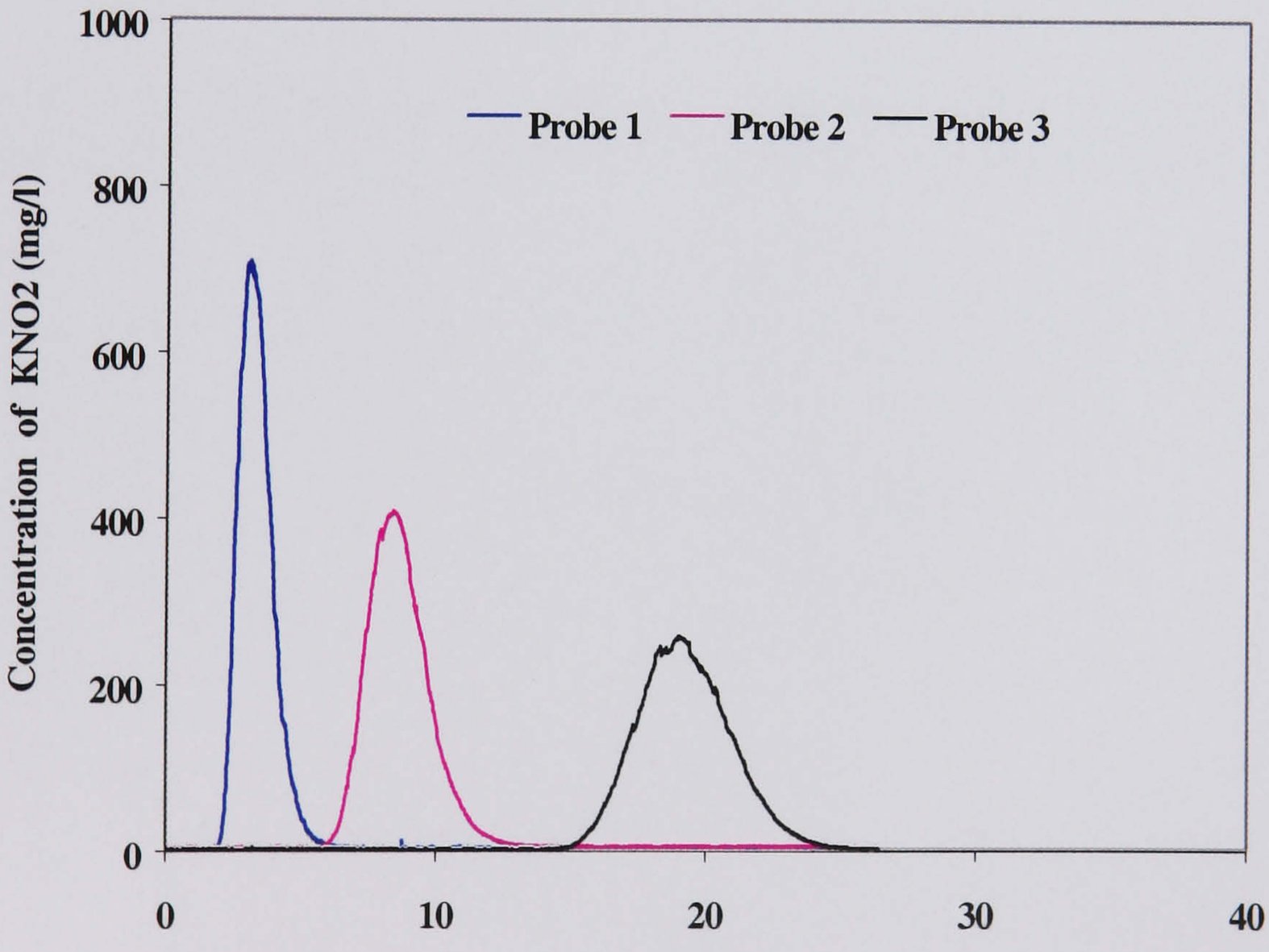

Figure A1.6. Concentration measurement,
$Re_o = 0$, $Re_n = 464$

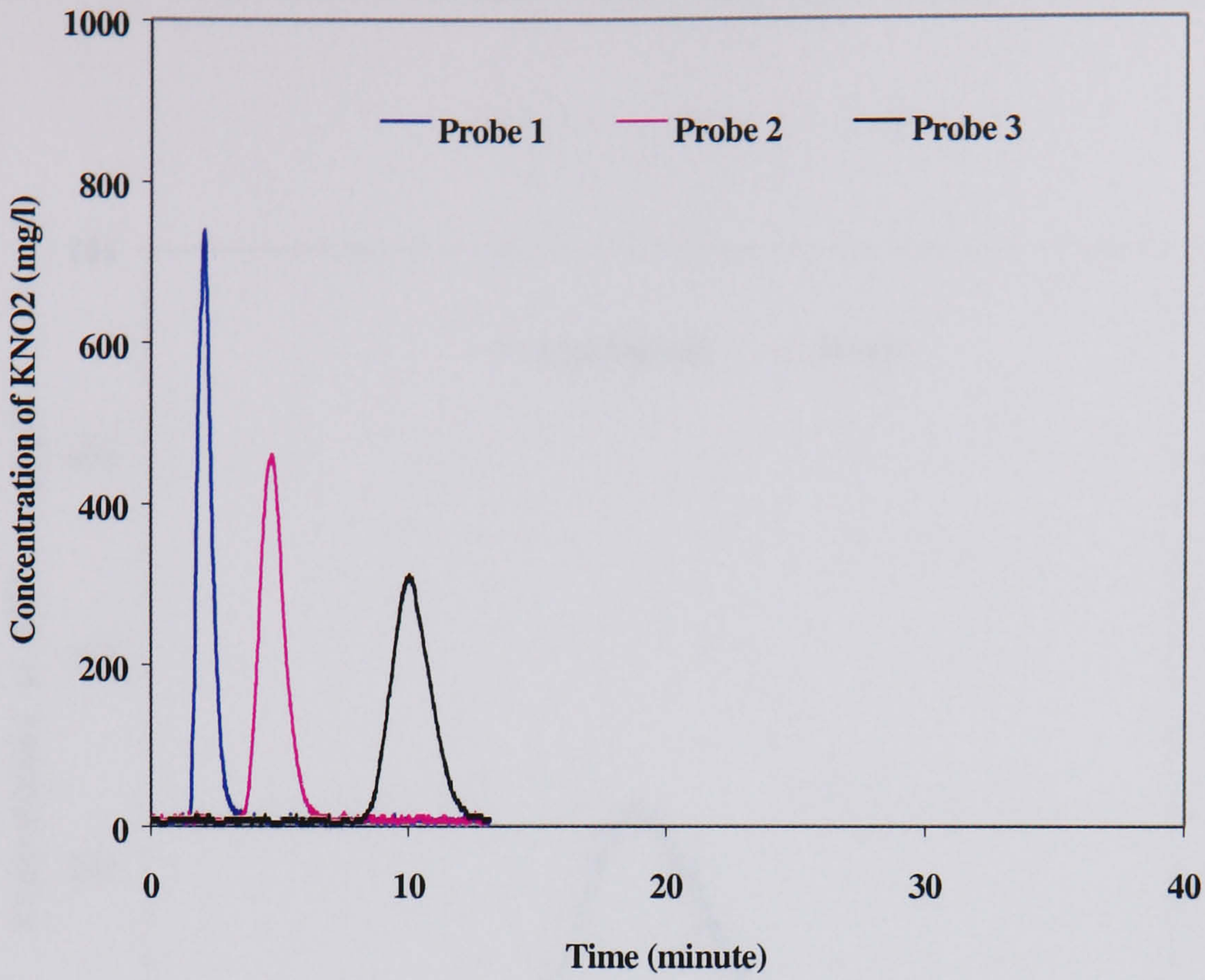

Figure A1.7. Concentration measurement, $Re_o = 0$, $Re_n = 1024$

PREDICTION OF CONCENTRATION PROFILE BY AXIAL DISPERSION MODEL

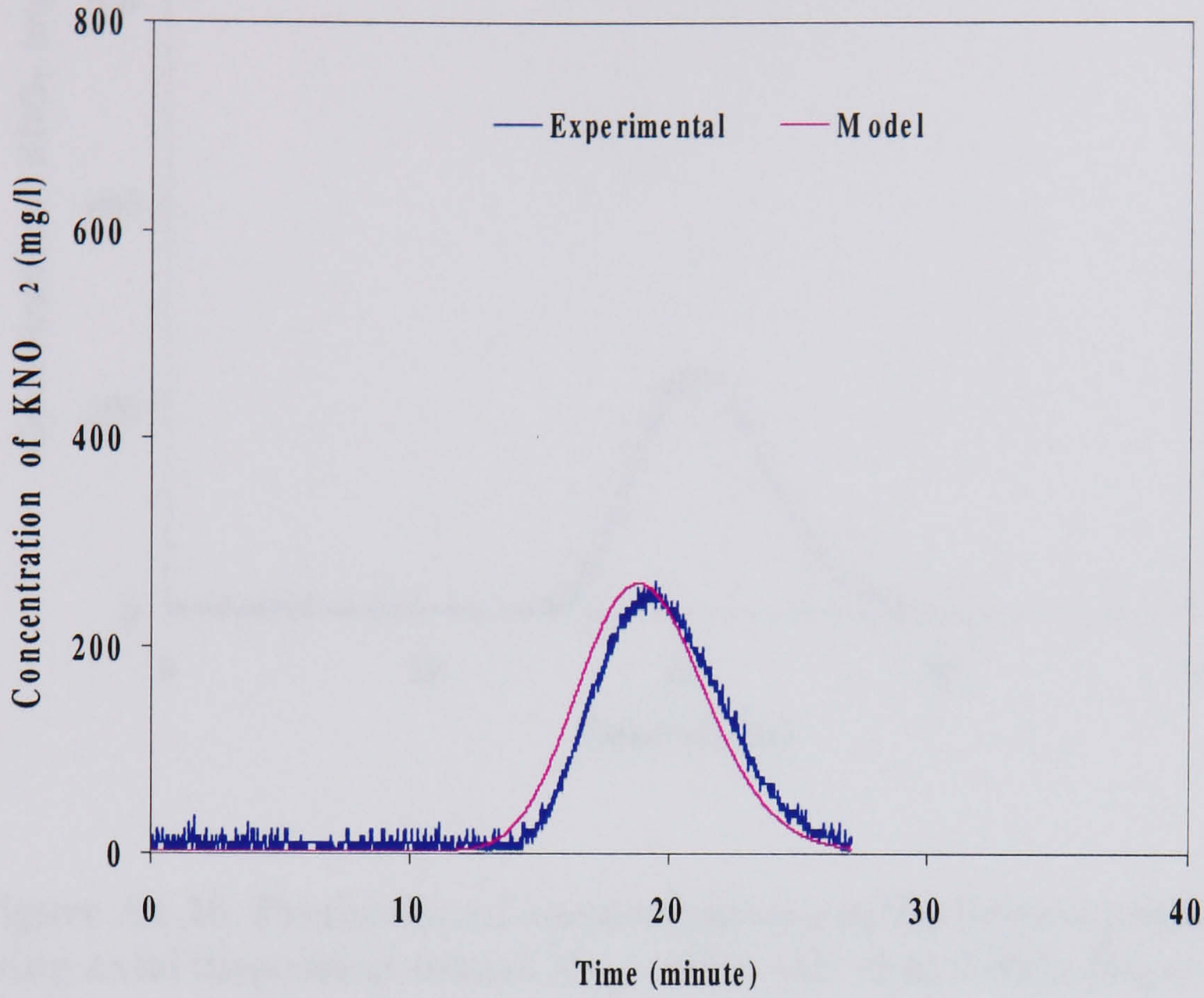

Figure A1.8. Prediction of concentration profile 3 from profile 1 using axial dispersion model, Re_o = 9036 (8 mm, 3 Hz), Re_n = 490

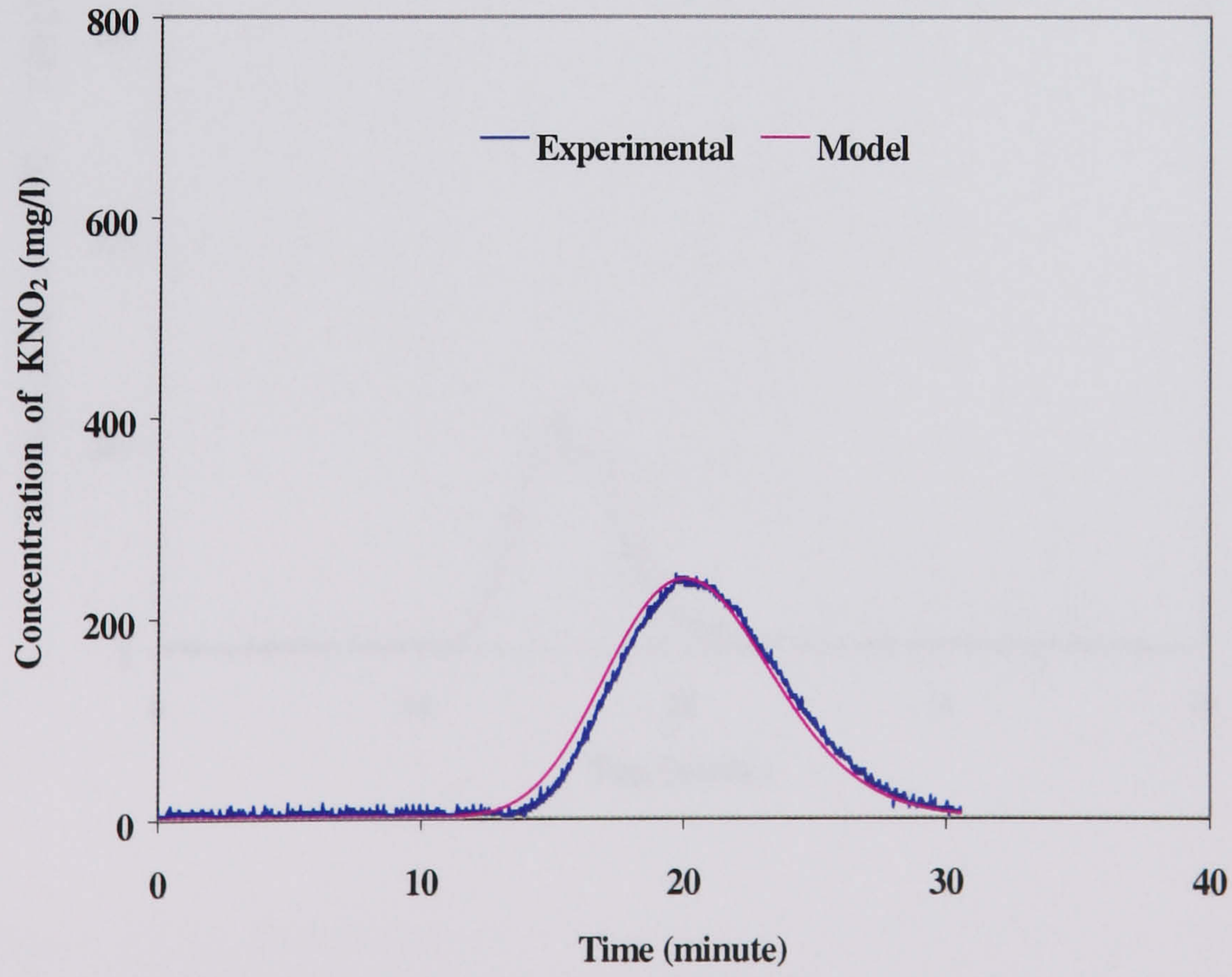

Figure A1.9. Prediction of concentration profile 3 from profile 1 using axial dispersion model, Re_o = 9036 (10 mm, 3 Hz), Re_n = 452

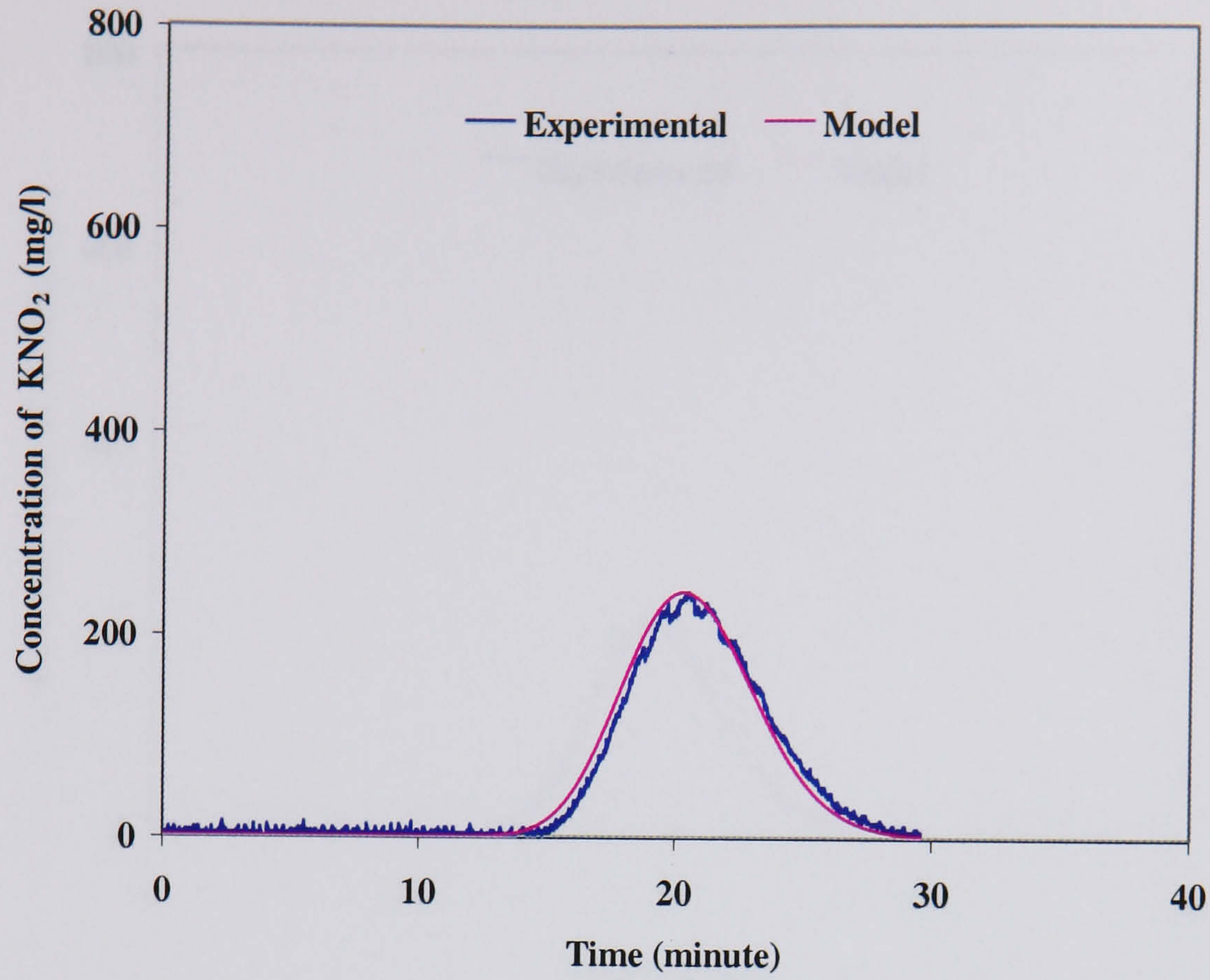

Figure A1.10. Prediction of concentration profile 3 from profile 1 using axial dispersion model, Re_o = 9036 (12 mm, 3 Hz), Re_n = 469

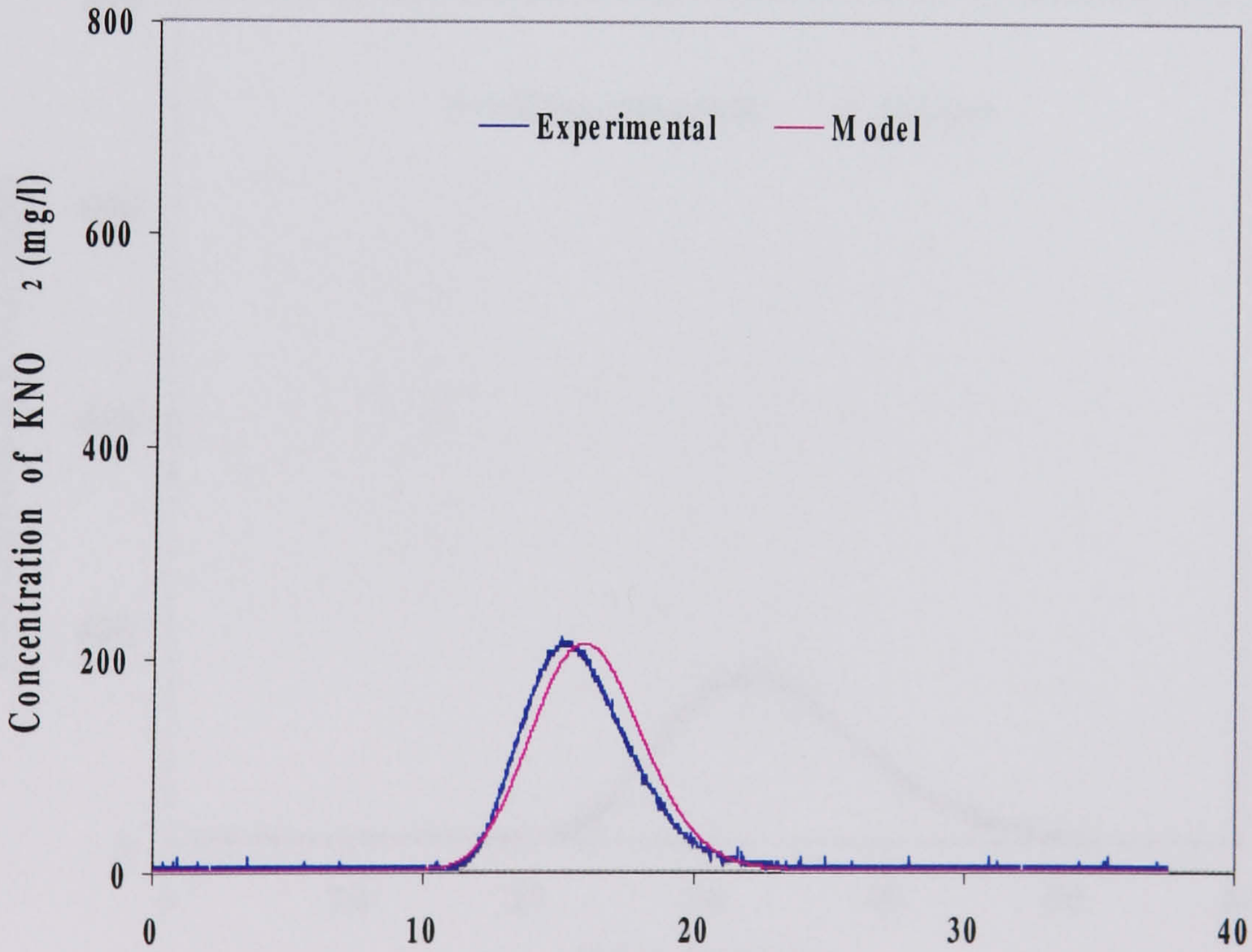

Figure A1.11. Prediction of concentration profile 3 from profile 1 using axial dispersion model, Re_o = 9036 (12 mm, 1 Hz), Re_n = 490

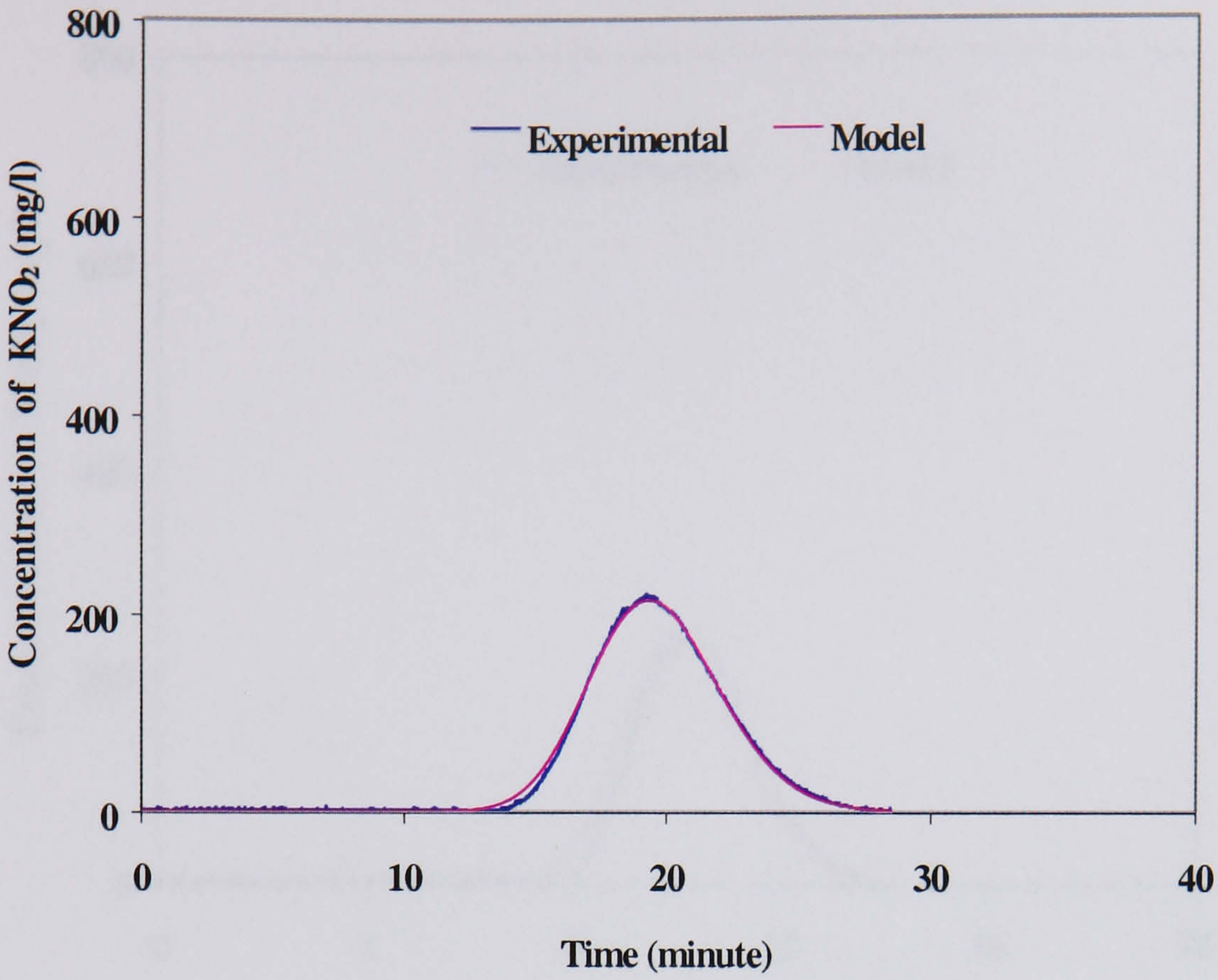

Figure A1.12. Prediction of concentration profile 3 from profile 1 using axial dispersion model, Re_o = 9036 (12 mm, 2 Hz), Re_n = 452

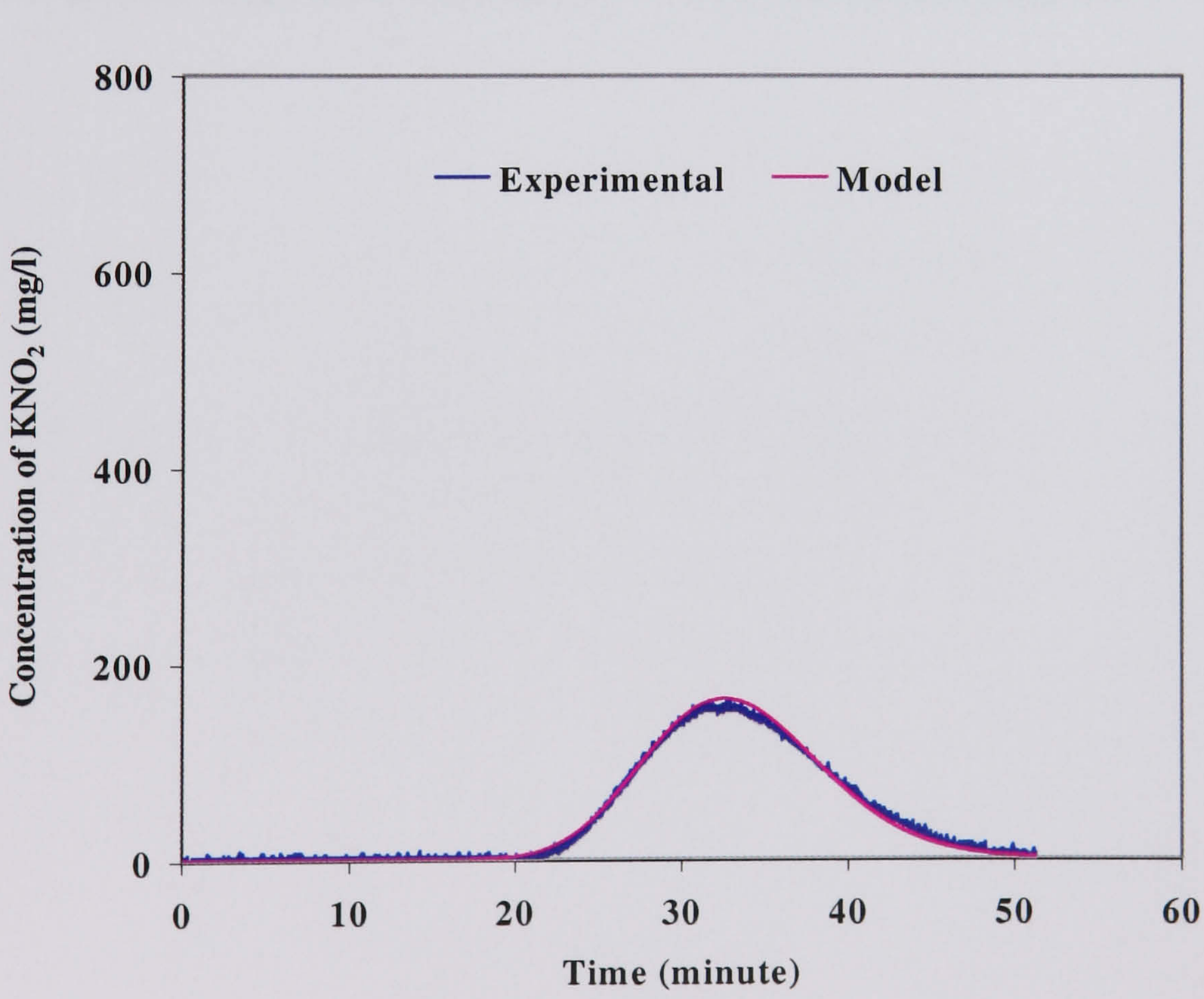

Figure A1.13. Prediction of concentration profile 3 from profile 1 using axial dispersion model, Re_o = 9036 (12 mm, 3 Hz), Re_n = 268

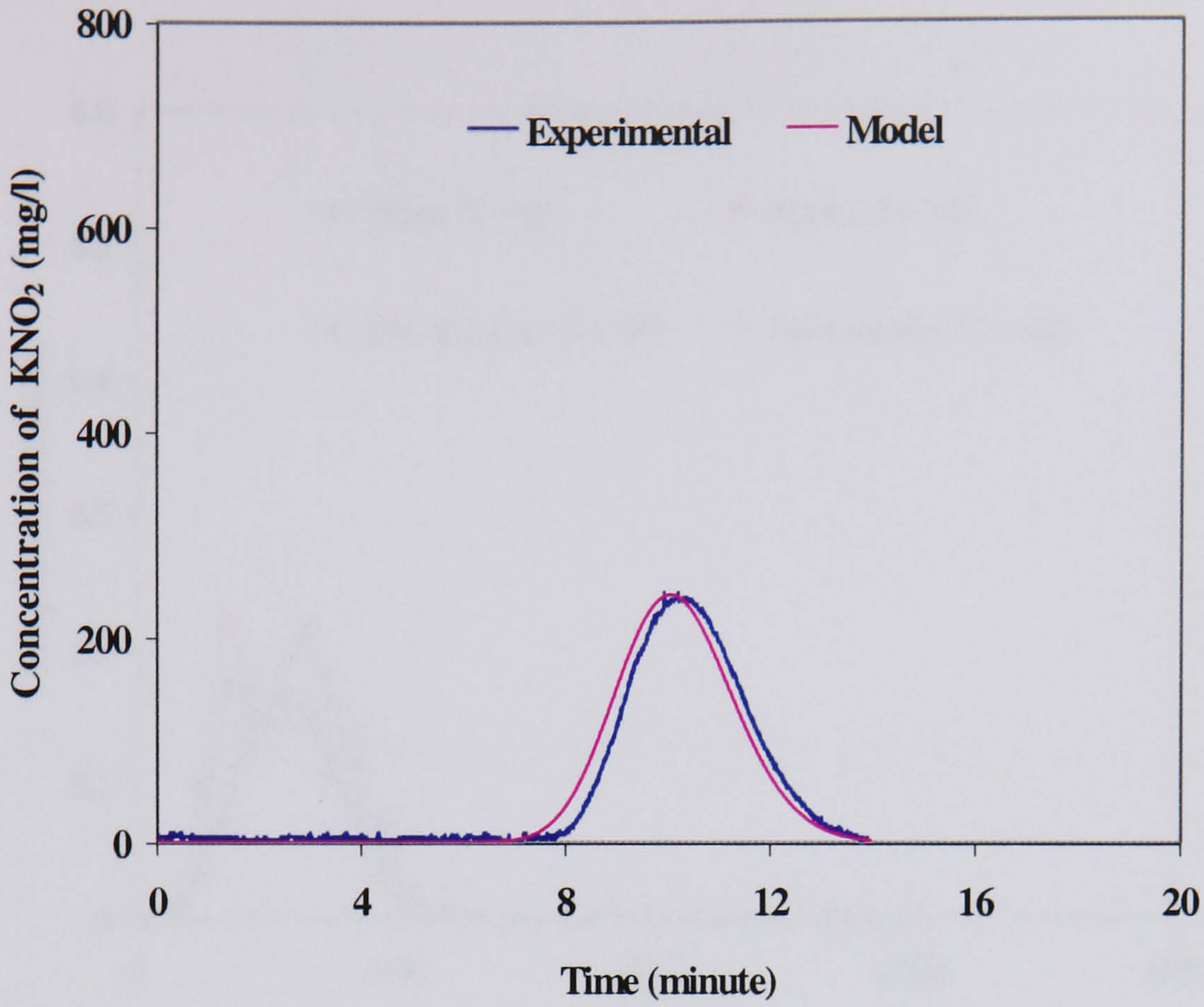

Figure A1.14. Prediction of concentration profile 3 from profile 1 using axial dispersion model, Re_o = 9036 (12 mm, 3 Hz), Re_n = 912

VARIATION OF DSD WITH FLOW LENGTH

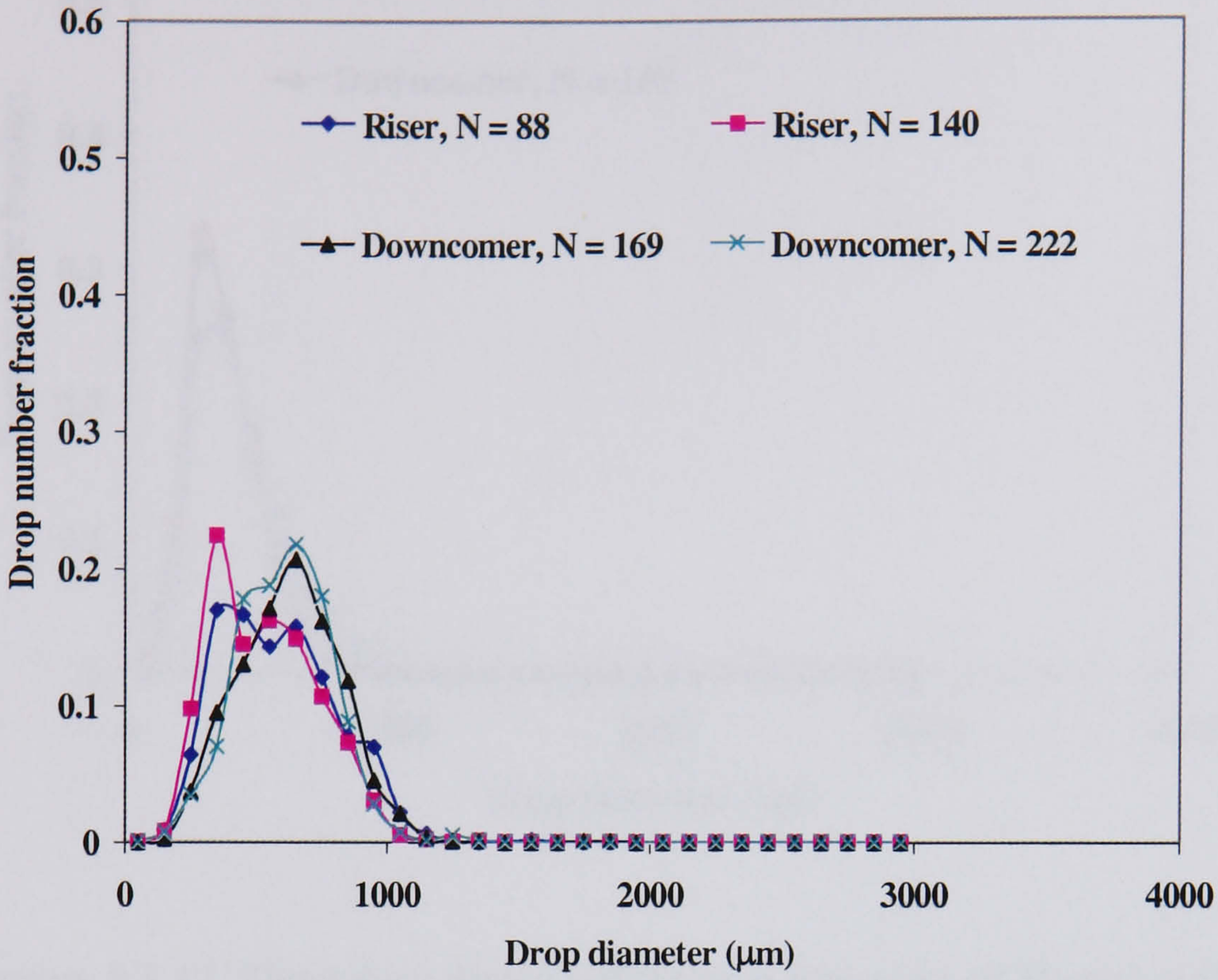

Figure A1.15. Drop size distribution as a function of flow length, Re_o = 7530 (x_o = 15 mm, f = 2 Hz); Re_n = 285

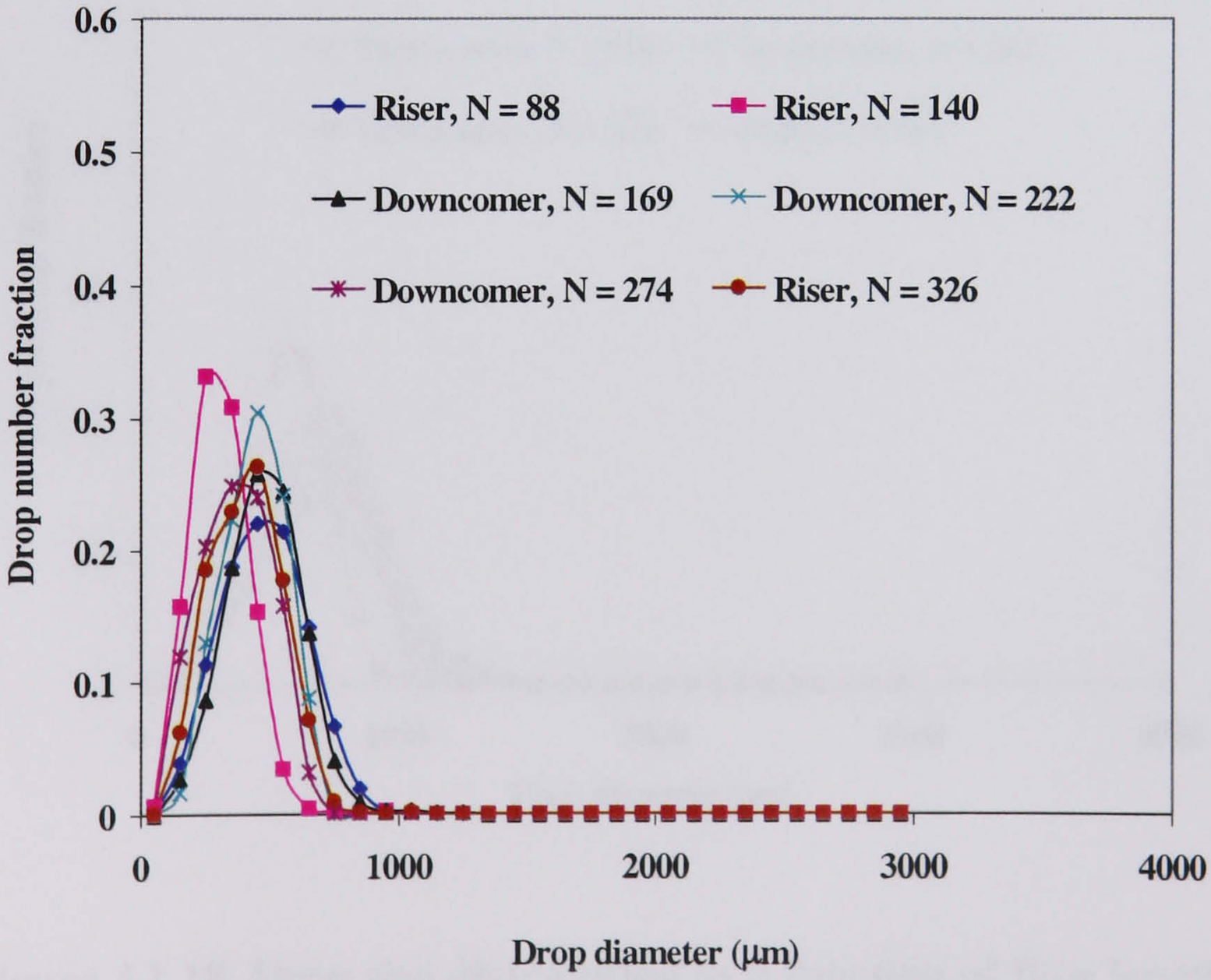

Figure A1.16. Drop size distribution as a function of flow length, Re_o = 9036 (x_o = 18 mm, f = 2 Hz); Re_n = 299

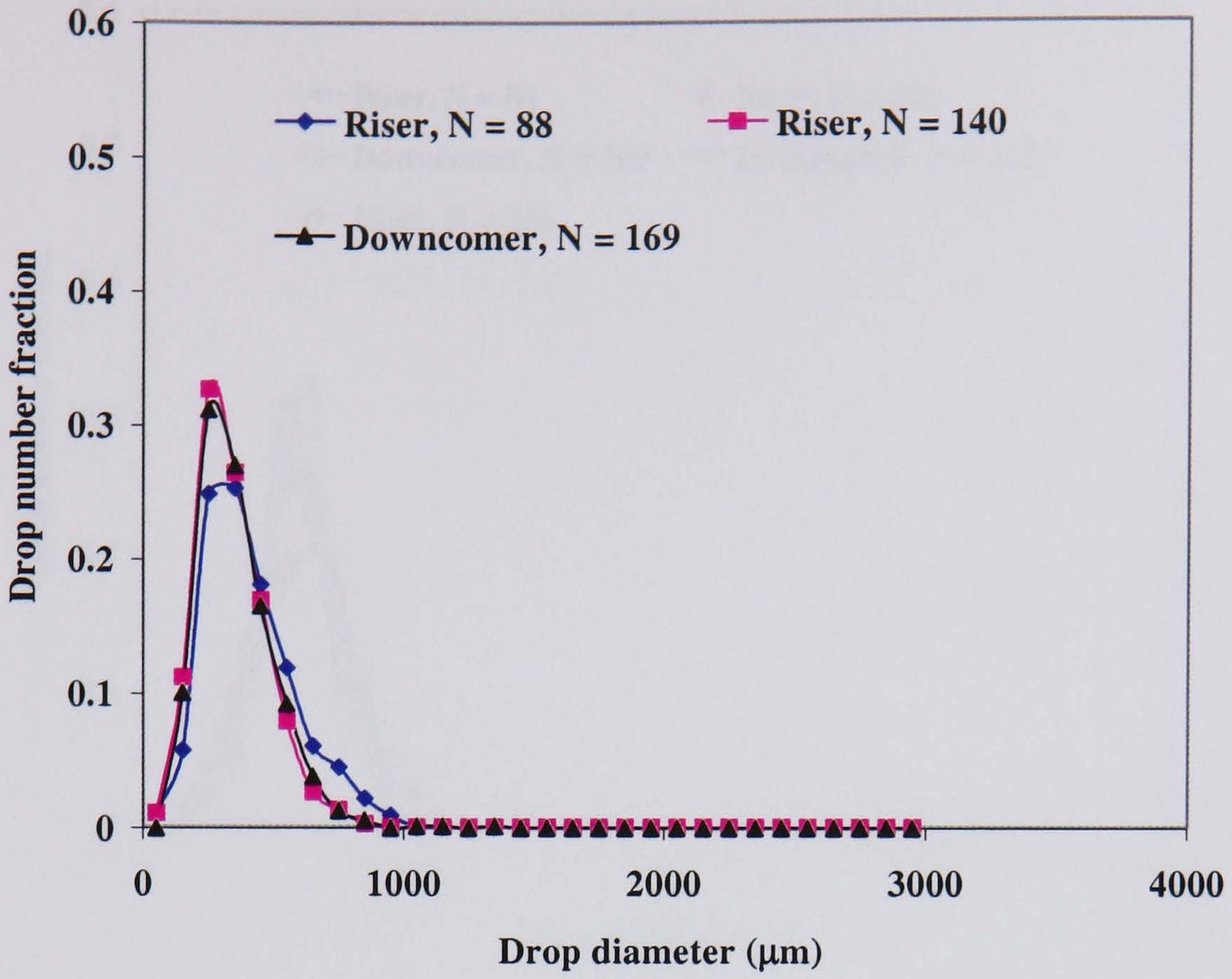

Figure A1.17. Drop size distribution as a function of flow length, Re_o = 13554 (x_o = 18 mm, f = 3 Hz); Re_n = 299

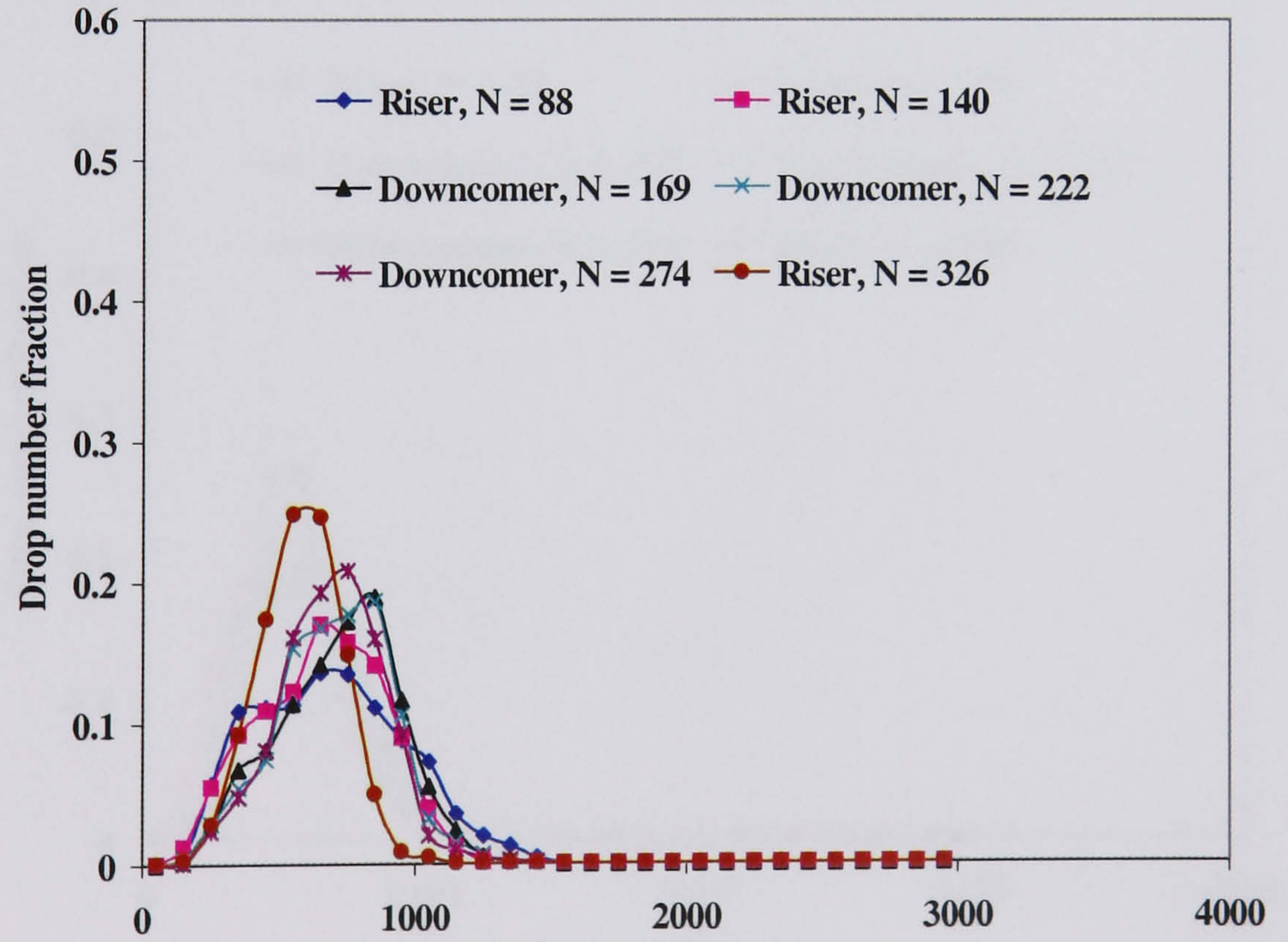

Figure A1.18. Drop size distribution as a function of flow length, Re_o = 7530 (x_o = 15 mm, f = 2 Hz); Re_n = 974

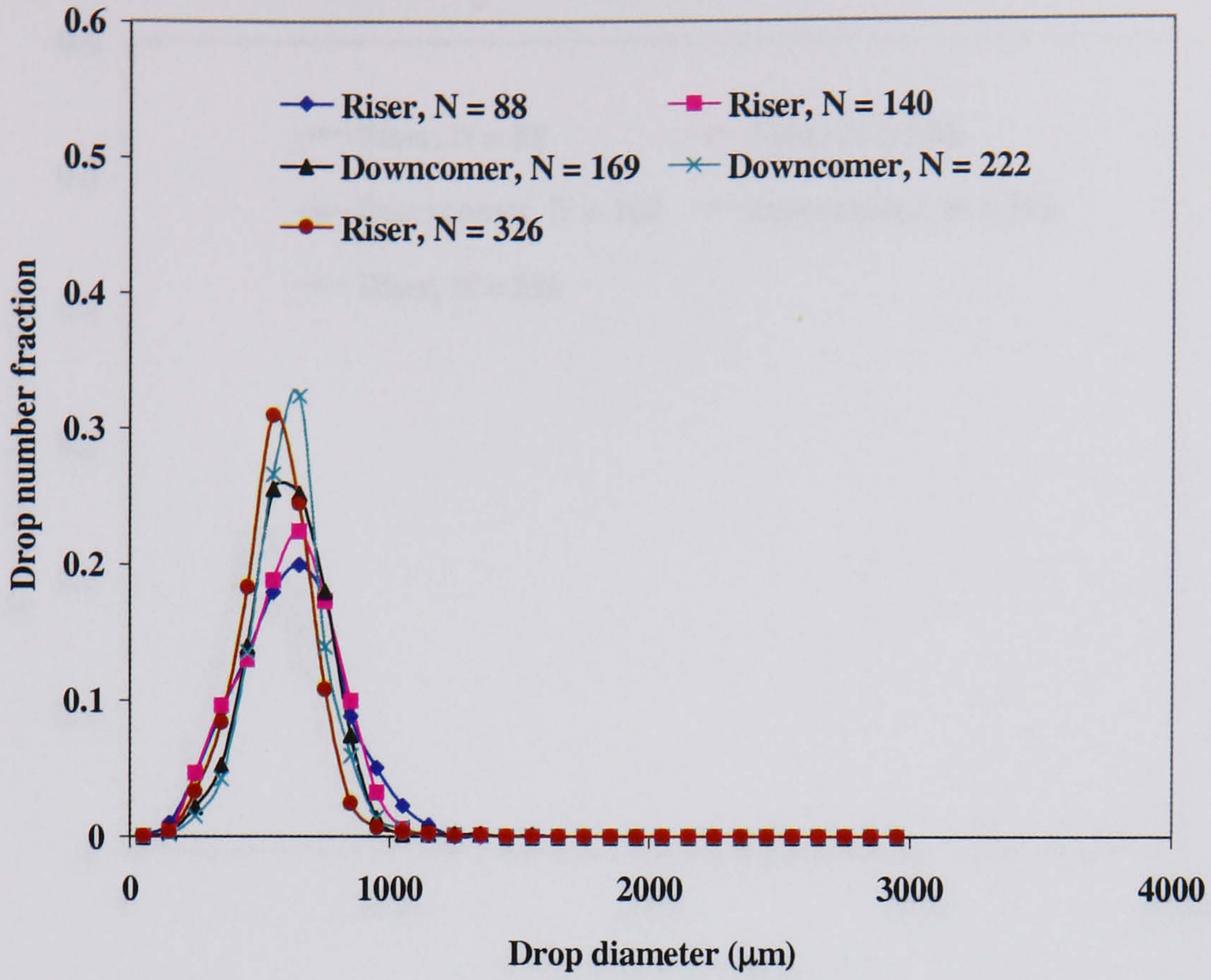

Figure A1.19. Drop size distribution as a function of flow length, Re_o = 9036 (x_o = 18 mm, f = 2 Hz); Re_n = 989

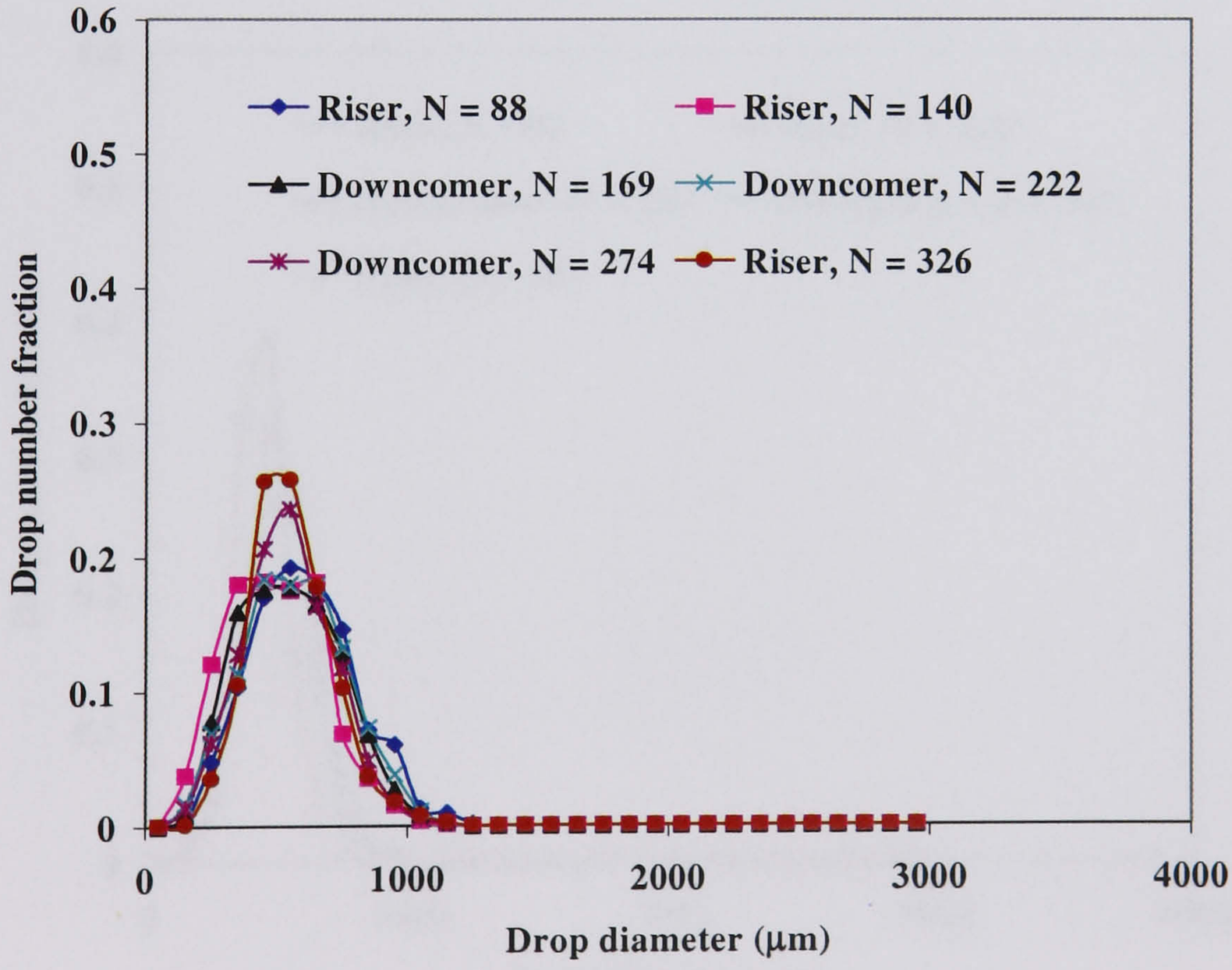

Figure A1.20. Drop size distribution as a function of flow length, Re_o = 11295 (x_o = 15 mm, f = 3 Hz); Re_n = 975

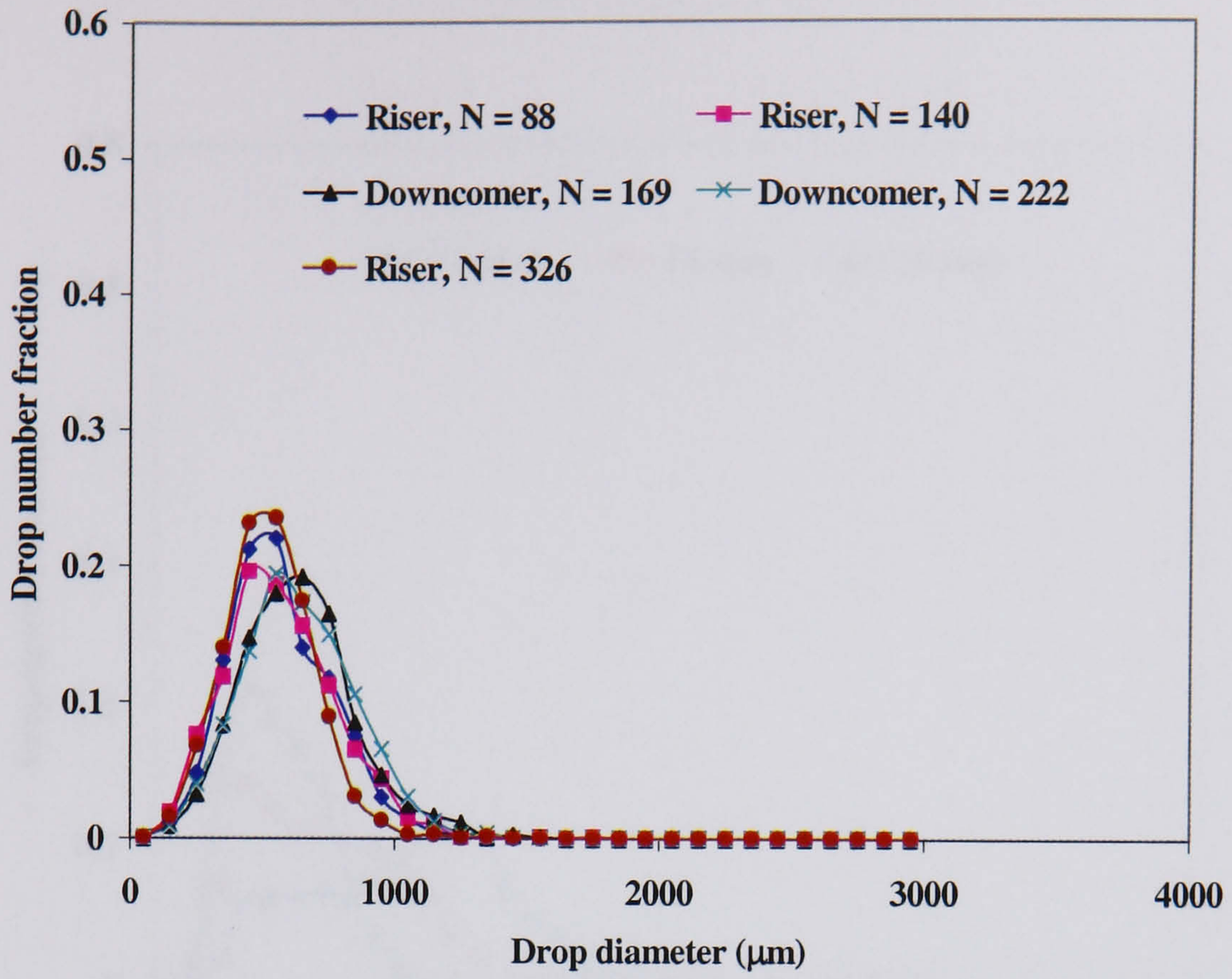

Figure A1.21. Drop size distribution as a function of flow length, Re_o = 13554 (x_o = 18 mm, f = 3 Hz); Re_n = 1006

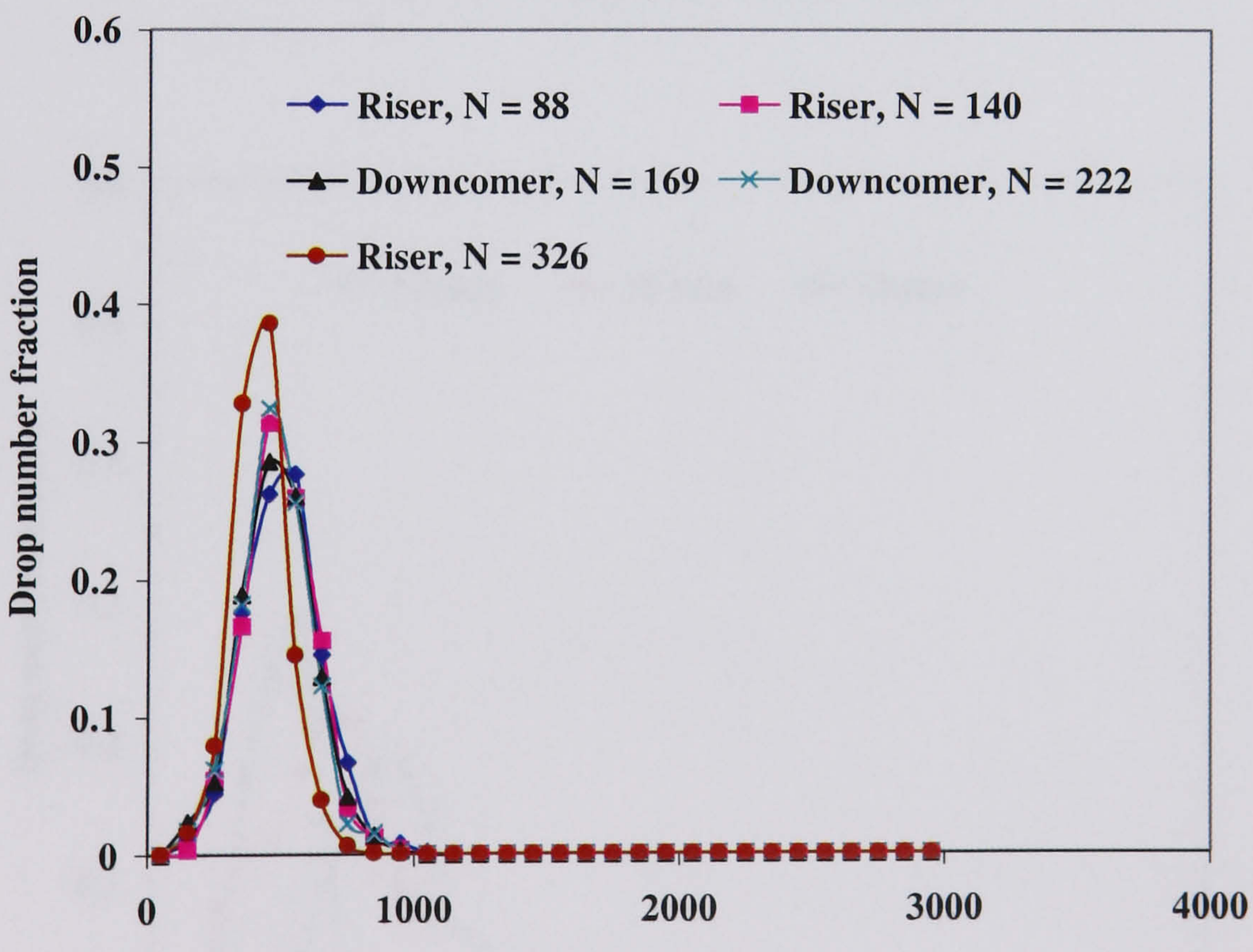

Figure A1.22. Drop size distribution as a function of flow length, Re_o = 15060 (x_o = 15 mm, f = 4 Hz); Re_n = 975

EFFECT OF OSCILLATION AMPLITUDE

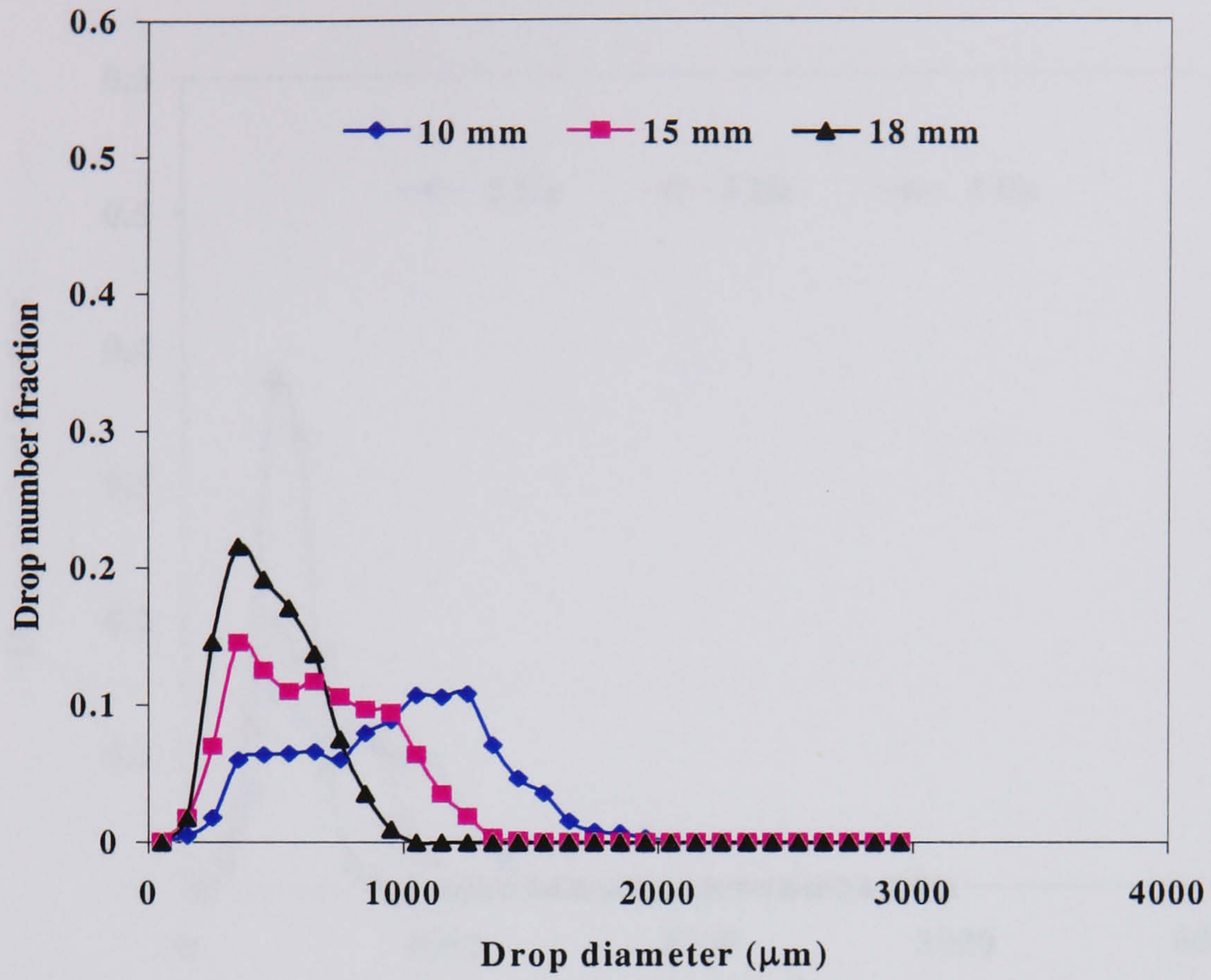

Figure A1.23. Effect oscillation amplitude on droplet size distribution (f = 2.0 Hz, Re_n = 554), Riser 1

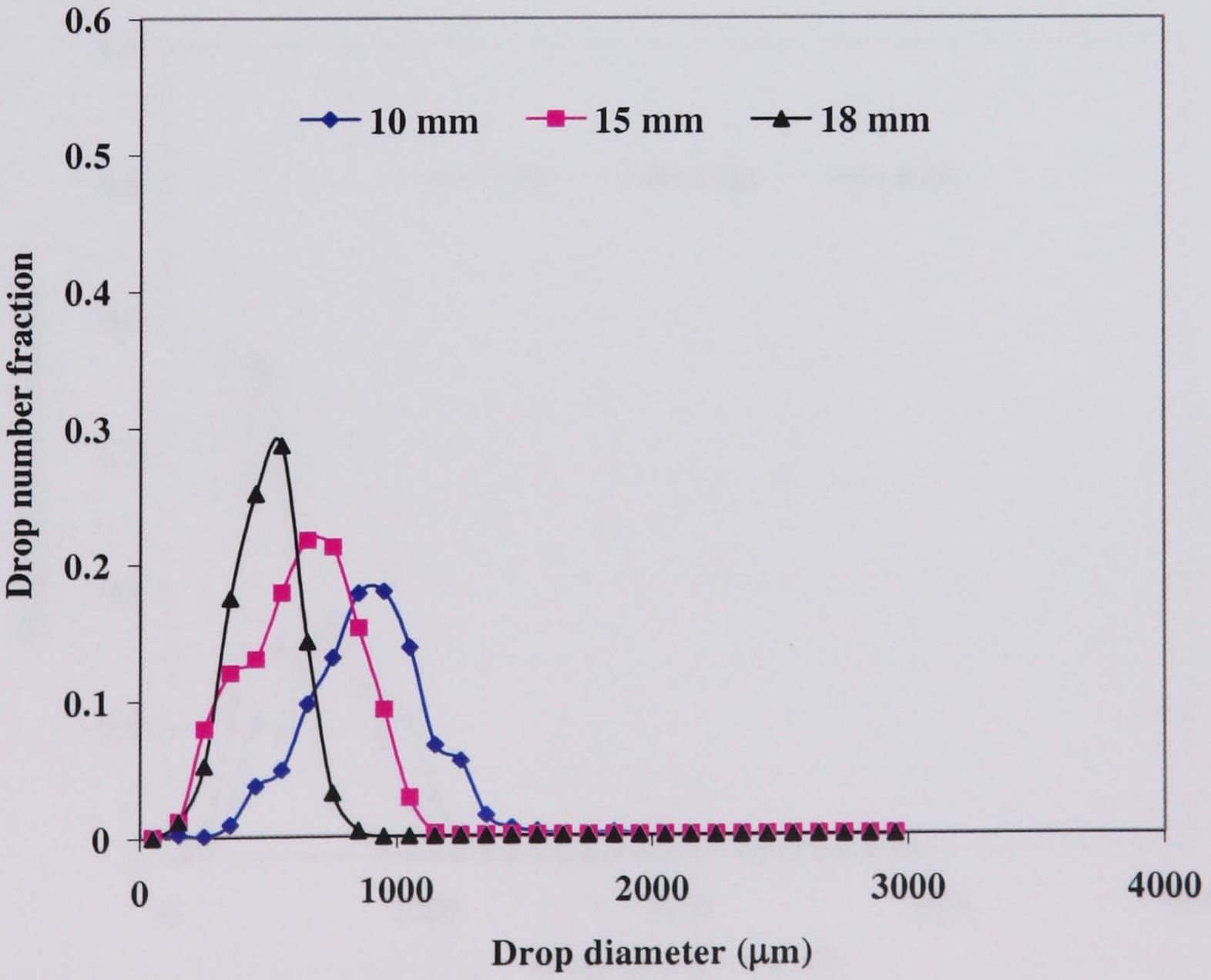

Figure A1.24. The effect oscillation amplitude on droplet size distribution (f = 2.0 Hz, Re_n= 554), Downcomer 2

EFFECT OF OSCILLATION FREQUENCY

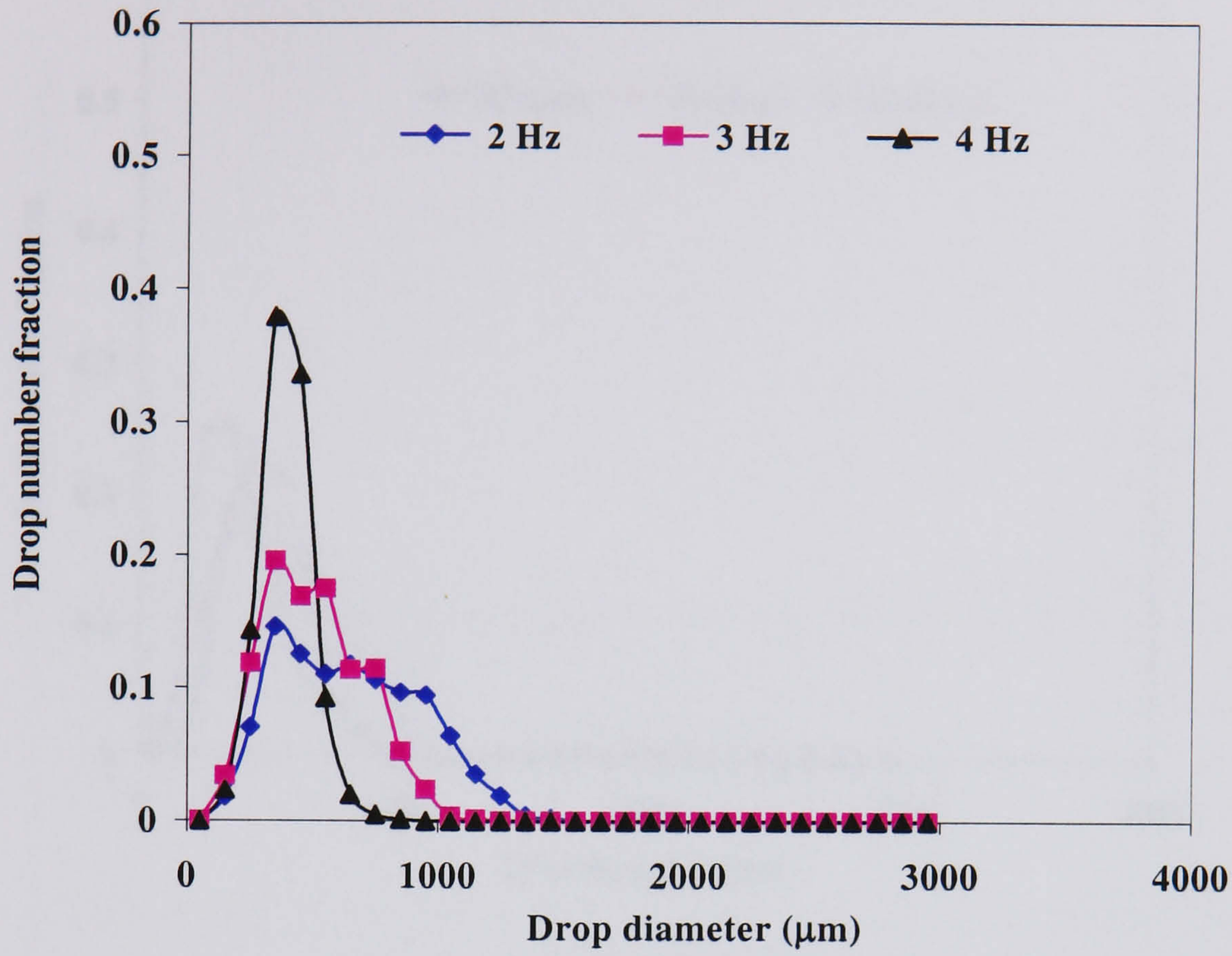

Figure A1.25. The effect oscillation frequency on droplet size distribution (x_o = 15 mm, Re_n = 554), Riser 1

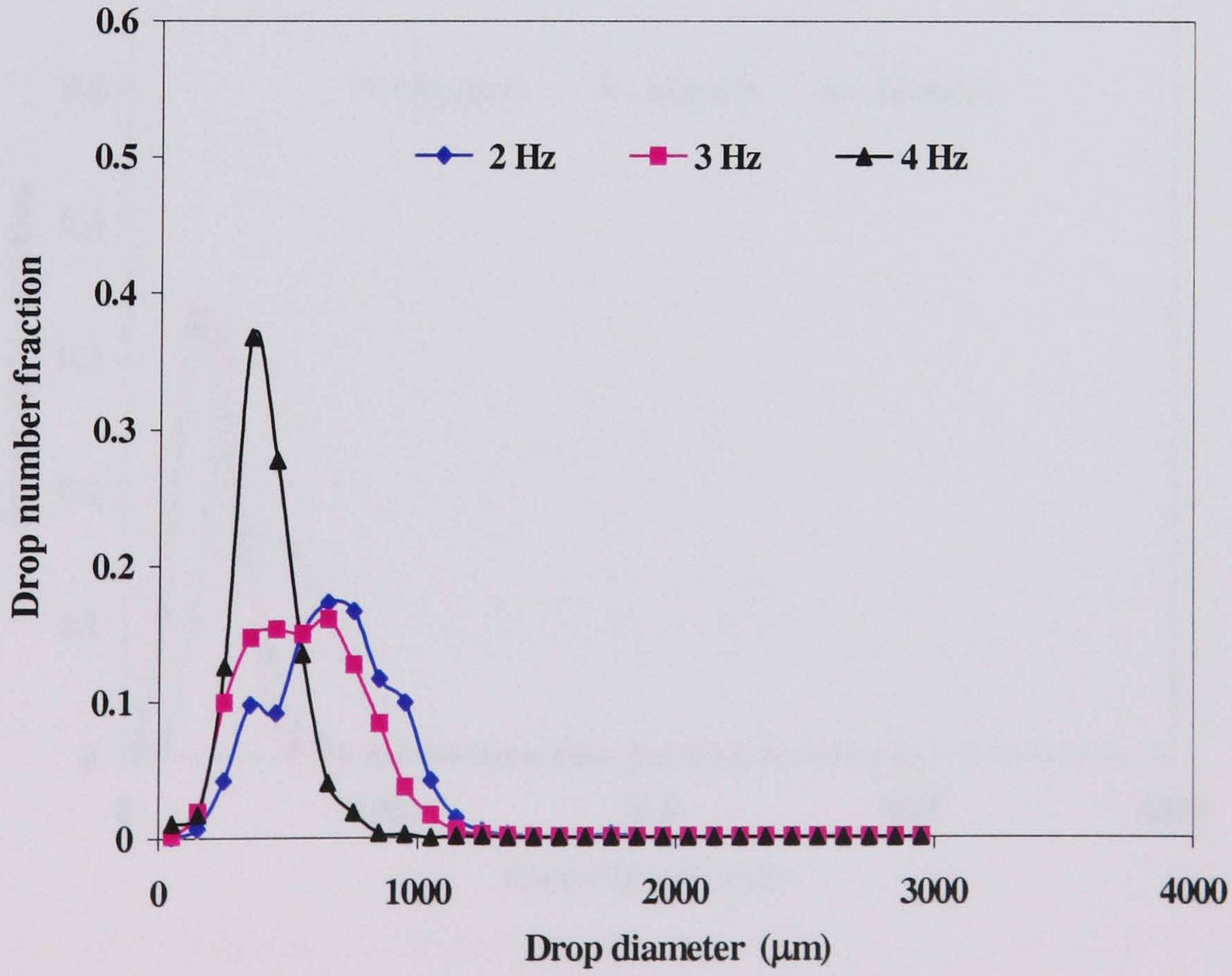

Figure A1.26. The effect oscillation frequency on droplet size distribution (x_o = 15 mm, Re_n = 554), Downcomer 2

EFFECT OF OSCILLATION VELOCITY

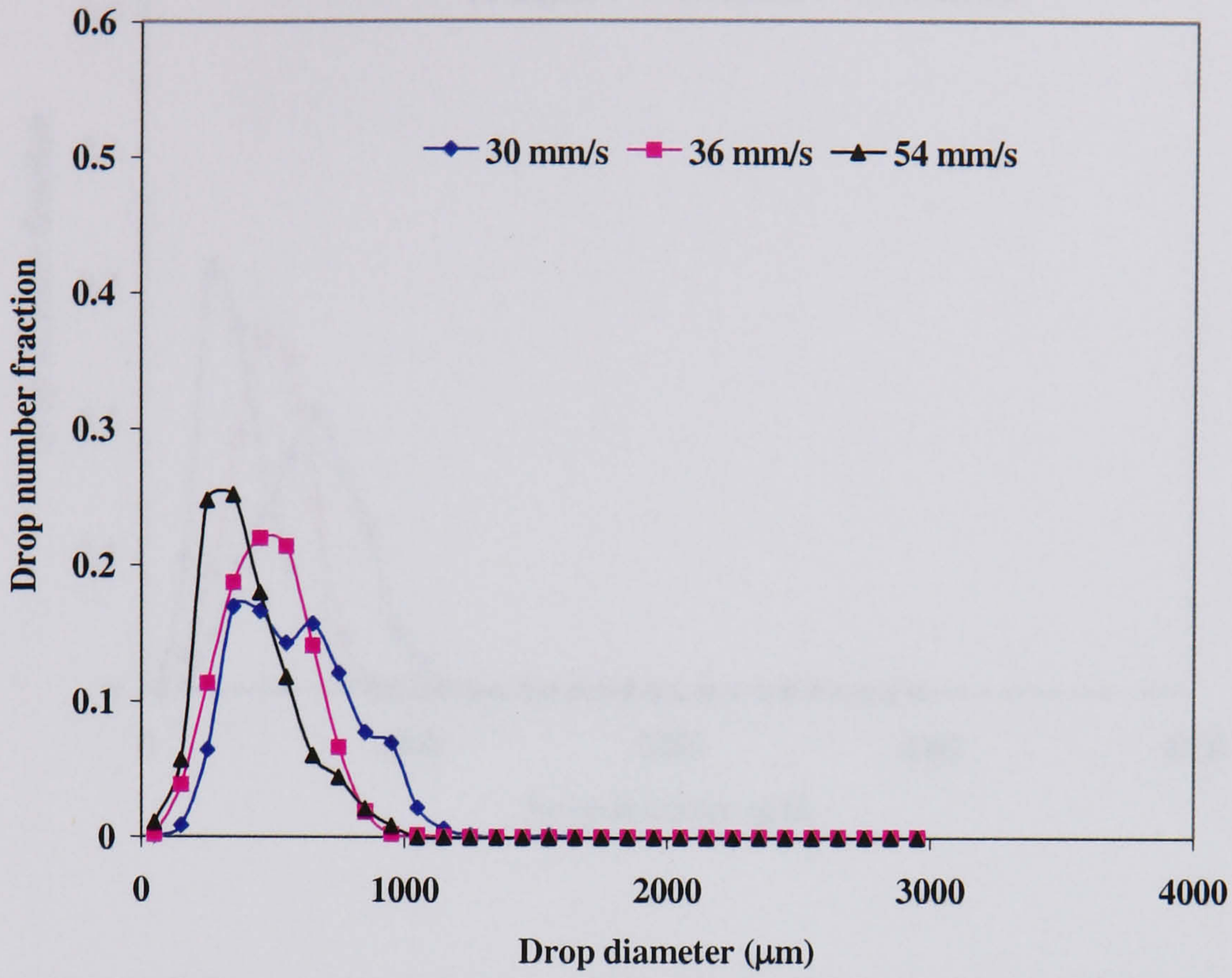

Figure A1.27. Effect of oscillation velocity on drop size distribution (DSD) (Re_n =289), Riser 1

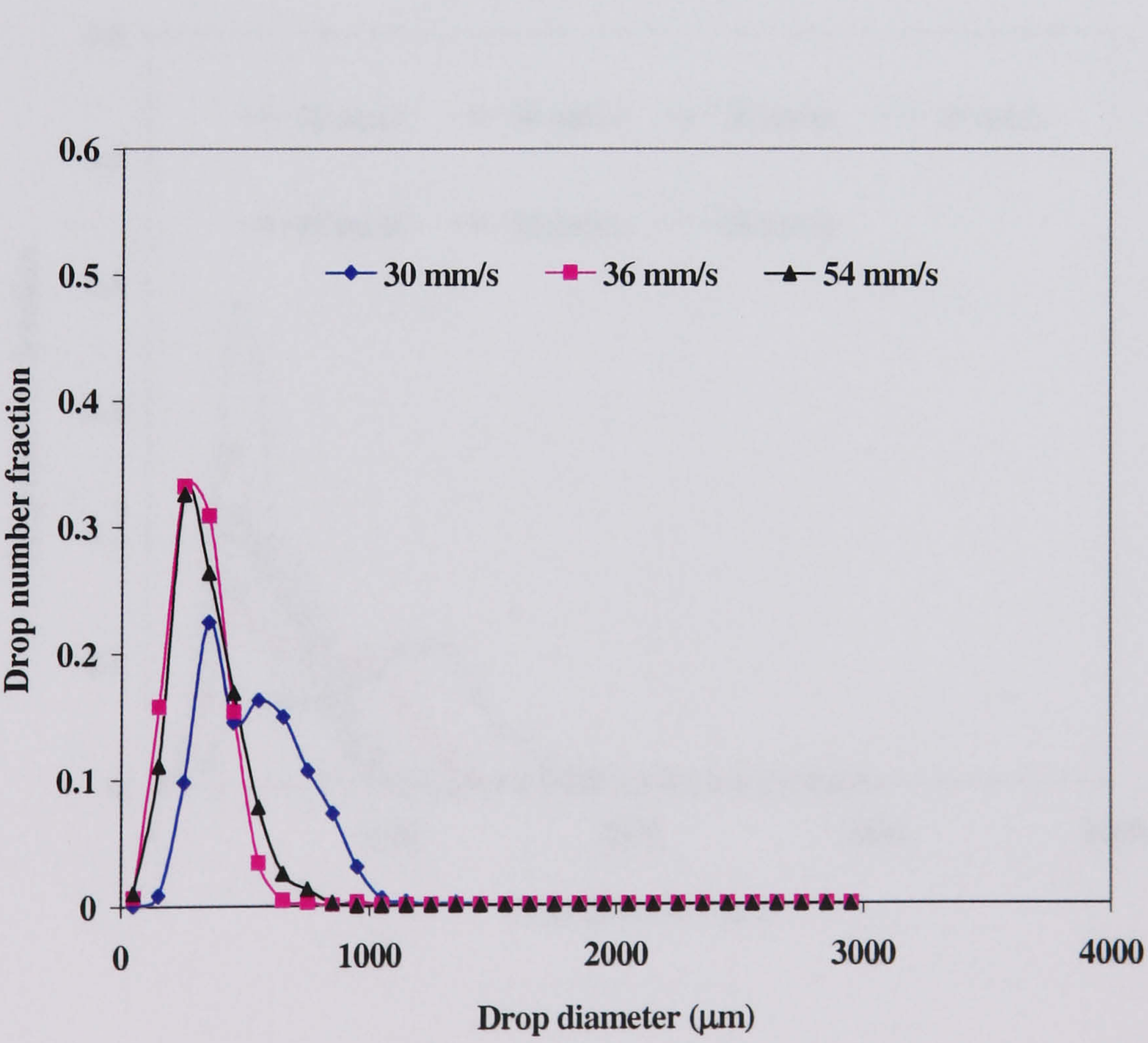

Figure A1.28. Effect of oscillation velocity on drop size distribution (DSD) (Re_n =289), Riser 2

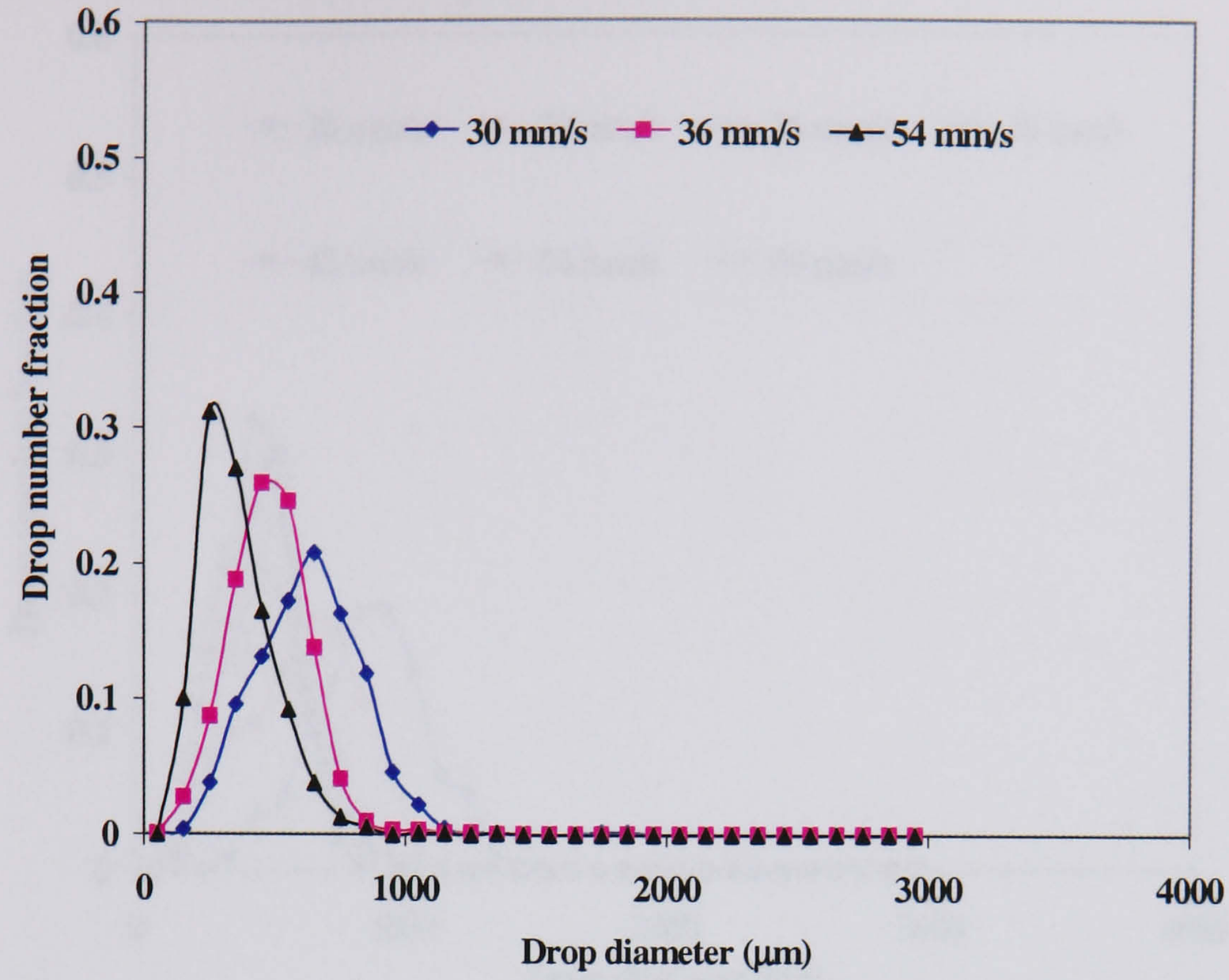

Figure A1.29. Effect of oscillation velocity on drop size distribution (DSD) (Re_n = 289), Downcomer 1

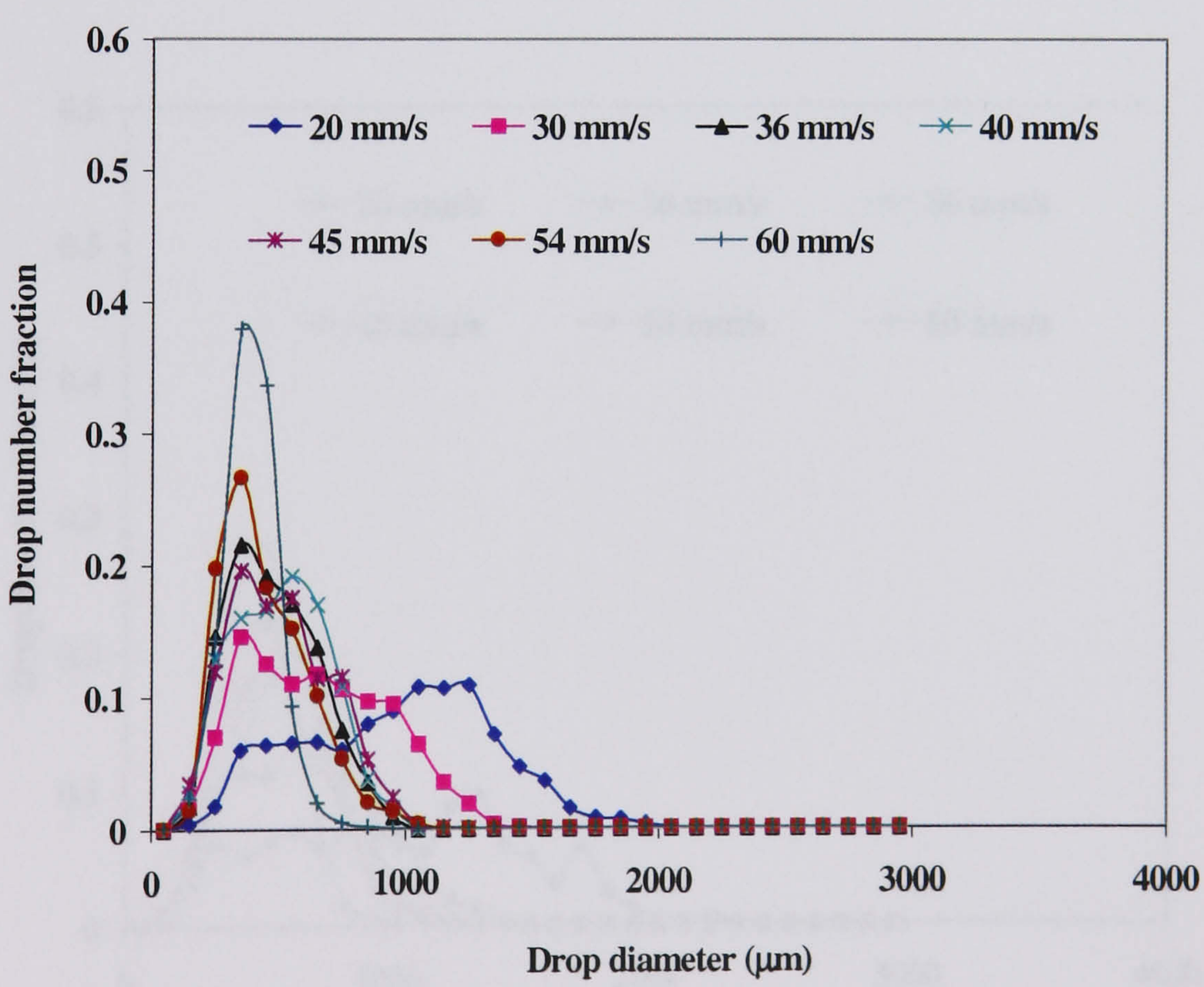

Figure A1.30. Effect of oscillation velocity on drop size distribution (DSD) (Re_n = 554), Riser 1

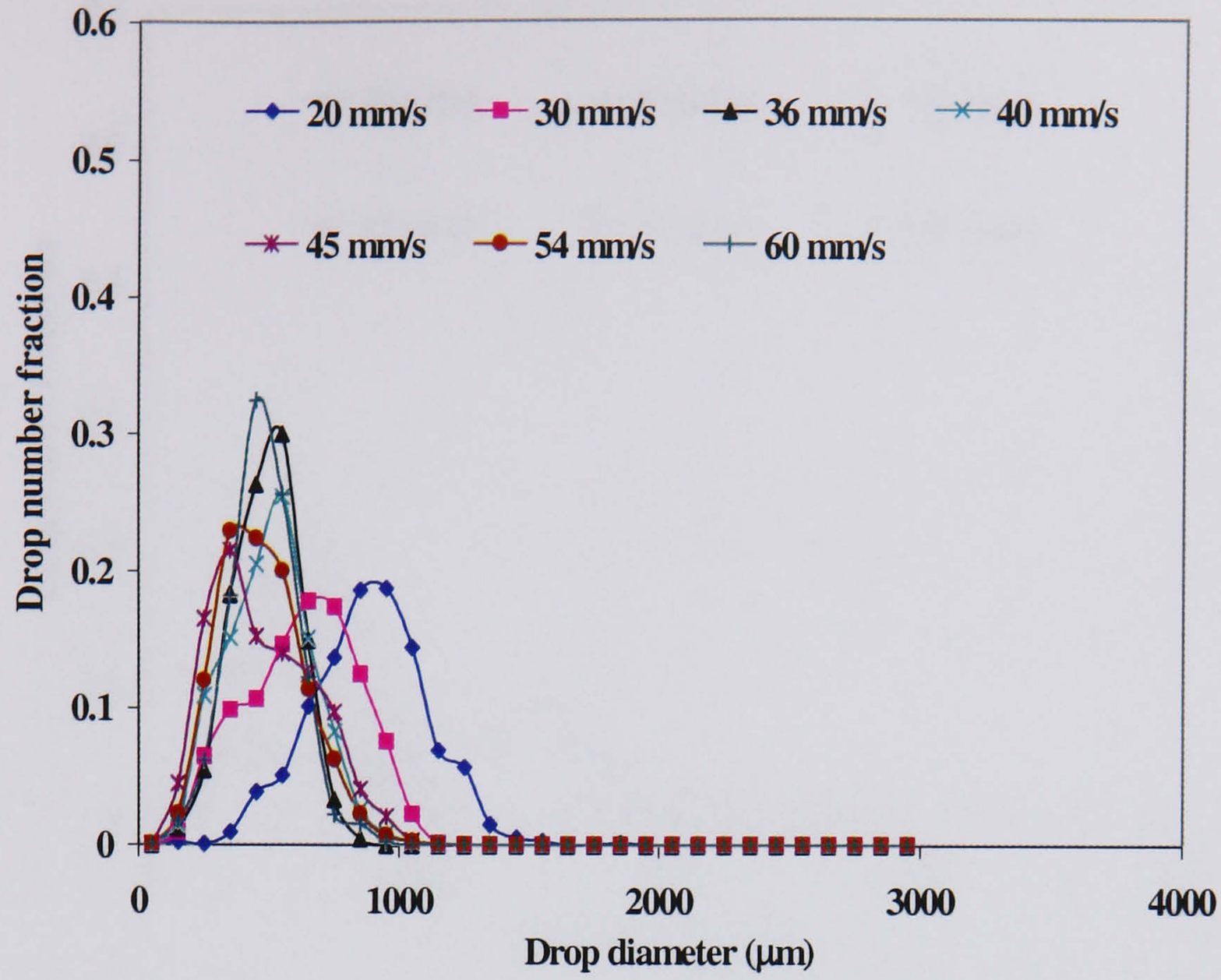

Figure A1.31. Effect of oscillation velocity on drop size distribution (DSD) (Re_n = 554), Downcomer 2

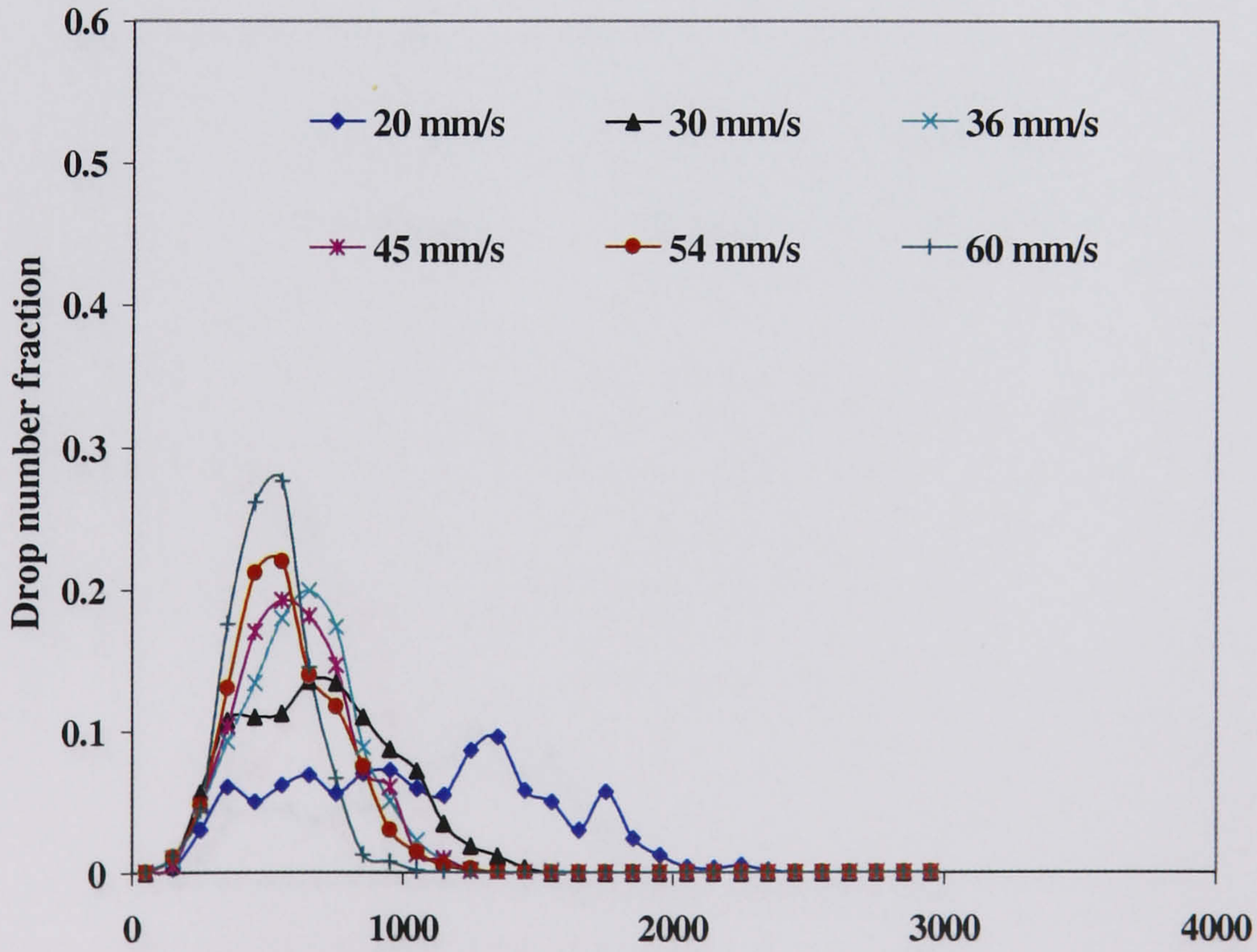

Figure A1.32. Effect of oscillation velocity on drop size distribution (DSD) (Re_n = 982), Riser 1

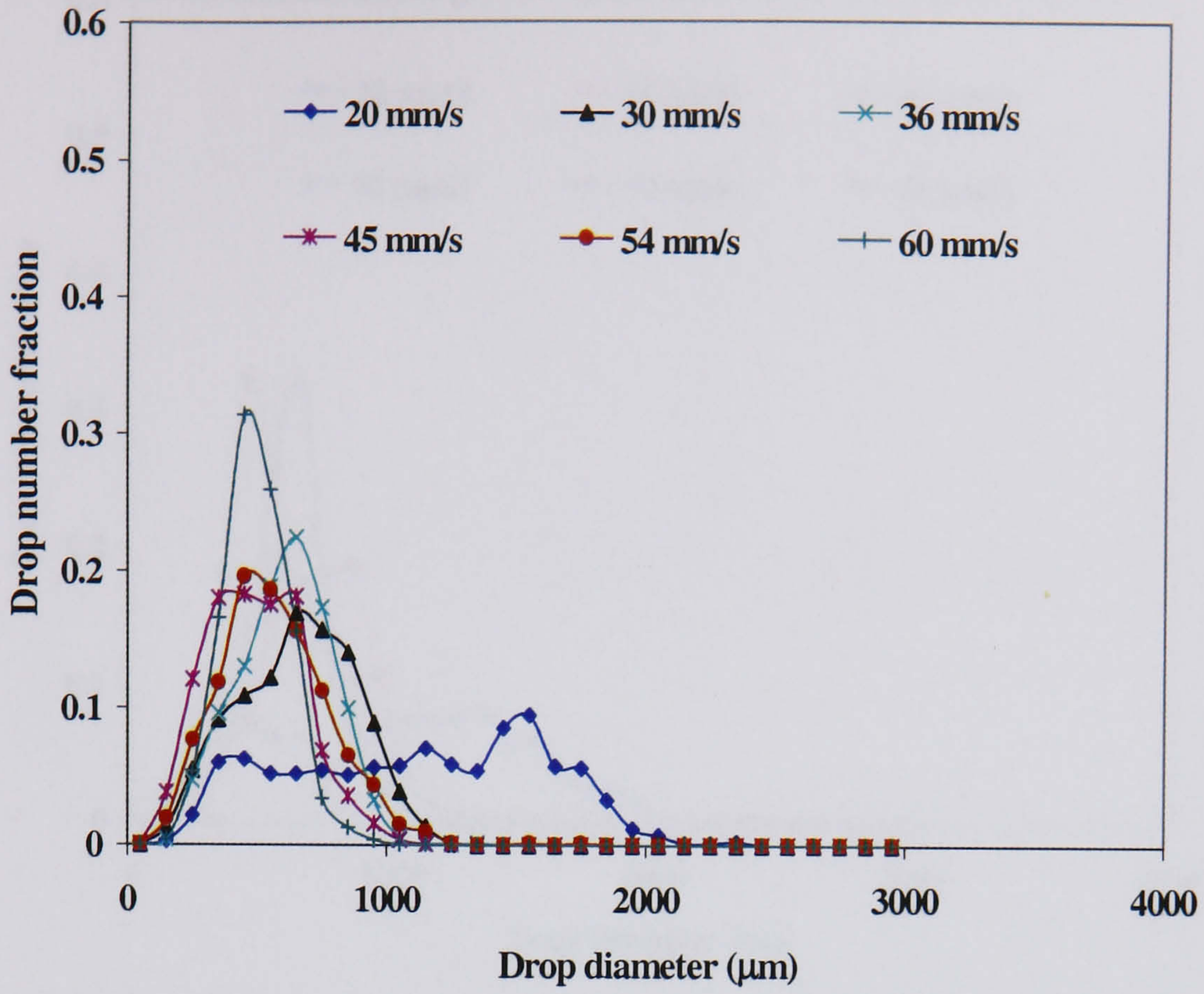

Figure A1.33. Effect of oscillation velocity on drop size distribution (DSD) (Re_n = 982), Riser 2

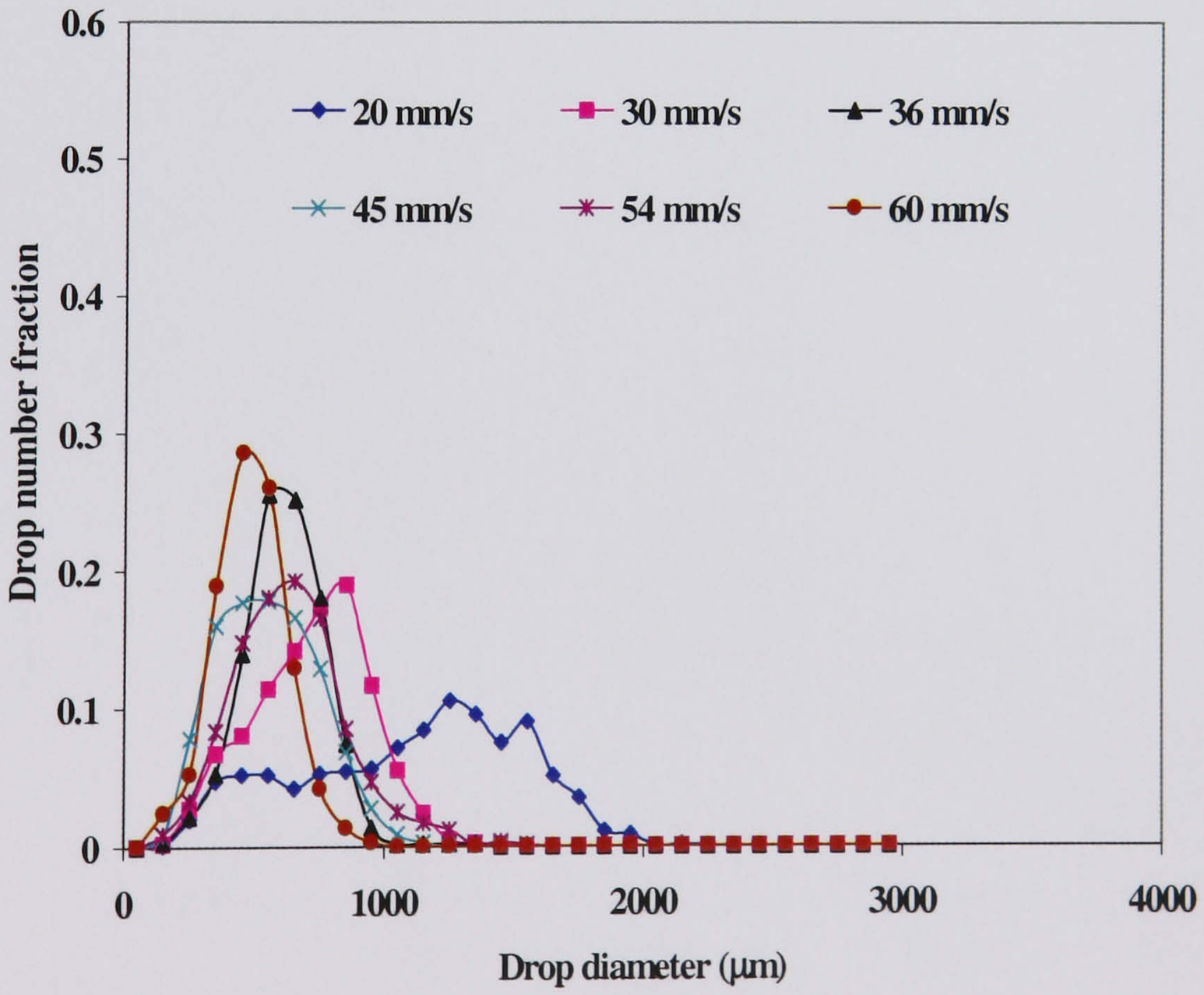

Figure A1.34. Effect of oscillation velocity on drop size distribution (DSD) (Re_n = 982), Downcomer 1

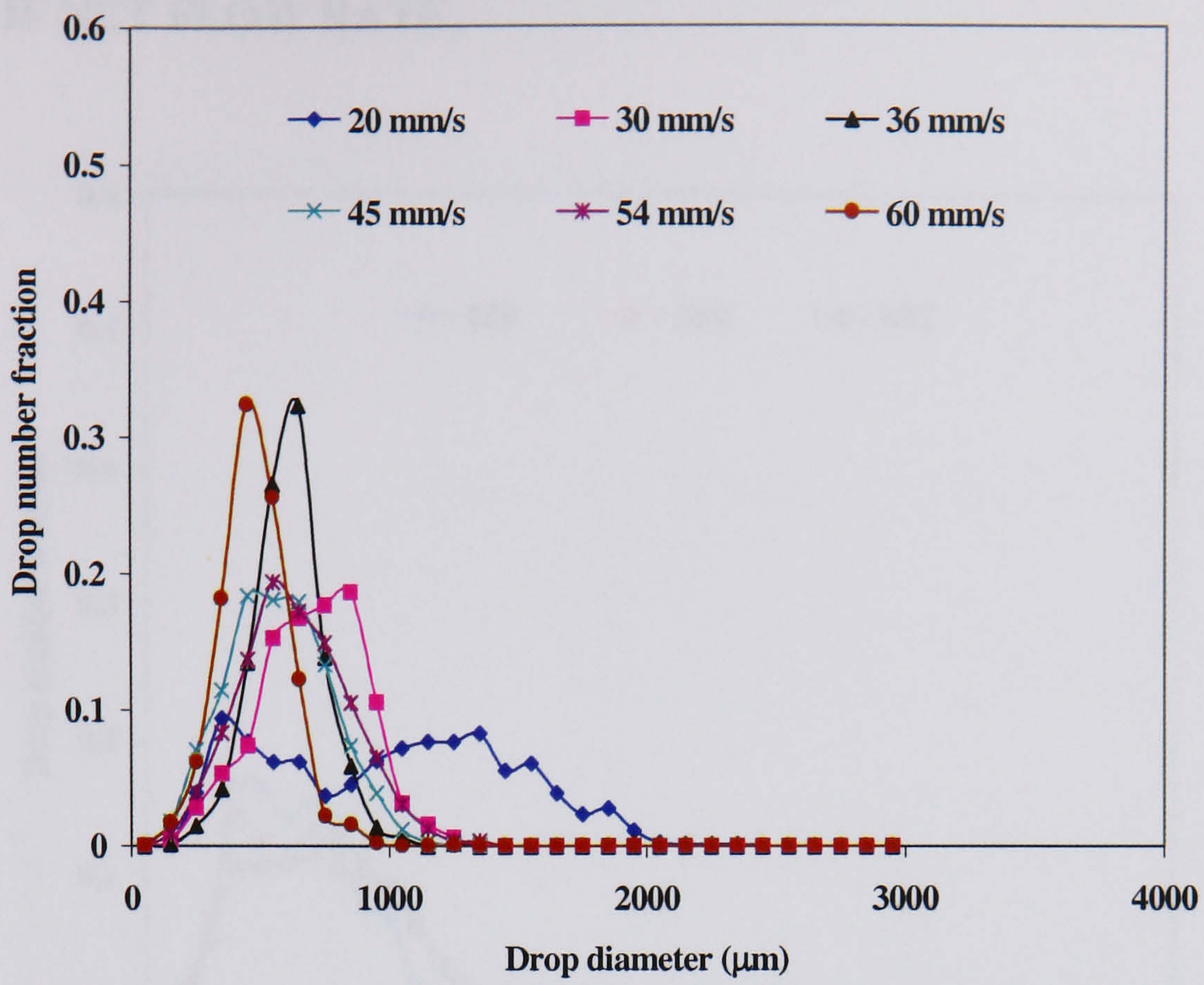

Figure A1.35. Effect of oscillation velocity on drop size distribution (DSD) (Re_n = 982), Downcomer 2

EFFECT OF NET FLOW RATE

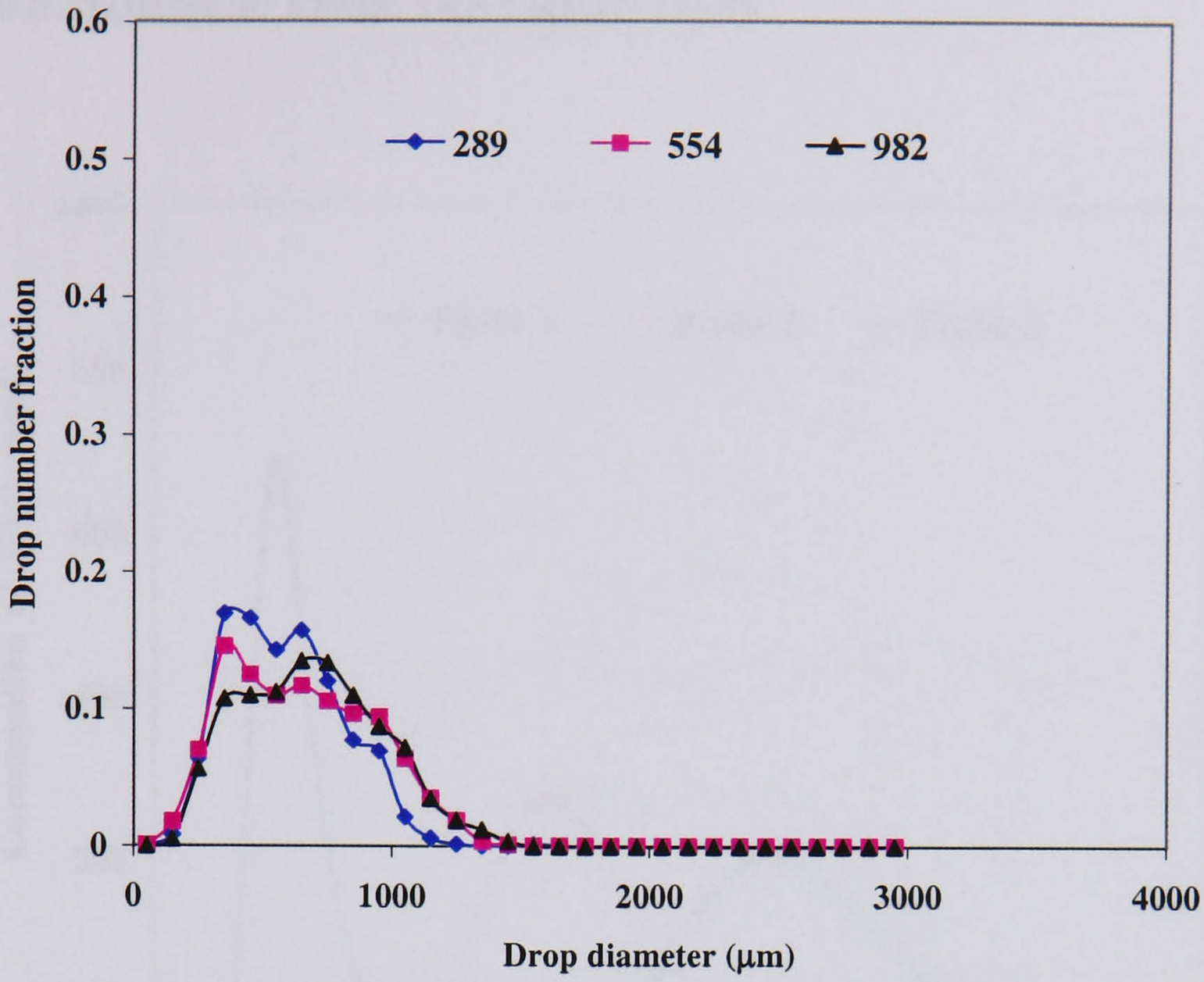

Figure A1.36. Effect of net flow rate on drop size distribution (x_o = 15 mm, f = 2 Hz), Riser 1

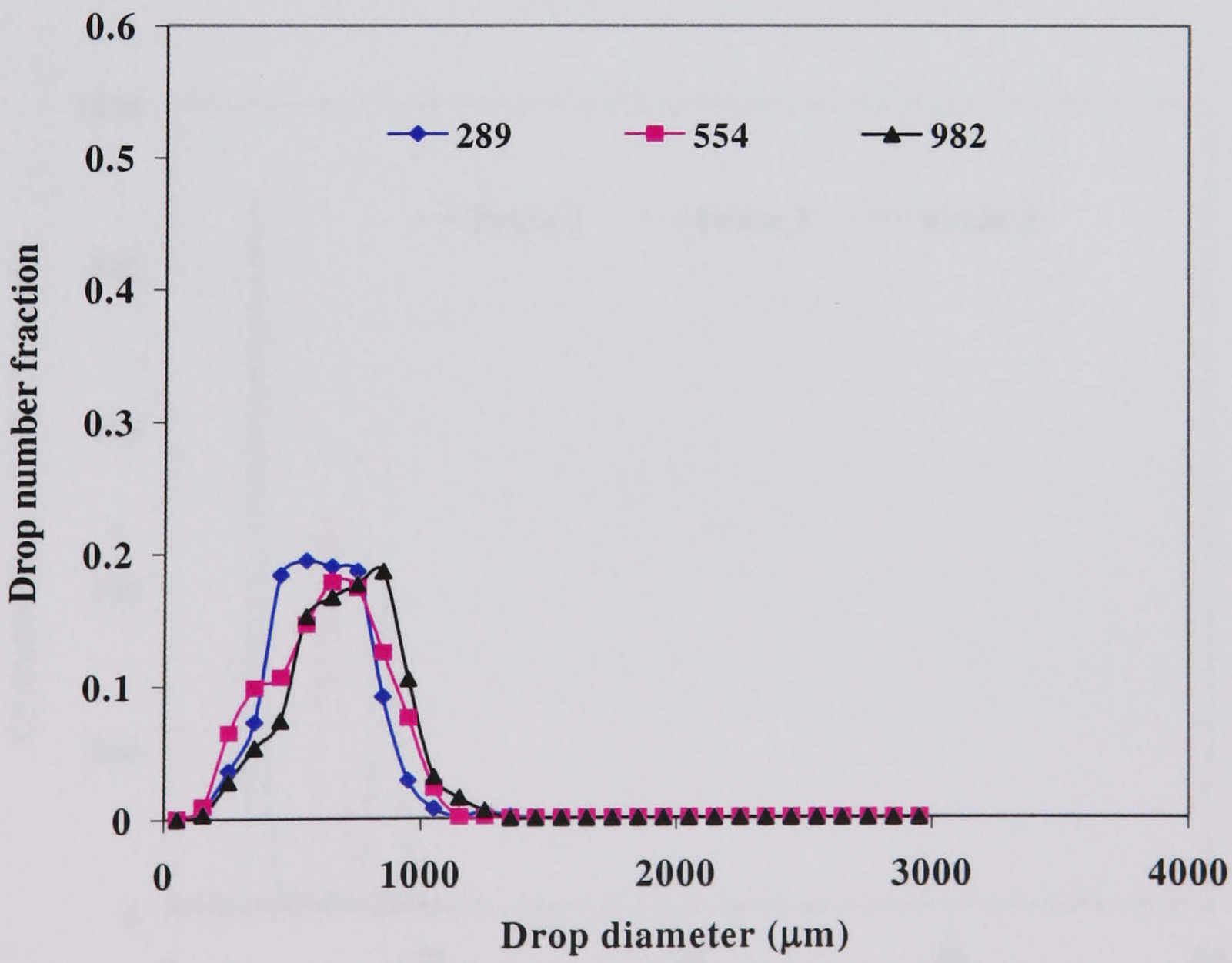

Figure A1.37. Effect of net flow rate on drop size distribution (x_o = 15 mm, f = 2 Hz), Downcomer 2

APPENDIX 2 CHARACTERISATION OF THE HORIZONTAL OBTR

TYPICAL RESIDENCE TIME DISTRIBUTION

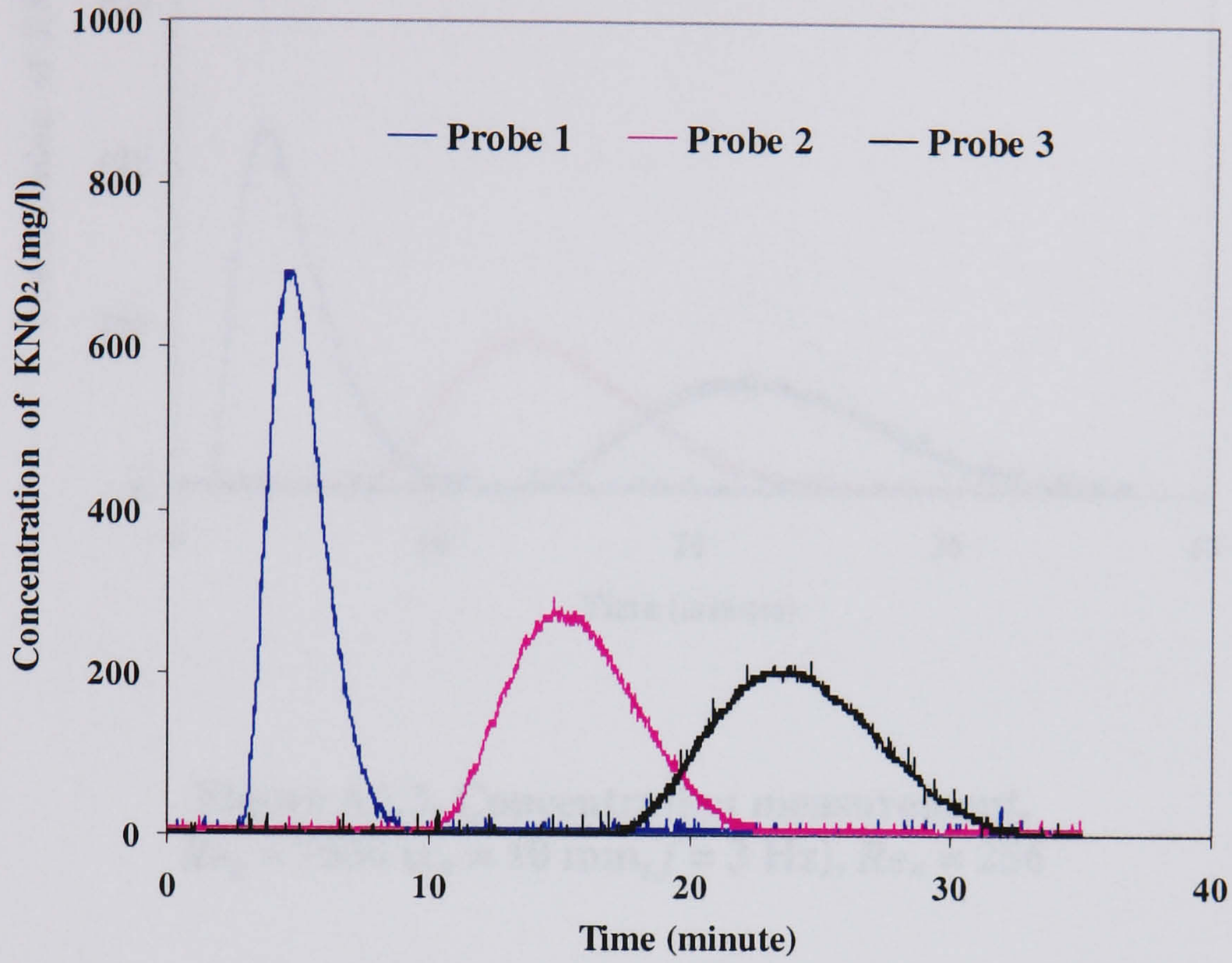

Figure A2.1. Concentration measurement, Re_o = 3012 (x_o = 4 mm, f = 3 Hz), Re_n = 266

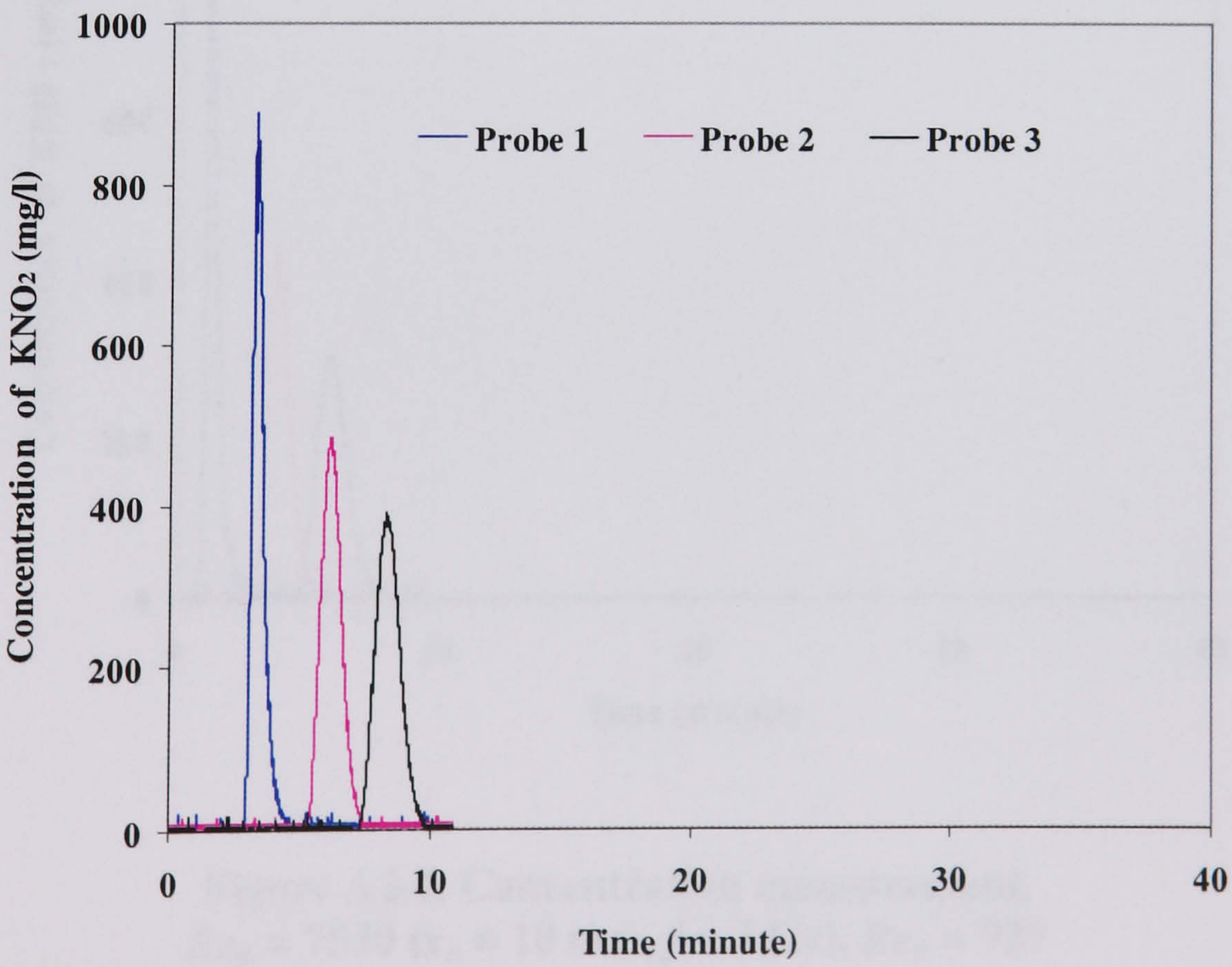

Figure A2.2. Concentration measurement, Re_o = 3012 (x_o = 4 mm, f = 3 Hz), Re_n = 955

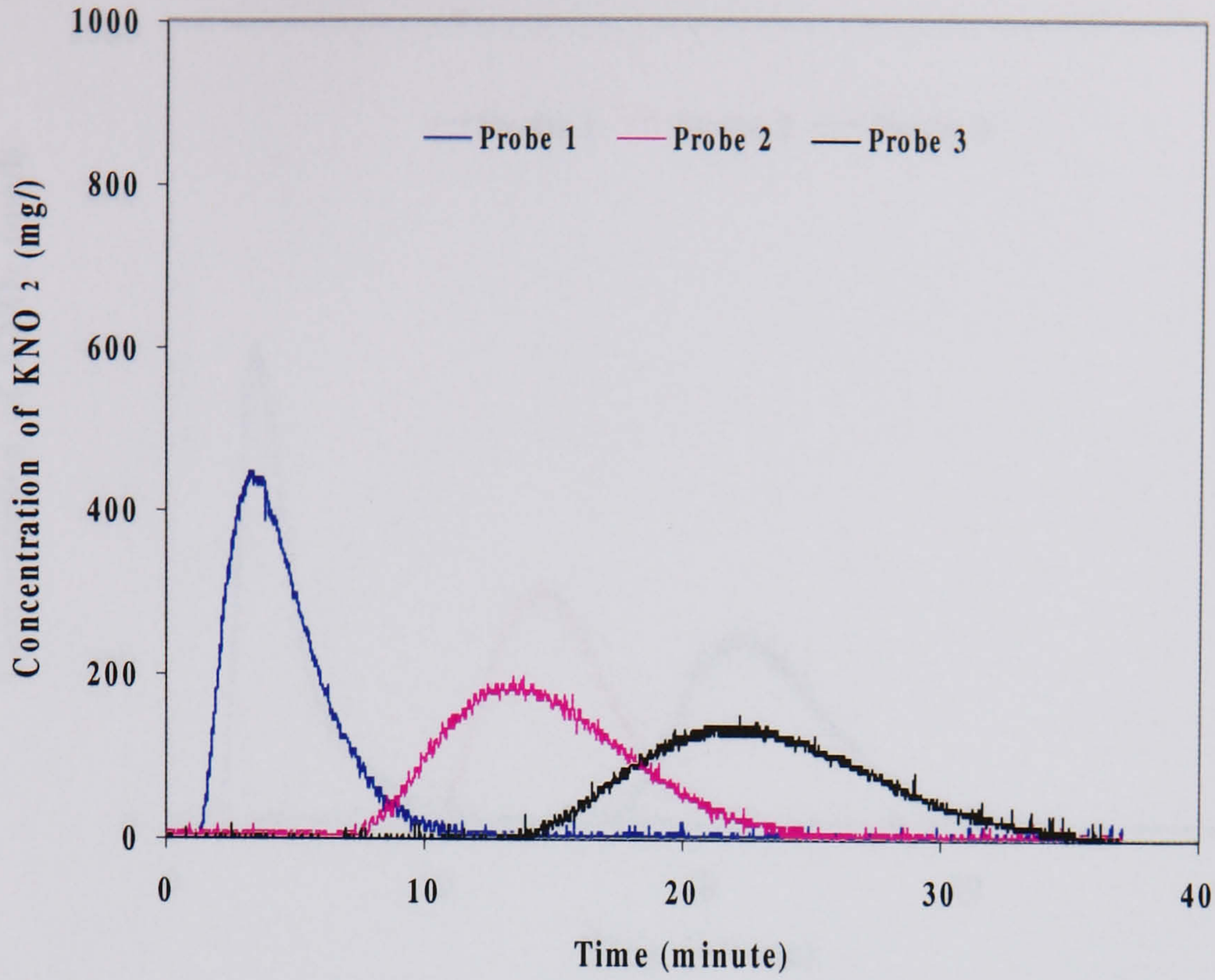

Figure A2.3. Concentration measurement, Re_o = 7530 (x_o = 10 mm, f = 3 Hz), Re_n = 256

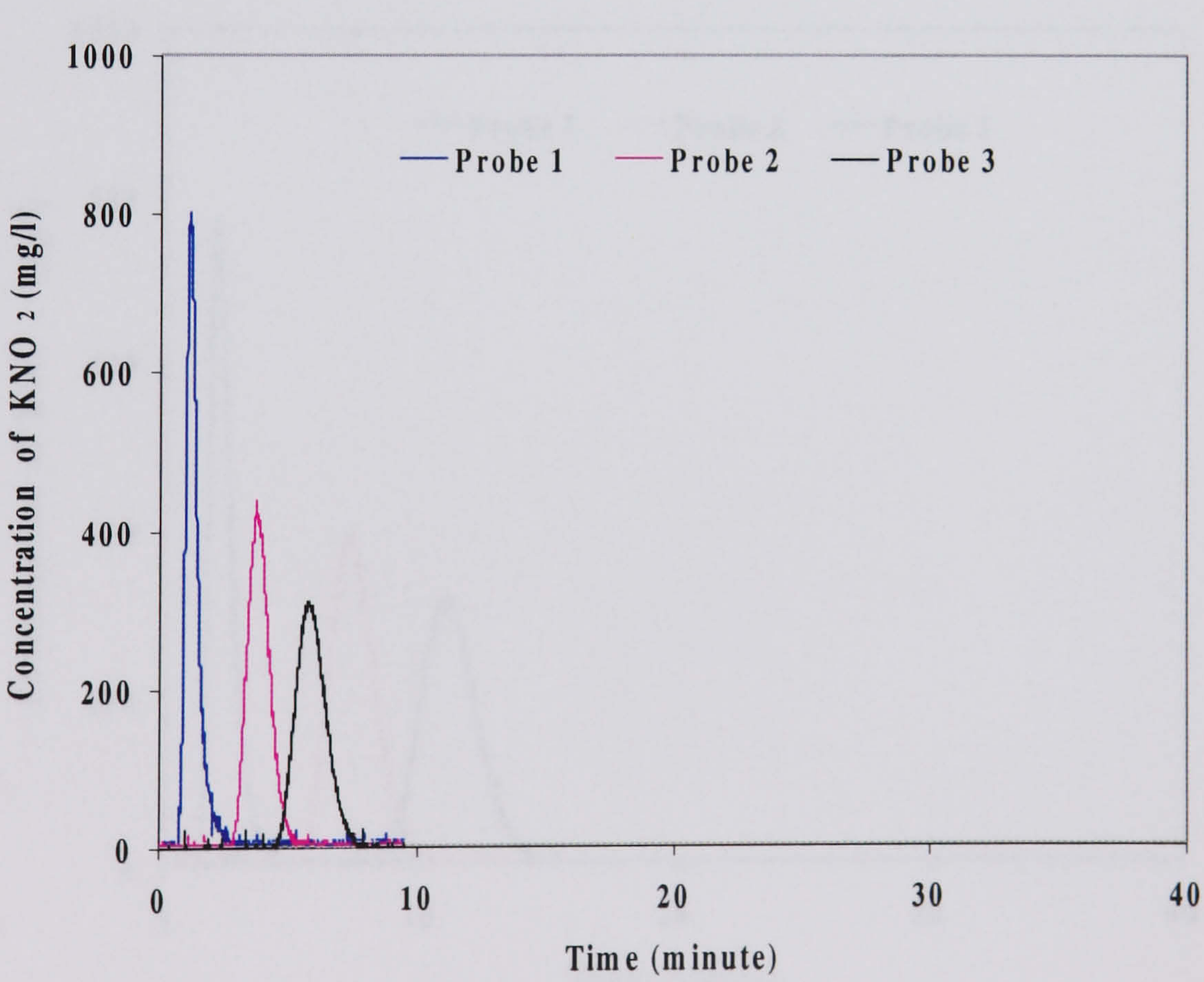

Figure A2.4. Concentration measurement, Re_o = 7530 (x_o = 10 mm, f = 3 Hz), Re_n = 987

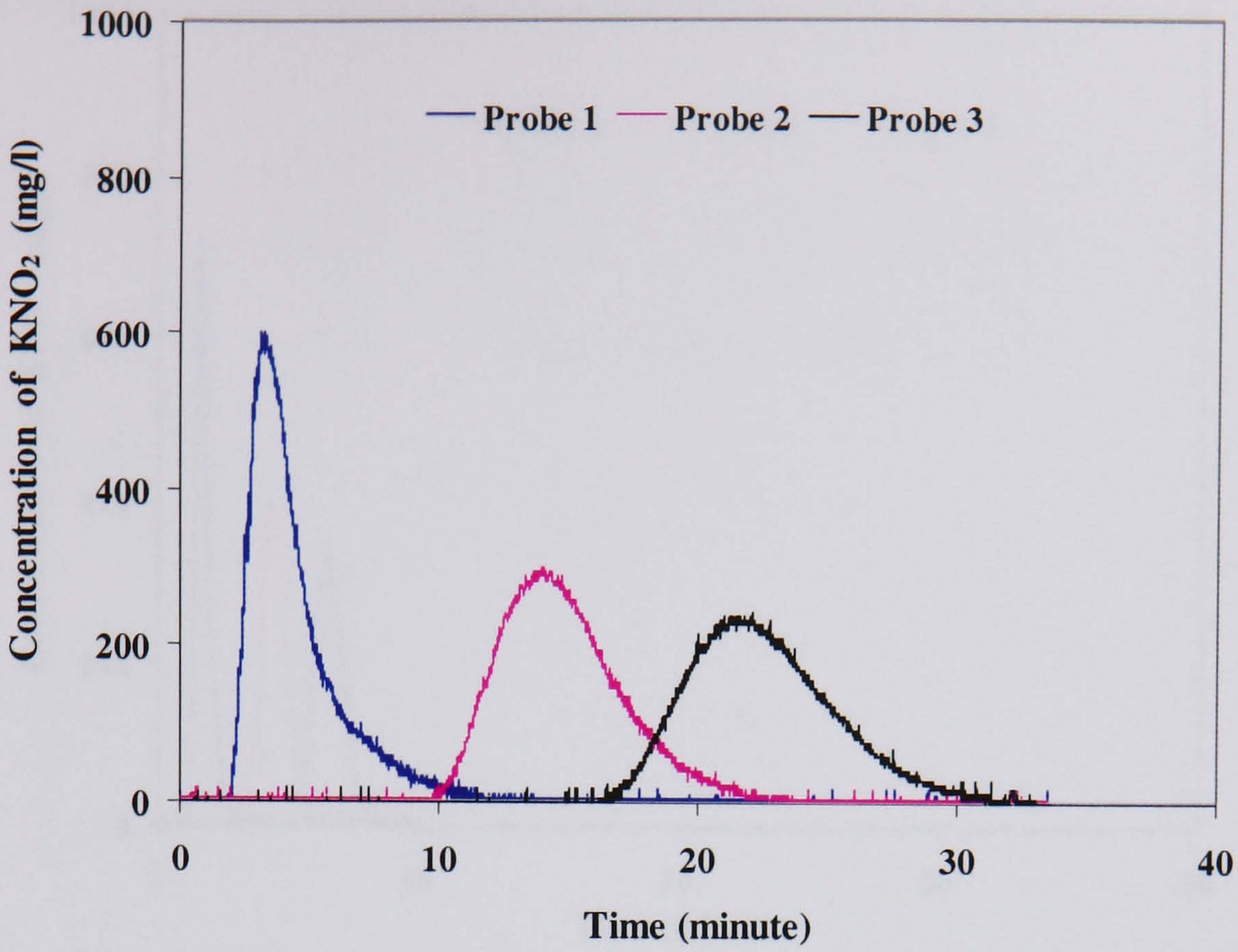

Figure A2.5. Concentration measurement,
$Re_o = 0$, $Re_n = 272$

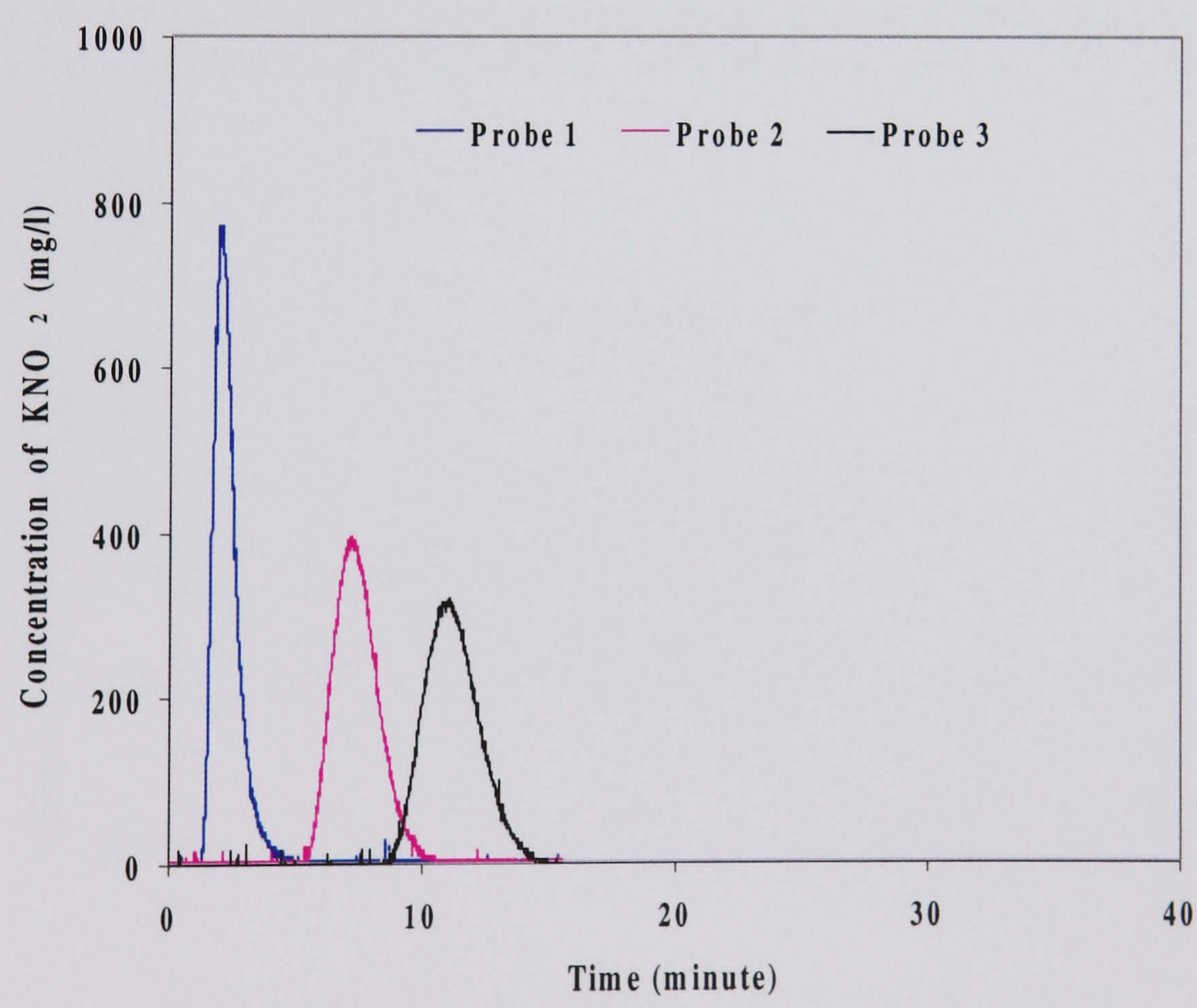

Figure A2.6. Concentration measurement,
$Re_o = 0$, $Re_n = 504$

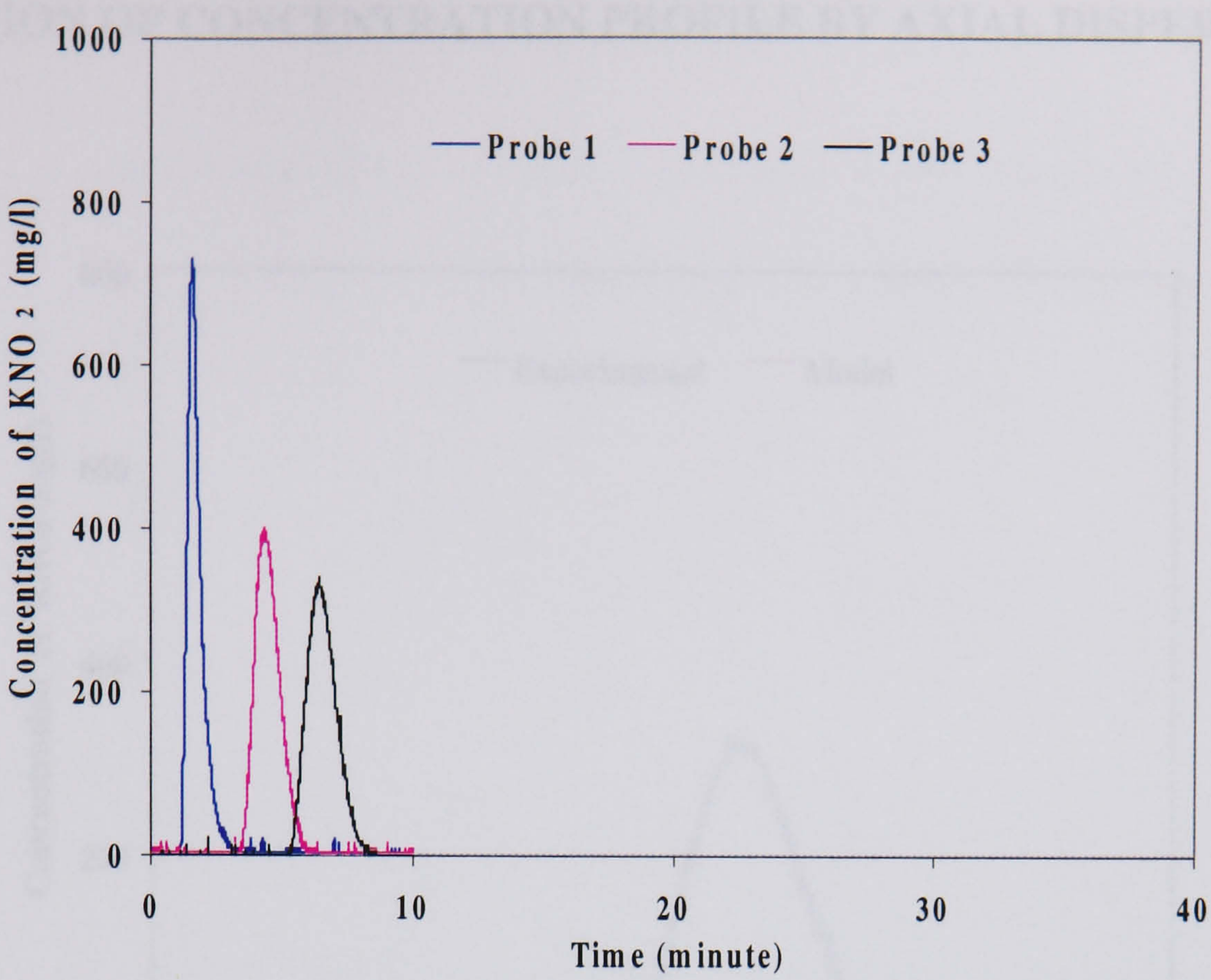

Figure A2.7. Concentration measurement,
$Re_o = 0$, $Re_n = 955$

PREDICTION OF CONCENTRATION PROFILE BY AXIAL DISPERSION MODEL

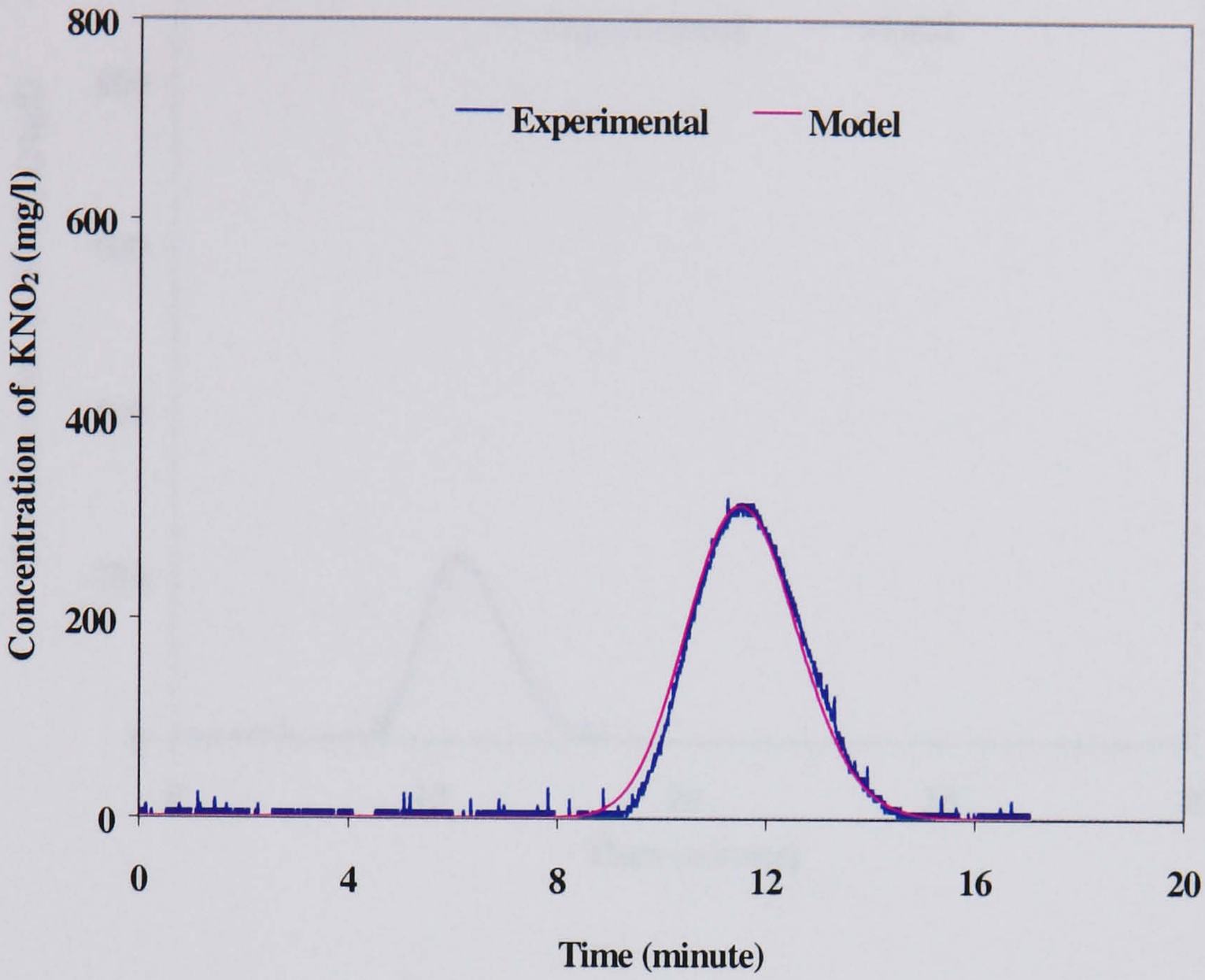

Figure A2.8. Prediction of concentration profile 3 from profile 1 using axial dispersion model, Re_o = 9036 (4 mm, 3 Hz), Re_n = 488

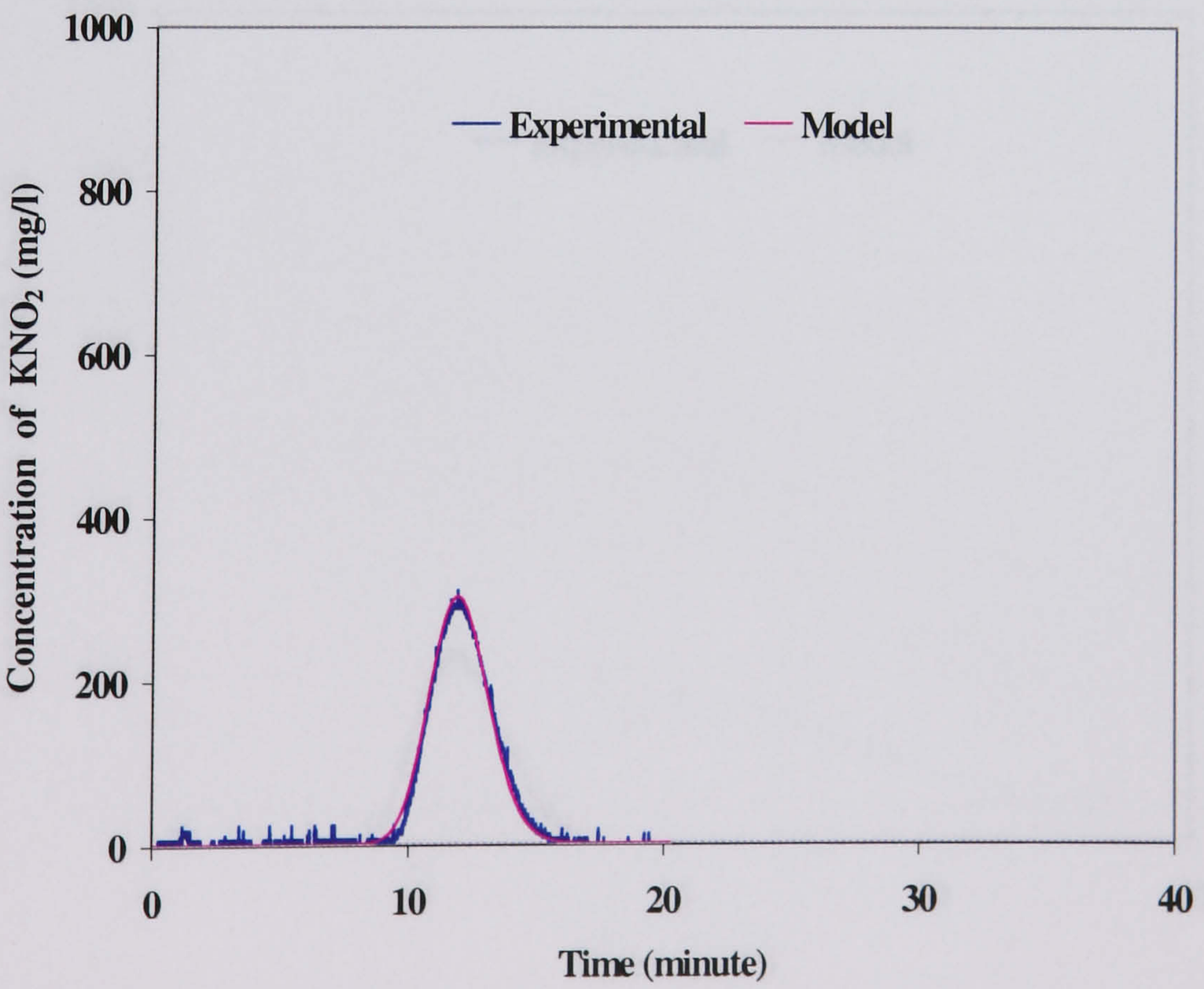

Figure A2.9. Prediction of concentration profile 3 from profile 1 using axial dispersion model, Re_o = 9036 (6 mm, 3 Hz), Re_n = 504

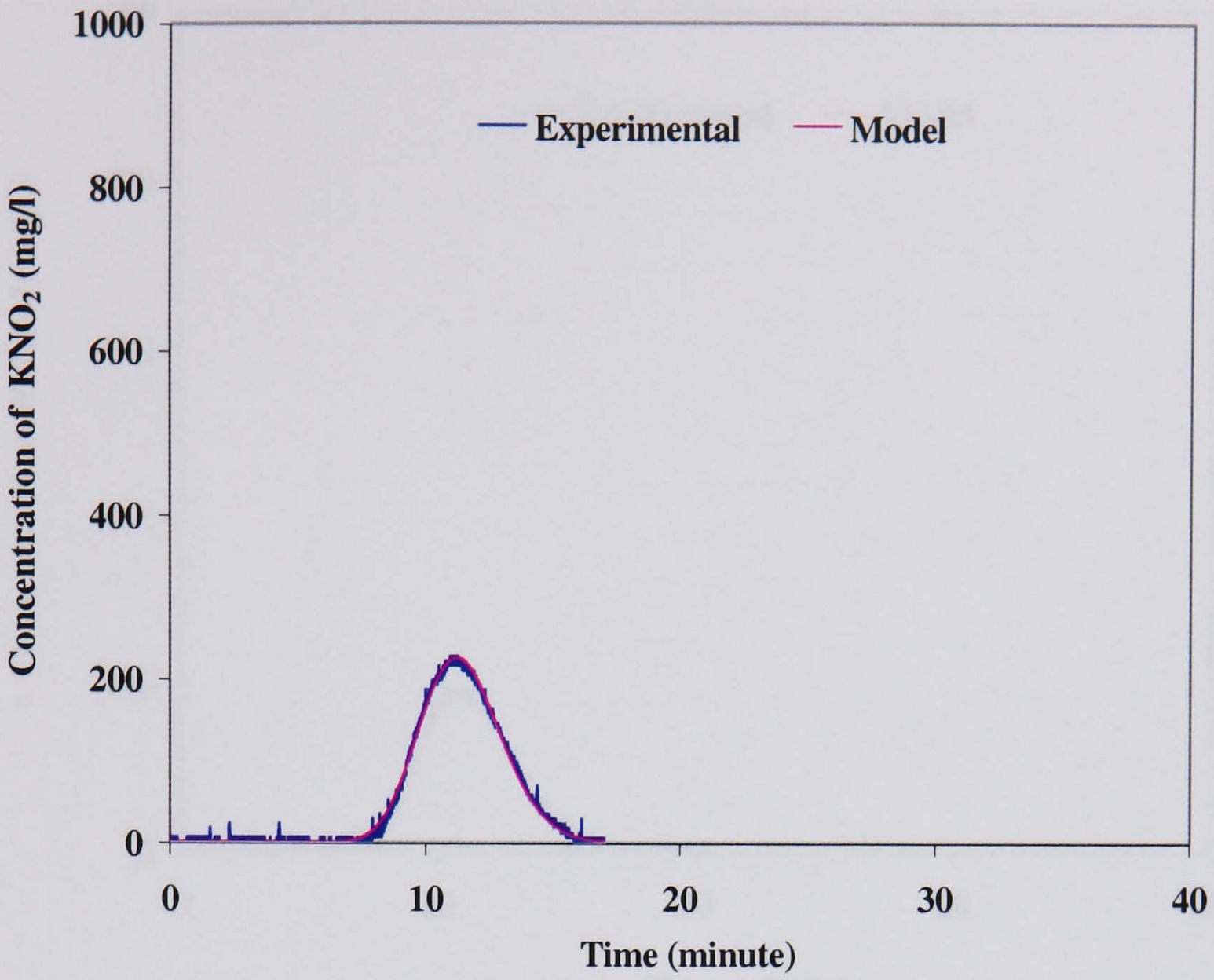

Figure A2.10. Prediction of concentration profile 3 from profile 1 using axial dispersion model, Re_o = 9036 (12 mm, 3 Hz), Re_n = 525

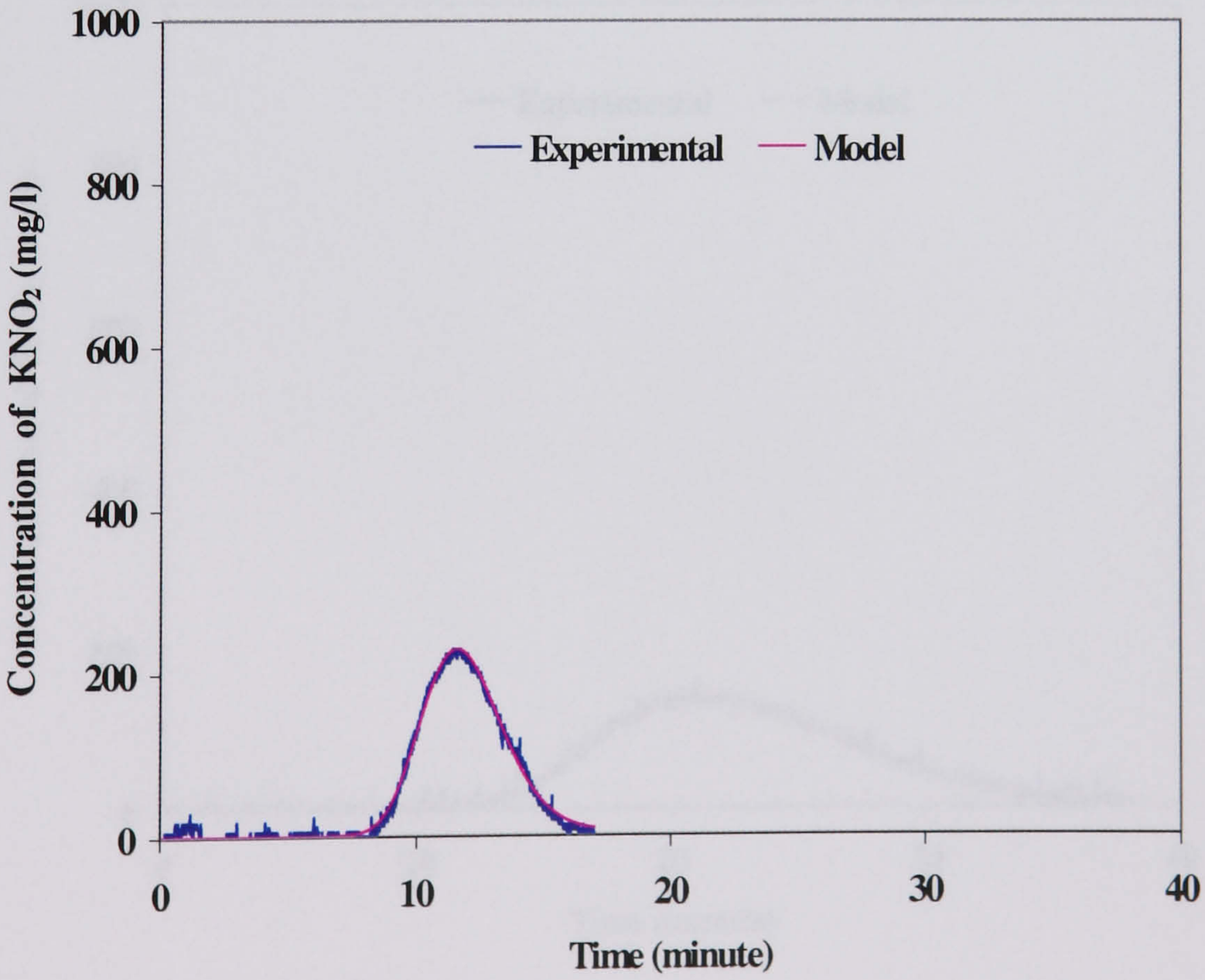

Figure A2.11. Prediction of concentration profile 3 from profile 1 using axial dispersion model, Re_o = 9036 (12 mm, 1 Hz), Re_n = 525

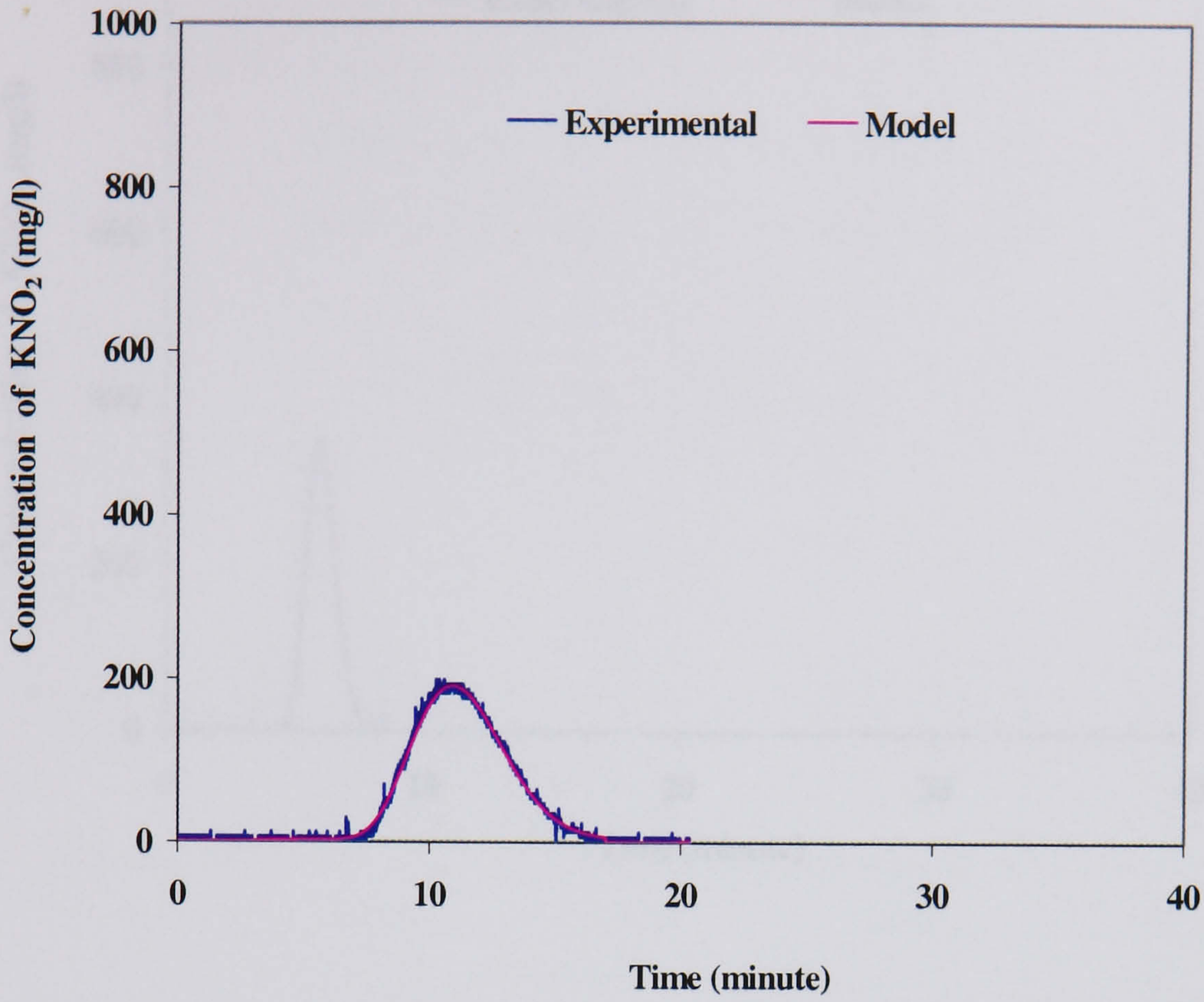

Figure A2.12. Prediction of concentration profile 3 from profile 1 using axial dispersion model, Re_o = 9036 (12 mm, 2 Hz), Re_n = 498

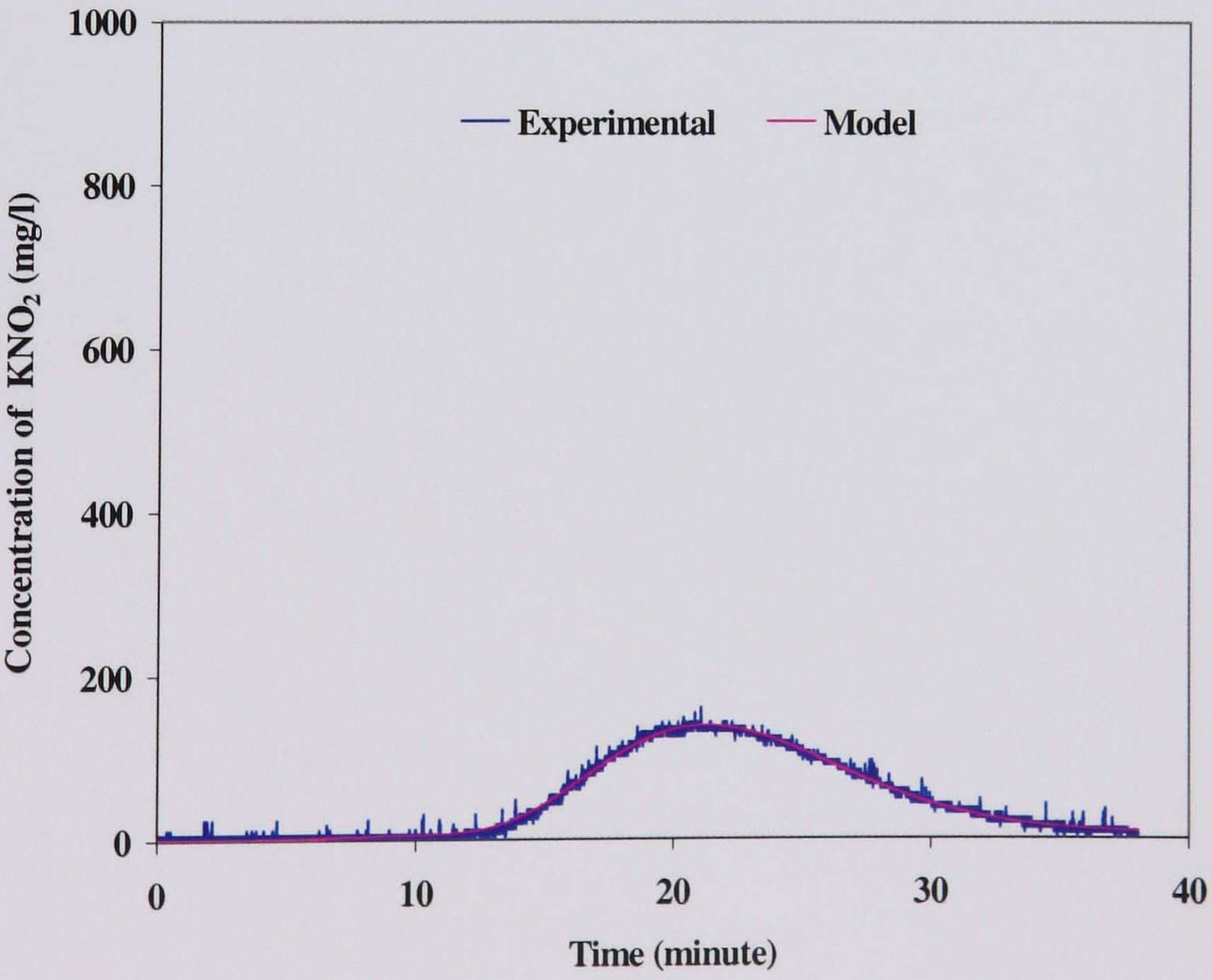

Figure A2.13. Prediction of concentration profile 3 from profile 1 using axial dispersion model, Re_o = 9036 (12 mm, 3 Hz), Re_n = 244

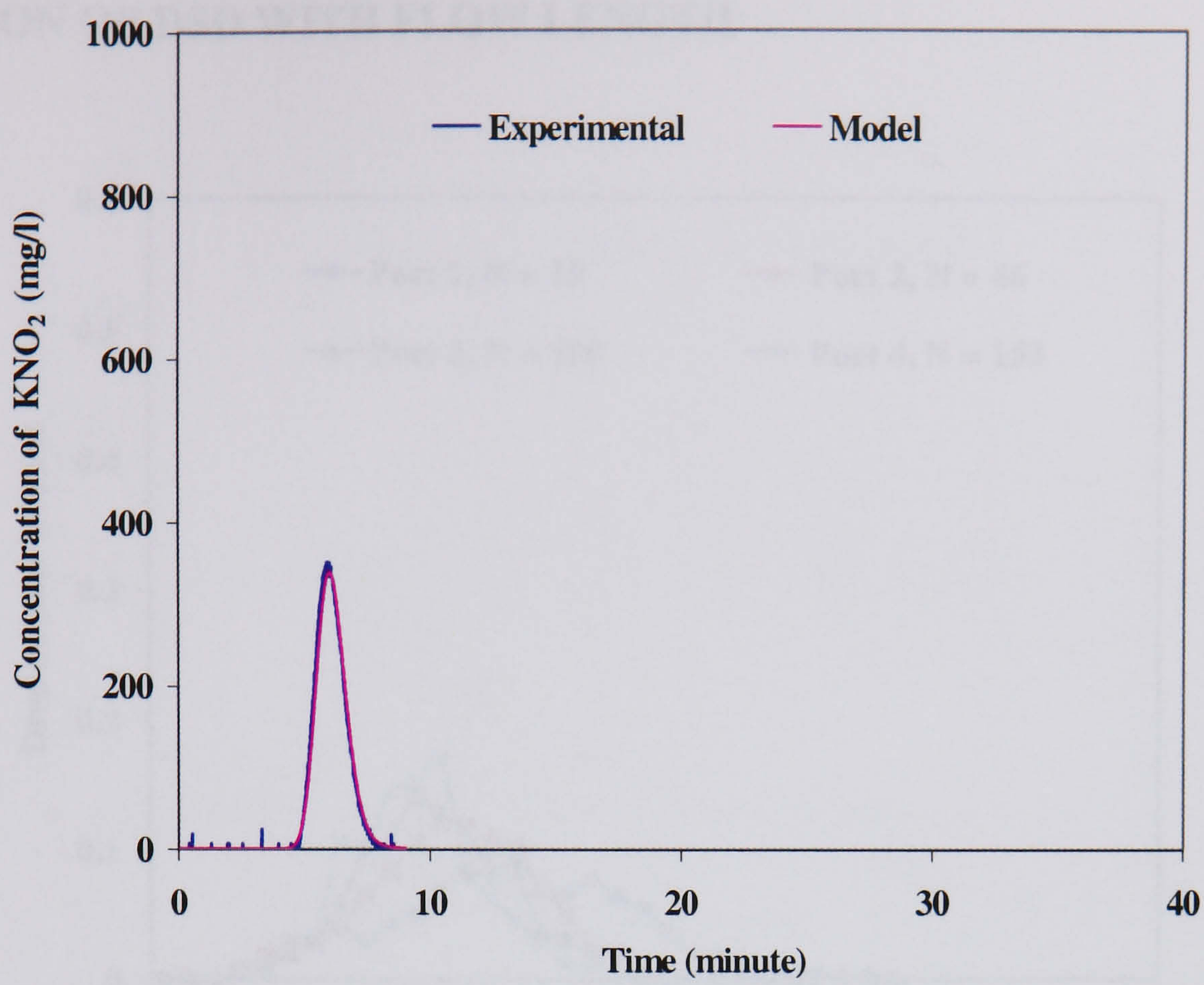

Figure A2.14. Prediction of concentration profile 3 from profile 1 using axial dispersion model, Re_o = 9036 (12 mm, 3 Hz), Re_n = 945

VARIATION OF DSD WITH FLOW LENGTH

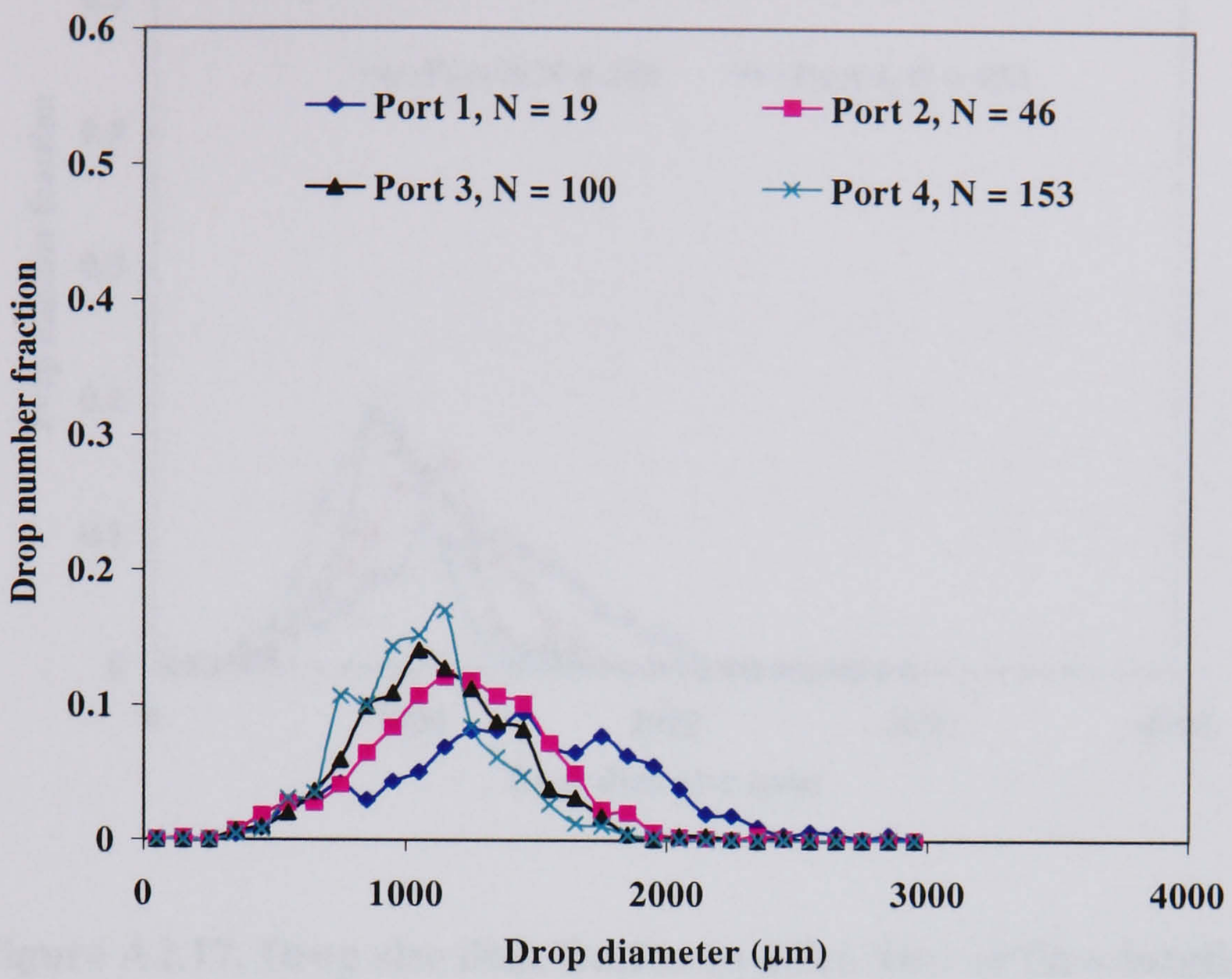

Figure A2.15. Drop size distribution as a function of flow length, Re_o = 3012 (x_o = 12 mm, f = 1 Hz); Re_n = 234

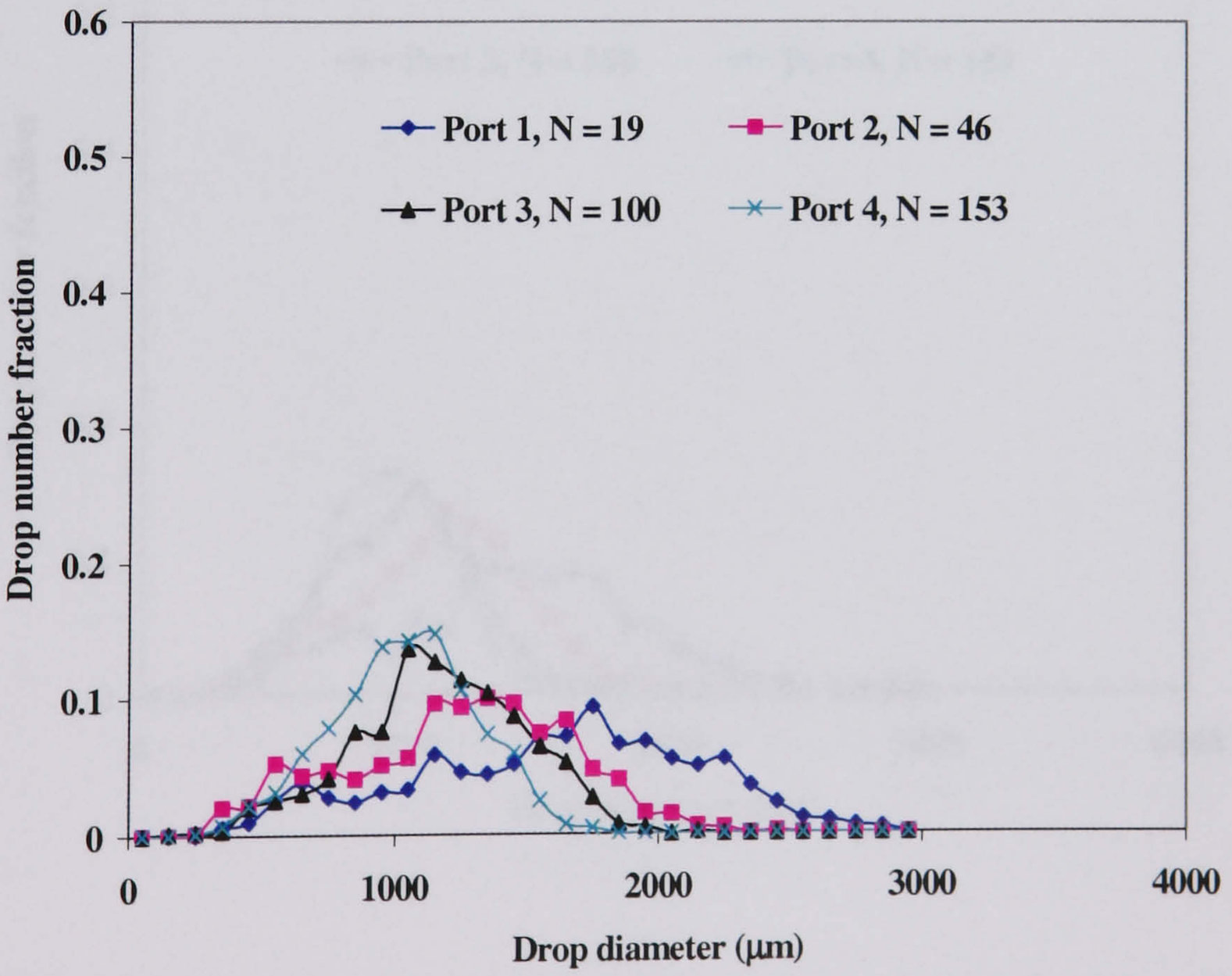

Figure A2.16. Drop size distribution as a function of flow length, Re_o = 3012 (x_o = 12 mm, f = 1 Hz); Re_n = 997

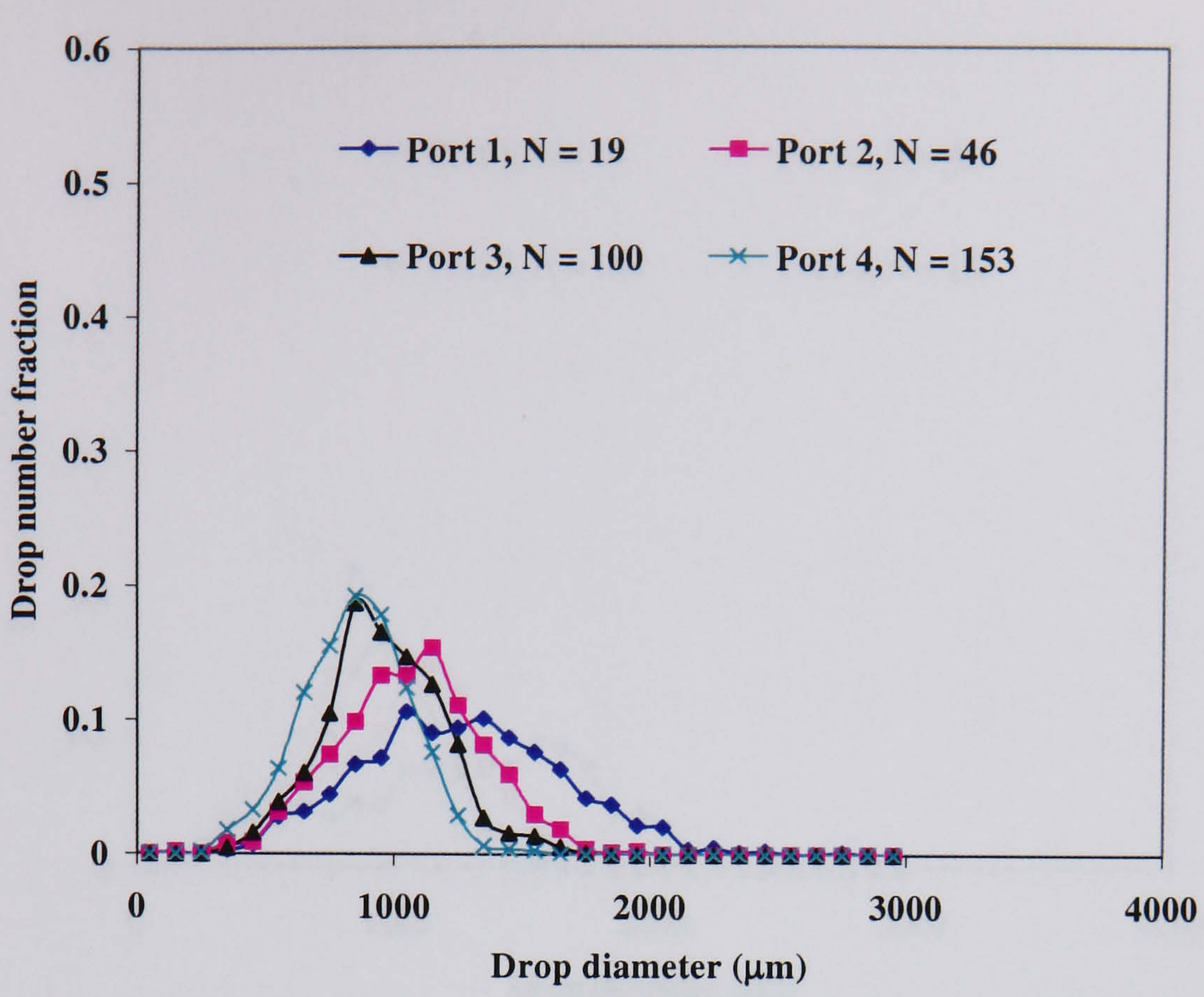

Figure A2.17. Drop size distribution as a function of flow length, Re_o = 3765 (x_o = 15 mm, f = 1 Hz); Re_n = 235

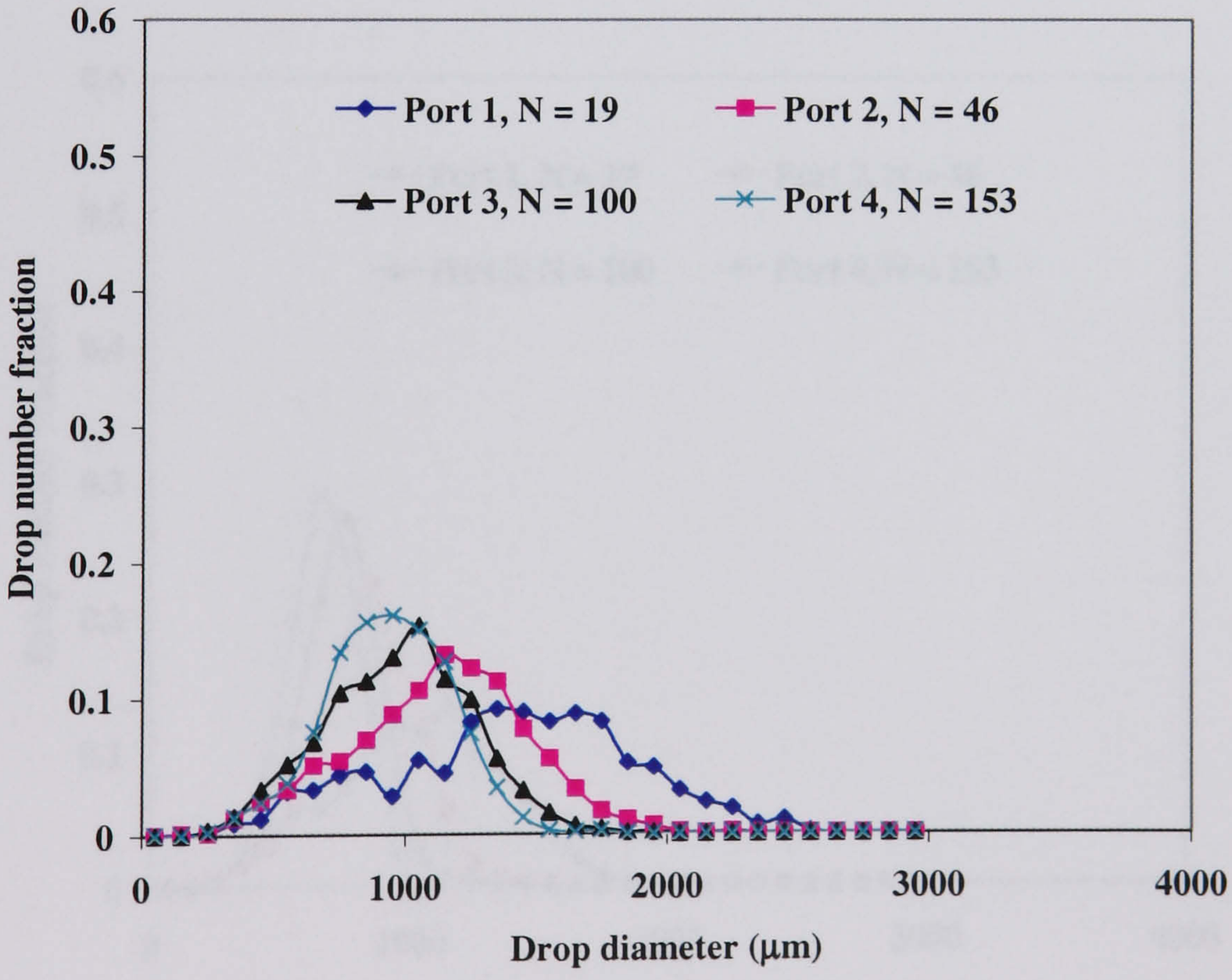

Figure A2.18. Drop size distribution as a function of flow length, Re_o = 3765 (x_o = 15 mm, f = 1 Hz); Re_n = 997

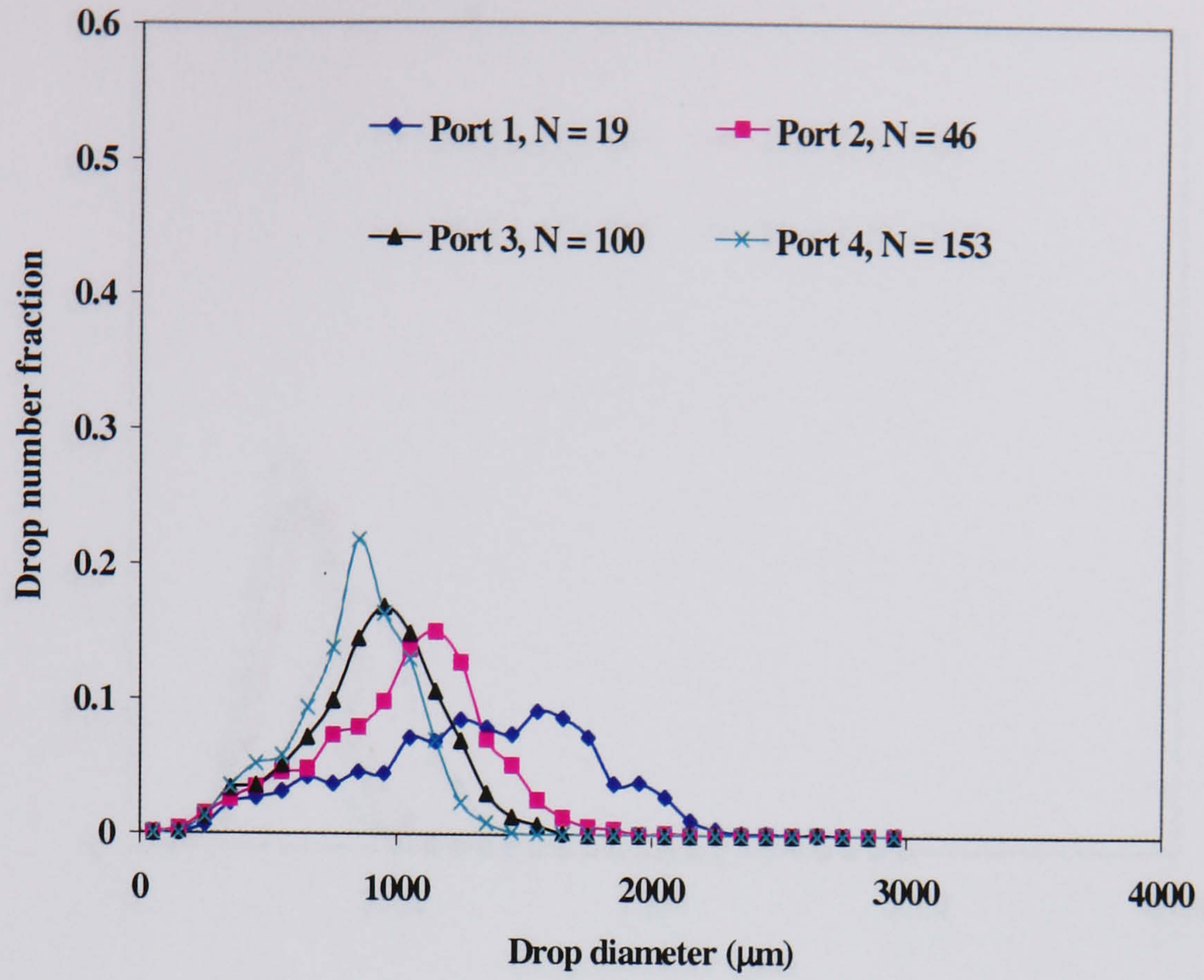

Figure A2.19. Drop size distribution as a function of flow length, Re_o = 4016 (x_o = 8 mm, f = 2 Hz); Re_n = 1004

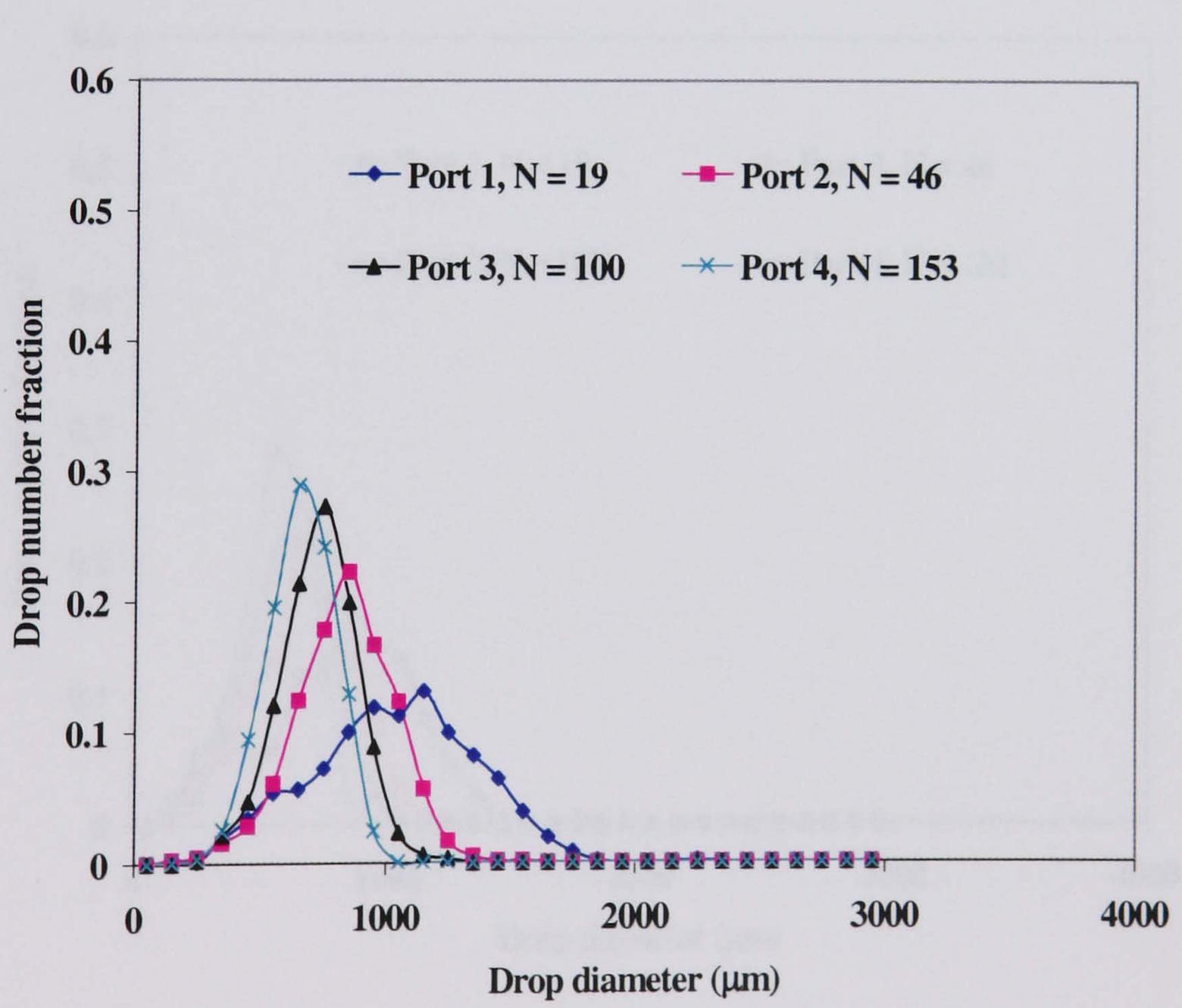

Figure A2.20. Drop size distribution as a function of flow length, Re_o = 5020 (x_o = 10 mm, f = 2 Hz); Re_n = 1010

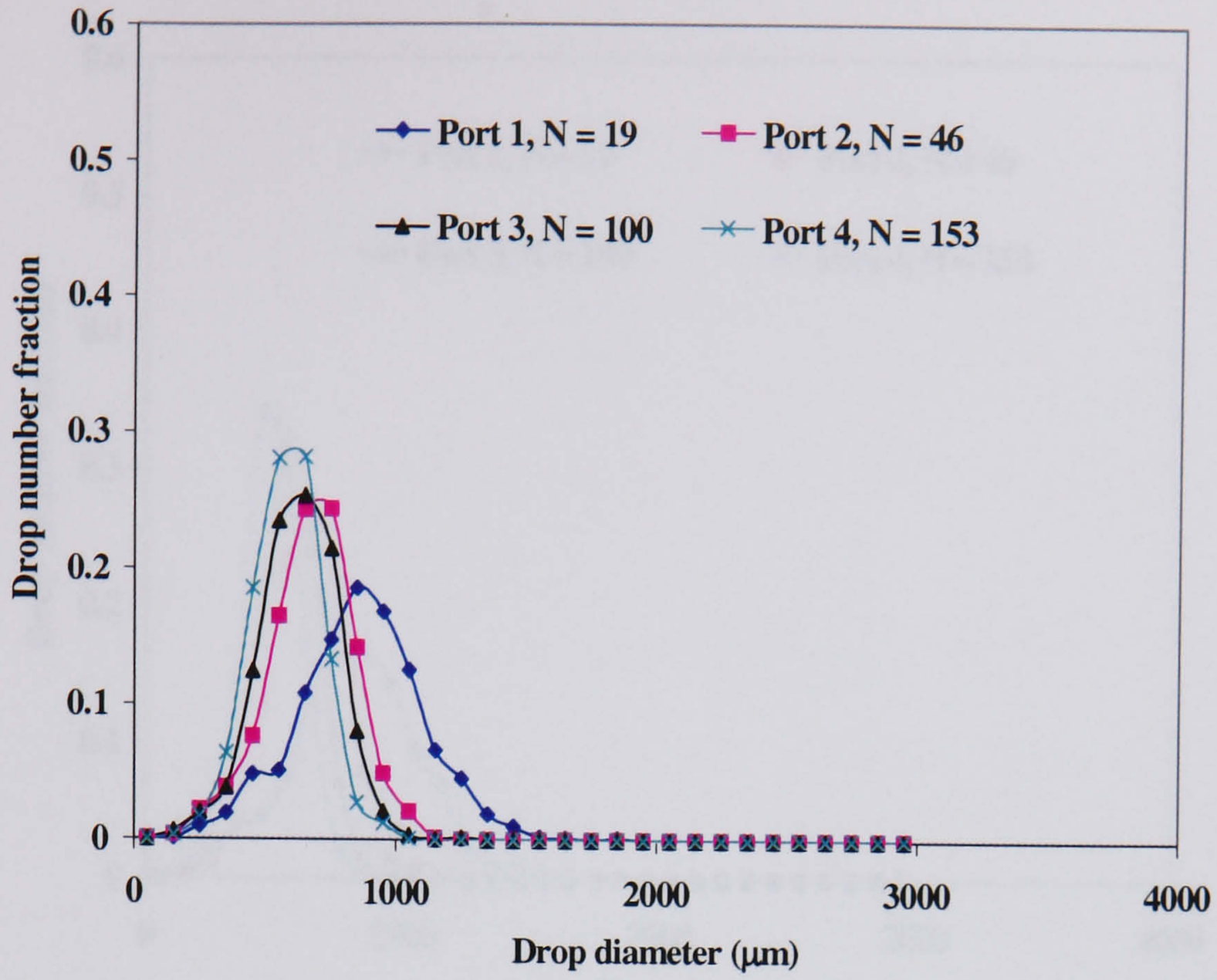

Figure A2.21. Drop size distribution as a function of flow length, Re_o = 6024 (x_o = 12 mm, f = 2 Hz); Re_n = 239

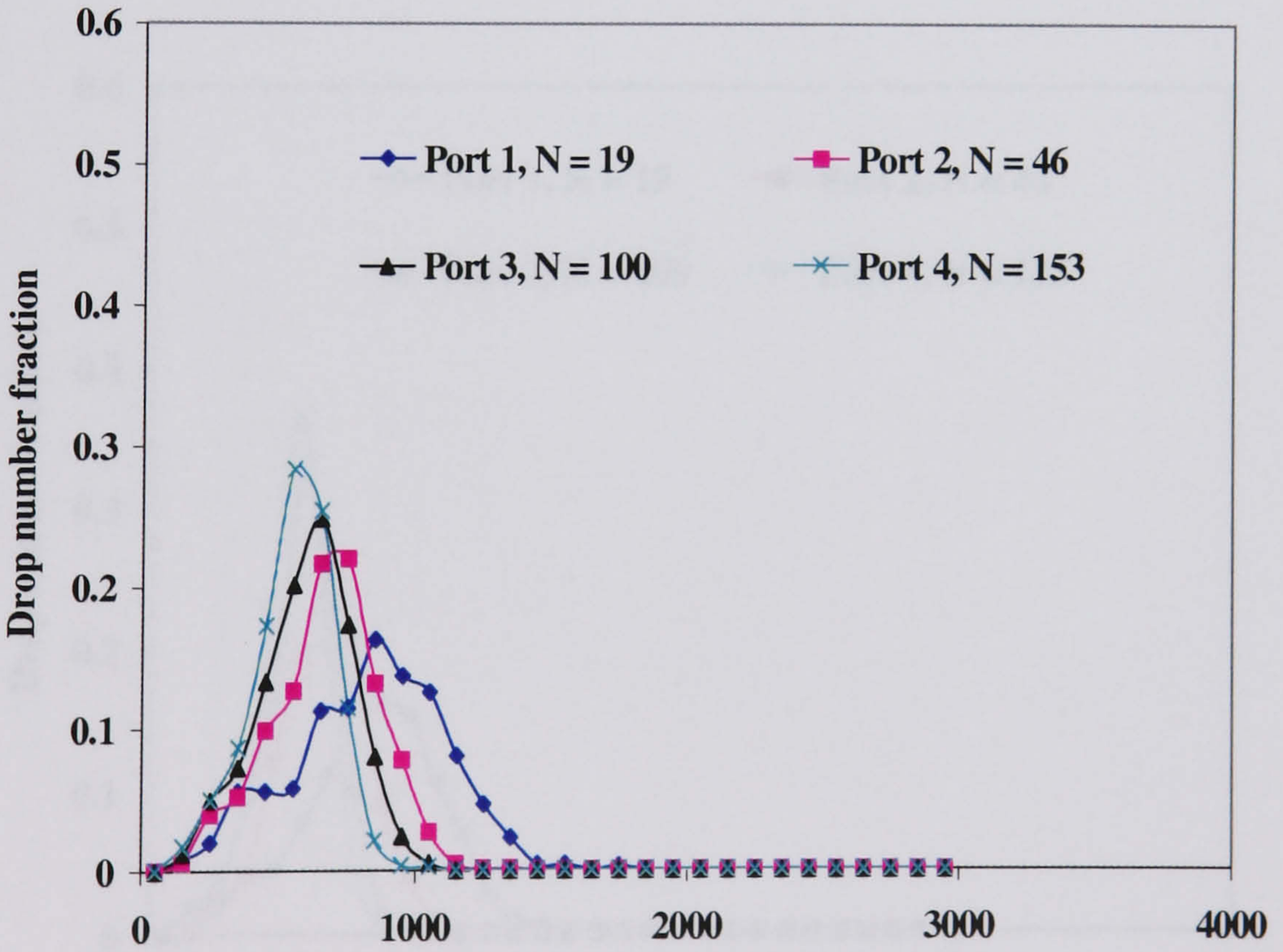

Figure A2.22. Drop size distribution as a function of flow length, Re_o = 6024 (x_o = 12 mm, f = 2 Hz); Re_n = 998

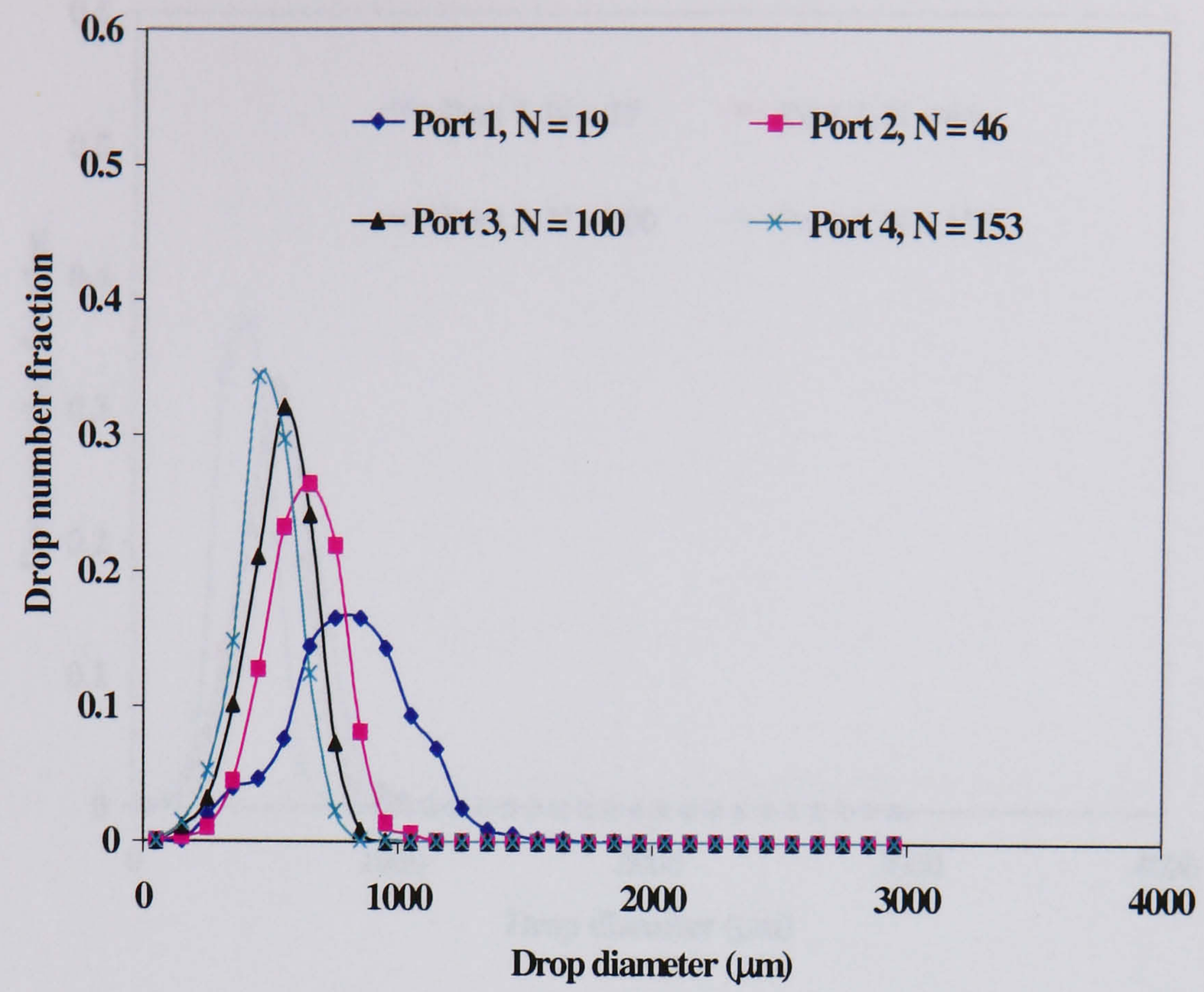

Figure A2.23. Drop size distribution as a function of flow length, Re_o = 7530 (x_o = 15 mm, f = 2 Hz); Re_n = 252

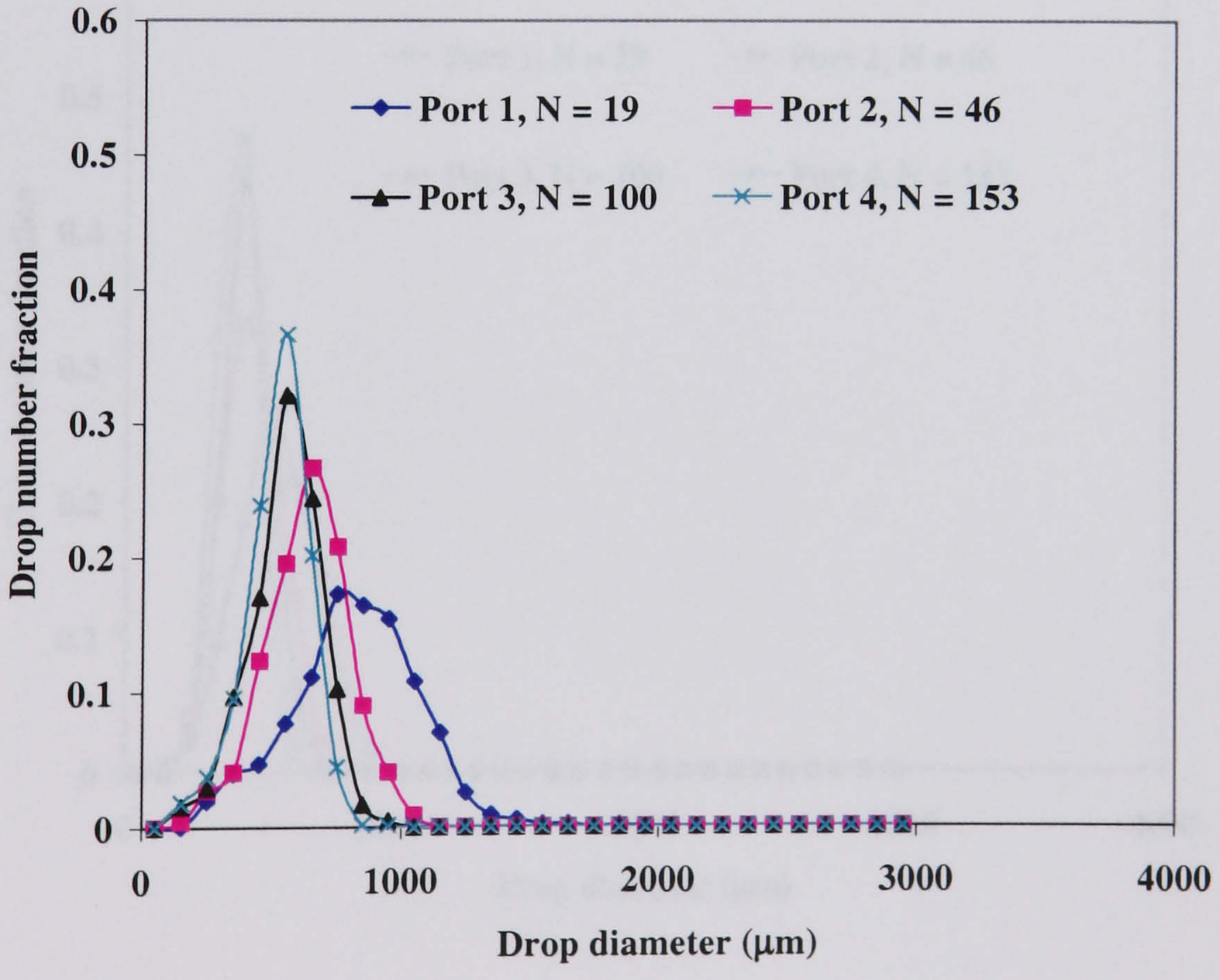

Figure A2.24. Drop size distribution as a function of flow length, Re_o = 7530 (x_o = 15 mm, f = 2 Hz); Re_n = 1016

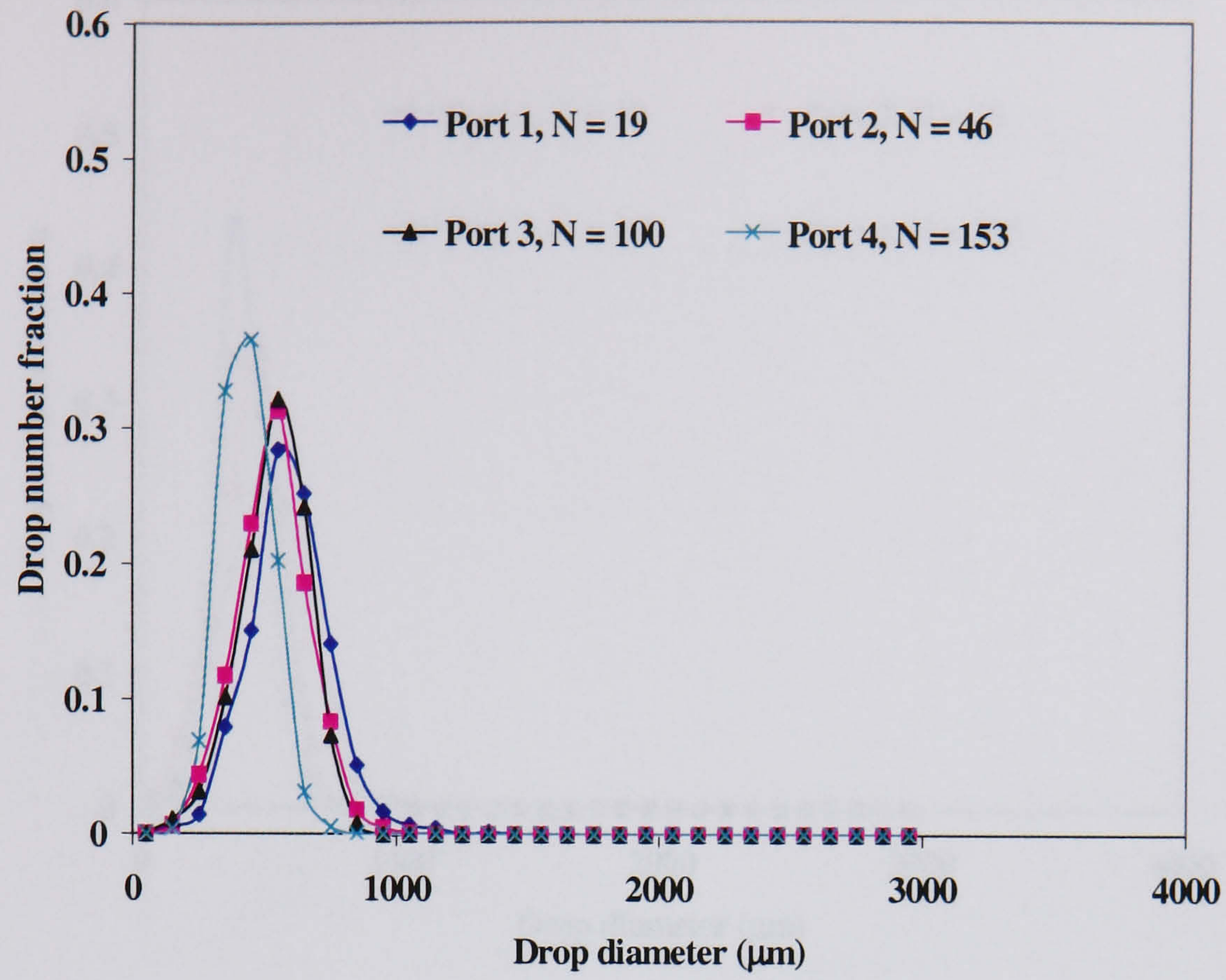

Figure A2.25. Drop size distribution as a function of flow length, Re_o = 9036 (x_o = 12 mm, f = 3 Hz); Re_n = 264

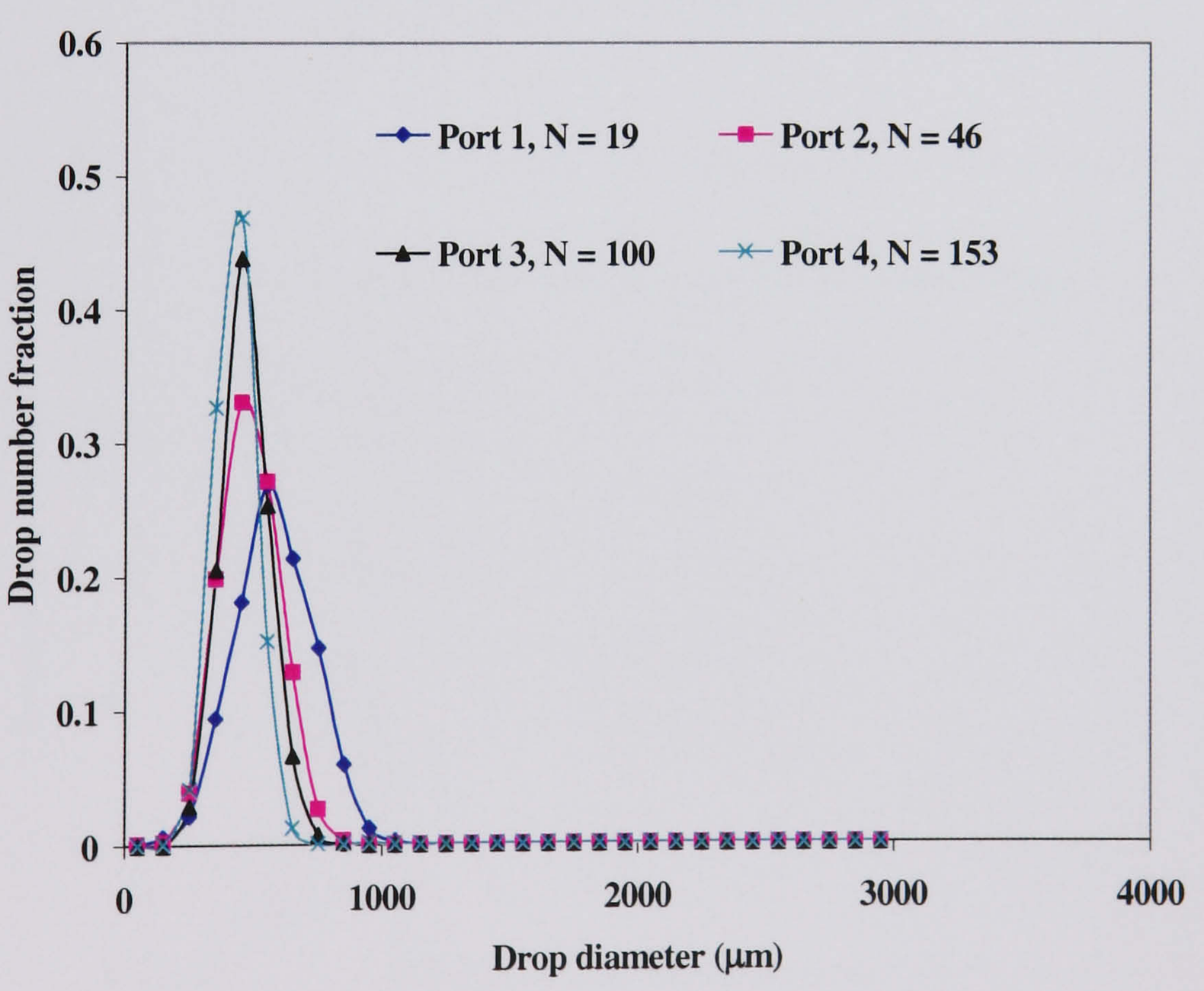

Figure A2.26. Drop size distribution as a function of flow length, Re_o = 9036 (x_o = 12 mm, f = 3 Hz); Re_n = 1016

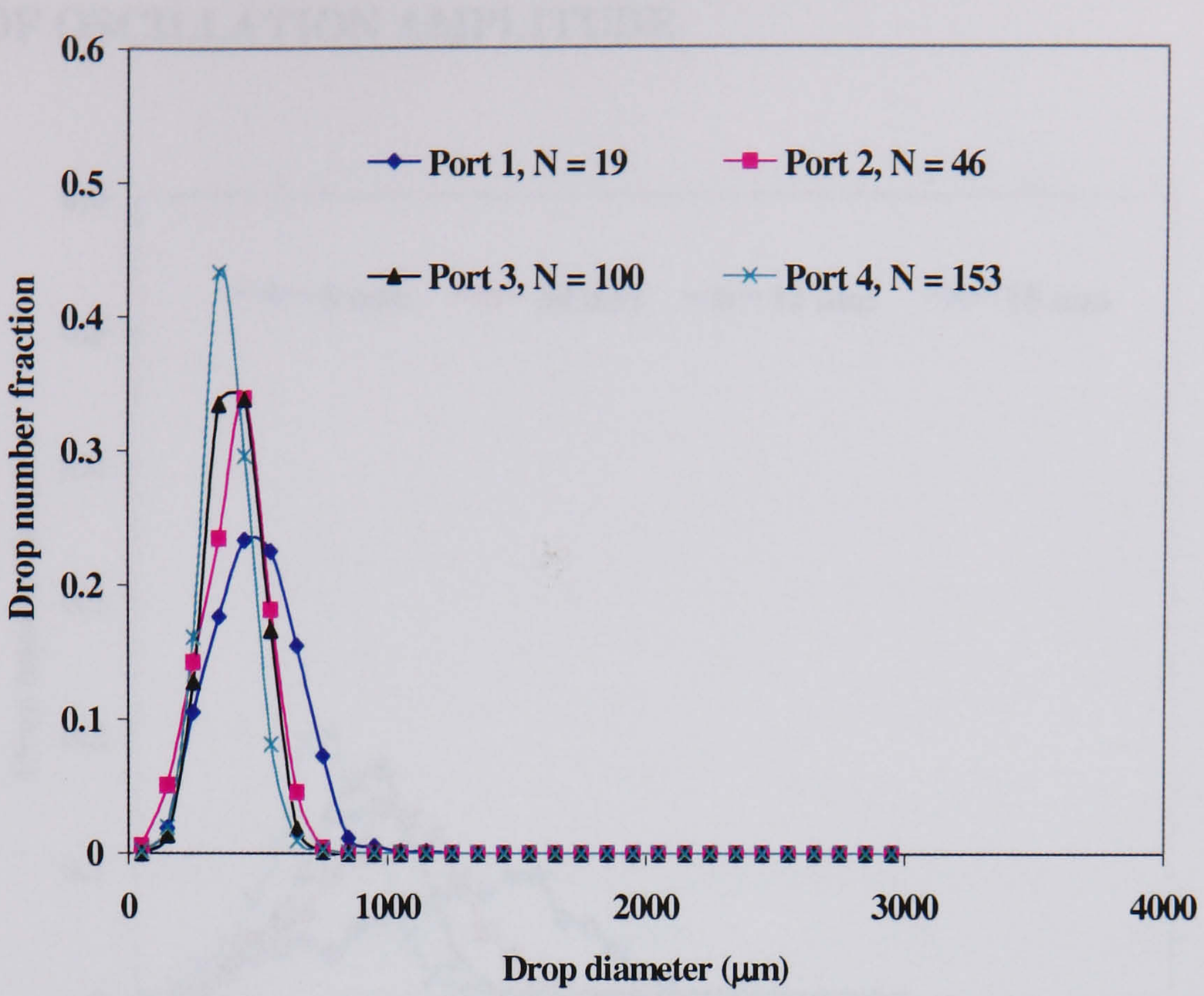

Figure A2.27. Drop size distribution as a function of flow length, Re_o = 11295 (x_o = 15 mm, f = 3 Hz); Re_n = 264

EFFECT OF OSCILLATION AMPLITUDE

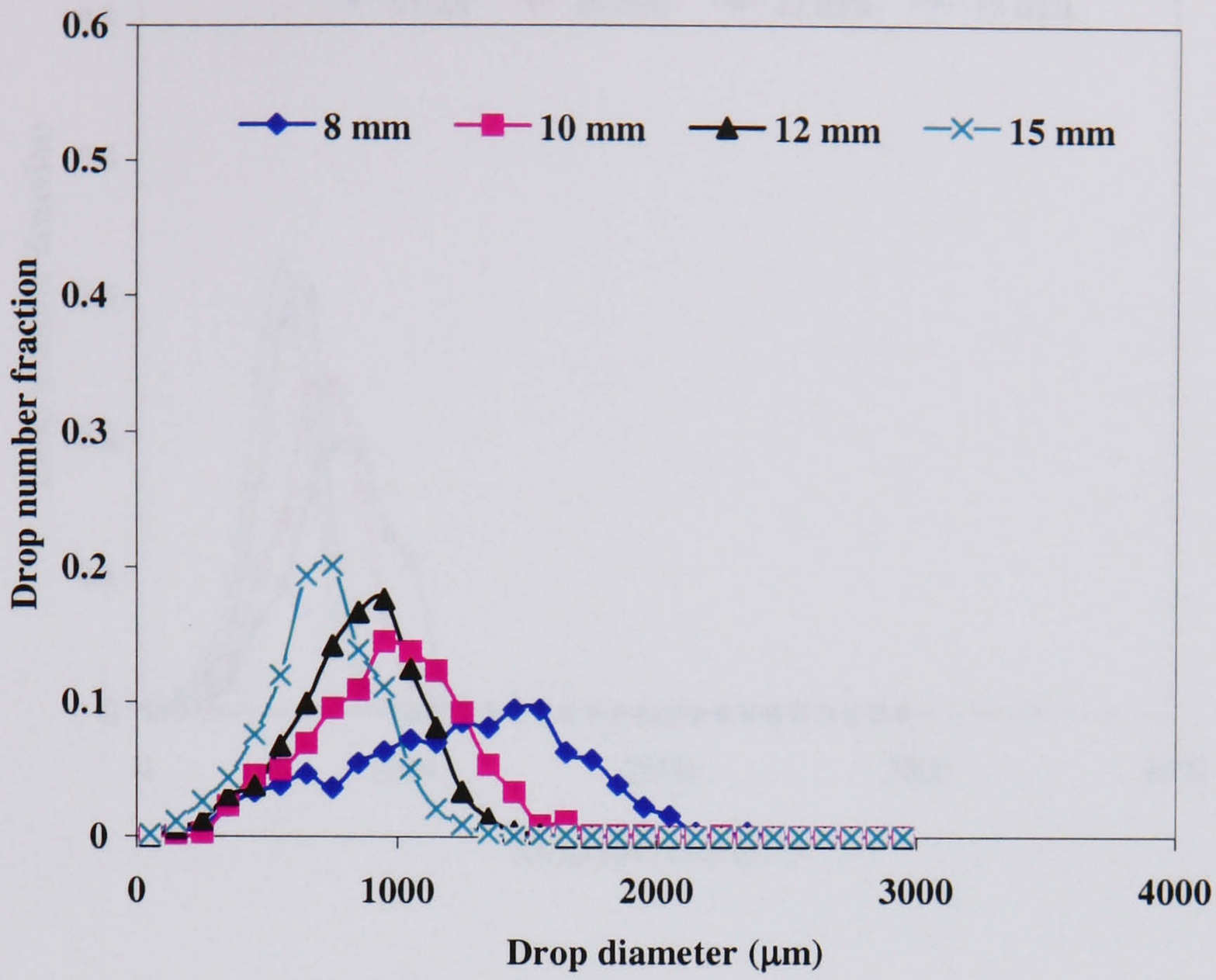

Figure A2.28. Effect of oscillation amplitude on droplet size distribution (f = 2.0 Hz, Re_n=541), Port 1

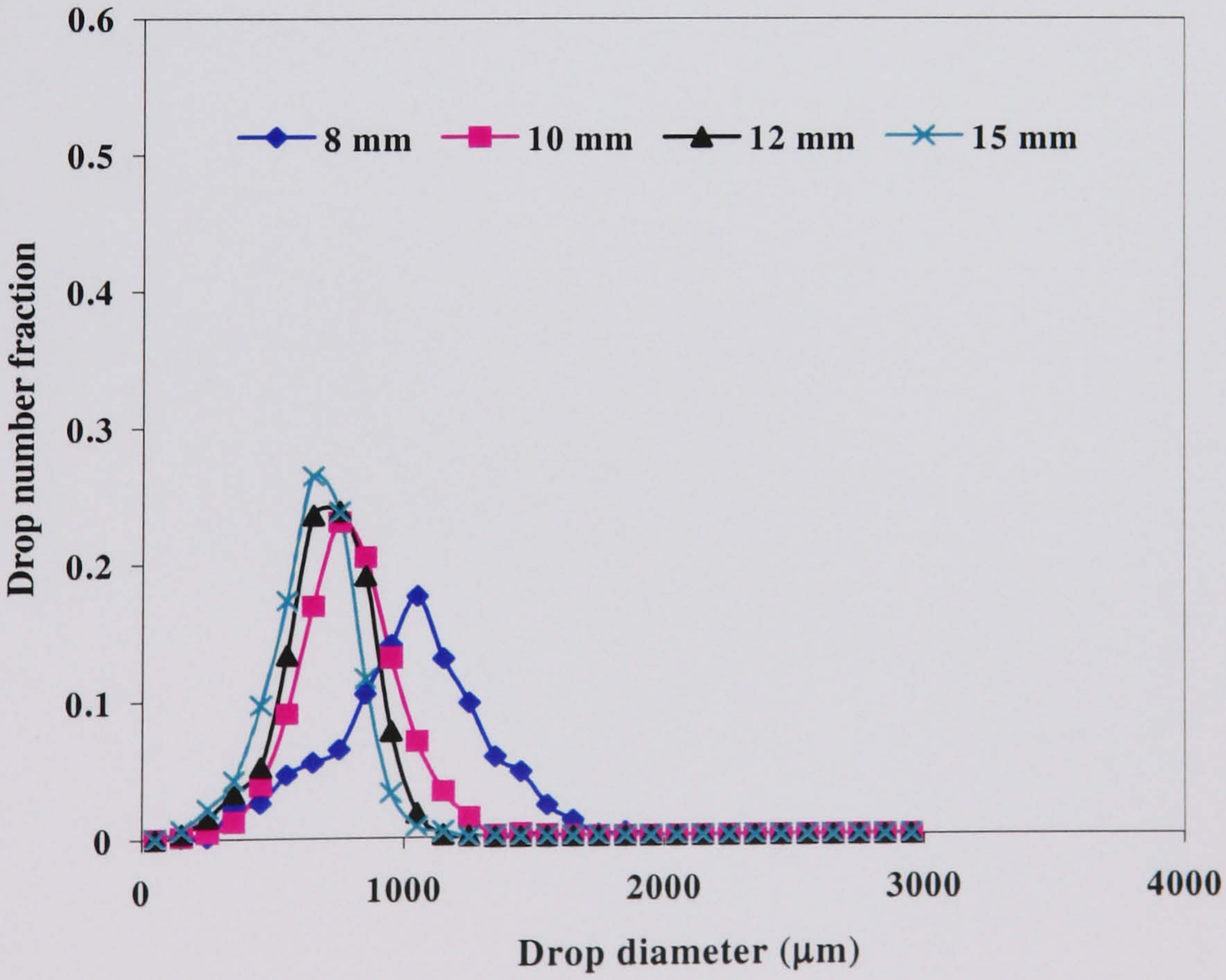

Figure A2.29. Effect of oscillation amplitude on droplet size distribution (f = 2.0 Hz, Re_n= 554), Port 2

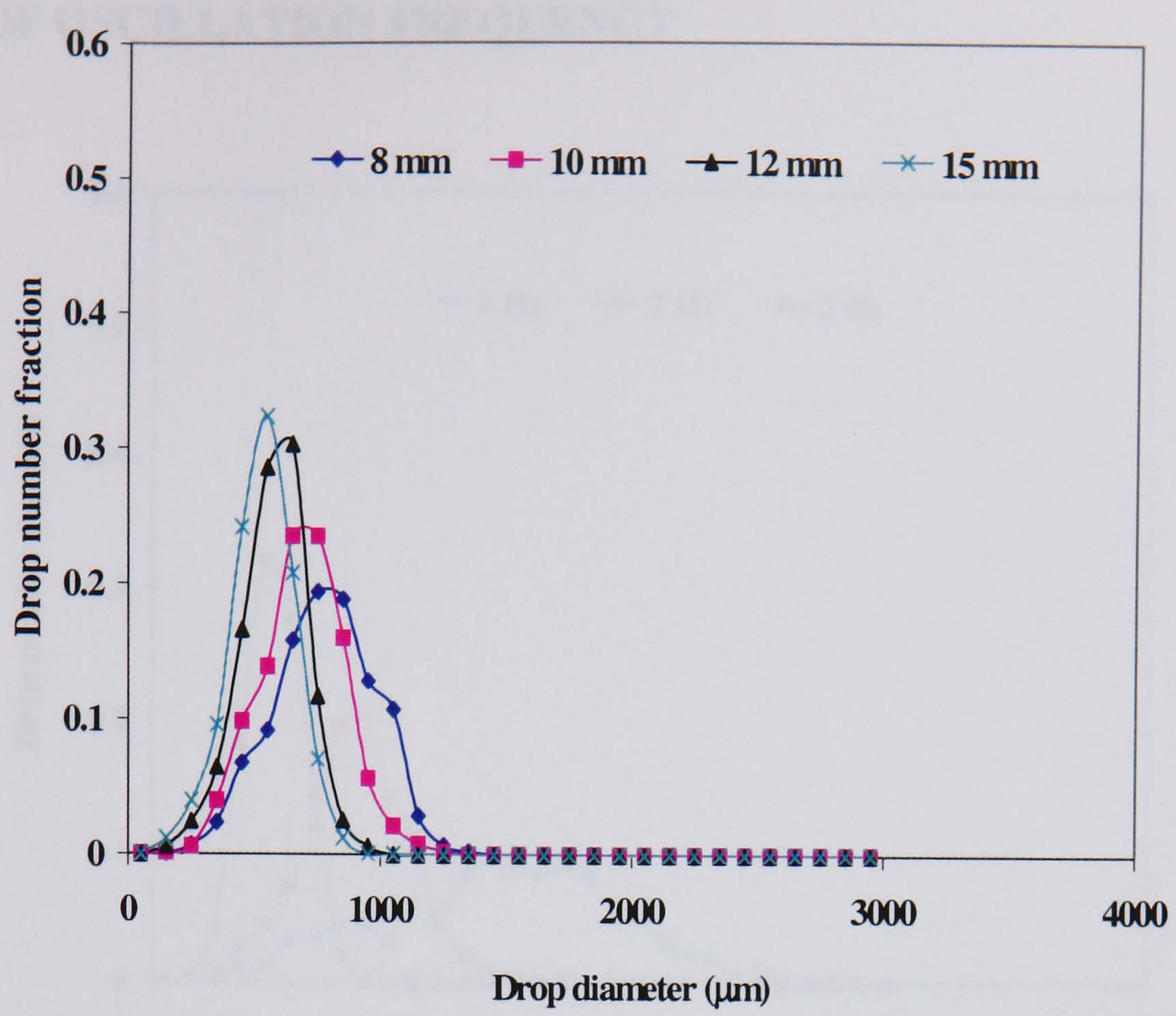

Figure A2.30. Effect of oscillation amplitude on droplet size distribution (f = 2.0 Hz, Re_n = 541), Port 4, (Horizontal OBTR).

EFFECT OF OSCILLATION FREQUENCY

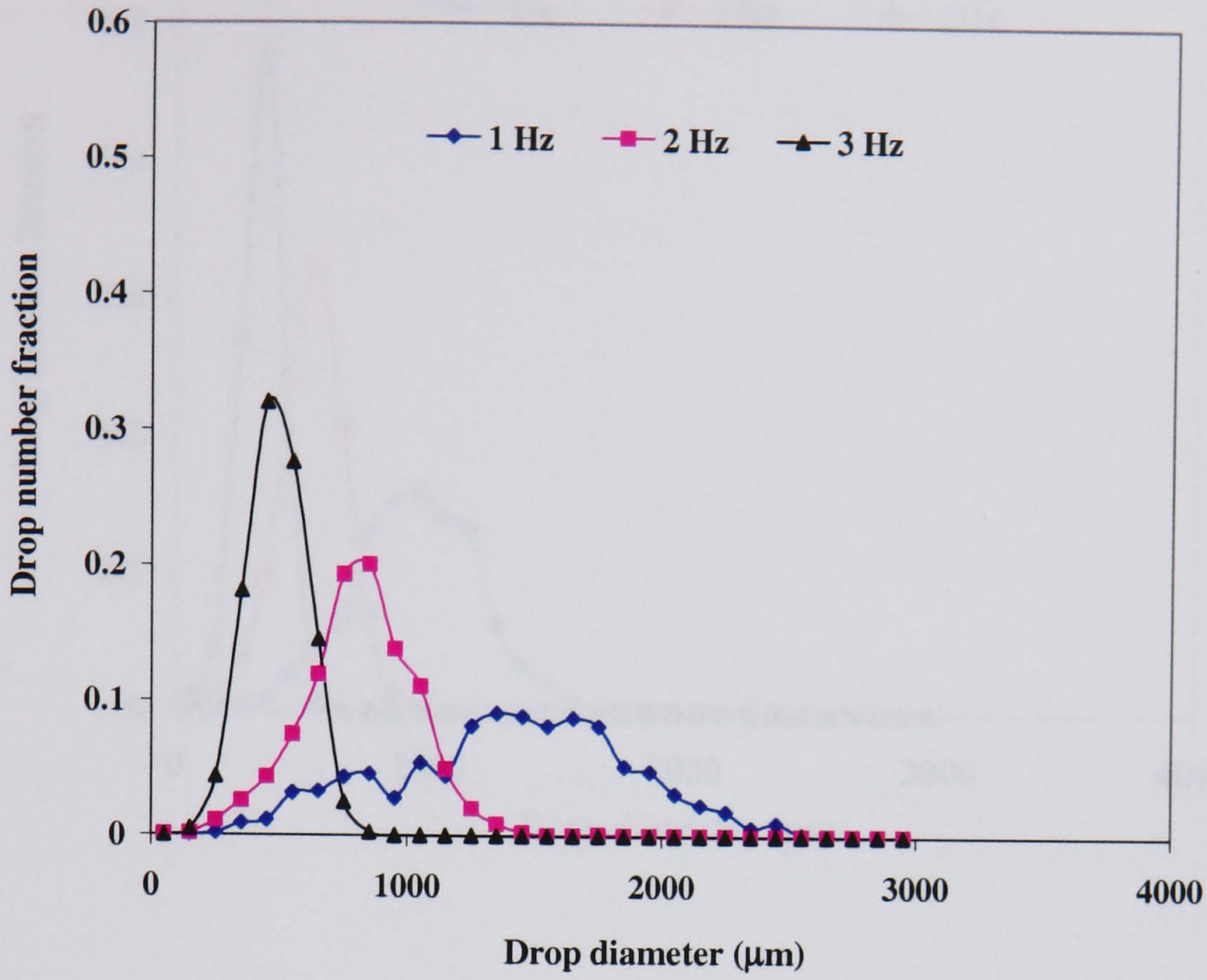

Figure A2.31. Effect of oscillation frequency on droplet size distribution (x_o = 15 mm, Re_n = 541), Port 1

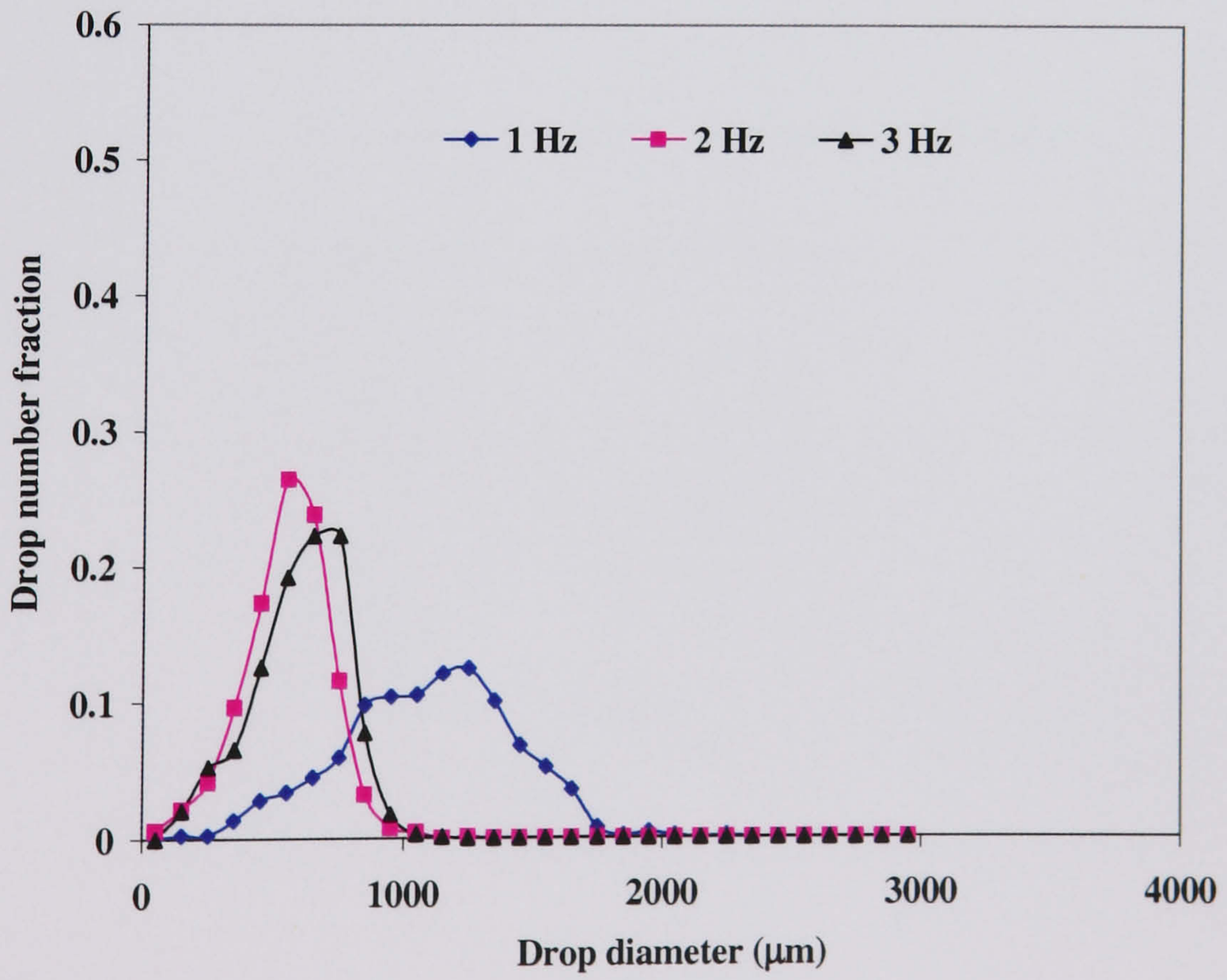

Figure A2.32. Effect of oscillation frequency on droplet size distribution (x_o = 15 mm, Re_n = 541), Port 2

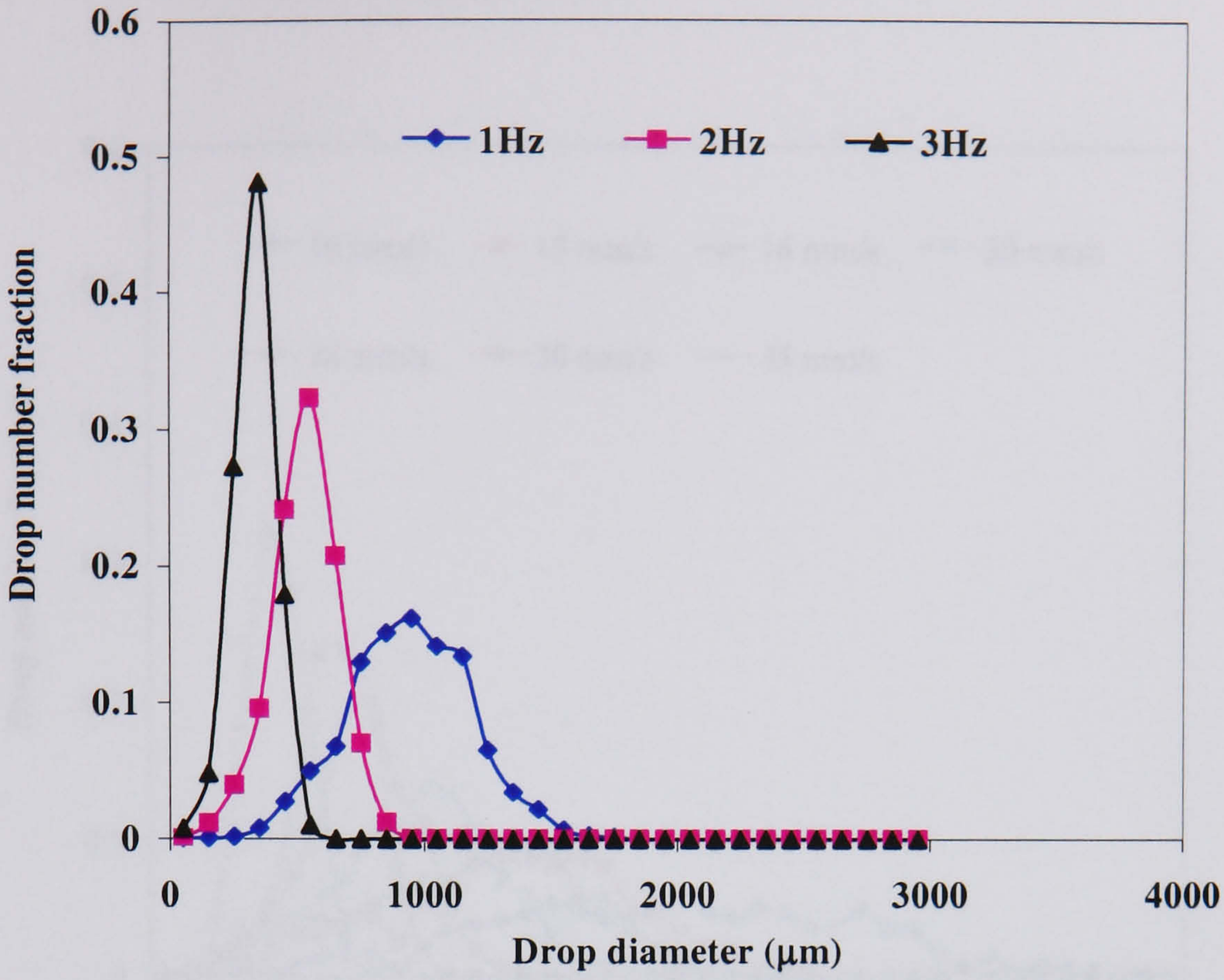

Figure A2.33. Effect of oscillation frequency on droplet size distribution (x_o = 15 mm, Re_n =541), Port 4

EFFECT OF OSCILLATION VELOCITY

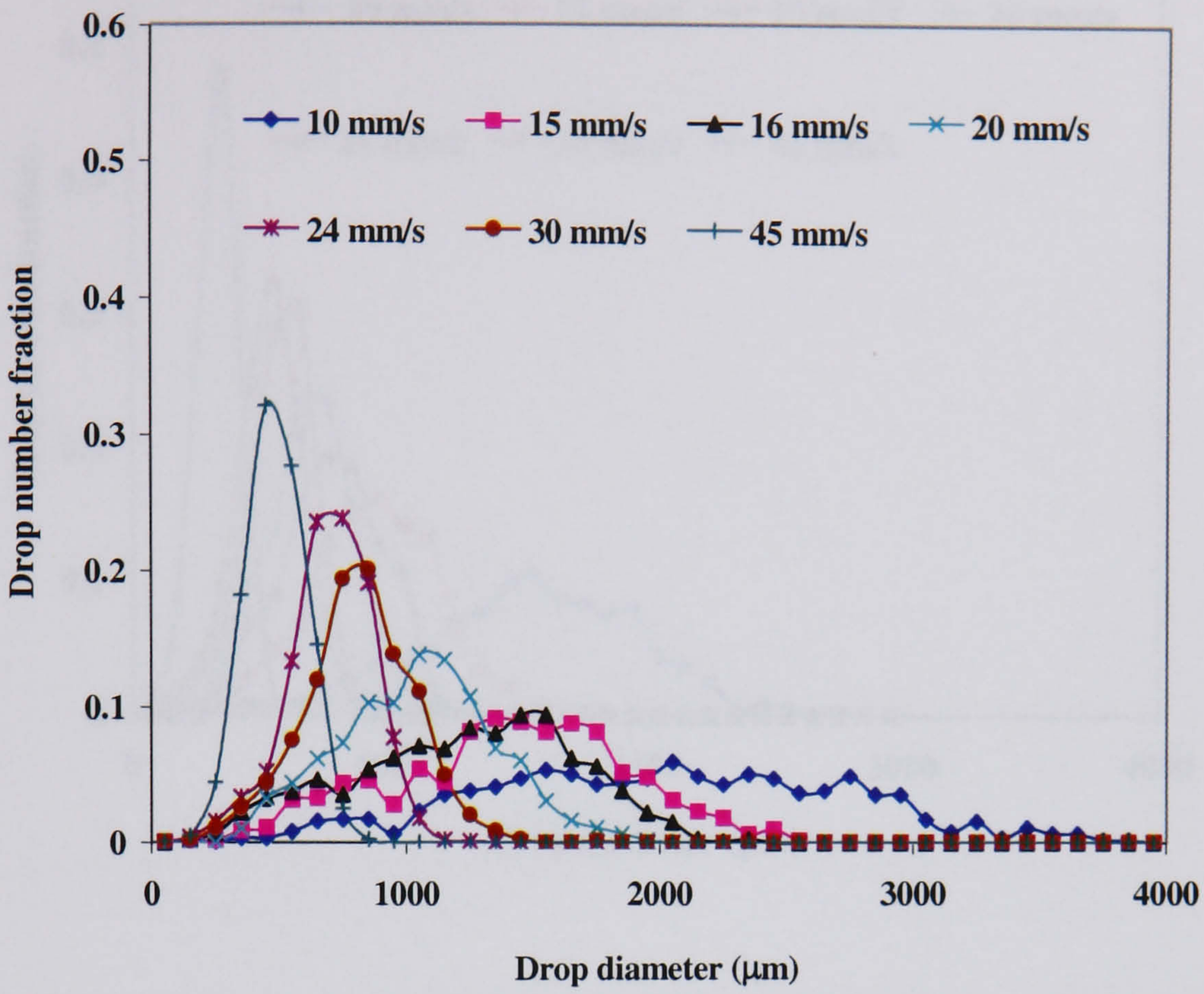

Figure A2.34. Effect of oscillation velocity on drop size distribution (DSD) (Re_n = 541), Port 1

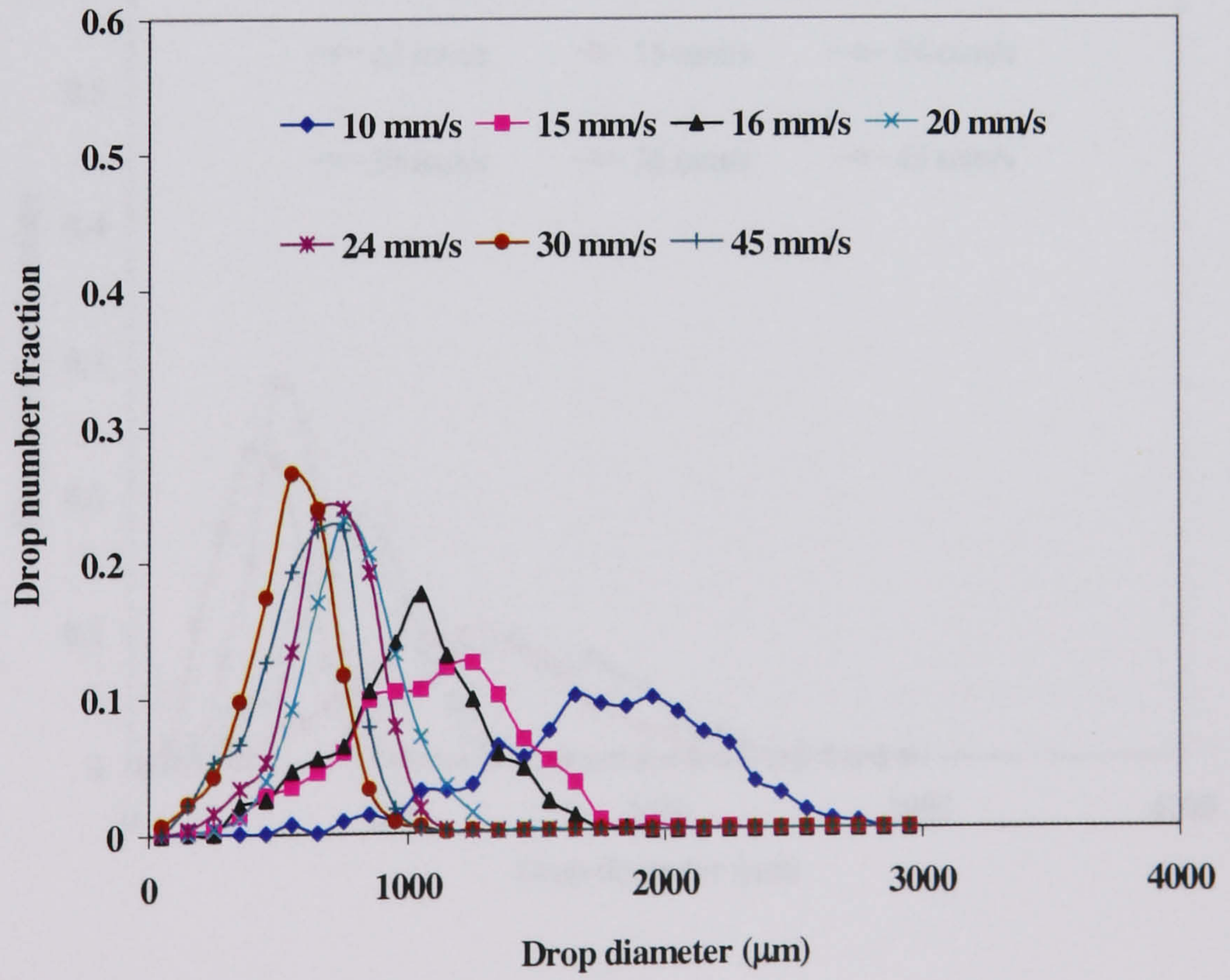

Figure A2.35. Effect of oscillation velocity on drop size distribution (DSD) (Re_n = 541), Port 2

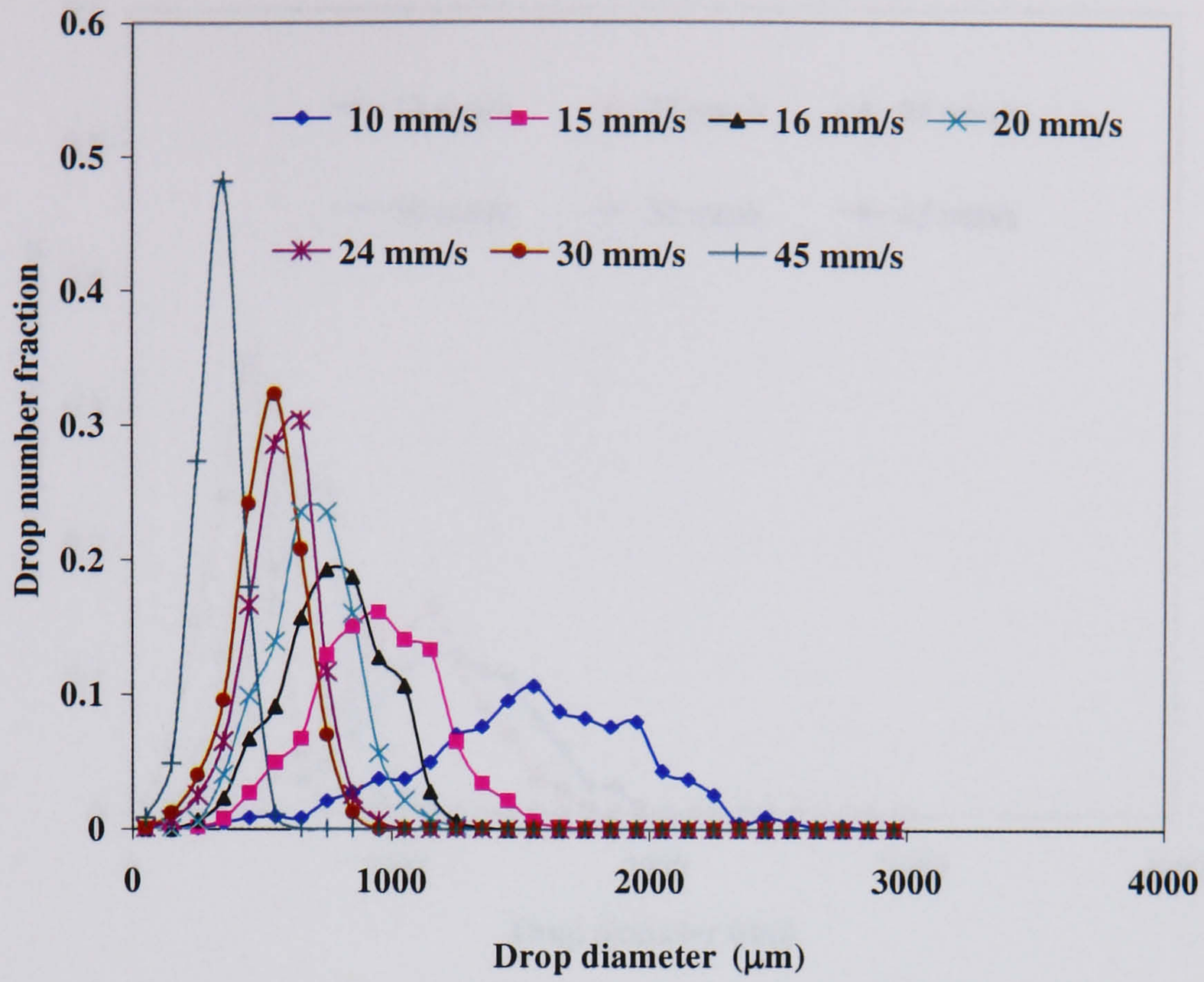

Figure A2.36. Effect of oscillation velocity on drop size distribution (DSD) (Re_n = 541), Port 4

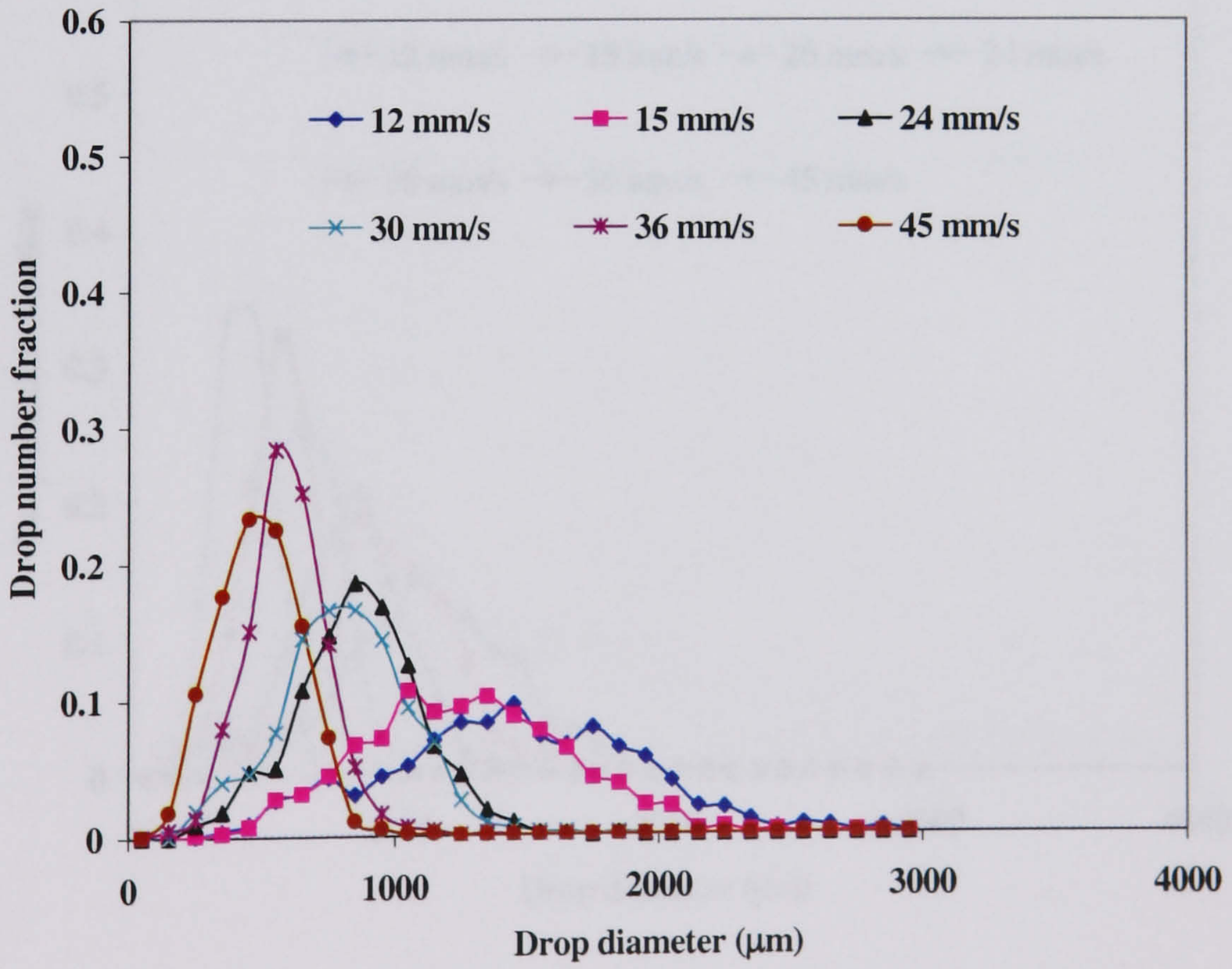

Figure A2.37. Effect of oscillation velocity on drop size distribution (DSD) (Re_n = 248), Port 1

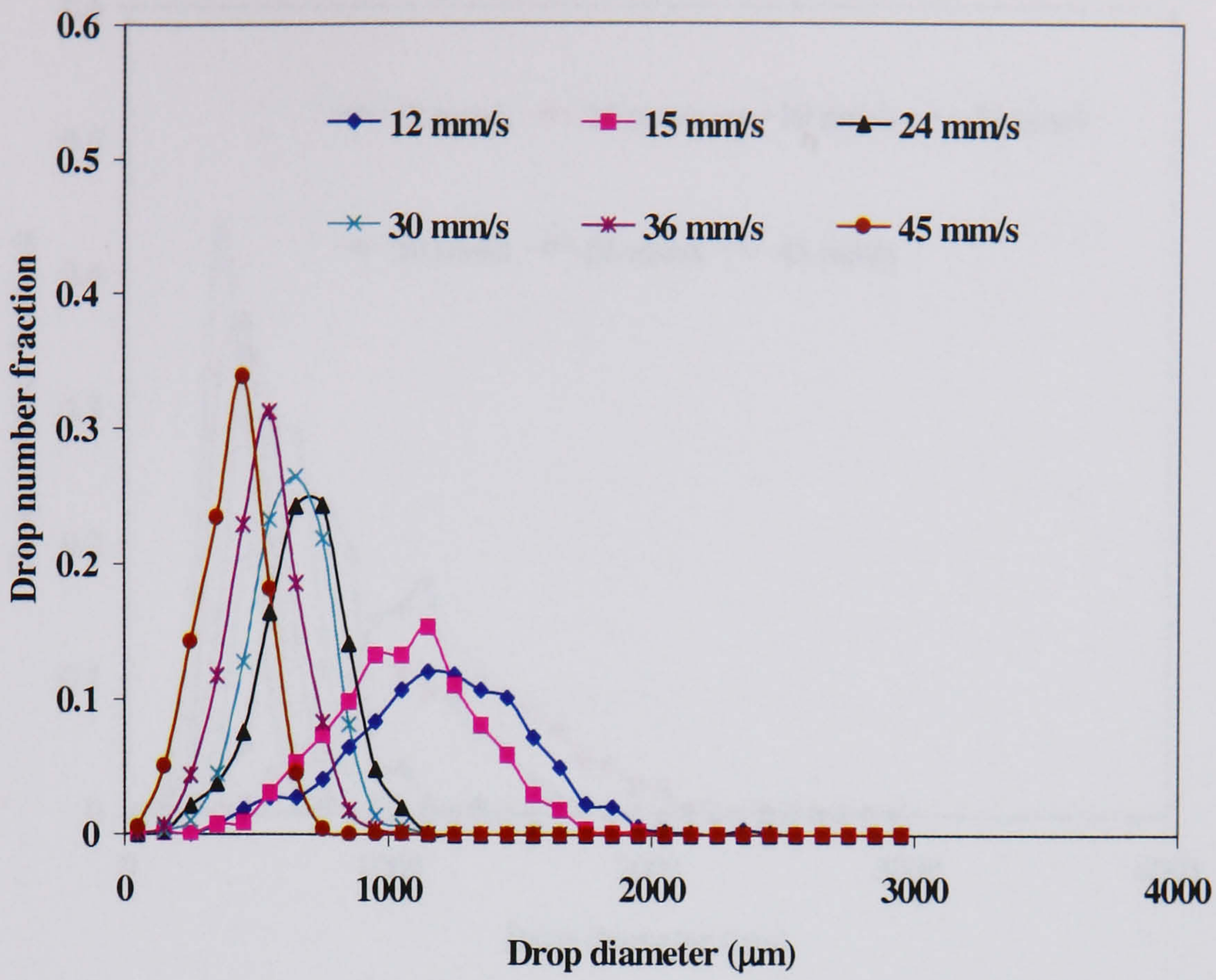

Figure A2.38. Effect of oscillation velocity on drop size distribution (DSD) (Re_n = 248), Port 2

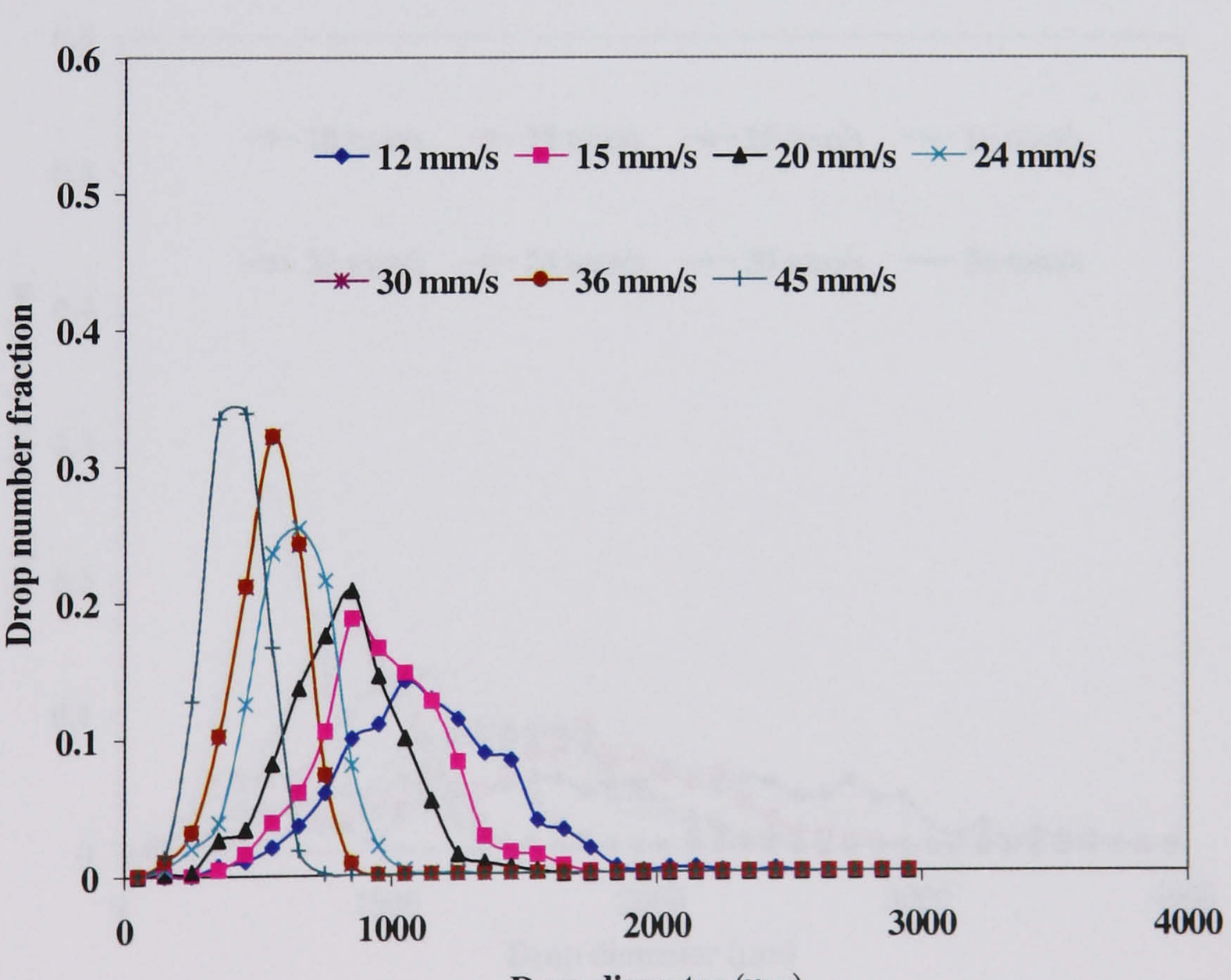

Figure A2.39. Effect of oscillation velocity on drop size distribution (DSD) (Re_n = 248), Port 3

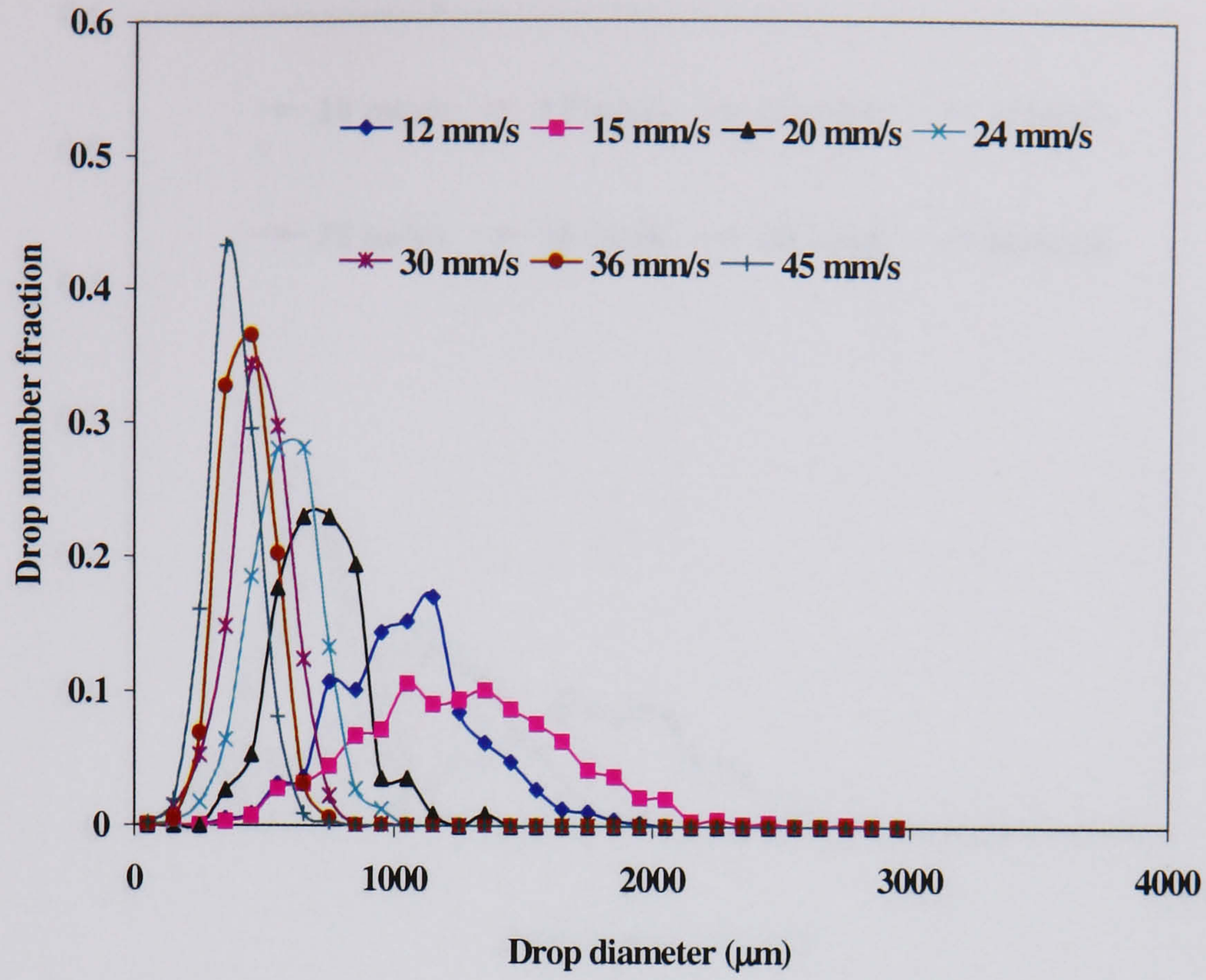

Figure A2.40. Effect of oscillation velocity on drop size distribution (DSD) (Re_n = 248), Port 4

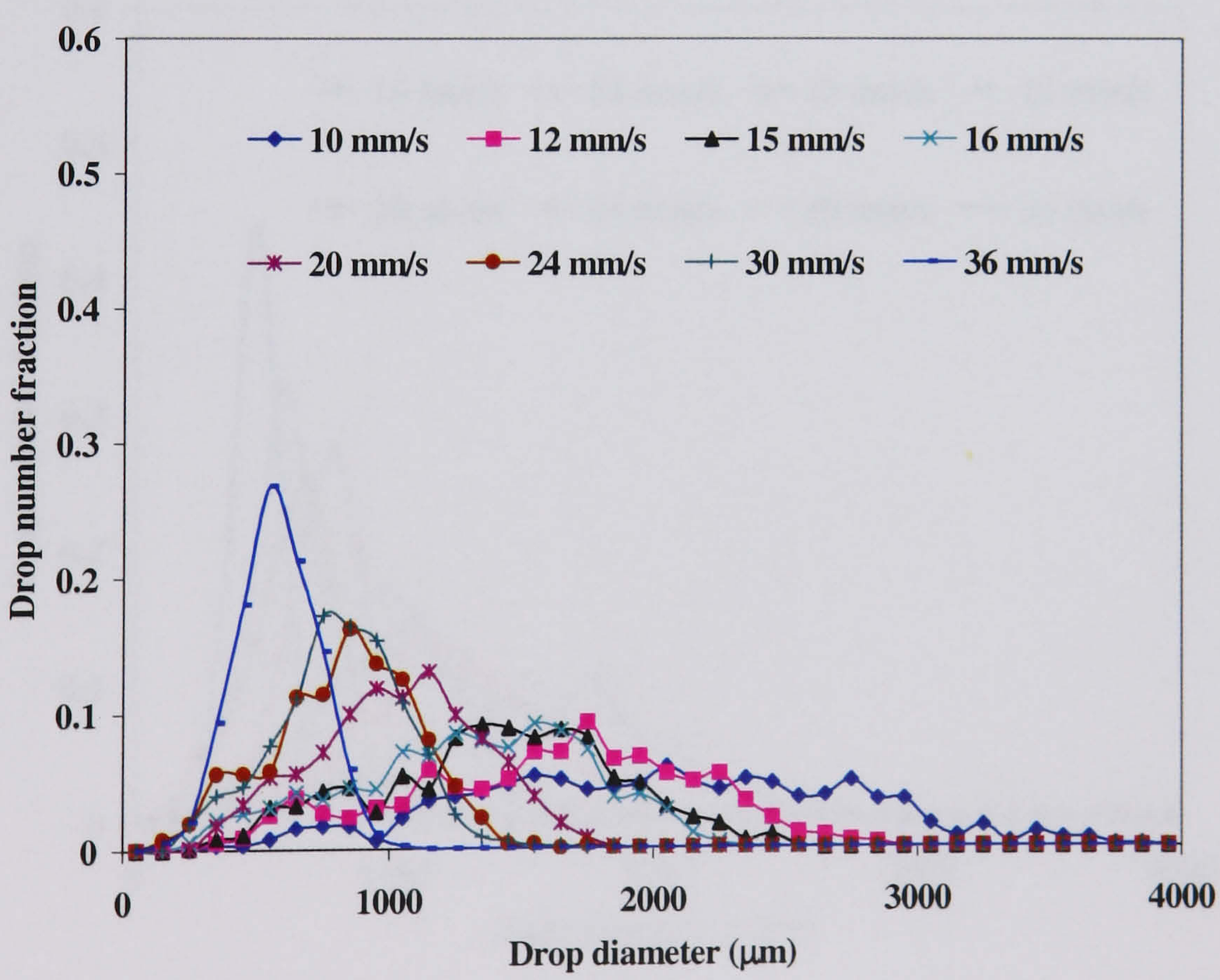

Figure A2.41. Effect of oscillation velocity on drop size distribution (DSD) (Re_n = 1002), Port 1

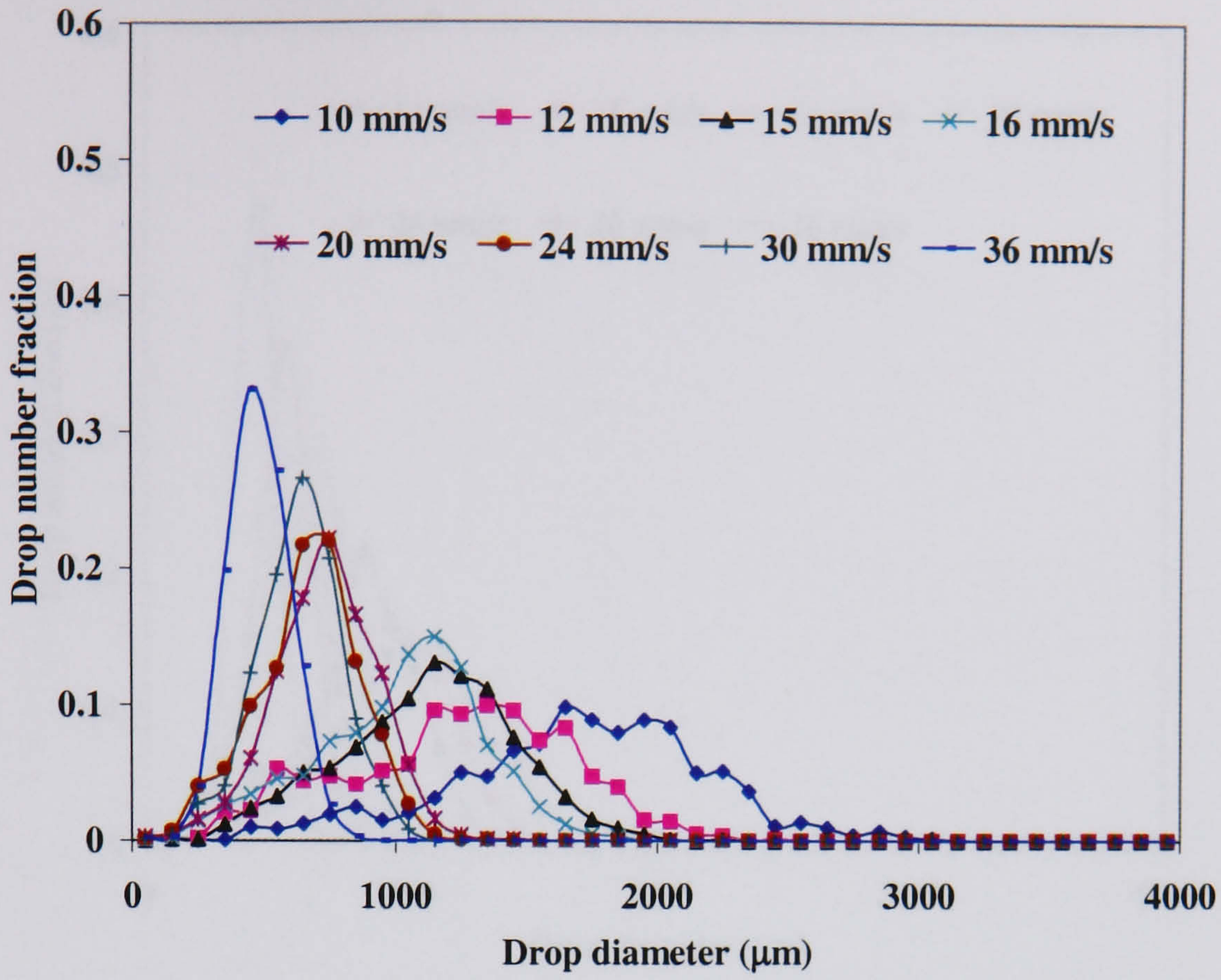

Figure A2.42. Effect of oscillation velocity on drop size distribution (DSD) (Re_n = 1002), Port 2

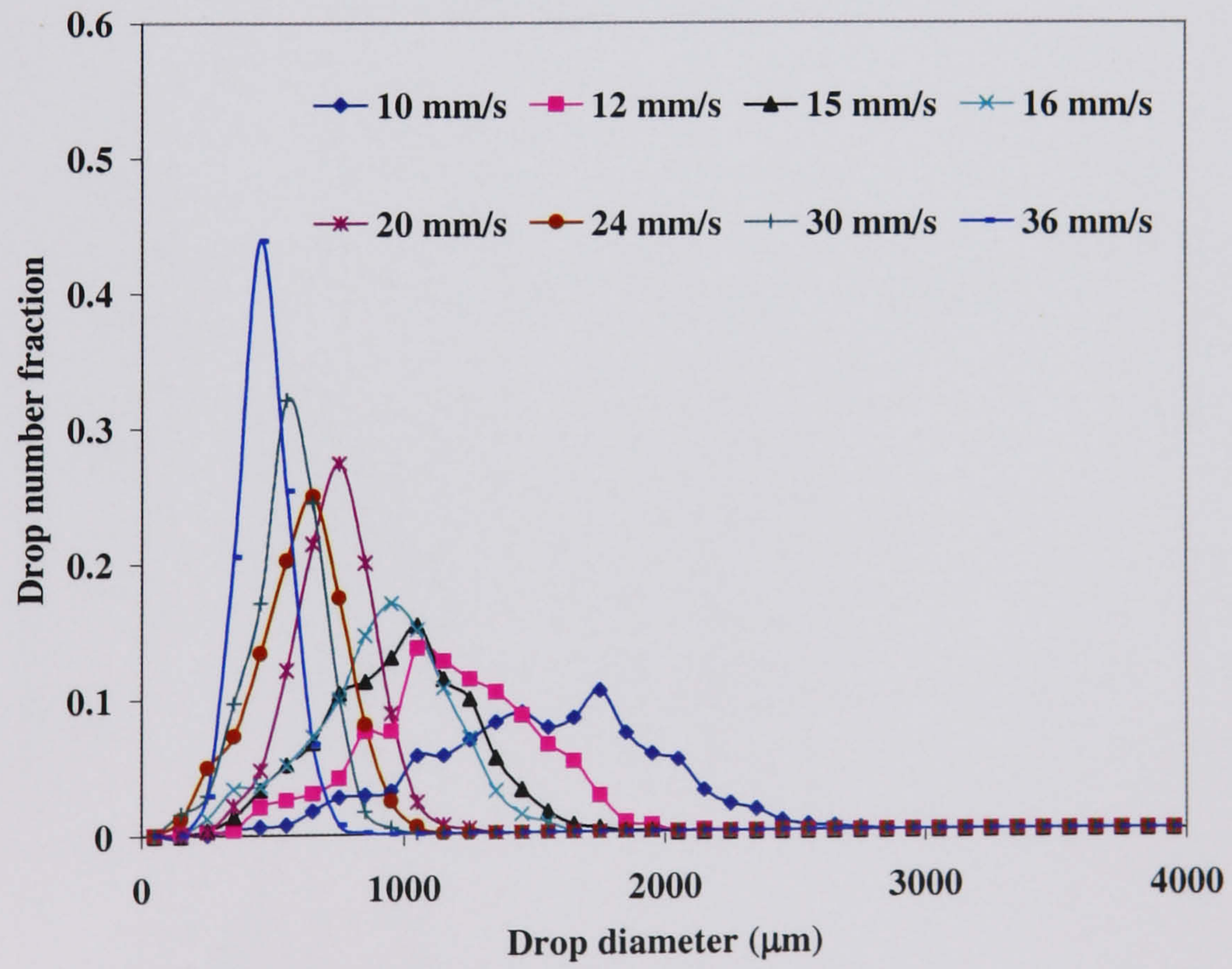

Figure A2.43. Effect of oscillation velocity on drop size distribution (DSD) (Re_n = 1002), Port 3

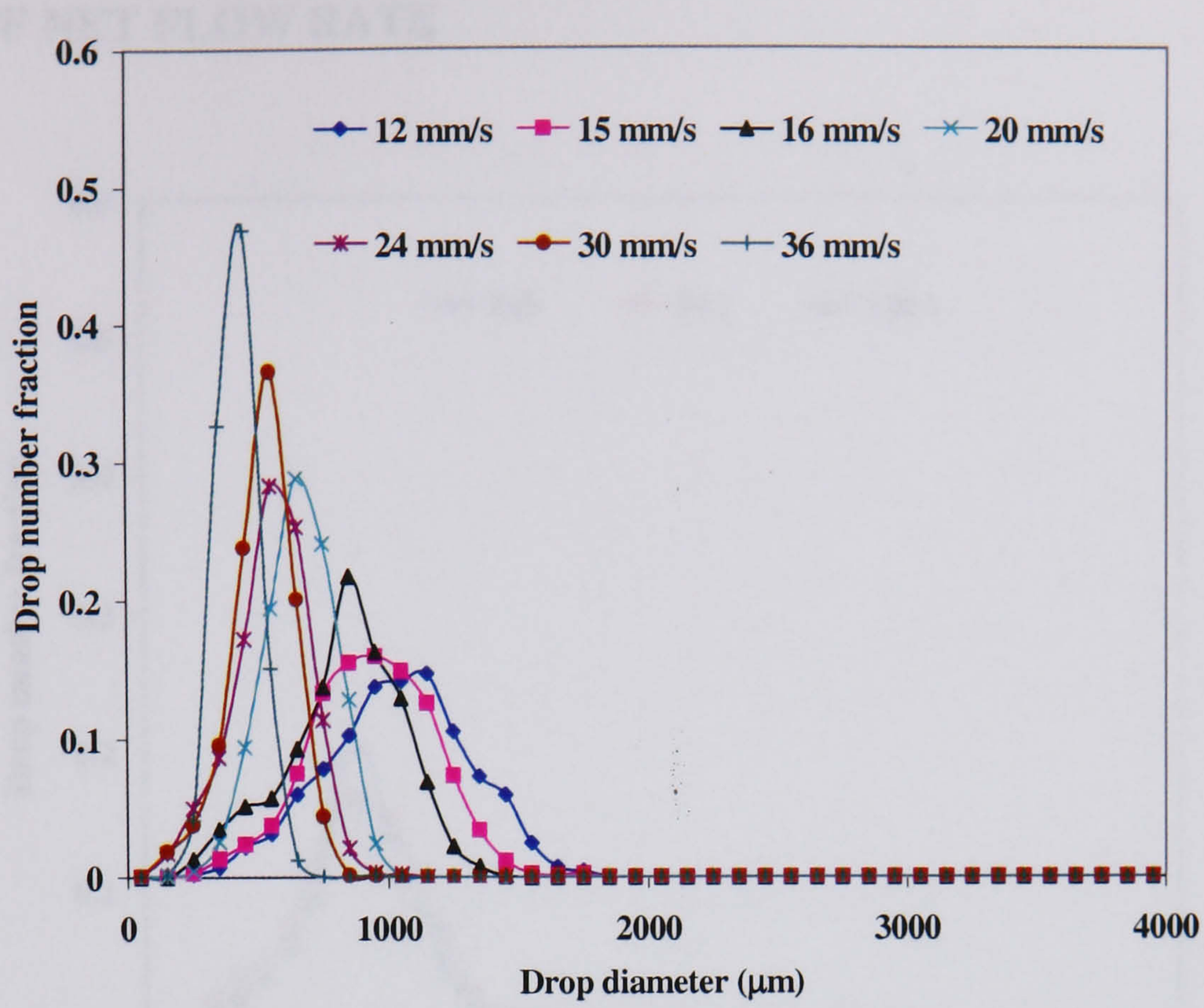

Figure A2.44. Effect of oscillation velocity on drop size distribution (DSD) (Re_n = 1002), Port 4

EFFECT OF NET FLOW RATE

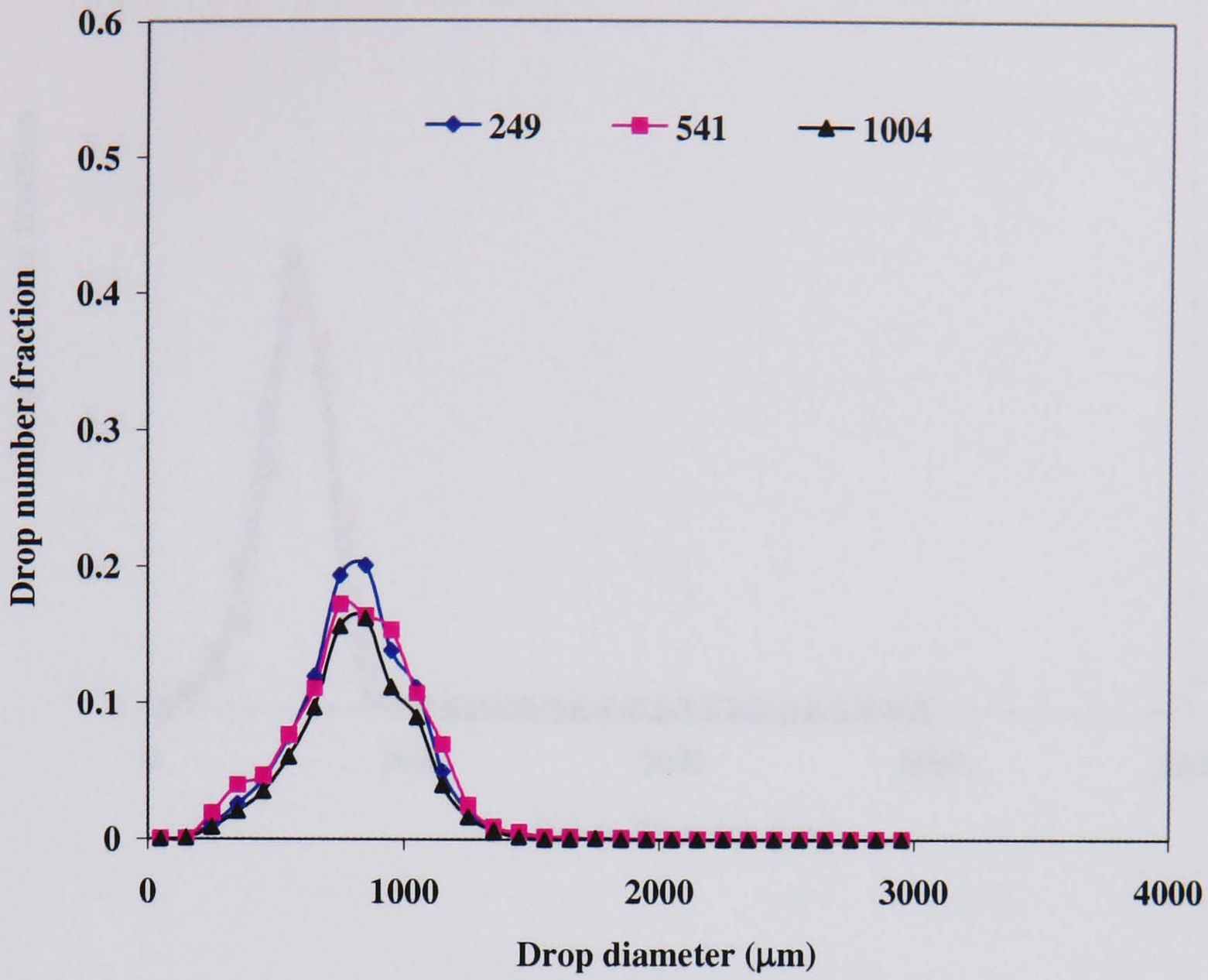

Figure A2.45. Effect of net flow rate on Sauter mean drop diameter, (x_o = 15 mm, f = 2 Hz), Port 1

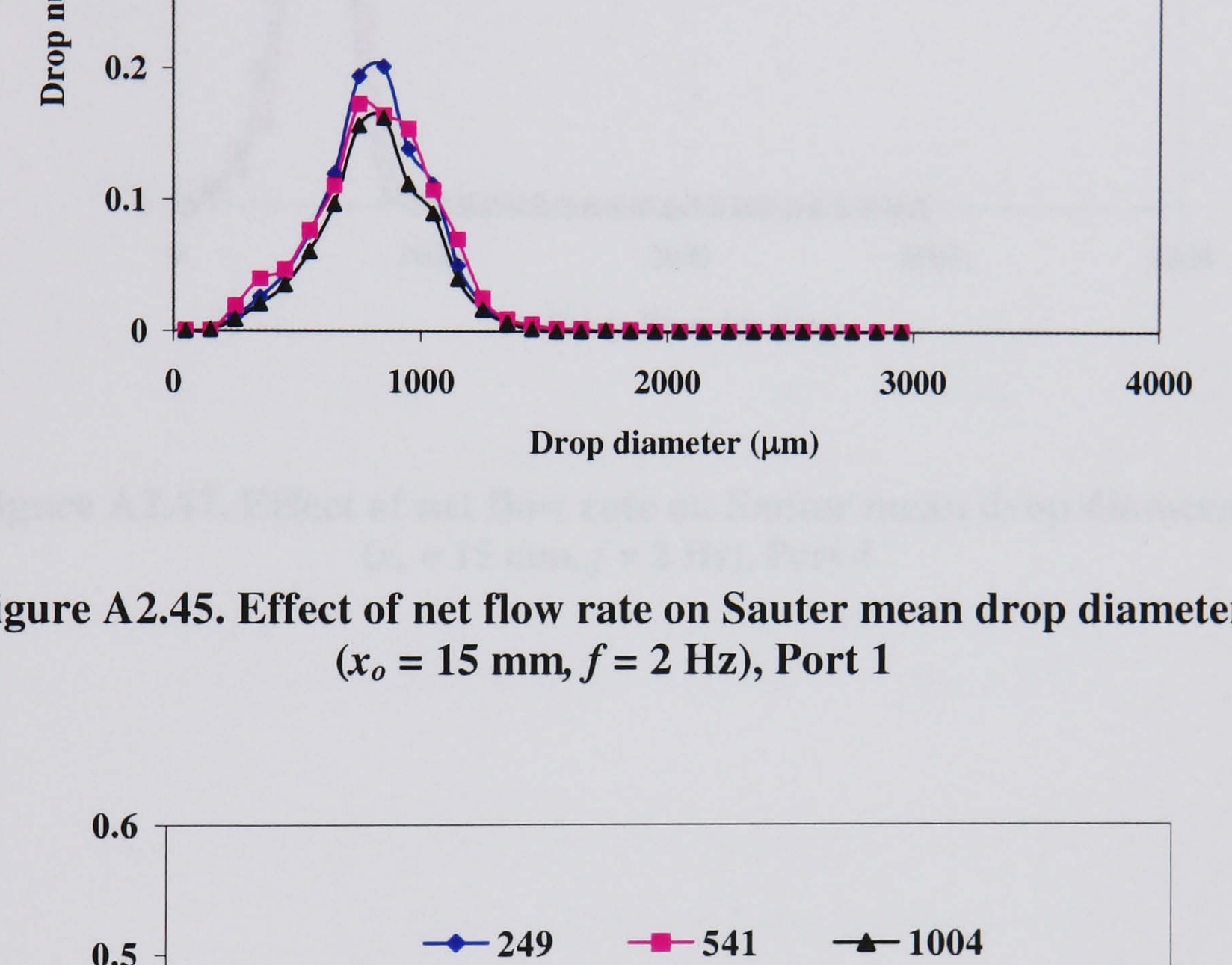

Figure A2.46. Effect of net flow rate on Sauter mean drop diameter, (x_o = 15 mm, f = 2 Hz), Port 2

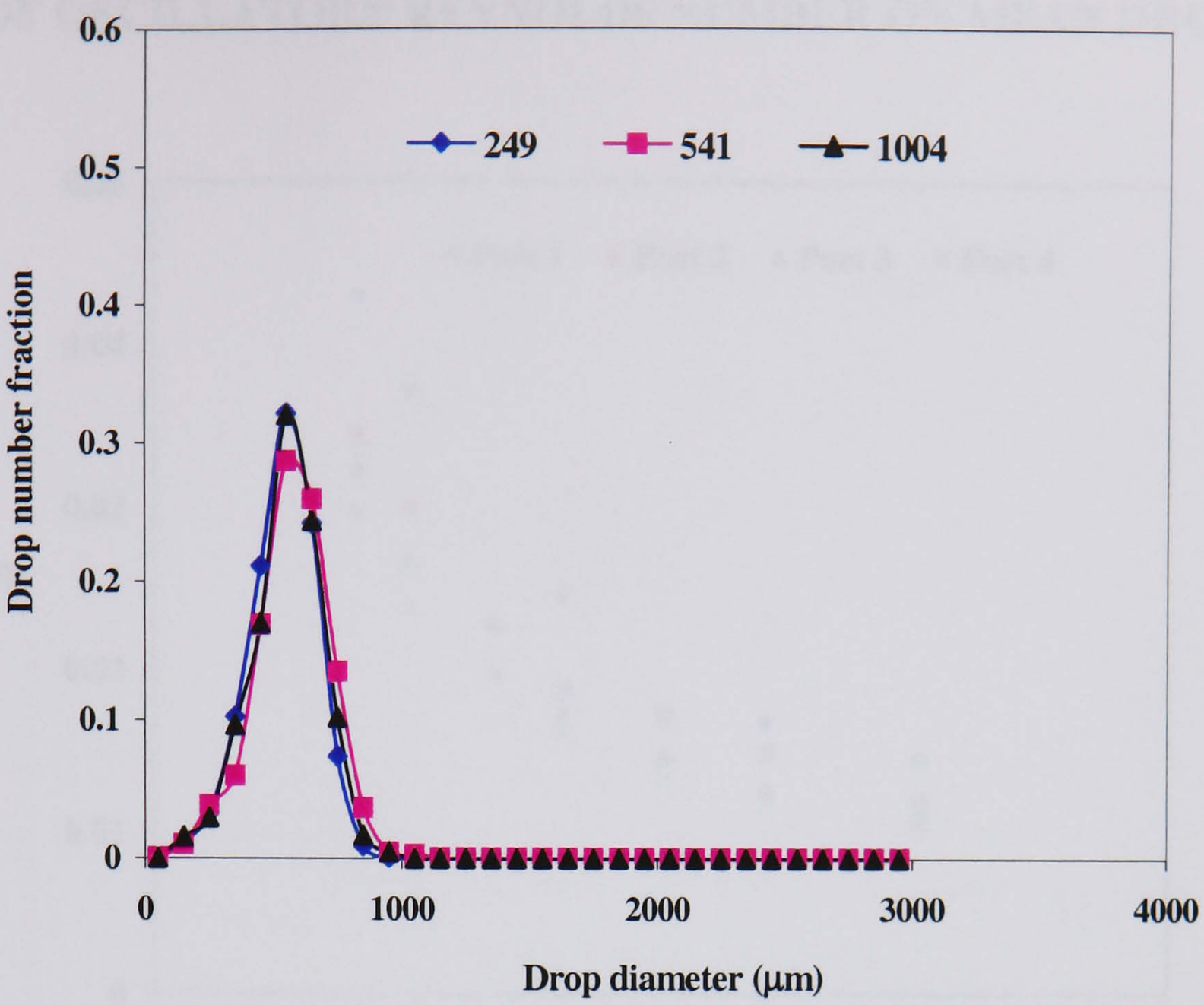

Figure A2.47. Effect of net flow rate on Sauter mean drop diameter, (x_o = 15 mm, f = 2 Hz), Port 4

EFFECT OF OSCILLATORY REYNOLDS NUMBER ON MEAN DROP SIZE

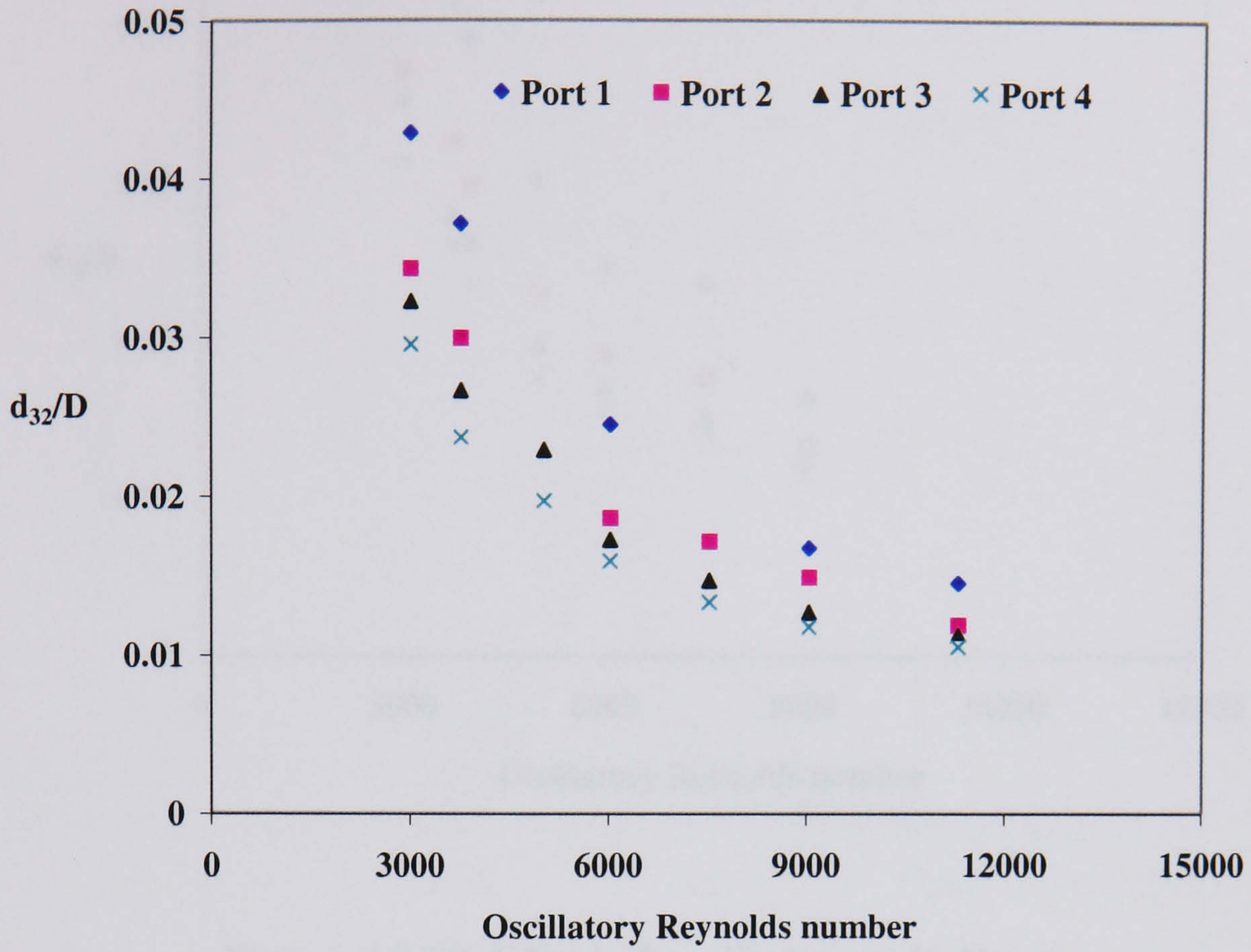

Figure A2.48. Effect of oscillatory Reynolds number on dimensionless mean drop diameter, Re_n = 249

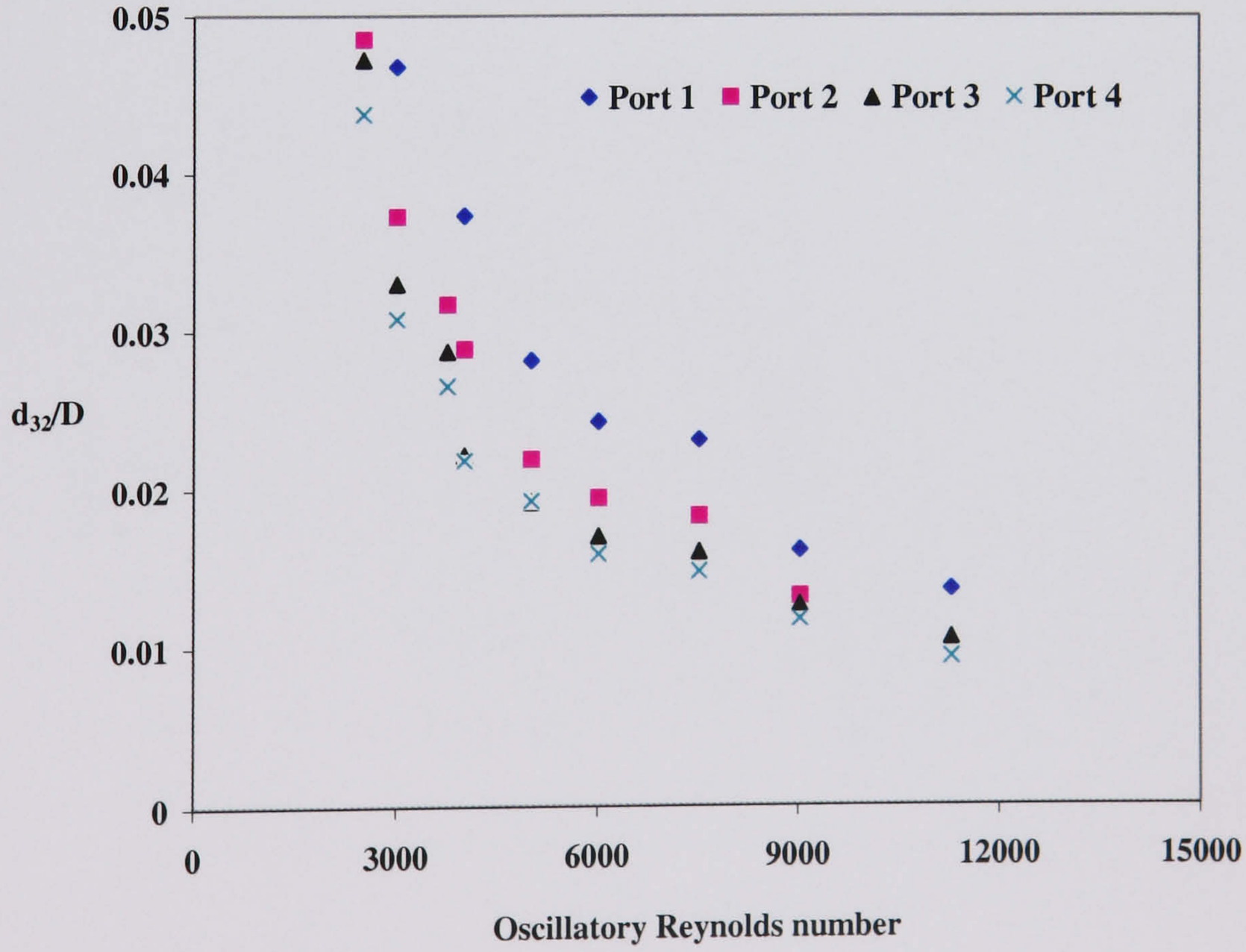

Figure A2.49. Effect of oscillation velocity on Sauter mean drop diameter, Re_n = 541

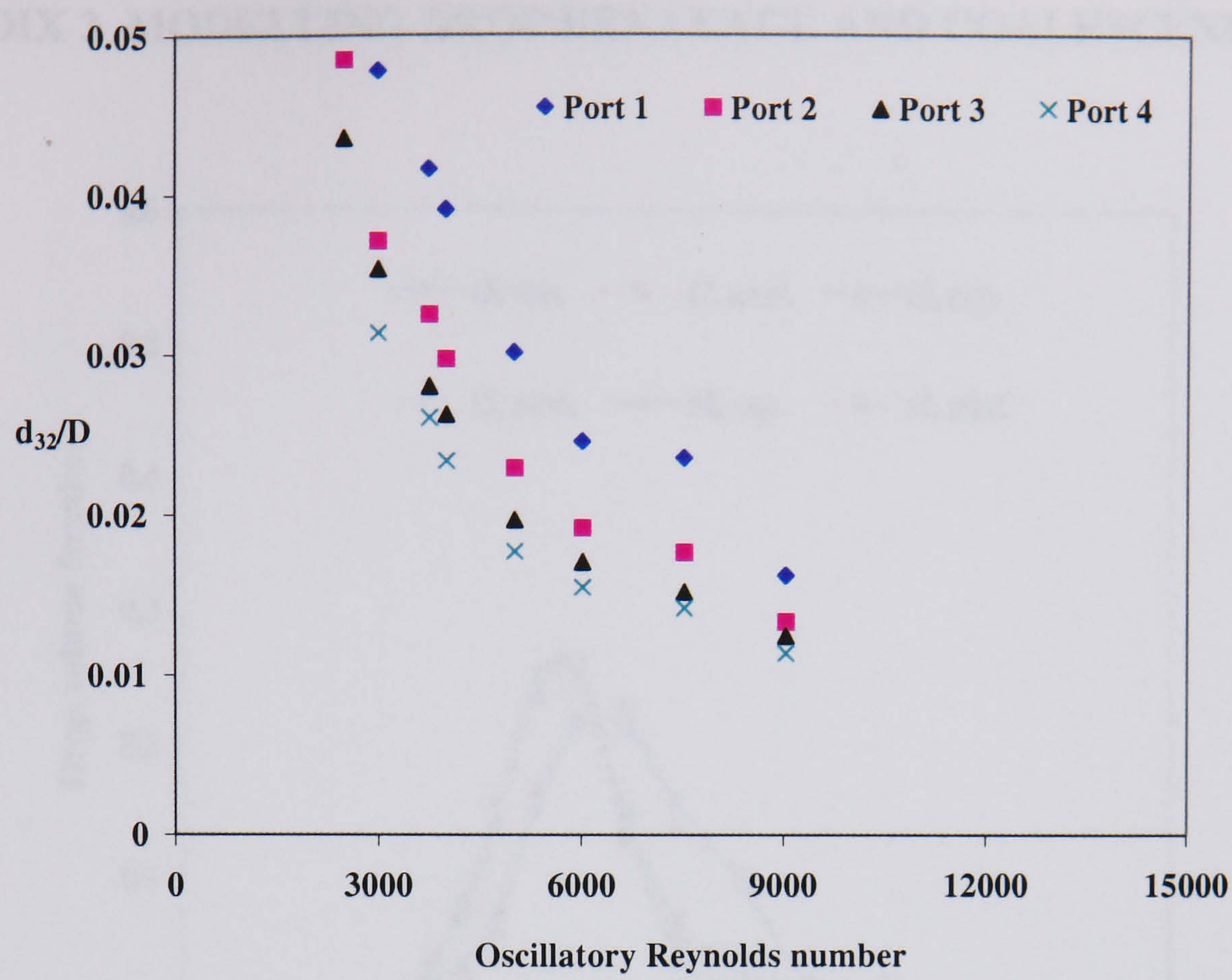

Figure A2.50. Effect of oscillation velocity on Sauter mean drop diameter, Re_n = 1004

APPENDIX 3 MODELLING DROP BREAKAGE AND COALESCENCE RATE

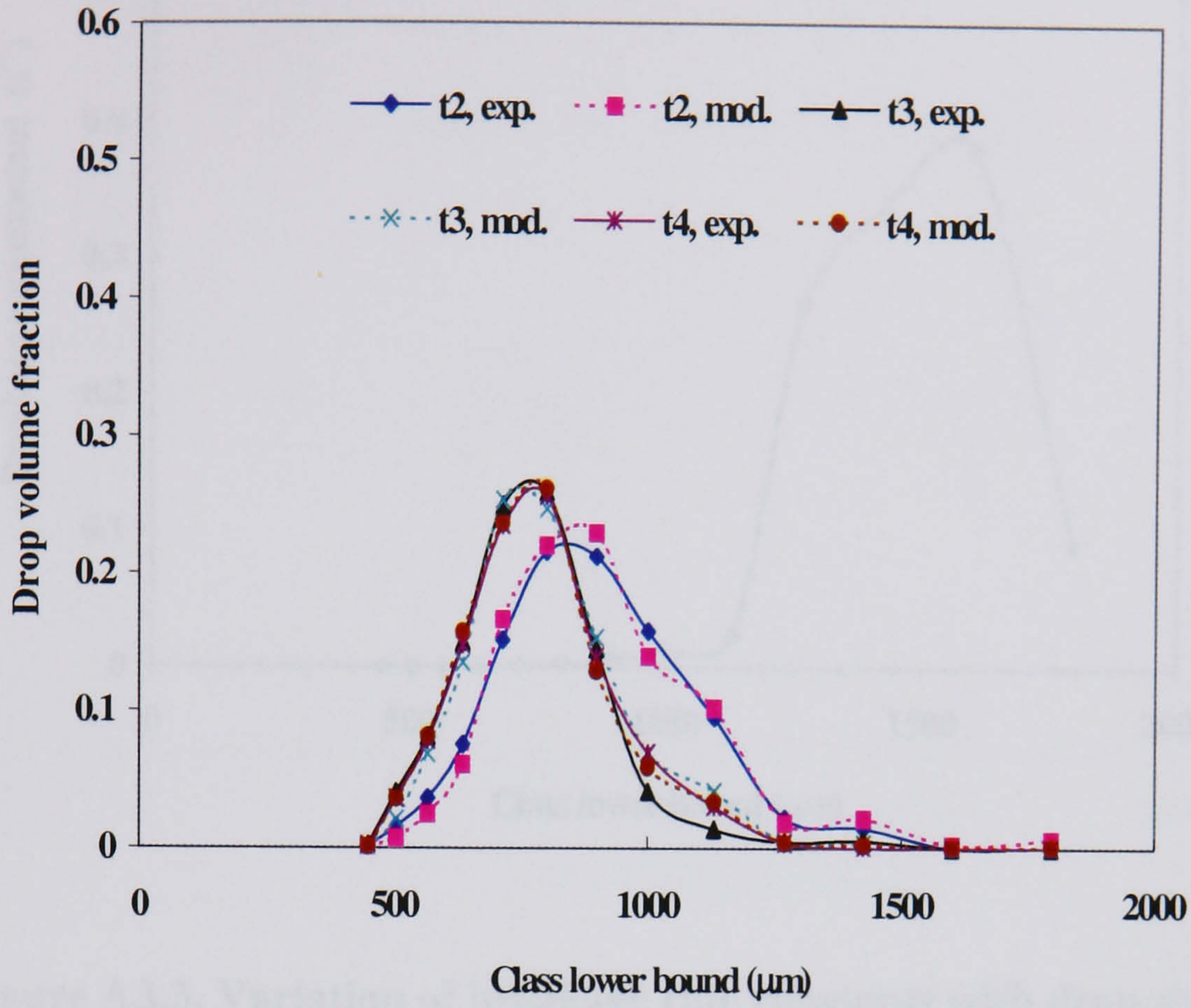

Figure A3.1. Experimental data and reconstructed distributions Re_o = 5020 (x_o = 10 mm, f = 2 Hz), Re_n = 541, χ^2 = 0.004487

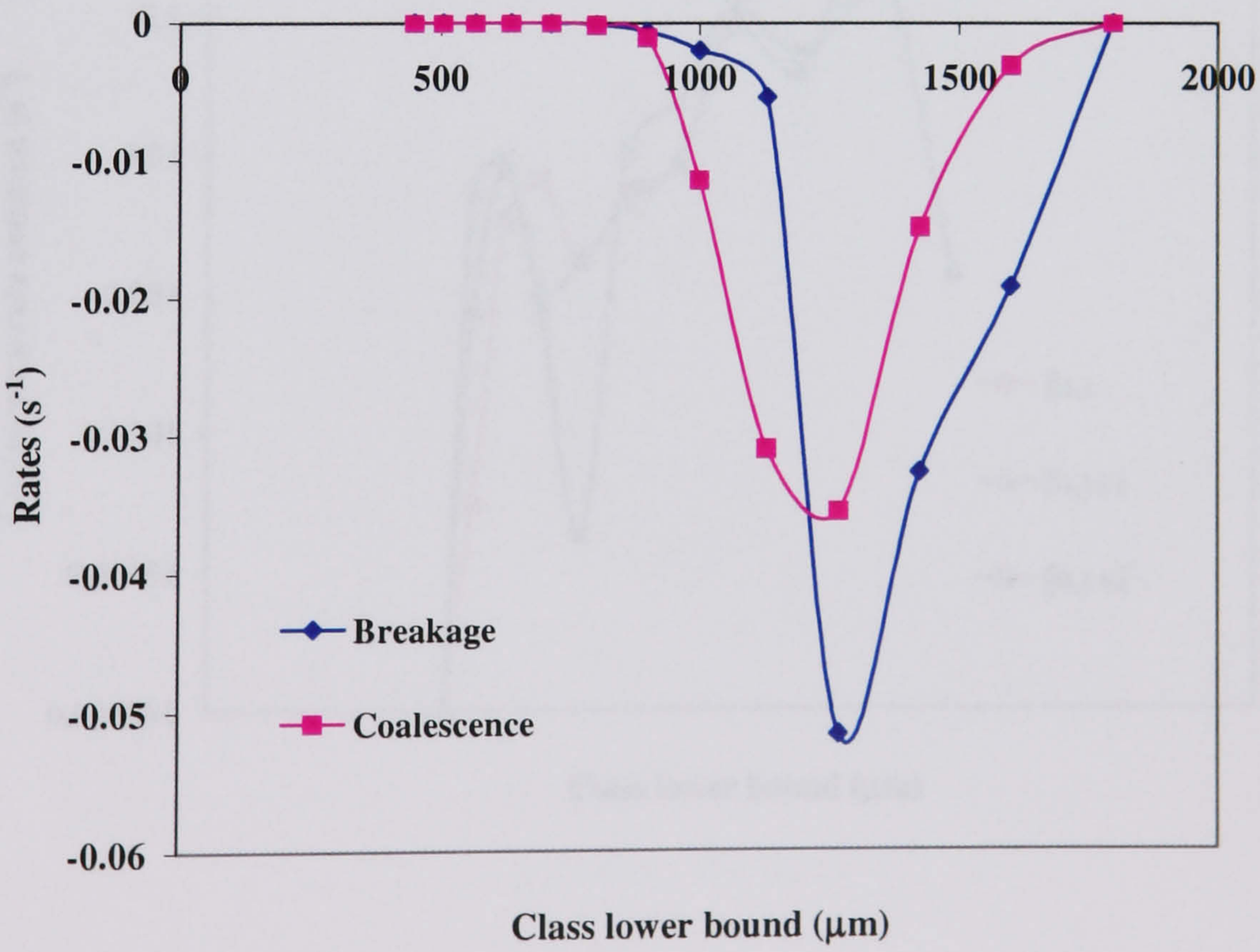

Figure A3.2. Breakage and total coalescence rates as functions of drop size, Re_o = 5020 (x_o = 10 mm, f = 2Hz), Re_n = 541, χ^2 = 0.004487

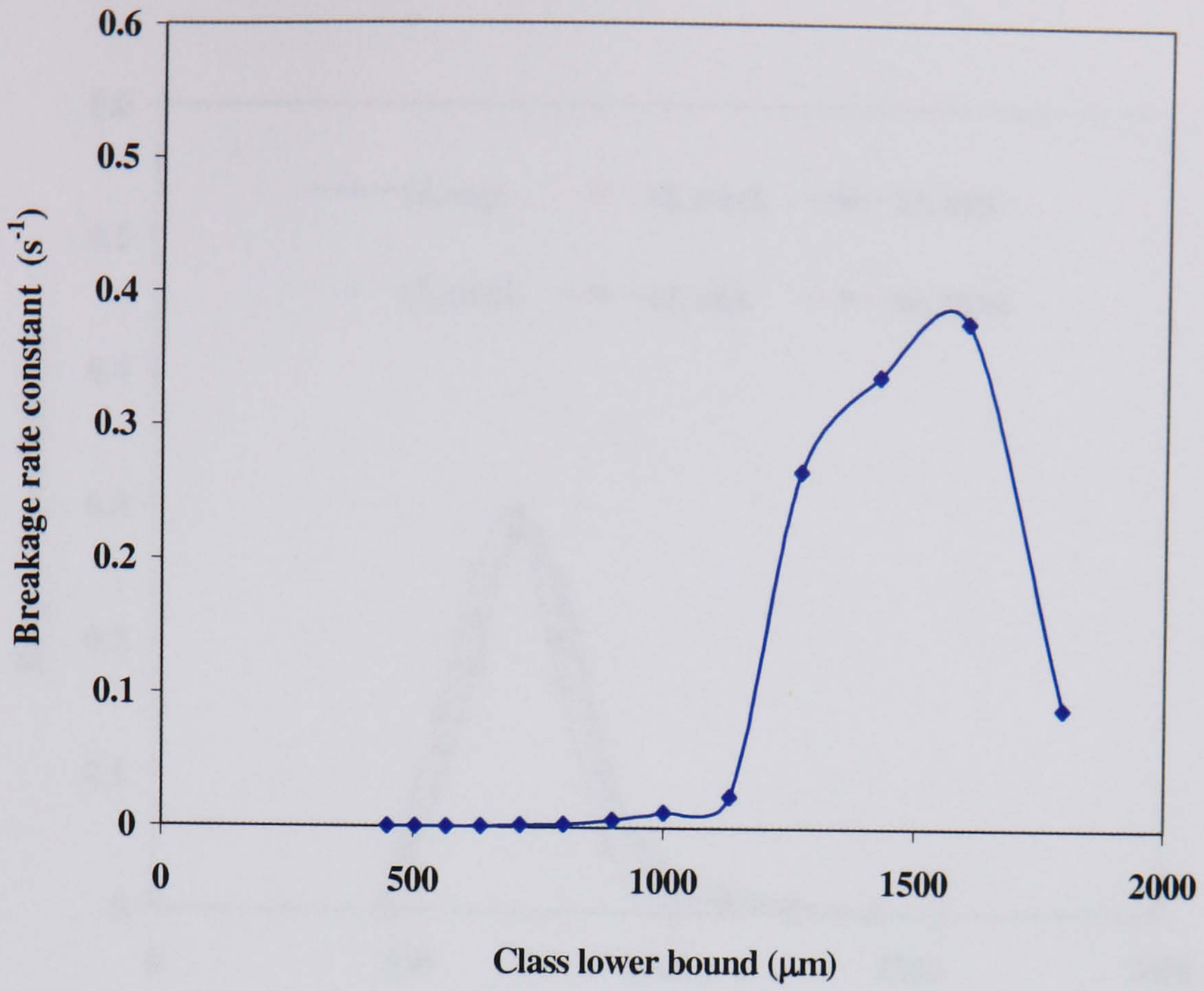

Figure A3.3. Variation of breakage rate constants with drop size, Re_o = 5020 (x_o = 10 mm, f = 2 Hz), Re_n = 541, χ^2 = 0.004487

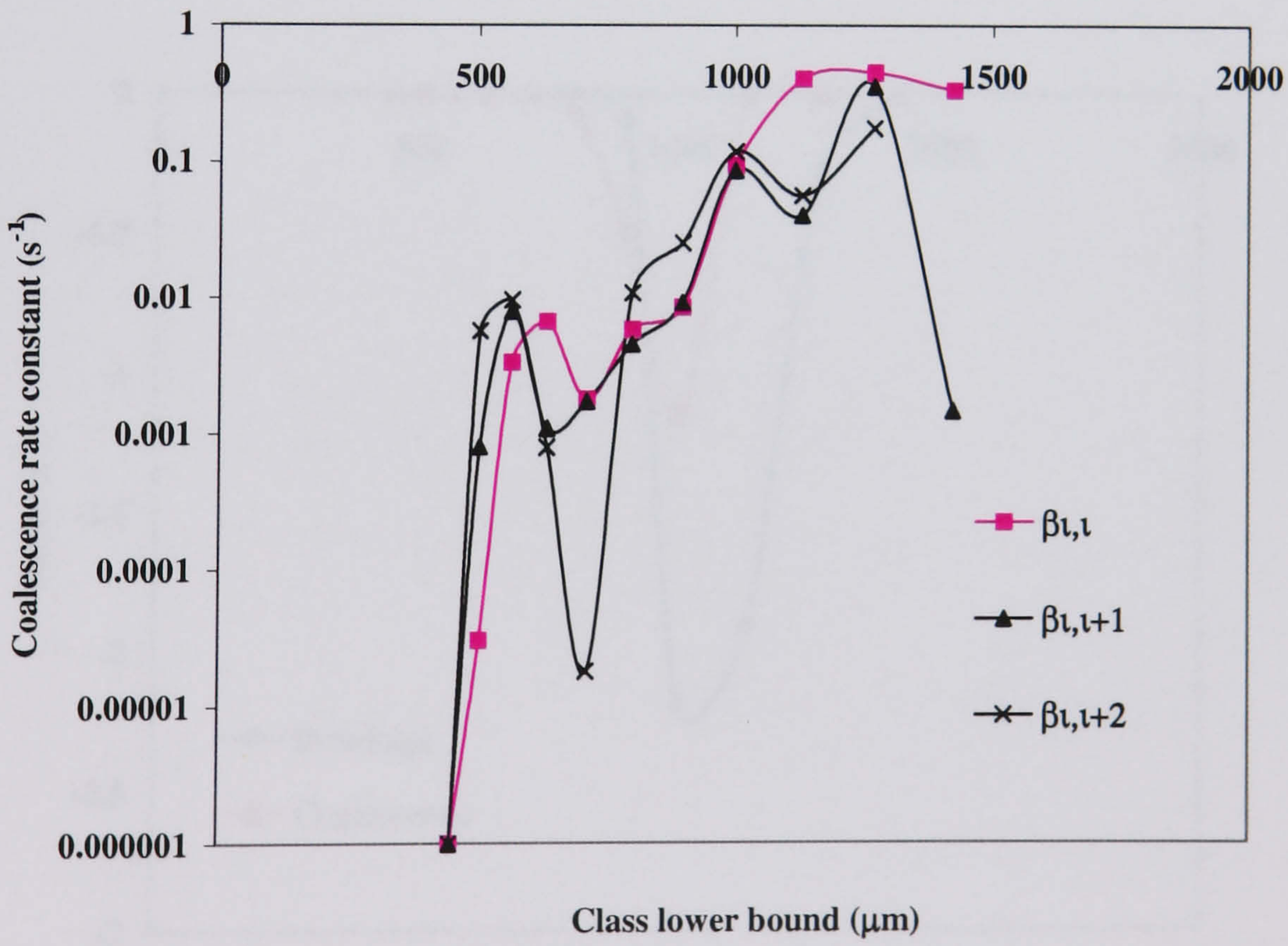

Figure A3.4. Variation of coalescence rate constants with drop size, Re_o = 5020 (x_o = 10 mm, f = 2 Hz), Re_n = 541, χ^2 = 0.004487

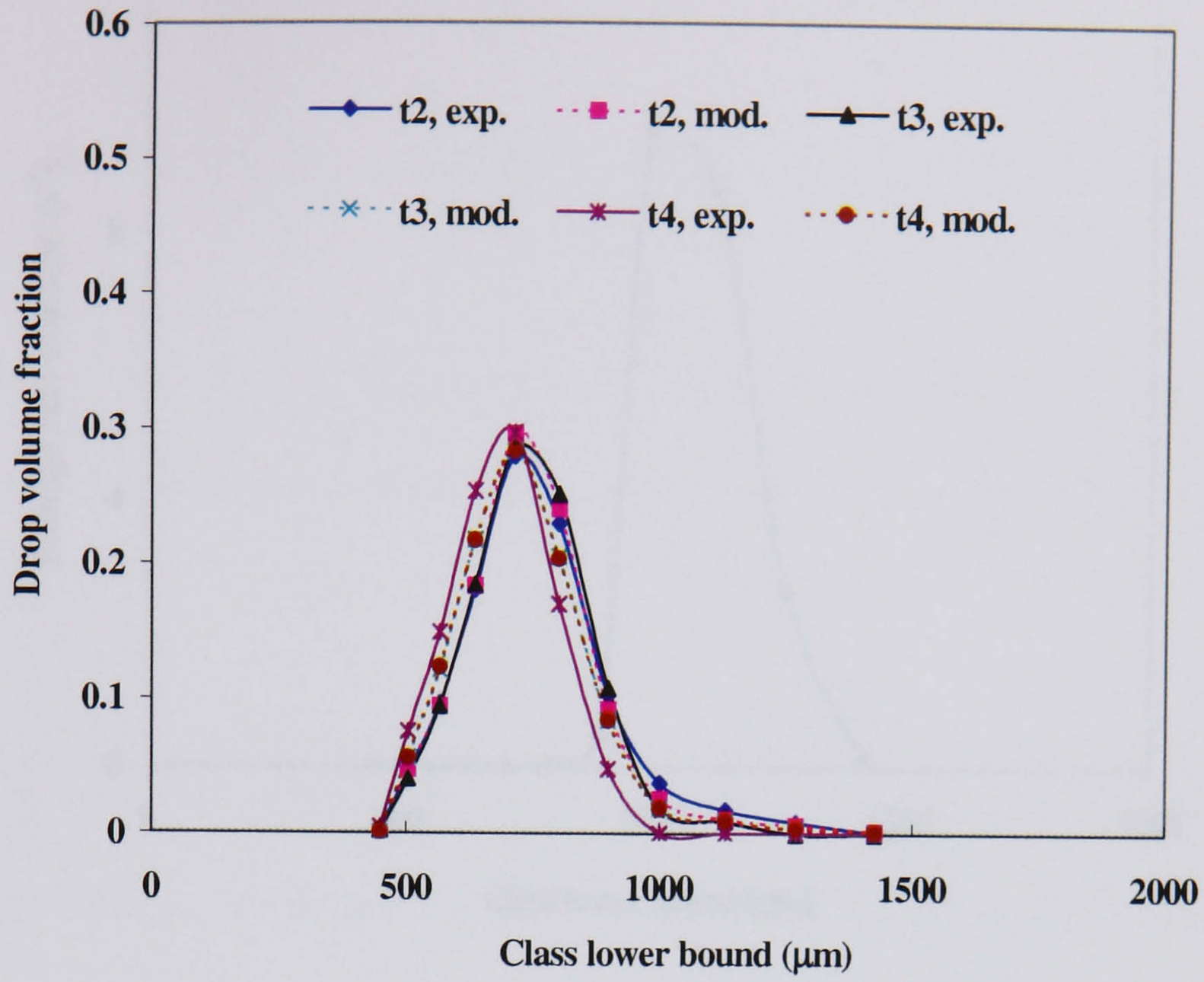

Figure A3.5. Experimental data and reconstructed distributions
Re_o = 7530 (x_o = 15 mm, f = 2 Hz), Re_n = 541, χ^2 = 0.00110575

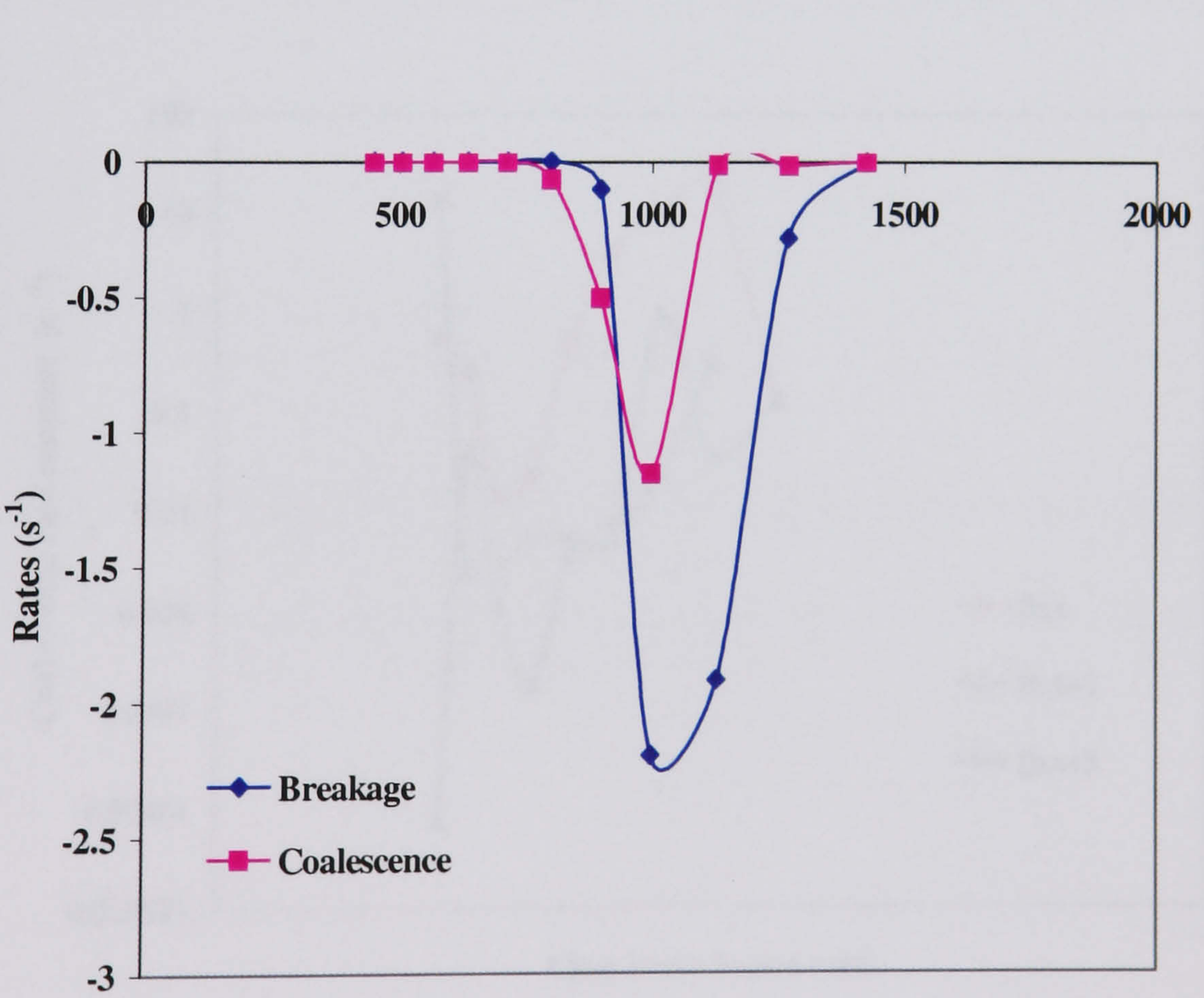

Figure A3.6. Breakage and total coalescence rates as functions of drop size,
Re_o = 7530 (x_o = 15 mm, f = 2Hz), Re_n = 541, χ^2 = 0.00110575

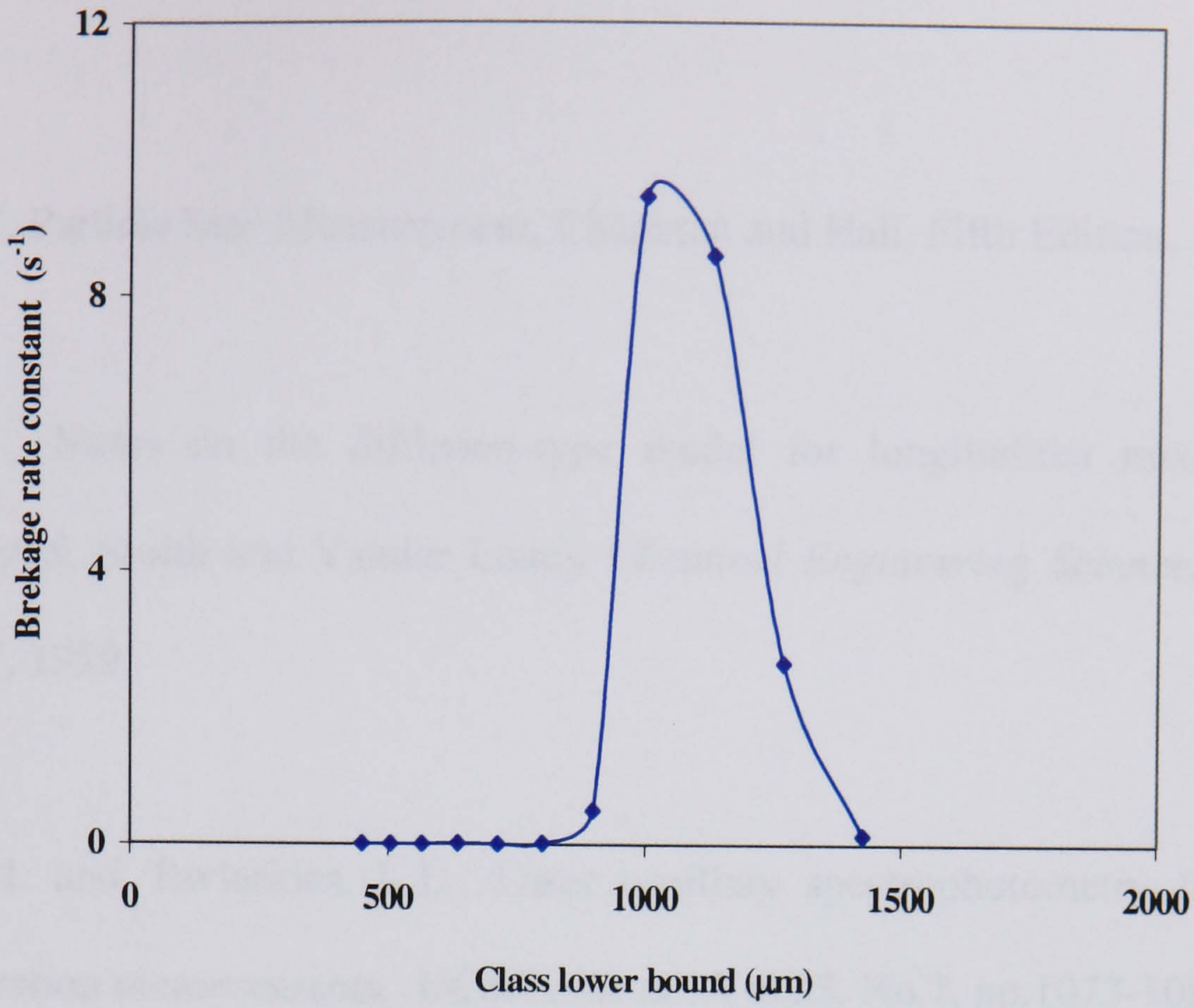

Figure A3.7. Variation of breakage rate constants with drop size, Re_o = 7530 (x_o = 15 mm, f = 2 Hz), Re_n = 541, χ^2 = 0.00110575

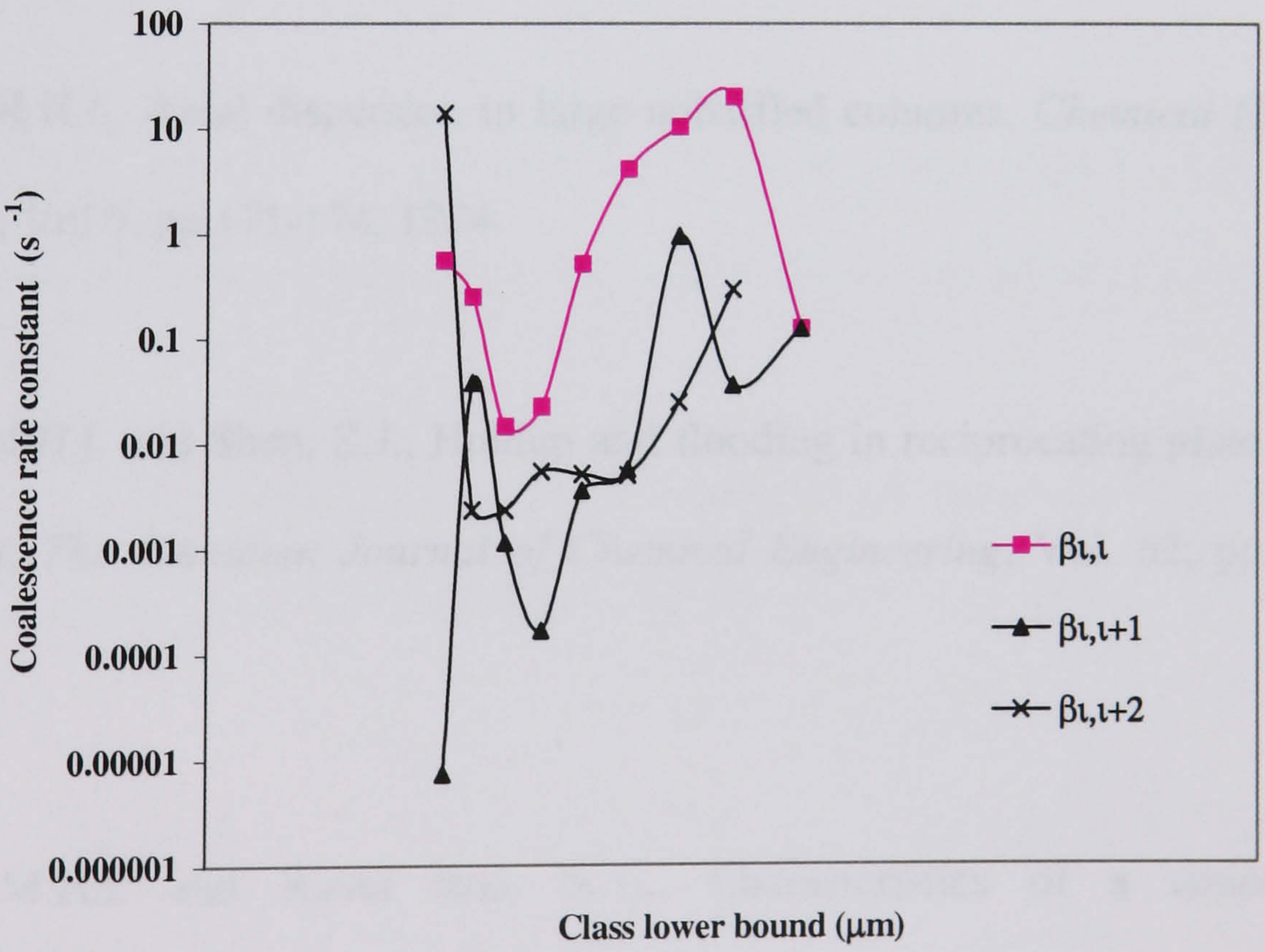

Figure A3.8. Variation of coalescence rate constants with drop size, Re_o = 7530 (x_o = 15 mm, f = 2 Hz), Re_n = 541, χ^2 = 0.0133909

REFERENCES

1. Allen, T. Particle Size Measurement, Chapman and Hall, Fifth Edition, 1997.

2. Aris, R., Notes on the diffusion-type model for longitudinal mixing in flow (Levenspiel, Smith and Vander Laan), *Chemical Engineering Science*, Vol. 9, pp. 266-267, 1959.

3. Bae, J.H. and Tavlarides, L.L., Laser capillary spectrophotometry for drop-size concentration measurements, *AIChE Journal*, Vol.35, No.7, pp.1073-1084, 1989.

4. Baird, M.H.I. and Lane, S.J., Drop size and hold-up in a reciprocating plate extraction column, *Chemical Engineering Science*, Vol.28, pp.947-955, 1973.

5. Baird, M.H.I., Axial dispersion in large unbaffled columns, *Chemical Engineering Journal*, Vol.9, pp.171-174, 1974.

6. Baird, M.H.I. and Shen, Z.J., Holdup and flooding in reciprocating plate extraction columns, *The Canadian Journal of Chemical Engineering*, Vol. 62, pp. 218-227, 1984.

7. Baird, M.H.I. and Rama Rao, N.V., Characteristics of a counter-current reciprocating plate column. II. Axial mixing and mass transfer, *The Canadian Journal of Chemical Engineering*, Vol.66, No.2, pp.222-231, 1988.

8. Baird, M.H.I. and RamaRao, N.V., Axial mixing in a 15 cm reciprocating plate bubble column, *The Canadian Journal of Chemical Engineering*, Vol.76, pp.370-377, 1998.

9. Bajpai, R.K., Ramkrishna, D. and Prokop, A., A coalescence redispersion model for drop-size distributions in an agitated vessel, *Chemical Engineering Science*, Vol. 31, pp.913-920, 1976.

10. Bischoff, K.B., Axial dispersion with time variable, *Chemical Engineering Science*, Vol. 19, pp. 989-990, 1964.

11. Boyadzhiev, L. and Spassov, M., On the size of drops in pulsed and vibrating plate extraction columns, *Chemical Engineering Science*, Vol. 37, No. 2, pp. 337-340, 1982.

12. Brown, D.E. and Pitt, K., Drop break-up in a stirred liquid-liquid contactor, *Institution of Chemical Engineering Symposium Series*, pp. 83-97, Chemeca '70.

13. Brown, D.E. and Pitt, K., Drop size distribution of non-coalescing liquid-liquid system, *Chemical Engineering Science*, Vol.27, pp. 577-583, 1972.

14. Brunold, C.R., Hunns, J.C.B., Mackley, M.R. and Thompson, J.W., Experimental observations of flow patterns and energy losses for oscillatory flow in ducts containing sharp edges, *Chemical Engineering Science,* Vol. 44, pp. 1227-1244, 1989.

15. Calabrese, R.V., Chang, T.P.K. and Dang, P.T., Drop break-up in turbulent stirred-tank contactors. Part I. Effect of dispersed-phase viscosity, *AIChE Journal*, Vol.32, No.4, pp.657-666, 1986.

16. Calabrese, R.V., Wang, C.Y. and Bryner, N.P., Drop break-up in turbulent stirred-tank contactors. Part III. Correlations for mean size and drop size distribution, *AIChE Journal*, Vol.32, No.4, pp.677-681, 1986.

17. Calderbank, P.H., Physical rate processes in industrial fermentation, Part 1: The interfacial area in gas-liquid contacting with mechanical agitation, *Transaction of Institution of Chemical Engineers*, Vol. 36, pp. 443-459, 1958.

18. Church, J.M. and Shinnar, R., Stabilising liquid-liquid dispersions by agitation, *Industrial Engineering and Chemistry*, Vol. 53, No. 6, pp. 479-484, 1961.

19. Coulaloglou, C.A. and Talvarides, L.L., Drop size distributions and coalescence frequencies of liquid-liquid dispersion in flow vessels, *AIChE Journal*, Vol. 22, pp.289-297, 1976.

20. Coulaloglou, C.A. and Talvarides, L.L., Description of interaction processes in agitated liquid-liquid dispersions, *Chemical Engineering Science*, Vol. 32, pp.1289-1297, 1977.

21. Danckwerts, P.V., Continuous flow systems, *Chemical Engineering Science*, Vol. 2, pp. 1-13, 1953.

22. Dickens, A.W., Mackley, M.R. and Williams, H.R., Experimental residence time distribution measurements for unsteady flow in baffled tubes, *Chemical Engineering Science*, Vol.44, No.7, pp.1471-1479, 1989.

23. Field, R.W., Wang. Y., Howell, J.A. and Mackley, M.R., Oscillatory flow within porous tubes containing wall or central baffles, *Chemical Engineering Research and Design*, Part A, Vol.72, No.5, pp.686-694, 1994.

24. Finnigan, S.M. and Howell, J.M., The effect of pulsatile flow on ultrafiltration fluxes in a baffled tubular membrane system, *Chemical Engineering Research and Design*, Vol. 67, pp. 278-282, 1989.

25. Giles, J.W., Hanson, C. and Marsland, J.G., Drop size distributions in agitated liquid-liquid systems with simultaneous interface mass transfer and chemical reaction, *Proceedings of the International Solvent Extraction Conference*, Hague, pp. 89-111, 1971.

26. Godfrey, J.C., Houlton, D.A., Marley, S.T., Marrocchelli, A. and Slater, M.J., Continuous phase axial mixing in pulsed sieve-plate liquid-liquid extraction columns, *Chemical Engineering Research and Design*, Vol.66, No.5, pp.445-457, 1988.

27. Godfrey, J.C. and Slater, M.J., Liquid-Liquid Extraction Equipment, John Wiley & Sons, Ltd., First edition, 1994.

28. Goebel, J.C., Booij, K. and Fortuin, J.M.H., Axial dispersion in single phase flow in pulsed packed columns, *Chemical Engineering Science,* Vol.41, No.12, pp. 3197-3203, 1986.

29. Goldmann, G. and Blass, E., Applications and experiences with measurement of particle size distribution by photoelectrical suction method in dispersed two-phase systems, CHISA, 14, 1984.

30. Gough, P., Ni, X. and Symes, K.C., Experimental flow visualisation in a modified pulsed baffled reactor, *Journal of Chemical Technology and Biotechnology*, Vol. 69, pp. 321-328, 1997.

31. Hafez, M.M., Baird, M.H.I. and Nirdosh, I., Flooding and axial dispersion in reciprocating plate extraction columns, *The Canadian Journal of Chemical Engineering*, Vol.57, No.2, pp.150-158, 1979.

32. Hayslett, M.S., *Statistics Made Simple*, W.H.Allen Publishing House, Second Edition, 1972.

33. Hewgill, M.R., Mackley, M.R., Pandit, A.B. and Pannu, S.S., Enhancement of gas-liquid mass transfer using oscillatory flow in a baffled tube, *Chemical Engineering Science*, Vol.48, No.4, pp.799-809, 1993.

34. Hounslow, M.J., Ryall, R.L. and Marshall, V.R., A discretised population balance for nucleation, growth and aggregation, *AIChE Journal*, Vol. 34, No.11, pp. 1821-1832, 1988.

35. Howell, J.A., Field, R.W. and Wu, D., Yeast cell microfiltration: flux enhancement in baffled and pulsatile flow systems, *Journal of Membrane Science*, Vol. (80), pp. 59-71, 1993.

36. Howes, T., On the dispersion of unsteady flow in baffled tube, Ph.D. Thesis, University of Cambridge, 1988.

37. Howes, T. and Mackley, M.R., Experimental axial dispersion for oscillatory flow through a baffled tube, *Chemical Engineering Science*, Vol.45, No.5, pp.1349-1358, 1990.

38. Howes, T., Mackley, M.R. and Roberts, E.P.L., The simulation of chaotic mixing and dispersion for periodic flows in baffled channels, *Chemical Engineering Science*, Vol.46, No.7, pp.1669-1677, 1991.

39. Ingham, J., Slater, M.J. and Retamales, J., Single phase axial mixing studies in pulsed sieve- plate liquid-liquid extraction columns, *Chemical Engineering Research and Design* Part A, Vol.73, No.A5, pp.492-496, 1995.

40. Jares, J. and Prochazka, J., Break-up of droplets in Karr reciprocating-plate extraction column, *Chemical Engineering Science*, Vol.42, No.2, pp.283-292, 1987.

41. Jealous, A.E. and Johnson, H.F., Power requirements for pulse generation in pulsed columns, *Industrial Engineering and Chemistry*, Vol. 47, pp.1159-1166, 1955.

42. Kagan, S.Z., Aerov, M.E., Lonik, V. and Volkova, T.S., Some hydrodynamic and mass-transfer problems in pulsed sieve-plate extractors, *International Chemical Engineering*, Vol. 5, pp. 656-661, 1965.

43. Kagan, S.Z., Veisbein, B.A., Trukhanov, V.G. and Muzychenko, L.A., Longitudinal mixing and its effect on mass transfer in pulsed screen extractors, *International Chemical Engineering*, Vol. 13, pp. 217-222, 1973.

44. Karr, A.E., Performance of a reciprocating plate extraction column, *AIChE Journal*, Vol. 5, No.4, pp. 446-452, 1959.

45. Karr, A.E. and Lo, T.C., Performance and scale-up of a reciprocating plate extraction column, *Proceeding of International Solvent Extraction conference* '71, The Hague, pp. 299-322.

46. Karr, A.E. and Lo, T.C., Scale-up of large diameter reciprocating plate extraction columns, *Chemical Engineering Progress*, Vol. 72, No. 11, pp. 68-70, 1976.

47. Karr, A.E., Gebert, W. and Wang, M., Extraction of whole fermentation broth with Karr reciprocating plate extraction column, *The Canadian Journal of Chemical Engineering*, Vol.58, pp.249-252, 1980.

48. Karr, A.E., Ramanujam, S., Lo, T.C. and Baird, M.H.I., Axial mixing and scale-up of reciprocating plate columns, *The Canadian Journal of Chemical Engineering*, Vol.65, No.3, pp.373-381, 1987.

49. Khemangkorn, V., Muratet, G. and Angelino, H., Study of dispersion in a pulsed perforated-plate column, *Proceedings of the International Solvent Extraction Conference*, pp. 429-435, 1977.

50. Kim, S.D. and Baird, M.H.I., Axial dispersion in a reciprocating plate extraction column, *The Canadian Journal of Chemical Engineering*, Vol. 54, pp.81-89, 1976a.

51. Kim, S.D. and Baird, M.H.I., Effect of hole size on hydrodynamics of a reciprocating perforated plate extraction column, *The Canadian Journal of Chemical Engineering*, Vol.54, pp.235-237, 1976b.

52. Kumar, A. and Hartland, S., Prediction of drop size in pulsed perforated-plate extraction columns, *Chemical Engineering Communication*, Vol. 44, pp. 163-182, 1986.

53. Laso, M., Steiner, L. and Hartland, S., Dynamic simulation of liquid-liquid agitated dispersions. I. Derivation of a simplified model, *Chemical Engineering Science*, Vol.42, No.10, pp.2429-2436, 1987.

54. Levenspiel, O. and Smith, W.K., Notes on the diffusion-type model for the longitudinal mixing of fluids in flow, *Chemical Engineering Science*, Vol. 6, pp. 227-233, 1957.

55. Levenspiel, O., *Chemical Reaction Engineering*, John Wiley & Sons, Ltd., Third Edition, 1999.

56. Litster, J.D., Smit, D.J. and Hounslow, M.J., Adjustable discretised population balance for growth and aggregation, *AIChE Journal*, Vol. 41, No. 3, pp.591-603, 1995.

57. Lo, T.C., Baird, M.H.I. and Hanson, C., Handbook of solvent extraction, John Wiley & Sons, Ltd., 1983.

58. Lo, T.C., Baird, M.H.I. and Rama Rao, N.V., The reciprocating plate column-Development and Applications, *Chemical Engineering Communications*, Vol. 116, pp. 67-88, 1991.

59. Long, J.T., Engineering for Nuclear Fuel Processing, Gordon and Breech, London, 1967.

60. Mackay, M.E., Mackley, M.R. and Wang, Y., Oscillatory flow within tubes containing wall or central baffles, *Chemical Engineering Research & Design*, Vol.69, No.A6, pp.506-513, 1991.

61. Mackley, M.R., Using oscillatory flow to improve performance, *The Chemical Engineer*, No. 433, pp. 18-20, 1987.

62. Mackley, M.R., Tweddle, G.M. and Wyatt, I.D., Experimental heat transfer measurements for pulsatile flow in baffled tubes, *Chemical Engineering Science*, Vol.45, No.5, pp.1237-1242, 1990.

63. Mackley, M.R. and Ni, X., Mixing and dispersion in a baffled tube for steady laminar and pulsatile flow, *Chemical Engineering Science*, Vol.46, No.12, pp.3139-3151, 1991.

64. Mackley, M.R. and Ni, X., Experimental fluid dispersion measurements in periodic baffled tube arrays, *Chemical Engineering Science*, Vol.48, No.18, pp.3293-3305, 1993.

65. Mackley, M.R., Smith, K.B. and Wise, N.P., The mixing and separation of particle suspensions using oscillatory flow in baffled tubes, *Chemical Engineering Research & Design*, Vol. 71, No.A6, pp.649-656, 1993.

66. Mackley, M.R. and Stonestreet, P., Heat transfer and associated energy dissipation for oscillatory flow in baffled tubes, *Chemical Engineering Science*, Vol.50, No.14, pp.2211-2224, 1995.

67. Mackley, M.R., Stonestreet, P., Roberts, E.P.L. and Ni, X., Residence time distribution enhancement in reactors using oscillatory flow, *Chemical Engineering Research and Design*, Part A, Vol.74, No.A5, pp.541-545, 1996.

68. McCoy, B.J. and Madden, A.J., Drop size in stirred liquid-liquid systems via encapsulation, *Chemical Engineering Science*, Vol. 24, pp. 419-421, 1969.

69. Mecklenburgh, J.C. and Hartland, S., The Theory of Backmixing, John Wiley & Sons, Ltd., London, First edition, 1975.

70. Miyanami, K., Tojo, K., and Yano, T., Liquid-phase mixing in a multistage vibrating-disk column with concurrent gas-liquid flow, *Journal of Chemical Engineering of Japan*, Vol. 6, No. 6, pp. 518-522, 1973.

71. Miyanami, K.K., Tojo, T.Y., Miyaji, K. and Minami, I., Drop size distributions and holdups in a multistage vibrating disk column, *Chemical Engineering Science*, Vol. 30, pp. 1415-1420, 1975.

72. Miyanami, K., Tojo, K., Minami, I. and Yano, T., Gas-liquid mass transfer in a vibrating disk column, *Chemical Engineering Science*, Vol. 33, pp. 601-608, 1978.

73. Miyauchi, T. and Vermeulen, T., Longitudinal flow dispersion in two-phase continuous flow operations, *Industrial Engineering and Chemistry Fundamentals*, Vol. 2, pp. 113-126, 1963.

74. Miyauchi, T. and Oya, H., Longitudinal dispersion in pulsed perforated-plate columns, *AIChE Journal*, Vol. 11, No.3, pp. 395-402, 1965.

75. Mlynek, Y. and Resnick, W., Drop sizes in agitated liquid-liquid systems, *AIChE Journal*, Vol. 18, pp. 122-127, 1972.

76. Nabli, M.A., Guiraud, P. and Gourdon, C., Numerical experimentation: a tool to calculate the axial dispersion coefficient in discs and doughnuts pulsed solvent extraction columns, *Chemical Engineering Science*, Vol.52, No.14, pp. 2353-2368, 1997.

77. Nanda, A.K. and Sharma, M.M., Effective interfacial area in liquid-liquid extraction, *Chemical Engineering Science*, Vol. 21, pp. 707-714, 1966.

78. Narsimhan, G., Ramkrishna, D. and Gupta, J.P., Breakage functions for droplets in agitated in liquid-liquid dispersion, *AIChE Journal*, Vol.30, pp.457-467, 1984.

79. Nelson, G., Scale –up study of suspension polymerisation in an oscillatory baffled reactor, Ph..D. Thesis, Heriot-Watt University, 2001.

80. Nemecek, M. and Prochazka, J., Longitudinal mixing in a vibrating-sieve-plate column two phase flow, *The Canadian Journal of Chemical Engineering*, Vol. 52, pp. 739-749, 1974.

81. Ni, X. and Mackley, M.R., Chemical reaction in batch pulsatile flow and stirred tank reactors, *Chemical Engineering Journal*, Vol. 52, pp. 107-114, 1993.

82. Ni, X., Gao, S. and Pritchard, D.W., A study of mass transfer in yeast in a pulsed baffle bioreactor, *Biotechnology and Bioengineering*, Vol.45, No.2, pp.165-175, 1995a.

83. Ni, X., Gao, S., Cumming, R.H. and Pritchard, D.W., A comparative study of mass transfer in yeast for a batch pulsed baffled bioreactor and a stirred-tank fermenter, *Chemical Engineering Science*, Vol.50, No.13, pp.2127-2136, 1995b.

84. Ni, X. and Gao, S., Mass transfer characteristics of a pilot pulsed baffled reactor, *Journal of Chemical Technology and Biotechnology*, Vol.65, No.1, pp.65-71, 1996a.

85. Ni, X. and Gao, S., Scale-up correlations for mass transfer coefficients in pulsed baffled reactors, *Chemical and Biochemical Engineering Journal*, Vol.63, No.3, pp.157-166, 1996b.

86. Ni, X., Bennett, D.C., Brogan, G., Struthers, A. and Wilson, S.F., A systematic study of the effect of geometrical parameters on mixing time in oscillatory baffled columns, *Chemical Engineering Research and Design*, Vol. 76, No. 5, pp. 635-642, 1998a.

87. Ni, X., Zhang, Y. and Mustafa, I., An investigation of droplet size and size distribution in methyl methacrylate suspensions in a batch oscillatory-baffled reactor, *Chemical Engineering Science*, Vol.53, No.16, pp.2903-2919, 1998.

88. Ni X., Zhang, Y. and Mustafa, I., Correlation of polymer particle size with droplet size in suspension polymerization of methyl methacrylate in a batch oscillatory-baffled reactor, *Chemical Engineering Science*, Vol.54, No.5, pp.841-850, 1999.

89. Ni, X., Johnstone, J.C., Symes, K.C., Grey, B.D. and Bennett, D.C., Suspension polymerisation of Acrylamide in an oscillatory baffled reactor: from drops to particles, *AIChE Journal*, Vol. 47, No. 8, pp. 1746-1757, 2001.

90. Ni, X., De Gelicourt, Y.S., Baird, M.H.I. and Rama Rao, N.V., Scale-up of single phase axial dispersion coefficients in batch and continuous oscillatory baffled tubes, *The Canadian Journal of Chemical Engineering*, Vol. 79, pp. 444-448, 2001a.

91. Ni, X., De Gelicourt, Y.S., Neil, J. and Howes, T., On the effect of tracer density on axial dispersion in a batch oscillatory baffled column, *Chemical Engineering Journal*, 2001b (accepted for publication).

92. Pietzsch, W. and Blass, E., A new method for the prediction of pulsed sieve-tray extractors, *Chemical Engineering & Technology*, Vol. 10, pp. 73-86, 1987.

93. Prabhakar, A., Srinidetan, G. and Varma, Y.B., Dispersed phase hold - up and drop size distribution in pulsed plate columns, *The Canadian Journal of Chemical Engineering*, Vol.66, No.2, pp.232-240, 1988.

94. Ramkrishna, D., The status of population balances, *Reviews in Chemical Engineering*, Vol. 3, pp. 49-95, 1985.

95. RamaRao, N.V., Srinivas, N.S. and Varma, Y.B.G., Dispersed phase hold-up and drop size distributions in reciprocating plate columns, *The Canadian Journal of Chemical Engineering*, Vol.61, No.2, pp.168-177, 1983.

96. RamaRao, N.V and Baird, M.H.I., Axial mixing and gas holdup with reciprocating doughnut plates, *The Canadian Journal of Chemical Engineering*, Vol.78, No.2, pp.261-264, 2000.

97. Reschke, M. and Schugerl, K., Continuous reactive extraction of Penicillin G in a Karr column, *Chemical Engineering Journal*, Vol. 31, pp. B19-B26, 1985.

98. Saye, B., On the interactions of droplets in oscillatory baffled columns, M.Phil. Thesis, Heriot-Watt University, 2001.

99. Sege, G. and Woodfield, F.W., Pulse column variables, *Chemical Engineering Progress*, Vol. 50, No. 8, pp. 396-402, 1954.

100. Sharma, R.N. and Baird, M.H.I., Solvent extraction of copper in a reciprocating plate column, *The Canadian Journal of Chemical Engineering*, Vol. 56, pp. 310-315, 1978.

101. Shinnar, R., On the behaviour of liquid dispersions in mixing vessels, *Fluid Mechanics*, 10, pp.259-275, 1960.

102. Smith, K., Scale-up of oscillatory baffled reactor, Ph.D. Thesis, University of Cambridge, 2000.

103. Sreenivasulu, K., Venkatanarasaiah, D. and Varma, Y.B.G., Drop size distributions in liquid pulsed columns, *Bioprocess Engineering*, Vol.17, No.3, pp.189- 195, 1997.

104. Stevens, G.W. and Baird, M.H.I., A model for axial mixing in reciprocating plate columns, *Chemical Engineering Science*, Vol.45, No.2, pp.457-465, 1990.

105. Stonestreet, P. and Baird, M.H.I., Energy dissipation in oscillatory flow within a baffled tube, *Chemical Engineering Research and Design*, Part A, Vol.73, No.A5, pp.503-511, 1995.

106. Tanaka, M., Local drop diameter variation in a stirred tank, *The Canadian Journal of Chemical Engineering*, Vol. 63, pp. 723-728, 1985.

107. Thibault, J. and Lounes, M., Axial dispersion in a reciprocating plate column, *The Canadian Journal of Chemical Engineering*, Vol.74, No.2, pp.187-194, 1996.

108. Tobin, T., Muralidhar, R., Wright, H. and Ramkrishna, D., Determination of coalescence in liquid-liquid dispersions: effect of drop size dependence, *Chemical Engineering Science,* Vol. 45, pp. 3491-3504, 1990.

109. Tojo, K., Miyanami, K. and Yano, T., Liquid-liquid extraction in a multistage vibrating disk column, *Journal of Chemical Engineering of Japan*, Vol. 8, No. 2, pp. 122-126, 1975a.

110. Tojo, K., Miyanami, K. and Yano, T., The effect of wave form of disk vibration on mass transfer in a MVDC with countercurrent liquid-liquid flow, *Journal of Chemical Engineering of Japan*, Vol. 8, No. 2, pp. 165-167, 1975b.

111. Tojo, K., Miyanami, K., Minami, I. and Yano, T., Power dissipation in a vibrating disk column, *Chemical Engineering Journal*, Vol. 17, pp. 211-218, 1979.

112. Tojo, K., Miyanami, K. and Yano, T., Design methods and performance characteristics of a MVDC extractor, *Industrial Engineering Chemistry Process Design and Development*, Vol. 19, pp. 459-465, 1980.

113. Tsouris, C. and Tavlarides, L.L., Breakage and coalescence models for drops in turbulent dispersions, *AIChE Journal*, Vol. 40, No. 3, pp. 395-406, 1994.

114. Valentas, K.J. and Amundson, N.R., Breakage and coalescence in dispersed phase systems, *Industrial Engineering and Chemistry Fundamentals*, Vol. 5, No. 2, 533-542 1966.

115. Van Dijick, W.J., US Patent 201186, 1935.

116. Van Heuven, J.W. and Beek, W.J., Power input, drop size and minimum stirrer speed for liquid-liquid dispersions in stirred vessels, *Proceedings of the International Solvent Extraction Conference*, Hague, pp. 70 -81, 1971.

117. Veljkovic, V. and Skala, D., Mass transfer characteristics in a gas-liquid reciprocating plate column – II, Interfacial area, *The Canadian Journal of Chemical Engineering*, Vol. 66, pp. 200 – 210, 1988.

118. Verhoff, F.H., Ross, S.L. and Curl, R.L., Breakage and coalescence in an agitated dispersion, experimental system and data reduction, *Industrial Engineering Chemistry and Fundamentals*, Vol. 16, No.3, pp. 371-376, 1977.

119. Vohradsky, J. and Sovova, H., Measurement of local velocities of drops in a liquid-liquid extraction vibrating plate column, *Chemical Engineering Science*, Vol. 45, No. 12, pp. 3563-3570, 1990.

120. Wang, C.Y. and Calabrese, R.V., Drop break-up in turbulent stirred-tank contactors. Part II. Relative influence of viscosity and interfacial tension, *AIChE Journal*, Vol.32, No.4, pp.667-676, 1986.

121. Weinstein, B. and Treybal, R.E., Liquid-liquid contacting in unbaffled agitated vessels, *AIChE Journal*, Vol. 19, pp. 304-312, 1973.

122. Wen, C.Y. and Fan, L.T., Models for Flow Systems and Chemical Reactors, Marcel Dekker, Inc., New York, 1975.

123. Wright, H. and Ramakrishna, D., Factors affecting coalescence frequency of droplets in a stirred liquid-liquid dispersion, *AIChE Journal*, Vol. 40, pp. 767-776, 1994.

124. Yang, N.S., Chen, B.H. and McMillan, A.F., Axial mixing and mass transfer in gas-liquid Karr columns, *Industrial Engineering Chemistry Process Design and Development*, Vol. 25, pp. 776-780, 1986.

125. Zerfa, M. and Brooks, B.W., Prediction of vinyl chloride drop sizes in stabilized liquid-liquid agitated dispersion, *Chemical Engineering Science*, Vol.51, No.12, pp.3223-3233, 1996.

126. Zhang, Y., A study of suspension polymerisation of methylmethacylate and styrene in an oscillatory baffled reactor, Ph.D. thesis, University of Strathclyde, 1998.

127. Zhang, Y., Ni, X. and Mustafa, I., A study of oil-water dispersion in a pulsed baffled reactor, *Journal of Chemical Technology and Biotechnology*, Vol.66, No.3, pp.305-311, 1996.